Doctoral Dissertation
Doctoral Program in Chemical Engineering (38th Cycle)

Sustainable High Capacity Lithium-Ion Battery Anodes: An Integrated Approach to Materials, Electrode Manufacturing and Environmental Impact

Elisa Ravesio
* * * * * *

Supervisors
Prof. Silvia Bodoardo, Supervisor
Dott. Daniele Versaci, Co-Supervisor
Dott. Valentina Sumini, Co-Supervisor

Doctoral Examination Committee:
Prof. Carlotta Francia, Politecnico di Torino
Dott. Mihaela-Ramona Buga, ICSI
Emanuel Lourenço, INEGI
Prof. Eliana Quartarone, Università di Pavia
Dott. Laida Otaegui, CIC energiGUNE

Politecnico di Torino
July, 2026

This thesis is licensed under a Creative Commons License, Attribution - Noncommercial - NoDerivative Works 4.0 International: see www.creativecommons.org. The text may be reproduced for non-commercial purposes, provided that credit is given to the original author.

This doctoral thesis was written at the end of the doctoral program funded by the project PNRR-NGEU which has received funding from the MUR – DM 352/2022.

I hereby declare that, the contents and organisation of this dissertation constitute my own original work and does not compromise in any way the rights of third parties, including those relating to the security of personal data.

Elisa Ravesio

……Elisa Ravesio……

Elisa Ravesio
Turin, April 14, 2026

Abstract

This doctoral research investigates the development of sustainable lithium-ion battery (LIB) anodes by integrating electrochemical performance, electrode manufacturing processes, and environmental impact assessment, driven by the need for high-energy-density storage technologies with reduced environmental impact of battery production.

The study explores the transition from conventional graphite to silicon-based anodes, including silicon-composite (~10% Si) and silicon-dominant (~80% Si) systems. Although silicon offers a significantly higher theoretical capacity, its implementation is limited by large volume changes during cycling, causing mechanical degradation, loss of electrode cohesion, and unstable electrochemical performance. To address these challenges, electrode formulation was optimized using aqueous binder systems and natural polysaccharides.

Slurry mixing, coating, and drying were systematically optimized at laboratory scale by evaluating different binders and processing conditions, while pilot-line activities were carried out at a preliminary level to assess process transferability. Graphite electrodes exhibited stable slurry properties and uniform coatings at both laboratory and pilot scale, confirming the robustness of conventional CMC/SBR systems. The introduction of silicon (10 wt% Si) increased sensitivity to formulation parameters, leading to slurry instability and coating inhomogeneity, further amplified at pilot scale. These effects became critical for silicon-dominant electrodes (80 wt% Si), where insufficient cohesion and poor adhesion to the current collector strongly affected electrode integrity and processability at pilot scale. Increasing silicon content therefore shifts the main challenges from electrochemical performance to processability and manufacturing stability.

Binder chemistry was identified as a key factor: while CMC/SBR systems showed limitations for silicon-based electrodes, PAA-based formulations improved active material dispersion, particle cohesion and adhesion at the current collector interface, and electrochemical performance, particularly for silicon-dominant systems. Natural polysaccharides, introduced at 1 wt% in the formulation, further influenced slurry rheology and coating quality. In addition, laser texturing of the copper current collector, particularly DLIP (Direct Laser Interference Patterning)-treated surfaces, enhanced electrode performance, highlighting the role of electrode–current collector interface.

A cradle-to-gate Life Cycle Assessment (LCA) based on primary experimental data showed that environmental impacts depend not only on material composition but also on process-related factors, especially energy-intensive steps such as drying. Per unit of capacity (1 Ah), silicon-based anodes reduced carbon footprint (kg CO_2-Eq) compared to graphite by ~40% for silicon-composite and up to ~97% for silicon-dominant systems. These benefits, however, depend on the selected functional unit and system boundaries. A sensitivity analysis comparing a global supply chain scenario, representative of current industrial conditions, with a European-based scenario highlighted the influence of electricity mix and transportation. A preliminary extension to the full-cell level evaluated the translation of these improvements at system level.

Overall, the work shows that advanced LIB anodes require an integrated approach in which material selection, manufacturing processes, and environmental sustainability are addressed simultaneously, with silicon-based materials playing a key role in enabling next-generation high-energy-density systems. The results of this study provide a basis for the future development of design-support tools in which material selection, electrode formulation, and process parameters are directly linked to both electrochemical performance and environmental impact.

Acknowledgment

I would like to open this Acknowledgements section in a slightly unconventional way, by expressing my gratitude to myself. Throughout these years, I never gave up and continuously strived to become a better version of myself.

This journey across Europe, from Italy to Spain and including Romania, would not have been possible without the support of many people. First and foremost, I would like to sincerely thank my supervisor, Prof. Silvia Bodoardo, for giving me the opportunity to undertake experiences I could not have even imagined. I am also deeply grateful to my co-supervisors, Ph.D. Daniele Versaci and Ph.D. Valentina Sumini, who guided me through two very different but equally enriching environments: the electrochemistry laboratories at Politecnico di Torino and the industrial context of Coesia. I would also like to thank Ph.D. Laida Otaegui and Ph.D. David Giraldo for their support during my research period at CIC energiGUNE. All the personal and professional growth I have experienced during these years would not have been possible without the many people I met along the way. Rather than risking to forget someone, I prefer to collectively thank everyone who contributed, directly or indirectly, to this journey.

A special mention goes to the staff of Equin'ozio, Giulia, Ciano, Silvia, the horses, and all the people who make that place my safe haven and a source of balance when things become challenging.

Finally, last but not least, I would like to thank my family. Despite difficulties, it has always remained close and supportive. In particular, I am deeply grateful to my mother, who has always been a constant and essential presence. And to my father, who is no longer here, but whose support I am sure has never truly left me.

Nothing is more frightening than the possibility that man may become what he is capable of becoming

Søren Kierkegaard

Table of Contents

List of Tables XII
List of Figures XIX
1. Introduction 1
1.1. Worldwide energy transition challenge 1
1.2. environmental sustainability and supply chain challenges 4
1.3. Goal of the dissertation 7
1.4. Summary of dissertation 8
1.5. Original Scientific Contributions of the Thesis 9
2. Li-ion Batteries (LIBs) 11
2.1. General overview of batteries 11
2.2. Fundamental parameters and terminology 13
2.3. Working mechanism of LIB 16
2.4. Components inside a LIB 21
2.4.1. Electrodes 23
2.4.1.1. Cathode materials 23
2.4.1.2. Anode Materials 28
2.4.1.3. Binders and Solvents 39
2.4.1.4. Current collectors 48
2.4.2. Electrolyte and Separators 49
2.4.2.1. Liquid Electrolyte (LE) 49
2.4.2.2. Gel polymer electrolyte (GPE) 51
2.4.2.3. Solid polymer electrolyte (SPE) 52
2.4.2.4. Ionic liquid (IL) 52
3. Battery Manufacturing 54
3.1. The TRL level 54
3.2. Overview about battery production 56
3.2.1. Electrode production 57
3.2.1.1. Mixing 58
3.2.1.2. Coating 60
3.2.1.3. Drying 62
3.2.1.4. Calendering 65
3.2.1.5. Slitting 67
3.2.2. Cells, modules and final battery pack assembly 67
3.2.3. Quality Control 67
3.3. Rheology 69
3.3.1. Formulas and definitions 70
3.3.2. Parameters 73
3.3.3. The rheometer and its working principle 75
3.3.4. Applications of rheology in the battery field 77
3.3.4.1. The most common geometries used for LIBs slurries 77
3.3.4.1.1. Rotational Tests 78
3.3.4.1.2. Dynamic Oscillatory Test 83
4. Life Cycle Assessment 87
4.1. The steps of a product life cycle and the related models 88
4.2. Key methodological parameter 91

4.3. The four phases of the LCA 92
4.4. Allocation rules 94
4.5. ReCiPe 2016: Midpoint impact categories and indicators 95
4.6. ReCiPe 2016: Endpoint Impact categories 101
4.7. Methodological approach of the EF 3.1 Method 102
4.8. Data quality, uncertainties quantification and sensitivity analysis 104
4.9. Criticism and limits of LCA 106
5. Experimental Section 109
5.1. Graphite Anodes 110
5.1.1. Small-Scale Production: Laboratory Level 111
5.1.1.1. Electrode Production 111
5.1.1.2. Electrochemical Characterization 113
5.1.1.2.1. Electrochemical Impedance Spectroscopy 113
5.1.1.2.2. Galvanostatic cycling - Baseline result: long cycling 116
5.1.1.2.3. Galvanostatic cycling - Baseline result: rate capability 121
5.1.1.2.4. Galvanostatic cycling - Optimizing the forming 125
5.1.1.2.5. The importance of the constant voltage step for anode half-cell characterization in galvanostatic cycling 127
5.1.2. Scale up process: Pilot-line Level 132
5.1.2.1. Slurry and Production Process Optimization 133
5.1.2.1.1. First trial 133
5.1.2.1.2. Second trial 138
5.1.2.1.3. Third trial 139
5.1.2.1.4. Fourth trial 140
5.1.2.1.5. Fifth trial 141
5.1.2.1.6. Sixth trial 141
5.1.3. Comparison between the two production processes: morphological characterization 145
5.1.4. Conclusion and final remarks 148
5.2. Manufacturing optimization of SC anodes from laboratory to pilot-line scale 149
5.2.1. Laboratory-scale investigation 150
5.2.1.1. Influence of binder chemistry on slurry processability 152
5.2.1.2. Electrochemical characterization of laboratory-processed electrodes 153
5.2.1.2.1. Reference CMC-based binders 155
5.2.1.2.1.1. Laminate no. 1 (92%, CMC) 156
5.2.1.2.1.2. Laminate no. 2 (92%, CMC_2) 161
5.2.1.2.1.3. Laminate no. 3 (95%, CMC) 162
5.2.1.2.2. PAA as single binder 165
5.2.1.2.2.1. Laminate no. 4 (95%, PAA250) 166
5.2.1.2.2.2. Laminate no. 5 (95%, PAA450) 166
5.2.1.2.3. LiPAA as single binder: effect of pre-lithiation 167
5.2.1.2.3.1. Laminate no. 6 (92%, LiPAA250) 168
5.2.1.2.3.2. Laminate no. 7 (95%, LiPAA250) 171
5.2.1.2.3.3. Laminate no. 8 (95%, LiPAA450) 174
5.2.1.2.4. LiPAA-based formulations with natural polysaccharide additives 176
5.2.1.2.4.1. Laminate no. 9 (92%, LiPAA250_TG) 177
5.2.1.2.4.2. Laminate no. 10 (92 wt.%, LiPAA250_CGN) 180
5.2.1.3. Processing-performance correlation at laboratory scale 183
5.2.2. Pilot-line manufacturing study 185
5.2.2.1. Electrode preparation and electrochemical validation at pilot scale of the reference CMC-based slurry 185
5.2.2.2. Li-PAA450-based slurry 190
5.2.3. Comparison of manufacturing behaviour at laboratory and pilot-line scale 191

5.2.4. Key outcomes and implications for silicon-anode manufacturability 193
5.3. Development of silicon anodes within the GIGAGREEN project: electrode production optimization process and laser-treated current collectors 194
5.3.1. Process optimization at laboratory scale 196
5.3.1.1. Trial no. 1 198
5.3.1.2. Trial no. 2 200
5.3.1.3. Trial no. 3 201
5.3.1.4. Trial no. 4 202
5.3.1.5. Trial no. 5 203
5.3.1.6. Trial no. 6 205
5.3.2. Electrochemical validation of optimized electrodes 205
5.3.3. Laser texturing of copper current collector 210
5.3.3.1. Impact of surface texturing on electrode fabrication and mass loading 211
5.3.3.2. Comparative electrochemical behaviour as a function of surface morphology 212
5.3.3.2.1. Pristine current collector (CuP) 213
5.3.3.2.2. LIPSS treatment (Cu1L) 215
5.3.3.2.3. LIPSS + micro-grooves treatment (Cu2L) 217
5.3.3.2.4. DLIP treatment (Cu3L) 220
5.3.3.3. Relationship between surface topology, interfacial resistance and electrochemical performance 222
5.3.4. Process implications and perspectives for scale-up 226
5.4. Nanoporous Silicon for the production of Si-dominant anodes 226
5.4.1. Small scale production: Laboratory Level 228
5.4.1.1. Electrode production 228
5.4.1.2. Electrochemical Characterization 231
5.4.1.3. PAA-based 232
5.4.1.3.1. First trial: PAA_1 233
5.4.1.3.2. Second trial: PAA_2 238
5.4.1.3.3. Third trial: PAA_3 240
5.4.1.4. PAA and additives 244
5.4.1.4.1. Addition of SBR: PAA_SBR 244
5.4.1.4.2. Addition of Sodium Alginate: PAA_Alg 247
5.4.1.4.3. Addition of Tragacanth Gum: PAA_TG 251
5.4.1.4.4. Addition of Pectin: PAA_Pec 254
5.4.1.5. Comparison between the additives 258
5.4.2. Scale up process: Pilot-Line Scale 261
5.4.2.1. Electrode production 262
5.4.3. Comparison between the production processes 263
5.4.4. Slurries optimization and further characterization at CIC energiGUNE Laboratories 264
5.4.4.1. Slurries optimization with a SF of 45 wt.% 266
5.4.4.2. Increase of the SF up to 60 wt.% 270
5.4.4.2.1. Single binder: PAA 272
5.4.4.2.2. PAA_Alg 278
5.4.4.2.3. PAA_Pec 282
5.4.4.2.4. PAA_CGN 287
5.4.4.2.5. PAA_TG 292
5.4.4.3. Comparison between the additives 296
5.4.5. Main Outcomes and Implications 304
5.5. Conclusion and final remarks 305
6. Life cycle assessment 307
6.1. Anode Production 309

6.1.1. Goal and scope definition 311
6.1.2. Definition of the functional units 312
6.1.3. System boundaries 312
6.1.4. LCI for the anodes preparation 313
6.1.4.1. Foreground system description 314
6.1.4.2. Material and energy inventory 314
6.1.5. Assumptions of the study 320
6.1.6. Limitations and outlook 323
6.1.7. LCIA methods 325
6.1.8. Sensitivity analysis 326
6.1.9. Data quality assessment and uncertainty analysis based on the Pedigree approach 328
6.1.10. LCIA: linking electrochemical performance and environmental impacts 329
6.1.10.1. Environmental impacts assessment of 1 Ah anode production in a global supply chain 330
6.1.10.2. Environmental impacts assessment of 1 kg anode production in a global supply chain 334
6.1.10.3. Material composition and the relative contribution of anode components to environmental impacts 337
6.1.10.4. Sensitivity analysis: how European supply chain impacts on the anodes production 340
6.1.10.5. Uncertainties evaluation through MCS 344
6.1.10.6. Evaluation of endpoint impact categories 352
6.2. Full cell production 355
6.2.1. Goal and scope definition 356
6.2.2. Definition of the functional units 356
6.2.3. System boundaries 357
6.2.4. LCI of the full cell assembly 358
6.2.4.1. Foreground system description 358
6.2.4.2. Material and energy inventory 358
6.2.5. Assumptions of the study 364
6.2.6. Limitations and outlook 365
6.2.7. LCIA methods 366
6.2.8. Data quality assessment and uncertainty analysis based on the Pedigree approach 366
6.2.9. LCIA: linking electrochemical performance and environmental impacts 367
6.2.9.1. Environmental impact assessment of 1 coin cell 368
6.2.9.2. Environmental impacts assessment of 1 kWh production in a global supply chain 370
6.2.9.3. Material composition and the relative contribution to environmental impacts 373
6.2.9.4. Uncertainties evaluation through MCS 376
6.2.9.5. Evaluation of endpoint impact categories 379
6.3. Methodological sensitivity: comparison between ReCiPe and EF Methods 381
6.3.1. Methodological Framework of EF vs ReCiPe 381
6.3.2. Comparison at anode production level 383
6.3.3. Comparison at full cell level 386
6.4. Main findings and implications 389
7. Conclusion and perspectives 391
References 393
Appendix A – List of Abbreviation 431
Appendix B – List of Publications 434
Appendix C – List of Oral/Poster Publications 436

List of Tables

Table 2.1 – Comparison of the properties of the commercialized rechargeable batteries, depending on their chemistry [15] 13
Table 2.2 – Percentage composition of the main components of cylindrical cells produced with different materials. LCO: Lithium Cobalt Oxide, NMC: Nickel Manganese Cobalt Oxide, LFP: Lithium Iron Phosphate [31] 22
Table 2.3 – Summary of the cited active materials and their specifications. Partially reproduced with permission from [61] 28
Table 2.4 – Summary of the most common anode material, divided into the lithium hosting mechanism and associated with their theoretical capacity, advantages and common issues [67] 29
Table 2.5 – Summary of the characteristics (lattice structure, cell volume and Si atomic volume) of the Li_xSi alloys formed during the lithiation process. Reproduced with permission from [91] 35
Table 2.6 – Common anode materials with their characteristic [112] 37
Table 2.7 – Summary of the binders used in my work with their advantages and main issues 47
Table 4.1 – Summary of the Impact Categories and relative Indicator proposed by the Impact Assessment method ReCiPe 2016 v1.03, midpoint (H) 96
Table 4.2 – Complete characterization framework of the EF 3.1 method, detailing the 16 midpoint impact categories and indicator metrics 103
Table 5.1 – Cycling protocol for the long cycling test for the baseline sample 116
Table 5.2 – Values of charge and discharge capacities, normalized by the electrode weight, and relative values of coulombic efficiency for some representative cycles for the baseline cycling protocol 117
Table 5.3 – Cycling protocol for rate capability test for the baseline sample 122
Table 5.4 – Values of charge and discharge capacities, normalized by electrode weight, and relative values of coulombic efficiency for some representative cycles for the baseline rate capability cycling protocol 123
Table 5.5 – Cycling protocol, with the improvement of the forming step 125
Table 5.6 – Values of charge and discharge capacities, normalized by electrode weight, and relative values of coulombic efficiency for some representative cycles for the improved forming test 126
Table 5.7 – Cycling protocol with the addition of the constant voltage step 128

Table 5.8 – Values of charge and discharge capacities, normalized by electrode weight, and relative values of coulombic efficiency for some representative cycles for the improved cycling protocol with the addition of the constant voltage step..... 130
Table 5.9 – Values of charge and discharge capacities and relative values of coulombic efficiency for some representative cycles for the electrode produced with the first trial at the pilot-line 137
Table 5.10 – Summary of the characteristics (dry thickness and ML) measured depending on the roll gap imposed for the coating. 142
Table 5.11 – Data for the electrode produce with the pilot-line 143
Table 5.12 – Summary of the electrodes prepared at the two different levels, with the imposed parameters (Solid Fraction and Wet Thickness) and relative parameters studied (Dry Thickness, ML and Areal Capacity)..... 145
Table 5.13 – Overview of the different laboratory trials performed on MTI SC anodes, reporting electrode composition and the corresponding sample code adopted throughout the manuscript. 150
Table 5.14 – Summary of the experimental trials carried out to optimize the slurry formulation and coating parameters of MTI SC anodes at laboratory scale. The table highlights the evolution of binder composition, SF and processing conditions, together with the main qualitative outcomes observed in terms of coating homogeneity and electrode manufacturability. 151
Table 5.15 – Summary of the laboratory-scale trials for MTI SC anodes, reporting binder composition, coating thickness and the resulting electrode properties. The areal capacity was calculated based on the material theoretical capacity *This one is the only sample produced with a SF of 47%..... 153
Table 5.16 – Cycling protocol applied along all the rate capability tests performed with silicon composite electrodes 154
Table 5.17 – Values of charge and discharge capacities, normalized by the electrode weight, and relative values of coulombic efficiency for some representative cycles for the electrodes produced with 92 wt.% of SC and using CMC and SBR as binders 159
Table 5.18 – Values of charge and discharge capacities, normalized by the electrode weight, and relative values of coulombic efficiency for some representative cycles for the electrodes produced with 95 wt.% of SC and using CMC and SBR as binders 163
Table 5.19 – Values of charge and discharge capacities, normalized by the electrode weight, and relative values of coulombic efficiency for some representative cycles for the electrodes produced with 92 wt.% of SC and using LiPAA250 as binder..... 169
Table 5.20 – Values of charge and discharge capacities, normalized by the electrode weight, and relative values of coulombic efficiency for some representative cycles for the electrodes produced with 95 wt.% of SC and using LiPAA250 as binder..... 172
Table 5.21 – Values of charge and discharge capacities, normalized by the electrode weight, and relative values of coulombic efficiency for some representative cycles for the electrodes produced with 95 wt.% of SC and using LiPAA450 as binder..... 175
Table 5.22 – Values of charge and discharge capacities, normalized by the electrode weight, and relative values of coulombic efficiency for some representative cycles for the electrodes produced with 92 wt.% of SC and using LiPAA250 and TG as binders 179

Table 5.23 – Values of charge and discharge capacities, normalized by the electrode weight, and relative values of coulombic efficiency for some representative cycles for the electrodes produced with 92 wt.% of SC and using LiPAA250 and CGN as binders 182
Table 5.24 – Summary of the electrode characteristics (dry thickness, ML, and areal capacity) as a function of the roll gap applied during the coating step for electrodes produced at pilot-line scale using CMC and SBR as binders. 186
Table 5.25 – Values of charge and discharge capacities, normalized by the electrode weight, and relative values of coulombic efficiency for some representative cycles for the electrodes produced at the pilot line, with 95 wt.% of SC and using CMC and SBR as binders 188
Table 5.26 – Summary of the electrode characteristics (dry thickness, ML, and areal capacity) as a function of the roll gap applied during the coating step for electrodes produced at pilot-line scale using LiPAA450 as binders. 191
Table 5.27 – Comparison of the electrode characteristics (dry thickness, ML and areal capacity) based on CMC and SBR composition, using different facilities 192
Table 5.28 – Comparison of the discharge capacity values of the CMC-SBR based electrodes depending on the two production processes 193
Table 5.29 – Summary of the experimental trials carried out to optimize the slurry formulation and coating parameters of Gigagreen SC anodes at laboratory scale. The table highlights the evolution of binder composition, SF and processing conditions, together with the main qualitative outcomes observed in terms of coating homogeneity and electrode manufacturability. 197
Table 5.30 – Summary of the laboratory-scale trials for Gigagreen SC anodes, reporting solid fraction, coating thickness and the resulting electrode properties. The areal capacity was calculated based on the material theoretical capacity. 197
Table 5.31 – Cycling protocol for the rate capability test coupled with the long term cycling, adopted for the electrochemical test throughout all the project, it was agreed between the partners 207
Table 5.32 – Values of charge and discharge capacities, normalized by the electrode weight, and relative values of coulombic efficiency for the electrodes produced with the optimized production process 208
Table 5.33 – Characteristics of the electrodes produced using the modified current collectors. The dry thickness was calculated excluding the current collectors 212
Table 5.34 – Values of charge and discharge capacities, normalized by the electrode weight, and relative values of coulombic efficiency for the electrodes produced with the pristine CC 213
Table 5.35 – Values of charge and discharge capacities, normalized by the electrode weight, and relative values of coulombic efficiency for the electrodes produced with the Cu1L 216
Table 5.36 – Values of charge and discharge capacities, normalized by the electrode weight, and relative values of coulombic efficiency for the electrodes produced with the Cu2L 218
Table 5.37 – Values of charge and discharge capacities, normalized by the electrode weight, and relative values of coulombic efficiency for the electrodes produced with the Cu3L 220

Table 5.38 – Discharge capacity values, including and excluding the CVS and relative capacity retention (%) of silicon-based electrodes prepared on different CCs. Values are reported as average ± standard deviation calculated from replicate cells. 223
Table 5.39 – Resistivity of the composite dry layer and interface resistance of electrodes produced with different laser-treated current collector 224
Table 5.40 – Summary of the experimental trials carried out to optimize the slurry formulation and coating parameters of silicon-dominant anodes at laboratory scale. The table highlights the evolution of binder composition, SF and processing conditions, together with the main qualitative outcomes observed in terms of coating homogeneity and electrode manufacturability. 229
Table 5.41 – Summary of the laboratory-scale trials for E-Magy SD anodes, reporting trial ID, coating thickness and the resulting electrode properties. 230
Table 5.42 – Cycling protocol adopted for the first charge-discharge test for silicon-dominant anodes 231
Table 5.43 – Cycling protocol adopted after the production optimization for the charge-discharge test for silicon-dominant anodes 232
Table 5.44 – Values of charge and discharge capacities, normalized by the electrode weight, and relative values of coulombic efficiency for some representative cycles for the electrodes produced with the first production trial using 10 wt.% PAA as binder. 235
Table 5.45 – Values of charge and discharge capacities, normalized by the electrode weight, and relative values of coulombic efficiency for some representative cycles for the electrodes produced with the optimized production process using 10 wt.% PAA as binder. 242
Table 5.46 – Values of charge and discharge capacities, normalized by the electrode weight, and relative values of coulombic efficiency for some representative cycles for the electrodes produced using 9 wt.% PAA and 1 wt.% SBR as binders. 246
Table 5.47 – Values of charge and discharge capacities, normalized by the electrode weight, and relative values of coulombic efficiency for some representative cycles for the electrodes produced using 9 wt.% PAA and 1 wt.% Alg as binders. 249
Table 5.48 – Values of charge and discharge capacities, normalized by the electrode weight, and relative values of coulombic efficiency for some representative cycles for the electrodes produced using 9 wt.% PAA and 1 wt.% TG as binders. 252
Table 5.49 – Values of charge and discharge capacities, normalized by the electrode weight, and relative values of coulombic efficiency for some representative cycles for the electrodes produced using 9 wt.% PAA and 1 wt.% Pec as binders. 255
Table 5.50 – Comparison between the dry thicknesses and ML of the electrodes produced at laboratory level at Polito 258
Table 5.51 – Selected electrochemical performance results used for comparison among the investigated electrodes produced at Polito. 260
Table 5.52 – Characteristics of the electrodes produced at pilot line with a SF of 45 wt.% and a formulation containing 10 wt.% PAA. 263
Table 5.53 – Comparison of the electrode's characteristics based on the different production processes. 263
Table 5.54 – Rheological testing protocol applied to the slurry to measure flow curve and thixotropic behavior 265

Table 5.55 – Rheological testing protocol applied to the slurry to measure creep recovery test 265
Table 5.56 – pH values of all the solutions produced starting from the solution of PAA and with the natural polysaccharides added to the system. 271
Table 5.57 – Characteristics of the electrodes produced at CIC energiGUNE with the different binder combinations 271
Table 5.58 – Cycling protocol adopted for electrochemical characterization of silicon-dominant electrodes produced at CIC energiGUNE 272
Table 5.59 – Values of charge and discharge capacities, normalized by the electrode weight, and relative values of coulombic efficiency for some representative cycles for the PAA-based electrodes produced at CIC energiGUNE. 276
Table 5.60 – Values of charge and discharge capacities, normalized by the electrode weight, and relative values of coulombic efficiency for some representative cycles for the PAA_Alg based electrodes produced at CIC energiGUNE. 281
Table 5.61 – Values of charge and discharge capacities, normalized by the electrode weight, and relative values of coulombic efficiency for some representative cycles for the PAA_Pec based electrodes produced at CIC energiGUNE. 285
Table 5.62 – Values of charge and discharge capacities, normalized by the electrode weight, and relative values of coulombic efficiency for some representative cycles for the PAA_CGN based electrodes produced at CIC energiGUNE. 290
Table 5.63 – Values of charge and discharge capacities, normalized by the electrode weight, and relative values of coulombic efficiency for some representative cycles for the PAA_TG based electrodes produced at CIC energiGUNE. 294
Table 5.64 – Selected electrochemical performance results used for comparison among the investigated electrodes produced at CIC energiGUNE. 302
Table 6.1 – Summary of key methodological parameters (system boundaries, functional units, and LCIA methods) across a selection of published battery LCAs. 310
Table 6.2 – Summary of the methodological setup adopted for the LCA of anode production 311
Table 6.3 – Material inputs, process parameters, and energy consumption associated with the mixing, coating, and drying steps for the production of G-A, SC-A, and SD-A anodes at laboratory scale. 315
Table 6.4 – Geographical origin of materials and energy inputs considered in the LCA of G-A, SC-A, and SD-A anodes, used for the assessment of transport-related impacts and supply-chain scenarios. 316
Table 6.5 – Amount of scraps produced during the punching step of anode production, depending on the electrode chemistry 317
Table 6.6 – Correspondence between experimental inputs and Ecoinvent 3.11 background datasets, including data quality classification and proxy identification for the anode manufacturing processes 318
Table 6.7 – Overview of the main properties of the G-A, SC-A, and SD-A anodes produced at laboratory scale 319
Table 6.8 – List of the 18 impact categories evaluated with the ReCiPe (2016) Midpoint method, with their abbreviations and measurement unit. 326
Table 6.9 – Number of laminates and electrodes required to achieve the capacity of 1 Ah 330

Table 6.10 – Life cycle environmental impacts calculated for the actual production of 1Ah of different types of anodes and relative percentage reduction, considering the G-A as the baseline 333
Table 6.11 – Number of laminates and electrodes required to achieve the capacity of 1 kg..... 334
Table 6.12 – Life cycle environmental impacts calculated for the actual production of 1kg of different types of anodes and relative percentage reduction, considering the graphite anode as the baseline..... 336
Table 6.13 – Monte Carlo simulation results for GW for the electrode production system per 1 Ah under both Global and European supply chain scenarios. 346
Table 6.14 – Monte Carlo simulation results for GW for the electrode production system per 1 kg under both Global and European supply chain scenarios. 347
Table 6.15 – Endpoint impact results for the production of 1 Ah and 1 kg of anodes under the actual global supply chain scenario..... 352
Table 6.16 – Endpoint impact results for the production of 1 Ah and 1 kg of anodes under the actual global supply chain scenario..... 353
Table 6.17 – Summary of the methodological setup adopted for the LCA of full cells 356
Table 6.18 – Material inputs, operating conditions, and energy requirements related to the mixing, coating, and drying stages of the production processes of G-A, SC-A, SD-A, and LFP electrodes at laboratory scale..... 359
Table 6.19 – Amount of scraps produced during the punching step of electrode production, depending on the electrode chemistry..... 360
Table 6.20 – Material inputs, operating conditions, and energy requirements related to the second drying and cell assembly for the production of full cells..... 361
Table 6.21 – Correspondence between experimental inputs and Ecoinvent 3.11 background datasets, including data quality classification and proxy identification for the full cell manufacturing processes..... 361
Table 6.22 – Overview of the main properties of the G-A, SC-A, SD-A anodes, and LFP cathode produced at laboratory scale. 363
Table 6.23 – Average discharge capacity for the full cells assembled with the different anode chemistries..... 364
Table 6.24 – Mass distribution of cell components for the three anode chemistries considering the complete coin cell configuration, including casing and spacers. Values are reported in grams and as weight percentage relative to the total cell mass..... 367
Table 6.25 – Mass distribution of cell components for the three anode chemistries excluding case and spacers. Values are reported in grams and weight percentage relative to the system..... 368
Table 6.26 – Midpoint impact category results for the three anode chemistries calculated using the FU of 1 coin cell..... 369
Table 6.27 – Number of coin cells required to reach the production of 1 kWh for the three anode chemistries, based on the experimentally measured cell capacities. 371
Table 6.28 – Midpoint impact category results for the three anode chemistries calculated using the FU of 1kWh..... 372
Table 6.29 – Monte Carlo simulation results for GW for the full cell system, considering both the FUs. 377

Table 6.30 – Endpoint impact category results for the three anode chemistries calculated using both the FUs. 380
Table 6.31 – Comparative results for 1 Ah of anode capacity across G-A, SC-A, and SD-A chemistries using EF 3.1 and ReCiPe 2016 approaches. 383
Table 6.32 – Comparative results for 1 kg of anode capacity across G-A, SC-A, and SD-A chemistries using EF 3.1 and ReCiPe 2016 approaches. 384
Table 6.33 – Comparative results for 1 coin cell production across G-A, SC-A, and SD-A chemistries using EF 3.1 and ReCiPe 2016 approaches. 386
Table 6.34 – Comparative results for 1 kWh of full cell capacity across G-A, SC-A, and SD-A chemistries using EF 3.1 and ReCiPe 2016 approaches. 387

List of Figures

Figure 1.1 – BATTERY 2030+ vision highlighting a chemistry-neutral strategy for the development of sustainable, high-performance batteries tailored to different applications, based on interconnected research themes and tools aimed at accelerating battery discovery and innovation [3]. 3

Figure 1.2 – Gigafactories and cathode active material (CAM) plants in Europe in 2026 [4]. 4

Figure 1.3 – Climate advantages associated with relocating the battery supply chain to Europe, quantified in terms of kg CO_2-Eq per kWh and as a percentage decrease relative to a supply chain dominated by Chinese production [5]. 5

Figure 1.4 – Global map showing the distribution of mineral reserves and exploration areas for key raw materials, based on data from the US Geological Survey International Minerals Statistics and Information [6]. 6

Figure 2.1 – Brief storyline of batteries. Reproduced with permission from [8]. 11

Figure 2.2 – Ragone plot of the most common batteries technologies [14]. 13

Figure 2.3 – Set-up of a lithium-ion battery (shown is the discharge process). Reproduced with permission from [8]. 17

Figure 2.4 – Schematic representation of the main components inside a LIB. As example, anode and cathode are represented by some of the most common material actually used for their production [22]. 19

Figure 2.5 – Typical discharge curve of a generic battery, where the main important polarization types are highlighted. Reproduced with permission from [23]. Copyright 2004 American Chemical Society. 20

Figure 2.6 – Generic composition of lithium-ion battery pack for EV applications. Reproduced from [29]. 21

Figure 2.7 – Comparison between the different percentage composition depending on LIBs geometry: a) Cylindrical; b) Pouch; c) Prismatic. The graphs are reproduced from the data provided in the work of Romero Guillèn et al. [30]. 22

Figure 2.8 – Crystal structures of three lithium-insertion materials, where Li^+ ions migrate through 2-D (layered), 3-D (spinel), and 1-D (olivine) diffusion frameworks. Reproduced from [37]. 24

Figure 2.9 – Crystal structures of layered LCO. Partially reproduced with permission from [41]. Copyright 2018 American Chemical Society. 25

Figure 2.10 – (a) The state-of-art NMC cathode materials, near-future NMC materials, and far-future cathode materials; (b) Schematic diagram of the positions of the various redox couples [36]. 26

Figure 2.11 – Atomic model of Ni-rich NMC811 layered oxide [51] 26
Figure 2.12 – Schematic structure of (a) disorder and (b) ordered LNMO and their charge/discharge curves. Partially reproduced with permission from [54] 27
Figure 2.13 – Crystal olivine structure of LFP. Reproduced with permission from [64] 28
Figure 2.14 – Summary of the next generation active material for anodes. Reproduced with permission from [66] 30
Figure 2.15 – Schematic illustration of the issues related to the use of lithium metal as anode, in particular: a) lithium dendrites formation mechanism; b) subsequent phenomenon after continuous cycles. Partially reproduced from [79] 31
Figure 2.16 – General representation of the intercalation mechanism of anode materials. Partially reproduced with permission from [66] 32
Figure 2.17 – Schematic illustration of the intercalation mechanism of lithium into the layered graphite structure, according to the model of Rüdorff and Hofmann (upper path) and Daumas and Herold (lower path) [83] 33
Figure 2.18 – More detailed mechanism of the intercalation and de-intercalation of lithium ions inside the layer of the graphite [83] 33
Figure 2.19 – General representation of the alloying mechanism of anode materials. Partially reproduced with permission from [66] 34
Figure 2.20 – Comparison between lithiation and de-lithiation curves of silicon at room temperature and higher temperature. Reproduced with permission from [91] 35
Figure 2.21 – Schematic illustrations of (a) the intrinsic properties of Si anodes and (b) the induced unfavorable electrochemical performances of Si-based LIB. Reproduced with permission from [93] 36
Figure 2.22 – General representation of the conversion mechanism of anode materials. Partially reproduced with permission from [66] 38
Figure 2.23 – Radar plot comparing the most important characteristics of common families of anode materials, previously discussed. Rearranged from [114] 39
Figure 2.24 – a) chemical structure of PVDF; b) chemical structure of NMP 40
Figure 2.25 – Chemical structure of a) CMC and b) SBR 42
Figure 2.26 – Monomeric unit of the PAA 42
Figure 2.27 – Sodium Alginate structure with its two units: 1-4-linked β-D-mannuronic acid (M-Block) and α-L-guluronic acid (G-Block) 44
Figure 2.28 – Chemical structure of TG 45
Figure 2.29 – Molecular structures of the three types of carrageenan, from left to right: κ-carrageenan, ι-carrageenan and λ-carrageenan 45
Figure 2.30 – Chemical structure of Pectin con CMC with the important focus on the glycosidic bond. Partially reported with permission from [184]. Copyright 2016 American Chemical Society 46
Figure 2.31 – Different types of solvents usually used in LIBs: a) EC; b) PC; c) DMC; d) DEC; e) EMC 50
Figure 2.32 – Chemical structures of the most common lithium salts actually used in LIBs: a) $LiPF_6$; b) LiFSI; c) LiTFSI 51
Figure 2.33 – Chemical structures of additives: a) FEC; b) VC 51
Figure 2.34 – Typical organic cations used in ILs: a) Pyrrolidinium; b) Pyridinium; c) Ammonium 53

Figure 3.1 – Technology Readiness Level scale for EV battery application [13]..... 55
Figure 3.2 – Complete flow chart of battery production process [228] 57
Figure 3.3 – Schematic presentation of the steps involved in electrode production process and the intermediate products [235]..... 58
Figure 3.4 – Different types of mixers used at different TRLs: a) Magnetic Stirrer; b) Ball milling; c) Homogenizer mixer used in Polito laboratories; d) Dispermat Mixer; e) Planetary Mixer; f) Complex homogenizer blades for higher TRL applications..... 59
Figure 3.5 – a) Doctor Blade coating method; b) Schematic working principle of the Doctor Blade 61
Figure 3.6 – a) Small Roll-to-roll system for the coating, on the right part of the instrument is located the oven; b) Schematic working process of the Reverse Comma Technique..... 62
Figure 3.7 – Comparison of a typical drying process for a NMP-processed cathode and a water-based anode. Reproduced with permission from [247]. Copyright 2017 American Chemical Society 63
Figure 3.8 – Schematic process of the drying steps [249] 64
Figure 3.9 – Schematic representation of the production process, with an important focus on the benefits of using water as a solvent in the production instead of NMP [117] 65
Figure 3.10 – Comparison of the different impact that can occur after the calendering step: a) important reduction of the electrode thickness; b) the excessive strength applied can bring to the fracture of the active material particles; c) the excessive strength applied can lead to the deformation of the current collector. Partially reproduced with permission from [255] 66
Figure 3.11 – Schematic representation of the electrode manufacturing process with the parameters involved in the production process and the relative analyses involved in the quality control [279]..... 68
Figure 3.12 – Representation of different types of flows and the parameters involves: a) shear flow; b) extensional flow. Reproduced with permission from [294] and [295] .. 70
Figure 3.13 – a) Representation of the velocity distribution of a flowing fluid with a fixed shear gap in case of the Two-Plates model; b) Representation of the concept of laminar flow: the fluid is ideally divided into layers. Reproduced from [292]..... 71
Figure 3.14 – Viscosity function of a polymer solution [292]..... 73
Figure 3.15 – Example of a rheometer produced by Anton Paar and its components. Reproduced from [296]..... 75
Figure 3.16 – Left: rotational movement. Right: oscillatory movement. Reproduced from [296] 76
Figure 3.17 – The most common geometries used for rheological measurements, from left to right: plate-plate, cone-plate, cylindrical, capillary [295]..... 76
Figure 3.18 – Most common types of geometry used in the LIBs field: a) plate-plate (PPG); b) cone-plate (CPG). Reproduced from [292]..... 78
Figure 3.19 – a) Time-dependent shear rate ramp; b) Viscous behaviour response to the shear rate ramp: 1) ideal viscous, 2) shear-thinning, 3) shear-thickening. Reproduced from [292]. 79
Figure 3.20 – Typical flow curve behavior of a shear-thinning material. Reproduced with permission from [247]. Copyright 2017 American Chemical Society..... 80

Figure 3.21 – First method to observe the thixotropic behavior, based on the evidence of the hysteresis effect observe evaluating the variation of shear stress: a) Setting of the time-dependent shear rate profile, divided into three time intervals; b) Back and forth flow curve, obtained changing the shear rate and representing the hysteresis area. Reproduced from [292] 81
Figure 3.22 – Second method to observe the thixotropic behavior: a) Setting of the experiment changing the value of shear rate for three times: 1) low shear rate, 2) high shear rate, 3) low shear rate; b) Time-dependent viscosity after the application of the three stages at different shear rates. Reproduced from [292] 82
Figure 3.23 – Working principle of a rheometer based on the oscillatory mode: a) Representation of the Two-Plates model for the oscillatory tests; b) Representation of the forces involved in the tests and the angle that they create between the two plates fixed at a certain distance [292] 84
Figure 3.24 – Comparison of the stress and strain waves depending on the type of material. Reproduced from [301] 85
Figure 3.25 – Example of oscillatory frequency sweep test on two different type of graphite at 25°C. Reproduced from [307] 86
Figure 4.1 – Schematic overview of the life cycle stages of LIB materials and components, starting from raw material extraction to end-of-life recycling [6] 89
Figure 4.2 – Graphical representation of all the steps involved for the production of a complete Life Cycle Inventory [318] 93
Figure 4.3 – Graphical representation of the connections between midpoint and endpoint indicators, based on the damage pathways proposed by the ReCiPe methods [343] 102
Figure 4.4 – Pedigree matrix adopted by the Ecoinvent Data Quality System 105
Figure 5.1 – a) Laminate produced at the first trial based on previous optimization; b) Weight distribution of the electrodes produced with the doctor blade at laboratory level 113
Figure 5.2 – Complexity of the inner cell components structure and relative circuit elements [366] 114
Figure 5.3 – a) Equivalent circuit for EIS adopted in this discussion; b) Simplification of the equivalent circuit when the cells do not yet have the SEI layer; c) Example of a Nyquist plot commonly observed with fresh graphite anodes, in absence of SEI layer . 115
Figure 5.4 – Values of charge and discharge capacity and relative coulombic efficiency for the baseline sample with long cycling protocol: a) Entire test, up to 500 cycles to highlight the inconstant values and the prominent capacity decay; b) Focus on the first 100 cycles to highlight the first capacity decay and its recovery; c) Focus on the first 30 cycles to highlight the stability at 0.1C and the decay when the current density is increased at 1C 117
Figure 5.5 – a) Charge/discharge curves for the forming cycles and b) their relative dQ/dV curves with a focus on the intercalation steps and the related voltage values 120
Figure 5.6 – Charge/discharge curves for some representative cycles: a) from cycle 6 to cycle 50; b) from cycle 100 to cycle 500 121
Figure 5.7 – Values of charge and discharge capacity and relative coulombic efficiency for the baseline sample with the rate capability protocol: a) Entire test, up to 500 cycles to highlight the inconstant values; b) Focus on the first 100 cycles to highlight

the first capacity decay and its recovery; c) Focus on the first 30 cycles to highlight the values for the forming step and the capacity decay after the increase in the current density 123
Figure 5.8 – Charge/discharge curves for some representative cycles for the baseline rate capability cycling protocol: a) Forming cycles; b) Curve for the rate capability test; c) Curves of the first part of long cycling test; d) Curves of the second part of long cycling test 124
Figure 5.9 – Values of charge and discharge capacities and relative coulombic efficiency for the cycling protocol with the improved forming step 126
Figure 5.10 – Charge/Discharge curves for the improved forming protocol test: a) First three cycles of the forming step; b) Rate capability test; c) Long cycling step 127
Figure 5.11 – Values of charge and discharge capacities highlighting the impact that the CVS had on the overall performance of the cell. 129
Figure 5.12 – Charge and discharge capacities and relative values of coulombic efficiency for the cell tested with the CVS: a) Entire test; b) Focus on the first 30 cycles 129
Figure 5.13 – Charge/discharge curves for the CC-CV cycling protocol: a) Forming step; b) Representative cycles at 1C 131
Figure 5.14 – Visual contribution of the CVS considering the discharge capacity for the graphite anode 131
Figure 5.15 – Facilities provided by MTI Corp. and used at Pilot-line level: a) Planetary Mixer; b) Roll-to-roll coating machine and oven; c) Hot rolling press 132
Figure 5.16 – Parameters that can be controlled by the reverse comma mechanism on the R2R machine provided by MTI: thickness deposition and roll gap, which was kept constant at 20 μm 134
Figure 5.17 – Photos related to the first trial of pilot-line deposition: a) the coating was just performed and the white arrow highlights the flow of the slurry; b) dried electrodes after drying step, the inhomogeneity after the coating is very evident 135
Figure 5.18 – a) The picture highlights the lack of homogeneity of the electrodes: ideally, each sheet can be divided into four sections; b) Weight distribution of the electrodes cut from the three sections of the sheet; c) Electrode characteristics related to the three sections 136
Figure 5.19 – Electrochemical results of the electrode produced at the pilot-line and tested with the CVS: a-b) Charge and Discharge Capacities and relative values of Coulombic Efficiency: a) whole test; b) zoom on the first 30 cycles; c-d) Charge/discharge curves for the CC-CV cycling protocol: a) Forming step; b) Representative cycles at 1C 137
Figure 5.20 – Photo of one of the electrodes produced in the second trial, the accumulation is still visible on the bottom side 138
Figure 5.21 – Photo of one of the electrodes produced in the third trial, the accumulation is still visible on the bottom side 139
Figure 5.22 – Photo of one part of the long electrode produced in the fourth trial 140
Figure 5.23 – Visual representation on the trend of dry thickness and mass loading reducing the roll gap during the production of graphite anodes 142
Figure 5.24 – Electrochemical results of the electrode produced with the optimized process (thickness: 100 μm) at the pilot-line and tested with the CVS: a-b) Charge and

Discharge Capacities and relative values of Coulombic Efficiency: a) whole test; b) zoom on the first 30 cycles; c-d) Charge/discharge curves for the CC-CV cycling protocol: a) Forming step; b) Representative cycles at 1C; e) CVS capacity contributions distinguished between the discharge and the CVS..... 144

Figure 5.25 – SEM images of the surface of the electrodes produced as previously described, focusing on highlighting the differences between the two production processes. Laboratory level: a) Doctor Blade; b) Doctor Blade and Hydraulic Press; Small Pilot-line level: c) Pilot-line; d) Pilot-line and Calender. For all the images the acquisition parameters were the same to have a proper comparison: Magnification 1,00 KX; WD 3,0 mm; EHT 5,00 kV..... 147

Figure 5.26 – SEM images of the folded anodes produced with the pilot-line: a-c) without calendering; b-d) calendering. a-b) Magnification: 300X; WD: a) 3,1 mm, b) 3,6 mm; EHT 5,00 kV. c-d) Magnification: 1KX; WD: a) 2,9 mm, b) 3,7 mm; EHT 5,00 kV 148

Figure 5.27 – Summary of the electrochemical behaviour of MTI SC electrodes prepared with different binders, including specific discharge capacity, coulombic efficiency of the first cycle and capacity retention during cycling. 155

Figure 5.28 – First laminate produced with 92 wt.% of SC and CMC and SBR, the unoptimized viscosity is evident for the defects on the edges of the deposition and the bad dispersion in the middle 157

Figure 5.29 – Electrochemical characterization of the electrodes produced with 92 wt.% of SC and using CMC and SBR as binders: a) Entire test; b) Focus on the rate capability test 158

Figure 5.30 – Charge/discharge curves for some representative cycles of the electrodes produced with 92 wt.% of SC and using CMC and SBR as binders: a) Forming cycles; b) Rate capability test; c) Long cycling..... 160

Figure 5.31 – CV test performed on 5 cycles for the electrodes produced with 92 wt.% of SC and using CMC and SBR as binders..... 161

Figure 5.32 – Second laminate produced with 92 wt.% of SC and CMC and SBR, the unoptimized viscosity is even more evident for the defects on the side of the deposition 161

Figure 5.33 – Electrode with a diameter of 15 mm obtained at the third trial, with 95 wt.% of SC and using CMC and SBR as binders, with homogeneous and smooth surface 162

Figure 5.34 – Electrochemical characterization of the electrodes produced with 95 wt.% of SC and using CMC and SBR as binders: a) Entire test; b) Focus on the rate capability test 163

Figure 5.35 – Charge/discharge curves for some representative cycles of the electrodes produced with 95 wt.% of SC and using CMC and SBR as binders: a) Forming cycles; b) Rate capability test; c) Long cycling..... 164

Figure 5.36 – CV test performed on 5 cycles for the electrodes produced with 95 wt.% of SC and using CMC and SBR as binders..... 165

Figure 5.37 – Laminate produced with 95 wt.% of SC and using PAA250 as binder: a) Total laminate, the excess of solvent is evident on the left side; b) Focus on the deposition inhomogeneities 166

Figure 5.38 – Laminate produced with 95 wt.% of SC and using PAA450 as binder, on the left side is evident the inhomogeneities related to the accumulation of the slurry.... 167
Figure 5.39 – Laminate produced with 92 wt.% of SC and LiPAA250 as binder, to be noted the tensions along the side highlighted with the red arrows..... 169
Figure 5.40 – Electrochemical characterization of the electrodes produced with 92 wt.% of SC and using LiPAA250 as binder: a) Entire test; b) Focus on the rate capability test..... 169
Figure 5.41 – Charge/discharge curves for some representative cycles of the electrodes produced with 92 wt.% of SC and using LiPAA250 as binder: a) Forming cycles; b) Rate capability test; c) Long cycling..... 170
Figure 5.42 – Laminate produced with 95 wt.% of SC and LiPAA250 as binder, to be noted the tensions along the side highlighted with the red arrow..... 171
Figure 5.43 – Electrochemical characterization of the electrodes produced with 95 wt.% of SC and using LiPAA250 as binder: a) Entire test; b) Focus on the rate capability test..... 172
Figure 5.44 – Charge/discharge curves for some representative cycles of the electrodes produced with 95 wt.% of SC and using LiPAA250 as binder: a) Forming cycles; b) Rate capability test; c) Long cycling..... 173
Figure 5.45 – CV test performed on 5 cycles for the electrodes produced with 95 wt.% of SC and using LiPAA250 as binder..... 174
Figure 5.46 – Laminate produced with 95 wt.% of silicon and LiPAA450 as binder, with a smooth and homogeneous surface..... 174
Figure 5.47 – Electrochemical characterization of the electrodes produced with 95 wt.% of SC and using LiPAA450 as binder: a) Entire test; b) Focus on the rate capability test..... 175
Figure 5.48 – Charge/discharge curves for some representative cycles of the electrodes produced with 95 wt.% of SC and using LiPAA450 as binder: a) Forming cycles; b) Rate capability test; c) Long cycling..... 176
Figure 5.49 – Laminate produced using 92 wt.% of SC and LiPAA250 as binder with the addition of 1 wt.% of tragacanth gum..... 178
Figure 5.50 – Electrochemical characterization of the electrodes produced with 92 wt.% of SC and using LiPAA250 and TG as binders: a) Entire test; b) Focus on the rate capability test..... 179
Figure 5.51 – Charge/discharge curves for some representative cycles of the electrodes produced with 92 wt.% of SC and using LiPAA250 and TG as binders: a) Forming cycles; b) Rate capability test; c) Long cycling..... 180
Figure 5.52 – Laminate produced with 92 wt.% of SC and using LiPAA250 as binder with the addition of 1 wt.% of Carrageenan..... 181
Figure 5.53 – Electrochemical characterization of the electrodes produced with 92 wt.% of SC and using LiPAA250 and CGN as binders: a) Entire test; b) Focus on the rate capability test..... 181
Figure 5.54 – Charge/discharge curves for some representative cycles of the electrodes produced with 92 wt.% of SC and using LiPAA250 and CGN as binders: a) Forming cycles; b) Rate capability test; c) Long cycling..... 183
Figure 5.55 – Comparison of the average discharge capacities of the electrodes produced at laboratory level: a) Entire test; b) Focus on the rate capability test..... 184

Figure 5.56 – Laminates produced at the pliot plant with the CMC-SBR composition at different thicknesses: a) 100 µm; b) 90 µm; c) 80 µm; d) 70 µm 186
Figure 5.57 – Electrochemical characterization of the electrodes produced at the pilot line, with 95 wt.% of SC and using CMC and SBR as binders: a) Entire test; b) Focus on the rate capability test 188
Figure 5.58 – Charge/discharge curves for some representative cycles of the electrodes produced at pilot line with 95 wt.% of SC and using CMC and SBR as binders: a) Forming cycles; b) Rate capability test; c) Long cycling..... 189
Figure 5.59 – CV test performed on 5 cycles for the electrodes produced at pilot line with 95 wt.% of SC and using CMC and SBR as binders 189
Figure 5.60 – Laminates produced at the pilot line with the LiPAA450 binder at different thicknesses: a) 100 µm; b) 90 µm; c) 80 µm..... 190
Figure 5.61 – Example of one 15 mm disc electrodes punched from the laminate produced with 80 µm wet slurry, the signs of the detachments are very evident along the borders..... 191
Figure 5.62 – Comparison of the discharge capacity of the CMC-SBR based electrodes depending on the two production processes 192
Figure 5.63 – Map of the European partners involved in the GIGAGREEN project [352]. 195
Figure 5.64 – Laminate produced at the first trial where the clumps and the inhomogeneities are very visible: a) Entire laminate; b) Focus on the clumps, macroscopically visible; c) Electrode with a diameter of 14 mm 199
Figure 5.65 – SEM of the surface of two different regions with evident pressed clumps 200
Figure 5.66 – Focus on the clumps presented on the dried laminate produced with the second trial 201
Figure 5.67 – Dry laminate produced with the third trial: a) Entire laminate; b) Focus on the clumps 201
Figure 5.68 – Dry laminate produced with the fourth trial: a) Entire laminate; b) Focus on the clumps; c) Electrode with a diameter of 14 mm 203
Figure 5.69 – Dry laminate produced with the fifth trial: a) Entire laminate; b) Focus on the clumps; c) Electrode with a diameter of 14 mm 204
Figure 5.70 – a) SEM of the surface of electrode produced with the fifth trial, for this image the acquisition parameters were Magnification 500 X; WD 3,0 mm; EHT 5,00 kV; b) Map of the electrode surface..... 204
Figure 5.71 – Electrochemical characterization of the electrodes produced with the optimized procedure: a) Entire test; b) Focus on the rate capability test 208
Figure 5.72 – Charge/discharge curves for some representative cycles of the electrodes produced with the optimized production process: a) Forming cycles; b) Rate capability test; c) Long cycling..... 209
Figure 5.73 – Copper current collector modified with three treatments: a-d) Cu1L; b-e) Cu2L; c-f) Cu3L. The SEM images were captured using a magnification of 10KX..... 211
Figure 5.74 – Electrochemical characterization of the electrodes produced with the pristine CC: a) Entire test; b) Focus on the rate capability test..... 213

Figure 5.75 – Charge/discharge curves for some representative cycles of the electrodes produced with the pristine CC: a) Forming cycles; b) Rate capability test; c) Long cycling 214
Figure 5.76 – Cyclic voltammetry performed on the CuP electrodes. The analysis was performed in the potential window between 0.1 V and 1.5 V with a scan rate of 0.1 mV s^{-1}. 215
Figure 5.77 – Electrochemical characterization of the electrodes produced with the Cu1L: a) Entire test; b) Focus on the rate capability test 215
Figure 5.78 – Charge/discharge curves for some representative cycles of the electrodes produced with the Cu1L: a) Forming cycles; b) Rate capability test; c) Long cycling... 216
Figure 5.79 – Cyclic voltammetry performed on the Cu1L electrodes. The analysis was performed in the potential window between 0.1 V and 1.5 V with a scan rate of 0.1 mV s^{-1}. 217
Figure 5.80 – Electrochemical characterization of the electrodes produced with the Cu2L: a) Entire test; b) Focus on the rate capability test 218
Figure 5.81 – Charge/discharge curves for some representative cycles of the electrodes produced with the Cu2L: a) Forming cycles; b) Rate capability test; c) Long cycling... 219
Figure 5.82 – Cyclic voltammetry performed on the Cu2L electrodes. The analysis was performed in the potential window between 0.1 V and 1.5 V with a scan rate of 0.1 mV s^{-1}. 219
Figure 5.83 – Electrochemical characterization of the electrodes produced with the Cu3L: a) Entire test; b) Focus on the rate capability test 220
Figure 5.84 – Charge/discharge curves for some representative cycles of the electrodes produced with the Cu3L: a) Forming cycles; b) Rate capability test; c) Long cycling... 221
Figure 5.85 – Cyclic voltammetry performed on the Cu3L electrodes. The analysis was performed in the potential window between 0.1 V and 1.5 V with a scan rate of 0.1 mV s^{-1}. 222
Figure 5.86 – Comparison of the discharge capacities of electrodes produced with laser-treated current collectors. Results are shown including the contribution of the CVS: a) the entire test; b) the rate capability test. Excluding the CVS:c) the entire test; d) the rate capability test. 223
Figure 5.87 – Comparison between the cyclic voltammetry of the electrodes produced with the laser treated CCs: a) Cycle 1; b) Cycle 3. 225
Figure 5.88 – SEM images of the silicon supplied by E-Magy at different magnifications: a) 500X; b) 2kX; c) 11kX. Reproduced from [469] 227
Figure 5.89 – Laminates produced during the first trial with a SF of 31% and a formulation containing 80 wt.% Si and 10 wt.% PAA, deposited at different wet thicknesses: a) 50 µm; b) 100 µm. 234
Figure 5.90 – Values of charge and discharge capacity and relative coulombic efficiency for the first production trial using 10 wt.% PAA as binder: a) Entire test, up to 120 cycles; b) Focus on the rate capability test. 235
Figure 5.91 – Charge/discharge profiles for some representative cycles for the first production trial using 10 wt.% PAA as binder: a) Forming cycles; b) Rate capability test; b) Long-term test. 237
Figure 5.92 – Cycling voltammetry for the first production trial using 10 wt.% PAA as binder. 238

Figure 5.93 – Laminates produced during the second trial with a SF of 45 wt.% and a formulation containing 80 wt.% Si and 10 wt.% PAA, deposited at different wet thicknesses: a) 50 µm; b) 100 µm. 239
Figure 5.94 – Values of charge and discharge capacity and relative coulombic efficiency for the optimized process using 10 wt.% PAA as binder: a) Entire test, up to 120 cycles; b) Focus on the rate capability test. 241
Figure 5.95 – SEM images produced with the optimized process using 10 wt.% PAA as binder at different magnification: a) 500X; b) 5kX. 241
Figure 5.96 – Charge/discharge profiles for some representative cycles for the optimized production process using 10 wt.% PAA as binder: a) Forming cycles; b) Rate capability test; b) Long-term test. 243
Figure 5.97 – Cycling voltammetry for the optimized production trial using 10 wt.% PAA as binder. 243
Figure 5.98 – Laminates produced with a SF of 45 wt.% and a formulation containing 9 wt.% PAA and 1 wt.% SBR, deposited at different wet thicknesses: a) 50 µm; b) 70 µm; c) 100 µm. 245
Figure 5.99 – Values of charge and discharge capacity and relative coulombic efficiency for the electrodes produced using 9 wt.% PAA and 1 wt.% SBR as binders: a) Entire test, up to 120 cycles; b) Focus on the rate capability test. 246
Figure 5.100 – Charge/discharge profiles for some representative cycles for the optimized production process using 9 wt.% PAA and 1 wt.% SBR as binders: a) Forming cycles; b) Rate capability test; b) Long-term test. 247
Figure 5.101 – Laminates produced with a SF of 45 wt.% and a formulation containing 9 wt.% PAA and 1 wt.% Alg, deposited at different wet thicknesses: a) 50 µm; b) 70 µm; c) 100 µm. 248
Figure 5.102 – Values of charge and discharge capacity and relative coulombic efficiency for the electrodes produced using 9 wt.% PAA and 1 wt.% Alg as binders: a) Entire test, up to 120 cycles; b) Focus on the rate capability test. 249
Figure 5.103 – Charge/discharge profiles for some representative cycles for the optimized production process using 9 wt.% PAA and 1 wt.% Alg as binders: a) Forming cycles; b) Rate capability test; b) Long-term test. 250
Figure 5.104 – Cycling voltammetry for the optimized production trial using 9 wt.% PAA and 1 wt.% Alg as binder. 250
Figure 5.105 – Laminates produced with a SF of 45 wt.% and a formulation containing 9 wt.% PAA and 1 wt.% TG, deposited at different wet thicknesses: a) 50 µm; b) 70 µm; c) 100 µm. 251
Figure 5.106 – Values of charge and discharge capacity and relative coulombic efficiency for the electrodes produced using 9 wt.% PAA and 1 wt.% TG as binders: a) Entire test, up to 120 cycles; b) Focus on the rate capability test. 252
Figure 5.107 – Charge/discharge profiles for some representative cycles for the optimized production process using 9 wt.% PAA and 1 wt.% TG as binders: a) Forming cycles; b) Rate capability test; b) Long-term test. 253
Figure 5.108 – Cycling voltammetry for the optimized production trial using 9 wt.% PAA and 1 wt.% TG as binder 253

Figure 5.109 – Laminates produced with a SF of 45 wt.% and a formulation containing 9 wt.% PAA and 1 wt.% Pec, deposited at different wet thicknesses: a) 50 µm; b) 70 µm; c) 100 µm. 254
Figure 5.110 – Values of charge and discharge capacity and relative coulombic efficiency for the electrodes produced using 9 wt.% PAA and 1 wt.% Pec as binders: a) Entire test, up to 120 cycles; b) Focus on the rate capability test. 255
Figure 5.111 – SEM images of the electrodes produced using 9 wt.% PAA and 1 wt.% Pec as binders at different magnification: a) 500X; b) 5kX. 256
Figure 5.112 – Charge/discharge profiles for some representative cycles for the optimized production process using 9 wt.% PAA and 1 wt.% Pec as binders: a) Forming cycles; b) Rate capability test; b) Long-term test. 257
Figure 5.113 – Cycling voltammetry for the optimized production trial using 9 wt.% PAA and 1 wt.% Pec as binder 257
Figure 5.114 – Graphical comparison between the dry thicknesses and ML of the electrodes produced at laboratory level at Polito 259
Figure 5.115 – Comparison of electrochemical performance of the electrodes produced at PoliTo based on the different binders combinations: a) Entire test, up to 120 cycles; b) Focus on the rate capability test. 261
Figure 5.116 – Coating process at pilot line level, highlighting the defects encountered during the production process. 262
Figure 5.117 – Slurry drying process observed during rheological measurements. .. 266
Figure 5.118 – Rheological characterization of the PAA and additive slurries: a) Flow curve and b) Creep recovery test. 267
Figure 5.119 – Laminates with a thickness of 70 µm produced with the PAA and the additives: a) PAA alone; b) Tragacanth Gum; c) Pectin and d) SBR. 268
Figure 5.120 – Chemical structures of a) PAA and b) SBR. 268
Figure 5.121 – a) Laminate produced with the PAA as binder and the graphite; b) Laminate complete with PAA graphite, carbon black and silicon; c) Flow curve with the comparison of the slurries produced with the different components; d) Creep recovery test with the comparison of the slurries produced with the different components. 269
Figure 5.122 – Comparison of the rheological measurement for the slurries produced with the PAA alone (black curve) and the PAA with the TG (red curve): a) Flow curve; b) Creep recovery test. 270
Figure 5.123 – Rheological characterization of the slurries produced with PAA alone: a) Flow curve; b) Creep recovery test. 273
Figure 5.124 – Laminates produced with a constant wet thickness of 50 µm and starting from the solution of PAA alone: a) PAA alone; b)PAA_Graphite; c) PAA_C45; d) PAA_C45_Graphite; d) PAA_Complete. 274
Figure 5.125 – Peel test performed o the laminates produced starting with the PAA alone solution: a) PAA alone; b)PAA_Graphite; c) PAA_C45; d) PAA_C45_Graphite; d) PAA_Complete. 275
Figure 5.126 – Values of charge and discharge capacity and relative coulombic efficiency for PAA-based electrodes produced at CIC energiGUNE: a) Entire test, up to 120 cycles; b) Focus on the rate capability test. 276

Figure 5.127 – Charge/discharge profiles for some representative cycles for PAA-based electrodes produced at CIC energiGUNE: a) Forming cycles; b) Rate capability test; b) Long-term test. 277
Figure 5.128 – Cycling voltammetry for the PAA-based electrodes produced at CIC energiGUNE..... 277
Figure 5.129 – Rheological characterization of the slurries produced with PAA_Alg: a) Flow curve and b) Creep recovery test. 278
Figure 5.130 – Laminates produced with a constant wet thickness of 50 µm and starting from the solution of PAA_Alg: a) PAA_Alg; b)PAA_Alg_C45; c) PAA_Alg_Complete. 279
Figure 5.131 – Peel test performed o the laminates produced starting with the PAA_Alg solution: a) PAA_Alg; b)PAA_Alg_C45, first replica; c) PAA_Alg_C45, second replica; d) PAA_Alg_Complete. 280
Figure 5.132 – Values of charge and discharge capacity and relative coulombic efficiency for PAA_Alg based electrodes produced at CIC energiGUNE: a) Entire test, up to 120 cycles; b) Focus on the rate capability test..... 281
Figure 5.133 – Charge/discharge profiles for some representative cycles for PAA_Alg based electrodes produced at CIC energiGUNE: a) Forming cycles; b) Rate capability test; b) Long-term test. 282
Figure 5.134 – Rheological characterization of the slurries produced with PAA_Pec: a) Flow curve and b) Creep recovery test. 283
Figure 5.135 – Laminates produced with a constant wet thickness of 50 µm and starting from the solution of PAA_Pec: a) PAA_Pec; b)PAA_Pec_C45; c) PAA_Pec_Complete. 283
Figure 5.136 – Peel test performed o the laminates produced starting with the PAA_Pec solution: a) PAA_Pec; b)PAA_Pec_C45; c) PAA_Pec_Complete. 284
Figure 5.137 – Values of charge and discharge capacity and relative coulombic efficiency for PAA_Pec based electrodes produced at CIC energiGUNE: a) Entire test, up to 120 cycles; b) Focus on the rate capability test..... 285
Figure 5.138 – Charge/discharge profiles for some representative cycles for PAA_Pec based electrodes produced at CIC energiGUNE: a) Forming cycles; b) Rate capability test; b) Long-term test. 286
Figure 5.139 – Cycling voltammetry for the PAA_Pec based electrodes produced at CIC energiGUNE. 286
Figure 5.140 – Rheological characterization of the slurries produced with PAA_CGN: a) Flow curve and b) Creep recovery test. 287
Figure 5.141 – Laminates produced with a constant wet thickness of 50 µm and starting from the solution of PAA_CGN: a) PAA_CGN; b)PAA_CGN_C45; c) PAA_CGN_Complete..... 288
Figure 5.142 – Peel test performed o the laminates produced starting with the PAA_CGN solution: a) PAA_CGN; b)PAA_CGN_C45; c) PAA_CGN_Complete. 289
Figure 5.143 – Values of charge and discharge capacity and relative coulombic efficiency for PAA_CGN based electrodes produced at CIC energiGUNE: a) Entire test, up to 120 cycles; b) Focus on the rate capability test..... 290

Figure 5.144 – Charge/discharge profiles for some representative cycles for PAA_CGN based electrodes produced at CIC energiGUNE: a) Forming cycles; b) Rate capability test; b) Long-term test. 291
Figure 5.145 – Cycling voltammetry for the PAA_CGN based electrodes produced at CIC energiGUNE. 291
Figure 5.146 – Rheological characterization of the slurries produced with PAA_TG: a) Flow curve and b) Creep recovery test. 292
Figure 5.147 – Laminates produced with a constant wet thickness of 50 µm and starting from the solution of PAA_TG: a) PAA_TG; b)PAA_TG_C45; c) PAA_TG_Complete. 293
Figure 5.148 – Peel test performed o the laminates produced starting with the PAA_TG solution: a) PAA_TG; b)PAA_TG_C45; c) PAA_TG_Complete. 293
Figure 5.149 – Values of charge and discharge capacity and relative coulombic efficiency for PAA_TG based electrodes produced at CIC energiGUNE: a) Entire test, up to 120 cycles; b) Focus on the rate capability test. 294
Figure 5.150 – Charge/discharge profiles for some representative cycles for PAA_TG based electrodes produced at CIC energiGUNE: a) Forming cycles; b) Rate capability test; b) Long-term test. 295
Figure 5.151 – Cycling voltammetry for the PAA_TG based electrodes produced at CIC energiGUNE. 295
Figure 5.152 – Rheological characterization of the slurries with the different additives: a) Flow curves of the binders alone; b) Hysteresis effect observe for the binders alone; c) Flow curve of the binders added with the C45; d) Flow curves of the complete slurries containing all the components (binders, graphite, C45 and silicon) 298
Figure 5.153 – Viscosity flow curve for silicon electrode slurry. Reproduced from [506] 299
Figure 5.154 – Evolution of measured SF during moisture balance analysis for complete slurry formulations at 60 wt.% SF. 300
Figure 5.155 – Comparison of the peel-test results based on the different binder compositions: a) PAA; b) PAA_Alg; c) PAA_Pec; d) PAA_CGN; e) PAA_TG 301
Figure 5.156 – Comparison of electrochemical performance of the electrodes produced at CIC energiGUNE based on the different binders combinations: a) Entire test, up to 120 cycles; b) Focus on the rate capability test. 302
Figure 5.157 – SEM images of the C) surface at different magnifications. Before cycling (500X): a), b). After cycling of the PAA-based electrodes: c), d) at 500X, e) at 1kX, and f) at 5kX. 303
Figure 6.1 – Schematic overview of the production and assembly steps involved in coin-cell fabrication, from slurry preparation to electrochemical testing. The red markers indicate the system boundaries adopted for the two LCAs considered in this study. 308
Figure 6.2 – The system boundary is indicated by the green rectangle, production steps are represented by red ovals, input materials and components by black ovals, and process outputs by blue squares. 313
Figure 6.3 – Schematic representation of electrode laminates produced at laboratory scale, showing the waste generated by manual punching process. 318
Figure 6.4 – Electrochemical results of the different anode materials tested in half-cell configuration using lithium metal as reference electrode: A) G-A; B) SC-A; C) SD-A. 320

Figure 6.5 – Pedigree matrix developed by Ecoinvent 328
Figure 6.6 – Relative percentage reduction of environmental impacts for 1 Ah of anode production across the impact categories 331
Figure 6.7 – Sankey diagram showing the contribution of different midpoint impact categories to the overall environmental impact of the three anode configurations (G-A, SC-A, SD-A). Each impact category is associated with a specific color, while the width of the flows represents their relative contribution. Due to scale differences, some contributions are not visually prominent, although all categories are reported for completeness. 332
Figure 6.8 – Relative percentage reduction of environmental impacts for 1 kg of anode production across the impact categories 335
Figure 6.9 – Relative contribution of anode components for G-A: a) including active material, conductive additive, binders, and current collector; b) excluding the current collector..... 338
Figure 6.10 – Relative contribution of anode components for SC-A: a) including active material, conductive additive, binders, and current collector; b) excluding the current collector. 339
Figure 6.11 – Relative contribution of anode components for SD-A: a) including active material, conductive additive, binders, and current collector; b) excluding the current collector. 339
Figure 6.12 – Comparison of the contribution of materials and processing steps to the overall environmental impact of G-A under different supply-chain scenarios: a) global and b) European. 341
Figure 6.13 – Comparison of the contribution of materials and processing steps to the overall environmental impact of SC-A under different supply-chain scenarios: a) global and b) European. 342
Figure 6.14 – Comparison of the contribution of materials and processing steps to the overall environmental impact of SD-A under different supply-chain scenarios: a) global and b) European. 342
Figure 6.15 – Comparison between the current global supply chain and the hypothetical European supply chain scenario: the percentage variation is shown for each case: values below zero indicate a reduction in impacts, whereas values above zero indicate an increase in impacts..... 343
Figure 6.16 – Normal distributions obtained from 10,000 MCS for GW related to the actual production of 1 Ah. For each chemistry, the upper panel shows the box plot including mean, median, and outliers, while the lower panel presents the corresponding frequency histogram: a) G-A; b) SC-A; c) SD-A. 346
Figure 6.17 – Normal distributions obtained from 10,000 MCS for GW related to the actual production of 1 kg. For each chemistry, the upper panel shows the box plot including mean, median, and outliers, while the lower panel presents the corresponding frequency histogram: a) G-A; b) SC-A; c) SD-A. 348
Figure 6.18 – Normal distributions obtained from 10,000 MCS for GW related to the theoretical European supply chain of 1 Ah. For each chemistry, the upper panel shows the box plot including mean, median, and outliers, while the lower panel presents the corresponding frequency histogram: a) G-A; b) SC-A; c) SD-A..... 349

Figure 6.19 – Normal distributions obtained from 10,000 MCS for GW related to the theoretical European supply chain of 1 kg. For each chemistry, the upper panel shows the box plot including mean, median, and outliers, while the lower panel presents the corresponding frequency histogram: a) G-A; b) SC-A; c) SD-A. 349
Figure 6.20 – Comparison of the normal distributions obtained from 10,000 MCS for GW across the three anode chemistries: (a) actual production of 1 Ah; (b) actual production of 1 kg; (c) European theoretical supply chain for 1 Ah; (d) European theoretical supply chain for 1 kg. 350
Figure 6.21 – Comparison of the MCS conducted for the actual global production and the theoretical European supply chain of 1 Ah: a) G-A; b) SC-A; c) SD-A. 351
Figure 6.22 – Percentage change in endpoint results under the European supply chain scenario relative to the actual global production [511]. 354
Figure 6.23 – The limit of the system boundaries is highlighted by the green rectangle, which include both the electrode manufacturing and full cell assembly processes, while production steps, input materials and components, and process outputs are represented by red ovals, black ovals, and blue squares, respectively. 357
Figure 6.24 – Average electrochemical results of the different full cells assembled with the different anode chemistries: A) G-A; B) SC-A; C) SD-A. 364
Figure 6.25 – Graphical representation of midpoint impact category results for the three anode chemistries calculated using the FU of 1 coin cell. 369
Figure 6.26 – Graphical representation of midpoint impact category results for the three anode chemistries calculated using the FU of 1 kWh. 372
Figure 6.27 – Relative contribution of full cell components produced using G-A as anode: a) including the entire assembly process, accounting for electricity, argon consumption in the glovebox, and all other components; b) excluding the assembly process, focusing only on anode, cathode, and electrolyte. 374
Figure 6.28 – Relative contribution of full cell components produced using SC-A as anode: a) including the entire assembly process, accounting for electricity, argon consumption in the glovebox, and all other components; b) excluding the assembly process, focusing only on anode, cathode, and electrolyte. 375
Figure 6.29 – Relative contribution of full cell components produced using SD-A as anode: a) including the entire assembly process, accounting for electricity, argon consumption in the glovebox, and all other components; b) excluding the assembly process, focusing only on anode, cathode, and electrolyte. 376
Figure 6.30 – Normal distributions obtained from 10,000 MCS for GW related to the full cell production using the FU of 1 coin cell. For each chemistry, the upper panel shows the box plot including mean, median, and outliers, while the lower panel presents the corresponding frequency histogram: a) G-A; b) SC-A; c) SD-A; d) Comparison between the three chemistries. 378
Figure 6.31 – Normal distributions obtained from 10,000 MCS for GW related to the full cell production using the FU of 1 kWh. For each chemistry, the upper panel shows the box plot including mean, median, and outliers, while the lower panel presents the corresponding frequency histogram: a) G-A; b) SC-A; c) SD-A; d) Comparison between the three chemistries. 379
Figure 6.32 – Percentage change in endpoint results depending on the anode chemistries and FUs: a) 1 coin cell; b) 1 kWh 380

Figure 6.33 – Comparative evaluation of GW impacts, contrasting the EF 3.1 and ReCiPe 2016 characterization models: a) 1 Ah of electrochemical capacity; b) 1 kg of manufactured anode. 386
Figure 6.34 – Comparative evaluation of GW impacts, contrasting the EF 3.1 and ReCiPe 2016 characterization models: a) 1 coin cell; b) 1 kWh..... 388

Chapter 1

1. Introduction

1.1. Worldwide energy transition challenge

The global energy system is undergoing a profound transformation driven by the urgent need to mitigate climate change. Anthropogenic greenhouse gas (GHG) emissions, largely associated with the combustion of fossil fuels for electricity generation, industry, and transportation, remain the primary driver of global warming. The transportation sector alone accounts for a significant fraction of global CO_2 emissions, with road transport representing the dominant share. The electrification of mobility, combined with the decarbonization of the electricity mix, is therefore considered one of the most effective strategies to reduce emissions in the coming decades. At the same time, the increasing utilization of renewable energy sources such as solar and wind introduces structural challenges to the stability of the power system. These sources are inherently intermittent, requiring efficient energy storage solutions to ensure grid reliability and load balancing. In this context, rechargeable batteries have become a key enabling technology.

Lithium-ion batteries (LIBs) currently dominate the electrochemical energy storage market due to their high gravimetric and volumetric energy density, high efficiency, and long cycle life. Their rapid technological development has enabled large-scale deployment in electric vehicles (EVs), stationary storage systems, and portable electronics. Despite their widespread adoption, current LIBs still face intrinsic limitations in terms of energy density and long-term environmental sustainability. In particular, the anode represents a key opportunity for improving energy density and enabling next-generation battery performance, especially when moving beyond conventional graphite toward higher-capacity materials. Graphite, which is currently the most used commercial anode material, offers excellent stability and cyclability but is limited by a intrinsically limited theoretical capacity

(~372 mAh g^{-1}). To overcome these limitations, significant research efforts are being directed toward the development of silicon-based anodes, which exhibit a much higher theoretical capacity (~4,200 mAh g^{-1}). However, the implementation of silicon introduces new challenges, including large volume expansion during cycling, mechanical instability, and difficulties in maintaining electrode integrity and processability. These aspects highlight the need for a comprehensive approach in which material design, electrode formulation, and manufacturing processes are optimized simultaneously, rather than independently.

Within this evolving energy panorama, the European Green Deal represents a strategic framework aimed at transforming the European Union into a modern, competitive and resource efficient economy [1]. It targets a reduction in greenhouse gas emissions of at least 50%, and progressively up to 55%, by 2030, while establishing the legally binding objective of climate neutrality by 2050 through the European Climate Law [2]. The initiative promotes a sustainable transition that balances environmental protection, economic viability and social equity.

In addition, the Green Deal supports investments in innovation, clean technologies and sustainable infrastructure. In this context, recent European research roadmaps highlight the need for a paradigm shift in battery development strategies, moving from incremental improvements toward a more integrated and accelerated research framework. In particular, the BATTERY 2030+ initiative proposes a chemistry-neutral approach aimed at enabling the discovery and optimization of next-generation batteries through advanced modelling, artificial intelligence and high-throughput experimentation. As schematically illustrated in ***Figure 1.1*** [3] of the roadmap, the future battery research ecosystem is expected to rely on a strongly interconnected loop between materials discovery, digital tools, and manufacturing innovation, ultimately accelerating the transition toward sustainable and high-performance energy storage systems.

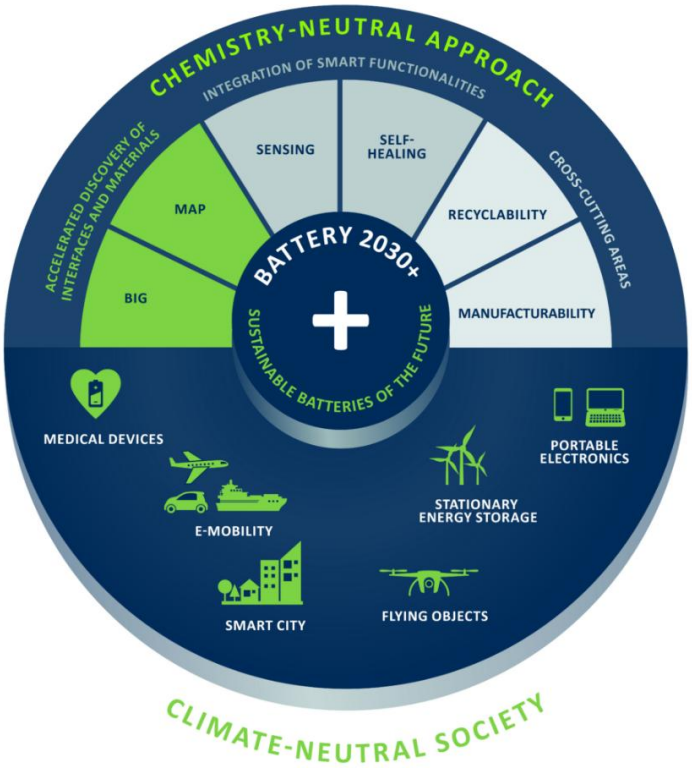

Figure 1.1 – BATTERY 2030+ vision highlighting a chemistry-neutral strategy for the development of sustainable, high-performance batteries tailored to different applications, based on interconnected research themes and tools aimed at accelerating battery discovery and innovation [3].

Alongside advances in battery materials and electrochemical performance, the industrialization of cell manufacturing has become a strategic priority. The rapid growth in global demand for electrochemical energy storage systems, particularly for electric mobility and stationary applications, has led to the emergence of so-called gigafactories: highly automated production facilities designed to manufacture battery cells at multi-GWh annual capacities. The deployment of such infrastructures is essential not only to reduce production costs through economies of scale, but also to secure supply chains and strengthen technological sovereignty. In this perspective, the European Union is actively promoting the establishment of gigafactories across its territory in order to support the electrification of transport, accelerate the energy transition, and reduce dependence on extra-European battery manufacturing hubs. A map illustrating the gigafactories active in Europe in 2026 is reported in ***Figure 1.2*** [4]. The increasing diffusion of these large-scale manufacturing plants is therefore expected to play a crucial role in enabling the widespread adoption of sustainable energy storage technologies in the coming decades.

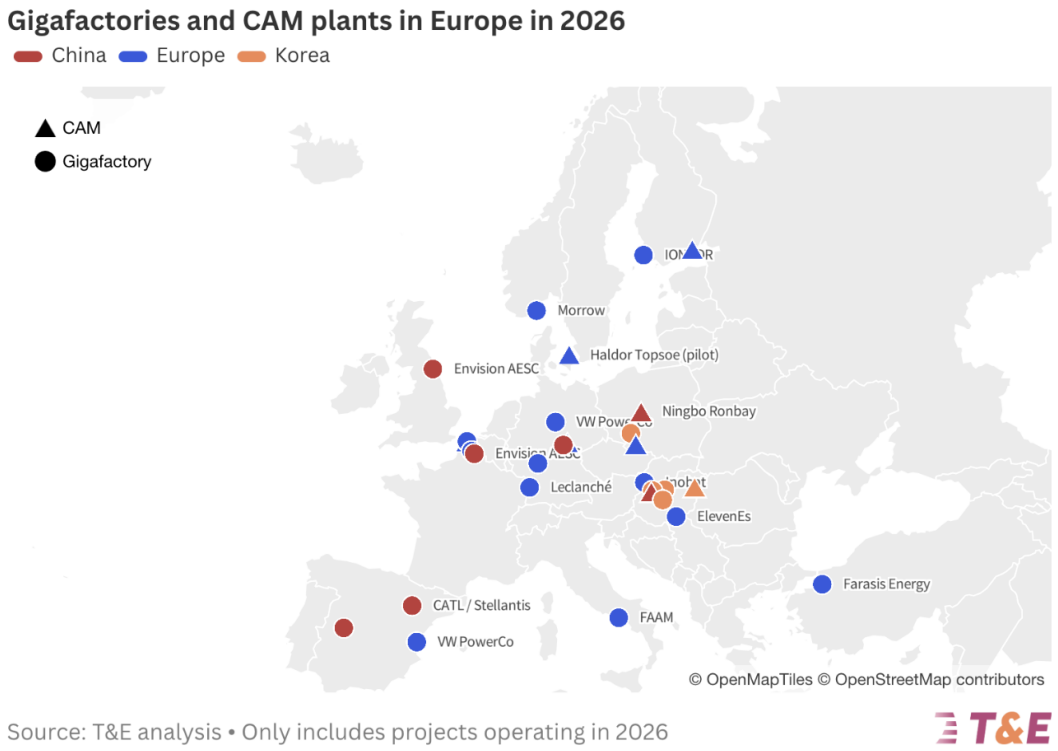

Figure 1.2 – Gigafactories and cathode active material (CAM) plants in Europe in 2026 [4].

Beyond material selection, the manufacturing process plays a crucial role in determining both the performance and the environmental impact of LIBs. In particular, electrode production based on slurry processing represents one of the most energy-intensive and technically critical steps. The preparation of the slurry, its rheological behavior, and the subsequent coating and drying steps directly influence electrode microstructure, adhesion, and electrochemical performance. At the same time, these processes significantly contribute to the overall energy consumption of battery manufacturing, especially during energy-intensive steps such as solvent evaporation. Therefore, optimizing electrode manufacturing requires balancing process efficiency, material utilization, and final electrode performance, especially when transitioning from laboratory-scale to pilot-line and industrial production.

1.2. environmental sustainability and supply chain challenges

Recent comparative analyses indicate that the carbon footprint of LIBs is strongly influenced by the geographical location of manufacturing and by the electricity mix used during production. In particular, batteries produced within Europe, especially when powered by predominantly renewable electricity, can exhibit significantly lower greenhouse gas emissions compared to those manufactured under more carbon-intensive supply chains. This effect is illustrated

in ***Figure 1.3*** [5], which compares the climate impact of different battery supply chain configurations. The results show that a European-based production powered mainly by renewable energy can reduce CO_2 emissions per kWh by more than 60% compared to a fully imported supply chain dominated by coal-based electricity. Even when considering the average European grid mix, a substantial reduction in carbon intensity is observed.

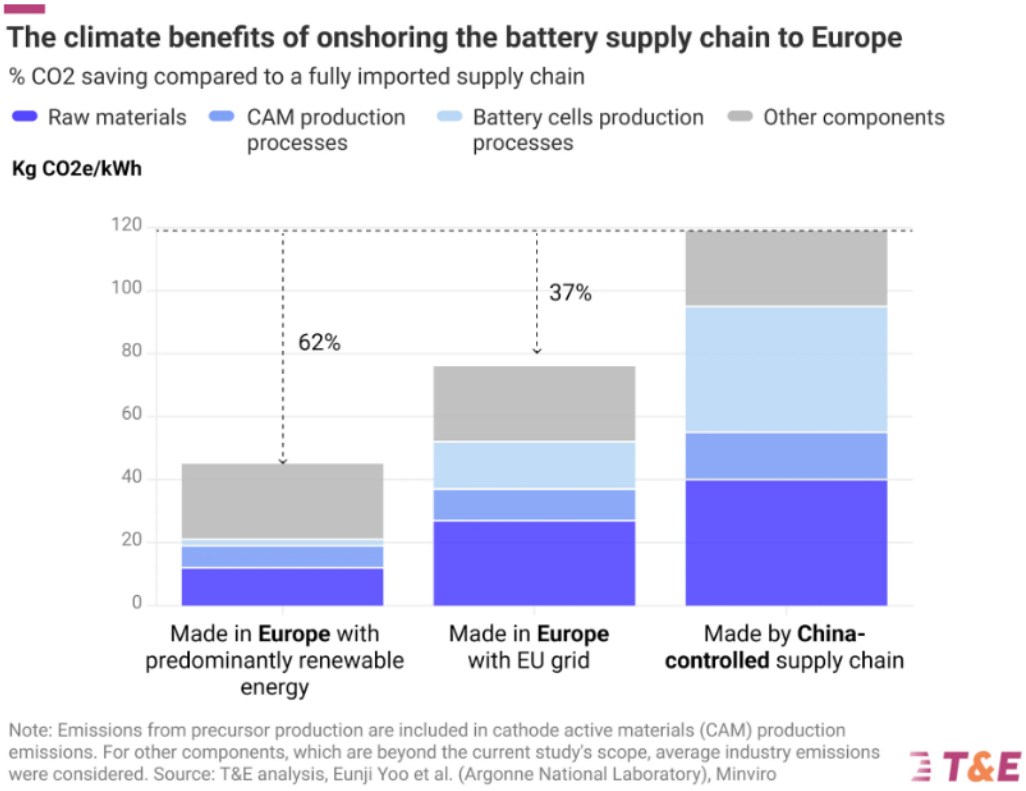

Figure 1.3 – Climate advantages associated with relocating the battery supply chain to Europe, quantified in terms of kg CO_2-Eq per kWh and as a percentage decrease relative to a supply chain dominated by Chinese production [5].

In addition, the extraction, synthesis and processing of raw materials represent the starting point of the entire battery production chain. These activities are geographically concentrated in a limited number of regions worldwide, often identified as critical hotspots (***Figure 1.4*** [6]). Such concentration reflects both the uneven distribution of mineral resources, including lithium, cobalt, nickel and natural graphite, and the localization of industrial processing capacities. This spatial imbalance can generate supply risks, price volatility and geopolitical dependencies, highlighting the importance of diversifying sourcing strategies and strengthening regional value chains. Consequently, securing access to raw materials and developing sustainable extraction and refining practices have become key priorities for the large-scale deployment of battery technologies.

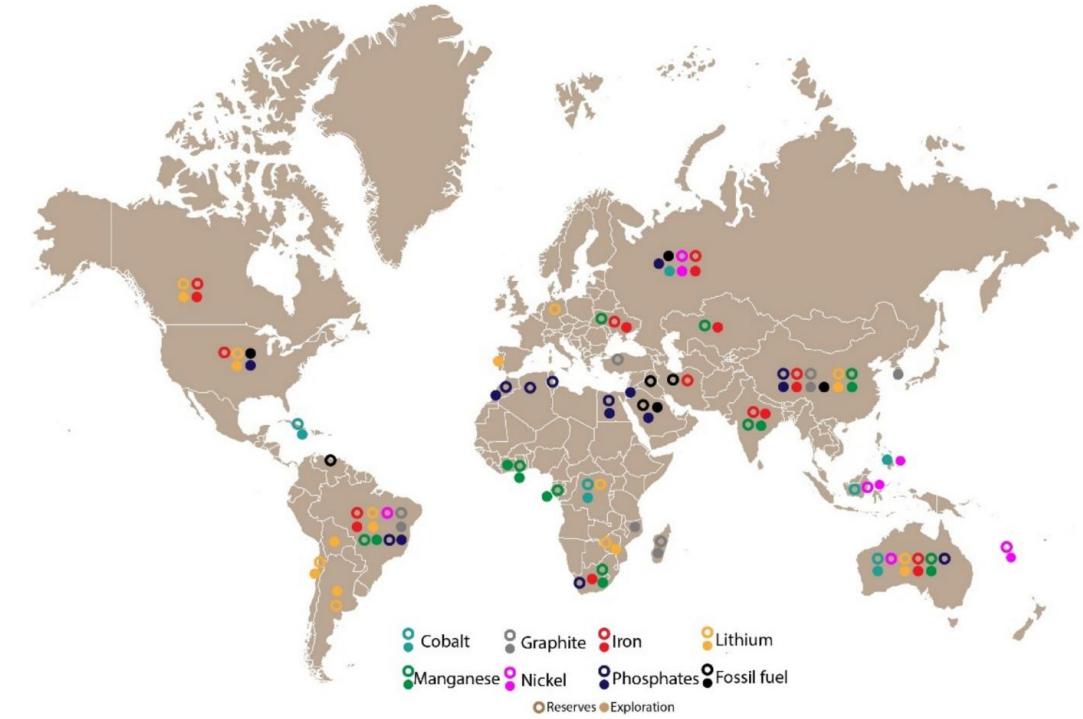

Figure 1.4 – Global map showing the distribution of mineral reserves and exploration areas for key raw materials, based on data from the US Geological Survey International Minerals Statistics and Information [6].

These considerations underline that battery environmental sustainability is not determined solely by material chemistry, but also by the origin of raw materials, manufacturing location, electricity mix, and overall process efficiency. For this reason, reducing emissions from battery production requires a comprehensive approach that combines technological improvements with changes in supply chains and the transition to cleaner energy sources. Beyond supply chain environmental sustainability, the technical performance of battery systems must also be evaluated, particularly when moving from cell-level parameters to full pack-level operation. One of the main challenges in this transition is the reduction in gravimetric and volumetric energy density, which can significantly affect the overall efficiency of the system. In addition, unwanted chemical and electrochemical side reactions may progressively lead to capacity fading during battery operation. From an industrial perspective, the commercial viability of advanced battery technologies also depends on manufacturing aspects, including process scalability and the design of solutions compatible with recycling and circular economy principles.

In this context, rechargeable batteries characterized by high efficiency represent a key enabling technology for energy storage across a wide range of applications, as also recognized within the European Green Deal framework. Their deployment can support the transition toward sustainable and smart mobility and contribute to the provision of clean, affordable and secure energy. In addition, rechargeable batteries can support industrial transformation toward a more

circular economy. In this context, Life Cycle Assessment (LCA) emerges as a key tool to quantitatively evaluate the environmental impact of battery production [7]. However, traditional LCA studies are often based on secondary data and are conducted independently from experimental research, limiting their ability to capture the real impact of process innovations. A more advanced approach consists in integrating LCA directly with experimental activities, using primary data collected during electrode production and testing. This enables a more accurate and dynamic evaluation of how changes in materials, formulations, and process parameters affect both environmental impacts and electrochemical performance. Such an integrated methodology is essential to identify effective strategies for reducing the environmental footprint of batteries while simultaneously improving their performance and manufacturability. This dual challenge, combining performance optimization and environmental sustainability, defines the core research problem addressed in this dissertation.

1.3. Goal of the dissertation

As discussed above, the simultaneous achievement of high performance and environmental sustainability represents a central challenge in modern lithium ion battery development. The main objective of this Ph.D. research is to develop an integrated framework for the design of LIB anodes in which electrochemical performance, manufacturing scalability, and environmental sustainability are addressed simultaneously rather than sequentially. Traditionally, battery research has focused primarily on maximizing electrochemical metrics such as specific capacity and cycle life, while environmental sustainability considerations have often been evaluated only at a later stage. This work challenges that approach by embedding LCA directly within the experimental development of electrode materials and processes.

The research investigates how each step of electrode manufacturing, from material selection and slurry formulation to mixing, coating, and drying, influences both technical performance and environmental impact. The availability of a small pilot line at Politecnico di Torino (Environmental Park), combined with experimental activities conducted at CIC energiGUNE, enabled the collection of primary foreground data under controlled and scalable conditions. These data constituted the basis for a quantitative LCA, performed in collaboration with COESIA, allowing a direct comparison of alternative material and process configurations.

Within this multi-objective perspective, the research was structured around three interconnected goals:

- ***Reduction of energy demand and process-related emissions*** through the optimization of aqueous electrode manufacturing, including the

replacement of organic solvents, increased deposition rates, and reduced drying time.

- ***Progressive enhancement of anode performance***, moving from conventional graphite to silicon-composite (10 wt% Si) and silicon-dominant (80 wt% Si) anodes, with the aim of increasing areal capacity and energy density while maintaining manufacturability.
- ***Development of advanced aqueous binder systems*** tailored for high-silicon-content electrodes, including the implementation of natural polysaccharides and the systematic investigation of slurry rheology to ensure mechanical integrity, process stability, and scalability.

By integrating laboratory experimentation, electrochemical characterization, and environmental assessment within a unified framework, this dissertation demonstrates that high-performance battery materials can be developed alongside sustainable manufacturing strategies, emphasizing the need to balance performance and environmental sustainability. Within this approach, it is worth noting that while circular economy benefits are qualitatively discussed, they are not analytically quantified in the final footprint evaluation, as the end-of-life (EoL) phase falls outside the cradle-to-gate boundaries of this study.

1.4. Summary of dissertation

The dissertation is structured to progressively connect fundamental battery principles, manufacturing aspects, experimental optimization, and environmental assessment within a single integrated framework.

Chapter 2 provides a comprehensive overview of LIBs, describing their working principles, key electrochemical mechanisms, and fundamental performance parameters. Particular attention is given to electrode materials, as these represent the central focus of this research, with an in-depth discussion of graphite and silicon-based anodes.

Chapter 3 focuses on battery manufacturing, introducing the concept of Technology Readiness Level (TRL) and outlining the main production steps, from raw materials to final pack assembly. A detailed analysis is devoted to electrode fabrication, including slurry preparation, coating, drying, and calendering. The chapter also presents the fundamentals of rheology and discusses its critical role in slurry-based electrode processing, highlighting the parameters that govern processability and scalability.

Chapter 4 introduces the LCA methodology adopted in this work. The chapter defines the system boundaries, functional unit, foreground and background data structure, and uncertainty assessment approach, establishing the methodological framework for the environmental sustainability evaluation.

Chapter 5 reports the experimental activities carried out during the Ph.D., structured into four main research lines corresponding to the different anode

chemistries investigated. The first section is dedicated to graphite-based anodes. It compares laboratory-scale production with small pilot-line manufacturing, analyzing how different facilities and process parameters influence electrode morphology, electrochemical performance, and reproducibility. Particular attention is given to the identification and resolution of critical issues related to electrochemical testing, followed by process optimization and detailed morphological and electrochemical characterization. The second section focuses on silicon-composite anodes produced using MTI materials. This part describes the development and stabilization of the production process for silicon composite-based electrodes, with additional emphasis on binder systems and the implementation of natural polysaccharides as functional additives to improve mechanical integrity and processability. The third section addresses silicon-composite anodes developed within the GIGAGREEN project framework. Here, the focus is on process development and optimization under project-specific constraints, highlighting the integration between material selection, manufacturing parameters, and electrochemical validation. The final section is devoted to silicon-dominant anodes. It presents the development and optimization of the production process for high-silicon-content electrodes, with particular emphasis on binder engineering and the use of natural polysaccharides as additives. A dedicated analysis of slurry rheology is included, based on experimental work conducted during the research period at CIC energiGUNE, to better understand process stability and scalability.

Chapter 6 presents the LCA results for the investigated anode production processes and includes a preliminary assessment at full-cell level, providing a comparative environmental sustainability analysis of the different chemistries. The chapter establishes a cradle-to-gate inventory derived from laboratory experiments and defines the scaling approach required for full-cell integration. To ensure a comprehensive overview, diverse impact assessment methodologies covering both midpoint and endpoint levels are utilized, while sensitivity analyses are applied to verify the robustness of the models.

The final chapter summarizes the main findings of the research and outlines perspectives for future developments, particularly in the integration of high-performance anode materials with sustainable manufacturing strategies.

1.5. Original Scientific Contributions of the Thesis

To clearly delineate the novel achievements of this work from the existing state of the art, this section highlights the primary scientific and technological contributions delivered by this dissertation. The core novelty of this research lies in its integrated, multi-objective approach, which simultaneously addresses material optimization, slurry rheology, pilot-scale manufacturability, and environmental environmental sustainability.

- ***Development of an Integrated Multi-Objective Framework***: to overcome the limitations of classic, fragmented development steps, this work establishes a comprehensive methodology that simultaneously addresses material selection, slurry rheology, electrode manufacturing scalability, and environmental sustainability. This integration represents a fundamental transition, shifting away from traditional sequential optimization processes that treat performance, processing, and ecological footprint as independent, consecutive steps. Instead, it treats them as inherently interconnected aspects, optimizing all target criteria in parallel to effectively bridge the gap between lab-scale discovery and pilot-scale production.
- ***Elucidation of the Silicon Scaling Gap***: A systematic comparative study from laboratory to pilot-line scale demonstrated that increasing the silicon content, from silicon-composite (~10 wt% Si) to silicon-dominant (~80 wt% Si) systems, shifts the primary failure bottlenecks from electrochemical degradation to processability, slurry instability, and mechanical cohesion issues during scale-up.
- ***Binder Engineering and Rheological Optimization***: The study identified poly(acrylic acid) (PAA)-based formulations as superior alternatives to conventional CMC/SBR compositions for high-silicon electrodes. Furthermore, it introduced the novel incorporation of specific natural polysaccharides as functional additives (at 1 wt%), providing a robust strategy to balance slurry rheology, enhance particle cohesion, and prevent mechanical defects during pilot-scale coating.
- ***Interfacial Engineering via Advanced Laser Texturing***: This research expanded current collector engineering by implementing Direct Laser Interference Patterning (DLIP) on copper foils. This specific surface modification lowered interfacial resistance and significantly enhanced mechanical adhesion at the electrode-current collector interface, directly translating into improved electrochemical capacity retention.
- ***Primary Experimental Data-Driven LCA***: Unlike literature studies reliant on secondary data, this work implements a cradle-to-gate LCA entirely built upon primary foreground data collected from actual laboratory production. The model quantifies up to a 40% carbon footprint reduction for silicon-composite and up to 97% for silicon-dominant anodes (considering 1 Ah as functional unit) compared to graphite. Furthermore, it provides a comprehensive sensitivity and uncertainty analysis comparing global and European supply chain scenarios.

Chapter 2

2. Li-ion Batteries (LIBs)

2.1. General overview of batteries

The origin of batteries dates back to the late 18th century, as well represented in ***Figure 2.*** [8], when the Italian scientist Alessandro Volta described for the first time a battery. After that, history passed through many revolutionary discoveries thanks to great scientists. Nevertheless, the most important improvement has occurred in the last 50 years, thanks to the introduction of lithium inside batteries, which has quickly led to their commercialization by Sony in 1991. This moment represented a turning point for the entire technology world and, as a result, a Nobel Prize was assigned in 2019 to John B. Goodenough, M. Stanley Whittingham and Akira Yoshino "for the development of lithium-ion batteries" [9].

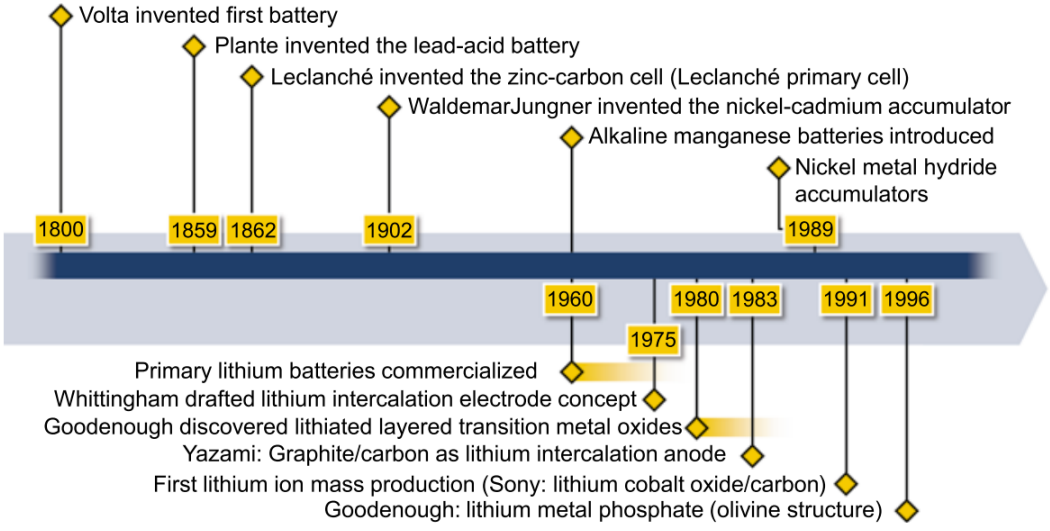

Figure 2.1 – Brief storyline of batteries. Reproduced with permission from [8]

Research and technological innovation have become increasingly important as the world faces a dramatic climate crisis largely driven by human activity. In this way, the use of fossil fuels to produce energy needs to be drastically reduced to limit emissions and reduce CO_2 and other molecules which are responsible for the climatic crisis [10]. Among the many technological innovations proposed, storing intermittent renewable energies (sun, wind, etc.) appears to be the most promising. This can be done using energy-storage systems, among which batteries are the most widely used, thanks to their high efficiency [11].

It is possible to divide the batteries into two different categories: the primary batteries and the secondary batteries. The primary batteries are systems that directly convert chemical energy into work, in this case, the electrochemical reaction that occurs inside the cell is not reversible. The secondary batteries are rechargeable system because the electrical energy is converted back into chemical energy, thanks to the reversibility of the electrochemical reaction during the charge step. The rechargeable batteries can be classified according to the cell chemistry, and some examples from the past to the present can include lead-acid, nickel-cadmium, nickel-metal-hydride and lithium-ion [12].

LIBs were first commercialized in 1991, and their market demand has since grown exponentially [13]. Currently, Li-ion batteries are widely diffused as rechargeable batteries in different fields of application, such as portable devices (cell phones, laptops, cameras) healthcare and medical equipment, electric vehicles, and large-scale energy storage systems.

Among all types, Li-ion batteries have become dominant in the market thanks to their high energy density, long lifespan, and high-temperature operation compared to other chemistries, such as lead-acid, alkaline or nickel-cadmium, as it is possible to observe in the Ragone plot reported in ***Figure 2.2*** [14]. Furthermore, LIBs are characterised by longer cycle life, higher cell voltage and very low self-discharge, which therefore prolongs their use. A great comparison of the characteristics between the different chemistries is summarized in ***Table 2.1*** [15]. However, lead-acid, alkaline or nickel-cadmium batteries are still used because of their convenience in terms of costs and safety issues.

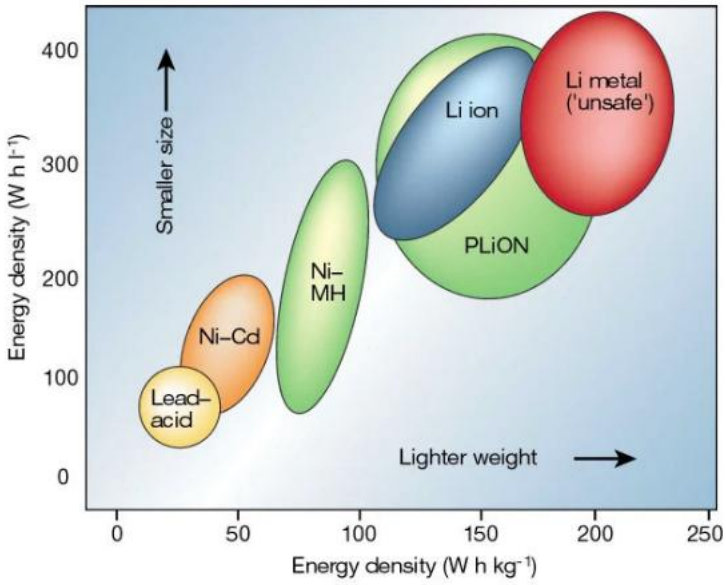

Figure 2.2 – Ragone plot of the most common batteries technologies [14]

Table 2.1 – Comparison of the properties of the commercialized rechargeable batteries, depending on their chemistry [15]

Properties	Rechargeable Battery Chemistry			
	Li-ion	**Lead Acid**	**NiMH**	**Ni–Cd**
Specific energy density (Wh/kg)	90–190	30–55	60–120	45–80
Cycle life (80% of initial capacity)	500–2000	200–300	300–500	1000
Cell voltage (V)	3.3–3.8	2.0	1.2	1.2
Self-discharge/month at 25 °C	<5%	5–15%	30%	20%
Safety	Protection circuit is mandatory		Thermally stable	
Commercialized in	1991	1881	1990	1950
Toxicity	Low	High	Low	High

Undoubtedly, many efforts have been made during the years to continually improve many aspects: starting from a higher energy density for electric vehicles (EV) applications, lower costs and environmental impact. Considering this aspect, the attention of the industry is focused on the development of electrode production processes based on water as a solvent and the choice of materials without the presence of critical raw materials. A greater discussion about the material involved and the production process will be given in the following chapters.

2.2. Fundamental parameters and terminology

Many parameters are currently used to characterize a cell, starting from the electrochemical performance, up to the economic or environmental aspects. These parameters depend on the specific chemistries used in the electrode production, which directly affect the chemical reactions, the transport phenomena and the diffusion kinetics. The most common cell parameters are described below [16–18].

- **Theoretical Capacity [Ah]** – This value is specific to a given compound, related to its molecular mass and chemical formulation, relative to the number of electrons that move inside the battery during an ideal charge-discharge process. It can be calculated using ***Equation 2.1***, where x is the number of moles of active material (AM) inside the electrode, n is the number of equivalent electrons involved in the electrochemical reactions and F is the Faraday constant.

$$Q_t = xnF$$

Equation 2.1

- **Capacity [C or Ah]** (or Nominal Capacity) – Total amount of electric charge that a power source can deliver under specific discharge conditions (discharging current, cut-off voltage, temperature, type and amount of AM). The capacity of a cell can be defined by the ***Equation 2.2***, which expresses capacity over a specified time range. Under constant-current conditions, ***Equation 2.2*** simplifies to ***Equation 2.3***.

$$Q = \int_{t1}^{t2} I(t)dt$$

Equation 2.2

$$Q = It$$

Equation 2.3

- **Specific Capacity [Ah g^{-1}]** – Defined as the capacity of an electrochemical cell expressed per unit of mass of AM.
- **Practical Capacity [Ah g^{-1}]** – Refers to the usable portion of the theoretical capacity of the electrode material. It is typically slightly lower than Specific Capacity, due to inefficiency and losses during regular operation of the battery.
- **Volumetric Capacity [Ah cm^{-3}]** – Defined as the capacity of an electrochemical cell expressed per unit volume of AM.
- **Mass loading (ML) [mg cm^{-2}]** – It is defined as the amount of AM on the considered area, expressed in mg cm^{-2} (***Equation 2.4***).

$$ML = \frac{(electrode\ weight - current\ collector\ weight) * active\ material\ ratio}{electrode\ area}$$

Equation 2.4

- **Areal Capacity (AC) [mAh cm^{-2}]** – It is defined as the capacity of the electrode per areal unit (***Equation 2.5***).

$$AC = \frac{ML * Theoretical\ Capacity}{1000}$$

Equation 2.5

- **Energy [Wh or J]** (or Nominal Energy) – Defined as the product of capacity and the average operating voltage delivered by the system.

$$E = QV$$

Equation 2.6

- **Specific Energy [Wh kg^{-1}]** (or Gravimetric Energy Density) – Represents the energy content per unit mass, typically in Watt-hours per kilogram. One watt-hour equals the consumption of one watt for one hour.
- **Energy Density [Wh m^{-3}]** – Represents the amount of energy stored per unit volume, typically reported in Watt-hours per cubic meter.
- **Power [W]** – Defined as the product of current and working voltage; equivalently, it represents the energy transferred per unit of time.

$$P = Vi = \frac{QV}{t} = \frac{E}{t}$$

Equation 2.7

- **C-rate** – Measures the rate of charge (or discharge) of a battery relative to its nominal capacity. The C-rate can be associated with the time required for full charge or discharge: *e.g.*, 1C corresponds to the current required to charge or discharge a cell completely in 1 hour.
- **Current density [A m^{-2}]** – Defined as the ratio of the total current flowing through the electrode to its geometric surface area:

$$j = \frac{I}{A}$$

Equation 2.8

- **Open-circuit voltage (OCV) [V]** – Represents the potential difference between the negative and positive electrodes under no-current conditions. The corresponding expression under standard conditions is given in ***Equation 2.9***:

$$OCV\ cell = E^0_{anode} - E^0_{cathode} = \Delta E^0 = -\frac{\Delta G^0}{nF}$$

Equation 2.9

- **Overpotential and overvoltage [η]** – It is the difference between the cell potential and the OCV, during the charge and discharge phase.
- **Coulombic Efficiency [%]** – Represents the efficiency with which electrons are transferred in a cell, expressed as the ratio between discharge and charge capacity accumulated during the previous charge phase.

$$CE = \frac{Q_{discharge}}{Q_{charge}}$$

Equation 2.10

- **Initial Coulombic Efficiency (ICE) [%] –** Refers to the Coulombic Efficiency of the first cycle. It is an important parameter to evaluate the irreversible reactions occurring during the first lithiation and de-lithiation processes.
- **Self-discharge** – Phenomenon corresponding to the spontaneous loss of battery capacity under open-circuit conditions, caused by internal chemical side reactions and/or micro-short-circuits.
- **Capacity retention [%]** – It is calculated as the ratio between the discharge capacity measured after a selected cycle number and the discharge capacity measured at the beginning of cycling, and is used as an indicator of electrochemical stability during long-term operation.
- **State of Charge (SoC) [%]** – It is defined as the ratio between the charge still available in the battery and the maximum charge it can deliver, expressed as a percentage (***Equation 2.11***). In the equation, Q refers to the capacity directly supplied to or delivered by the battery; Q_0 indicates the battery's initial capacity, and Q_{max} represents its maximum storable capacity.

$$SoC = \frac{Q + Q_0}{Q_{max}} \cdot 100$$

Equation 2.11

- **State of Health (SoH) [%]** – It refers to the state of health of the battery, indicating how much it has degraded compared to the initial value. It is generally calculated as the ratio between the current capacity and the initial value, expressed as a percentage, and provides an estimate of how long it takes to reach the end of life.
- **Cycle life** – Indicates how many times the battery can be charged/discharged before its performance deteriorates. More specifically, it corresponds to the number of complete charge-discharge cycles before the capacity drops below a fixed threshold (typically 80% of the original capacity). This parameter strongly depends on the materials used and the operating conditions (*e.g.*, temperature, charge/discharge rate).

2.3. Working mechanism of LIB

LIBs are complex electrochemical systems that can be organized into multiple hierarchical levels, of increasing complexity: the basic unit is the cell; multiple cells are assembled into modules, and modules are finally combined into battery packs. The entire system is managed by the Battery Management System (BMS),

responsible for monitoring, balancing, and ensuring the reliability of the battery operation [19]. This Ph.D. work is focused only on the basic unit of a battery, so the work was carried out at the cell level.

Inside a Li-ion cell, there are four main components responsible for proper operation (schematically shown in ***Figure 2.3*** [8]):

- Anode (– , negative pole, during discharge): site of oxidation, where electrons are released. The anode is commonly made of carbonaceous materials such as graphite, which can reversibly intercalate lithium ions between graphene planes.
- Cathode (+ , positive pole, during discharge): site of reduction, where electrons are inserted. The cathode generally consists of transition-metals oxides with a stable crystal lattice; their layered or tunneled structures provide pathways for lithium-ion diffusion.
- Electrolyte: medium through which Li-ions move between electrodes via the separator. It is typically composed of lithium salt dissolved in organic carbonate solvents.
- Separator: a porous, electrically insulating membrane that separates the electrodes to prevent short-circuits while allowing ionic conduction. Common materials include polyethylene (PE) and polypropylene (PP)-based polymers.

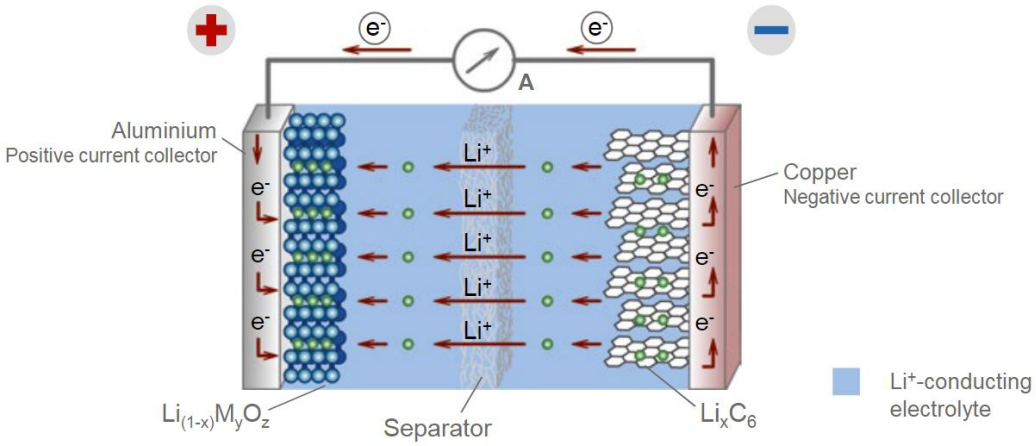

Figure 2.3 – Set-up of a lithium-ion battery (shown is the discharge process). Reproduced with permission from [8]

In general, batteries are devices that convert chemical energy stored in the AMs into electrical energy through electrochemical reduction-oxidation (redox) reactions [20]. The overall electrochemical process can be described as two half-reactions, oxidation and reduction, occurring simultaneously. Oxidation is the reaction associated with the loss of one or more electrons from a chemical species, while reduction is the reaction where one or more electrons are accepted on a chemical species. These two species involved in the redox reaction are called redox pairs. Specifically, in LIBs, the species involved in redox reactions are

located on the opposite electrodes of the battery: cathode (site of reduction) and anode (site of oxidation).

It is possible to write the overall reaction (***Equation 2.12***) that occurs inside of a LIB, considering the anode half-reaction with a graphite-based anode (LiC_6, ***Equation 2.13***) and a cathode half-reaction with a generic metal oxide ($Li_xM^nO_y$, ***Equation 2.14***) where M is a transition metal (Mn, Ni, Co) [21]:

Full reaction (Discharge)

$$Li_xC_6 + Li_{(x-1)}M^{n+1}O_{ys} \rightleftharpoons C_6 + Li_xM^nO_y$$

Equation 2.12

Anode reaction (LiC_6)

$$Li_xC_6 \rightleftharpoons C_6 + xLi^+ + e^-$$

Equation 2.13

Cathode reaction ($Li_xM^nO_y$)

$$Li_{(x-1)}M^{n+1}O_y + xLi^+ + e^- \rightleftharpoons Li_xM^nO_y$$

Equation 2.14

As already mentioned, LIBs are rechargeable systems, meaning that the reactions are reversible and can proceed in both directions: hence, the cell can be charged or discharged. In ***Figure 2.4*** [22], both the charge and the discharge steps are described. During discharge, well represented by the green arrows, electrons flow from the anode, which is oxidized through the external circuit up to the cathode, which is reduced. In this way, the battery can provide electricity to the external world. Meanwhile, charge neutrality is maintained by the migration of Li-ions from anode to the cathode through the electrolyte. After the complete discharge of a LIB, it must be recharged, and this process is exactly the reverse of the discharge. During charging, the non-spontaneous process, the applied current extracts electrons from the positive electrode and drives them to the negative electrode, forcing Li^+ ions to migrate in the same direction through the electrolyte This alternating movement of Li-ions between the electrodes is commonly known as *shuttling* or *rocking chair* mechanism.

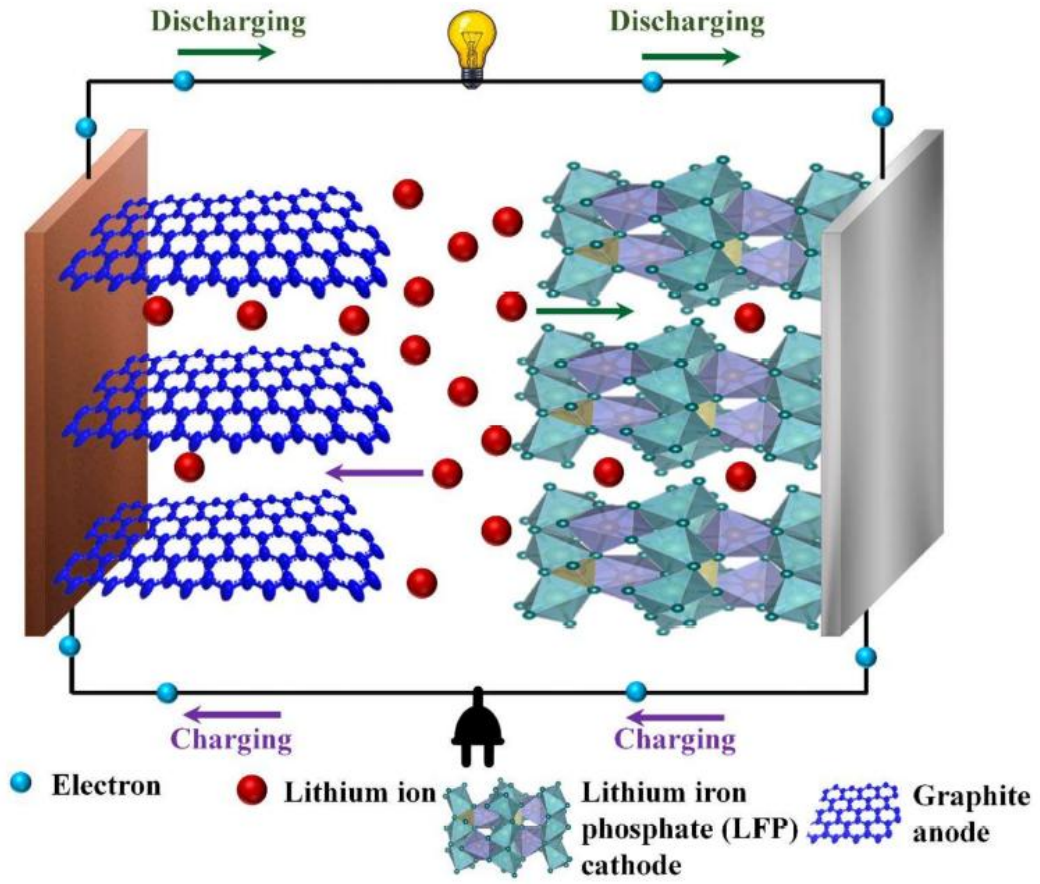

Figure 2.4 – Schematic representation of the main components inside a LIB. As example, anode and cathode are represented by some of the most common material actually used for their production [22]

The theoretical amount of electrical energy that an electrochemical cell can deliver is determined by the cell potential and the number of electrons transferred between electrodes [23]. In this way, it is possible to define the Gibbs free energy (ΔG) (***Equation 2.15***) as the change in internal energy:

$$\Delta G = -nFE$$

Equation 2.15

Where n is the number of electrons transferred in the reaction, F is the Faraday constant (product of electron charge and Avogadro's number) and E is the voltage of the cell, which directly depends on the electrochemical reaction considered [24]. Based on ***Equation 2.15***, the energy produced can be increased in two ways: first, by using AMs that exchange a greater number of electrons, and second, by increasing the potential difference between the electrodes. The latter approach has motivated extensive research on the development of high-voltage cathode materials [25,26].

However, these considerations are valid only at the theoretical level; in real applications, the system is far more complex involving additional reactions and kinetic limitations. During battery operation, charge-transfer and mass-transport

introduce kinetic limitations that cause polarization and reduce efficiency. Consequently, the actual available energy is lower than the theoretical one, as part of the energy is dissipated as heat due to polarization losses.

From the typical discharge curve of a battery, reported in ***Figure 2.5*** [23], it is possible to identify three main types of polarization, described below [27,28].

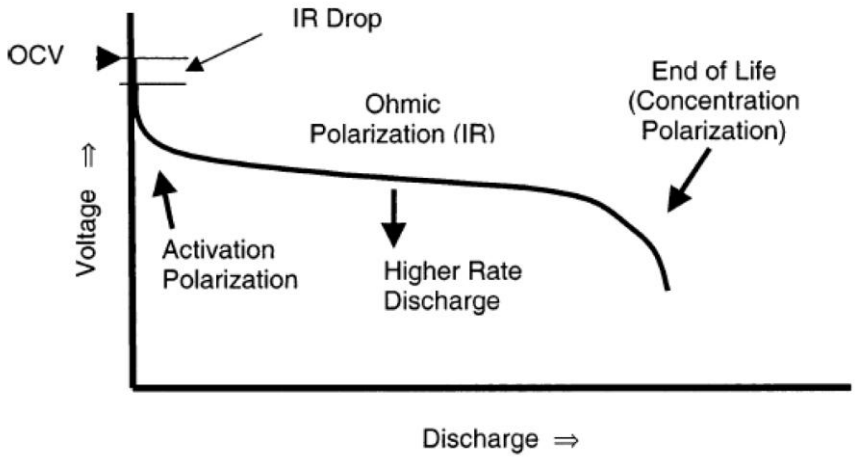

Figure 2.5 – Typical discharge curve of a generic battery, where the main important polarization types are highlighted. Reproduced with permission from [23]. Copyright 2004 American Chemical Society.

- ***Activation polarization*** (also called *electrochemical polarization*): corresponds to the initial voltage drop during discharge. It is due to slow electrode-reaction kinetics at the electrode-electrolyte interface.
- ***Ohmic polarization***: results from the internal resistance of cell components and contact losses between them, causing a voltage drop during the operation. The intensity is directly proportional to the applied current: the higher the current, the greater the voltage drop.
- ***Concentration polarization***: it occurs at the electrode surface and is due to differences in lithium-ion concentration between the electrode interface and the bulk electrolyte. These concentration gradients lead to uneven ion distribution within the electrolyte phase. The main cause of this effect is the mass-transfer resistance experienced by ions as they move through the electrolyte and separator, from one electrode to the other. As a result, the limited availability of lithium ions at the electrode surface slows the electrochemical reactions, producing an additional voltage drop in the discharge curve.

Hence, it is possible to define the value of the polarization (η) as the difference between the voltage of the cell at open circuit (E_{OCV}) and the terminal cell voltage after the discharge process (E_T):

$$\eta = E_{OCV} - E_T$$

Equation 0.16

Analyzing the discharge curves is an essential method to properly characterize the cell. Their shape allows the determination of total capacity and evaluation of how operating conditions, like temperature or current density, affect final performance.

In conclusion, Li-ion cells are highly complex systems, and their available energy depends primarily on electrode reactions. However, the involvement of multiple materials and interfaces slows charge-transfer kinetics and ion diffusion, leading to energy losses. Therefore, optimized separator and electrolyte selection, electrode manufacturing, and cell design play a crucial role in enhancing performance.

2.4. Components inside a LIB

A deeper understanding of battery performance requires examining the physical structure and materials composition of the cell. A battery pack is an integrated system composed of numerous components that must work synergically to ensure proper operation (***Figure 2.6***) [29]. Depending on the target application, cells can be manufactured in different formats, and these geometries have a strong influence on how materials are distributed inside the device (***Figure 2.7***) [30]. For example, while separator and electrolyte contents are comparable across designs, pouch cells (***Figure 2.7b***) require roughly one-third less casing material than the other cell formats.

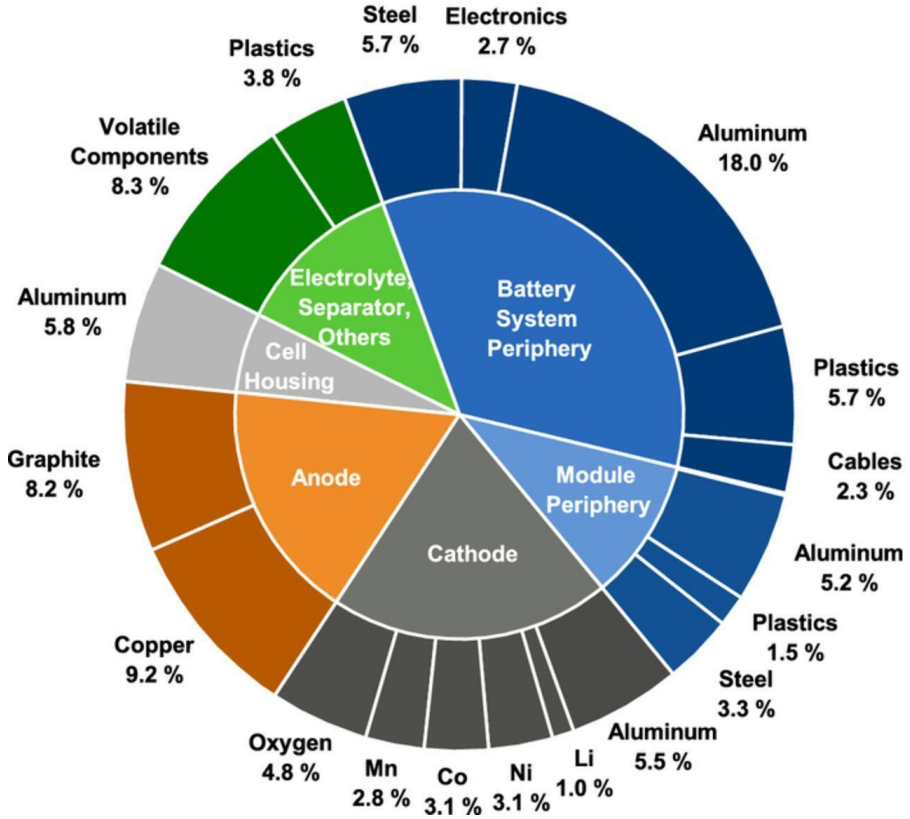

Figure 2.6 – Generic composition of lithium-ion battery pack for EV applications. Reproduced from [29]

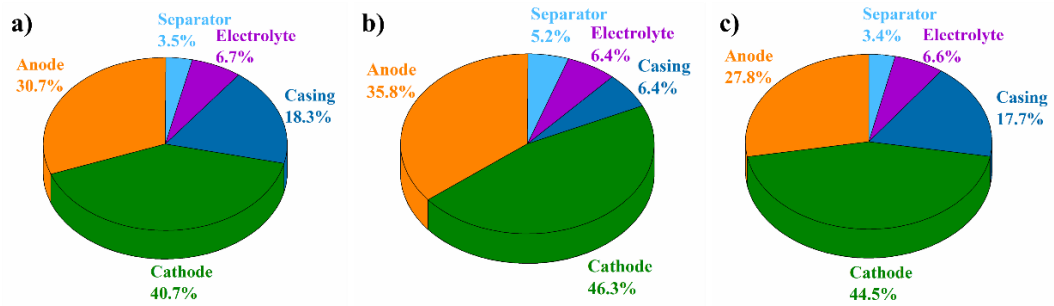

Figure 2.7 – Comparison between the different percentage composition depending on LIBs geometry: a) Cylindrical; b) Pouch; c) Prismatic. The graphs are reproduced from the data provided in the work of Romero Guillèn et al. [30]

For cylindrical cells, as for the other architectures, the choice of materials further modifies the overall composition, as shown in ***Table 2.2*** by Golubkov et al. [31]. As consistently reported across the literature [32,33], the electrodes account for more than half of the total cell mass. This is directly reflected in cost analysis: the combined cost of the electrode materials (both anode and cathode), including the current collectors (CC) typically represents 60-80% of the total production cost of a battery pack, including cells and module assembly and a basic BMS [34]. Although the separator contributes to the smallest mass fraction, it is essential for preventing internal short circuits while permitting lithium-ion transport through its porous structure. The electrolyte, which can constitute a significant portion of the cell depending on the format, ensures ion transport between anode and cathode. It is usually a liquid solution of organic solvents with dissolved lithium salts.

Table 2.2 – Percentage composition of the main components of cylindrical cells produced with different materials. LCO: Lithium Cobalt Oxide, NMC: Nickel Manganese Cobalt Oxide, LFP: Lithium Iron Phosphate [31]

Component	***LCO/NMC***	***NMC***	***LFP***
Casing	17 %	22 %	27 %
Cathode CC	4 %	7 %	6 %
Cathode AM	41 %	26 %	25 %
Anode CC	7 %	17 %	10 %
Anode AM	18 %	15 %	13 %
Electrolyte	10 %	10 %	16 %
Separator	3 %	3 %	3 %

The choice of the correct combination of the components is fundamental for achieving performance targets, including energy density, power density,

durability, and cost. The following sections will provide a more detailed discussion of each component.

2.4.1. Electrodes

As previously discussed, the electrodes are the components where the electrochemical reactions take place; therefore, their composition has a strong influence on the overall performance of the cell. Electrodes are prepared by mixing several components with a suitable solvent for producing the so-called *slurry* [35]:

- ***Active Material*** (AM): responsible for the redox reactions occurring both at the anode and the cathode. The materials used for the two electrodes are different in terms of chemistry and structure. They are characterized by several parameters such as operating voltage, specific capacity, and lithiation/ de-lithiation mechanism. The selection of electrode material allows for tailoring the cell properties to the intended application.
- ***Conductive Additive*** (CA): carbonaceous materials added in small amounts to enhance electronic conductivity within the electrode.
- ***Polymeric Binder***: ensures cohesion among AM particles and CAs, and adhesion to the CC. It has to be dissolved in a suitable solvent to achieve homogeneous dispersion of all components in the slurry.

After mixing, the slurry is coated onto the ***Current Collector*** (CC), which is copper foil for negative electrode and aluminum foil for the positive electrode, which ensures electrical conduction from the electrodes to the external circuit.

2.4.1.1. Cathode materials

As previously discussed, the cathode is the electrode where the reduction occurs during discharge. This process is enabled by transition-metal-based materials which are directly involved in the electrochemical reaction. This redox process occurs with the variation of the oxidation state of the transition metal and the simultaneous insertion (or extraction) of lithium ions within the oxide structure. However, the associated phase transitions and structural strain can significantly affect the overall battery performance [36]. Cathode materials for LIBs are generally classified into three main structural families: layered, spinel, and olivine structures (***Figure 2.8*** [37]).

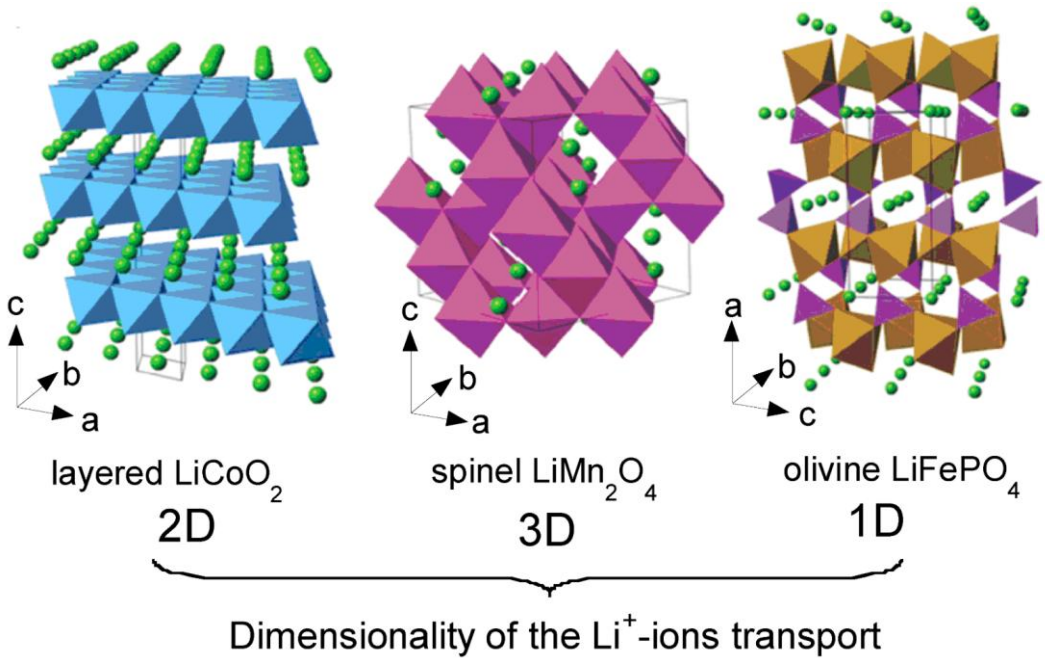

Figure 2.8 – Crystal structures of three lithium-insertion materials, where Li^+ ions migrate through 2-D (layered), 3-D (spinel), and 1-D (olivine) diffusion frameworks. Reproduced from [37]

Over the years, numerous materials [38–40] have been proposed to meet the increasing demand for cathode materials offering higher capacity, energy density, cycling stability, as well as improved safety and lower cost. The first cathode material used in commercial LIBs, introduced by Sony in 1991, was Li_xCoO_2 (**LCO**). This material was considered innovative due to its layered structure (***Figure 2.9*** [41]), which enables the reversible intercalation of Li-ions at potential around 4V, thus providing a high operating voltage [42]. LCO exhibits a high theoretical capacity (274 mAh g^{-1}) and volumetric capacity (1363 mAh cm^{-3}) [40]. These properties contributed to its widespread use as a cathode material, ensuring high energy density; however, several disadvantages limit its overall performance. Firstly, the practical capacity (140 mAh g^{-1}) is much lower compared to the theoretical value. Only about half of the lithium can be extracted from the structure; further extraction induces a structural transition that causes rapid capacity decay [36]. Secondly, LCO has limited electronic conductivity; therefore, the addition of conductive carbon is required to ensure proper operation [43]. Furthermore, during normal operation, elevated temperatures can cause the decomposition of LCO, releasing oxygen that reacts with the organic carbonate electrolyte to form CO_2, CO, and other gaseous species. If generated in large quantities, these gases can trigger thermal runaway, potentially leading to battery explosion [44]. For these reasons, LCO is considered one of the least thermally stable cathode materials among those commercially available [40]. Another critical issue associated with this material is its high cobalt content, which

contributes to elevated costs and raises ethical concerns regarding cobalt extraction in developing countries [45].

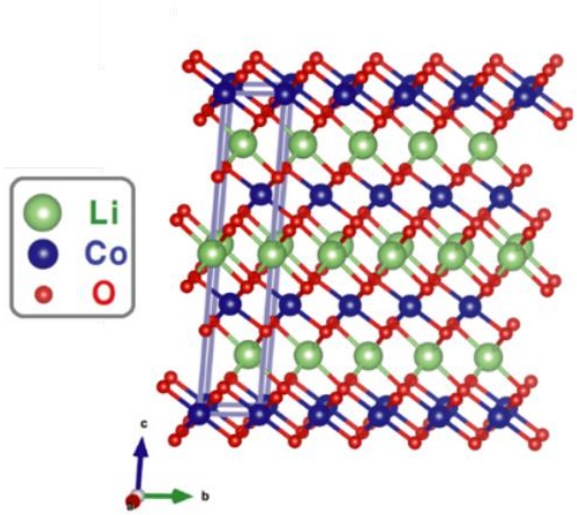

Figure 2.9 – Crystal structures of layered LCO. Partially reproduced with permission from [41]. Copyright 2018 American Chemical Society.

Driven by the demand for improved performance, many alternative layered oxides such as $LiNiO_2$, $LiMnO_2$, and their derivatives have been developed, among which the $LiNi_xMn_yCo_{1-x-y}O_2$ (NMC) family has become one of the most widely used and best-performing cathode materials [46].

Figure 2.10 [36] presents the state-of-the-art and future perspective of NMC materials, along with the redox couples associated with their electrochemical behavior. Different NMC compositions have been developed depending on the transition-metal ratios. The first variant is the so-called **NMC111** (or NMC333, $LiNi_{0.33}Mn_{0.33}Co_{0.33}O_2$) in which the atomic ratio of Ni, Mn, and Co is 1:1:1 [46]. This layered material exhibits a high operating voltage (≈3.7 V), a theoretical capacity of about 155 mAh g^{-1} and high energy density [36]. These advantages result from the synergistic combination of the transition-metal ions within the layered structure. The high reversible capacity originates mainly from the Ni^{3+}/Ni^{4+} redox couple [46,47]. Meanwhile, Mn^{4+} contributes to both structural and thermal stability during cycling, as its oxidation state remains unchanged throughout the charge/discharge process [36,47,48]. The presence of Co, together with the other transition metals, enhances both rate capability and specific capacity [36].

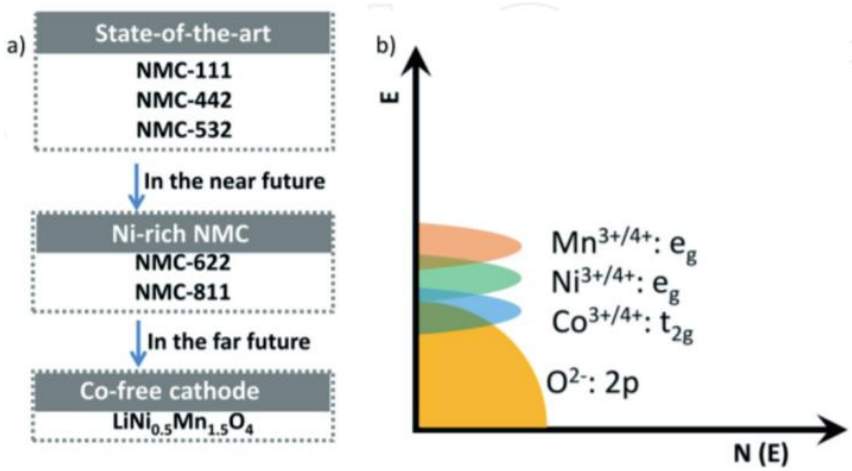

Figure 2.10 – (a) The state-of-art NMC cathode materials, near-future NMC materials, and far-future cathode materials; (b) Schematic diagram of the positions of the various redox couples [36]

Because of cobalt's high cost, toxicity, and ethical concerns, its content in the NMC structure has been progressively reduced [49], in favor of a higher Ni proportion [46]. Consequently, new NMC compositions such as NMC532 ($LiNi_{0.5}Mn_{0.3}Co_{0.2}O_2$), NMC622 ($LiNi_{0.6}Mn_{0.2}Co_{0.2}O_2$) and **NMC811** ($LiNi_{0.8}Mn_{0.1}Co_{0.1}O_2$), have been developed and are now commercially available, thanks to the progressively higher theoretical capacity up to ~200 mAh g^{-1} [50]. The typical layered structure of NMC811 is shown in ***Figure 2.11*** [51]. The increasing Ni-content in these structures is directly associated with higher capacity; however, it also leads to reduced thermal stability [52]. This undesirable effect arises from the enhanced dissolution of transition-metal ions, which react with the electrolyte and ultimately reduce the cell capacity, as clearly demonstrated in the comparative study by Son et al. [53].

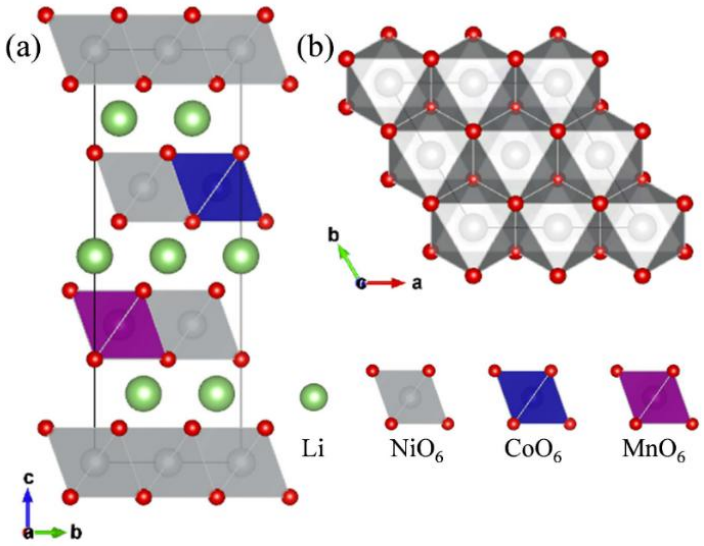

Figure 2.11 – Atomic model of Ni-rich NMC811 layered oxide [51]

The future of cathode AMs lies in high voltage, cobalt-free compounds, such as the promising $LiNi_{0.5}Mn_{1.5}O_4$ (**LNMO)** [54]. This spinel exhibits a high operating voltage (≈4.7 V vs Li/Li^+) and a theoretical capacity of approximately 147 mAh g^{-1} [55–57]. Furthermore, LNMO delivers the highest specific energy (≈650 Wh kg^{-1}) among the reported layered oxides [36,54], and the absence of Co significantly reduces cost and mitigates the ethical issues associated with its extraction [49,50]. LNMO possesses a stable spinel crystal structure [49,56,57] which differs substantially from the layered NMC family (***Figure 2.12*** [54]). Two spinel variants, ordered and disordered, can be synthetized, each exhibiting distinct electrochemical behaviour and structural stability [59]. However, LNMO has not yet been widely implemented in commercial batteries due to several drawbacks. First, the transition-metal cations (in particular Mn) are subjected to leaching during cycling, which affects the crystal structure and leads to a loss of electrochemical performance. Secondly, the electrolytes commonly used for conventional cathodes are unstable at the high operating of LNMO, leading to severe electrolyte decomposition and reduced the overall system safety [60].

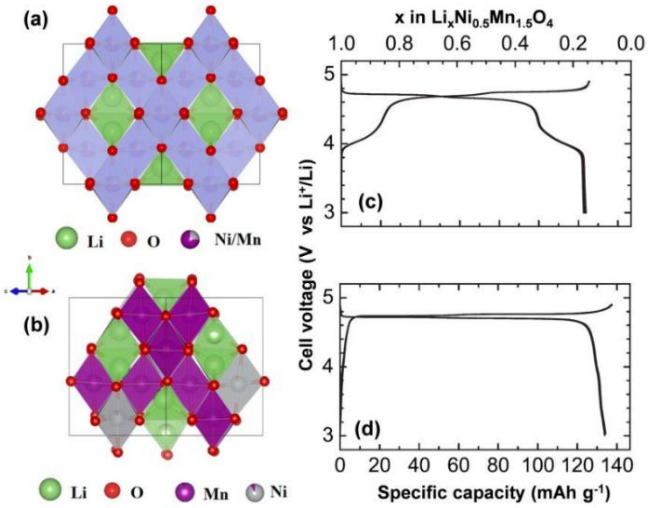

Figure 2.12 – Schematic structure of (a) disorder and (b) ordered LNMO and their charge/discharge curves. Partially reproduced with permission from [54]

Another widely used cathode AM is $LiFePO_4$ (**LFP**), which is commercially produced by several manufactures and extensively employed in applications such as electrical buses and cars in China [61] and stationary energy storage systems requiring long cycle life and high safety. These applications are enabled by its low cost and the strong chemical bonds associated with the presence of iron instead of cobalt, which make the material intrinsically safe [62]. LFP exhibits a high theoretical capacity (≈170 mAh g^{-1}) but a lower energy density compared with previous materials (about 175 Wh kg^{-1} at cell level and 125 Wh kg^{-1} at pack level [63]). Moreover, it has intrinsically low electronic conductivity [62]. Unlike the previously mentioned layered and spinel cathodes, LFP adopts an olivine crystal structure (***Figure 2.13*** [64]).

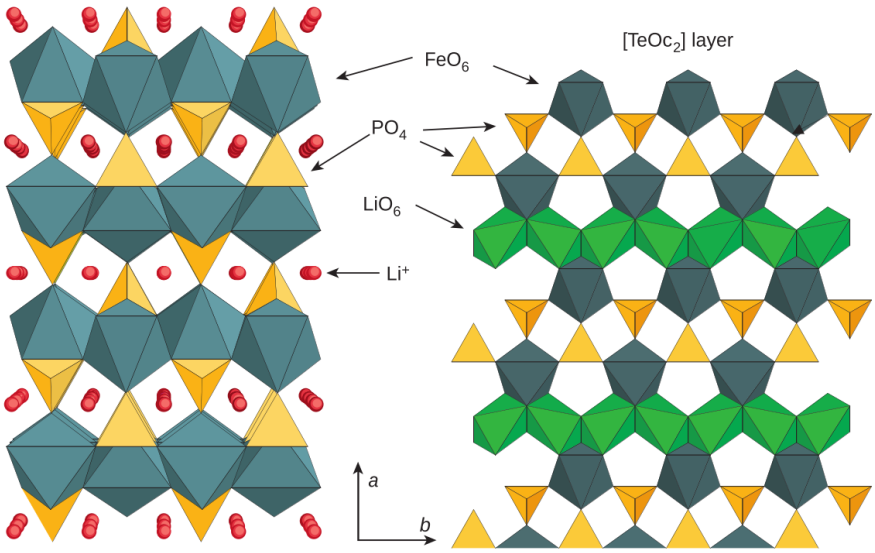

Figure 2.13 – Crystal olivine structure of LFP. Reproduced with permission from [64]

Table 2.3 [61] summarizes some of the most important characteristics of the positive electrode AMs discussed above. The practical specific capacity refers to the AM itself; it is usually expressed in mAh g^{-1} and is a useful parameter to compare the performance of different cathode materials. Specific energy, on the other hand, is evaluated at the cell or battery level when a specific voltage is applied and is expressed in Wh kg^{-1}.

Table 2.3 – Summary of the cited active materials and their specifications. Partially reproduced with permission from [61]

Code	Stoichiometry	Structure type	Practical specific capacity (mAh g^{-1})	Average potential (V vs. Li^+/Li)	Specific energy active material combination (Wh kg^{-1})
LFP	$LiFePO_4$	phospho olivine	165	3.45	379
LFMP	$LiMn_{0.7}Fe_{0.3}PO_4$	phospho olivine	155	3.90	412
LCP	$LiCoPO_4$	phospho olivine	150	4.75	492
LCO	$LiCoO_2$	layered oxide	150	3.90	402
NMC_{111}	$LiNi_{0.33}Mn_{0.33}Co_{0.33}O_2$	layered oxide	160	3.70	399
NMC_{532}	$LiNi_{0.5}Mn_{0.3}Co_{0.2}O_2$	layered oxide	165	3.70	407
NMC_{622}	$LiNi_{0.6}Mn_{0.2}Co_{0.2}O_2$	layered oxide	170	3.70	416
NCA	$LiNi_{0.8}Co_{0.15}Al_{0.05}O_2$	layered oxide	188	3.70	445
NMC_{811}	$LiNi_{0.8}Mn_{0.1}Co_{0.1}O_2$	layered oxide	190	3.70	448
LNO	$LiNiO_2$	layered oxide	240	3.75	526
LRLO	$Li[Li_{0.2}Ni_{0.2}Mn_{0.6-x}M_x]O_2$	layered oxide	280	3.75	575
LMO	$LiMn_2O_4$	spinel	110	4.10	337
LMNO	$LiNi_{0.5}Mn_{1.5}O_4$	spinel	140	4.70	464
L_2MNO	$Li_2Ni_{0.5}Mn_{1.5}O_4$	spinel (tetragonal)	280	3.70	567

2.4.1.2. Anode Materials

The anode is the electrode where oxidation occurs during discharge; therefore, the materials used must be capable of hosting lithium ions through different mechanisms. Anode materials can be classified into different families based on their lithium-hosting mechanism, each characterized by specific advantages and limitations [65,66]:

1. Lithium reduction: lithium ions are reduced from Li^+ to Li^0, this mechanism occurs exclusively in the presence of metallic lithium.
2. Intercalation: lithium ions are reversibly inserted between the layers of host materials
3. Alloying: lithium ions form alloys with elements such as Si, Sn, Sb, Al and Ge
4. Conversion: lithium ions participate in conversion-type redox reactions that form new species during cycling

A comprehensive summary of the most widely studied anode materials is reported in ***Table 2.4*** [67], organized according to the different families and including their theoretical capacities, advantages and common challenges. In the following sections, some of these materials will be discussed in greater detail.

Table 2.4 – Summary of the most common anode material, divided into the lithium hosting mechanism and associated with their theoretical capacity, advantages and common issues [67]

Active anode material	Theoretical capacity ($mAh\ g^{-1}$)	Advantages	Common issues
Insertion/de-insertion materials			
A. Carbonaceous	200-600	➢ Good working potential	❖ Low coulombic efficiency
a. Hard carbons	1116	➢ Low cost	❖ High voltage hysteresis
b. CNTS	780/1116	➢ Good safety	❖ High irreversible capacity
c. Graphene			
B. Titanium oxides	175	➢ Extreme safety	❖ Very low capacity
a. $LiTi_4O_5$	330	➢ Good cycle life	❖ Low energy density
b. TiO_2		➢ Low cost	
		➢ High power capability	
Alloy/de-alloy materials			
a. Silicon	4212	➢ Higher specific capacities	❖ Large irreversible capacity
b. Germanium	1624	➢ High energy density	❖ Huge capacity fading
c. Tin	993	➢ Good safety	❖ Poor cycling
d. Antimony	660		
e. Tin oxide	790		
f. SiO	1600		
Conversion materials			
a. Metal oxides(Fe_2O_3, Fe_3O_4, CoO , Co_3O_4, Mn_xO_y, Cu_2O/CuO, NiO, Cr_2O_3, RuO_2, MoO_2/MoO_3 etc.)	500−1200	➢ High capacity ➢ High energy ➢ Low cost ➢ Environmentally compatibility	❖ Low coulumbic efficiency ❖ Unstable SEI formation ❖ Large potential hysteresis ❖ Poor cycle life
b. Metal phoshides/sulfides/nitrides (MXy; M = Fe, Mn, Ni, Cu, Co etc. and X = P, S, N)	500−1800	➢ High specific capacity ➢ Low operation potential and Low polarization than counter oxides	❖ Poor capacity retention ❖ Short cycle life ❖ High cost of production

More generally, some essential characteristics can be identified to define a good anode material [65]:

- Lightweight and capable of storing as many lithium ions as possible, to achieve high specific capacity
- Low redox potential vs. Li^+/Li^0, to maximize the overall cell voltage
- High electronic and ionic conductivities
- Insoluble in electrolyte solvents and chemically stable towards lithium salts
- Safe, with high thermal stability and no toxic effects
- Cheap and environmentally friendly

Figure 2.14 [66] shows the most widely used and studied anode AMs. Some of them meet the characteristics described above, whereas others, such as titanium

oxides, are limited by a higher operating voltage compared to alternative materials. Some of these materials will be discussed in greater detail in the following sections.

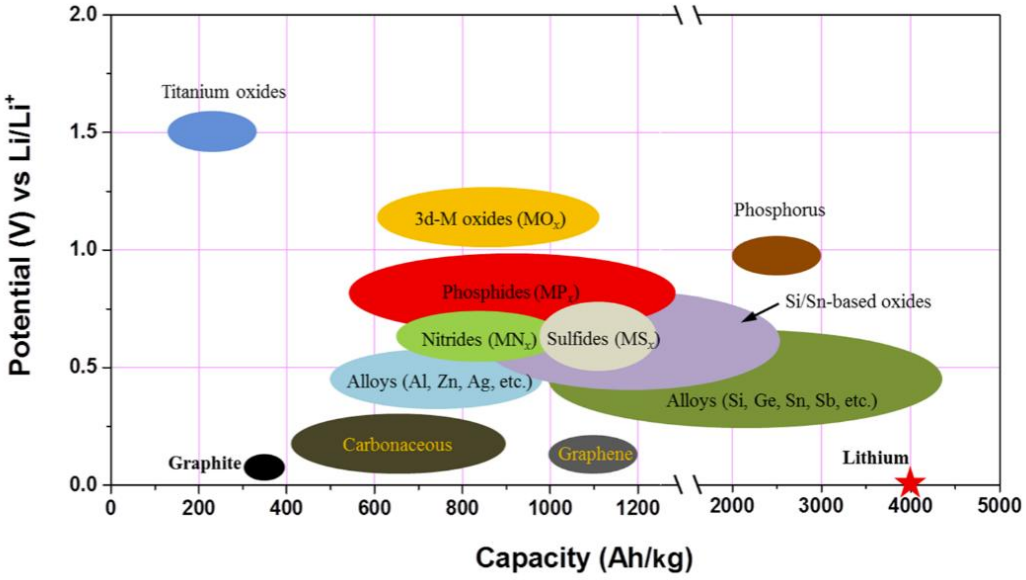

Figure 2.14 – Summary of the next generation active material for anodes. Reproduced with permission from [66]

One of the main aspects affecting the use, research, and development of anode materials is the formation of the ***Solid Electrolyte Interface*** (SEI). The SEI is defined as a layer which is formed on the anode surface during the initial charge-discharge cycles [68]. It plays an essential role in the stability and performance of LIBs, acting as a chemical junction between the electrode and the electrolyte, like a sort of passivation layer [69]. More in detail, the SEI performs several crucial functions. First, it acts as a protective barrier on the anode surface, preventing further electrolyte decomposition and limiting unwanted side reactions. It also behaves as an electronic insulator, preventing electrons from directly reacting with the electrolyte. At the same time, it remains permeable to lithium ions, allowing normal charge and discharge processes [69,70].

The chemical composition of the SEI is highly complex [71], as it depends on most of the materials present inside the cell. It is typically 10-50 nm thick and composed of numerous chemical species [69]. Several studies describe the SEI as a bilayer structure, with an outer organic-rich layer and an inner inorganic layer containing compounds such as lithium carbonate or lithium fluoride [68,69,72]. The main contribution to the SEI formation arises from the decomposition of electrolyte solvents, lithium sats and additives; however, several studies have shown that binders used in electrode production can also have a non-negligible impact on SEI composition [70,73,74]. The most common SEI components can be identified by the decomposition pathways of the electrolyte constituents [75,76].

Achieving a stable SEI layer remains one of the main challenges in improving the overall performance of lithium-based batteries. Nevertheless, its exact formation mechanism, composition, and functionality are still not fully understood [69]. One of the major limitations of next-generation anode materials, such as silicon-based anodes, is the continuous breaking and reformation of the SEI layer, which results in excessive SEI growth and increased cell resistance.

1) Lithium reduction

Lithium reduction is one of the fundamental electrochemical reactions, where lithium changes its oxidation state from Li^+ to Li^0, and it is typical in lithium metal batteries (LMBs), where lithium metal is used as an anode. Lithium exhibits the highest theoretical specific capacity among pure anode materials (3860 mAh g^{-1}), and the lowest electrode potential (-3,045 V vs. SHE), making it an attractive candidate for high-energy battery systems [77]. However, its use is associated with several critical disadvantages [78].

A graphical summary of these mechanisms is shown in ***Figure 2.15*** [79], highlighting the substantial morphological changes occurring at the lithium electrode during cycling. One of the most critical issues is the growth of lithium dendrites (***Figure 2.15a***), which can penetrate the separator and cause internal short circuits [67,80]. Second, during repeated cycling, freshly exposed lithium reacts continuously with the electrolyte, leading to ongoing SEI formation and degradation and electrolyte consumption. This causes capacity fade and increases internal resistance. Additionally, the formation of "dead Li" (***Figure 2.15b***), caused by the electrical and/or electrochemical isolation of active lithium from the bulk electrode, leads to further capacity loss [80].

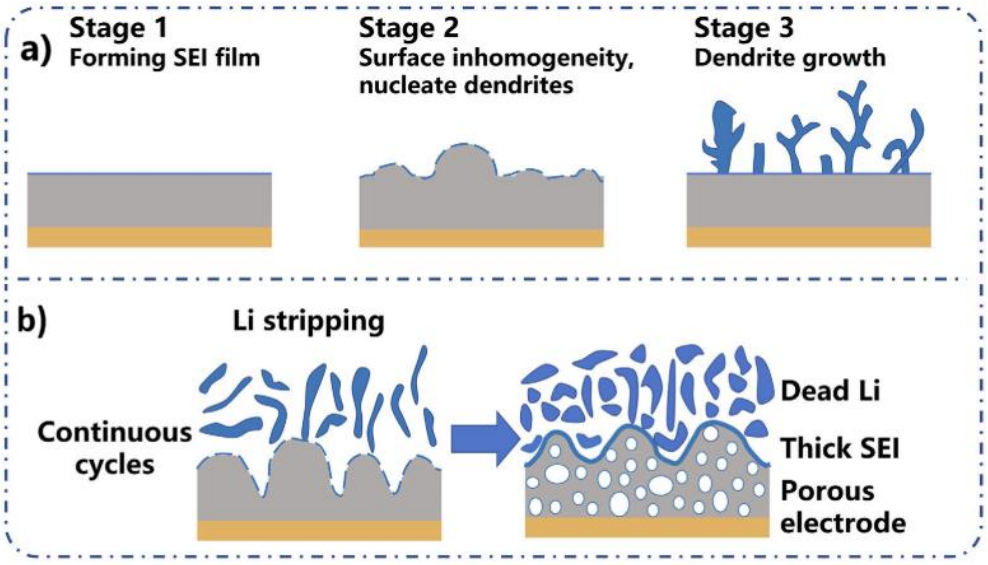

Figure 2.15 – Schematic illustration of the issues related to the use of lithium metal as anode, in particular: a) lithium dendrites formation mechanism; b) subsequent phenomenon after continuous cycles. Partially reproduced from [79]

However, lithium metal anodes are successfully employed in some solid-state battery systems, where polymer or solid electrolytes mitigate dendrite formation and improve safety [81].

2) Intercalation mechanism

The intercalation mechanism relies on the insertion of lithium ions between the planes of layered host materials. Among the most commonly used commercial anode materials, two main families can be identified: carbonaceous materials (with graphite as the primary representative) and titanium oxides. ***Figure 2.16*** [66] provides a schematic representation of the intercalation mechanism, together with a brief summary of its main advantages and limitations.

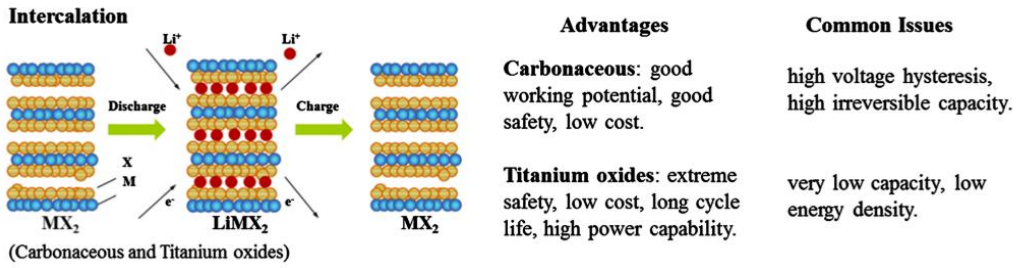

Figure 2.16 – General representation of the intercalation mechanism of anode materials. Partially reproduced with permission from [66]

Natural or synthetic graphite is currently the most widely used commercial anode material due to its low cost and ease of processing. Both forms have been extensively evaluated and generally exhibit comparable electrochemical performance; however, natural graphite is typically cheaper and easier to process, provided that adequate purification and particle morphology control are applied [82]. Typically, graphite has a theoretical capacity of ~372 mAh g^{-1} [83] and an operating potential of ~0.1 V vs Li^+/Li [84]. Graphite also benefits from the formation of a stable SEI layer during the first cycles [85].

Graphite operates via an intercalation mechanism due to its layered structure. Two theoretical models describing this mechanism are shown in ***Figure 2.17*** [83]. The Rüdorff-Hofman Model (upper), proposed in 1938, suggests lithiation proceeds with one graphene layer at a time; however, some transitions, such as Stage 3 → Stage 2, require energetically unfavorable rearrangements and remain unclear. The lithiation process continues until complete formation of the LiC_6 phase [86,87]. Daumas and Herold later proposed a modified model (lower) where intercalation proceeds through local "islands" enabled by the flexibility of the graphene layer, eventually forming fully lithiated LiC_6.

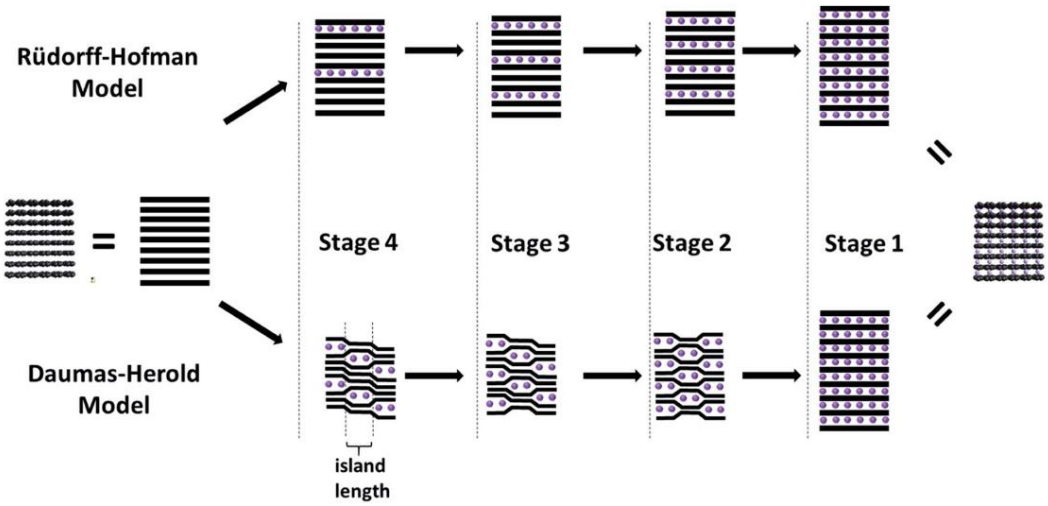

Figure 2.17 – Schematic illustration of the intercalation mechanism of lithium into the layered graphite structure, according to the model of Rüdorff and Hofmann (upper path) and Daumas and Herold (lower path) [83]

A more detailed description of the intercalation process can be obtained by correlating it with the discharge curve of a typical graphite electrode, as shown in ***Figure 2.18*** [83]. The actual intercalation mechanism is more complex than the two models previously suggest, due to the presence of additional intermediate *L-stages*. These stages are characterized by a disordered distribution of lithium ions within the graphene layers. These stages allow a more accurate description of the intercalation behavior. The corresponding phase transitions can be monitored electrochemically through the appearance of voltage plateaus in galvanostatic discharge curves.

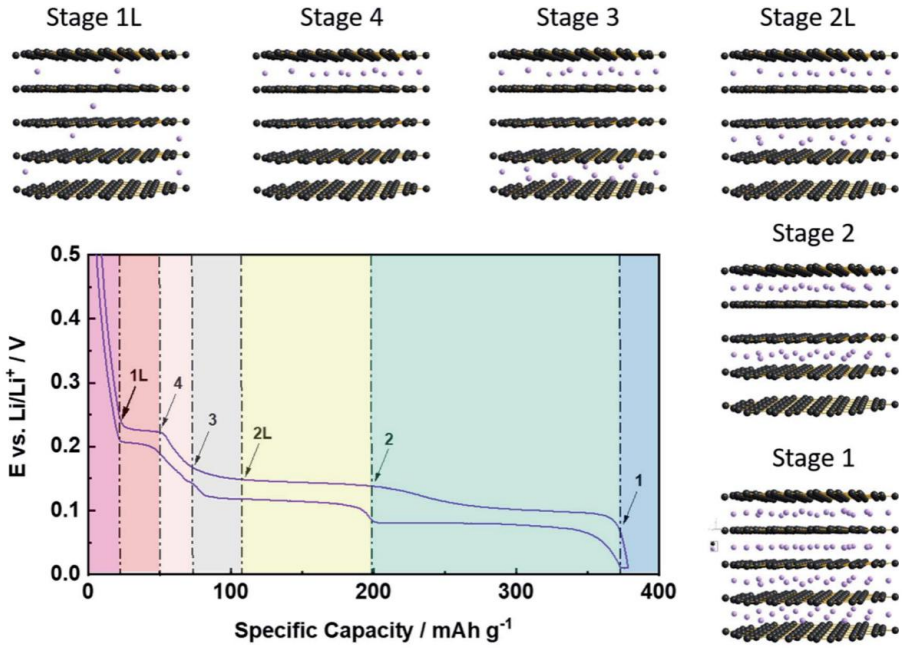

Figure 2.18 – More detailed mechanism of the intercalation and de-intercalation of lithium ions inside the layer of the graphite [83]

However, graphite also presents some limitations. Natural graphite is currently classified as a critical raw material, with supply risks comparable to those of rare earth elements [88]. Consequently, research efforts are increasingly directed toward the development of higher energy density anode materials.

3) Alloying mechanism

To achieve higher specific capacities, new anode materials are required, and among the various options, those operating through an alloying mechanism are particularly promising. The alloying mechanism is based on the ability of certain elements to form an alloy with lithium. A schematic representation is shown in ***Figure 2.19*** [66]. The most common elements in this category include Si, Ge, Sn and P, all of which exhibit higher specific capacities and higher energy densities than graphite. However, these advantages are accompanied by significant challenges in practical applications.

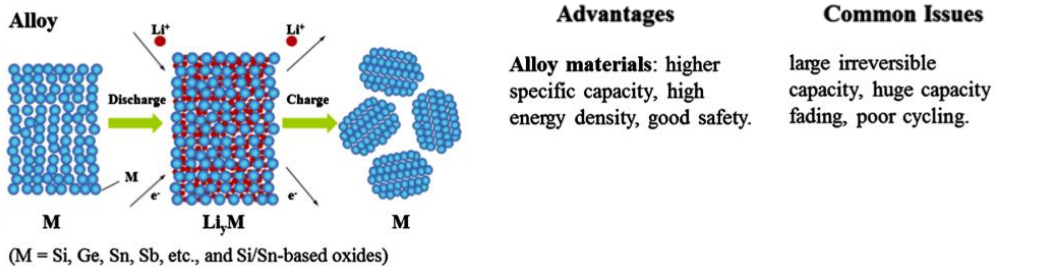

Figure 2.19 – General representation of the alloying mechanism of anode materials. Partially reproduced with permission from [66]

Among these materials, **silicon** (including its derived forms, such as silicon composites, silicon oxide, nanowires, and nanotubes) is considered the most promising. Silicon exhibits an exceptionally high theoretical specific capacity of ~4200 mAh g^{-1} and a volumetric capacity of ~9786 mAh cm^{-3} [61,86], along with an attractive electrochemical potential (~0.06 V vs Li^+/Li) [89]. In addition, silicon is abundant, non-toxic, and environmental-friendly, making it an appealing candidate for large-scale applications [61].

Unlike graphite, silicon undergoes alloying reactions, forming multiple Li-Si phases during lithiation [90]. ***Figure 2.20*** [91] shows the lithiation/de-lithiation curves of silicon at room temperature and at 450°C. At room temperature, the initial steep voltage decrease corresponds to a solid-solution region, where lithium ions diffuse into the silicon lattice without major structural rearrangement. The subsequent plateau at ~0.1 V vs Li^+/Li corresponds to the formation of amorphous alloy Li_xSi from crystalline silicon. When the potential drops below ~50 mV, the amorphous alloy converts into the crystalline $Li_{15}Si_4$ phase. At higher temperatures, additional intermediate steps become visible, as summarized in

Table 2.5 [91], where each lithiation stage is associated with distinct lattice structures and significant volume expansion.

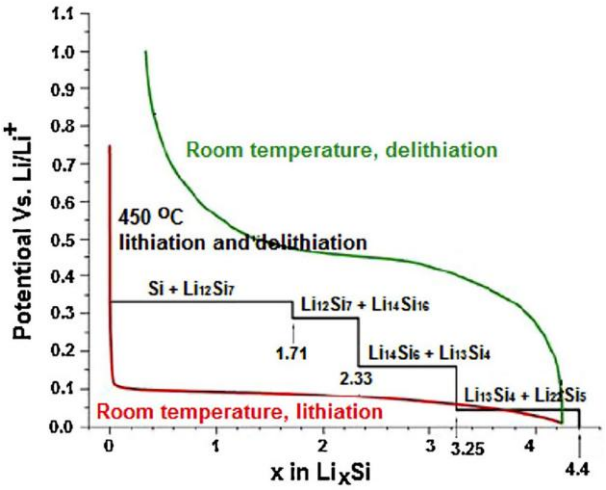

Figure 2.20 – Comparison between lithiation and de-lithiation curves of silicon at room temperature and higher temperature. Reproduced with permission from [91]

Table 2.5 – Summary of the characteristics (lattice structure, cell volume and Si atomic volume) of the Li_xSi alloys formed during the lithiation process. Reproduced with permission from [91]

Si-Li alloy	Lattice structure	Cell volume	Si atomic volume
Si	Cubic	160.2	20.0
$Li_{12}Si_7(Li_{1.71}Si)$	Orthorhombic	243.6	58.0
$Li_{14}Si_6(Li_{2.33}Si)$	Rhombohedral	308.9	51.5
$Li_{13}Si_4(Li_{3.25}Si)$	Orthorhombic	538.4	67.3
$Li_{22}Si_5(Li_{4.4}Si)$	Cubic	659.2	82.4

This behavior is the origin of the exceptionally high capacity of silicon: because of the alloying mechanism, each Si atom can host 4.4 lithium ions, but this is also the reason for the major drawback of using silicon as a full anode material [86]. During the lithiation/de-lithiation processes occurring in charge/discharge cycling, silicon undergoes a dramatic volume change of ~300-400%, which generates severe mechanical stress in the electrode [92–94]. For silicon-based anodes, this expansion is significantly higher than the ~10% volume change of fully lithiated graphite [68]. The resulting stress induces cracking and pulverization of the electrode, leading to loss of contact both between the silicon particles and between the AM and the CC. These degradation processes are directly responsible for the loss of CE and capacity typically observed in silicon anodes [61,93,95].

Silicon also suffers from intrinsically low electronic conductivity (~10^{-5} S cm^{-1}) and very slow lithium-ion diffusion (~10^{-14} cm^2 s^{-1}) [93]. Furthermore, although a SEI layer forms during the initial cycles, the repeated volume expansion and

contraction continuously fractures and reforms the SEI, resulting in persistent electrolyte consumption and performance decay. ***Figure 2.21*** [93] summarizes silicon main limitations.

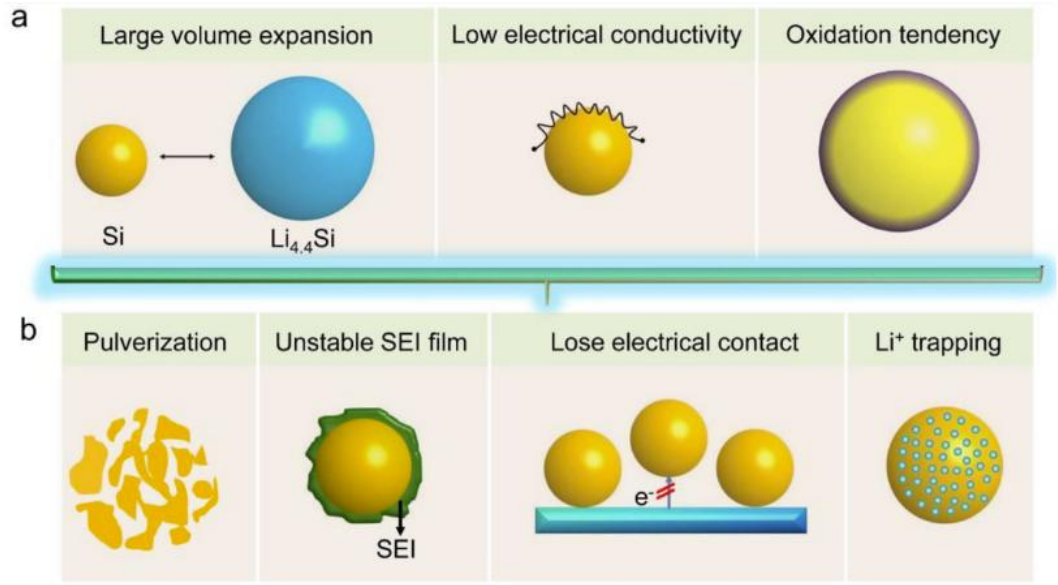

Figure 2.21 – Schematic illustrations of (a) the intrinsic properties of Si anodes and (b) the induced unfavorable electrochemical performances of Si-based LIB. Reproduced with permission from [93]

Therefore, these drawbacks make it necessary to engineer silicon-based anodes to control volume expansion and improve cycling stability. This major drawback can be partially mitigated by using silicon composites (Si-C) or silicon oxides (SiO_x) instead of pure silicon. However, these materials still undergo volume changes of up to ~200% during cycling [96]. Such approaches can help to reduce pulverization, but the origin and structure of the carbon component strongly influence the final electrochemical performance, meaning that each composite requires careful characterization prior to application [97].

Over the years, several strategies have been proposed to mitigate the expansion issue, acting at different structural levels:

- Designing materials with controlled morphology and size, such as micrometric [98] and nanometric particles [99], nanowires [100] or mesoporous structure [101]. In the case of silicon composites, synthesis routes can also generate complex architectures, including core-shell structures [102] and nanotubes [103].
- Using suitable binders capable of accommodating mechanical expansion, such as strong polymeric networks with high cohesive strength [104]. For example, the development of three-dimensional polymer enriched in hydrogen-bonding sites can provide self-healing behavior, improving electrode stability [105].

- Limiting the lithiation depth to avoid the fully lithiated phase, thereby reducing volume change and preventing particle pulverization [106].

Even with these strategies, the use of high Si-content anodes remains a major challenge for next-generation LIBs [91,107,108]. Commercial anodes currently contain approximately 10% silicon [109,110], either from engineered Si-C composites or from simply blending small amounts of silicon with graphite. However, such silicon content is insufficient to meet future energy-density targets, and further development is required to increase the silicon fraction to at least ~50% while maintaining cycling stability [111].

Table 2.6 [112] summarizes the main characteristics of the anode materials discussed so far. It is evident that lithium metal offers the lowest density and the highest theoretical specific capacity, exceeded only by silicon. However, the issues associated with lithium metal remain critical, preventing widespread adoption. For this reason, research continues toward identifying and optimizing alternative anode materials that can combine high energy density with acceptable cycle life and safety.

Table 2.6 – Common anode materials with their characteristic [112]

Materials	Li	C	Si
Density (g cm^{-3})	0.53	2.25	2.33
Lithiated phase	Li	LiC_6	$Li_{4.4}Si$
Theoretical specific capacity (mAh g^{-1})	3862	372	4200
Theoretical charge density (mAh cm^{-3})	2047	837	9786
Volume change (%)	100	12	320
Potential vs. Li (~V)	0	0.05	0.4

4) Conversion mechanism

The last family of anode materials includes various transition metal oxides, sulfides, fluorides, and selenides, generally represented by the formula M_aX_b where M corresponds to Mn, Fe, Co, Ni or Cu, and X represents O, S, F or Se (***Figure 2.22*** [66]). The conversion mechanism occurs during lithiation, where lithium ions participate in redox reactions to form Li_nX and metallic M. During de-lithiation, Li_nX and M are reconverted to Li and M_aX_b, allowing the reaction to proceed reversibly.

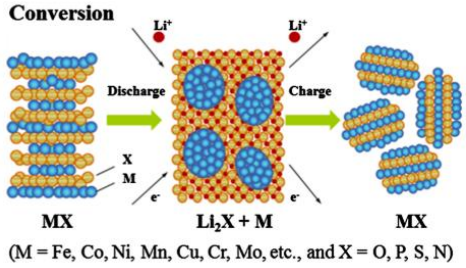

Advantages	Common Issues
Metal oxides: high capacity, low cost, environmental benignity.	low coulombic efficiency, unstable SEI, poor cycling.
Metal phosphides/sulfides/nitrides: high capacity, low operation potential and low polarization.	poor capacity retention, short cycle life, high cost of production.

Figure 2.22 – General representation of the conversion mechanism of anode materials. Partially reproduced with permission from [66]

These materials are characterized by high theoretical specific capacities (typically 700-1200 mAh g^{-1}) and volumetric capacities of 4000-5500 mAh cm^{-3} [66]. However, similar to alloying-type anodes, conversion-type materials suffer from severe volume changes, unstable SEI formations, structural pulverization, and morphological degradation, which lead to rapid capacity fading and poor cycling stability [113].

In conclusion, a summary of the anode material families discussed above is shown in ***Figure 2.23*** [114]. Carbon-based materials, which represent the current commercial state-of-the-art, are the least expensive and offer good stability, but their electrochemical performance is insufficient to meet the energy-density requirements of next-generation batteries. Intercalation-type transition metal oxides provide advantages in safety and cycling stability but suffer from relatively low specific capacity. Alloying-type anodes offer extremely high capacities, but their practical use is limited by severe volume changes and poor cycle life. Finally, conversion-type transition metal compounds exhibit balanced performance across several metrics, yet they do not excel in any single category. Therefore, no existing material class simultaneously maximizes cost, energy density, cycling stability, and safety, and research continues toward improved solutions.

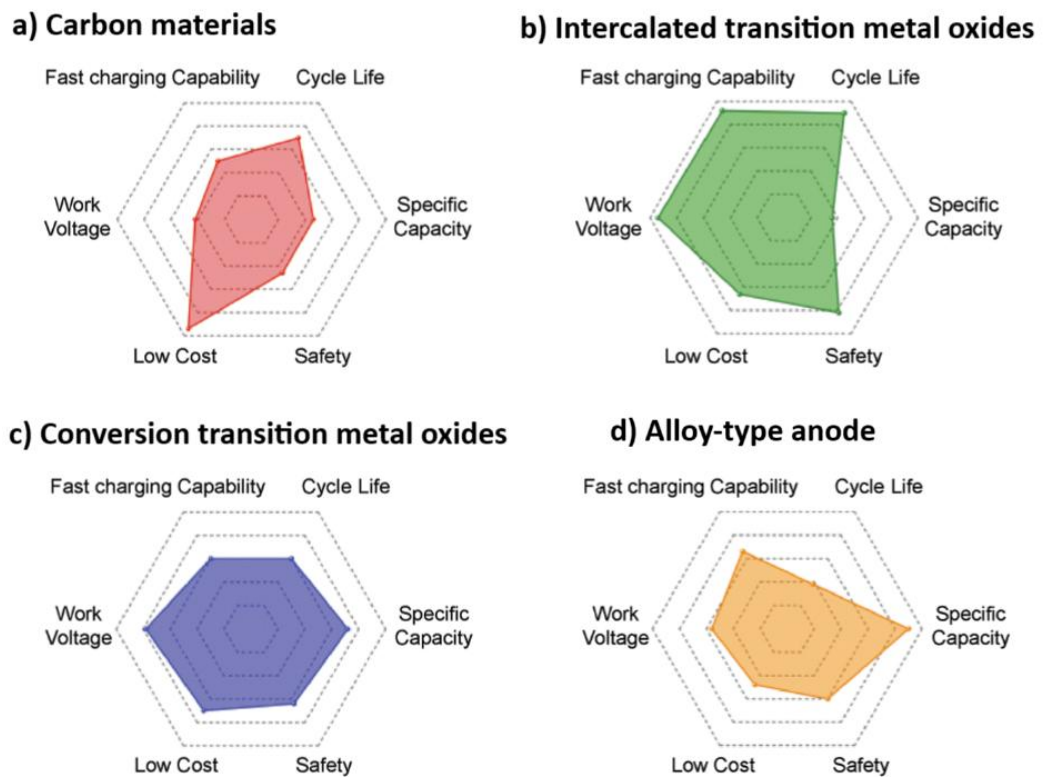

Figure 2.23 – Radar plot comparing the most important characteristics of common families of anode materials, previously discussed. Rearranged from [114]

2.4.1.3. Binders and Solvents

Binders act as the structural matrix that holds the AM and CA together ensuring their adhesion to the CC. Typically, binders are polymeric materials dissolved in a suitable solvent to form a slurry in which the solid particles are uniformly dispersed. As with any other component used in electrode manufacturing, binders must satisfy several requirements to be considered suitable for LIB applications [115,116]:

- *Electrochemical performance*: the binder must provide strong adhesion among AM, CA and CC, support ionic and electronic conductivity, minimize parasitic reactions and ensure cycling stability and capacity retention.
- *Mechanical properties*: the binder must combine strength and flexibility to maintain electrode structural integrity during both manufacturing and battery operation, preventing particles and preserving long-term stability.
- *Thermal stability*: the binder should resist decomposition during cell operation and during electrode drying, where temperatures commonly reach 100-200 °C.
- *Cost-effectiveness and scalability*: especially relevant for large-scale production, as binder cost can significantly influence final battery price.

- *Environmental impact*: increasing attention is placed on using environmentally benign, low-toxicity and low-carbon-footprint binders, and on avoiding solvents and materials that are difficult to recover or recycle.

Once these material-level requirements are satisfied, additional processing-related characteristics must also be ensured [115,116]:

- *Stable slurry viscosity*: essential for achieving uniform coating, homogeneous active-material distribution, and controlled porosity.
- *High solubility in the selected solvent*: to minimize solvent usage and facilitate recovery, particularly important when the solvent is toxic or expensive.

The interaction between the binder and the electrolyte is also critical. The binder must be chemically compatible and electrochemically stable to prevent side reactions. A moderate degree of swelling in the electrolyte improves electrolyte wetting and ionic transport, but excessive swelling compromises mechanical integrity and adhesion, leading to particle detachment [117].

The choice of binder is strongly dependent on the AM. Different polymer structures result in different dominant interactions between polymer chains. For example, polyvinylidene fluoride (PVDF) (***Figure 2.24a***) forms mainly weak Van der Waals interactions, which offer high structural reversibility but poor mechanical strength. Instead, binders that rely on strong covalent bonding create rigid networks with limited adaptability. For silicon-based anodes, an ideal binder must form ionic or hydrogen-bonding networks that are strong enough to maintain cohesion but sufficiently reversible to accommodate volume expansion [118].

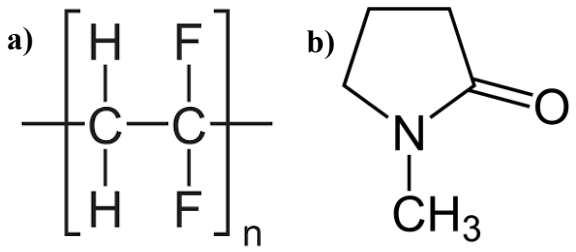

Figure 2.24 – a) chemical structure of PVDF; b) chemical structure of NMP

Currently, the dominant binder is PVDF, especially for cathode formulation, dissolved in N-Methyl Pyrrolidone (NMP) (***Figure 2.24b***) [119,120]. NMP is an organic solvent, widely used in electrode fabrication due to its strong solvation power and compatibility with PVDF. Its widespread adoption is mainly due to its excellent electrochemical stability (up to ~5 V), high melting point, resistance to common solvents, and compatibility with most cathode materials [121–124].

The major issue associated with the use of PVDF and NMP is that both are toxic and expensive. In Europe, NMP has been classified under REACH (Registration, Evaluation, Authorisation and Restriction of Chemicals –

Regulation of the European Union [125]) as a substance of very high concern, due to its human reproductive and development toxicity, including documented teratogenic effects [61,120]. Consequently, electrode drying must be carefully controlled to ensure operator safety and to allow efficient solvent recovery. Solvent recycling can account for over 3% of the total battery pack cost [126]. In addition, at temperatures above 45°C, PVDF can react exothermically with lithium and lithiated graphite to form LiF, generating heat and potentially promoting thermal runaway [115,127].

These drawbacks drive research toward water-based binders, which also offer significant cost reductions. Water-based processing requires lower drying temperatures [127,128] and relies on cheaper aqueous binders compared to PVDF [120]. Moreover, due to different interaction mechanisms, the binder content can be reduced: PVDF-based electrodes typically require ~10 wt% binder, whereas aqueous systems may require only ~5 wt% [129]. A techno-economic analysis by Wood et al. (2015) demonstrated that switching from NMP to water in multilayer pouch cell fabrication can reduce electrode manufacturing costs by over 90% [128].

Research on replacing organic solvents with water has been ongoing for more than two decades [130], but full substitution remains challenging. Aqueous processing of cathodes may lead to metal dissolution during processing [122], pH-induced corrosion of aluminum CC [131], and instability of layered oxide structures in the presence of water and oxygen [122,132]. Nevertheless, water-based binders are already the industrial standard for graphite anodes and LFP cathodes, while for NMC and LNMO cathodes replacing PVDF remains challenging [122].

Among the many alternatives proposed [124,133–135], only one aqueous binder is currently established commercially: carboxymethyl cellulose (CMC) (***Figure 2.25a***). CMC is a water-soluble cellulose derivative composed of β-linked glucopyranose units with variable degrees of carboxymethyl substitution. It is widely used as an anode binder (typically in its sodium salt form) due to its high adhesion strength and lower solvent uptake compared to PVDF, which contributes to improved cycling stability [136]. Furthermore, lower binder loading can be used while maintaining mechanical integrity [129]. During electrode fabrication, the pH and degree of substitution must be carefully controlled, as they strongly influence the mechanical properties of the resulting electrode film [137].

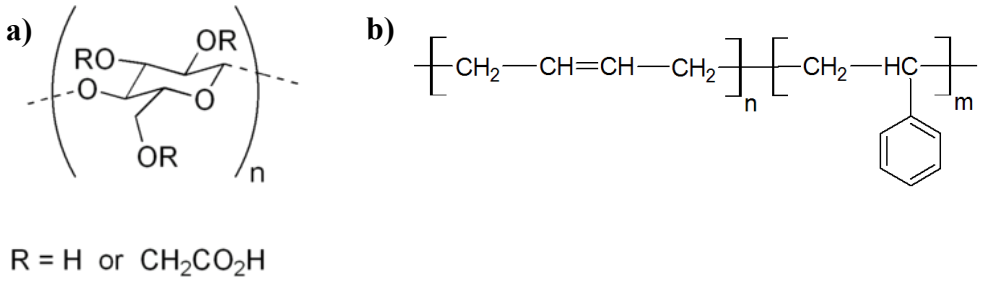

Figure 2.25 – Chemical structure of a) CMC and b) SBR

However, the CMC polymeric network alone is not sufficient to guarantee electrode integrity throughout the entire production process, especially at higher TRL levels. Therefore, the addition of rubber components such as Styrene Butadiene Rubber (SBR) (***Figure 2.25b***) is indispensable at the industrial scale [129]. The CMC/SBR mixture represents the current state-of-the-art binder formulation for anodes and is used both for fully graphite electrodes and for electrodes containing small amounts of silicon. When compared to PVDF-based electrodes, CMC-based systems exhibit lower first-cycle irreversible capacity loss (ICL) due to the faster and more uniform SEI formation driven by better interactions between carbon surfaces and CMC [120].

When moving from graphite to high-silicon-content anodes, the role of binder becomes even more critical. The binders must not only accommodate the large volume of expansion of silicon but must also promote the formation of a stable SEI. Although CMC provides better electrochemical performance than PVDF, it still does not represent the optimal binder for silicon-based anodes. Numerous alternatives to the CMC/SBR have been proposed in the literature [120,138–140], some of which show promising industrial applications and improved sustainability. Among them, polyacrylic acid (PAA) (***Figure 2.26***) has demonstrated superior mechanical properties and improved cycling stability, making it one of the most promising binders for silicon-containing anodes [141–143].

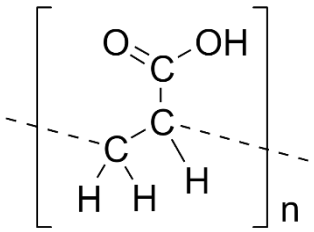

Figure 2.26 – Monomeric unit of the PAA

PAA is a synthetic polymer based on acrylic acid as its monomeric unit. It is water-soluble and becomes negatively charged when the carboxyl groups are dissociated. PAA is already widely used in pharmaceuticals, cosmetics, paints,

and food products, where it acts as a dispersing, suspending, or emulsifying agent. Its use in the food industry is permitted following safety and biocompatible approval by the European Food Safety Authority [144]. PAA is commercially available in different molecular weights (MWs); in the battery field, medium MWs (250-500 kDa) are commonly used, although the optimal value is still debated, and different results are reported in the literature [145–147].

The improved performance of PAA compared to the CMC/SBR system is mainly attributed to its higher density of carboxyl functional groups, which enables stronger interactions with silicon. These groups can form hydrogen bonds and ester linkages with hydroxyl groups present on the silicon surface [148]. As a result, PAA can create a more cohesive polymer network surrounding the silicon nanoparticles, limiting particle pulverization and reducing the loss of contact between the AM and the CC [142,149]. PAA also influences the rheology of the slurry, which directly affects electrode morphology at both the micro- and meso-scale [136,137].

However, PAA also has limitations. It is hygroscopic, which can negatively affect electrochemical performance [150]. Like other linear polymers, the number of interaction sites with silicon is limited, and the resulting network is often not strong enough to withstand large volume changes during cycling. While hydrogen-bonding interactions are reversible and can provide some degree of self-healing, they lack mechanical strength. On the other hand, covalent bonding provides higher strength but cannot reform once broken, leading to electrode cracking, particle pulverization, loss of electrical contact and unstable SEI formation over cycling [150].

This means that an optimal binder solution has not yet been identified, and further research is still required. Several approaches have been proposed in the literature. A first strategy involves partial neutralization of PAA with LiOH or NaOH to obtain LiPAA or NaPAA [151,152]. This simple modification can improve the performance of silicon-graphite electrodes, since LiPAA exhibits a lower water uptake compared to unmodified PAA, resulting in improved electrode stability [148].

Natural polymer strategies have also been widely explored. PAA has been grafted onto complementary polymers such as CMC [153–158] or combined with SBR [159]. In addition, a broad range of plant- and animal-derived polysaccharides has been investigated as standalone binders, co-binders, additives, or as components of crosslinked networks. Similar to the CMC–SBR system, where SBR enhances the mechanical robustness of CMC, selected natural polysaccharides can reinforce linear polymer binders and improve electrode integrity and cycling stability. This research direction is directly relevant to the work developed in this Ph.D. project.

Among biopolymer-based binders, chitosan is one of the most studied examples from animal-derived sources [136,160–165]. From plant-derived

sources, the available options are significantly broader and include xanthan gum [166,167], guar gum [168], sodium alginate [136,165,169–171], tragacanth gum [172,173], carrageenan [124,174,175], pectin [176–179], and many others. These materials are already widely used in the food and cosmetic industries as gelling agents, thickeners, moisture stabilizers, and dispersants. In the present work, the focus has been placed on sodium alginate, tragacanth gum, carrageenan and pectin, and therefore only these materials will be discussed in the following section.

Sodium alginate (Na-Alg) is a co-polymer composed of 1-4-linked β-D-mannuronic acid (M) and α-L-guluronic acid (G), as shown in ***Figure 2.27***, and contains a high density of carboxyl groups, similar to CMC and PAA [136]. It is typically extracted from brown algae in the form of sodium salt and is already used in cosmetics, food, and biomedical applications. More than a decade ago, it was demonstrated that sodium alginate can improve the electrochemical performance of silicon-based anode: Feng et al. [171], reported slightly lower ICE, compared to other aqueous binders, but significantly higher capacity retention after extended cycling. This improvement is attributed to its superior mechanical properties relative to PVDF. A further enhancement can be obtained by crosslinking Na-Alg with chitosan, forming a self-healing polymeric network with a tensile strength more than double compared to PVDF, and markedly improved electrochemical performance [165]. Mechanical robustness remains one of the key factors supporting Na-Alg as a promising binder for silicon-based anode [180]. However, Na-Alg exhibits environment-dependent rheological behavior. The polymer backbone carries negative charges, and in the absence of dissolved ions the chains are stiff and extended. In contrast, in the presence of cations such as Na^+ or Li^+, the polymer adopts random coil conformation [173]. Therefore, controlling the ionic composition of the slurry is critical for achieving reproducible electrode structure and performance.

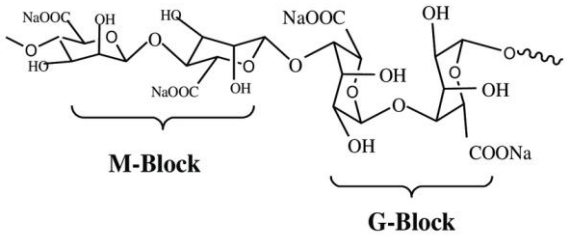

Figure 2.27 – Sodium Alginate structure with its two units: 1-4-linked β-D-mannuronic acid (M-Block) and α-L-guluronic acid (G-Block)

Tragacanth gum (TG) is a natural polysaccharide obtained as an exudate from various species of the *Astragalus* genus. TG consists of two main fractions: *tragacanthin*, which is highly water-soluble, and *bassorin*, which is only partially soluble but forms a high-viscosity gel in aqueous media [173]. A representative structural scheme is shown in ***Figure 2.28.*** The use of TG as a binder in LIB

electrodes has been very limited. Only a small number of studies report its applications as binder for high-voltage cathode [182] and for graphite anodes [172]. TG has also been investigated in supercapacitors electrodes but to the best of current knowledge, no reports exist on its use in silicon-based anodes. Therefore, this specific application remains essentially unexplored.

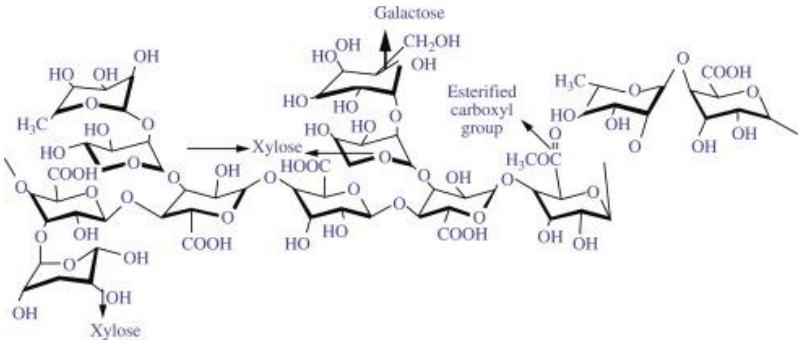

Figure 2.28 – Chemical structure of TG

Carrageenan (CGN) is a family of polysaccharides typically extracted from red algae. Its structure is similar to alginate but contains sulfonate groups. Depending on the number and position of these sulfonate groups, three main types can be distinguished: κ-carrageenan, ι-carrageenan and λ-carrageenan, as shown in ***Figure 2.29***. As in the case of TG, the use of CGN as a binder for LIBs has been limited, and the available studies are scattered across different electrode materials. When used as binders without fraction selection, the family is generally characterized by the absence of carboxylic groups, preventing the formation of hydrogen bonding interactions with the silicon surface. As a result, the polymer network tends to be weak, leading to poor electrode integrity and reduced electrochemical performance [183]. This behavior was confirmed in graphite anodes, where Cuesta et al. [124] reported severe loss of capacity due to detachment of the AM from the CC. However, opposite behavior was observed when λ-carrageenan was specifically employed as a binder for silicon anode [174]. In that study, λ-carrageenan was intentionally selected to maximize the density of functional groups able to interact with the silicon, and the presence of sulfonate groups was also found to enhance ionic conductivity in the electrode.

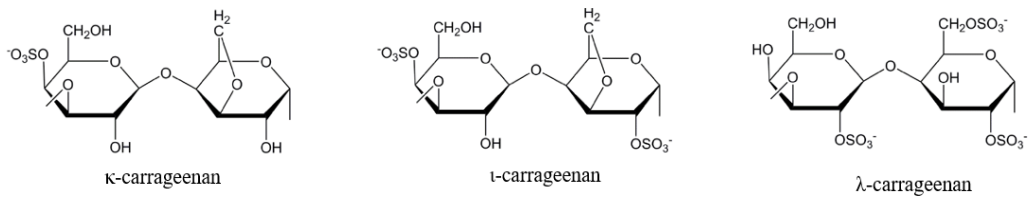

Figure 2.29 – Molecular structures of the three types of carrageenan, from left to right: κ-carrageenan, ι-carrageenan and λ-carrageenan

Pectin (Pec) is a rarely studied binder for LIBs application. In literature, it appears both as a primary binder and as an additive to other dominant systems. Pectin is a natural linear polysaccharide composed of galacturonic acid units linked through α-(1→4)-glycosidic bonds [116]. It is commonly extracted from citrus or apple peels and is widely used in the food industry as a thickening and gelling agent. Despite its promising chemical functionality, its use in LIBs remains limited. One of the most notable studies employing pectin as a pure binder was conducted by Yoon et al. [184], who reported that electrodes retained remarkably high capacity even after 500 cycles, outperforming CMC-based electrodes. This behavior is closely related to the polymer's chemical structure: as shown in ***Figure 2.30*** [184], pectin and CMC share similar representation units, but differ in the configuration of the glycosidic bond, α in pectin and β in CMC. The α-(1→4) linkage in pectin allows elastic deformation of the polymeric chains through conformational changes of the pyranose ring from the chair to the boat configuration, providing an estimated elongation capability of about 18%. In contrast, the β-linkage in CMC does not allow such flexibility, which explains its inferior mechanical adaptability and poorer performance as a silicon-anode binder. Pectin has also been investigated as a co-binder or additive to improve the performance of other polymers. For example, Wang et al. [177] demonstrated that combining pectin with PAA results in a strong 3D crosslinked network, due to the abundant hydroxyl and carboxyl functional groups present in both polymers. However, the proportion between the two components must be carefully controlled: excessive pectin or PAA content can make the binder too rigid, reducing its ability to accommodate silicon expansion and lowering the adhesive strength on the electrode.

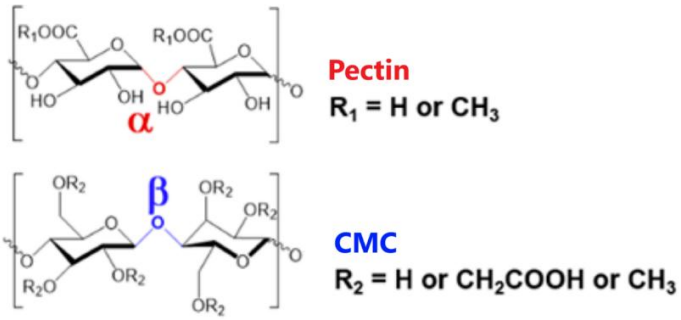

Figure 2.30 – Chemical structure of Pectin con CMC with the important focus on the glycosidic bond. Partially reported with permission from [184]. Copyright 2016 American Chemical Society.

This section has presented some representative examples of binders currently investigated for silicon-anode applications. As summarized in ***Table 2.7***, each compound examined in this Ph.D. work shows specific advantages and limitations related to its chemical structure and interaction with electrode components. At present, the identification of an optimal binder system (either pure or composite) for silicon-based anodes and its large-scale commercialization remains an open

challenge. The work presented in this thesis is intended as a contribution toward understanding and improving this complex and still evolving field.

Table 2.7 – Summary of the binders used in my work with their advantages and main issues

Name	*Chemical Structure and Functional Groups*	*Environmental and Sustainable Aspects*	*Advantage*	*Main Issues*
PVDF	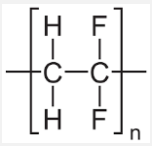 Difluoromethylene Methylene	High carbon footprint Requires hazardous organic solvents (NMP) Non-biodegradable	Excellent electrochemical stability (up to 5 v) High melting point Strong chemical resistance to solvents Good compatibility with cathode materials	Requires toxic solvent (NMP) Exothermic reaction with lithium Poor performance with silicon-based anodes
CMC	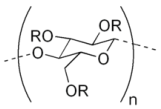 R = H or CH_2CO_2H Carboxylate Hydroxyl	Bio-derived from renewable wood/cotton cellulose Water-soluble Fully biodegradable Non-toxic	Water-soluble Cost-effective Small amount required (< 5 wt%) High adhesive strength Low solvent uptake Reduced first cycle irreversible capacity loss	Poor mechanical strength Requires rubber additive Limited performance with silicon-based anodes
PAA	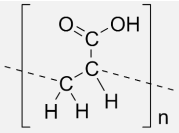 Carboxylic Acid	Synthetic (petroleum-derived) but water-soluble Non-biodegradable	Water-soluble High density of carboxyl groups Linear polymer chain allows good dispersion	High amount required (≥ 10 wt%) Hygroscopic behavior
Alg	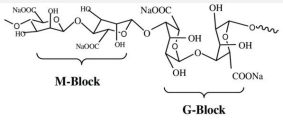 Carboxylate Hydroxyl	Sourced from renewable marine biomass (brown algae) Water-soluble Fully biodegradable	Water-soluble Rich in carboxyl groups Excellent mechanical robustness	High hydrophilicity Rheological properties sensitive to ionic composition
TG	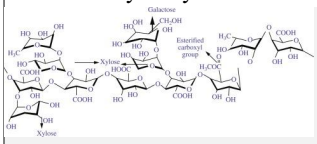 Hydroxyl Carboxylic Acid	Plant-derived natural exudate Minimal, low-energy physical processing/extraction Renewable Non-toxic Fully biodegradable.	Water-soluble Contains carboxyl groups Branched structure improves flexibility	Two fractions with different solubility and viscosity ratios
CGN	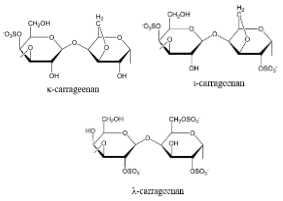 Sulfate ester Hydroxyl	Bio-extracted from sustainable red seaweed Water-soluble Fully biodegradable	Water-soluble Abundant hydroxyl groups Sulfonate groups enhance ionic conductivity	Poor adhesion to CC Weak Si interaction due to the absence of carboxyl groups
Pec	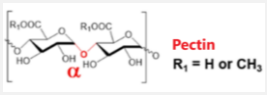 Carboxylic Acid Hydroxyl	Upcycled from agro-industrial waste (citrus peels/apple pomace), promoting circular economy principles Renewable Water-soluble Fully biodegradable Non toxic	Water-soluble Rich in carboxyl groups Linear α-(1→4) glycosidic bond increases elasticity	Very few studies available Limited data on long-term stability

2.4.1.4. Current collectors

The CC is a key component in LIBs, accounting for approximately 15% of the total battery weight [185]. Its primary function is to provide mechanical support for the AM layers deposited on its surface [186,187] and to ensure efficient electron transport to and from the AMs. Maintaining good contact between the CC and the electrode layer is therefore critical for minimizing resistance and ensuring long-term electrochemical stability over repeated charge/discharge cycles [186–188]. In addition to its electrical role, the CC must exhibit suitable mechanical properties, including strength, flexibility, and durability, to withstand the roll-to-roll coating process and in different cell formats (cylindrical, prismatic or pouch) [189]. As with other battery components, the CC also contributes to the overall cost and environmental footprint of the system. These impacts can be mitigated by reducing CC mass or improving its recyclability and integration into circular economic frameworks after EoL [185].

Copper (Cu) and aluminum (Al) are the two standard CCs: copper for the negative electrode and aluminum for the positive electrode. This choice comes from their electrochemical stability window. Copper remains stable between 0 and 2 V but oxidizes at higher potentials [190], whereas aluminum forms a passivating Al_2O_3 layer at high voltages that prevents further metal dissolution into the electrolyte [187]. However, aluminum cannot be employed for anodes since it forms a Li-Al alloy below 1 V [186].

During cycling, detachment of the AM from the CC, particularly in silicon-based anodes where large volume expansion occurs, can lead to cracking and increased resistance, reducing lithium-ion transport and accelerating capacity fading [191]. Corrosion and unwanted reactions, especially between fluorinated electrolyte components and aluminum, can further produce HF, posing safety risks [192].

The morphology and surface structure of CCs significantly influence electrode performance [191–194]. Thinner foils increase the proportion of AM and thus improve energy density. Moreover, surface modification treatments can enhance CE, specific capacity, and capacity retention by improving electrode adhesion and reducing interfacial resistance [187,188]. These include conductive coatings to enhance electronic contact, or three-dimensional structuring to increase surface area [193]. Common examples include carbon coatings [195] and graphene layers [196], both of which improve high-rate capability and inhibit corrosion [195–197]. Alternatively, chemical etching of aluminum with strong acidic or basic solutions increases surface roughness and improve adhesion, but also introduces higher production costs and environmental concerns, emphasizing the need for cleaner and more cost-effective methods [198,199].

An emerging approach involves the use of laser surface texturing on both aluminum and copper foils. This technique can create controlled three-

dimensional surface patterns that enhance electrochemical performance by improving adhesion and charge distribution [200–204]. Although still relatively unexplored, laser texturing represents a promising alternative to traditional surface treatments.

During this Ph.D. project, within the framework of Gigagreen Project, the impact of laser treatment on both anode and cathode CCs was investigated using two different laser sources. Treated CCs were supplied by project partners, whereas electrochemical characterization was conducted within this work. These collaborations led to the publication of two scientific articles [205,206].

2.4.2. Electrolyte and Separators

Another fundamental component of LIBs is the electrolyte, which enables the transport of Li-ions between the cathode and anode. Electrolytes can be broadly classified according to the amount of organic solvent present [207]: systems entirely based on organic solvents are referred to as *liquid electrolytes*; those containing only a limited amount of solvent are *gel polymeric electrolytes*; and systems with no solvent correspond to *solid polymer electrolytes*. A separate category is represented by *ionic liquids*, which are increasingly investigated due to their high thermal stability [208].

Given the vast research landscape surrounding electrolyte technologies, this chapter focuses only on the aspects directly relevant to the present Ph.D. work, with brief mentions of alternative systems, where relevant.

2.4.2.1. Liquid Electrolyte (LE)

The most common electrolytes used in LIBs are *liquid electrolytes*, consisting of one or more organic solvents in which a lithium salt is dissolved. Suitable electrolyte solvents must satisfy several key requirements [207,209]:

a. High dielectric constant to effectively dissolve the lithium salt
b. High electrolytic conductivity
c. Low viscosity
d. High chemical and electrochemical stability, with full inertness toward all cell components
e. Liquid nature under all operating conditions
f. Wide operation temperature range
g. Safe, low toxic, economical

The solvents of families that best fulfill these criteria are organic esters and ethers. In practice, carbonate-based solvents are the most widely used. These include cyclic carbonates such as ethylene carbonate (EC) and propylene carbonate (PC), as well as linear carbonates such as dimethyl carbonate (DMC), diethyl carbonate (DEC), and ethyl methyl carbonate (EMC) [209]. Their

chemical structures are shown in ***Figure 2.31***. Since no single solvent can meet all requirements simultaneously, mixtures of cyclic and linear carbonates are typically employed, allowing the electrolyte to achieve the desired balance of dielectric constant, viscosity, stability, and conductivity [207].

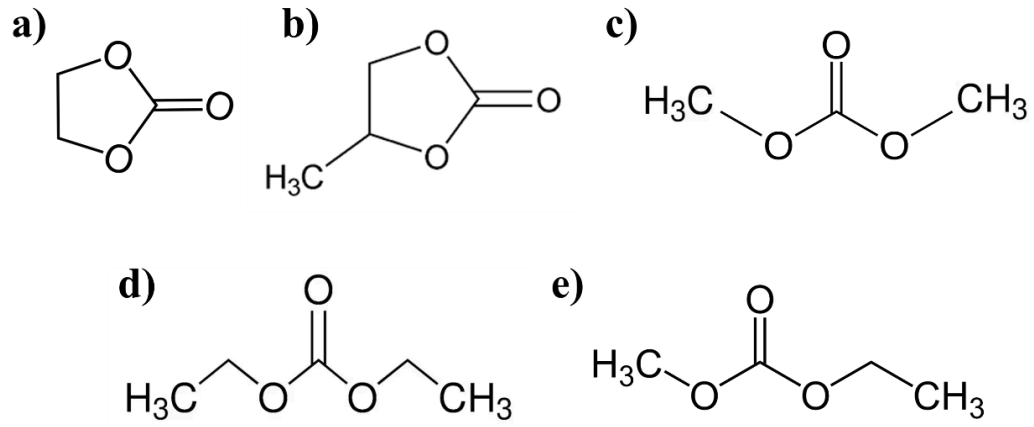

Figure 2.31 – Different types of solvents usually used in LIBs: a) EC; b) PC; c) DMC; d) DEC; e) EMC

Within this solvent mixture, one lithium salt is typically dissolved, as this configuration provides the most predictable physicochemical behavior. However, in some formulations multiple salts may be combined to fine-tune properties such as ionic conductivity, SEI formation, or high-voltage stability. As for solvents, lithium salts must meet several essential requirements [207,210]:

a. Complete solubility in the chosen solvent system
b. High mobility of the Li^+ cation
c. Chemical and electrochemical stability across the full operating potential window, without reacting with cell components
d. Ability to contribute to the formation of a stable SEI
e. Low toxic and low cost

Among the available salts, $LiPF_6$ is the most widely used because it combines high ionic mobility with good solubility in carbonate-based solvents, resulting in one of the highest conductivities among commercial electrolytes [207]. However, at high voltages it can promote passivation of the aluminum CC on the cathode side [211]. Since the anion strongly influences ionic conductivity and interfacial behavior, alternative salts such as LiFSI [212] and LiTFSI [210] have been explored, showing promising electrochemical performance. Their chemical structures are presented in ***Figure 2.32***.

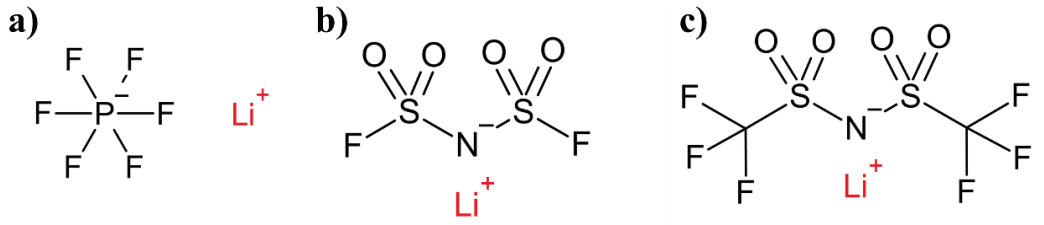

Figure 2.32 – Chemical structures of the most common lithium salts actually used in LIBs: a) $LiPF_6$; b) LiFSI; c) LiTFSI

Finally, LEs can be supplemented with specific additives to increase or modulate targeted properties [211]. Additives may promote the formation of a stable SEI layer, limit cathode dissolution, or modify electrolyte characteristics such as ionic conductivity and viscosity [213]. In this Ph.D. work, only a limited number of additives were employed, focusing on those suited for anode operation. Both selected additives belong to carbonate family: fluoroethylene carbonate (FEC) (***Figure 2.33a***), widely used to extend the cycle life of silicon anodes by stabilizing their SEI [214] and vinyl carbonate (VC) (***Figure 2.33b***), known for reducing the first-cycle irreversible capacity of graphite anodes [215].

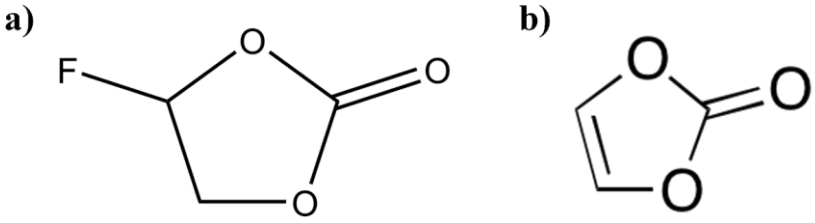

Figure 2.33 – Chemical structures of additives: a) FEC; b) VC

The LEs remain the most widely used system due to their high ionic conductivity (10^{-3}-10^{-2} S cm^{-1}) [216]. However, their use requires coupling with a polymeric semipermeable separator, which prevents internal short circuits while allowing Li^+ to transport. The separator must also withstand mechanical stresses during cell assembly, particularly in jelly-roll or z-folding stacking. Commercial separators are available in several materials, including cellulose or PP or PE, selecting according to the requirements of each specific application [208].

Despite their advantages, liquid electrolytes also present notable drawbacks, including the risk of leakage, flammability, and a relatively narrow electrochemical stability window (typically below 5 V) [216]. These limitations have driven research toward alternative electrolyte technologies.

2.4.2.2. Gel polymer electrolyte (GPE)

GPEs are inherently complex systems composed of lithium salt, a polymer matrix, and a controlled amount of organic solvent. The polymer acts as a

structural framework that immobilizes the solvent molecules, thereby improving the overall stability of the electrolyte [217]. The small quantity of organic solvent functions as a plasticizer, enhancing the mobility of the polymer chains and facilitating ionic transport [218].

In principle, GPEs aim to combine the ionic diffusivity of liquid electrolytes with the mechanical integrity of solids, as a polymer network supports the entire system. This hybrid behavior enhances safety and enables operation over a wider temperature range [219]. However, similar to LEs, GPEs may still experience leakage if their mechanical strength is insufficient [216].

2.4.2.3. Solid polymer electrolyte (SPE)

SPEs consist of a polymer matrix mixed with lithium salt, without any addition of LEs. This solvent-free formulation improves the overall safety of the system. Their chemical structure also provides higher thermal and mechanical stability compared to liquid or gel-based systems [216]. Moreover, SPEs simultaneously act as separators, physically isolating the two electrodes and preventing short circuits in a more controlled and effective manner [218].

Despite these advantages, SPEs face two major challenges. The first is the poor interfacial contact between the electrode surfaces and the solid electrolyte, which limits charge-transfer efficiency. The second is their low ionic conductivity, typically in the range of 10^{-8}-10^{-6} S cm^{-1}, far below that of conventional LEs [220].

2.4.2.4. Ionic liquid (IL)

ILs are organic salts, often referred to as molten salts, with melting points typically below 100 °C. They are synthesized by combining asymmetric organic cations such as pyrrolidinium (***Figure 2.34a***), pyridinium (***Figure 2.34b***) or ammonium (***Figure 2.34c***) with weakly coordinating organic or inorganic anions [221]. Some of the most common anions are shown in ***Figure 2.32***. The wide range of possible cation-anion combinations provides significant flexibility in designing ILs properties tailored to specific applications [222].

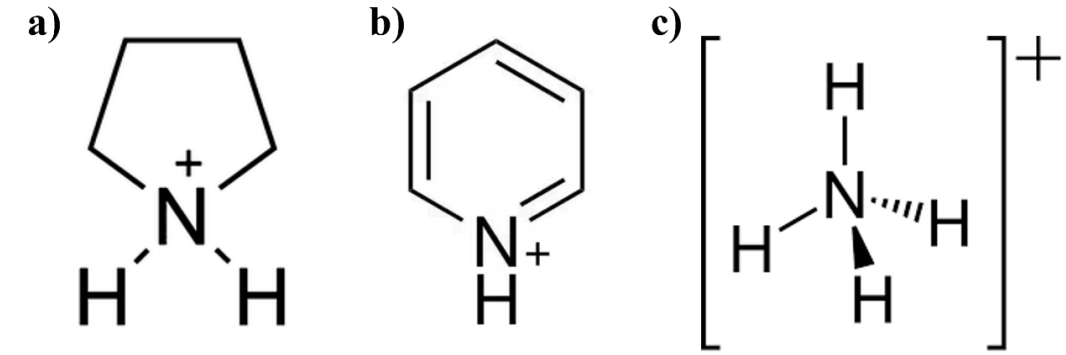

Figure 2.34 – Typical organic cations used in ILs: a) Pyrrolidinium; b) Pyridinium; c) Ammonium

ILs exhibit several advantageous characteristics for use in LIBs: high thermal and chemical stability, a wide electrochemical stability window, non-flammability, and ionic conductivity comparable to that of LEs [222]. However, their very high viscosity results in poor compatibility with commercially used separators, leading to inadequate wettability. In addition, their production costs remain considerably higher than those of standard electrolyte components [208]. For these reasons, the integration of ILs into commercial batteries is still challenging and remains an active area of research.

Chapter 3

3. Battery Manufacturing

LIBs are now widely deployed, yet their cost remains relatively higher. A major reason is the price of the material involved: AMs alone account for roughly 50% of the total cost of a cell [111]. This explains why a substantial part of current research targets innovative AMs that reduce the use of critical raw materials or provide higher volumetric capacity. Considering all cell components together (AMs, separator, electrolytes and case) the amount can reach up to 75% of the total cost of a LIB [223,224]. When shifting the perspective to a full battery pack, electrode manufacturing accounts for a range of approximately 27–40% of the total production cost [225]. Consequently, optimizing electrode manufacturing at the industrial scale has become a key challenge for cost reduction. Possible strategies include adopting more sustainable materials, developing more efficient and environmentally friendly processing methods, and redesigning production to facilitate battery reuse and recycling [226].

This chapter is structured in two main sections: the first focuses on the electrode manufacturing process, while the second provides an extensive overview of rheology and its relevance to LIB electrode formulation and processing.

3.1. The TRL level

Before describing the electrode manufacturing process, it is necessary to introduce the concept of Technology Readiness Level (TRL) and its relevance in the battery field. TRLs assess technological maturity and measure how close a technology is to market introduction, as shown in ***Figure 3.1*** [13].

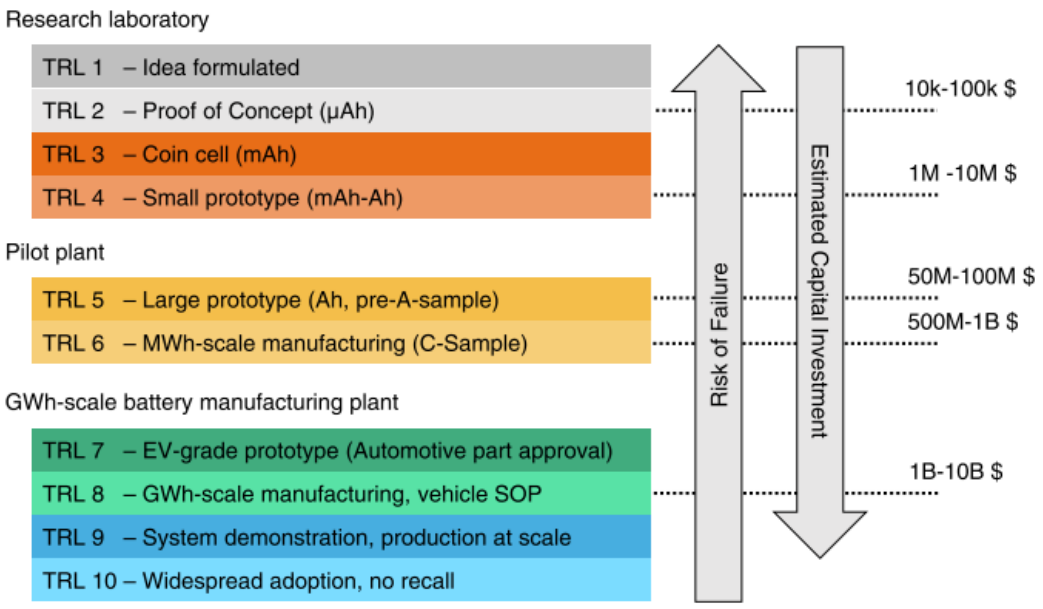

Figure 3.1 – Technology Readiness Level scale for EV battery application [13]

At low TRLs, where research is typically conducted in universities or research centers, the risk of failure is very high because new materials are developed and tested under conditions that often differ substantially from real-world applications. In the battery field, for example, electrochemical testing is usually carried out in coin cells, a format convenient for laboratory studies but distant from EV application. Production at this stage is discontinuous, allowing broad exploration of material candidates. However, most AMs developed at early stages never progress to industrial level, due to poor scalability, high production costs, or safety concerns that prevent transition to higher TRLs [227]. On the other hand, at industrial scale of Gigafactories, where the TRL exceeds 7, production is continuous, fully automated, and based on materials and processes that are already optimized, with the sole objective of massive manufacturing.

A substantial gap exists between early-stage research and industrial production, largely due to the limited availability of intermediate TRL facilities. These environments are extremely expensive and require significant space, which is why they are scarce in European panorama. Thus, the pilot-lines represent an essential bridge with multiple essential roles [13,227]:

- Assess scalability of laboratory formulations.
- Investigate process parameters and their interactions.
- Predict suitable process parameters.
- Validate cell design choices.
- Develop and test prototype cells.
- Optimize quality control procedures.
- Identify cost-reduction opportunities without compromising safety.

- Detect and mitigate production bottlenecks.

Overall, pilot-line facilities offer a realistic preview of industrial manufacturing, using equipment farcloser to industrial-scale tools than laboratory facilities. One key advantage is the possibility to work with semi-continuous processes, enabling meaningful process optimization while avoiding the enormous time and material losses that would occur if testing were carried out directly on a full industrial line [227].

Thanks to the pilot plant located at Environmental Park Laboratories in Turin, a central objective of this Ph.D. work was to compare the electrode manufacturing process at laboratory scale (TRL 3) with that of a pilot-line level (TRL 4-5). This comparison made it possible to identify bottlenecks, limitations, and improvements that emerge as TRL increases in the production of electrodes for LIBs application.

3.2. Overview about battery production

A representative flowchart of the multi-step production process is shown in ***Figure 3.2*** [228]. The entire procedure can be grouped into three main stages: electrode manufacturing, cell assembly and cell finishing. Electrode production is the core of battery manufacturing and involves the fabrication of both anodes and cathodes. The second stage is cell assembly, during which the electrodes are combined with the separator, filled with electrolyte and partially sealed in the appropriate casing. The third stage is cell finishing, where cells undergo formation: they are charged and discharged at low current to allow the development of stable SEI and cathode electrolyte interphase (CEI) layers on the electrodes. This step is notoriously slow and may require weeks or even months, making it the primary bottleneck of LIBs production [227,229]. After formation, the cells are refilled with electrolyte and sealed completely. Once individual cells are completed, they are assembled into modules, which are subsequently integrated into battery pack. This pack is then connected to a Battery Management System (BMS) to ensure proper and safe operation [230].

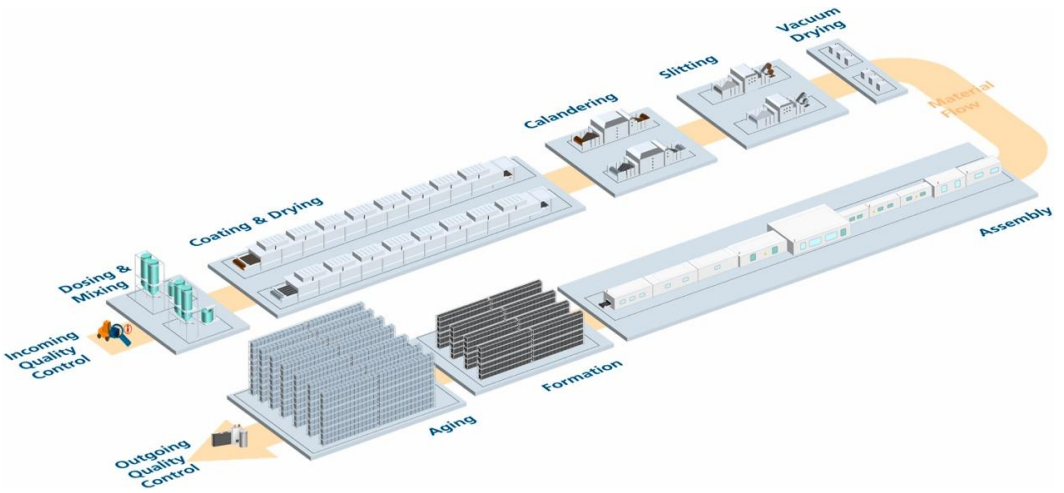

Figure 3.2 – Complete flow chart of battery production process [228]

Li-ion batteries can be manufactured in three main geometries: cylindrical, prismatic and pouch cells [231]. These configurations share the same electrode manufacturing process, while the major differences arise during cell assembly, as each geometry requires specific equipment and handling methods. For instance, cylindrical cells are typically produced using the jelly-roll process, whereas pouch cells are assembled through z-folding. The selection of a particular cell format depends on the requirements of the final application [232].

3.2.1. Electrode production

The process of fabricating electrodes plays a crucial role in shaping the ultimate performance of a battery, as it impacts the morphology and interface characteristics. These directly influence key parameters such as porosity, pore size, tortuosity, and the effective transport coefficient. The actual production process used in the industry is based on wet production involving the use of a solvent for properly dissolving the powders. However, several researchers are focusing on the drastic reduction of the use of solvent, for example, by using extrusion as a proper technique for the mixing and coating in case of high-viscosity mixtures [233]. The ultimate step in this direction is the development of the fully dry process, which completely eliminates solvents and represents one of the most challenging approaches to improve production sustainability [234]. In this chapter, however, only the wet processing will be investigated.

The complete electrode production process can be divided into four main steps (Mixing, Coating, Drying and Calendering), as schematically shown in ***Figure 3.3*** [235]. Each of these steps will be discussed in detail, with particular attention to the differences between low TRL laboratory equipment and medium TRL pilot line facilities. During this Ph.D. project, electrodes were produced at both TRL levels and systematically compared, with the analysis mainly focused on

electrochemical performance as well as rheological behaviour and mechanical properties of the dried electrodes.

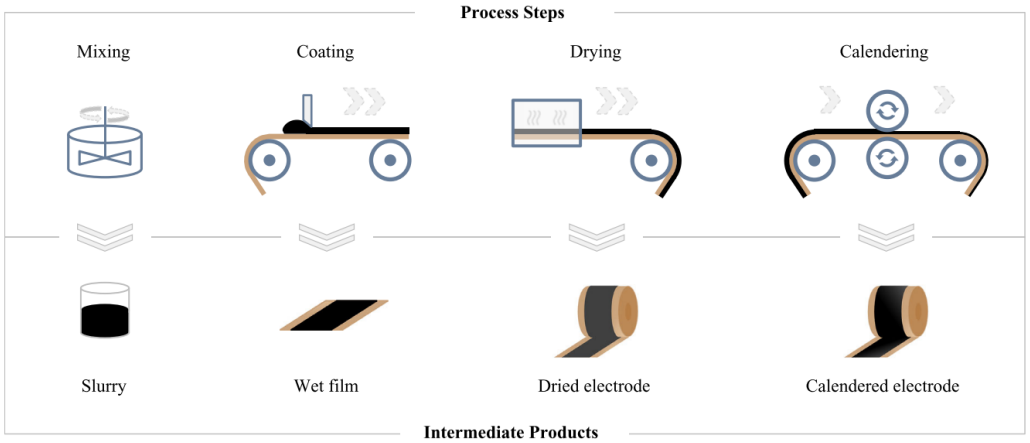

Figure 3.3 – Schematic presentation of the steps involved in electrode production process and the intermediate products [235]

3.2.1.1. Mixing

The first step is the ***mixing step***, where the AM, CA and binder are dispersed in the proper solvent to produce the *wet slurry*. This step is the most important of all the production processes because it is responsible for the optimal homogenization of the materials and directly affects all the other steps. Considering the whole electrode production process, the mixing step is the longest one, because it requires many hours and its contribution to the total manufacturing cost can be around 8% [236]. Many variables can affect this step, starting from the time and the rotating speed that are applied during the mixing. The rotating speed is usually expressed in rpm (rotations per minute), and the achievable or recommended rpm range depends on the specific instrument configuration, geometry, and motor design. Second, the shape and the dimension of the mixer used, which can be very different at different TRLs, impacting on the processability of the slurry and requiring further tuning and optimization of the process [227]. Furthermore, depending on the facility, it is also possible to perform this step under vacuum to favor the degassing of the slurry, especially in case of NMP slurries.

Going more in detail of the facilities normally involved in this step, it is possible to identify some typical ones depending on the amount of slurry and thus the TRL: for example, for small amounts of slurry, the use of a magnetic stirrer (***Figure 3.4a***), ball milling (***Figure 3.4b***) or ultrasonic homogenization is preferred thanks to their effectiveness [226]. However, some limitations do not make them suitable to be used on a larger scale, for example, the magnetic stirrer cannot properly mix high-viscosity slurries, leading to the presence of clumps and agglomeration. In addition, none of them can properly perform the target in the industrial process of three liters per minute of slurry [237]. For this motivation,

when more slurry is involved, other types of mixers have to be preferred, with bigger tanks and different geometries, like homogenizers (***Figure 3.4c,d***), planetary mixers (***Figure 3.4e***), more complex high-speed mixers (***Figure 3.4f***) [226] and extruders [233]. It is not that easy to properly divide the mixers depending on the TRL application but generally, low TRLs are associated with a batch size that is less than 2 L, the pilot level can reach up to 60 L, and the industrial level mixers can process 2000 L of slurries [227].

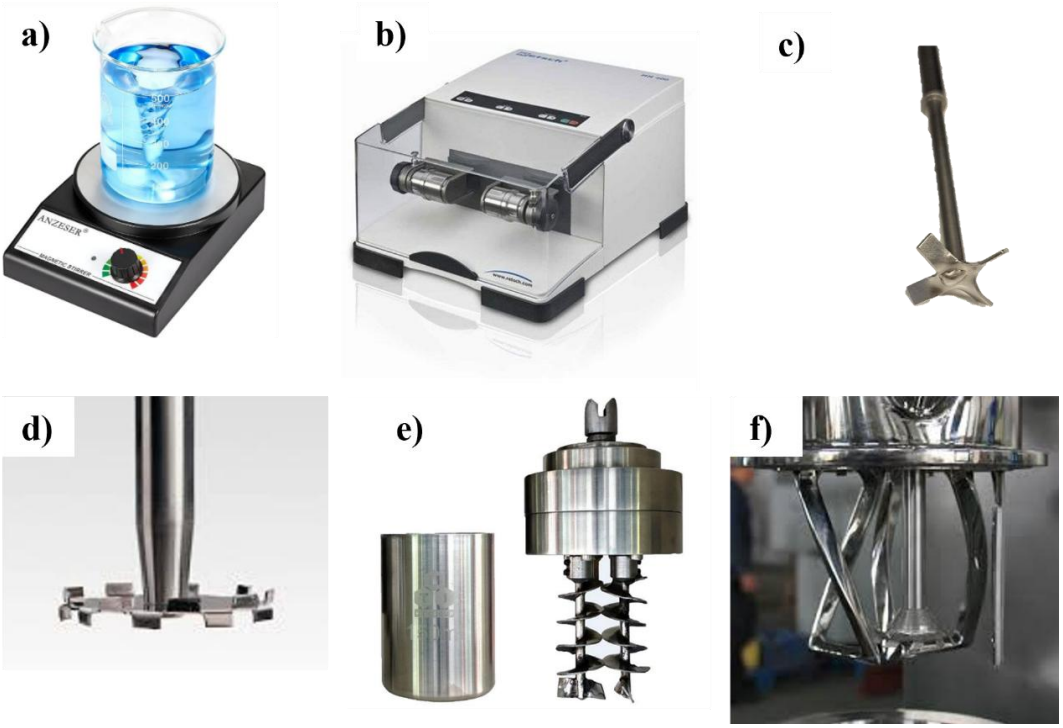

Figure 3.4 – Different types of mixers used at different TRLs: a) Magnetic Stirrer; b) Ball milling; c) Homogenizer mixer used in Polito laboratories; d) Dispermat Mixer; e) Planetary Mixer; f) Complex homogenizer blades for higher TRL applications

Mixing requires more time compared to the coating and drying steps, but it is fundamental to carry it out in the proper way, in order to avoid spontaneous processes like sedimentation or agglomeration that lead to a non-homogeneous slurry and negatively influence the deposition step. It is well established that multi-step, sequential addition of components promotes effective dispersion of powders in the solvent, and that the order of addition can alter the final properties of the slurry [238,239].

Y. He et al. [240] suggested the importance of rheological properties (solid fraction, viscosity, shear rate, storage modulus) of the slurry in all the successive steps of the production: to reach the higher electrochemical performance, a deeper knowledge of the "microenvironmental of AM" (ME@AM) could be the first step. ME@AM is the local space around the single particle of AM and can be used to evaluate the quality of ion and electron transport. Hence, the structure of the microenvironment of the electrode can be strictly associated with the slurry

rheological properties not only in the mixing step, but also in all the following steps.

The most reliable way to evaluate slurry viscosity is through rheological measurements performed with a rheometer, as discussed in detail later in this chapter. However, such measurements can only be carried out if the slurry viscosity falls within the instrument's measurable range. In practice, this creates a preliminary challenge: before testing, the actual viscosity is unknown, yet the slurry must already be formulated within an appropriate range to allow accurate rheological characterization and ensure suitability for subsequent processing steps. A preliminary indication of viscosity can instead be obtained from the solid fraction (SF), defined as the ratio between the total mass of solids and the total mass of the slurry (***Equation 3.1***).

$$SF(\%) = \frac{S}{S+L} \cdot 100$$

Equation 3.1

Where S represents the sum of all the solid components (AM, CA, binder) and L represents the amount of the solvent added. The value of the solid fraction has been demonstrated to be a fundamental parameter to calculate before performing the mixing: a higher amount of solid, for example, promotes the dispersion of the CA, thanks to a higher shear stress [223]. A low value of solid fraction can have a negative impact on the subsequent production steps, especially the coating [241]. However, the SF has to be considered only as an indicative parameter for the production process, and a deeper investigation with a rheometer must be done.

In fact, the viscosity of the electrode slurry is a key parameter in the production of LIB electrodes, as it determines the processability, homogeneity, and quality of the coating. Proper control of viscosity ensures uniform dispersion of the AM, binder, and CA, preventing sedimentation or agglomeration during mixing. It also enables smooth and defect-free coating on the CC, directly influencing the electrode's thickness, porosity, and adhesion. Moreover, the viscosity reflects the internal interactions within the slurry, such as particle-binder network formation and solvent content, making it a critical indicator for both formulation optimization and process reproducibility. Therefore, viscosity measurement is essential to guarantee consistent electrode performance and reliable large-scale manufacturing. Further discussion on the general principles of rheology and their application in this field will be presented later in this chapter.

3.2.1.2. Coating

Once the slurry is properly mixed, the subsequent step is the ***coating step***, which is the core of the electrode production: the wet slurry is deposited on the

CC, with a deposition that has to be as homogeneous as possible, so the final result is strictly related to the mixing process [223].

This step is the most divergent depending on the TRL for the different systems of deposition: due to the small amount of slurry normally used at the laboratory level, the coating is performed with very simple instruments like a doctor blade (an example is reported in ***Figure 3.5***). This simple tool permits to manually set the desired thickness for the wet slurry (from a few dozen µm to a few hundred µm), permitting a great flexibility during production. However, doctor blade technique permits the coating only of a small area per time (dozen cm^2), with a very low speed, of only some cm min^{-1}, and high variability due to manual thickness adjustment. Therefore, this approach is suitable for early-stage research purposes, for example, in the case of preliminary analysis after the synthesis of new AMs, where only a very small amount of material is available.

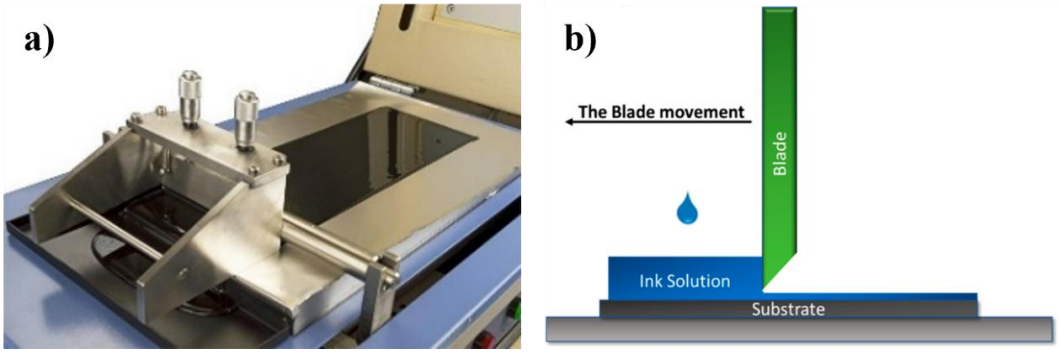

Figure 3.5 – a) Doctor Blade coating method; b) Schematic working principle of the Doctor Blade

For the up scaling of the process to the industrial level, this simple instrument is not able to guarantee a high production rate. So the actual state-of-the-art, for high TRL electrode manufacturing, is the slot-die coater [233], one of the most common systems is the roll-to-roll coater (***Figure 3.6a***) based on the Reverse Comma technology (***Figure 3.6b***) [237]. This technology is the one used during this Ph.D. work. Alternative technologies include tape casting, which is similar to the previously described doctor blade technique, and slot-die coating, where the slurry is extruded through a narrow slit of controlled thickness and directly deposited onto a moving substrate. Actually, modern coaters can operate at 50 m min^{-1} [225] with the additional advantage of integrating the drying and calendering step in line, enabling a continuous production process.

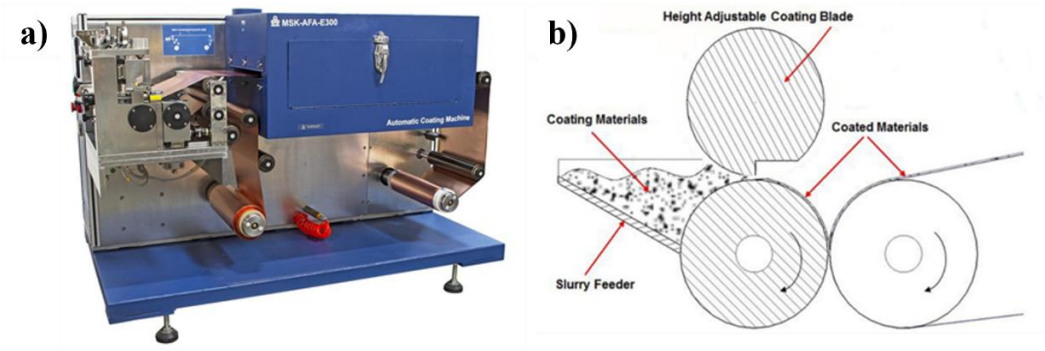

Figure 3.6 – a) Small Roll-to-roll system for the coating, on the right part of the instrument is located the oven; b) Schematic working process of the Reverse Comma Technique

In conclusion, the coating process is affected by multiple parameters, which may be related either to the intrinsic properties of the slurry (*e.g.*, viscosity) or to the operating conditions of the equipment. Starting from the slurry characteristics, if the viscosity is too low, during the deposition, it is possible to observe phenomena like phase separation. On the other hand, if the viscosity is too high a homogeneous deposition is not guaranteed. Another slurry parameter that should be carefully monitored is the storage modulus, which is closely related to the electrode microstructure. In particular, it reflects the network formed by the conductive carbon particles, which can influence the final electrochemical performance of the cell [242]. Regarding the machine parameters that can be controlled during the coating step, they are mainly two: the thickness of the deposition and the speed. The speed can affect especially the adhesion of the slurry to the CC, while the imposed thickness plays one of the most important roles in the ML [237].

3.2.1.3. Drying

After the coating step, the solvent is evaporated from the wet electrode during the ***drying step***. This is considered one of the most expensive steps of the whole electrode manufacturing process, because it is very energy consuming as it normally involves multiple steps at high temperature. This aspect becomes particularly evident when NMP is used as the solvent, as it requires a strictly controlled environment for safety reasons. Moreover, both NMP handling and recovery significantly increase processing costs [243]. Conversely, the use of greener solvents, such as water, represents a more cost-effective and sustainable option. However, complete removal of water is essential to ensure proper electrode performance [244].

At small TRLs, the drying process is typically non-continuous and the wet electrode is manually moved from the coater to the (vacuum) oven, where it is dried for several hours. In contrast, at industrial level, the oven is integrated inline, with the coater, so the drying time is lower and depends on the coating

speed and the length of the drying chamber [111,227]. Although coating and drying are performed in a continuous configuration, their operating cost remains significantly higher than that of the mixing step, mainly due to the energy demand associated with solvent removal [225]. At industrial scale, this step requires significantly shorter times (typically 2-3 minutes) than at the laboratory scale. However, at a coating speed of 50 m min^{-1}, the dryer would need to be approximately 150 m long, resulting in substantial costs in terms of energy consumption and required floor space [245].

The actual state-of-the-art of drying is based on a convective process, which can remove the solvent thanks to heated air blown from proper nozzles [246]. This step is commonly a multistep process, based on connected ovens with different temperatures (***Figure 3.7*** [247]). The graph clearly represents the different sections inside the oven and the relative temperature, correlated to the residual amount of solvents during the drying process. The graph aims to compare the different behaviors of NMP and water which depend on their chemical properties. Even if the drying step seems to have similar operating costs for both solvents, it has to be taken into account that NMP must be collected and recovered, meaning that the use of water permits a total energy consumption which is 25.7% lower [248].

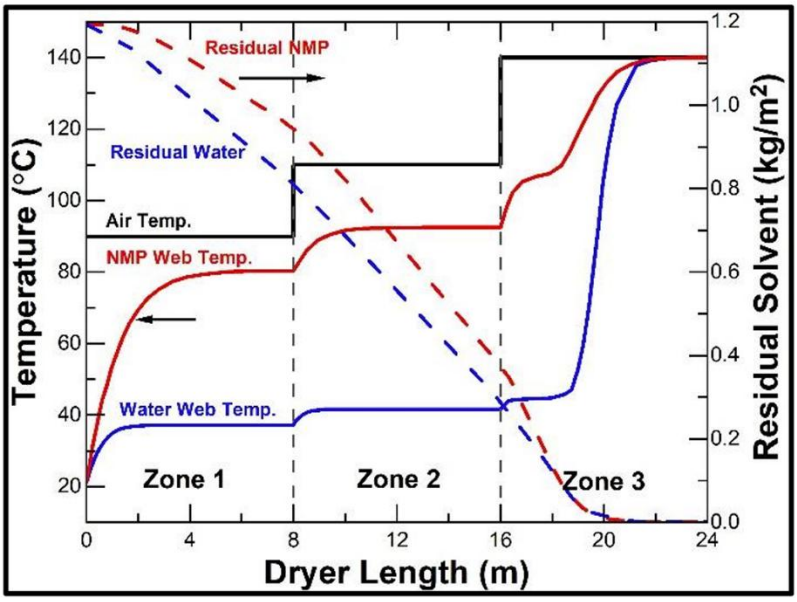

Figure 3.7 – Comparison of a typical drying process for a NMP-processed cathode and a water-based anode. Reproduced with permission from [247]. Copyright 2017 American Chemical Society

Two main stages of solvent evaporation can be identified (***Figure 3.8***) [249]. Starting from the wet film of the just coated electrode (***Figure 3.8a***), the first step is related to the larger volume of solvent evaporation associated with film shrinkage (***Figure 3.8b***), where the thickness of the electrode is drastically reduced. During this stage, the evaporation occurs mainly from the top surface of

the electrode and the thickness is reduced until the solid particles make contact with each other. During the second part of the drying (***Figure 3.8c,d***), the thickness remains constant and the solvent continues to evaporate thanks to capillary transport across the AM particles [250]. This stage is called pore emptying because the solvent is mainly removed from the AM pores [225]. The resulting dried electrode (***Figure 3.8e***) should be characterized by a uniform distribution of all the components.

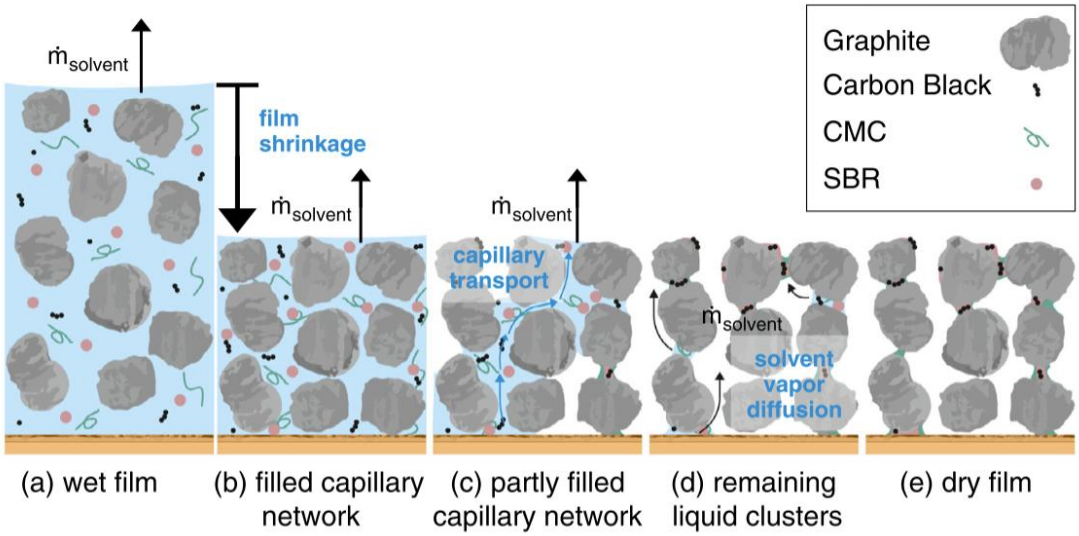

Figure 3.8 – Schematic process of the drying steps [249]

During the drying process, multiple physical phenomena occur inside the wet slurry [251]: evaporation, convection, diffusion and sedimentation. Under typical electrode manufacturing conditions sedimentation effects can generally be neglected [252]. Also in this step, the viscosity plays a fundamental role: in fact, higher value of solid fraction can drastically speed up the drying process, reducing the energy cost in this step [224,253]. Haarmann et al. [223] were able to demonstrate that increasing the solid content of a cathode slurry from 65% up to 75% allowed a decrease in the energy costs of this step of around 12%. However, if the drying rate or temperature are too high, the binder is not able to reach a homogeneous dispersion, with a fast migration towards the electrode surface [246], leading to an uneven distribution that finally causes poor adhesion to the CC [250]. Thus, a correct balance between the drying rate and the oven length is mandatory to satisfy industrial production requirements and ensure the proper drying process.

The use of water has to be preferred not only in relation to the drying step, but it can also greatly simplify all the previous steps of the electrode production, as reported in ***Figure 3.9*** [117], where the author compared the use of NMP or water in the production process. It is clearly evident that the use of NMP has a great impact due to its high toxicity and the entire production process needs to be

engineered in order to avoid its dispersion in the air. On the contrary, the use of water permits reducing the strict working conditions, and thus the overall costs are dramatically reduced.

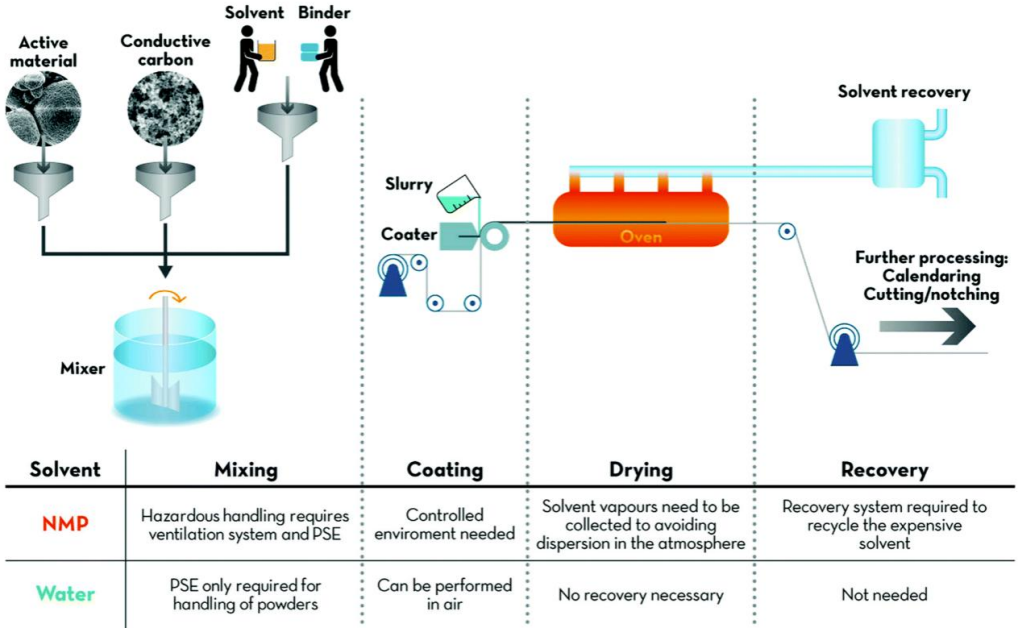

Solvent	Mixing	Coating	Drying	Recovery
NMP	Hazardous handling requires ventilation system and PSE	Controlled enviroment needed	Solvent vapours need to be collected to avoiding dispersion in the atmosphere	Recovery system required to recycle the expensive solvent
Water	PSE only required for handling of powders	Can be performed in air	No recovery necessary	Not needed

Figure 3.9 – Schematic representation of the production process, with an important focus on the benefits of using water as a solvent in the production instead of NMP [117]

Several innovative approaches have been proposed to accelerate solvent removal, including the coupling of conventional convection with electromagnetic waves. Among these, the most promising is infrared drying, offering the potential to reduce the required oven length by up to 90% [254]. Other coupled methods actually, under evaluation are laser and microwave drying process. Alternatively, a different type of drying method is based on Joule heating, using induction to generate alternating magnetic fields able to heat the electrode [245].

3.2.1.4. Calendering

Once the slurry is completely dried, the electrodes are subjected to subsequent ***calendering*** steps. The calender machine is typically made of two stainless steel rolls with an imposed gap between them, where the dried electrodes are gradually thinned to the desired thickness [111]. The calendering step has the aim of reducing the thickness (***Figure 3.10a***) and reduce the porosity of the electrode. Therefore, calendaring process leads to multiple positive effects [255]: first, an increase in volumetric energy density, secondly, a decrease in the tortuosity. Furthermore, it increases both the contact between the particles of AM and CA but also with the CC, leading to an increased the electronic conductivity [256]. Due to the strong modification of the electrode microstructure induced by

calendering, a deeper understanding and optimization of this step are required. For this reason, several modelling approaches have been proposed in the literature to describe the evolution of porosity, particle contacts and transport pathways within the compressed electrode structure [256–259].

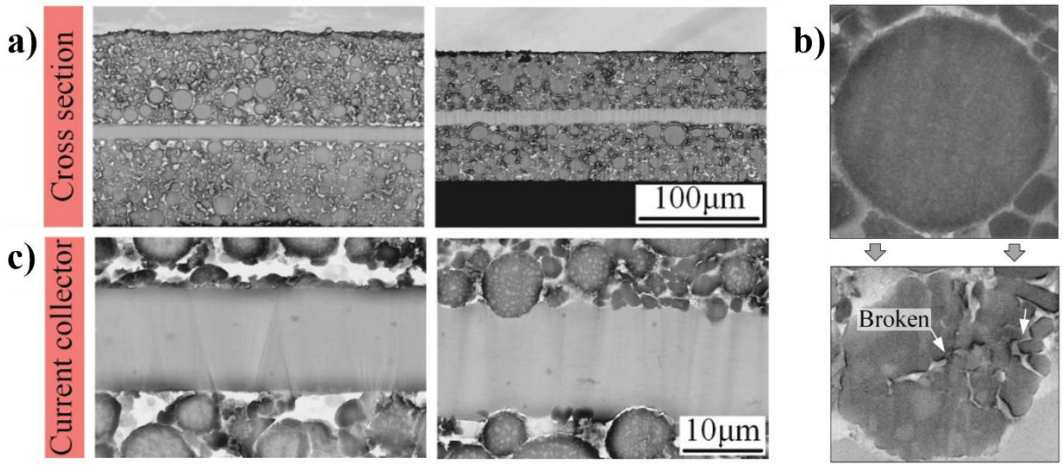

Figure 3.10 – Comparison of the different impact that can occur after the calendering step: a) important reduction of the electrode thickness; b) the excessive strength applied can bring to the fracture of the active material particles; c) the excessive strength applied can lead to the deformation of the current collector. Partially reproduced with permission from [255]

Numerous studies have demonstrated that calendering the electrode with high pressure leads to the fragmentation of nanoparticles (***Figure 3.10b***) and deformation of the CCs (***Figure 3.10c***), decreasing the final specific capacity and lower CE [260]. However, concerning the cathode side, a decrease in porosity of about 30% has been confirmed to be the optimal value both for NMC [261] and LFP [262], balancing the ionic conductivity of high porosity and the good electronic conductivity of low porosity [256].

Considering the graphite anodes, a reduction of the porosity between 40% and 50% is the production target to obtain the most performing anodes [263]. A moderate compaction of the graphite anodes permits improving the electrolyte wettability thanks to a sort of alignment of the graphite particles [264]. However, avoiding excessive compression in case of graphite anodes is mandatory to allow the graphite to maintain a proper porosity and pore size distribution for facing the dimensional change during the lithiation step, even though the variation of the volume is only around 10% [264,265].

Concerning the use of silicon in anode applications, calendering becomes more challenging as the silicon content increases, which is reflected in the often contradictory results reported in the literature [266–270]. This can be directly related to the possibility of the anode structure to collapse after the application of pressure, leading to an excessive reduction of porosity [264]. The consequence is the limiting space for silicon expansion during the lithiation step: if the electrodes are compressed as is normally due for the graphite anodes, the silicon experiences

even greater stress during the lithiation step because it has no more space to expand, leading to a poor electrochemical performance.

3.2.1.5. Slitting

The subsequent step, the last one which can be considered part of electrode production, is ***punching***, ***cutting*** or ***slitting*** aimed at producing electrodes with the desired dimensions. This step is strictly dependent on the final geometry of the cell: in the case of pouch cell, the electrodes are cut and stacked, only in a second time they are assembled in the pouch cell configuration. While in case of the prismatic or cylindrical configuration, the electrodes are slitted and directly assembled [271].

The state of the art of the cutting process is die cutting, although this widely used technology is limited by the shape of the cutter, and if a redesign is desired, a different tool must be purchased [272]. Over the years, laser cutting has been proposed as a valid alternative thanks to its high versatility and faster process, though some degradation phenomena can occur on the surface of the AMs [273].

3.2.2. Cells, modules and final battery pack assembly

Once the electrodes are finished, they are ready to be ***assembled*** into the cells with the separators, ***filled*** with the electrolyte, and then the entire cell is ready for the final sealing. The electrolyte filling is a cost-intensive step for the highly controlled environment, which is necessary to avoid the degradation of lithium salts during the electrolyte filling process [274]. In addition, the improper or inhomogeneous wetting of the electrodes inside the cells is one of the most common causes of poor performance [275]. The cell can be considered completely isolated from the external atmosphere once the final side is sealed.

The subsequent step is the ***forming*** of the cell by performing numerous and long charge and discharge cycles to ensure the correct formation of the SEI layer [276]. The forming procedures are generally highly complex to guarantee the best battery performance and are therefore often subject to industrial secrecy [277]. The gases produced during the SEI formation are generally removed and new electrolyte is added to complete the formation of the cell [278]. Once the forming process is completed, the cells can be assembled into modules and finally into packs, with the integration of the BMS and tailored to the final application.

3.2.3. Quality Control

Along the entire production process, multiple control systems are required at different levels to ensure proper operating conditions, process safety and high battery performance. These techniques are generally classified as in-line, where the instrument is integrated directly into the production line and provides real-

time feedback, or off-line, where the analysis is carried out separately and in parallel to manufacturing. In-line inspection accelerates production by immediately identifying defects, whereas some analyses are too slow to be integrated into continuous processing. The complexity of the quality controls involved in battery production is shown in ***Figure 3.11*** [279], where each step of electrode manufacturing is described with the parameters involved in the process and the relative analyses available.

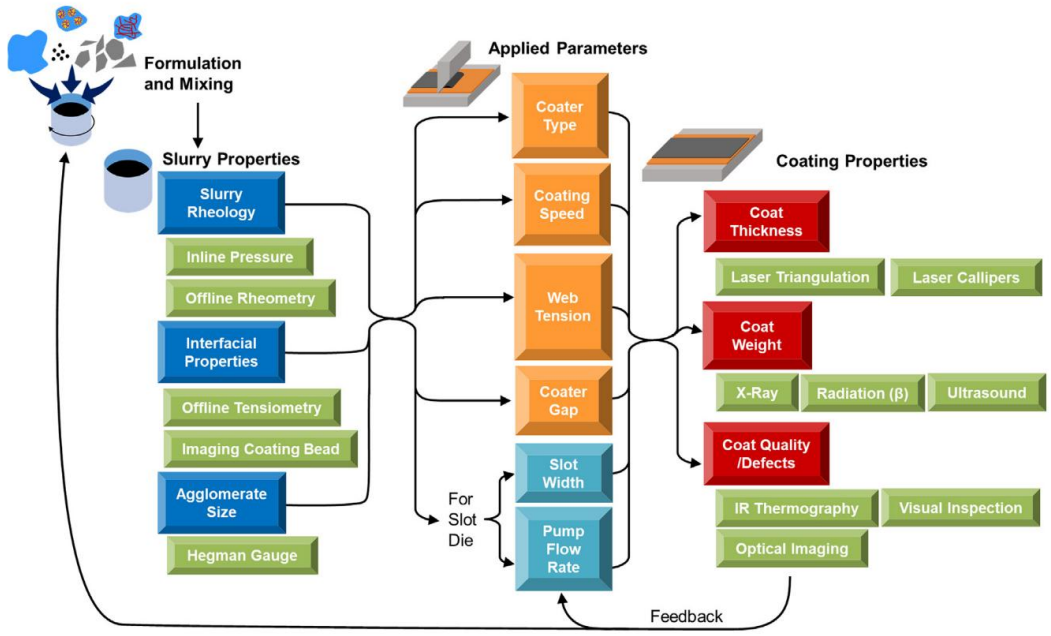

Figure 3.11 – Schematic representation of the electrode manufacturing process with the parameters involved in the production process and the relative analyses involved in the quality control [279]

Before mixing, the AM can be characterized to determine particle-size distribution by laser diffraction or dynamic light scattering and its chemical composition can be confirmed using IR and Raman spectroscopy. After mixing, the viscosity of the slurry must be verified to confirm that it lies within the appropriate range for the coating step. Rheological measurements necessarily require an off-line equipment, and their principles will be discussed later in this chapter.

During electrode manufacturing, the coated surface is monitored to verify thickness uniformity, surface morphology, and the presence of defects such as cracking or delamination, as well as unwanted particles, which can severely affect electrochemical performance and cell safety [280]. Several automated inspection systems are used for this purpose, including conventional optical imaging [281,282], non-destructive thermal imaging [283], infrared particle detection [284], laser-based calipers [285] and X-ray radiography (2D imaging) [285] or X-ray computed tomography (CT) (3D imaging) [286,287]. After cell assembly, CT inspection is widely recognized as one of the most useful industrial-scale

technology to reveal internal defects, including misalignment, foil wrinkles or dendrite formation [288]. Laser-beam technology is also employed for detecting gas formation after sealing pouch-cells [289]. However, techniques such as CT scanning require several hours to fully inspect a single cell, making them an additional bottleneck in quality control.

Quality control is a mandatory procedure in battery manufacturing, ensuring that production meets the strict standards required to commercialize batteries with highest performance and guaranteed safety.

3.3. Rheology

Rheology is a complex science, the branch of physics that deals with the flow and deformation of matter, describing the relationship between force, deformation and time [290]. In the beginning, the term was mainly referred to as a science for describing the flow of liquids (in Greek *rhei* or *rheo* mean *to flow*) and the deformations of solids. Actually, the term has become more general with the rheology that wants to find an answer to the question *How does a material respond to a force?*¸ and they refer to this force in terms of "stress" [291].

Rheology concerns the description of materials made of complex microstructure with the use of simple equations (rheological material functions) extracted from continuum mechanic. Thus, the physical and chemical properties of a material directly affect the rheological behaviour, allowing to understand the correlation between these properties and the processing of materials. Specifically, the rheological study of material, both liquid or solid, enables us to gain deeper insight into the relationship between deformations and flows and how these can be affected by strains, stresses and time. For this, it is widely applied in numerous fields like cosmetics, construction materials and petroleum, generally, every time that a material has to be handled. One explicative example can be toothpaste because proper viscosity is required to squeeze it out of the tube to have a competitive product on the market.

Ideally, it is possible to distinguish the materials into two families: solid and liquid. A material is defined as *solid* when its shape is fixed and does not change if a stress is applied. On the contrary, a material is defined as *liquid* when it is able to continuously change its shape, even when the stress applied is very small. Real materials are typically complex systems combining solid and liquid behaviour. This behaviour is called *viscoelasticity* [292]. In addition, for rheological studies, it also becomes important to define the "timescale of the observations": it is possible to observe different behaviours if the time considered is very short or long enough. The most illustrative experiment of this concept is the *Pitch Drop experiment*: in 1927 Professor Thomas Parnell started this experiment to demonstrate that even the pitch, which is almost considered a solid, over longer timescales, it behaves like a liquid, observing the fall of some drops [293].

It is possible to define different types of flows which can directly affect the rheological properties of complex fluids [294]:

1. Shear Flows (***Figure 3.12a***): in the presence of rigid walls, adjacent particles move over or past each other, forming laminar elements. In this type of flow, the shear is applied to the bottom and the top of the sample in two opposite directions, generating a gradient of velocity inside the sample, with the top moving faster [295].
2. Extensional Flows (***Figure 3.12b***): in the absence of rigid walls, adjacent particles move away from or towards each other, typical behaviour of liquids and gases. It occurs when the force is applied in opposite directions along the entire sample [295]. Studying this type of rheology requires specific experimental setups.
3. Complex or Mixed Flows: collect all the other types of flow

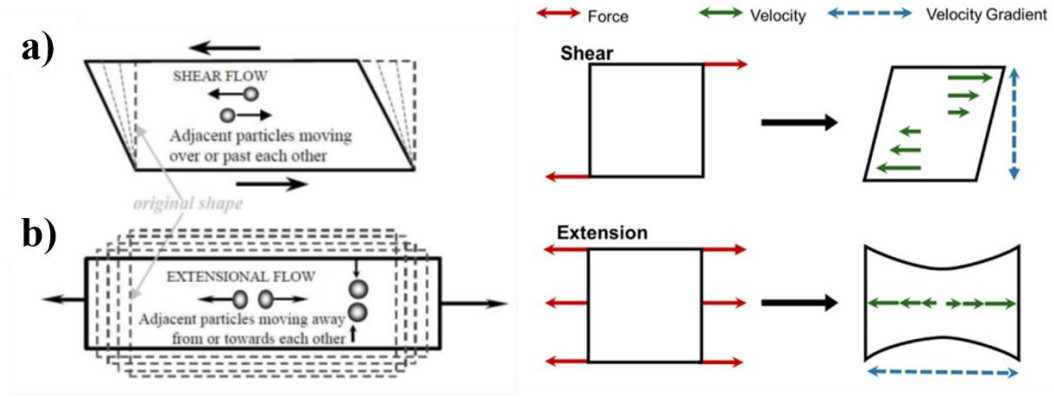

Figure 3.12 – Representation of different types of flows and the parameters involves: a) shear flow; b) extensional flow. Reproduced with permission from [294] and [295]

3.3.1. Formulas and definitions

For a proper and easier description of the parameters used in rheology, it is useful to introduce the two-plates model (***Figure 3.13a*** [292]): the lower plate is fixed, while the upper plate, with area A, is moved by applying a shear force F at a constant velocity v. The distance between the two plates is fixed at h. Considering this model, two shear conditions are necessary to calculate the rheological parameters accurately:

- There must be adhesion between the sample and the plates.
- The flow must remain laminar (***Figure 3.13b*** [292]), ensuring homogeneous deformation: this assumption allows the flow to be described as multiple layers, with no turbulences or vortices.

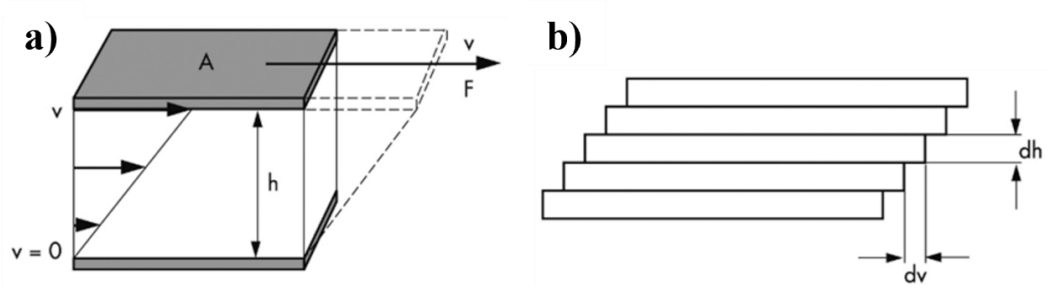

Figure 3.13 – a) Representation of the velocity distribution of a flowing fluid with a fixed shear gap in case of the Two-Plates model; b) Representation of the concept of laminar flow: the fluid is ideally divided into layers. Reproduced from [292]

To provide a clear basis for the rheological concepts discussed in this chapter, some fundamental definitions commonly used in rheology are introduced below.

- **Shear stress** – The shear stress is the force applied per unit area and can be calculated with the formula reported in ***Equation 3.2***. Where F is the shear force expressed in Newton (N) and A is the shear area expressed in m^2. The measuring unit of the shear stress is Pa (Pascal).

$$\tau = \frac{F}{A}$$

Equation 3.2

- **Shear strain** (or **shear deformation**) – The shear strain is the measure of the deformation of a material due to the shear stress and permits to describe how much a material is distorted from its original shape. The shear strain is calculated based on ***Equation 3.3***, where *s* is the deflection path expressed in m and *h* is the shear gap expressed in m. Shear strain is a dimensionless quantity.

$$\gamma = \frac{s}{h}$$

Equation 3.3

- **Shear rate** – The shear rate is the measure of the rate at which adjacent layers of fluid move with respect to each other. It is also referred to as the rate of deformation or shear gradient. The shear rate is calculated based on ***Equation 3.4***, where *v* is the velocity expressed in m s^{-1}, and *h* is the shear gap expressed in m. Thus, its unit of measurement is s^{-1}.

$$\dot{\gamma} = \frac{v}{h}$$

Equation 3.4

- **Viscosity** – Viscosity depends on multiple parameters that occur when the molecules of flowing fluids are characterized by relative motion between one another, in combination with internal frictional forces. For ideal viscous fluids, at a constant temperature, the viscosity is described as the measure of the resistance of a fluid to flow or to deform under an applied force (***Equation 3.5***). Where τ is the shear stress expressed in Pa, and $\dot{\gamma}$ is the shear rate, expressed in s^{-1}, thus its measuring unit is Pa·s. These parameters can only be precisely measured if there are laminar flow conditions and there is a uniform flow.

$$\eta = \frac{\tau}{\dot{\gamma}}$$

Equation 3.5

- **Shear modulus** – The shear modulus measures the rigidity of a material or its resistance to deformation under shear stress. It is an intrinsic property of the material: depending on the chemical structure, the presence of stronger intermolecular or crystalline forces leads to higher values of G. The shear rate is calculated based on ***Equation 3.6***, where τ is the shear stress and γ is the shear strain, thus the measuring unit is Pa. In the case of a fluid, its shear modulus is zero.

$$G = \frac{\tau}{\gamma}$$

Equation 3.6

- **Complex shear modulus** – A measure of the viscoelasticity behaviour, described as the response to oscillatory shear stress. It is obtained by combining the elastic and viscous properties of the material (***Equation 3.7***), where i is the imaginary unit, G' is defined as the storage modulus and represents the elastic contribution of a material that behaves like a solid, and G'' is defined as the loss modulus and refers to the viscous component, which describes a liquid-like material.

$$G^* = G' + iG''$$

Equation 3.7

- **Flowpoint (**or **Damping factor**) – Describes the behaviour of a viscoelastic material, indicating whether the viscous or elastic contribution dominates. It is calculated from ***Equation 3.8***: when tanδ>1 (G''>G') the material behaves more like a viscous liquid, while when tanδ<1 (G''<G') the material behaves more like a solid with elastic contribution.

$$\tan\delta\left(\frac{G'}{G''}\right)$$

Equation 3.8

3.3.2. Parameters

The parameters that can affect the rheological properties of a material are multiple, and they can be divided into two big categories: internal and external. The internal ones are intrinsic to the material and cannot be changed during the rheological analysis, while the external ones depend on the analysis conditions and can be freely modified.

Internal parameters

Based on the physicochemical characteristics of the material, it is possible to highlight some characteristics that can affect the interaction forces between molecules, causing attraction or repulsion, whose macroscopic behaviour is related to a more or less viscous response. These aspects are particularly evident in the case of polymers, distinguishing between the steady-state conditions, when polymers can be described as random coils with some fixed connections with the other molecules, and the shear process when the molecules are oriented in the shear direction.

In ***Figure 3.14*** [292] is reported the ideal viscosity function of a polymer solution in absence of cross-linking between the molecules. Depending on the applied shear rate it is possible to highlight three regions related on the behaviour of the polymer:

1) First Newtonian range: the viscosity is constant.
2) Shear-thinning range: the viscosity can be described by a shear-dependent function.
3) Second Newtonian range: after the complete detanglement of the polymeric molecules, the viscosity becomes constant once more.

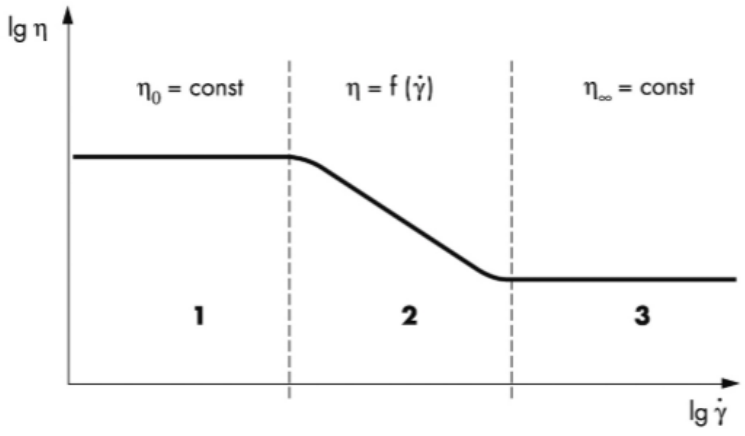

Figure 3.14 – Viscosity function of a polymer solution [292]

The way of representing the viscosity depending on the shear rate is very ideal, however, it permits to understand that the internal characteristics of the molecules can greatly affect the final viscosity of a solution.

- Concentration: for low/concentration polymer solutions, the interaction between the molecules is very low, thus the viscosity is lower. In more concentrated solutions, the entanglement between individual molecules is more frequent, causing an increase in viscosity.
- MW distribution: considering the same concentration, smaller polymers show lower viscosity because the interaction between them is less effective. In the case of larger polymers, the interaction between them promotes entanglement, causing a greater increase in viscosity.
- Chain branching: the more a polymer is characterized by branches, the stronger the interaction between molecules can become, increasing the viscosity.
- Polarity: in the presence of polar groups, dipole interactions can modify the interactions between molecules
- Copolymerization
- Polymer mixtures
- Suspended solid particles
- Solvent polymer interactions
- Chain rigidity

External parameters

Based on the analysis conditions, they can be tailored during the analysis to study the properties of the material under a wide range of conditions.

- Temperature: different range of interest depending on the material studied. The temperature affects the viscosity according to the Arrhenius relationship.
- Pressure: the isostatic pressure leads to an exponential increase in viscosity.
- Shear rate: depending on the degree of loading (low or high shear conditions), it is possible to divide the materials into two different behaviours. The fluids are defined as *Newtonian* when the shear rate and the shear stress are directly proportional, and *non-Newtonian* when the two values are not directly proportional. In this case, the materials are distinguished as *shear-thinning* when the viscosity decreases with an increase of the shear rate and as *shear-thickening* when the viscosity increases as the shear rate increases. The non-Newtonian fluids are characterized by the Weissenberg effect (rod climbing).
- Time: rheological phenomena related to time can be divided into two categories. Reversible effects describe materials that temporarily change their viscosity under a constant shear rate and then gradually recover to their original state once the shear is removed. This includes *thixotropy*, where viscosity

decreases during steady shear, and *rheopexy*, where viscosity increases under shear stress conditions. In contrast, non-reversible effects involve structural changes that do not spontaneously recover once the shear stress is removed. Examples include ageing or phase separation, where the material evolves over time in ways that permanently modify its rheological behavior.

- Electrical field
- Magnetic field

3.3.3. The rheometer and its working principle

A rheometer is a quite complex machine whose example structure is represented in ***Figure 3.15*** [296]. The working principle is based on the measurement of the torque and the deflection angle of the sampler. The precise measurement of these values is possible thanks to the air bearing, which maintains all the entire system in the absence of friction. During every type of measurement, the rheometer applies a specific current that corresponds to a predetermined torque. The sample generates resistance, or a counteracting torque, to this applied setting, and the resulting deflection angle is precisely measured by the rheometer's system.

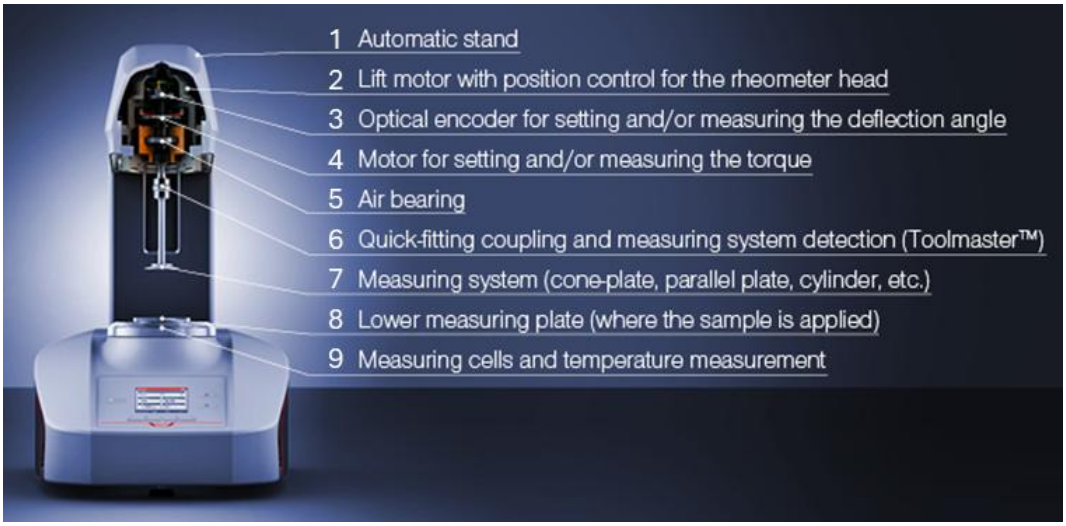

Figure 3.15 – Example of a rheometer produced by Anton Paar and its components. Reproduced from [296]

Starting from the deflection angle and time, it is possible to calculate the speed. Modern rheometers can operate by setting either the torque or the speed, with the other parameter being measured. Essentially, the current, and thereby the torque, is applied, and the parameter (torque or speed) is adjusted using a rapid controller, while the speed is subsequently measured. However, users are generally more interested in rheological parameters, which are derived from the measured values of torque, deflection angle, and speed using conversion factors,

which will not be further discussed. Additional parameters, such as viscosity, are not directly measured but are instead calculated.

The working mode of a rheometer is based on two different movements of the sampler (***Figure 3.16*** [296]):

- Rotational test: this type of test is based on the rotation in a single direction of the sampler along its axis. This setting is generally used to measure viscosity.
- Oscillatory test: in this type of test, the sampler moves with an oscillatory movement back and forth along the axis with a preset frequency. This test is mainly performed to evaluate the viscoelastic properties of a sample.

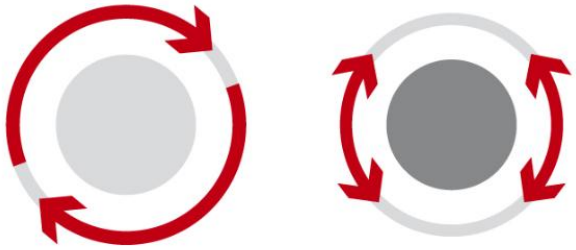

Figure 3.16 – Left: rotational movement. Right: oscillatory movement. Reproduced from [296]

The so called "sampler" can have very different geometries, some common examples are reported in ***Figure 3.17*** [295]. Depending on the shear rate range of interest and on the characteristics of the sample, it is useful to choose one geometry rather than another. This detail is very important because if the wrong one is chosen, it is possible to work outside the working range of the instrument, generating results that are not useful. Thus, this is a challenging aspect of setting up the instrument because, before the start of the measurement it is necessary to know at least the approximate viscosity of the sample.

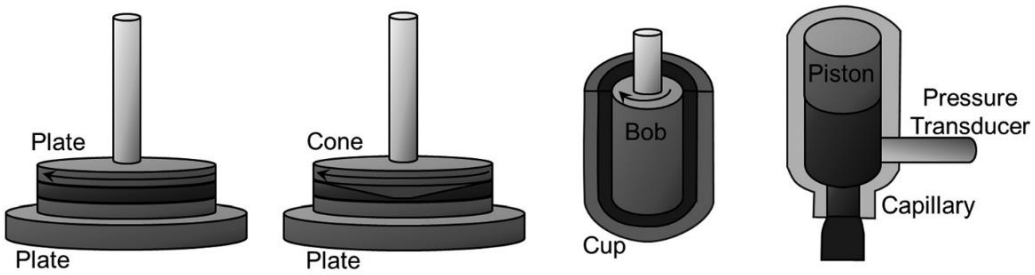

Figure 3.17 – The most common geometries used for rheological measurements, from left to right: plate-plate, cone-plate, cylindrical, capillary [295]

3.3.4. Applications of rheology in the battery field

Rheology has a fundamental role in LIBs manufacturing, especially during the electrode manufacturing, since all the steps can be strongly affected if the slurry viscosity is not the optimal one. It is possible to define the LIBs slurries as non-Newtonian complex mixtures, made of a polymeric binder dissolved in water or organic solvent and suspended particles of different sizes and shapes [297]. The measurement of the viscosity of a slurry is already a widely used method to evaluate its stability and processability during the production process [225].

Being able to monitor the viscosity every production step allows for avoiding the formation of defects in the electrode, like agglomeration or phase separation [298]. Generally, it is possible to identify multiple types of rheology depending on the production step: slurry preparation rheology during the mixing, processing rheology during the coating, drying rheology, and calendering rheology. Rheological measurements can also find a good application in the development of the electrolytes, tailoring the amount of solvents, salts and additives to improve the wettability of the electrode surface [240].

Regarding the electrode production, the mixing step is the one that is affected the most by the rheology. In fact, if the slurry is too viscous, the mixing is harder, and controlling the particle dispersion becomes more challenging. However, working with a slurry whose viscosity is too low could be advantageous for mixing, but can negatively affect the coating, leading to inhomogeneous distribution of the slurry on the CC. The drying rheology is quite challenging because during the evaporation of the solvent, the multiple phenomena that occur lead to the rheological transition from viscoelasticity to thixotropy [251]. The calendering rheology can be quite simply described as the compression rheology that occurs during the thickness reduction [240].

The slurries used in the battery production are characterized by a non-Newtonian behaviour with shear-thinning properties [295]. Generally, higher viscosity at low shear rate is preferred to avoid sedimentation [299]. Galek at al. suggested the viscosity range of 0.5 – 20 Pa·s [300], as the proper one for the coating step: values lower than 0.5 Pa·s are related to too liquid slurries leading to an uneven distribution, as well as for values over 20 Pa·s when the viscosity is too high that the coating blade removes the material during the process.

3.3.4.1. The most common geometries used for LIBs slurries

As already reported above, the geometries that can be used in rheological measurements are different, depending on the type of sample and the desired application. In case of the battery field, where the slurries are normally quite viscous, the Two-Plates (or Plate-Plate Geometry, PPG) (***Figure 3.18a*** [292]) and

the Cone-Plate Geometry (CPG) (***Figure 3.18b*** [292]) are the most commonly chosen ones.

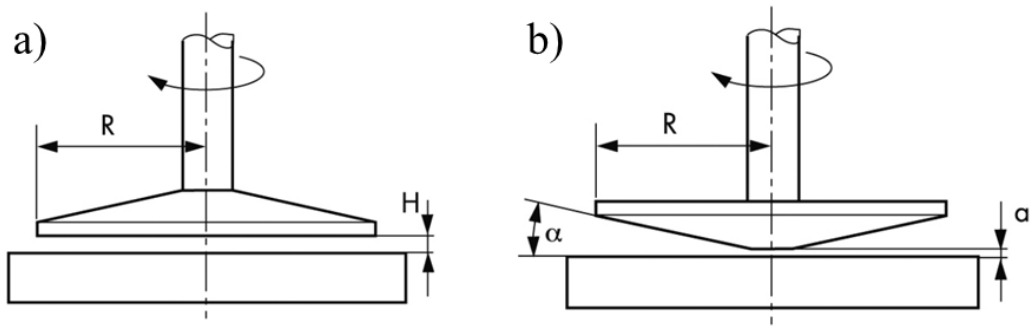

Figure 3.18 – Most common types of geometry used in the LIBs field: a) plate-plate (PPG); b) cone-plate (CPG). Reproduced from [292]

The two geometries are very similar and their application in the LIBs can be considered almost the same, without specific differences. However, it is possible to highlight some cases when the CPG is not the proper one, and this is strictly related to its geometry: the cone is a truncated cone characterised by a very low angle α of 1° and a fixed gap between the cone and the lower plate. The limitation in the use of the CPG is related to this infinitesimally small space, because this gap is normally fixed by the producer and is very important to guarantee the best working conditions for the instrument, avoiding the friction between the two parts. In case of suspensions made of particles or agglomerations, these can remain trapped in the small gap, causing a distortion in the results. For this reason, the gap should be at least one order of magnitude larger than the dimensions of these particles, and this is not always the situation. Thus, the PPG is the most chosen one [295].

Below the types of analyses normally used in the LIBs field are reported, however, it is important to highlight that the nomenclature can be different depending on the manual or article considered. This is the source of the great confusion that is associated with this type of experiments. Being as clear as possible, the conditions of each experiment are described, together with the results provided by the instrument and their relevance for assessing whether a slurry is suitable for industrial production.

3.3.4.1.1. Rotational Tests

Rotational test base their operation on the rotation of the upper geometry in the same direction but with different velocities. The common aims of these tests are based on the study of the deformation and flow properties of the matter, such as the measure of the viscosity or the thixotropic behaviour.

Flow curves

This type of analysis is a type of rotational test, based on the rotation of the upper plate while the lower plate is fixed. In case of non-Newtonian sample, as in LIBs slurries, it is impossible to define a single value of viscosity, but it is possible to define a value of shear rate and then measure the viscosity. Consequently, a flow curve test is performed by gradually increasing the rotational speed or shear rate along a fixed range (***Figure 3.19a***), thus the sample resistance at this movement is measured, and in this way the viscosity is calculated at different shear rates. In this way, it is possible to measure the viscosity at different shear-rate conditions, permitting a deeper understanding of the stability and processability of the electrode slurry.

The measured viscosity can be of different types (***Figure 3.19b***):

1) *Ideal-viscous*: when the shear rate changes, the viscosity is not affected. This type of behaviour is defined as *Newtonian flow behaviour*.
2) *Shear-thinning* (or pseudoplasticity): at the increase of the shear rate, the viscosity decreases. This is the typical behaviour of emulsions, suspensions and dispersions because the particles can be orientated, deformed or disaggregated, and the polymers are stretched during the application of the shear rate.
3) *Shear-thickening* (or dilatant behaviour): with the increase of the shear rate, the viscosity also increases. This behaviour is quite rare and is typical of highly concentrated suspensions with the particles that are densely packed, and a liquid is added as a plasticizer. When the shear rate is applied, the particles of the suspension disjoin and the plasticizer is no longer sufficient to guarantee the proper lubrication between the particles.

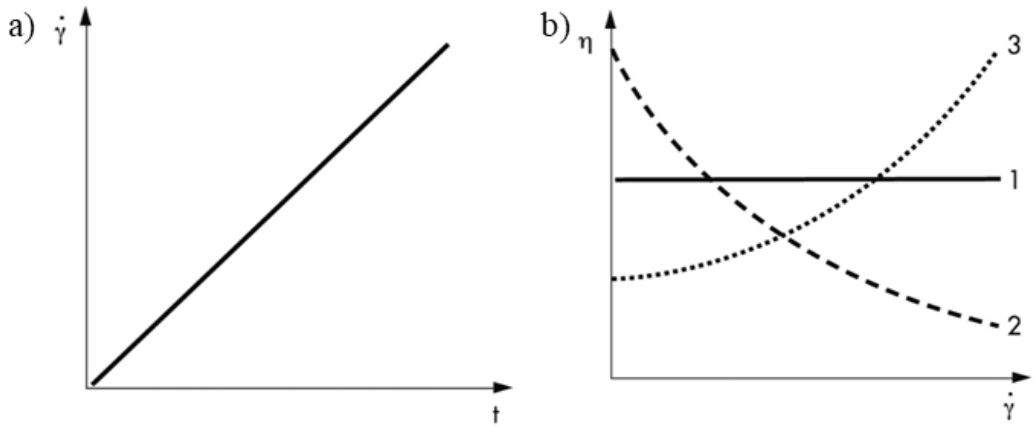

Figure 3.19 – a) Time-dependent shear rate ramp; b) Viscous behaviour response to the shear rate ramp: 1) ideal viscous, 2) shear-thinning, 3) shear-thickening. Reproduced from [292].

An optimal formulation for LIBs applications should exhibit a shear-thinning behaviour, with high viscosity when no (or very small) shear rate is applied. For example, after the coating the slurry should remain stable and avoid phase separation of the components. At the same time, at higher shear rates, especially during the coating step, a lower viscosity is preferred, allowing a simpler and more homogeneous deposition. An example of this desired behaviour is reported in ***Figure 3.20*** [247]:

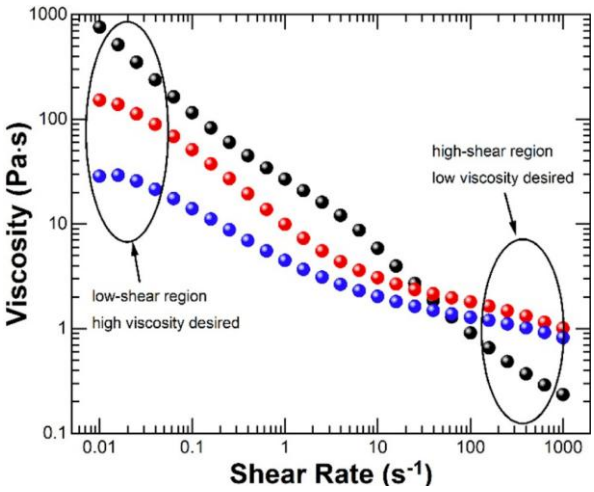

Figure 3.20 – Typical flow curve behavior of a shear-thinning material. Reproduced with permission from [247]. Copyright 2017 American Chemical Society

Thixotropic Behaviour

The thixotropic behaviour is a time-dependent behaviour [301], typical of shear-thinning materials, such as LIBs slurries. Ideally, this behaviour can be considered as the ability of a material to recover its previous structure after the application of a force, evaluating the response of the material both in terms of shear stress and viscosity [302]. It is important to highlight that this type of behaviour cannot be properly quantified because it depends on a large number of variables: during the application of a force, the material is subjected to internal microstructure changes that lead to the changes in viscosity. Depending on the test conditions is possible to compare different samples but is not possible to assign a single numerical value to the thixotropic behaviour.

Below are reported a couple of test that can be used to highlight the presence of this behaviour: in both of the cases, the shear rate is varied over time, but in the case of the *Hysteresis effect*, this variation is gradual, while in case of the *3ITT test* (3 Interval Thixotropic Test), the variation is sharp.

Hysteresis effect

As already mentioned, the hysteresis effect, or *thixotropic loop* [301], is the behaviour associated with the variation of the shear stress depending on the

gradual variation of the shear rate. Practically, the setup of this experiment is quite easy and an explicative scheme is reported in ***Figure 3.21a*** [292]. The test is divided into three steps:

1) Increase of the shear rate: during this step the shear rate is gradually increased and the material is subjected to stress-induced microstructural changes.
2) Stable shear rate: during this step the shear rate is maintained constant for a certain period, causing another further degradation of the structure.
3) Decrease of the shear rate: during the last step the shear rate is gradually decreased up to the starting value, in this way the material structure starts to recover depending on the internal characteristics.

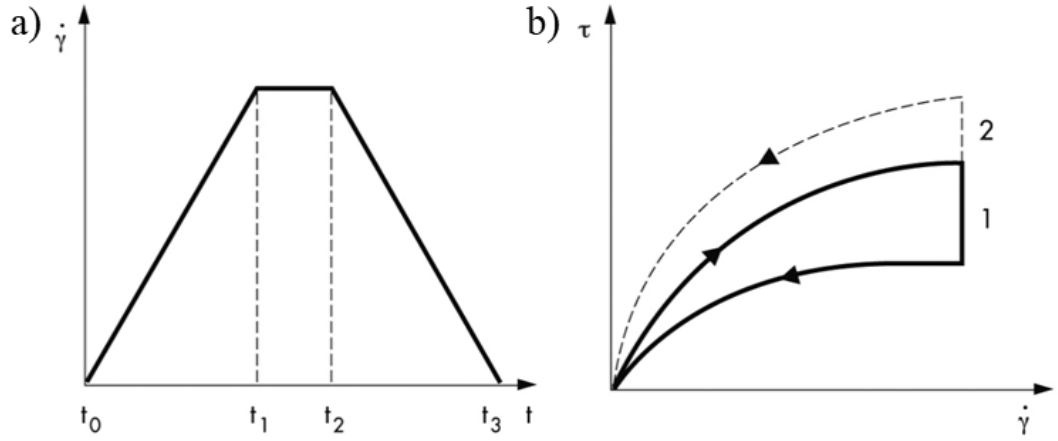

Figure 3.21 – First method to observe the thixotropic behavior, based on the evidence of the hysteresis effect observe evaluating the variation of shear stress: a) Setting of the time-dependent shear rate profile, divided into three time intervals; b) Back and forth flow curve, obtained changing the shear rate and representing the hysteresis area. Reproduced from [292]

In ***Figure 3.21b*** [292] the most common response is presented, which is generally observed with this type of test:

1) The first response is the increase in the shear stress proportional to the increase in the shear rate.
2) During the second step, the shear rate is constant, thus an increase or a decrease in shear stress can be observed.
3) The shear stress decreases according to the decrease in shear rate up to the starting point, closing the loop.

Thus, it becomes evident that it is possible to distinguish between two behaviors: the one described by number 1 is the *thixotropic behavior*, characterized by positive values of this area, while for curve number 2, the value of the area is negative and this is called *rheopectic behavior*. This second behavior will not be further discussed.

3 Interval Thixotropic Test (or Creep test)

The 3 interval thixotropic test (3 ITT) [295], also known as 3-Interval Time Test [147] or Creep test, is another simple test that permits the evaluation of the thixotropic behaviour of a material. Compared to the previous one, in this case the variation in shear rate is sharp, as reported in ***Figure 3.22a*** [292], but ideally the three steps remain the same:

1) Low shear rate is considered as a steady-state step: during this step, the applied shear rate is constant, thus, no changes occur inside the material.
2) High shear rate: the shear rate is increased, causing an abrupt change in the microstructure of the material, which can be observed as a great change in the viscosity.
3) Low shear rate: the applied shear rate is the same as before, with the material gradually able to recover its structure to the previous steady-state conditions.

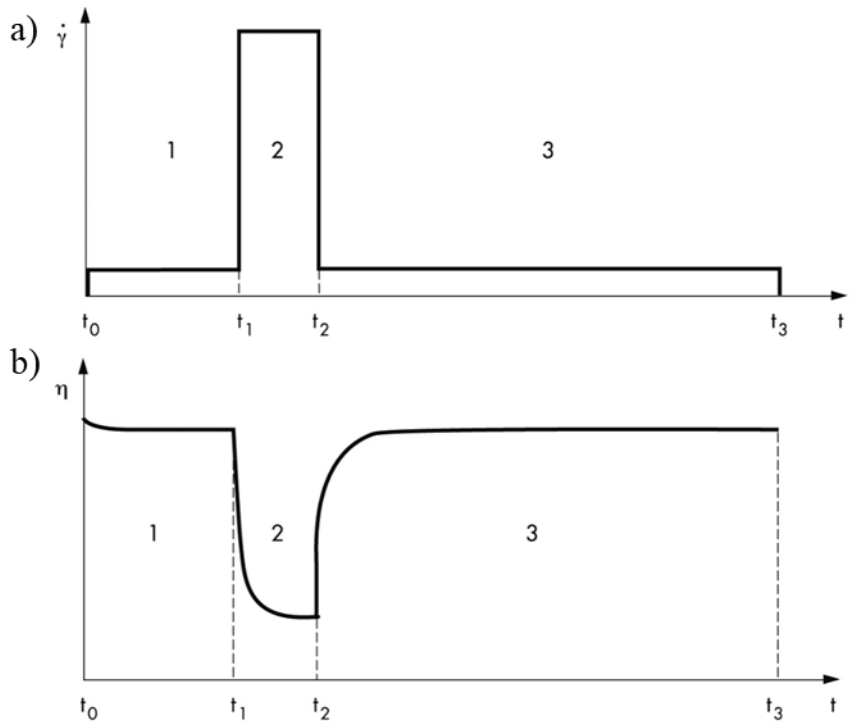

Figure 3.22 – Second method to observe the thixotropic behavior: a) Setting of the experiment changing the value of shear rate for three times: 1) low shear rate, 2) high shear rate, 3) low shear rate; b) Time-dependent viscosity after the application of the three stages at different shear rates. Reproduced from [292]

The most common viscosity response of a material is reported in ***Figure 3.22b*** [292]: it is clearly evident that the sudden application of different shear rates causes important changes in the viscosity.

1) During the first step, at constant low shear rate, no changes in the viscosity are observed because the material is not subjected to any stress.

This is an important step because it permits to evaluate the stability of a material in the absence of external forces: if a variation in viscosity is observed, this means that the microstructure is subjected to changes, such as some chemical bonds that are rearranged.

2) The sudden application of a higher shear rate causes an immediate decrease of the viscosity that gradually reaches a plateau after the rearrangement of the microstructure of the material.
3) After the removal of the high shear rate, the material gradually recovers its original structure. Depending on the final slope, it is possible to identify if a material is more subject to thixotropic behaviour or not. If the material is not able to recover, some degradation phenomena have occurred, causing an irreversible change in the structure of the material.

It is possible to define the *thixotropic index* [303] (or shear thinning index) as the ratio between the viscosity measured at the first low-shear-rate step and the viscosity measured at higher shear rate. The higher the value of this number, the more the sample has a shear thinning behaviour.

In the battery field this could be a very useful test that permits to "simulate" the behaviour of a slurry during some production steps, however, its application is quite rare [147,295,304,305]. The first one can be associated to a rest time of the slurry right after the mixing step and the coating. If some changes occur during this time, this means that the slurry undergoes some structural changes that cannot be controlled. The second step is associated with the coating step, when a force is applied on the slurry by the coating machine and a decrease in viscosity is the desired behaviour to guarantee a good deposition. The third step permits a better understanding of the slurry behaviour during the drying step: in this case, the microstructure is recovered, thus it is important that the viscosity reaches the same value as before, otherwise, some irreversible reactions have occurred, changing the properties and potentially leading to phase separation or precipitation.

3.3.4.1.2. Dynamic Oscillatory Test

A rheometer used in the oscillatory mode permits the study the viscoelastic properties of a material, distinguishing between elastic and viscous properties. The rheometer working conditions, in case of the PPG, are reported in ***Figure 3.23a*** [292]: the upper plate is made to oscillate back and forth, generating a variation in the angle between the upper and the lower plate (***Figure 3.23b*** [292]).

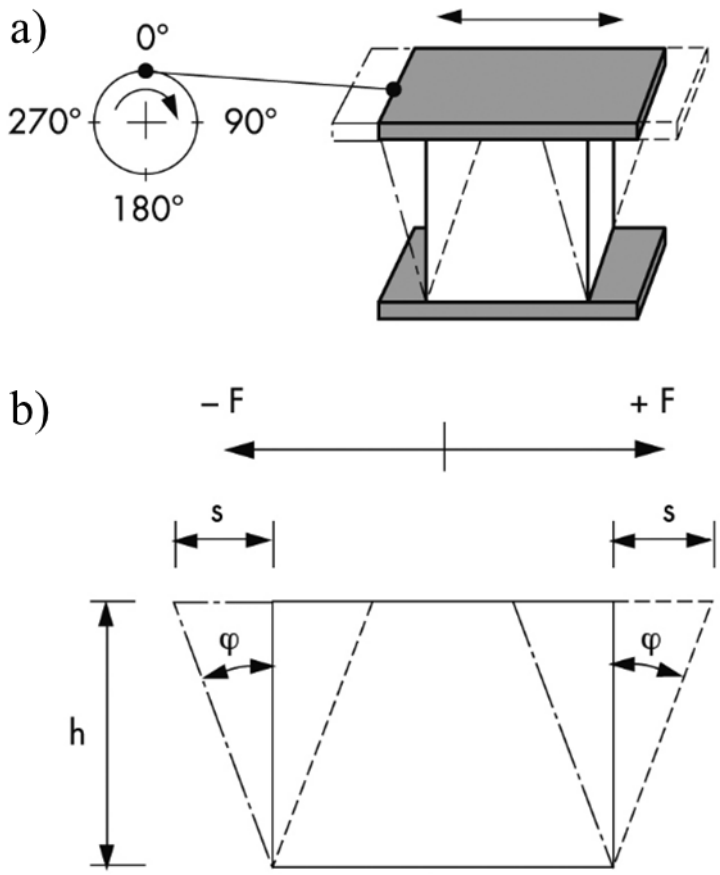

Figure 3.23 – Working principle of a rheometer based on the oscillatory mode: a) Representation of the Two-Plates model for the oscillatory tests; b) Representation of the forces involved in the tests and the angle that they create between the two plates fixed at a certain distance [292]

The viscoelasticity is a parameter strictly related to the molecular structure of the sample and, from a fluid mechanics point of view, has an impact only in situations that are not considered steady-flow conditions, like accelerated or decelerated flows [297]. Thus, oscillatory tests can be a useful instrument to better understand the behaviour of the slurry, for example during the coating step. Even though the potential applications of this technique are very interesting, in literature the examples are very few, therefore, only few examples are reported below [225].

Oscillatory measurements are generally carried out under oscillatory conditions, varying the shear stress or the frequency of the rotation and providing as a response the strain. This strain can be classified into three types, depending on the characteristics of the sample: pure elastic, viscoelastic and pure viscous. A clear schematic representation of this concept is reported in ***Figure 3.24*** [301]:

- Pure Elastic: when the maximum stress is applied, the maximum strain is also observed, with the two curves being in phase.

- Pure Viscous: when the maximum stress is applied, the strain is at zero, with a shift between the phases of the two curves of 90°.
- Viscoelastic Behaviour: this complex behaviour is between the two pure ones, with the two curves of stress and strain not being in phase, with an angle between 0° and 90°.

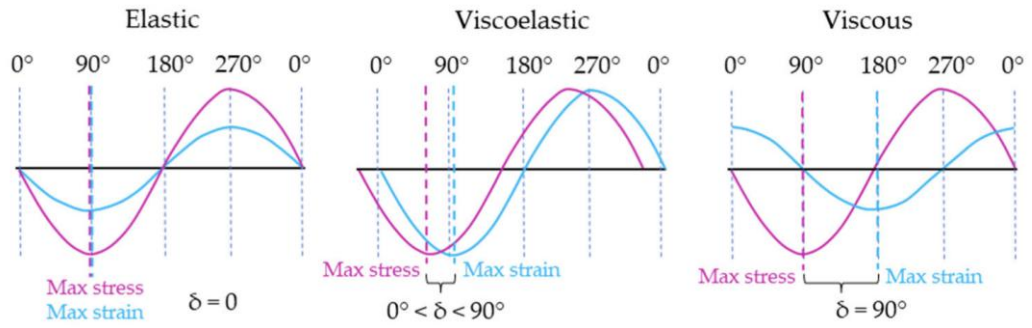

Figure 3.24 – Comparison of the stress and strain waves depending on the type of material. Reproduced from [301]

From a mathematical point of view, it is possible to express the amount of strain as the G* value (***Equation 3.7***), with the two components G' (storage modulus) and G'' (loss modulus) [306]. Thus, in the case of a viscoelastic sample, it is possible to distinguish two co-existing behaviours but with one dominating the other, depending on the values of the two moduli:

- If G'>G'', the contribution of the elastic component is higher than the viscous component. In this case, the external force is not sufficient to break the internal structure of the sample, and the behaviour is gel-similar. This is the typical behaviour of polymer solutions and solid/liquid suspensions at low values of strain.
- If G'<G'', the contribution of the viscous component is higher than the elastic one. In this case, the external force is so high that the internal structure is destroyed and the sample behaves like a viscous liquid.

Oscillatory amplitude sweep

The oscillatory amplitude sweep test is based on the variation of the amplitude of the shear stress (or strain) applied to the sample, while the frequency is maintained constant. The results of this test are the curve G' and G'' that usually form a plateau, and this region is highlighted as the linear viscoelastic region (LVR), where the sample can be tested while avoiding the degradation of its structure [301]. Every time that an oscillatory test is conducted on an unknown sample, the oscillatory amplitude sweep should be performed in advance to determine the LVR.

Oscillatory frequency sweep

In this case, the shear stress (and so the strain) is maintained constant in the LVR (determined with the previous test), while the oscillation frequency is increased. The frequency sweep test is useful to better understand the internal structure of the sample and its time-dependent response in a non-destructive way [301]. An example of this test is reported in ***Figure 3.25*** [307].

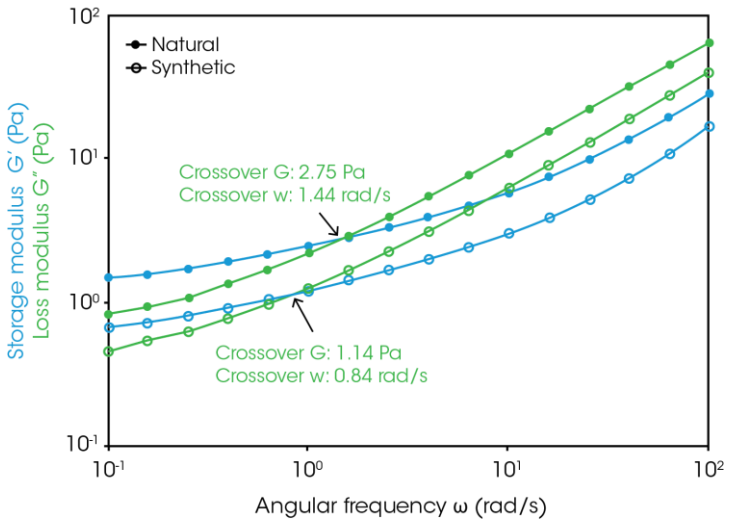

Figure 3.25 – Example of oscillatory frequency sweep test on two different type of graphite at 25°C. Reproduced from [307]

At high frequency, the sample has a behavior that can be considered similar to the coating step, when the LIBs slurry is subjected to high deformation from external force, while at low frequency, the comparison is made with the drying step [301]. The intersection point between the curves G' and G'' is called *flowpoint* and can be calculated as the tangent of the angle formed by the two curves (***Equation 3.8***). Once again, it is possible to divide the behavior into two, depending on which G is greater:

- If G'>G'', the value of tanδ is less than 1: the sample is characterized by the dominance of solid-like behavior.
- If G'<G'', the value of tanδ is greater than 1: the sample has a liquid-like behavior.

One problem associated with this test occurs at high frequency because the material can escape from the gap due to inertial forces. One solution can be to change the temperature and thus extended the frequency range, however, this is not always possible for instrument limitations [295].

Regarding the application of the oscillatory test in the LIBs field, it is possible to find some examples in the literature, even though it is less frequently used compared to a simple flow curve [225,297,308].

Chapter 4

4. Life Cycle Assessment

LCA is a methodology used inside the strategy of the circular economy to evaluate the environmental impacts of a product throughout its entire life, with the aim of increasing resource efficiency and minimize environmental disadvantages. This methodological framework is particularly relevant in the context of battery research, where environmental impacts are strongly influenced by both material selection and manufacturing conditions.

The LCA is a quantitative and standardized working method developed in the early 1990s and based on the ISO 14040-44 [309,310]. Within the European Green Deal, the European Commission defined the LCA as the *best framework for assessing the potential environmental impacts of products* [311]. Hence, during the years was developed the European Platform on LCA (EPLCA) [312], with the aim to contribute to the improvement of LCA methods for evaluating supply chains and managing waste at the end of a product's life. Inside the EPLCA, different LCA projects [313] are hosted like the Plastics LCA, Consumption Footprint, Food System Analysis and the Carbon Footprint of Batteries (CFB) for electric vehicles [314].

The standardization of the LCA methodology represented a fundamental step toward the development of Environmental Product Declarations (EPDs) [7]. An EPD is a Type III environmental declaration, meaning a standardized and independently verified environmental label based on quantified LCA results and compliant with the ISO 14025 standard, which provides transparent and reliable information on the environmental impacts of a product. To ensure that LCAs are developed using consistent, objective, and comparable data, each product category is governed by specific Product Category Rules (PCRs) [315]. These documents define the rules, requirements, and methodological guidelines that must be followed when producing an EPD for a given product category.

Regarding the LIBs field, PCRs for batteries are still under development [316] with the expected promulgation timeline in the first months of 2026. Therefore,

performing an LCA on LIBs is still a complex process with high variability depending on multiple factors. Still, there is a need to develop a suitable procedure to evaluate the environmental impacts related to each stage involved in LIBs life [6].

To effectively address the challenges of emerging battery technologies characterized by a low TRL, a prospective LCA (P-LCA) approach is required [317]. Conventional, retrospective LCAs evaluate existing industrial processes operating at mature economies of scale. However, applying such standard frameworks to emerging components, like silicon-based anodes, would lead to unfair comparisons and misleading conclusions, as laboratory or pilot-scale processes inherently suffer from unoptimized energy efficiencies and material configurations. The utility of P-LCA within this thesis lies in its capacity to "bridge the scale-up gap". By projecting the foreground system from current laboratory configurations to a simulated future industrial scale, P-LCA enables a fair, anticipatory environmental evaluation. This methodology allows the identification of environmental hot-spots and potential trade-offs before commercialization, guiding the environmental sustainable development of next-generation energy storage systems. It is worth noting that while the application of P-LCA is rapidly expanding in literature, a universally standardized scaling methodology within the ISO framework is still lacking, making the rigorous harmonization of inventory upscaling a core methodological effort of this research.

4.1. The steps of a product life cycle and the related models

Behind the LCA stands Life Cycle Thinking (LCT), which is a systematic approach to evaluate the environmental (LCA), economic (Life Cycle Costing, LCC) and social (sLCA) impacts of a product throughout its entire life, starting from raw material extraction to EoL treatments [318].

For every product, it is possible to identify the different stages of its life cycle [319]. ***Figure 4.*** [6] highlights these phases specifically for LIBs. In general, it is possible to distinguish four main phases: Production and Construction Phase (A), Use and Maintenance Phase (B), EoL Phase (C), which, in some cases, can be followed by the Beyond EoL Phase (D). Each stage includes multiple processes and involves various actors, making the life cycle of a product a highly complex system [320].

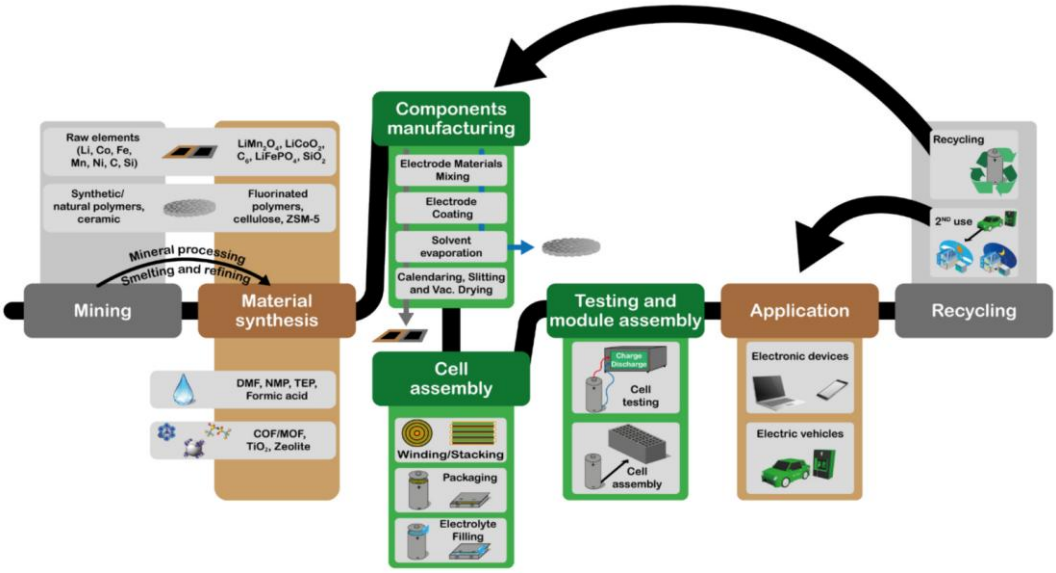

Figure 4.1 – Schematic overview of the life cycle stages of LIB materials and components, starting from raw material extraction to end-of-life recycling [6]

The production and construction phase begins with the extraction of the raw materials, hence, for choosing the best ones, their environmental impacts are studied and the most sustainable are chosen. Among all the factors, some like emissions, energy consumption and resource depletion are the ones considered, therefore the use of recycled or renewable materials is usually the best option. The extraction of raw materials for LIBs applications is an openly debated topic, both for ethical and sustainability point of view, especially for elements like lithium and cobalt [321]. During this phase, the transportation of the raw materials, of some components or reagents and of the final product between different locations is also taken into consideration. Multiple parameters can be controlled, like fuel consumption, distance and the relative emissions. In order to reach a more sustainable process, the use of greener vehicles or technology, as well as shorter distances has to be preferred. The manufacturing stage focuses on the production phase itself. Generally, during this stage the raw materials are treated with specific processes involving water use and electricity consumption, while at the same time generating some wastes other than the product itself. The use of electricity from renewable resources or the choice of lower-impact processes can improve the sustainability of the whole process.

The use and maintenance phase considers the lifespan of the product. Its complexity lies in the need to account for operational energy and water consumption, as well as maintenance activities and potential repair processes. These additional elements introduce a significant number of parameters that can influence the overall assessment. Products that minimize maintenance activities and promote the proper use to reach maximum efficiency, can improve

sustainability. In the specific case of LIBs, extending the battery lifespan can substantially improve their environmental performance [322].

The EoL phase includes all the stages that occur when a product reaches its end of life. It covers activities such as deconstruction, transportation, and waste management, where the associated impacts, such as electricity or water consumption, can be assessed. In case of LIBs used in the EV sector, batteries typically exit the use phase when their SoC drops below 80% of the initial value [323].

Finally, the beyond EoL (D): entering the cycle loops of the circular economy can significantly improve the sustainability of a product. A product can be re-used, for example becoming a second-hand object, recovered, or recycled, thereby re-entering the life cycle and reducing the need for virgin resources. The sustainability outcome varies according to the EoL pathway selected. In case of LIBs for EV applications, several options are available, including their repurposing in stationary energy storage systems, where high energy density is no longer a critical requirement [324].

Depending on the phases considered in the LCA, it is possible to identify multiple models, which permit to define the system boundaries of the study [325]:

- **Cradle-to-cradle (A-B-C-D)** – This is the most complete type of LCA and so the most complex to realize. It represents the idea of the circular economy when a product at the end of its life is reused or recycled to enter once again in the life cycle.
- **Cradle-to-grave (A-B-C)** – This approach considers all life cycle stages of a product, from raw material extraction to its end-of-life treatment. It is the most common LCA model because it provides a comprehensive overview of the product's total environmental impact. For example, although producing a textile bag requires more resources than manufacturing a plastic bag, its significantly higher number of reuse cycles can lead to better overall sustainability performance. This model is typically used for the development of the EPDs.
- **Cradle-to-gate (A)** – This system boundary considers only the production stage of a product, from raw material extraction up to the point at which the product leaves the factory. As the analysis is limited to upstream and core processes, data requirements are relatively contained, making data collection simpler and faster compared to full life cycle approaches. For this reason, cradle-to-gate studies often represent an effective starting point for LCA assessments. Inside a company, it can be a useful tool to evaluate and consequently improve the sustainability performance of production process.
- **Gate-to-gate** – This system boundary focuses on a specific segment of the production process, considering only the operations that occur between the

input and output gates of a particular manufacturing stage. In this case, the output from one process becomes the input for the next-one. This approach is useful when analyzing or optimizing specific production steps, and it can be integrated with other system boundaries to construct the full LCA.

4.2. Key methodological parameter

To perform an LCA, different software tools are available online, some free like OpenLCA, developed by GreenDelta [326], while others must be purchased like SimaPro, developed by PRé Sustainability [327] or GaBi, developed by Sphera [328]. These tools allow practitioners to model product systems using datasets from dedicated databases. Among the most widely used is the Ecoinvent database, known for its completeness and regular updates, which offers extensive sector coverage and multiple system models. For this Ph.D. project, the LCA modelling has been carried out using OpenLCA 2.4 in combination with the Ecoinvent 3.11 database [329]. Before starting the description of the steps involved in the production of an LCA, some definitions must be provided [309,310,325,330]:

- **Functional Unit (FU)** – It is a quantified unit (e.g. 1 kg, 1 kWh, 1 item) needed for the description of the function studied in the assessment. It is the basis for all the calculations, being the reference point for the normalization of inputs and outputs and allowing a proper qualitative and quantitative comparison between different systems.
- **Unit process** – It is the "*smallest element of a product system for which input and output data are quantified*" [309]. Generally, it can be associated with a single step or operation step in the life of a product, but it can be a merge of multiple unit processes to set up a new and more complete unit process, depending on the LCA to be carried out. The connection of multiple unit processes allows to produce the full LCA.
- **Reference flows** – They represents the amount of material, energy and resources needed to fulfil the FU. They are linked to reference amounts, like mass, volume or energy, and associated with the relative unit of measurement. Reference flows are divided into *input flows* (material, energy and resources) when their amount is set as input quantity in the process, or *output flows* when they describe the product, the waste or the emissions that the process produces. Products and wastes of one process can become the materials or resources for another process. Resources are defined as inputs that enter in the LCA directly from the environment, without further treatment, thus they are never considered as outputs from other processes. The emission flows are peculiar, because they refer to materials which can be released into the environment

without further effect, and they cannot be involved in other processes as input parameters.

- **Multifunctional processes** – In this case, a single process has more than one function, leading to the production of more than one product or being involved in the recycling process, where it involves the management of waste and the production of a secondary product. If it is not possible to divide the process into simpler unit processes, the ISO 14044 sets some rules called allocation procedures to properly calculate the multifunctional process impact.
- **System boundaries** – A set of rules needed to define the limit of the studied system, in particular which unit processes have to be included. As previously introduced, the most common types of system boundaries are the Cradle-to-Gate and the Cradle-to-Grave.
- **Foreground system** – It collects all the foreground processes which are directly related to the product system. It is mainly modelled with primary data, which are first-hand data collected from the industry. They can generally be easily changed because the flows in the process can be modified both quantitatively and qualitatively.
- **Background system** – This system collects all the processes that are more general and not directly related to the desired product. These processes are easily modelled with the support of LCI databases, and they represent average industry data, like the electricity supplier or the waste management system.
- **Product system** – It is the whole production process, which collects all the unit processes, starting from the raw material to the EoL process, linked together with the relative flows, including also all the input and output considered.

4.3. The four phases of the LCA

To perform a complete and consistent LCA requires significant time and effort, and before starting it is essential to define the four key phases, as established by the ISO 14040 and 14044 standards [309,310]. These principles are further supported and operationalized at the European level through frameworks such as the Environmental Footprint methods [331–333]. These steps are strictly related to each other, making the performance of an LCA an iterative process, where inputs, flows and parameters can be changed along the process. In the present research, this structured approach enables a systematic comparison of alternative electrode materials and production processes from an environmental perspective.

- **Definition of Scope and Goal** – During this preliminary step, it is fundamental to set the aim of the study, defining its application, explaining the reasons for

developing the study and choosing the proper audience. In addition, some methodological parameters have to be defined: functional unit, system boundaries, impact categories and data quality requirements, as well as the limits of the analysis.

- **Production of the Life Cycle Inventory (LCI)** – The complexity associated with the development of LCI is shown in ***Figure 4.2*** [318]. The objective of the LCI step is to identify and quantify all materials, emissions, waste streams and energy consumption associated with the process under investigation, which can involve multiple stages of a product's life cycle. This step is typically the most complex as the volume of data and the effort required for data collection are often substantial. Data are generally classified into two categories: *primary data*, which are the ones directly collected from the specific process or manufacturer, and *secondary data*, which are values derived from literature, theoretical estimations or average industry datasets. These data can be further distinguished based on their role in the system: *input data* refer to the resources consumed, in terms of raw materials, electricity and water consumption, but also the transportation costs and emissions. The *output data* include final products, co-products, waste streams and emissions to air, water and soil.

Figure 4.2 – Graphical representation of all the steps involved for the production of a complete Life Cycle Inventory [318]

- **Definition of the Life Cycle Impact Assessment –** This phase aims to evaluate the potential environmental impacts associated with various inputs and outputs, as well as to select impact categories based on the scope of analysis. Numerous LCIA methods exist, and the selection may be either discretionary or dictated by specific guidelines. The most commonly applied impact assessment methods include IPCC (Intergovernmental Panel on Climate Change) [334], ReCiPe [335], TRACI (Tool for Reduction and Assessment of

Chemicals and Other Environmental Impacts) [336] and GREET (Greenhous gases, Regulated Emissions, and Energy use in Technologies) [337]. These methods are routinely updated with new versions. IPCC is internationally recognized for climate change assessment; ReCiPe encompasses all impact categories and is likely the most widely used; TRACI was created by the United States Environmental Protection Agency; and GREET, developed by the Department of Energy, focuses on energy systems, related technologies, and fuels. In addition, specialized methods address particular impact categories, such as ecotoxicity (USEtox), material usage (Crustal Scarcity Indicator), or energy resources (Cumulative Energy Demand).

- **Data interpretation** – After all the steps, the final data are collected and used to evaluate their impact on the chosen categories. These data can be used to compare different production processes or to propose some exploring strategies to mitigate the impacts.

4.4. Allocation rules

In LCA practice, industrial processes rarely produce a single output. Most chemical and engineering systems generate multiple valuable co-products or involve recycling loops where waste is transformed into secondary raw materials [338]. Because the environment interacts with an industrial plant as a whole, a significant methodological challenge arises when trying to isolate the environmental impacts of a single product. Deciding how to partition the total inputs of resources and outputs of emissions among the various co-products is a well-known source of uncertainty in literature, and it requires clear methodological choices governed by international standards [309,310].

To resolve this issue, the ISO 14044:2006 [310] standard outlines a strict hierarchical procedure, prioritizing solutions that avoid allocation entirely. The first and most preferred option is the sub-division of the process into smaller, distinct unit operations, which allows the practitioner to isolate the specific material and energy flows dedicated exclusively to the product of interest. Accordingly, this sub-division strategy was prioritized in the present Ph.D. project. Wherever detailed primary data were directly collected during this research, the manufacturing chains under investigation were broken down into individual unit processes, thereby minimizing the reliance on broader allocation metrics and ensuring a higher level of inventory accuracy. When sub-division is not technically possible, the standard recommends system expansion, also known as the substitution approach. This strategy enlarges the system boundaries to include the functions of the co-products, assuming they displace conventionally produced alternatives on the global market. The environmental impacts of these replaced products are then subtracted from the main system, reducing the overall impact of the main process.

When avoiding allocation is impossible, practitioners must partition the environmental impacts based on causal relationships. The first choice is to look for physical parameters, such as the relative mass or energy content of the outputs. Mass allocation is widely favored in chemical engineering due to its baseline stability, while energy allocation is typically applied to co-generation systems where the primary utility is defined by the calorific value of the flows. However, if physical parameters fail to reflect the true economic drivers of the industrial process, such as when a low-mass co-product possesses a very high market value, the allocation must be based on alternative relationships. In such cases, economic allocation is applied, distributing the environmental impacts according to the relative market value of each co-product based on its percentage share of the total revenue generated by the process.

In practical modeling, these theoretical guidelines are directly operationalized through the selection of the system model within the LCI database. When utilizing OpenLCA 2.4 in combination with Ecoinvent 3.11, the choice of the database version fundamentally alters how multi-product datasets behave [329]. For instance, the allocation cut-off model establishes that the primary producer is responsible for the full environmental impact up to the point where a material becomes waste, meaning that secondary materials enter downstream processes burden-free, and no recycling benefits are granted at the end of life. Conversely, the consequential model employs system expansion to capture the broader consequences of market shifts and institutional decisions, identifying which marginal technologies are affected by a change in supply or demand. Because the choice between these different allocation methods can significantly alter the final environmental profile of a product, it is standard academic practice to evaluate their influence through a dedicated sensitivity analysis, ensuring that the final conclusions of the assessment are robust and transparent.

4.5. ReCiPe 2016: Midpoint impact categories and indicators

During the LCIA step, emissions and resource uses identified in the inventory are classified into impact categories to provide a comprehensive assessment of a wide range of environmental issues. The Product Environmental Footprint and Environmental Footprint methods [339] define 18 impact categories regularly updated, to cover all the environmental aspects that can be affected by the emissions. These categories are based on the combination of multiple factors that have an impact on a single environmental effect and they are periodically updated by a scientific commission. Each impact category is associated with a specific midpoint indicator, which quantifies the contribution of different elementary flows to a single environmental effect [325]. These impact indicators are defined as *midpoint impact indicators*, because they refer to environmental mechanisms

which are directly measurable and are typically subject to lower uncertainty [340]. All the impact categories and the relative midpoint impact indicators are reported in ***Table 4.*** [329], following the Impact Assessment method ReCiPe 2016 v.1.03, midpoint (H) [341]. According to Tolomeo et al. [342], this specific framework represents the most widely adopted characterization method within the current literature. Such indicators are especially useful for emerging battery technologies, as they allow the identification of environmental trade-offs associated with performance improvements.

Table 4.1 – Summary of the Impact Categories and relative Indicator proposed by the Impact Assessment method ReCiPe 2016 v1.03, midpoint (H)

Impact Category	***Impact Indicator***	***Unit***
Acidification: terrestrial (TA)	Terrestrial Acidification Potential (TAP)	kg SO_2 eq
Climate Change (GW)	Global Warming Potential (GWP)	kg CO_2 eq
Ecotoxicity: freshwater (FE)	Freshwater Ecotoxicity Potential (FETP)	kg 1,4-DCB eq
Ecotoxicity: marine (ME)	Marine Ecotoxicity Potential (METP)	kg 1,4-DCB eq
Ecotoxicity: terrestrial (TE)	Terrestrial Ecotoxicity Potential (TETP)	kg 1,4-DCB eq
Eutrophication: marine (MET)	Marine Eutrophication Potential (MEP)	kg N eq
Eutrophication: terrestrial (TET)	Terrestrial Eutrophication Potential (TEP)	kg N eq
Eutrophication: freshwater (FET)	Freshwater Eutrophication Potential (FEP)	kg P ep
Human toxicity: carcinogenic (CHT)	Human Toxicity Potential: carcinogenic (HTPc)	kg 1,4-DCB eq
Human toxicity: non-carcinogenic (NCHT)	Human Toxicity Potential: non-carcinogenic (HTPnc)	kg 1,4-DCB eq
Ionising radiation (IR)	Ionising Radiation Potential (IRP)	kBq Co-60 eq
Land use (LU)	Agricultural Land Occupation (LOP)	m^2*a crop eq
Particulate matter (PMF)	Particulate Matter Formation Potential (PMFP)	kg PM2.5 eq
Photochemical oxidant formation: human health (POFHH)	Photochemical Oxidant Formation Potential: Humans (HOFP)	kg NO_x eq
Photochemical oxidant formation: terrestrial ecosystem (POFTE)	Photochemical Oxidant Formation Potential: Ecosystems (EOFP)	kg NO_x eq
Resource use: fossils (FRS)	Fossil Fuel Potential (FFP)	kg oil eq
Resource use: minerals and metals (MRU)	Surplus Ore Potential (SOP)	kg Cu eq
Stratospheric ozone depletion (SOD)	Ozone Depletion Potential (ODP)	kg CFC-11 eq
Water use (WC)	Water Consumption Potential (WCP)	m^3

Acidification – This effect is related to the increase of the acidic characteristics of the environment, caused by the decrease of the acid neutralising capacity of soils or aquatic ecosystems. The decrease in pH is due to the addition of hydrogen ions in the environmental system or the reduction of cations able to remove the hydrogen ions from the same ecosystem. The acidification is a natural and cycling process which can be dramatically promoted by human activity, with the emission into the atmosphere of gases like sulphur oxides, nitrogen oxides, ammonia and strong acids. These acids have a great solubility in water, thus, they enter very fast in the water cycle, creating the phenomenon of the "acid rain". Generally, the acidification is a short-time effect which lasts a few days and is localized in regions with high pollution of the atmosphere. Hence, the geology can have a great effect on avoiding the acidification of the soil, for example, in presence of calcareous soils, characterized by a high amount of calcium carbonate able to neutralize the hydrogen ions. The impact indicator chosen for this category is the kilogram of sulphur dioxide equivalent (kg SO_2 eq). The acidifying potential of various chemical substances is converted into SO_2 equivalents based on their relative capacity to contribute to acidification.

Climate Change – This category is one of the most known categories in the LCA, because it is widely used alone to perform the "Carbon Footprint" of a product. It refers to the increase of the average global temperature due to the increase of the GHG from the anthropogenic activities. The excessive human contribution, due to the combustion of fossil fuels, like coal, oil and natural gas and the associated deforestation leads to the unfortunately widely known global warming (GW). The effects are observed all around the world and are associated with an increasing amount of uncontrolled and dramatic natural phenomena (tropical cyclones, flooding, droughts, wildfires and so on), with the consequent impacts on multiple ecosystems and human activities like agriculture. The accumulation of GHG in the atmosphere creates a barrier which limits the passage of solar radiation, favouring the heat accumulation between this layer and the surface of the Earth. The impact indicator used to describe this category is the kilogram of carbon dioxide equivalent (kg CO_2 eq). Even though the impact indicator refers to CO_2, many other gases contribute to the climate change, like methane or nitrous oxide, whose impact is calculated, balanced and converted into kg CO_2 eq.

Ecotoxicity (freshwater, marine, terrestrial) – This category refers to the potential toxic impact of a process or a product on an ecosystem. To evaluate the toxicity of a chemical, multiple factors other than toxicity have to be considered: 1) emitted quantity, 2) mobility, 3) persistence, 4) exposure patterns and bioavailability, 5) toxicity. Taking into account all these parameters makes this category very complex and difficult to globally evaluate. For example, there are some chemicals that are very toxic but undergo a fast degradation process which prevents them from reaching the target organism, making them almost harmless.

Other chemicals can have lower toxicity impact but be present in the environment in high quantities and with long persistence, making them very dangerous. Hence, environmental conditions can have an impact on the ecotoxicity of a substance. The main sources of this type of pollution are related to all the chemicals involved in industrial production processes. The effect on an organism can be very different depending on the chemical, from changes in photosynthetic activity and reduced growth in plants, to the reduced mobility and increased mortality in animals. The impact indicator is kilogram of 1,4-dichlorobenzene equivalent (kg 1,4-DCB eq), which is a typical emission in urban air with impacts on ecosystem toxicity but also human toxicity.

Eutrophication (marine, terrestrial, freshwater) – The eutrophication is the effect that occurs in an ecosystem when the nutrients are unbalanced, favouring the growth of only some species and leading to the death of other species. The substances responsible for this effect are the ones which contain nitrogen (N) or phosphorus (P), which are essential macronutrients. The nutrient enrichment of an ecosystem is based on all the substances which have a certain amount of bioavailable phosphorus or nitrogen. The aquatic ecosystems (marine and freshwater) are the most affected because the eutrophication effect is very common for some algae species. These species can grow in an uncontrolled way causing an excessive biomass production which leads to water-quality degradation. In particular, if this phenomenon happens in a confined ecosystem like a lake, the excessive consumption of oxygen from the algae causes the death of all the other flora and fauna species, and the lake is destined to become a swamp. In case of terrestrial eutrophication, this is mainly due to atmospheric deposition and has the biggest impact on plants able to fix atmospheric nitrogen. The eutrophication effect can be classified as having local impact because it highly depends on the ecosystem itself and on the human contribution. The N-rich and S-rich compounds are typically contained in inorganic fertilizers, emitted as pollution from incineration processes or derived from household wastewater and fish farming. There are two impact indicators for this category, depending on which is the limiting chemical compound: for freshwater, phosphorous is the limiting one, thus the reference unit is kg P eq, while for marine and terrestrial systems it is kg N eq.

Human toxicity (cancer, non-cancer) – This category is partially overlapping with the Ecotoxicity category, because the parameters considered to evaluate the toxicity of a substance are the same but with the focus on human health. The effect of emissions into the environment can affect the whole population or be more localized, for example for specific workers or consumers categories. Depending on the classification of the substance (cancerogenic), it is possible to distinguish between cancerogenic toxicity and non-cancerogenic toxicity. For

both categories, the impact indicator is the same as the one for ecotoxicity, kg 1,4-DCB eq.

Ionising radiation – This impact category is one of the newest ones, and it evaluates the impact of ionising radiation (radioactivity) on human health. This category refers to nuclear energy production operating in normal conditions, it is not related to nuclear accidents. The potential impact is calculated on human health, based on the conversion of ionising radiation into the equivalent of kilobecquerels of Cobalt 60 equivalent (kBq Co-60 eq).

Land use – This category evaluates the impact that all anthropogenic activities have on soil areas, such as agricultural production, raw materials extraction or urban settlements. The consequences on a finite resource such as soil are multiple and very different: biodiversity decline due to the ecosystems modification and species loss, changes in soil organic matter or erosion of the soil itself. Concrete surfaces typical of urban and industrial have substituted the soil, with the loss of all the typical functions, such as rainwater management. This category evaluates the impacts on biodiversity and ecosystem services, as well as the potential properties: biotic production, carbon sequestration, freshwater regulation, water purification, desertification regulation and erosion regulation. The impact indicator for this category is the $m^2 \cdot a$ crop eq, which represents the area multiplied by the year for a land occupancy with a specific use as a cropland.

Particulate matter (PM) formation – This category refers to the impact that PM of different shapes and dimensions have on human health. PM pollution is a worldwide matter which is responsible for an average of 1 to 5 premature deaths. Their effect on human health is mainly related to respiratory issues, leading to chronic and acute diseases, lung cancers but also cardiovascular diseases and diabetes, with a significant reduction of life expectancy. PMs can be divided into two categories depending on their source: primary PM are the ones directly emitted as in the case of transportations or heating systems, secondary PM are the particles formed through chemical reactions in the atmosphere. The chemicals involved in these reactions are already named as polluting substances in other categories: nitrogen oxides, sulphur oxides, ammonia and volatile organic compounds. PMs are also classified depending on their aerodynamic diameter: if the diameter is less than 10 µm they are considered respirable particles and named PM_{10}, if the diameter is less than 2.5 µm the particles are defined $PM_{2.5}$. These are the most dangerous ones because they are able to penetrate deeper into the lungs and thus are taken as the indicator for this category (kg PM2.5 eq).

Photochemical oxidant formation – This category addresses all the chemical reactions that are able to form reactive oxygen compounds like ozone, using solar light as a catalyst. These reactions are very complex and take place in the lower layer of atmosphere, called troposphere. They occur in the presence of both volatile organic compounds (VOC) and nitrogen oxides (NO_x). The sources of

these compounds are numerous and widely spread, thus this phenomenon can be localized and non-linear, depending also on meteorological conditions. The reactive oxygen compounds are very dangerous for human and animals respiratory systems when inhaled. In case of high concentration of pollutants, the symptoms can be very severe with consequences that can lead to chronic respiratory illnesses or even death. For plants, these compounds can react with the surface of the leaves or directly enter inside, damaging the organs responsible for photosynthesis. This has an impact on the growth rate, for example causing a loss in the agricultural field. The main sources of VOC and NO_x are related to the transportation sector and industrial processes, especially when organic solvents are involved. The impact indicator, both for human health and terrestrial ecosystems, is based on kilograms of NO_x equivalents (kg NO_x eq).

Resources use (fossils, minerals and metals) – The term resource refers to all the materials involved in human activities and extracted from nature. In this category the resources considered are the abiotic resources, which are the non-biological resources extracted from the ground: fossil fuels, minerals and metals. The impact that this category aims to evaluate is the loss of these resources, based on the idea that the high consumption of resources today will oblige future generations to more difficult extractions. The resources can be distinguished into two categories: consumptive resources and dispersive resources. Consumptive resources are the resources converted into other products in an irreversible way, like the combustion of fuels. Dispersive resources, typically minerals and metals, are not properly lost but are used in a way that causes them to be dispersed in the ecosphere with less accessibility for further extractions. For fossils fuels, the impact indicator is kilograms of oil equivalents (kg oil eq), while for minerals and metals it is the surplus ore potential and it is expressed in kilograms of copper equivalent (kg Cu eq).

Stratospheric ozone depletion – The ozone (O_3) is a reactive molecule present in lower atmospheric layers as a pollutant, and in larger amounts in higher altitudes, where it forms the stratospheric ozone layer. In this latter case, the presence of this layer is fundamental to protect human health and ecosystems from hazardous ultraviolet radiation (UV-B). However, due to anthropogenic activities, this layer has been subjected to depletion, reducing the protection from the UV radiation. The effects on human health are mainly associated with skin damage and cancers, eye illness like cataracts and also irritation to the respiratory ways. As with humans, the radiation can cause similar epidermal damages to animals. For the ecosystems, the photosynthetic organisms are the most damaged because their photosynthesis yield is reduced. The depletion of ozone is due to chlorine and bromine compounds in the atmosphere, in particular the trichlorofluoromethane (also known as Freon-11), and more in general the chlorofluorocarbons (CFCs). These chemicals react with the ozone in the atmosphere, reducing its

concentration and leading to reduced protection of the ozone layer. Hence, the impact indicator is expressed in kilograms of CFC-11 equivalent (kg CFC-11 eq).

Water use – This category refers to the local impact of water use on human and ecosystem life. Water is a renewable resource in sufficient quantity to meet all needs. However, its availability depends on the region and on the season, while the human demand is continuously increasing. This leads to localized issues also in relation to the climate change effect, with droughts and floodings that alter its availability. Scarcity or degradation caused by freshwater pollution leads to a water deprivation of ecosystems like rivers and lakes, causing the loss of flora and fauna species. The impact of water deprivation on humanity can affect domestic users, the agricultural sector and aquaculture workers. The impact indicator is expressed in cubic meters (m^3).

4.6. ReCiPe 2016: Endpoint Impact categories

After calculating the midpoint impact indicators, these results can be further aggregated along the damage pathways defined in the ReCiPe method [343]. This approach allows the identification of three categories defined as Damage Categories [344] or "Areas of Protection" (AoP), described by *endpoint impact indicators* [340]. These endpoint categories represent downstream environmental mechanisms that are generally more meaningful from a decision-making perspective, although they are also more difficult to quantify due to higher uncertainty and the complexity of the underlying cause-effect chains [325]. The difficulties related to the proper calculation are due to the complexity of the pathways and currently not all of them are considered in the calculations [343]. A schematic representation of the correlation between the midpoint and the endpoint indicators is reported in ***Figure 4.3***: red arrows highlight the connection between the impact categories and the damage category of Human Health (HH) (expressed in Disability-Adjusted Life Years, DALY), green arrows describe the Natural Environment (NE) connections (expressed in species loss over time) and finally the black arrows are for the Natural Resources (NR) category (expressed in 2013 USD).

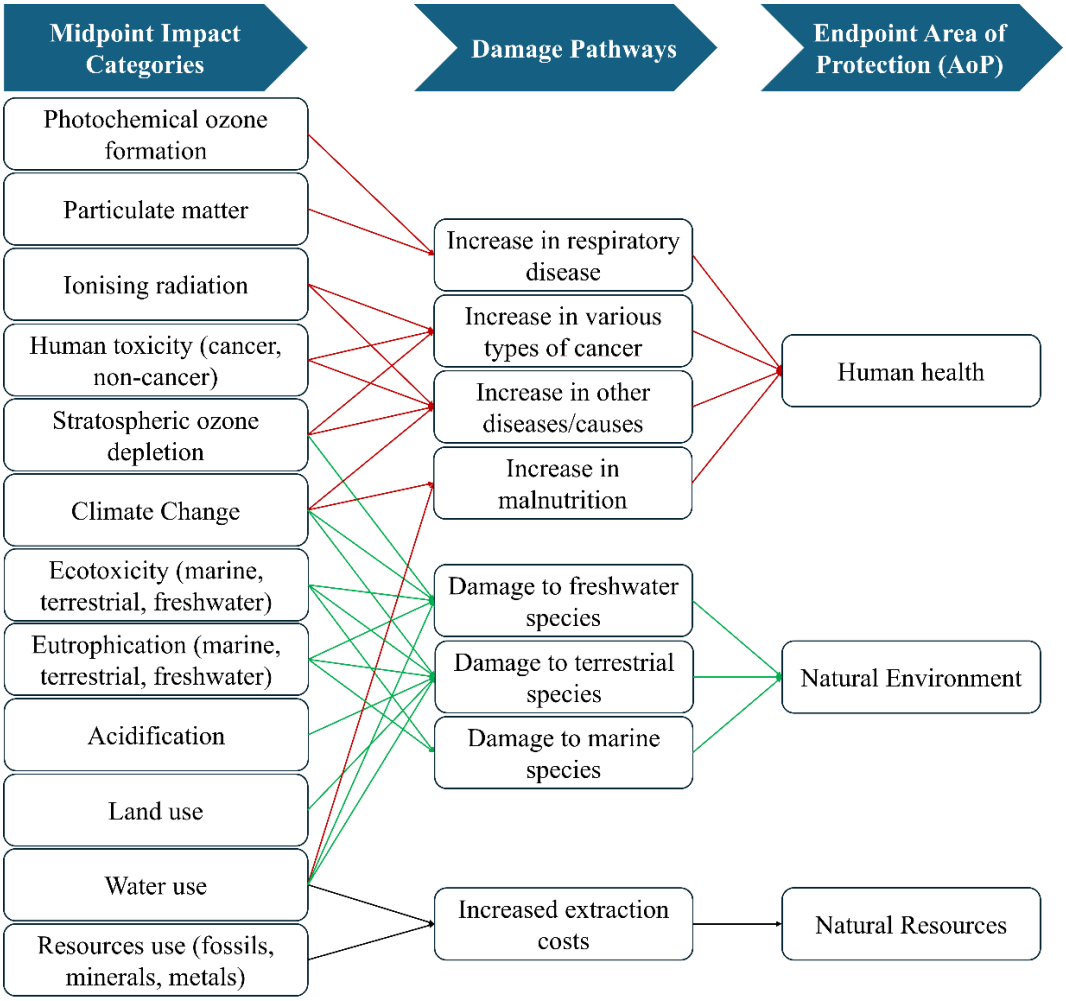

Figure 4.3 – Graphical representation of the connections between midpoint and endpoint indicators, based on the damage pathways proposed by the ReCiPe methods [343]

4.7. Methodological approach of the EF 3.1 Method

To provide a comprehensive and policy-relevant evaluation, the EF 3.1 method [345] is implemented alongside the ReCiPe 2016 Midpoint (H) approach. Although both methods operate primarily at the midpoint level, key distinctions exist regarding their institutional purpose, characterization models, and specific indicator structures. ReCiPe 2016 is widely recognized as a global academic standard that reflects consensus within the scientific community [342]. In contrast, EF 3.1, developed by the European Commission's Joint Research Centre (JRC), represents the mandatory approach for Product Environmental Footprint (PEF) compliance within the European Union. This makes it an essential tool for aligned battery supply-chain assessments under current European regulations.

A fundamental structural difference between the two frameworks lies in their approach to endpoint and damage modelling. ReCiPe 2016 provides distinct quantitative characterization factors at both the midpoint and endpoint levels. This

approach maps environmental interventions to physical damages within specific AoPs, quantifying impacts such as HH degradation or ecosystem quality degradation (expressed in species loss over time).

Conversely, the EF 3.1 method operates strictly as a midpoint framework and deliberately avoids physical endpoint damage pathways due to their high intrinsic scientific uncertainty. Although EF 3.1 targets the same three overarching AoPs (HH, NE, and NR), the transition from its 16 midpoint indicators to an aggregated evaluation is achieved through standardized normalization and institutional weighting factors established by the European Commission. This step converts the midpoint results into a single, dimensionless macro-indicator known as the "Single Score," expressed in points (Pt) or millipoints (mPt).

Furthermore, the two methods differ significantly in their specific environmental mechanisms and modeling choices for individual categories:

- **Climate Change Granularity**: EF 3.1 introduces a high level of detail by explicitly subdividing the total GWP into three independent sub-indicators: fossil, biogenic, and land-use emissions.
- **Water Consumption Modeling**: For the assessment of water depletion, EF 3.1 implements the advanced AWARE (Available Water Remaining) model to quantify user deprivation potential, whereas ReCiPe relies on a different water consumption index.
- **Toxicity Characterization**: EF 3.1 incorporates the USEtox model, expressed in Comparative Toxic Units for humans (CTUh) and ecosystems (CTUe), for both human toxicity and freshwater ecotoxicity. ReCiPe, conversely, evaluates these categories through chemical equivalents based on 1,4-dichlorobenzene (1,4-DCB-eq).

The EF 3.1 method aggregates elementary flows into 16 core environmental impact categories. A comprehensive breakdown of these categories, including their associated midpoint indicators, reference units, and underlying reference models, is compiled in ***Table 4.2***.

Table 4.2 – Complete characterization framework of the EF 3.1 method, detailing the 16 midpoint impact categories and indicator metrics.

Impact Category	***Impact Indicator***	***Unit***
Acidification (TA)	Accumulated Exceedance (AE)	mol H^+ eq
Climate Change: total (GW)	Global Warming Potential (GWP100)	kg CO_2 eq
Climate Change: biogenic (GW-bio)	GWP100 - Biogenic fraction	kg CO_2 eq
Climate Change: fossil (GW-fos)	GWP100 - Fossil fraction	kg CO_2 eq
Climate Change: land use	GWP100 - Land use change	kg CO_2 eq

(GW-lu)		
Ecotoxicity: freshwater (FE)	Comparative Toxic Unit for ecosystems	CTUe
Ecotoxicity: freshwater, inorganics (FE-inorg)	Comparative Toxic Unit for ecosystems	CTUe
Ecotoxicity: freshwater, organics (FE-org)	Comparative Toxic Unit for ecosystems	CTUe
Resource Use: fossils (FRS)	Abiotic Depletion Potential (ADP-fossil)	MJ
Eutrophication: freshwater (FET)	Nutrients fraction reaching freshwater	kg P eq
Eutrophication: marine (MET)	Nutrients fraction reaching marine water	kg N eq
Eutrophication: terrestrial (TET)	Accumulated Exceedance (AE)	mol N eq
Human Toxicity: carcinogenic (CHT)	Comparative Toxic Unit for humans	CTUh
Human Toxicity: carcinogenic, inorganics (CHT-inorg)	Comparative Toxic Unit for humans	CTUh
Human Toxicity: carcinogenic, organics (CHT-org)	Comparative Toxic Unit for humans	CTUh
Human Toxicity: non-carcinogenic (NCHT)	Comparative Toxic Unit for humans	CTUh
Human Toxicity: non-carcinogenic, inorganics (NCHT-ionrg)	Comparative Toxic Unit for humans	CTUh
Human Toxicity: non-carcinogenic, organics (NCHT-org)	Comparative Toxic Unit for humans	CTUh
Ionising Radiation (LU)	Human exposure efficiency	kBq U235 eq
Land Use (IR)	Soil Quality Index	dimensionless
Resource Use: minerals/metals (MRU)	Abiotic Depletion Potential (ADP-elements)	kg Sb eq
Ozone Depletion (SOD)	Ozone Depletion Potential (ODP)	kg CFC-11 eq
Particulate Matter (PMF)	Potential impact on human health	disease incidence
Photochemical Oxidant Formation: Human Health (POFHH)	Tropospheric ozone concentration	kg NMVOC eq
Water Use (WC)	User Deprivation Potential	m^3 world eq. deprived

4.8. Data quality, uncertainties quantification and sensitivity analysis

Along all the calculations it is important not to forget that all the data are subjected to a great degree of uncertainties, mainly due to the difficulties in

obtaining primary data. Taking into account the uncertainties involved in the life cycle assessment results is fundamental for the credibility and reliability of an LCA study [346]. Addressing uncertainty is crucial in laboratory-scale battery studies, where primary data variability and technological immaturity can significantly influence environmental assessment results. The uncertainties are widely spread along all the LCA process, in fact, they can be associated with the chosen model for the calculations, the functional unit or the system boundaries, and variability related to the time or the place of data collection [325]. Generally, it is possible to identify two types of uncertainties: variability, when there is an error related to data collection, and epistemic, when there is a lack of information, for example related to a specific industrial process [347]. These should be included with the discrepancies identified within databases such as Ecoinvent 3.11, since not all flows are kept up to date and some data may be significantly outdated. To calculate the amount of uncertainties in LCA, one of the possible methods is the Pedigree matrix approach [322]. In ***Figure 4.4*** the Pedigree Matrix developed by the Ecoinvent Data Quality System is reported. This system permits quantifying the uncertainties even in case of absence of specific values, like standard deviation. The uncertainties are qualitatively distributed in 5 categories and for each category, an evaluation from 1 to 5 is assigned, where 1 is the score related to the lowest level of uncertainty and 5 to the highest one. These values are associated with *uncertainty factors* which are used to calculate the final uncertainty.

	1	2	3	4	5
Reliability	Verified data based on measurements	Verified data partly based on assumptions or non-verified data based on measurements	Non-verified data partly based on qualified estimates	Qualified estimate (e.g. by industrial expert)	Non-qualified estimates
Completeness	Representative data from all sites relevant for the market considered, over and adequate period to even out normal fluctuations	Representative data from > 50% of the sites relevant for the market considered, over an adequate period to even out normal fluctuations	Representative data from only some sites (<< 50%) relevant for the market considered or > 50% of sites but from shorter periods	Representative data from only one site relevant for the market considered or some sites but from shorter periods	Representativeness unknown or data from a small number of sites and from shorter periods
Temporal Correlation	Less than 3 years of difference to the time period of the data set	Less than 6 years of difference to the time period of the data set	Less than 10 years of difference to the time period of the data set	Less than 15 years of difference to the time period of the data set	Age of data unknown or more than 15 years of difference to the time period of the data set
Geographical Correlation	Data from area under study	Average data from larger area in which the area under study is included	Data from area with similar production conditions	Data from area with slightly similar production conditions	Data from unknown or distinctly different area (North America instead of Middle East, OECD-Europe instead of Russia)
Further Technological Correlation	Data from enterprises, processes and materials under study	Data from processes and materials under study (i.e. identical technology) but from different enterprises	Data from processes and materials under study but from different technology	Data on related processes or materials	Data on related processes on laboratory scale or from different technology

Figure 4.4 – Pedigree matrix adopted by the Ecoinvent Data Quality System

- **Reliability** – Refers to the quality of the data, which can be verified by measurements and in this case is the most reliable one, or only partially

verified by measurements, in the worst cases, the data are only based on assumptions.

- **Completeness** – Refers to the accuracy of data collection, for example, it is important if the value is an average over a long time or refers to only a single data collection, so that it is possible to calculate an average value, avoiding the use of overestimated or underestimated values.
- **Temporal Correlation** – Refers to how recent the data are, if they were collected in a short enough time range to be still representative for the calculations.
- **Geographical correlation** – It is important to take into account the region, the state or more in general the area where the process is considered. The different electricity sources or other aspects that depend on the area, can greatly affect the final results.
- **Further technology correlation** – Not always all the data are directly available, and when possible, the best choice should be the direct data collection on the production site. When this is not possible, multiple approaches can be used, like considering the same machine produced by different companies, similar technologies or different TRL.

After the assignment of the values, the uncertainties are quantified through statistical calculations, and the most widely used method to calculate the uncertainty propagation is the Monte Carlo Simulation. Through a specific number of iterations, depending on the user, the statistical analysis generates random numbers based on the data to generate the standard deviation, arithmetic mean and median, and finally to generate a probability distribution [325].

Based on the data obtained for the uncertainties calculation, a perturbation analysis, which is often referred to as a sensitivity analysis, even though this is not the entirely accurate, can be performed. In this case, it is possible to identify two different applications: in the proper perturbation analysis, an input parameter is modified and the new result permits calculating the sensitivity by comparing it with the base value. Another application is the scenario analysis, which occurs when a discrete choice like the functional unit or the system boundaries is modified. This type of application permits comparing different scenarios, for example during the development of new technologies, to evaluate if they are advantageous or not, compared to the current ones [325].

4.9. Criticism and limits of LCA

Even though the LCA is a widely adopted and common method for evaluating the environmental impacts associated with a product's life cycle, it is essential to recognize that it presents several criticisms and limitations [348–350]. An

interesting review on bibliometric analysis performed by Moutik et al. [351], highlighted that there are significant variations in the conclusions of LCA research studies. Knowing the reasons behind these discrepancies permits conducting a more reliable and robust assessment.

- **Quality of data and their availability**: the amount of data required to perform an LCA across all the supply chain is very big and in most cases they are very difficult to obtain. Ideally, high-quality primary data should be used for the process under investigation; however, this occurs only rarely. Most often, secondary data are employed, which may be incomplete or inconsistent, leading to inaccuracies in the results [348]. In addition, these secondary data often reflect older technologies and processes, while newer, potentially more sustainable alternatives, are not taken into account.
- **Methodological inconsistencies**: the scope and the system boundaries defined before performing the assessment determine the outcomes. This permits high flexibility among different studies, however, it creates many difficulties in comparisons. In addition, the choice of FU and the LCIA method can greatly affect the results and can lead to misrepresentations of the actual environmental impact [348].
- **Temporal and geographical limitations**: time and geographical specificity are generally not well represented in conventional LCA. For example, it is not always possible to account for the exact region in which a production process takes place, even though environmental impacts can be highly location-dependent. Likewise, some impacts occur over specific timeframes, but LCA commonly evaluates them on a non-temporal scale, limiting the precision of the assessment.
- **Exclusion of social and economic aspects**: the standard LCA is only focused on environmental impacts, while the social and economical impact are, in most cases, not considered. As briefly cited before, LCC and sLCA have been developed for these specific assessments.
- **Simplification of complex systems**: to produce a whole and complete LCA requires a lot of time, expertise and investment, meaning that it is an expensive tool not affordable for all companies. Therefore, the simplification of complex systems, for example assuming linear cause-and-effect relationships, is applied very often, to speed up the process. However, these simplifications may overlook cumulative, synergistic, or non-linear effects that characterize real environmental systems.
- **Application of the performed assessment**: even though the ISO standards are already quite widespread, there is still high variability in how these studies are performed, especially if these studies are used for marketing purposes [349].

Without adequate context or understanding, results may be misinterpreted. Moreover, using LCA as a decision-support tool for strategic planning can be problematic due to the inherent limitations discussed above.

Despite these non-negligible challenges, LCA remains a powerful tool for supporting environmental decision-making. Conducting an LCA while acknowledging and addressing these limitations leads to more complete and trustworthy results. Furthermore, database providers are continually improving the quality and availability of primary data, helping mitigate one of the most significant sources of uncertainty. Overall, the integration of LCA within battery research provides a quantitative basis for guiding material development and process optimization toward truly sustainable energy storage solutions.

Chapter 5

5. Experimental Section

In this chapter, the results obtained for the production process of different anode chemistries at different TRL levels are presented, to identify the best compromise between suitable processability properties and electrochemical performance. Initially, all the materials tested were prepared at the laboratory scale, which required only small quantities. After producing suitable electrodes, some trials were conducted at the pilot-line to understand the impact of the different facilities on the production process.

The first material tested was a graphite powder (Actilion GHDR 15-4) supplied by Imerys Timcal. Due to its widespread use in commercial batteries, the graphite anode production process is already widely known and patented, allowing a rapid optimization of the production process both at laboratory and pilot-line level. However, the electrochemical characterization required significant optimization efforts, as the baseline testing protocol led to strong capacity decay at higher current densities, unstable cycling behaviour and lower-than-expected ICE. In particular, the formation procedure and the introduction of a constant voltage step (CVS) proved essential to achieve stable lithiation kinetics and performance values comparable with those expected for commercial graphite anodes.

The second material investigated was a silicon composite (SC) provided by MTI Corp. Similarly to graphite, the production processes of these SC-based electrodes were optimized at both laboratory and pilot-line levels, in order to identify suitable operating conditions ensuring homogeneous coatings and reproducible electrode properties. However, compared to graphite, the presence of silicon introduced additional challenges related to the large volume changes occurring during lithiation and delithiation, which can compromise electrode integrity and long-term cycling stability. For this reason, the scope of the study was extended to the introduction of different binder systems aimed not only at improving slurry processability and coating quality, but also at enhancing the

mechanical cohesion of the electrode structure, the adhesion to the CC and the overall electrochemical stability. Particular attention was devoted to the development of more sustainable formulations, through the partial substitution of conventional binders with natural polysaccharides, with the objective of improving both the environmental compatibility of the process and the functional performance of the electrodes.

A second SC, supplied by Nanomakers within the Gigagreen project [352], was also investigated. Owing to the close collaboration with the supplier, the optimization of electrode production at laboratory level was achieved rapidly with consistent electrochemical behaviour. Furthermore, in line with the project objectives, a laser-textured CC was incorporated into the electrode fabrication process to enhance the adhesion of the AM to the CC.

The final material tested was silicon supplied by E-Magy. The use of this nanoporous silicon is particularly advantageous, as the intrinsic pore network provides internal buffering space that facilitates the accommodation of volume changes during repeated lithiation and delithiation. In particular, during my research period at CIC energiGUNE laboratories, an in-depth characterization of the slurry properties was carried out. As in the previous case, also with this material, natural polysaccharides were selected as additives to improve both the slurry processability and the electrochemical performance.

5.1. Graphite Anodes

Graphite is currently the most widely used anode material for LIBs, as discussed in ***Chapter 2*** due to its large availability, low price and easy manufacturability [82]. Both natural and synthetic graphite are commercially available: from an electrochemical point of view, the difference between the two is negligible, but from an ethical and economic point of view, the impact could be great and synthetic graphite is often preferred [353].

The main objective of this part of the work was to compare the production process at the laboratory scale with that at the pilot-line scale. The main difference between the two processes is due to the different facilities involved, which are described in ***Chapter 3***. Thus, the first part of this Ph.D. work was focused on the production of graphite anodes at laboratory scale level, with particular attention to the quality of the dry laminates. Homogeneity distribution and reproducibility were evaluated through measurements of dry thickness and mass distribution. The electrode morphology was investigated by SEM (Scanning Electron Microscopy). Successively, the electrodes were electrochemically characterized with Electrochemical Impedance Spectroscopy (EIS), and galvanostatic charge-discharge tests.

The second part concerned the optimization of the production process at pilot-line scale, providing a comprehensive description of the issues encountered and

the solutions applied during multiple trials. The electrodes were characterized with the same techniques previously cited (both morphological and electrochemical) to conclude the chapter with a comparison between the different TRLs.

All the graphite electrodes produced during this Ph.D. work were coated on a 6 µm Cu CC, purchased from MTI Corp. [354], using water as solvent, to guarantee the sustainability of the process, in accordance with the requirements of the scholarship. In addition, carbon black C45 was selected as CA because its surface functional groups promote good wettability and dispersion in water-based slurries, supporting stable electrode processing and homogeneous coating quality [355].

5.1.1. Small-Scale Production: Laboratory Level

5.1.1.1. Electrode Production

The slurry prepared at laboratory scale was based on a formulation already used for graphite-based anode manufacturing. This composition is in line with an already published patent about the industrial anode production [356], with the important recommendation not to exceed the total amount of binder [357]. In fact, in commercial electrodes, the binder content ranges between 2 and 5% [358]. A 1:2 ratio between CMC and SBR was chosen to achieve a good balance between the thickening and stabilizing properties of CMC and the good adhesion and cohesion properties provided by SBR [359]. Therefore, the composition ratio among the components was 95:2:1:2. Further details, about each component, are provided below. All these components were dissolved in MilliQ water with a controlled SF of 40 wt.%.

- 95 wt.% corresponds to the AM, in this case graphite supplied by Imerys (C-NERGY^{TM} Actilion GHDR 15-4), with the theoretical capacity of 364 mAh g^{-1} declared by the supplier
- 2 wt.% corresponds to the CA, in this case the carbon black C45 (Imerys Timcal)
- 1 wt.% is the amount of CMC 2200 (Daicel Corporation)
- 2 wt.% is the amount of SBR supplied by MTI Corp., containing 18 wt.% solid content

The electrode manufacturing process was conducted in a very small batch: the mixing procedure was performed in a 5 mL beaker using a magnetic stirrer (***Figure 3.4a***). To determine the proper amount of material, the calculation started by considering 1 g of solid material as a starting point. The order of material addition during slurry preparation can significantly influence rheological behavior and component dispersion, ultimately leading to distinct electrode microstructures

and ultimately to measurable differences in electrochemical performance of the resulting electrodes [360,361]. The mixing process is detailed below:

1) The 0.01 g of CMC were diluted in 1.5 mL of MilliQ water and kept stirring at high speed (around 1,600 rpm) for 1 h.
2) 0.02 g of C45 were added and the solution was kept stirring for 1 h at 1,600 rpm.
3) 0.95 g of graphite were then slowly added. Once all the powder was incorporated, the mixture was kept stirring for an additional 1 h.
4) The final step was the addition of 0.02 g of SBR. In this case the material was supplied as a suspension with a solid content of 18 wt.%, thus, 0.11 g of the suspension were added instead. In this step, both the mixing speed and duration were reduced by half to prevent degradation of the rubber.

The graphite slurry was coated on the 6 µm CC with a tape casting process, using an Automatic Film Applicator (TQC SHEEN Standard AB4120). The wet thickness was set to 100 µm adopting a Doctor Blade. As a manual technique was used, the produced electrodes were affected by some variability with a limited reproducibility. The coating speed was controlled and set at 10 mm s^{-1}. The laminate was dried in the oven at 50°C for 1 hour (***Figure 5.a***). Subsequently, the electrodes were punched into 15 mm diameter discs using a manual punch and pressed under a pressure of 1 ton with a hydraulic press. Finally, the electrodes were weighted and some preliminary considerations about the laminate were made:

- A visual inspection indicates that the laminate electrode foil was homogeneous with no observable macroscopic defects like cracks or delamination.
- The average thickness of the active layer was 34 ± 3 µm, excluding the CC. Although no specific tolerance values for thickness uniformity are readily available in the literature, this value is in line with the range suggested by Yourey et al. [362].
- The average total weight of the electrodes was 14.17 ± 0.44 mg, with a weight of 9.1 mg ascribable to the CC, for the considered area. The weight distribution is reported in ***Figure 5.b***.
- The average ML was 2.73 ± 0.24 mg cm^{-2}. This value falls within the range reported by the authors previously cited [362].
- The areal capacity of these laminates was calculated as 0.99 ± 0.09 mAh cm^{-2}.

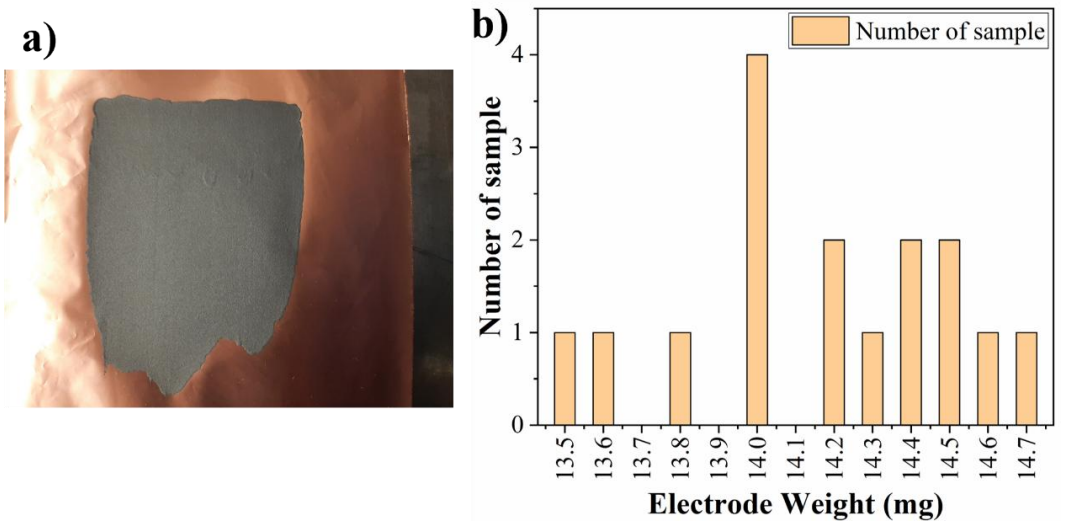

Figure 5.1 – a) Laminate produced at the first trial based on previous optimization; b) Weight distribution of the electrodes produced with the doctor blade at laboratory level

5.1.1.2. Electrochemical Characterization

All the electrodes were tested in coin-cell 2032 geometry, and all the coin cells were assembled inside a controlled-ambient glovebox filled with Argon (O_2 < 1ppm, H_2O < 1ppm). All the electrochemical results presented here were performed in half-cell configuration, with the graphite electrode as the working electrode and lithium chips (MTI Corp, with a diameter of 15.6 mm and a thickness of 0.56 mm) as counter electrodes. A glass fiber GF/A (Whatman, 18 mm diameter, 0.65 mm thickness) was used as separator soaked with 150 µL of electrolyte (1M $LiPF_6$ in EC:DEC 1:1). The electrolyte was added in large excess so as not to make it a limiting component of the system. The choice of using the half-cell configuration, with lithium as the counter electrode, is mainly due to its stable reference potential and the large specific capacity, which prevents the working electrode from becoming the limiting component. Thus, the half-cell configuration is very useful to study the behavior of the AM, while keeping in mind that in a full cell the behavior is not exactly the same, because further parameters have to be taken into account [363].

5.1.1.2.1. Electrochemical Impedance Spectroscopy

The electrochemical impedance spectroscopy (EIS) is a non-destructive technique widely used in LIBs [364]. The tests were performed with a Bio-Logic® VSP-3e multichannel potentiostat. The frequency range for the acquisition of the spectrum was set between 100 mHz and 100 kHz, with a sinusoidal amplitude of 10 mV.

EIS measurement was performed before the other electrochemical tests to evaluate the internal resistance of the cell and to make a preliminary screening of

the quality of the cells. The impedance response is a complex response, composed of contributions from multiple processes: electrolyte resistance in the high-frequency range, charge-transfer reactions and double-layer effects at the interphase between electrode and electrolyte in the mid-frequency range, and diffusion processes at low frequencies [364]. The complexity of this technique lies in the complexity of the inner structure of a battery [365], composed of multiple layers that can be described by a complex equivalent model (***Figure 5.2*** [366]).

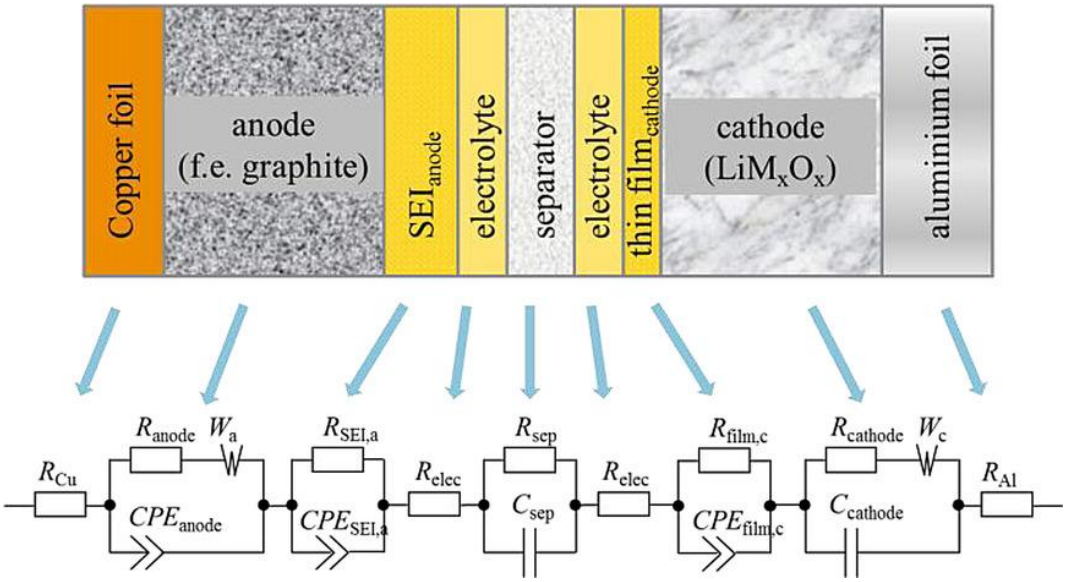

Figure 5.2 – Complexity of the inner cell components structure and relative circuit elements [366]

In this work, a simplified model was adopted, as the cells were assembled using lithium as the reference electrode. The equivalent circuit shown in ***Figure 5.3a*** was generally used to describe the individual contributions [367,368], distinguishing between resistance and capacitance. The components of the equivalent model used in this work are:

a) R_{el}: it refers to the bulk resistance, which includes the electrolyte, CC, and wires
b) CPE_{sei} + R_{sei}: it refers to the contribution of the SEI layer, distinguishing between the capacitance and resistance
c) R_{ct} + CPE_{ct}: it refers to the charge-transfer contribution, again distinguishing between resistance and capacitance
d) W_{diff}: it refers to the semi-infinite diffusion processes

However, when the cell impedance was measured before electrochemical testing, the SEI layer had not yet fully formed; therefore, the model could be further simplified (***Figure 5.3b***). The resulting Nyquist plot of this simplified model is shown in ***Figure 5.3c***. The spectrum consists of a single semicircle in the high to medium frequency regions and a linear diffusion contribution in the low-frequency region [369]. The control of the internal resistance is a key aspect in

battery operation, since excessive resistance leads to increased polarization and heat generation, potentially affecting both performance and safety [370]. In the present Ph.D. work, EIS measurements were employed exclusively as a preliminary diagnostic tool on freshly assembled cells, with the aim of evaluating the quality of cell assembly and identifying samples suitable for subsequent electrochemical testing. Based on the acquired data, the impedance spectra were fitted using Z-view software to extract the resistance values. Cells showing bulk resistance (R_{el}) in the range of 5–10 Ω and charge-transfer resistance (R_{ct}) between 40 and 70 Ω were considered acceptable for further electrochemical investigations [206].

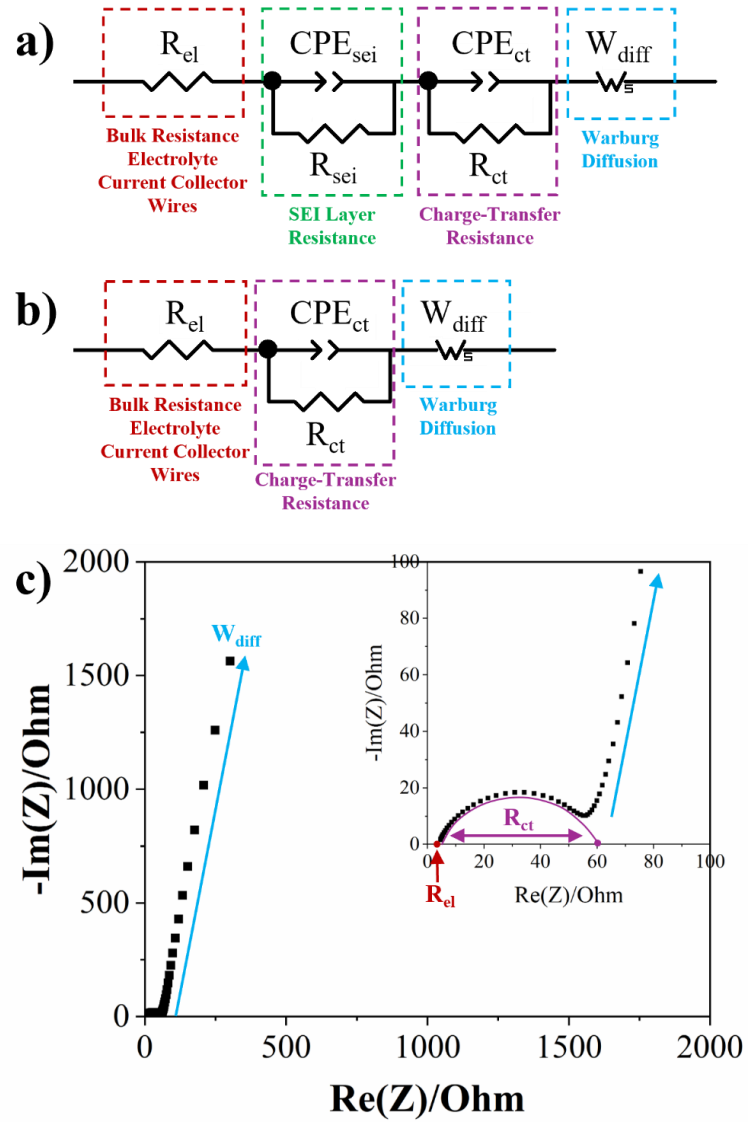

Figure 5.3 – a) Equivalent circuit for EIS adopted in this discussion; b) Simplification of the equivalent circuit when the cells do not yet have the SEI layer; c) Example of a Nyquist plot commonly observed with fresh graphite anodes, in absence of SEI layer

5.1.1.2.2. Galvanostatic cycling - Baseline result: long cycling

To evaluate the electrochemical stability of the as-assembled half-cells employing the baseline graphite anode, a preliminary long-term galvanostatic cycling test was performed (***Table 5.1****Table 5.*). The protocol was based on constant current steps (CCS), in which the applied current was maintained constant during both discharge and charge, and included 5 formation cycles at 0.1C followed by extended cycling at 1C to investigate the long-term behaviour of the AM.

Table 5.1 – Cycling protocol for the long cycling test for the baseline sample

Cycle	***Mode***	***Discharge***	***Charge***
1-5	*Formation*	*CCS: 0.1C*	*CCS: 0.1C*
6-500	*Long Cycling*	*CCS: 1C*	*CCS: 1C*

The electrochemical results are reported in ***Figure 5.4***. Considering the full cycling process (***Figure 5.4a***), the cell exhibited a significant capacity decay just after the increase in the current density from 0.1C to 1C, with approximately 15 cycles showing a capacity of ~ 80 mAh g^{-1}. However, the specific capacity values began to recover after around 35 cycles, remaining almost stable for 150 cycles. Subsequently, the cell underwent an irreversible and irregular decay, reaching a capacity of 78.56 mAh g^{-1} at the 500^{th} cycle (***Table 5.2***).

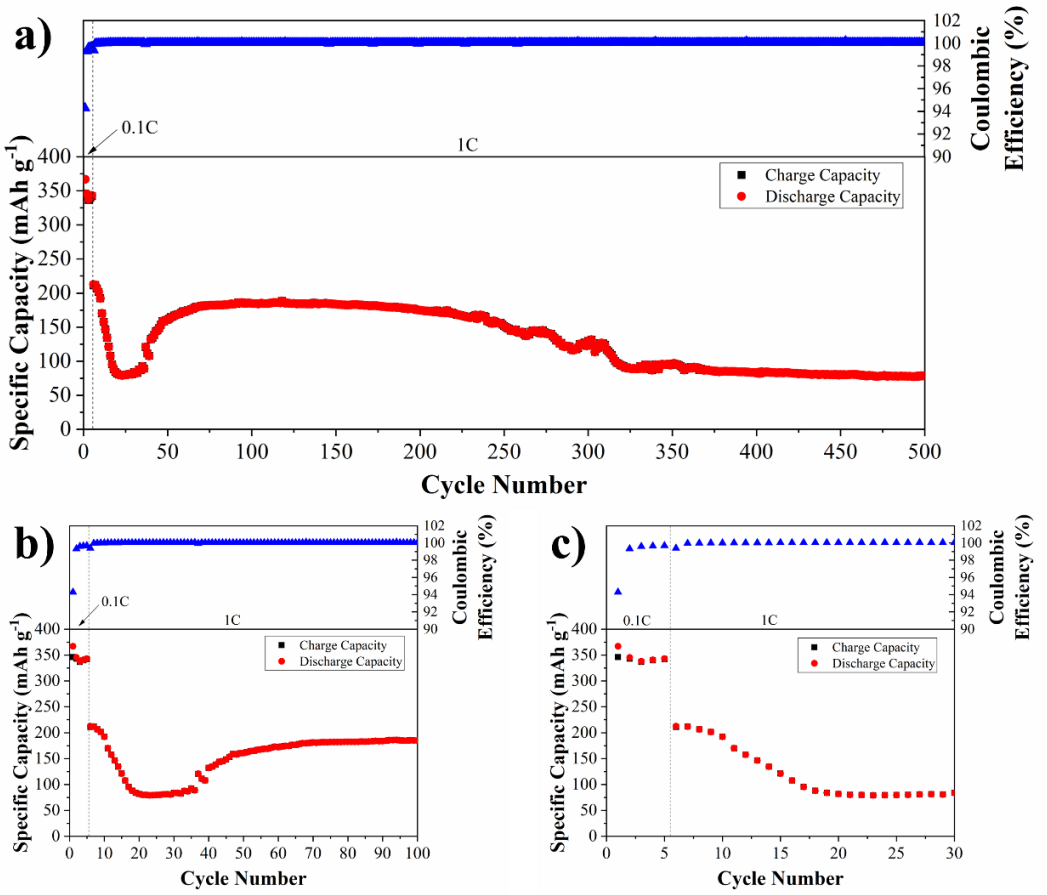

Figure 5.4 – Values of charge and discharge capacity and relative coulombic efficiency for the baseline sample with long cycling protocol: a) Entire test, up to 500 cycles to highlight the inconstant values and the prominent capacity decay; b) Focus on the first 100 cycles to highlight the first capacity decay and its recovery; c) Focus on the first 30 cycles to highlight the stability at 0.1C and the decay when the current density is increased at 1C

Table 5.2 – Values of charge and discharge capacities, normalized by the electrode weight, and relative values of coulombic efficiency for some representative cycles for the baseline cycling protocol

Cycle	*C-rate*	*Charge Capacity (mAh g^{-1})*	*Discharge Capacity (mAh g^{-1})*	*Coulombic Efficiency (%)*
1	*0.1C*	*346.00*	*366.96*	*94.29*
2		*342.97*	*345.33*	*99.32*
3		*336.60*	*337.96*	*99.60*
6	*1C*	*211.09*	*212.36*	*99.40*
10		*192.08*	*192.06*	*100.01*
20		*81.67*	*81.65*	*100.04*
30		*83.67*	*83.64*	*100.04*
50		*160.70*	*160.66*	*100.03*
100		*184.44*	*184.77*	*100.04*
200		*174.69*	*174.61*	*100.04*
300		*129.55*	*129.49*	*100.05*
400		*83.28*	*83.24*	*100.05*
500		*78.60*	*78.56*	*100.05*

A more detailed analysis of the first 100 cycles (***Figure 5.4b***) shows that the sharp decrease in both discharge and charge capacity occurs when the applied current is increased to 1C. The origin of this capacity decay is complex and mainly related to interfacial processes occurring at the graphite surface during cycling. Li-ions first diffuse from the electrolyte into the pores and channels of the electrode. Once they reach the graphite surface, they must pass through the SEI before finally intercalating into the graphite layers [371]. Hence, the chemistry, the thickness and the stability of the SEI layer can greatly affect the diffusion of the ions inside the electrode [372,373]. Among these phenomena, one of the most relevant is the kinetic limitation occurring at high current densities. Under these conditions, Li-ions do not have sufficient time to homogeneously diffuse into the graphite structure, leading to increased polarization within the cell. This effect is well described by Weng et al. [374], thanks to their X-Ray Diffraction (XRD) analysis and Inverse Fast Fourier Transform (iFFT) images.

Another undesired phenomenon that can occur at the electrode surface is lithium plating, where the Li-ions are reduced to metallic lithium. Lithium plating on graphite surface is typically an irreversible reaction, which consumes lithium ions increasing the internal resistance and leading to capacity decay. In addition, the continued plating during repeated charge/discharge process promotes dendrites formation, which can cause internal short circuits [375]. This was confirmed by Lu et al. [376] who were able to identify the lithium plating phenomenon thanks to operando optical microscopy observations during the process of charge and discharge of a graphite electrode. They were able to confirm the creation of an irreversible layer when a current density of 0.5C was applied to their electrodes.

Another effect that has an impact on the capacity is the structural stress that occurs inside the graphite particles after repeated lithium intercalation/de-intercalation cycles. This stress reduces the ionic and electronic conductivity, due to the generation of particle cracking, localized lattice strain and disordered surface structure [377,378]. Furthermore, it is important to cite also the diffusion-controlled Li-ions trapping effect, which occurs when, after repeated insertion and de-insertion cycles, Li-ions inside the material require progressively more and more time to diffuse, preventing their complete de-intercalation [372].

After only 15 cycles the discharge capacity decreased by around 130 mAh g^{-1}: at the 6^{th} cycle the value was 211.09 mAh g^{-1} while at the 20^{th} cycle it reached 81.67 mAh g^{-1} (***Table 5.2***). The capacity recovery became even more evident and at the 100^{th} cycle, the discharge capacity was 184.44 mAh g^{-1}, which means that the difference compared to the 6^{th} cycle is less than 27 mAh g^{-1}. The observed capacity recovery is likely the result of multiple overlapping mechanisms occurring simultaneously:

- **Structural relaxation**: the multiple intercalation/de-intercalation of lithium ions inside the graphite layers leads to a gradual expansion between these layers, with the consequence of the increase in the diffusion kinetics of the ions [378].
- **SEI maturation**: the porous and organic-compound-based SEI, it gradually becomes denser and mainly composed of inorganic compounds. This change reduces further parasitic reactions with the AM surface, increases the lithium diffusion coefficient, reduces the charge-transfer resistance and improves the overall interface stability, withstanding the slight volume expansion of graphite during intercalation, without cracking [379].
- **Lithium redistribution**: working at low voltage, the half-cell can face lithium plating on the graphite surface. During subsequent cycling under more favorable kinetic conditions, such as reduced current density, moderately increased temperature or improved interfacial stability due to SEI maturation, part of the plated lithium can be stripped and re-intercalate into the graphite structure, partially restoring the reversible capacity [229,378].
- **Electrode wetting improvement**: the electrolyte gains access to more pores, allowing the utilization of a larger fraction of the AM [378].

Figure 5.5a reports the detailed charge/discharge curves for the first three forming cycles. The black dashed line describes the first cycle, the second cycle is the red curve, and the third cycle is the blue curve. The first discharge curve differs in shape from the other two. This difference is typically attributable to SEI formation. All discharge curves exhibit three distinct plateaus, which are evident in both the charging and the discharging steps. These plateaus are associated with the different stage structures that coexist in graphite when lithium ions are inserted between the layers [378]. In ***Figure 5.5b***, the relative dQ/dV profiles are also reported, which highlight the multiple stage reaction behaviour. The voltage plateaus, and consequently the corresponding peaks in dQ/dV profiles, represent the voltage range in which two lithiation phases coexist within the material. In this way, it is possible to identify the different lithiation stages of graphite and the corresponding voltages at which they occur.

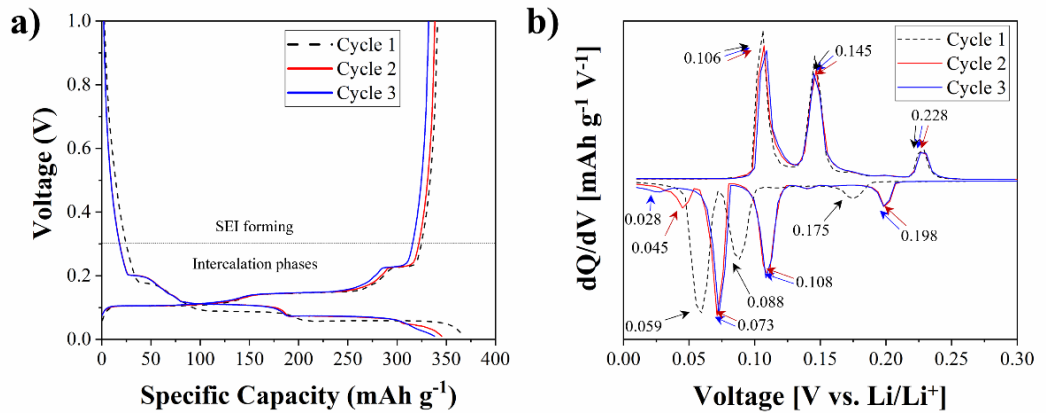

Figure 5.5 – a) Charge/discharge curves for the forming cycles and b) their relative dQ/dV curves with a focus on the intercalation steps and the related voltage values

Generally, the lithiation stages can be divided into "dilute" ones, when the potential is above 0.076 V and the sites are only partially occupied by Li-ions, and the "dense" ones, when the potential is below that value, and the layers begin to be fully occupied [380]. When compared to the literature [381–389] the charge/discharge profiles reported in ***Figure 5.5*** encompass all lithium intercalation steps within graphite and can be ideally divided into different regions depending on the potential range.

- 1.5 < V < 0.80 V: SEI formation. As already discussed in ***Chapter 2***, during this step, the lithium salts, possible additives, and the electrolyte solvents undergo partial degradation reactions on the surface of the electrode [387–389].
- 0.80 < V < 0.20: diluted phase (Stage 1'). The graphite is subjected to a partial reduction when the lithium ions start to be inserted into the layers.
- 0.20 < V < 0.10: Stage 4 → 3 → 2, where lithium ions are progressively intercalated between closely spaced layers [386]. Each lithiation stage is described as a graphite intercalation compound (GIC) where the lithiation steps are described as an alternation of graphene layers and lithium ions. For example, Stage 1 corresponds to one graphene layer alternating with one lithium layer, while Stage 2 consists of two graphene layers and a lithium layer, and so on [390].
- 0.10 < V < 0.00: Stage 1, where lithium ions are intercalated in every graphene layer. This step requires more time because the movement of Li-ions is limited by their high amount.

Moving to higher cycle numbers, the corresponding charge–discharge curves are reported in ***Figure 5.6***. Focusing on the profiles shown in ***Figure 5.6a***, a clear capacity decay can be observed from cycle 6 (pink) to cycle 20 (dark orange), as evidenced by the progressive shortening of the voltage plateaus and the simultaneous increase in overpotential. As previously discussed, this behaviour is

associated with an increase in internal resistance, which leads to reduced ionic and electronic transport within the electrode [377,378]. At cycle 35 (light orange) the capacity starts to be recovered, with slightly longer plateaus, and this is even more evident in cycle 50 (light green). When higher cycle numbers are considered (***Figure 5.6 b***), the most evident trend is the gradual decay of the capacity from cycle 100 to cycle 500.

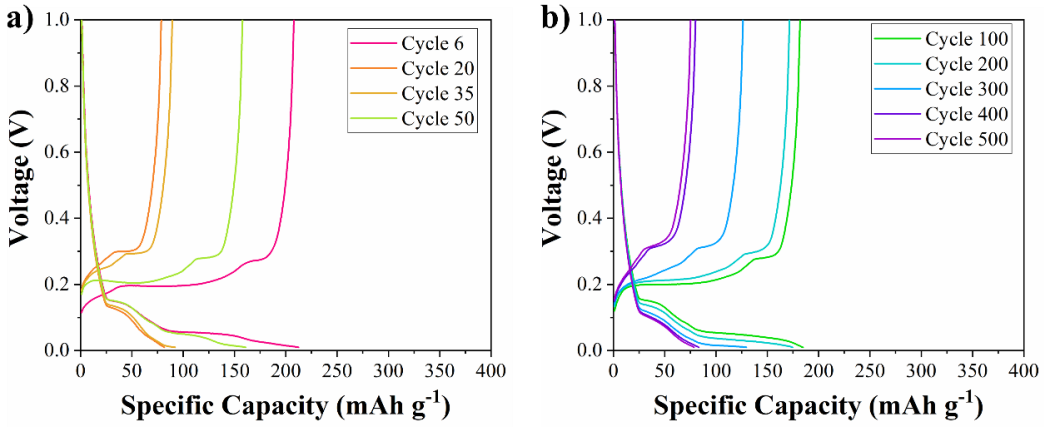

Figure 5.6 – Charge/discharge curves for some representative cycles: a) from cycle 6 to cycle 50; b) from cycle 100 to cycle 500

Another important aspect to consider is the CE. In full cells, it represents a key indicator of cell quality, as it reflects the amount of lithium irreversibly lost during cycling. In half-cell configuration, however, its significance is reduced due to the large lithium reservoir available at the counter electrode, which prevents a reliable quantification of lithium consumption [391]. Moreover, lithium plating on the graphite surface may further complicate the interpretation of the electrochemical response [392].

According to the data reported in ***Figure 5.4*** and ***Table 5.2***, the ICE was 94.29%, corresponding to an irreversible capacity loss of about 5.71%, which is lower than the value declared in the technical data sheet [393]. The subsequent formation cycles showed CE values between 99.30% and 99.70%. When the current density was increased to 1C, the CE progressively increased from approximately 99.40% to values exceeding 105% after prolonged cycling. Although such values are not physically meaningful, they can be attributed to the intrinsic limitation of the half-cell configuration, where the excess lithium available at the counter electrode may compensate for lithium losses, leading to apparently overestimated CE values [391].

5.1.1.2.3. Galvanostatic cycling - Baseline result: rate capability

Additional electrochemical test useful to understand the rate performance of an AM is the rate capability test. For this type of test increasing current densities are applied to the cell in order to evaluate how much the C-rates affect the electrochemical performance of the system. The whole protocol adopted in this

study is reported in ***Table 5.3***. The initial 5 cycles at a constant current of 0.1C are considered as forming step, as previously mentioned. Subsequently, three different steps, at increasing current densities (0.2C; 0.5C; 1C), are performed. The fourth step (recovering step) is, once again, a step at low current density: this step is especially important in the case of newly synthesized AM, because it allows highlighting the presence or absence of relevant degradation phenomena.

Table 5.3 – Cycling protocol for rate capability test for the baseline sample

Cycle	***Mode***	***Discharge***	***Charge***
1-5	*Formation*	*CCS: 0.1C*	*CCS: 0.1C*
6-10	*Rate Capability*	*CCS: 0.2C*	*CCS: 0.2C*
11-15	*Rate Capability*	*CCS: 0.5C*	*CCS: 0.5C*
16-20	*Rate Capability*	*CCS: 1C*	*CCS: 1C*
21-23	*Recovering*	*CCS: 0.1C*	*CCS: 0.1C*
24-500	*Long Cycling*	*CCS: 1C*	*CCS: 1C*

The results presented in ***Figure 5.7*** are quite similar to the previous ones (***Figure 5.4***), since the capacity dramatically decreases whenever the current density is increased at 1C, both during the rate capability and the longer cycling test. Focusing on the rate capability test (***Figure 5.7c***) during the first five forming cycles, the values of charge/discharge capacities are comparable with the ones of the previous test, with a discharge capacity of 364.83 mAh g^{-1}, 340.82 mAh g^{-1} and 337.63 mAh g^{-1}, respectively for the first, second and third cycle at 0.1C (***Table 5.4***). Increasing the current density at 0.2C the values are still acceptable, with a discharge specific capacity of 326.03 mAh g^{-1} at the 10^{th} cycle. However, further increasing the current density, a gradual decay of the capacity was observable: at 0.5 C the discharge capacity decreased up to 261.32 mAh g^{-1}, at 1C the capacity reached the value of 155.64 mAh g^{-1}. The capacity decrease in correspondence to an applied current density of 0.5C is in accordance with the study done by Lu et al. [376], thanks to in operando analysis of the irreversible lithium plating on the electrode surface.

The recovering step led to capacity values close to those obtained during the forming cycles, indicating that the capacity decrease observed during the rate capability test was mainly governed by kinetic limitations rather than by irreversible degradation phenomena, such as continuous SEI growth, lithium trapping within the graphite structure, electrical isolation of AM particles or irreversible lithium plating. Nonetheless, when the current density was increased again to 1C, a new capacity decay was observed, similarly to what was reported in the previous test. Despite comparable initial capacity values, the two cycling protocols led to markedly different electrochemical responses. In the present case, the capacity recovery occurred almost immediately after the initial drop (***Figure 5.7b***), whereas in the previous test several additional cycles were required before a

similar trend could be observed (***Figure 5.4b***). This behaviour clearly highlights the strong influence of the cycling protocol on the electrochemical performance of the graphite electrodes.

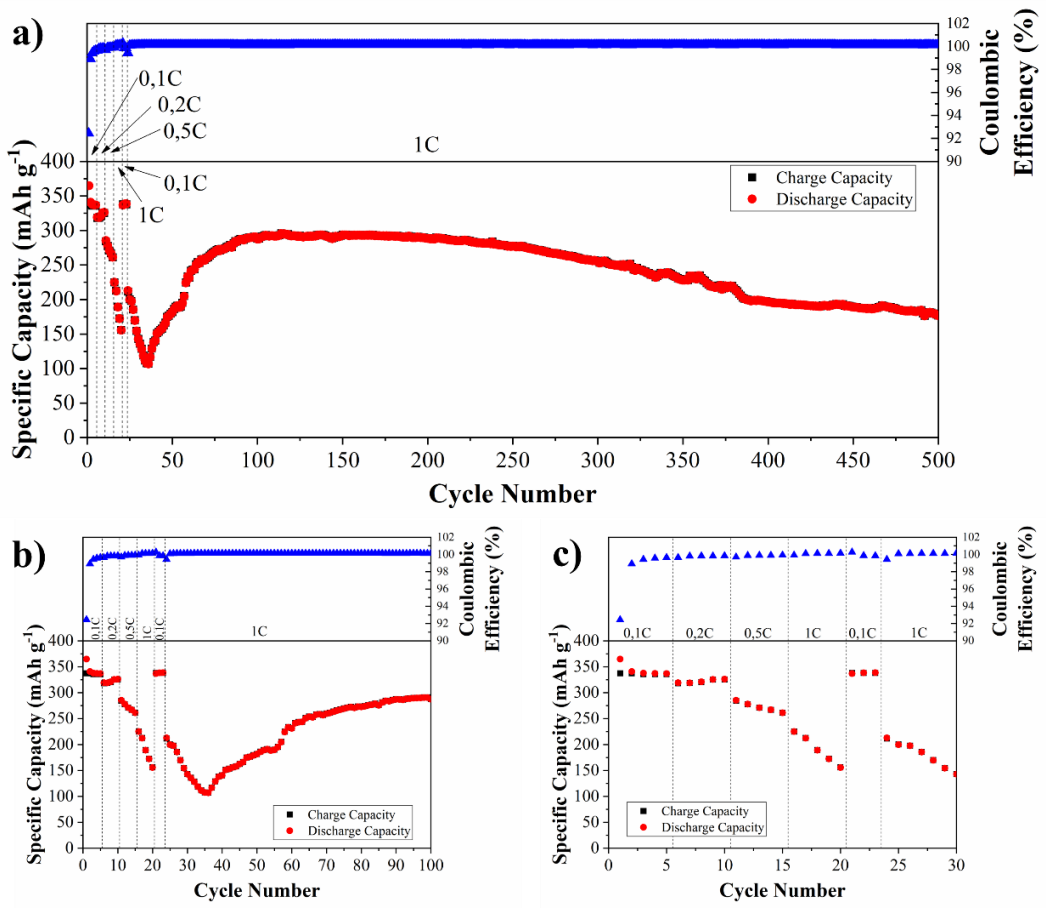

Figure 5.7 – Values of charge and discharge capacity and relative coulombic efficiency for the baseline sample with the rate capability protocol: a) Entire test, up to 500 cycles to highlight the inconstant values; b) Focus on the first 100 cycles to highlight the first capacity decay and its recovery; c) Focus on the first 30 cycles to highlight the values for the forming step and the capacity decay after the increase in the current density

Table 5.4 – Values of charge and discharge capacities, normalized by electrode weight, and relative values of coulombic efficiency for some representative cycles for the baseline rate capability cycling protocol

Cycle	***C-rate***	***Charge Capacity (mAh g^{-1})***	***Discharge Capacity (mAh g^{-1})***	***Coulombic Efficiency (%)***
1	*0.1C*	*337.28*	*364.83*	*92.45*
2		*337.17*	*340.82*	*98.93*
3		*335.72*	*337.63*	*99.43*
10	*0.2C*	*325.54*	*326.03*	*99.85*
15	*0.5C*	*261.11*	*261.32*	*99.92*
20	*1C*	*155.86*	*155.64*	*100.14*
23	*0.1C*	*338.05*	*338.53*	*99.86*
24	*1C*	*211.57*	*212.79*	*99.43*
30		*142.91*	*142.71*	*100.14*
36		*106.90*	*106.75*	*100.15*

50	*181.55*	*181.28*	*100.15*
100	*287.93*	*287.52*	*100.14*
200	*288.83*	*288.41*	*100.15*
300	*255.57*	*255.22*	*100.14*
400	*196.93*	*196.65*	*100.14*
500	*173.02*	*172.78*	*100.14*

Considering the charge/discharge curves of the forming step (***Figure 5.8a***), the shape was exactly the same as for the previous sample: all the plateaus are clearly evident at the same voltage values, meaning a good reproducibility of the process. Considering the rate capability test (***Figure 5.8b***), a gradual capacity decrease is observed: starting from the dark green cycle at 0.1C, the plateaus are progressively shorter up to cycle 20 at 1C (orange). When the current density is reduced to 0.1C once again (cycle 23, red curve), the material is able to completely recover the capacity, thanks to a perfect overlap with cycle 5 profiles.

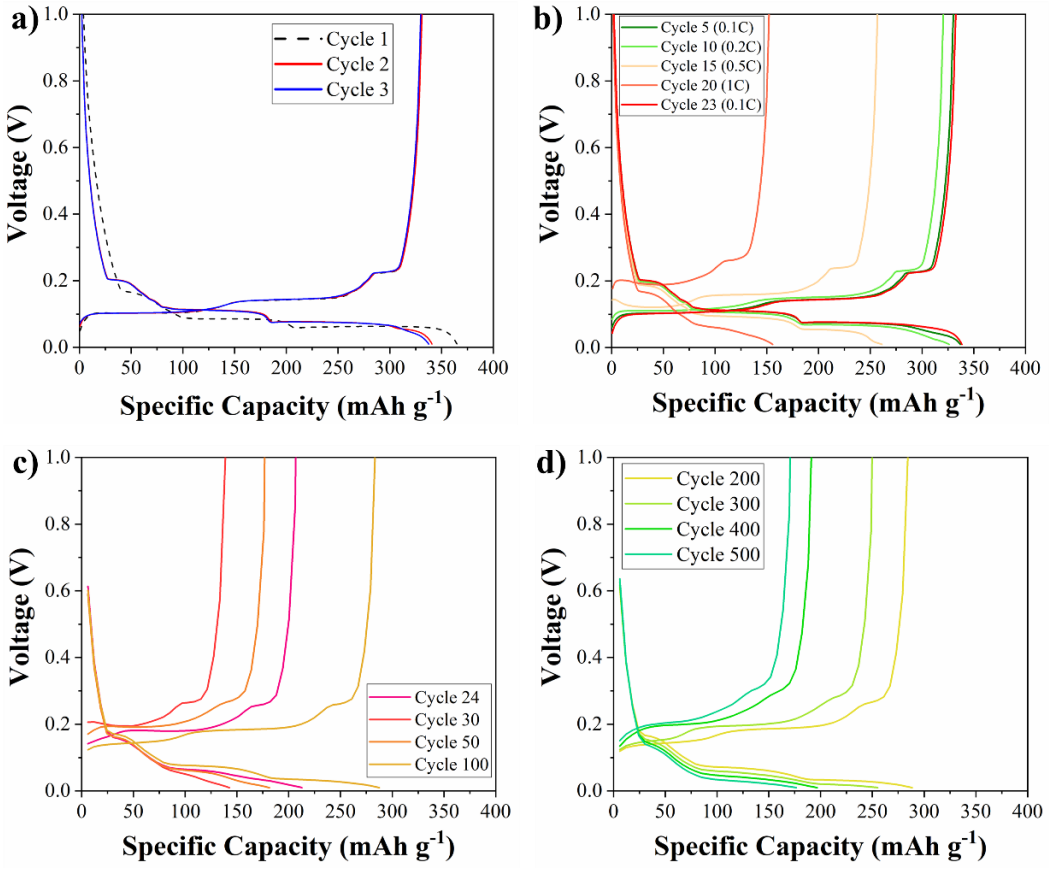

Figure 5.8 – Charge/discharge curves for some representative cycles for the baseline rate capability cycling protocol: a) Forming cycles; b) Curve for the rate capability test; c) Curves of the first part of long cycling test; d) Curves of the second part of long cycling test

During the long-term cycling stage, a behaviour similar to that observed in the previous test was detected, with an initial capacity decay followed by a

progressive recovery (***Figure 5.8c***). After the increase in current density, the discharge plateaus became shorter, indicating a temporary performance loss. However, the capacity recovered rapidly within the subsequent cycles and reached stable values close to 290 mAh g^{-1}, which were maintained over an extended cycling period. At higher cycle numbers (***Figure 5.8d***), a gradual capacity fade was again observed, although the final discharge capacity at the end of the test remained significantly higher than that measured for the previous sample, highlighting the improved long-term electrochemical stability under the adopted cycling protocol.

The results were much better than those of the previous sample; nevertheless, they are still not acceptable considering that the AM is commercial and the production process reflects the industrial production.

5.1.1.2.4. Galvanostatic cycling - Optimizing the forming

The rate capability test previously reported demonstrated the huge impact of the cycling protocol on the final electrochemical behaviour of the cells. Thus, the results presented in this section are focused on the improvement of the cell forming process. To do this, some variations were introduced in the cycling protocol, increasing the number of the initial cycles and decreasing the applied current density (***Table 5.5***). In particular, the first step consisted of 10 cycles at 0.05C. After these, a rate capability test was performed, followed by a short test at 1C, which concluded the experiment. The choice of this protocol was based on the aim of improving SEI formation: as already widely discussed in ***Chapter 2***, the SEI acts as a protective layer that prevents continuous electrolyte decomposition and solvent co-intercalation into graphitic layers during subsequent cycles [14,15]. Imperfect SEI layers can expose fresh graphite to the electrolyte, cause continuous electrolyte decomposition, and lead to graphite exfoliation [16–18]. The cell formation protocol is, therefore, essential to create a stable SEI layer and minimize active lithium loss, electrolyte depletion, and capacity fade over the lifetime of the battery [229].

Table 5.5 – Cycling protocol, with the improvement of the forming step

Cycle	***Mode***	***Discharge***	***Charge***
1-10	*Formation*	*CCS: 0.05C*	*CCS: 0.05C*
11-15	*Rate Capability*	*CCS: 0.1C*	*CCS: 0.1C*
16-20	*Rate Capability*	*CCS: 0.2C*	*CCS: 0.2C*
21-25	*Rate Capability*	*CCS: 0.5C*	*CCS: 0.5C*
26-70	*Long Cycling*	*CCS: 1C*	*CCS: 1C*

As observable in ***Figure 5.9***, this protocol improves the specific capacity stability for the first 20 cycles, with an average discharge capacity of around 350 mAh g^{-1} and 340 mAh g^{-1} respectively at 0.05C and 0.2C (***Table 5.6***). However,

increasing the current density, the specific capacity drops sharply, reaching 190.48 mAh g^{-1} at 0.5C and 75.78 mAh g^{-1} at 1C. Although after 15 cycles, the capacity started to recover again the test was stopped at the 70th.

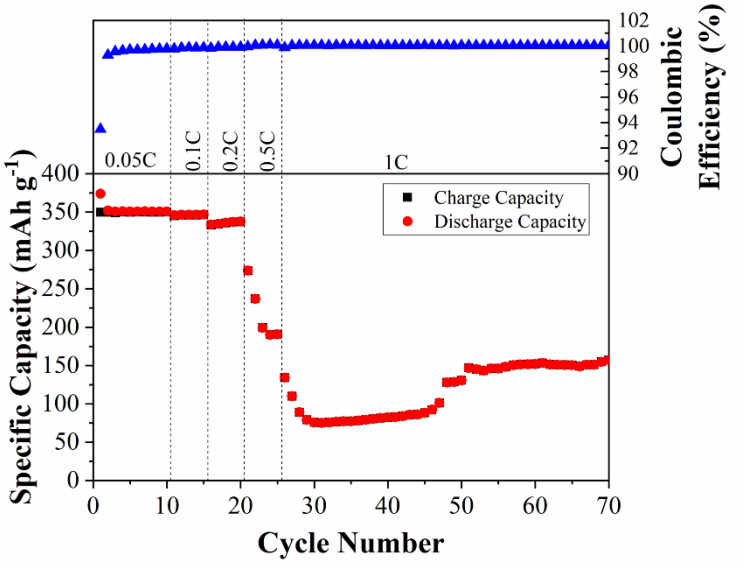

Figure 5.9 – Values of charge and discharge capacities and relative coulombic efficiency for the cycling protocol with the improved forming step

Table 5.6 – Values of charge and discharge capacities, normalized by electrode weight, and relative values of coulombic efficiency for some representative cycles for the improved forming test

Cycle	***C-rate***	***Charge Capacity (mAh g^{-1})***	***Discharge Capacity (mAh g^{-1})***	***Coulombic Efficiency (%)***
1	*0.05C*	*349.70*	*374.06*	*93.49*
2		*349.65*	*352.19*	*99.28*
3		*349.29*	*350.82*	*99.57*
15	*0.1C*	*346.34*	*346.80*	*99.87*
20	*0.2C*	*337.37*	*337.66*	*99.92*
25	*0.5C*	*190.63*	*190.48*	*100.08*
26	*1C*	*133.96*	*134.14*	*99.86*
30		*75.82*	*75.78*	*100.06*
50		*130.68*	*130.63*	*100.04*
70		*157.10*	*157.04*	*100.04*

Focusing on the charge/discharge curves, in the case of the forming steps (***Figure 5.10a***) the shape is the same as in the previous samples, with the three plateaus both in charge and in discharge. In the case of the rate capability test (***Figure 5.10b***), the curves clearly show the expected trend: the dark red curves of cycle 10 (0.05C) are almost overlapped with those of the red curves of cycle 15 (0.1C), meaning that doubling the current density in this case just led to a slight decrease in the capacity. Even at 0.2C, the decrease in the capacity is still negligible, with all the plateaus long and well defined. However, the increase in

the current density to 0.5C led to a relevant capacity decrease confirmed by the shortening of the plateaus.

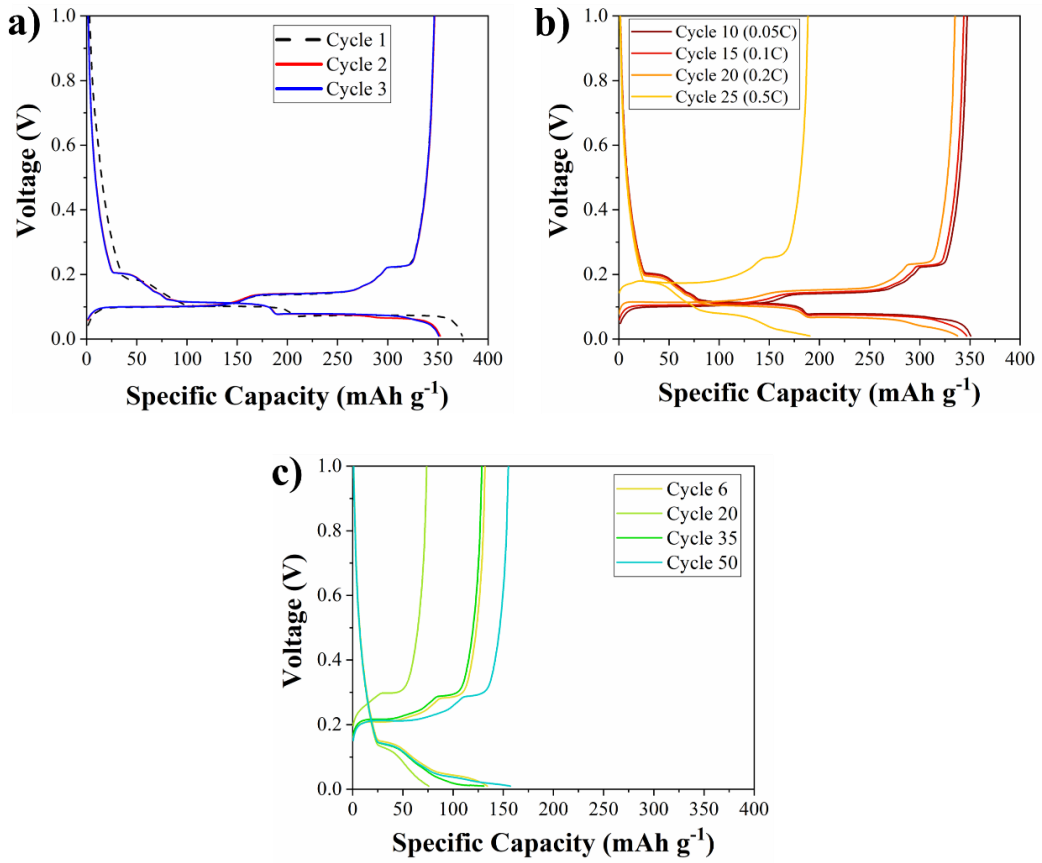

Figure 5.10 – Charge/Discharge curves for the improved forming protocol test: a) First three cycles of the forming step; b) Rate capability test; c) Long cycling step

Although the formation protocol was optimized, this adjustment alone was not sufficient to enhance the electrochemical performance at high C-rates, and a pronounced capacity decay was still observed during prolonged cycling.

5.1.1.2.5. The importance of the constant voltage step for anode half-cell characterization in galvanostatic cycling

To overcome the issue related to the poor electrochemical performance, a different cycling protocol has been chosen: this protocol, defined as CC-CV (Constant Current – Constant Voltage), adds a step of constant voltage after the discharge step at constant current. The addition of this step can be used to mitigate the capacity loss related to the slow diffusion of Li-ions inside the AM structure, permitting the ions to fully intercalate inside the graphite [372]. In addition, especially at higher C-rates, adopting a simple CCS, the Li^+ intercalation is incomplete because lithium ions saturate the graphite surface, favoring lithium plating [376]. On the contrary, during the delithiation step, some Li-ions trapped

deep inside the electrode become inaccessible, ultimately leading to a drop in the overall capacity [394].

Therefore, as reported in ***Table 5.7***, the CVS was added to all the cycling protocols. The main idea was to better understand the impact of this step on the overall electrochemical performance of the cell. Thus, the cycling protocol started with the forming step: the discharge CCS is performed by applying 0.1C, then the CVS is performed by maintaining the voltage at a constant value of 10 mV up to when the current reaches the value of 0.05C, and finally the cell is charged with a CCS with a current value of 0.1C, for 10 cycles.

Table 5.7 – Cycling protocol with the addition of the constant voltage step

Cycle	***Mode***	***Discharge***	***Charge***
1-10	*Formation*	*CCS: 0.1C* *CVS: 0.01V / 0.05 C*	*CCS: 0.1C*
11-60	*Cycling*	*CCS: 1C* *CVS: 0.01V / 0.05 C*	*CCS: 1C*
61-100	*Cycling*	*CCS: 1C*	*CCS: 1C*

As for the forming step, during the subsequent 50 cycles, the CVS was maintained under the same conditions. Finally, for a further 40 cycles, the CVS was omitted to better analyze the consequence of the addition of this step on the performance of the cell.

The evidence of the impact of the CVS on the performance of a graphite half-cell is observable in ***Figure 5.11***: during the first 10 cycles, when the current density is low, the charge and discharge capacities are almost overlapped. However, in the cycles between the 11^{th} and the 60^{th}, the contribution of the CVS becomes clear: the red dots are the values for the total discharge capacity, while the blue triangles are the values for the CCS without considering the capacity measured in the CVS. During this step at 1C it is evident how much the CVS contributed to the total measured discharge capacity. However, after the 60^{th} cycle, the removal of the CVS led to a noticeable capacity decay, both charge and discharge. This behaviour is associated with the increase in internal resistance and cell polarization in the absence of the CVS step. As a consequence, the cut-off potential is reached earlier during lithiation, limiting the extent of Li-ion intercalation and resulting in a reduced capacity during the subsequent delithiation process.

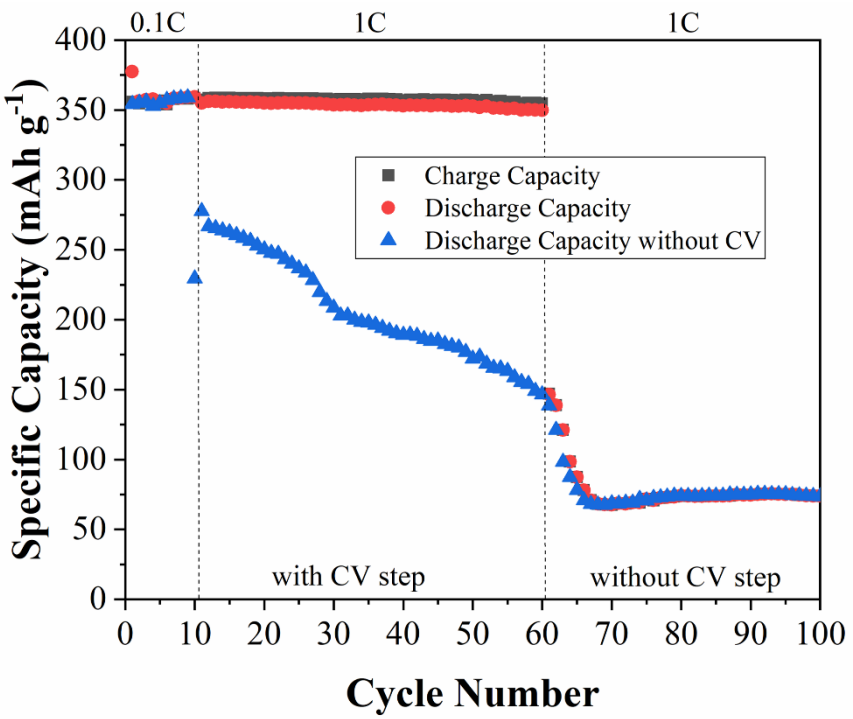

Figure 5.11 – Values of charge and discharge capacities highlighting the impact that the CVS had on the overall performance of the cell.

Once the importance of the CVS was confirmed, another cell was assembled to go deeper into the contribution of this step during a normal test: during this test the cycling protocol was simplified with 5 forming cycles at 0.1C and the CVS at 0.01V and 0.05C. After the forming step, 95 cycles were performed at 1C, with the CVS at 0.01V and 0.05C. The overall capacity values of charge and discharge and the relative values of coulombic efficiency are reported in ***Figure 5.12a***. In comparison with the previous test, the new protocol provides a stable capacity slightly over 335 mAh g^{-1} for the entire test (***Table 5.8***). Focusing on the first cycles (***Figure 5.12b***) the consistency of charge and discharge is evident, especially when the current density was increased from 0.1C up to 1C.

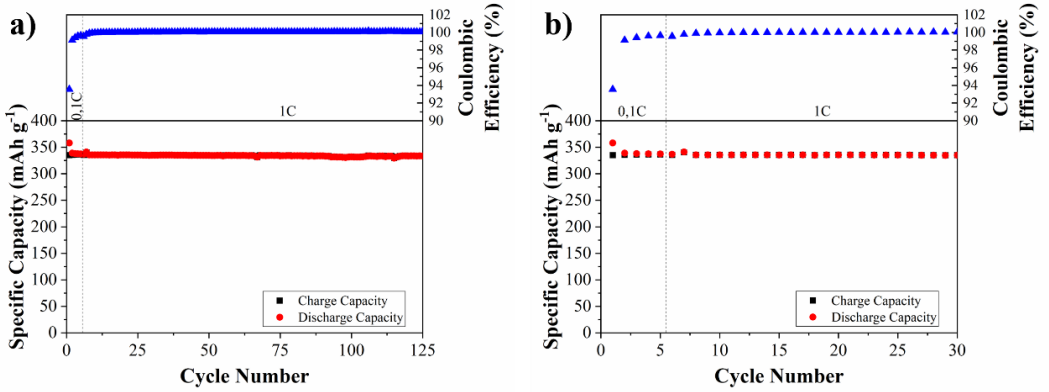

Figure 5.12 – Charge and discharge capacities and relative values of coulombic efficiency for the cell tested with the CVS: a) Entire test; b) Focus on the first 30 cycles

Table 5.8 – Values of charge and discharge capacities, normalized by electrode weight, and relative values of coulombic efficiency for some representative cycles for the improved cycling protocol with the addition of the constant voltage step

Cycle	***C-rate***	***Charge Capacity (mAh g^{-1})***	***Discharge Capacity (mAh g^{-1})***	***Coulombic Efficiency (%)***
1	*0.1C*	*335.02*	*358.09*	*93.56*
2		*335.92*	*338.90*	*99.12*
3		*336.19*	*338.19*	*99.41*
6	*1C*	*335.36*	*336.83*	*99.56*
10		*335.43*	*335.54*	*99.97*
20		*335.71*	*335.64*	*100.02*
30		*335.31*	*335.12*	*100.06*
50		*334.85*	*334.60*	*100.07*
125		*333.93*	*333.45*	*100.08*

According to these results, the impact of the CVS is evident: adding this step allowed obtaining charge and discharge values that are in line with the expected performance of a commercial graphite anode. The presence of this step is particularly evident at higher C-rate. In fact, focusing on the charge/discharge curves reported in ***Figure 5.13***, the profiles observed during the formation cycles (***Figure 5.13a***) at a current density of 0.1C are comparable to those of the previous samples. While, the most important difference appeared in ***Figure 5.13b***, when the current density was increased to 1C, where the voltage was maintained constant, permitting the full lithiation of the graphite. This behavior is in line with what was observed by Zhang et al. [395]: whenever the current density is increased, the different lithiation stages become less evident, with the plateaus gradually shortened. Nonetheless, the almost complete lithiation was confirmed by the charging curves (delithiation step in this system), where the plateaus are comparable with the ones of the forming step, even though they are less evident. As a result, the capacity retention of this cell (calculated considering the discharge capacity, from cycle 10 to cycle 125) was 99.33%.

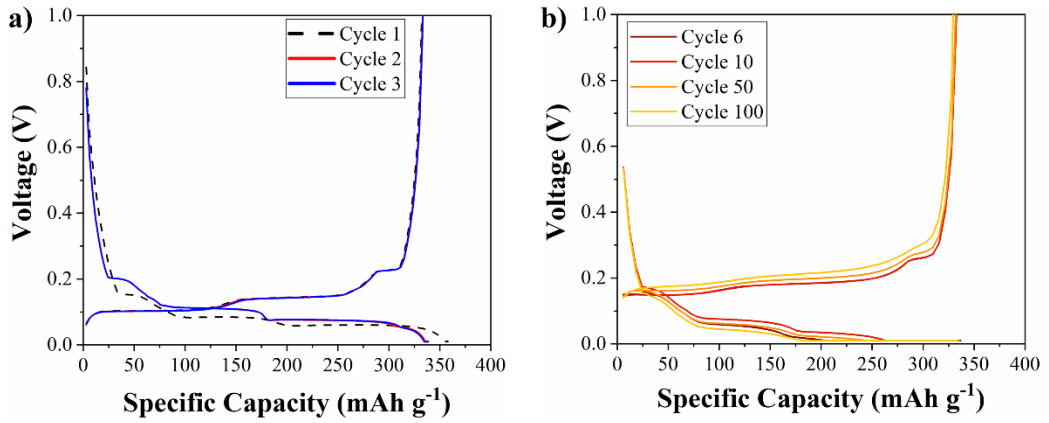

Figure 5.13 – Charge/discharge curves for the CC-CV cycling protocol: a) Forming step; b) Representative cycles at 1C

As previously discussed, CVS can be considered as an additional lithiation stage of graphite, during which Li-ions progressively fill all layers simultaneously [380]. In this way, it was possible to overcome the poor electrochemical performance observed in these graphite half-cells. However, it is important to quantify the contribution of the CVS to the total measured discharge capacity per cycle. As shown in ***Figure 5.14***, the contribution of the CVS during the forming cycles was almost negligible, with values on the order of only a few mAh g^{-1}. When the current density was increased, the contribution of the CVS progressively increased (green bar), demonstrating that this step becomes essential at higher C-rates. The capacity retention, calculated from the specific discharge capacity associated with the CCS between cycle 10 and cycle 125, was 66.61%.

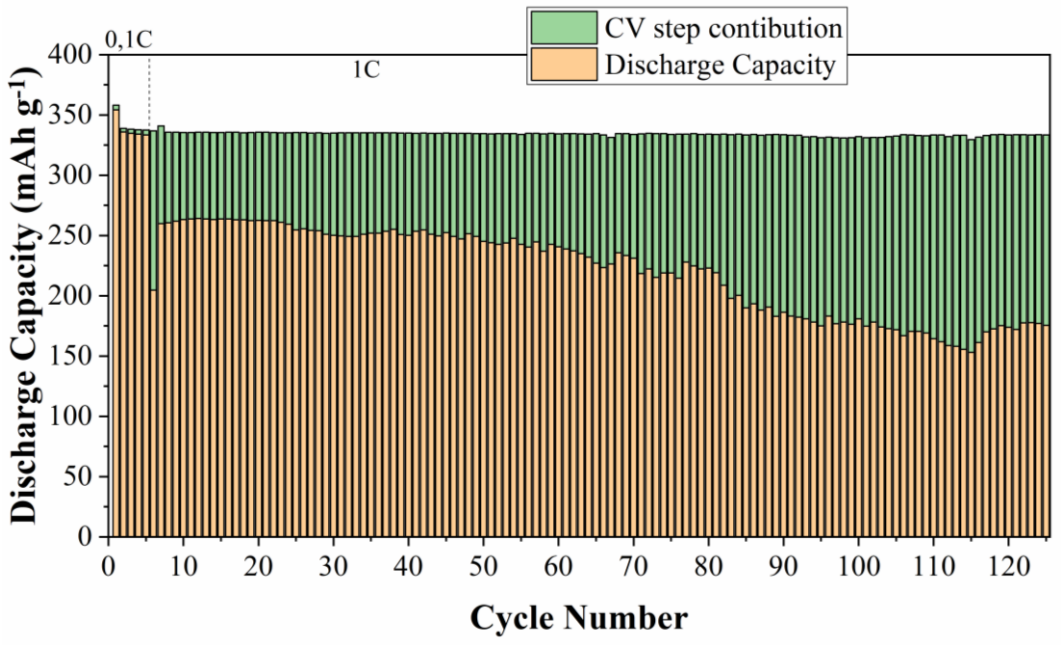

Figure 5.14 – Visual contribution of the CVS considering the discharge capacity for the graphite anode

5.1.2. Scale up process: Pilot-line Level

Once the cycling procedure had been optimized with the electrodes prepared at laboratory level, the focus was shifted to the pilot-line scale for electrode preparation. As previously discussed in ***Chapter 3***, the facilities involved are very different; hence, the same production conditions can lead to very different results. The different facilities employed for anode production are described in detail below (***Figure 5.15***):

- **Planetary Vacuum Mixer** (MTI Corp.): this planetary mixer differs from the laboratory-scale one primarily in its geometry, as it is equipped with two propellers that rotate on their own axes while simultaneously rotating around a central axis. Its maximum rotational speed is 600 rpm, and it allows vacuum control to ensure proper slurry degassing. The container has a maximum volume of 150 mL; however, the optimal working volume to achieve a better dispersion was one of the parameters investigated during slurry preparation.
- **Roll-to-Roll (R2R) Coating System** (MTI Corp.): this technology enables coating and drying to be performed simultaneously, significantly increasing the production rate. However, it is important to properly balance all the parameters involved in both of the processes. The deposition system is based on the reverse comma coating, which is substantially different from the tape-casting technique used at the laboratory scale.
- **Hot Rolling Press** (MTI Corp.): calendering represents the final step in electrode production. However, with this equipment, it was not possible to precisely control the applied pressure; therefore, this step was evaluated only qualitatively.

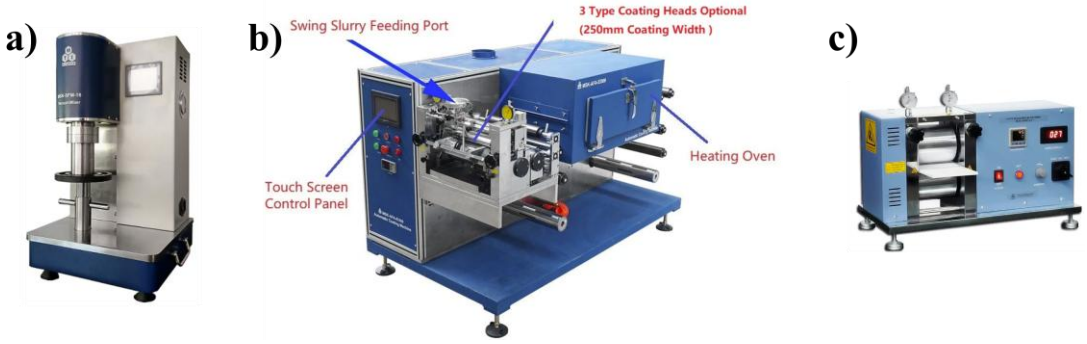

Figure 5.15 – Facilities provided by MTI Corp. and used at Pilot-line level: a) Planetary Mixer; b) Roll-to-roll coating machine and oven; c) Hot rolling press

The calendering step was challenging because the electrodes were calendered using a process composed of 10 forward passes and 10 backward passes at 80°C, with no particular changes observed in the final thickness of the dried electrodes.

Nevertheless, morphological characterization performed by Field Emission Scanning Electron Microscopy (FESEM) allowed the observation of a slight increase in the adhesion of the dried AM to the CC surface.

5.1.2.1. Slurry and Production Process Optimization

The change of facilities led to multiple issues/challenges during both the mixing and the coating; thus, great efforts were made to obtain homogeneous electrodes that could be electrochemically tested and compared with those produced at laboratory level. Multiple preparations were carried out on the pilot-line, based on the same composition as the laboratory level (95% AM: 2% CA; 1% CMC; 2% SBR), as widely discussed in ***Section 5.1.1.1***. However, the total amount of materials involved was dramatically increased, going from 1 g in the previous preparation up to tens of grams. The trials performed, together with the related issues, as well as the problems encountered and the solutions proposed and applied, are reported below.

During the scale-up to pilot-line production, scrap generation represents a key aspect to be considered. In the present work, relatively high scrap levels (around 30%) were observed, which can be considered acceptable during the optimization phase. However, these values remain significantly higher than those typically reported for stabilized industrial production (5-12%) [396]. For this reason, ongoing efforts are focused not only on optimizing the overall process, but also on specifically reducing scrap generation to approach industrially relevant values.

5.1.2.1.1. First trial

The first trial consisted of a scale-up in terms of material quantity, following the same procedure adopted at laboratory level. The main change was the increase in the total batch mass from 1 g to 10 g.

1) A total of 0.1 g of CMC was diluted in 14.8 mL of MilliQ water to obtain a SF of 40 wt.%. The mixture was stirred at the maximum speed of the mixer (600 rpm) for 1 hour.
2) Subsequently, 0.2 g of C45 was added, and the suspension was stirred for an additional 1 hour at the same speed.
3) Finally, 9.5 g of graphite was slowly added. Once all the powder was incorporated, the slurry was stirred again for 1 hour.
4) The final step consisted of adding 0.2 g of SBR. Since the SBR was supplied as a suspension with a solid content of 50 wt.%, a total of 0.4 g was added. The mixing speed was reduced to 100 rpm to avoid the degradation of the rubber and the solution was kept stirring for 30 minutes.

At the end of the mixing step, the slurry was visually inspected. The homogeneity was comparable to that obtained in the previous case; however, a lower apparent viscosity was qualitatively observed. This effect illustrates how different facilities impact the production process. Another aspect that should be considered is the total amount of slurry inside the vessel: the filling of the container can also have an impact on proper mixing. If the quantity is too low, the blades are not able to catch and mix all the powders, while an excessively high quantity could spill out of the tank due to centrifugal effects.

The slurry was then coated with the R2R system, where multiple parameters need to be tailored to obtain the desired electrodes: the two most important are the coating speed and the deposition thickness ***(Figure 5.16***). For all the preliminary trials presented in this section, the coating speed was 300 mm/min, while the wet thickness was varied depending on the application. One sensitive parameter is the Roll Gap (***Figure 5.16***): this gap is the distance between the roll used to transfer the slurry (left one) and the roll which collects the slurry on the CC (right one). This gap can be described as a space where the slurry accumulates before being coated, but if this region is too wide, the slurry simply drips down whereas if it is too narrow, the CC is damaged. During all the preparations performed with the R2R machine, this Roll Gap was maintained constant at 20 µm for all the trials.

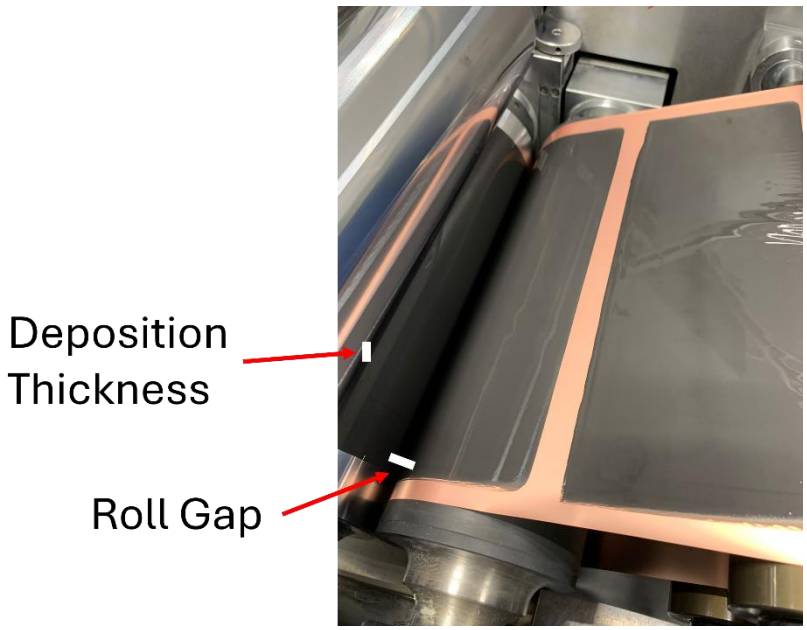

Figure 5.16 – Parameters that can be controlled by the reverse comma mechanism on the R2R machine provided by MTI: thickness deposition and roll gap, which was kept constant at 20 µm

When using this semi-automatic machine, it is important to consider that the oven is directly connected to the coater: this means that the deposition speed also affects the residence time of the slurry inside the oven. For all the trials, the temperature imposed was set to 80°C, and considering that the oven length is 70 cm, the drying step lasted approximately 2.30 minutes. For this study the

electrodes were coated with a width of 9 cm. This process is automated and the parameter can be set in advance prior to the coating step. This constraint was necessary because the calendering machine has a width of 10 cm.

Figure 5.17a shows the ongoing coating step: the wet slurry appeared homogeneous and the edges were well defined, however, after drying (***Figure 5.17b***) several inhomogeneities were observed. Inside a single sheet, slurry accumulation was observed on one side (which was not completely dried after passing through the oven), and the presence of "waves" along the entire sheet. The accumulation was caused by slight leaking occurring immediately after the coating step, as indicated by the white arrow in ***Figure 5.17a***. This further confirmed the excessively low viscosity of the slurry observed after the mixing step, indicating that additional optimization was required to address this issue.

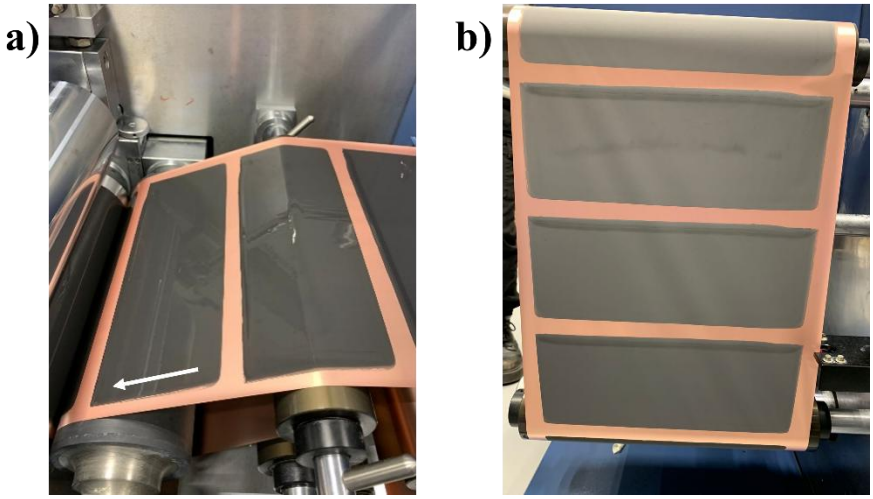

Figure 5.17 – Photos related to the first trial of pilot-line deposition: a) the coating was just performed and the white arrow highlights the flow of the slurry; b) dried electrodes after drying step, the inhomogeneity after the coating is very evident

Due to the high degree of inhomogeneity, these electrodes were not calendered. The significant inhomogeneity was confirmed by measuring the thickness and the ML of the electrodes: in ***Figure 5.18a***, one of the single sheets is shown with the corresponding measured values. The thickness was calculated as the average of multiple measurements, and the CC was not taken into account. The ML was calculated after cutting the electrodes into discs with a diameter of 15 mm, whose weight distribution is reported in ***Figure 5.18b***. The presence of three distinct distributions is clearly evident, and the corresponding data for dry thickness, weight and ML are presented in ***Figure 5.18c***. These data were collected along the long side of the sheet, and along this direction the distributions appear more acceptable.

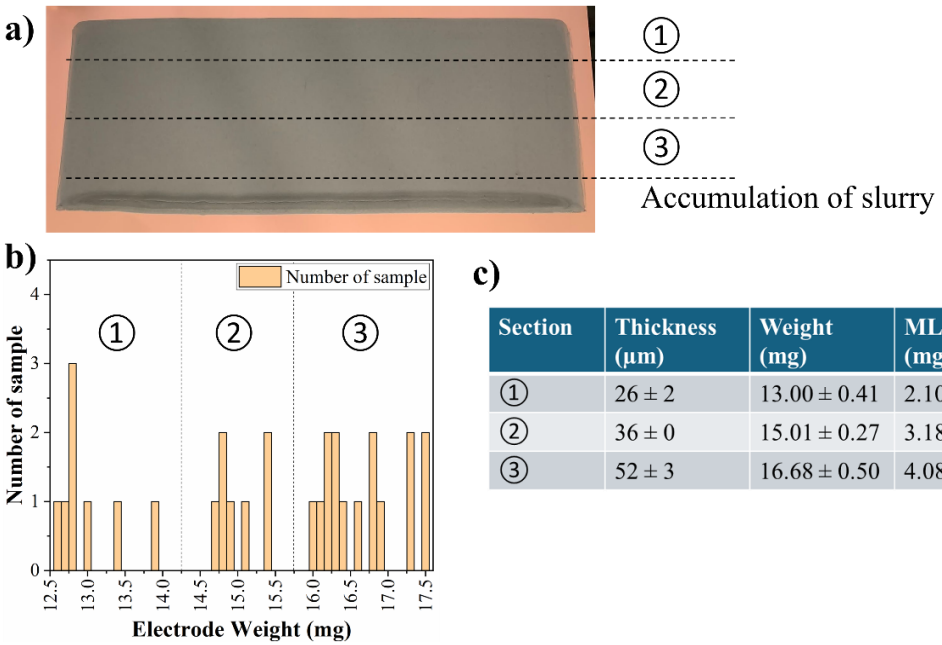

c)

Section	Thickness (µm)	Weight (mg)	ML (mg cm^{-2})
①	26 ± 2	13.00 ± 0.41	2.10 ± 0.22
②	36 ± 0	15.01 ± 0.27	3.18 ± 0.14
③	52 ± 3	16.68 ± 0.50	4.08 ± 0.27

Figure 5.18 – a) The picture highlights the lack of homogeneity of the electrodes: ideally, each sheet can be divided into four sections; b) Weight distribution of the electrodes cut from the three sections of the sheet; c) Electrode characteristics related to the three sections

One electrode from section ① was electrochemically tested to compare the performance with an electrode with similar ML but produced using a different process. The cell was assembled in the same way as the previous ones, and the results are reported in ***Figure 5.19***. These results confirmed that the inhomogeneities of the dry laminate led to poor electrochemical performance, with a lower ICE (below 90% instead of 93%, ***Table 5.9***) and strongly oscillating capacity values during the test (***Figure 5.19a***). Considering the charge/discharge profiles ***Figure 5.19d***, cycle 6 and cycle 10 already show lower performance compared to the profiles reported in ***Figure 5.13b***. In addition, the high polarization observed at cycles 50 and 100 confirms the instability previously observed in the capacity values.

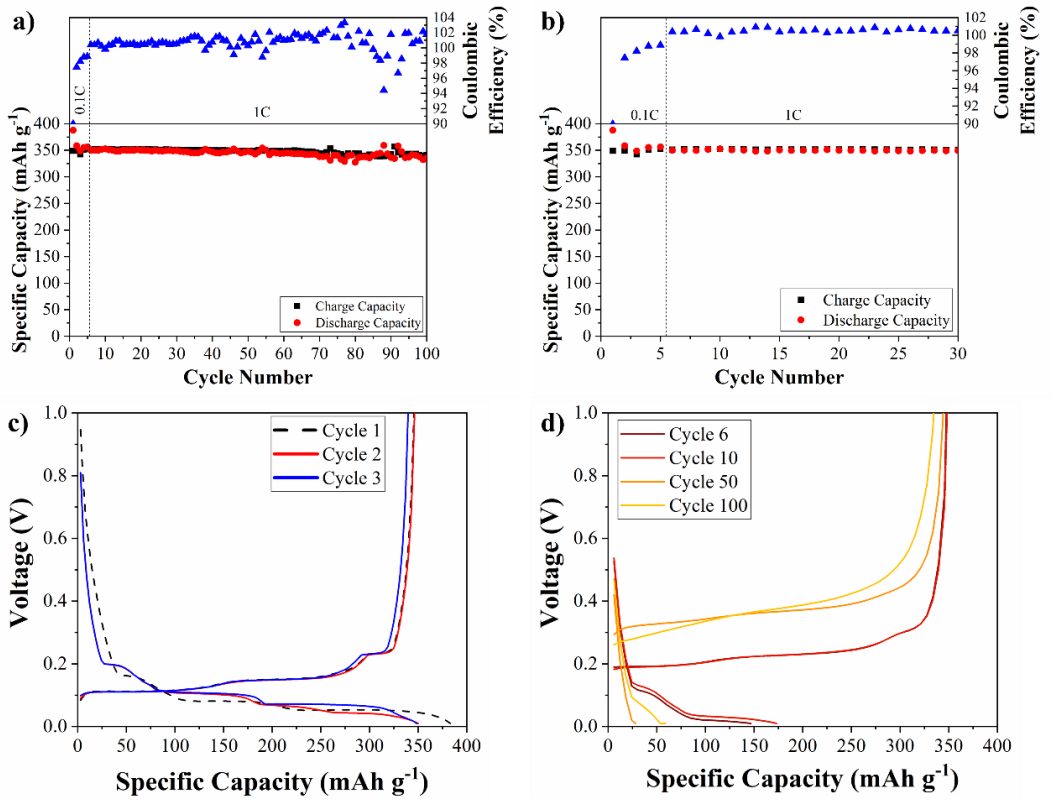

Figure 5.19 – Electrochemical results of the electrode produced at the pilot-line and tested with the CVS: a-b) Charge and Discharge Capacities and relative values of Coulombic Efficiency: a) whole test; b) zoom on the first 30 cycles; c-d) Charge/discharge curves for the CC-CV cycling protocol: a) Forming step; b) Representative cycles at 1C

Table 5.9 – Values of charge and discharge capacities and relative values of coulombic efficiency for some representative cycles for the electrode produced with the first trial at the pilot-line

Cycle	***C-rate***	***Charge Capacity (mAh g^{-1})***	***Discharge Capacity (mAh g^{-1})***	***Coulombic Efficiency (%)***
1	*0.1C*	*348.78*	*387.68*	*89.97*
2		*349.24*	*358.40*	*97.44*
3		*342.43*	*348.68*	*98.20*
6	*1C*	*351.24*	*349.82*	*100.41*
10		*352.09*	*352.66*	*99.84*
20		*351.54*	*349.91*	*100.47*
30		*351.10*	*349.30*	*100.52*
50		*348.78*	*347.83*	*100.27*
125		*323.82*	*327.92*	*98.75*

These results confirm that the observed limitations were mainly related to the production process, and that further process optimization was necessary to obtain electrochemically acceptable anodes.

5.1.2.1.2. Second trial

To overcome the issue of the first trial, it was chosen to double (from 10 g to 20 g) the total amount of material inside the vessel, and the production process is presented below:

1) A total of 0.2 g of CMC was diluted in 24.04 mL of MilliQ water; in this way, the SF was increased from 40% to 45%. The mixture was kept stirring at the highest speed (600 rpm) for 1 hour.
2) 0.4 g of C45 was added and the solution was kept stirring for 1 hour at the maximum speed.
3) 19 g of graphite was finally slowly added, and once all the powder was incorporated, the solution was once again kept stirring for 1 hour.
4) The final step was the addition of 0.4 g of SBR; however, in this case the material was already suspended in solvent with a solid content of 50 wt.%, thus 0.8 g was added. In this case, the mixing speed was reduced to 100 rpm to avoid degradation of the rubber, and the solution was kept stirring for 30 minutes.

All the coating parameters were maintained the same as in the previous trial.

In ***Figure 5.20*** it is possible to observe one of the dried electrode sheets produced in this second trial: the surface appears more homogeneous, without any "waves" caused by improper viscosity. However, on one side of the sheet, slurry accumulation was still observed, indicating that the viscosity was still too low. The calendering step was performed, as previously described, after the removal of the side affected by slurry accumulation.

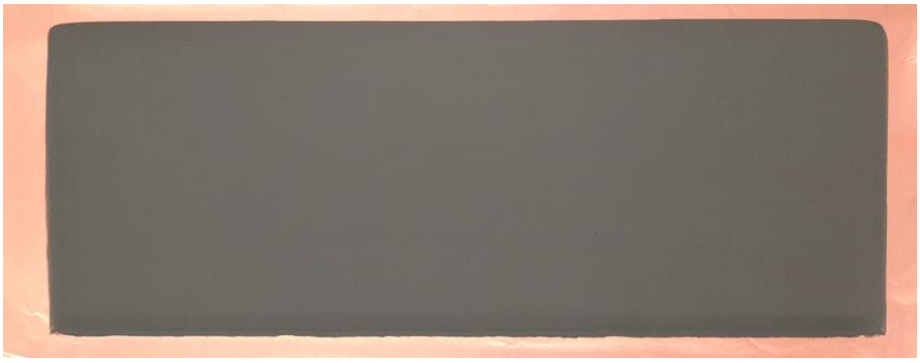

Figure 5.20 – Photo of one of the electrodes produced in the second trial, the accumulation is still visible on the bottom side

The dry thickness of these electrodes was more uniform than in the previous trial, with an average value of 54 ± 3 µm, calculated without considering the CC. This means that, in terms of dispersion on the surface of the CC, this process was significantly improved. Similarly, for the ML, the homogeneity was improved,

with an average value of 6.20 ± 0.66 mg cm^{-2}. The calculated AC was 2.26 ± 0.24 mAh cm^{-2}.

Even though the samples appear better compared to the first trial, the accumulation of slurry on one side cannot be considered acceptable, because approximately 1 cm of the sheet was not suitable for use.

5.1.2.1.3. Third trial

The third trial aimed to permanently remove the accumulation of the slurry. Thus, the focus was solely on the SF, which was increased to 50 wt.%: compared to the previous trial, the amount of water added was limited to 19.60 mL. All the other mixing and coating parameters were not changed.

As it is possible to observe in ***Figure 5.21***, the surface of the dried electrode was smooth and homogeneous, even though a small accumulation on one side was still present. As previously described, the calendering step was carried out after removing the portion of the electrode affected by slurry accumulation. The increase in the SF led to an increase in all the parameters checked:

- Dry Thickness: 77 ± 3 µm
- ML: 7.84 ± 0.92 mg cm^{-2}
- AC: 2.85 ± 0.33 mAh cm^{-2}

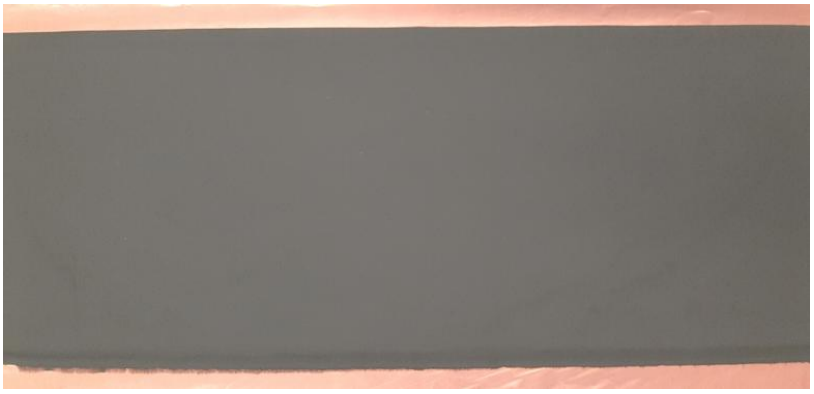

Figure 5.21 – Photo of one of the electrodes produced in the third trial, the accumulation is still visible on the bottom side

As expected, increasing the SF promoted a greater deposition of AM on the CC, leading to higher dry thickness and ML values. Overall, the electrodes show good quality; however, the small accumulation still remains an unacceptable characteristic of the production process. To reduce the amount of scrap, future electrodes will be produced as a single long sheet, without interruption of the coating process.

5.1.2.1.4. Fourth trial

For the fourth trial the composition, the SF and the mixing process were exactly the same as in the previous trial, but for the coating step, it was decided to interrupt the production of single sheets in favor of a single long deposition. All the other parameters (coating speed, wet thickness and oven temperature) were maintained the same.

This change led to the absence of slurry accumulation and hence to the production of very uniform electrodes (***Figure 5.22***). With the amount of materials mixed for this slurry, a length of around 2 m was coated. After cutting the electrode into sheets with a width of approximately 9 cm, the calendering step was performed as previously described. The average thickness and ML were measured from samples collected along the entire length:

- Dry Thickness: 60 ± 4 µm
- ML: 5.22 ± 0.21 mg cm^{-2}
- AC: 1.90 ± 0.08 mAh cm^{-2}

Figure 5.22 – Photo of one part of the long electrode produced in the fourth trial

Considering the electrodes' length and comparing these results with those obtained in the previous trial using a different deposition geometry, the values are improved in terms of dispersion. Regarding thickness, the difference was not particularly evident, whereas for ML, the improvement was significant, with a strong reduction in the standard deviation. These results indicate that along the entire deposition length, the distribution was highly homogeneous, confirming that an SF of 50 wt.% was the most suitable option.

5.1.2.1.5. Fifth trial

In this trial, the focus was on obtaining electrodes with the same ML as at laboratory level; thus, the deposited wet thickness was decreased from 100 µm to 80 µm. In addition, the total amount of material was doubled to obtain longer electrode sheet:

- 38 g of Graphite
- 0.8 g of C45
- 0.4 g of CMC
- 0.8 g of SBR, corresponding to 1.6 g of SBR suspension
- 39.20 mL of MilliQ water

All the other parameters, both for mixing and coating, were kept unchanged.

The electrodes thus obtained were as uniform as in the previous trial, with slight differences in terms of thickness and ML; however, these values were consistent with the decrease in deposited thickness:

- Dry Thickness: 46 ± 2 µm
- ML: 4.10 ± 0.28 mg cm^{-2}
- Areal Capacity: 1.49 ± 0.10 mAh cm^{-2}

These values are significantly higher than those obtained at laboratory level, where the ML was around 2.70 mg cm^{-2}. Therefore, subsequent trials were mainly aimed at investigating the optimal deposition thickness required to achieve the desired ML.

5.1.2.1.6. Sixth trial

The last attempt was carried out to better understand the impact of deposition thickness on the resulting ML. For this purpose, a single batch of slurry was prepared, increasing the total amount of material to 50 g in order to ensure sufficient slurry for all the wet thickness investigated:

- 47.5 g of Graphite
- 1 g of C45
- 0.5 g of CMC
- 1 g of SBR, corresponding to 2 g of SBR suspension

For the coating step, the deposition speed was kept unchanged, but different wet thicknesses were imposed. After drying, the electrode was cut into sheets approximately 9 cm wide and subsequently calendered as previously described. The electrodes were then punched into discs with a diameter of 15 mm and characterized. The corresponding dry thickness and ML values were measured

and reported in ***Table 5.10***, while a graphical representation of these results is shown in ***Figure 5.23***.

Table 5.10 – Summary of the characteristics (dry thickness and ML) measured depending on the roll gap imposed for the coating.

Roll Gap (µm)	***Dry Thickness (µm)***	***Mass Loading (mg cm^{-2})***	***Areal Capacity (mAh cm^{-2})***
120	*72 ± 1*	*6.58 ± 0.00*	*2.45 ± 0.00*
110	*66 ± 1*	*6.02 ± 0.03*	*2.19 ± 0.01*
100	*60 ± 1*	*5.29 ± 0.14*	*1.92 ± 0.05*
90	*57 ± 2*	*5.03 ± 0.06*	*1.83 ± 0.02*
80	*50 ± 1*	*4.51 ± 0.08*	*1.64 ± 0.03*
70	*44 ± 1*	*3.89 ± 0.11*	*1.42 ± 0.04*
55	*41 ± 1*	*3.73 ± 0.09*	*1.36 ± 0.03*

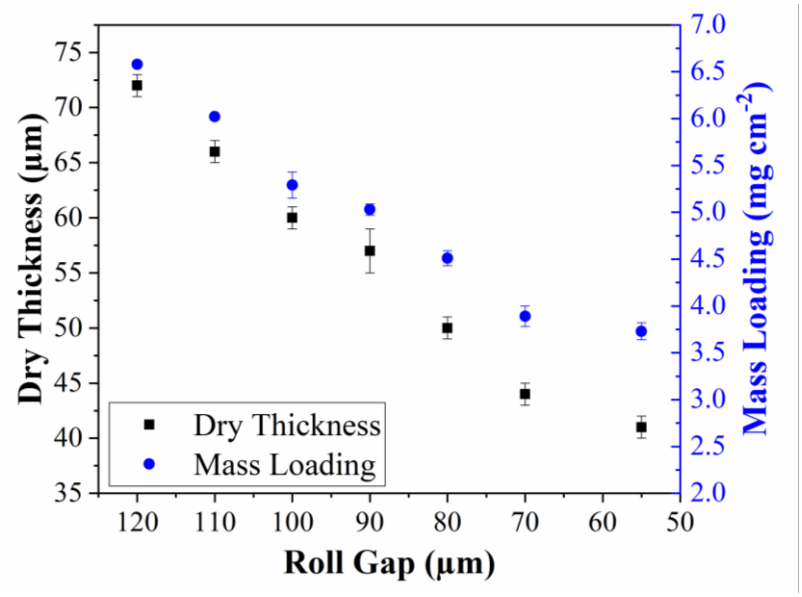

Figure 5.23 – Visual representation on the trend of dry thickness and mass loading reducing the roll gap during the production of graphite anodes

The trend was evident with a reduction of around 6 µm in terms of dry thickness every 10 µm decrease in the roll gap. The last point at a roll gap of 55 µm interrupted this reduction trend, marking the onset of a plateau. The same trend was also observed for the ML, with a reduction of around 0.5 mg cm^{-2} every 10 µm reduction of the roll gap. As for the thickness, a plateau appeared to start at 55 µm; hence, this value was considered the lower limit of roll gap for this production process. However, the ML value obtained with the thinnest deposition was not low enough for direct comparison with the electrodes produced using the doctor blade technique.

Therefore, in this case, the electrodes with an areal capacity of around 2.00 mAh cm^{-2} were selected for the electrochemical characterization, in line with commercial values [397]. The electrodes produced on the pilot-line were

assembled under exactly the same conditions as those produced at the laboratory level: the same coin-cell configuration, the same amount of electrolyte and the same testing conditions. This working procedure allowed a consistent comparison between the two production levels, even when the ML differed.

The electrochemical results are collected in ***Table 5.11*** and ***Figure 5.24***. These results are characterized by higher capacity throughout the test, with a discharge capacity that remained constant at around 350 mAh g^{-1} for all cycles. This value is around 15 mAh g^{-1} higher than that obtained for the doctor blade electrode (***Figure 5.12***). This improvement may be attributed to the enhanced homogeneity achieved through the pilot-line process, even though the ML is higher, with a value of 4.10 mg cm^{-2}.

Table 5.11 – Data for the electrode produce with the pilot-line

Cycle	***C-rate***	***Charge Capacity (mAh g^{-1})***	***Discharge Capacity (mAh g^{-1})***	***Coulombic Efficiency (%)***
1	*0.1C*	*351.43*	*373.14*	*94.18*
2		*352.21*	*354.67*	*99.31*
3		*352.31*	*353.98*	*99.53*
6	*1C*	*351.67*	*353.28*	*99.54*
10		*351.96*	*352.20*	*99.93*
20		*351.53*	*351.65*	*99.97*
30		*351.70*	*351.77*	*99.98*
50		*351.34*	*351.33*	*100.00*
100		*349.56*	*349.36*	*100.06*

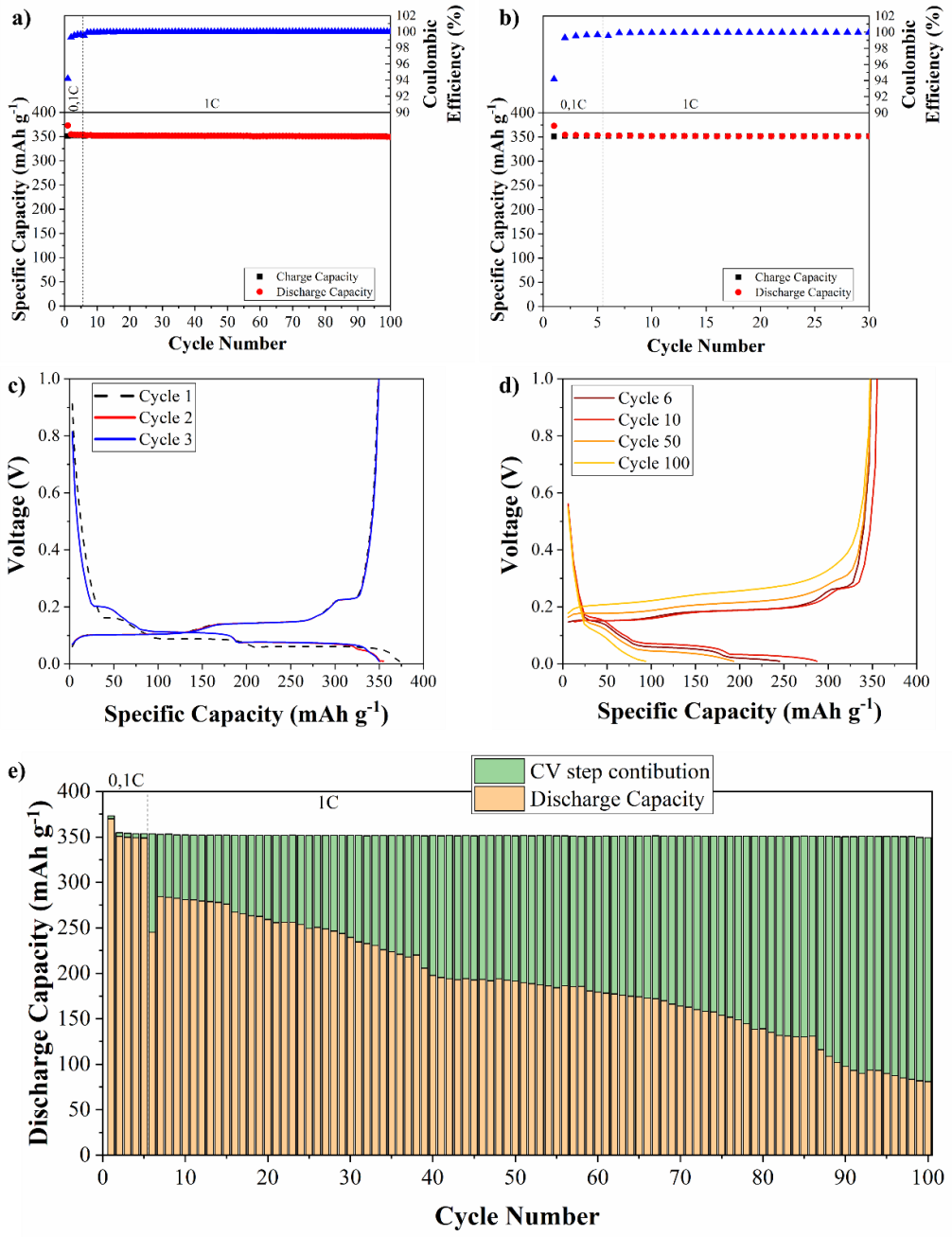

Figure 5.24 – Electrochemical results of the electrode produced with the optimized process (thickness: 100 µm) at the pilot-line and tested with the CVS: a-b) Charge and Discharge Capacities and relative values of Coulombic Efficiency: a) whole test; b) zoom on the first 30 cycles; c-d) Charge/discharge curves for the CC-CV cycling protocol: a) Forming step; b) Representative cycles at 1C; e) CVS capacity contributions distinguished between the discharge and the CVS

However, some differences have been observed at higher cycle numbers, with higher polarization between the curves when cycle 50 was reached (***Figure 5.24d***). This effect is reflected in ***Figure 5.24e***, where the contribution of the CVS is compared with the contribution of the discharge step. Regarding the formation cycles, the contribution of the CVS was comparable to that of the doctor blade electrode (***Figure 5.14***), with almost negligible values. Nevertheless, when long-

term cycling at 1C was performed, the CVS contribution became more significant than in the other case, confirming that cell polarization affected the electrochemical performance.

5.1.3. Comparison between the two production processes: morphological characterization

In ***Table 5.12*** a comprehensive summary of all the electrodes prepared at both laboratory level and pilot-line level is reported, with the parameters evaluated to enable a comparison between them. As it is possible to observe, at laboratory level it was possible to produce electrodes with the lower values of dry thickness and ML, and it was not possible to reproduce these values using the pilot-line facilities. The optimization required to obtain an acceptable coating significantly affected these parameters. However, it is important to highlight that all the graphite anodes produced on the pilot-line can be considered acceptable for application in a full cell, after proper N/P balancing.

Table 5.12 – Summary of the electrodes prepared at the two different levels, with the imposed parameters (Solid Fraction and Wet Thickness) and relative parameters studied (Dry Thickness, ML and Areal Capacity)

N° of Trial	***Solid Fraction (%)***	***Wet Thickness (µm)***	***Dry Thickness (µm)***	***Mass Loading (mg cm^{-2})***	***Areal Capacity (mAh cm^{-2})***
			Laboratory Level		
1	*40*	*100*	*34 ± 3*	*2.73 ± 0.24*	*0.99 ± 0.09*
			Pilot-line Level		
1	*40*	*100*	*--*	*--*	*--*
2	*45*	*100*	*54 ± 3*	*6.20 ± 0.66*	*2.26 ± 0.24*
3	*50*	*100*	*77 ± 3*	*7.84 ± 0.92*	*2.85 ± 0.33*
4	*50*	*100*	*60 ± 4*	*5.22 ± 0.21*	*1.90 ± 0.08*
5	*50*	*80*	*46 ± 2*	*4.10 ± 0.28*	*1.49 ± 0.10*
6	*50*	*120*	*72 ± 1*	*6.58 ± 0.00*	*2.45 ± 0.00*
		110	*66 ± 1*	*6.02 ± 0.03*	*2.19 ± 0.01*
		100	*60 ± 1*	*5.29 ± 0.14*	*1.92 ± 0.05*
		90	*57 ± 2*	*5.03 ± 0.06*	*1.83 ± 0.02*
		80	*50 ± 1*	*4.51 ± 0.08*	*1.64 ± 0.03*
		70	*44 ± 1*	*3.89 ± 0.11*	*1.42 ± 0.04*
		55	*41 ± 1*	*3.73 ± 0.09*	*1.36 ± 0.03*

One of the advantages of the use of the pilot-line is related to the higher production rate, with only one trial that permits the production of multiple meters of dry electrodes and allows the thickness to be varied directly during coating, as was done in the last trial. This approach increases the investigation potential by allowing multiple thicknesses to be evaluated from a single mixing procedure, thereby reducing variability associated with different production days [398].

Secondly, the R2R facility increases the reproducibility of the process thanks to the higher degree of automation; however, the instrument calibration was

performed manually, and therefore, some differences can be observed depending on the operator. Nevertheless, the high reproducibility was confirmed by the comparison between pilot-line trial no. 4 and no. 6: both were produced with a wet thickness of 100 µm and the difference between the electrodes was negligible. The comparison between trial no. 5 and no. 6, with an 80 µm wet thickness deposition, led to slightly different values, likely related to the manual adjustment of the gap between the rolls of the facility.

Lab-scale electrode surfaces were further characterized by FESEM to compare electrodes produced using different facilities through morphological analysis and to identify inhomogeneities, clumps, or agglomerates that may affect electrochemical performance. For a proper comparison of the samples, the analysis conditions were kept as constant as possible, especially with respect to magnification. In the case of complex samples, the working distance (WD) and the electron high tension (EHT) were slightly adjusted to obtain optimal focus.

The first images acquired (***Figure 5.25***) correspond to the electrode surfaces, with the aim of identifying differences related to the production process and to the effect of pressing or calendering. ***Figure 5.25a*** shows the surface of the electrodes produced at laboratory level with the doctor blade technique, while ***Figure 5.25c*** shows the surface of the electrodes produced at pilot-line level with the R2R technology. By comparing the two images, no evident differences related to the production process were observed. ***Figure 5.25b*** shows the surface of the electrode produced at lab-scale level after the pressing with a hydrostatic press, while ***Figure 5.25d*** shows the surface of the electrode produced with the R2R and pressed using the calendering machine. For both samples, the expectation was to observe reduced porosity and a decrease in the empty spaces between particles. However, this effect was not observed in either case, confirming the absence of significant variations in the dry thickness as previously discussed.

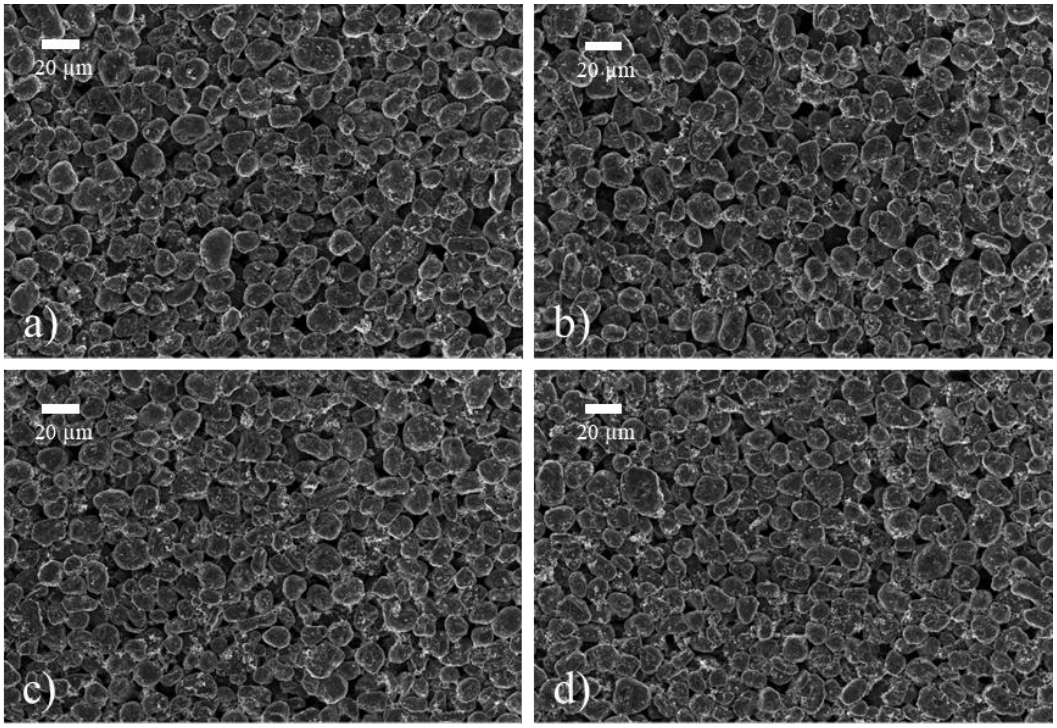

Figure 5.25 – SEM images of the surface of the electrodes produced as previously described, focusing on highlighting the differences between the two production processes. Laboratory level: a) Doctor Blade; b) Doctor Blade and Hydraulic Press; Small Pilot-line level: c) Pilot-line; d) Pilot-line and Calender. For all the images the acquisition parameters were the same to have a proper comparison: Magnification 1,00 KX; WD 3,0 mm; EHT 5,00 kV

A further characterization was performed to compare the effect of the calendering press on the adhesion of the dry layer to the CC. To this end, the electrodes were folded, and this stress point was observed with the microscope, looking for the presence of cracks or detachment (***Figure 5.26***). The uncalendered electrode (***Figure 5.26a***) was characterized by a partial removal of the dry layer in the upper right corner of the image and a slight detachment in the lower left corner. In the case of the calendered electrode (***Figure 5.26b***), no equally evident effects were observed; however, some large cracks formed after the application of the folding stress. By focusing on the edges of these electrodes (***Figure 5.26c,d***) at higher magnifications, the higher adhesion after the calendering step was more evident. However, this analysis confirmed what was previously observed, namely that the calendering step did not affect the dry thickness of the electrode because, when comparing the thickness values, a negligible difference of 1-2 µm was observe.

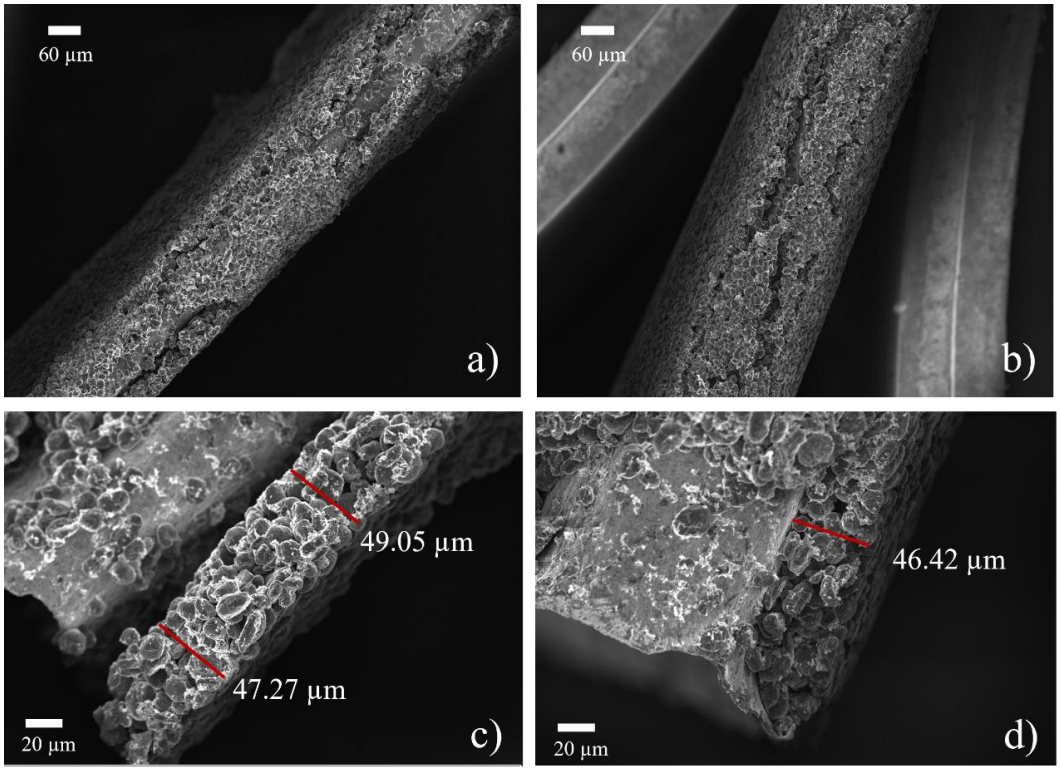

Figure 5.26 – SEM images of the folded anodes produced with the pilot-line: a-c) without calendering; b-d) calendering. a-b) Magnification: 300X; WD: a) 3,1 mm, b) 3,6 mm; EHT 5,00 kV. c-d) Magnification: 1KX; WD: a) 2,9 mm, b) 3,7 mm; EHT 5,00 kV

5.1.4. Conclusion and final remarks

This chapter examined the production and electrochemical behaviour of graphite anodes across different TRLs with the objective of identifying a scalable manufacturing approach without compromising performance. A systematic comparison between laboratory-scale and pilot-line processes was conducted through slurry optimization, coating control, morphological characterization and electrochemical testing.

At laboratory scale, aqueous processing combined with doctor blade coating enabled the fabrication of well-controlled graphite electrodes. However, electrochemical testing revealed that conventional CCS protocols can lead to a significant underestimation of reversible capacity in half-cell configuration, particularly at high C-rates. The adoption of a CVS proved necessary to ensure complete lithiation and to obtain electrochemical responses representative of commercial graphite behaviour. Scaling up to pilot-line facilities introduced substantial process constraints, demonstrating the critical role of equipment design and operating parameters in determining electrode quality. Initial trials were strongly affected by poor slurry rheology control and discontinuous deposition, resulting in severe inhomogeneities and unstable electrochemical performance. Progressive optimization of SF, batch volume and coating strategy enabled

continuous R2R processing and the production of long, uniform electrodes with improved thickness and ML distributions. Although the lowest ML achieved at laboratory scale could not be directly replicated, the optimized pilot-line electrodes delivered comparable or superior electrochemical performance under identical testing conditions, confirming their technological relevance and suitability for subsequent full-cell implementation.

Overall, this work demonstrates that graphite remains a highly processable and robust benchmark material for studying scale-up effects in LIB manufacturing. More importantly, it highlights that both production processes and electrochemical testing protocols must be carefully adapted when moving across TRLs. The insights gained in this chapter provide a solid methodological framework for the subsequent investigation of more complex anode chemistries, such as those involving silicon at different contents, where processability limitations and electrochemical sensitivity are expected to be even more pronounced.

5.2. Manufacturing optimization of SC anodes from laboratory to pilot-line scale

This chapter focuses on the laboratory-scale optimization of SC electrodes, with particular attention to the processing parameters that govern their manufacturability, electrochemical performance and scalability. Unlike conventional graphite anodes, the introduction of silicon leads to significantly higher sensitivity to manufacturing conditions, making process optimization a critical step toward industrial implementation. Following the in-depth investigation of graphite as an anode material, the research focus was extended to SC anodes, which offer the potential to increase electrode capacity and, consequently, the energy density of the final battery. However, as widely described in ***Chapter 2***, silicon-based materials suffer from major drawbacks, the most critical of which is the large volume changes occurring within the electrode during cycling. To mitigate this issue, several strategies can be adopted, ranging from the synthesis of silicon with tailored shapes or dimensions to the use of elastic binders capable of limiting volume variation. For this reason, a systematic experimental campaign was carried out to identify the formulation and processing conditions required to achieve homogeneous, mechanically stable and electrochemically reliable SC anodes.

In this section, the production process of SC electrodes is described and optimized at both laboratory and pilot-line levels, following the same approach adopted for graphite anodes. The SC used in this work was supplied by MTI [399] and is characterized by a nominal silicon content of approximately 10 wt.%, consistent with current commercial formulations [400]. The first part of the chapter addresses the optimization of electrode manufacturing at laboratory scale,

including the evaluation of alternative binder systems and the analysis of the resulting electrode characteristics. Subsequently, the electrodes were electrochemically tested in order to assess the impact of formulation parameters on cycling performance.

The second part of the chapter focuses on the scale-up of the most promising formulations identified at laboratory level, to evaluate their suitability for industrial implementation. The corresponding electrochemical results are then presented and discussed. Finally, a comparison between laboratory- and pilot-line production is provided in order to highlight the main processing challenges and to identify the key conclusions derived from this work.

5.2.1. Laboratory-scale investigation

As previously done for graphite, the laboratory-scale optimization represented the basis for the subsequent scale-up at the pilot-line level. To systematically investigate the processability of SC electrodes and identify suitable conditions for scalable manufacturing, a series of experimental trials was therefore carried out by progressively modifying the slurry formulation. Compared to graphite, in the initial phase the amount of AM was slightly reduced (92 wt.%) in favor of a higher amount of binder, in order to promote the dispersion of the SC in water-based systems and to accommodate/mitigate the expansion and contraction occurring during the lithiation and delithiation. After confirming successful processing, the AM content was increased to 95% to achieve values comparable to those adopted for graphite anodes.

Initially, the same binder system used for graphite anodes, composed of CMC and SBR, was employed. However, based on the experimental results obtained and in agreement with the literature, this binder system does not represent the optimal choice for silicon-based anodes [401]. Consequently, the investigation was extended to PAA and its lithiated form LiPAA [402], considering two different MWs (250.000 and 450.000 g mol^{-1}). In addition, two natural polysaccharides, TG and CGN, were evaluated to assess their influence on slurry processability and to promote a more sustainable electrode fabrication route. For clarity, the different electrode formulations investigated in this work and the corresponding sample codes adopted throughout the discussion are summarized in ***Table 5.13***.

Table 5.13 – Overview of the different laboratory trials performed on MTI SC anodes, reporting electrode composition and the corresponding sample code adopted throughout the manuscript.

Trial Number	***Composition***	***Trial ID***
1	92:2:2:4 (SC:C45:CMC:SBR)	92%, CMC
2	92:2:2:4 (SC:C45:CMC:SBR)	92%, CMC_2

3	95:2:1:2 (SC:C45:CMC:SBR)	95%, CMC
4	95:2:3 (SC:C45:PAA250)	95%, PAA250
5	95:2:3 (SC:C45:PAA450)	95%, PAA450
6	92:2:6 (SC:C45:LiPAA250)	92%, LiPAA250
7	95:2:3 (SC:C45:LiPAA250)	95%, LiPAA250
8	95:2:3 (SC:C45:LiPAA450)	95%, LiPAA450
9	92:2:5:1 (SC:C45:LiPAA250:TG)	92%, LiPAA250_TG
10	92:2:5:1 (SC:C45:LiPAA250:CGN)	92%, LiPAA250_CGN

A concise overview of the iterative optimization strategy, including the main formulation changes and the qualitative outcomes in terms of coating homogeneity and manufacturability, is reported in ***Table 5.14***. Further details on the motivation behind each trial, related processing and electrochemical implications are provided in the following sections.

Table 5.14 – Summary of the experimental trials carried out to optimize the slurry formulation and coating parameters of MTI SC anodes at laboratory scale. The table highlights the evolution of binder composition, SF and processing conditions, together with the main qualitative outcomes observed in terms of coating homogeneity and electrode manufacturability.

Trial Number	***Trial ID***	***Solid Fraction***	***Changes adopted***	***Main conclusions***
1	92%, CMC	47%	First CMC/SBR trial at 92 wt.% AM; extra water added during mixing because the viscosity blocked the stirrer.	Poor slurry processability, edge recession, bad powder dispersion, highly inhomogeneous laminate.
2	92%, CMC_2	50%	Same CMC/SBR system, SF increased from 47 to 50% and second water addition avoided.	Coating quality still poor and no further characterization performed.
3	95%, CMC	50%	AM increased from 92 to 95 wt.%; binder reduced; new SBR batch with 50 wt.% solids used.	Better surface homogeneity than previous CMC trials, but some edge defects remained; ML unexpectedly decreased, likely due to improved coating homogeneity.
4	95%, PAA250	50%	Shift from CMC/SBR to PAA250 as single binder.	Severe inhomogeneities and solvent/powder segregation across the laminate; no further characterization.
5	95%, PAA450	50%	Same PAA approach but MW increased from 250.000 to 450.000 g mol^{-1}.	Viscosity increase still insufficient; slurry accumulated on one side and laminate remained inhomogeneous; no further characterization.

6	92%, LiPAA250	50%	Pre-lithiated PAA introduced; AM reduced to 92 wt.% to favor coating and binder support.	Clear improvement vs CMC/SBR at same AM; more homogeneous laminate, though central defects and edge tensions were present.
7	95%, LiPAA250	50%	Same LiPAA250 binder, but AM increased from 92 to 95 wt.% and binder reduced to 3 wt.%.	Very good surface homogeneity and no visible surface defects; only edge tensions remained. Better than CMC/SBR analogue.
8	95%, LiPAA450	50%	LiPAA MW increased from 250.000 to 450.000 g mol^{-1}.	Best laminate quality among lab trials: highly homogeneous, no central or edge defects.
9	92%, LiPAA250_TG	50%	1 wt.% TG added, reducing LiPAA by 1%; overnight solubilization step introduced.	Surface highly homogeneous and edge tensions disappeared, but dry thickness and ML decreased, suggesting reduced slurry viscosity and later worse electrochemical behavior.
10	92%, LiPAA250_CGN	50%	1 wt.% CGN added instead of TG, again reducing LiPAA by 1%.	Smooth and homogeneous laminate with fewer tensions, but small detachments from the CC after punching indicated weaker adhesion; dry thickness and ML lower than LiPAA case.

5.2.1.1. Influence of binder chemistry on slurry processability

Four different binder-based slurry groups were prepared at laboratory scale using different binder systems in order to assess their influence on the cycling performance of SC anodes. The first group employed CMC and SBR binders, providing a reference for comparison with graphite electrodes. The second group was formulated with as-received PAA, with two different MWs (250.000 and 450.000 g mol^{-1}). The third group involved the pre-lithiation of PAA, again evaluating both MWs. Finally, the fourth group included natural polysaccharides, introduced alongside the lower MW PAA to enhance slurry processability and electrode performance.

Some discrepancies in the electrode characteristics (dry thickness and ML) and electrochemical performance were related to the influence that binder chemistry can have on the microstructure of the electrode [401] and to the manual adjustment of the doctor blade during the coating step. The results reported in ***Table 5.15*** highlight the strong sensitivity of SC electrodes to formulation changes. In particular, variations in binder chemistry significantly affected slurry behaviour during coating, leading to measurable differences in dry thickness and ML even when the same wet thickness of 100 µm was applied. Electrodes prepared with LiPAA binders generally exhibited higher dry thickness and ML compared to CMC/SBR-based systems, suggesting improved structural stability during drying. Conversely, the introduction of natural polysaccharides resulted in a reduction of both parameters, indicating a possible decrease in slurry viscosity

and packing density of the AM. These observations confirm that binder selection plays a crucial role not only in electrochemical stability but also in determining the final electrode microstructure and manufacturability. A detailed discussion of the individual trials is provided in the following sections.

*Table 5.15 – Summary of the laboratory-scale trials for MTI SC anodes, reporting binder composition, coating thickness and the resulting electrode properties. The areal capacity was calculated based on the material theoretical capacity *This one is the only sample produced with a SF of 47%.*

Trial Number	***Trial ID***	***Wet Thickness (µm)***	***Dry Thickness (µm)***	***Mass Loading (mg cm^{-2})***	***Areal Capacity (mAh cm^{-2})***
1	92%, CMC*	100	*46 ± 1*	*4.12 ± 0.08*	*1.85 ± 0.03*
2	92%, CMC_2	100	--	--	--
3	95%, CMC	100	--	*3.76 ± 0.20*	*1.69 ± 0.09*
4	95%, PAA250	100	--	--	--
5	95%, PAA450	100	--	--	--
6	92%, LiPAA250	100	*53 ± 3*	*4.26 ± 0.14*	*1.92 ± 0.06*
7	95%, LiPAA250	100	*49 ± 2*	*4.24 ± 0.18*	*1.91 ± 0.08*
8	95%, LiPAA450	100	*57 ± 2*	*4.41 ± 0.30*	*1.98 ± 0.13*
9	92%, LiPAA250_TG	100	*42 ± 2*	*3.24 ± 0.28*	*1.46 ± 0.13*
10	92%, LiPAA250_CGN	100	*40 ± 1*	*3.40 ± 0.18*	*1.53 ± 0.08*

5.2.1.2. Electrochemical characterization of laboratory-processed electrodes

After the punching process, the electrodes underwent a second drying step under vacuum at 120 °C for 4 h. Coin cells were assembled in CR2032 geometry inside an argon-filled glovebox (O_2 < 1ppm, H_2O < 1ppm), using lithium metal as counter electrode. A glass-fiber separator (GF/A, Whatman) soaked with 150 µL of electrolyte consisting of 1 M $LiPF_6$ in EC:DEC (1:1 v/v) with 10 wt.% FEC and 2 wt.% VC was employed to enhance the interfacial stability of silicon-based electrodes [403]. The electrolyte was added in excess to ensure that it did not act as a limiting component of the system.

The coin cells were tested according to a protocol (***Table 5.16***) including five formation cycles, a rate capability test, and long-term cycling at a fixed C-rate, identical for all experiments. For each type of laminate, at least three cells were tested to evaluate the reproducibility of the prepared electrodes and to enable a

proper statistical evaluation. Cells were tested in the voltage window of 0.01-1.5 V. As for the graphite anodes and according to the literature [400], a CVS was also applied, with the potential set at 10 mV for all the cycles and the current limitation tailored to the applied current density. It is worth noting that the application of a CVS at 0.01 V until the current decays to a defined cut-off value (0.01C), as adopted here, is a common practice for the electrochemical testing of silicon-based anodes in half-cell configuration [404,405]. The duration of this step can vary among cycles and electrodes, since the current decay at low potentials is controlled by time-dependent interfacial and transport phenomena; consequently, reaching a fixed current limit does not necessarily occur within a constant time [406]. As already widely discussed for the graphite anodes, operating in half-cell configuration using lithium as the counter electrode represents a limitation for the proper evaluation of the CE, as its almost limitless availability prevents an accurate evaluation. Nevertheless, the values are reported for completeness and specific comments are provided when considered useful for the overall discussion.

Table 5.16 – Cycling protocol applied along all the rate capability tests performed with silicon composite electrodes

Cycle	***Mode***	***Discharge***	***Charge***
1-5	*Formation*	*CCS: 0.1C* *CVS: 0.01V, 0.01C*	*CCS: 0.1C*
6-10	*Rate Capability*	*CCS: 0.2C* *CVS: 0.01V, 0.02C*	*CCS: 0.2C*
11-15	*Rate Capability*	*CCS: 0.5C* *CVS: 0.01V, 0.05C*	*CCS: 0.5C*
16-20	*Rate Capability*	*CCS: 1C* *CVS: 0.01V, 0.1C*	*CCS: 1C*
21-25	*Rate Capability*	*CCS: 2C* *CVS: 0.01V, 0.2C*	*CCS: 2C*
26-125	*Long Cycling*	*CCS: 1C* *CVS: 0.01V, 0.1C*	*CCS: 1C*

An initial overview of the electrochemical performance obtained for selected SC electrodes with different binder systems is reported in ***Figure 5.27***, where the discharge capacities at cycle 1 and cycle 20 differ significantly between the binder systems adopted, as well as the ICE and the capacity retention. This value was calculated as the ratio of the discharge capacity at cycle 125 to that at cycle 30, further confirming the strong influence of binder chemistry on the performance of SC anodes. While comparable first-cycle capacities were obtained for several formulations, significant differences emerged in terms of CE and capacity retention. LiPAA-based electrodes showed the most balanced behaviour, combining relatively high initial efficiency with improved capacity retention during cycling. In contrast, electrodes containing natural polysaccharides exhibited a marked deterioration in long-term performance, despite showing

acceptable initial capacities. This behaviour suggests that the mechanical stability and interfacial properties provided by these additives were not sufficient to accommodate the volume changes of silicon during cycling. Overall, these trends indicate that the optimization of binder chemistry is a key parameter for achieving both stable electrochemical performance and scalable electrode manufacturing.

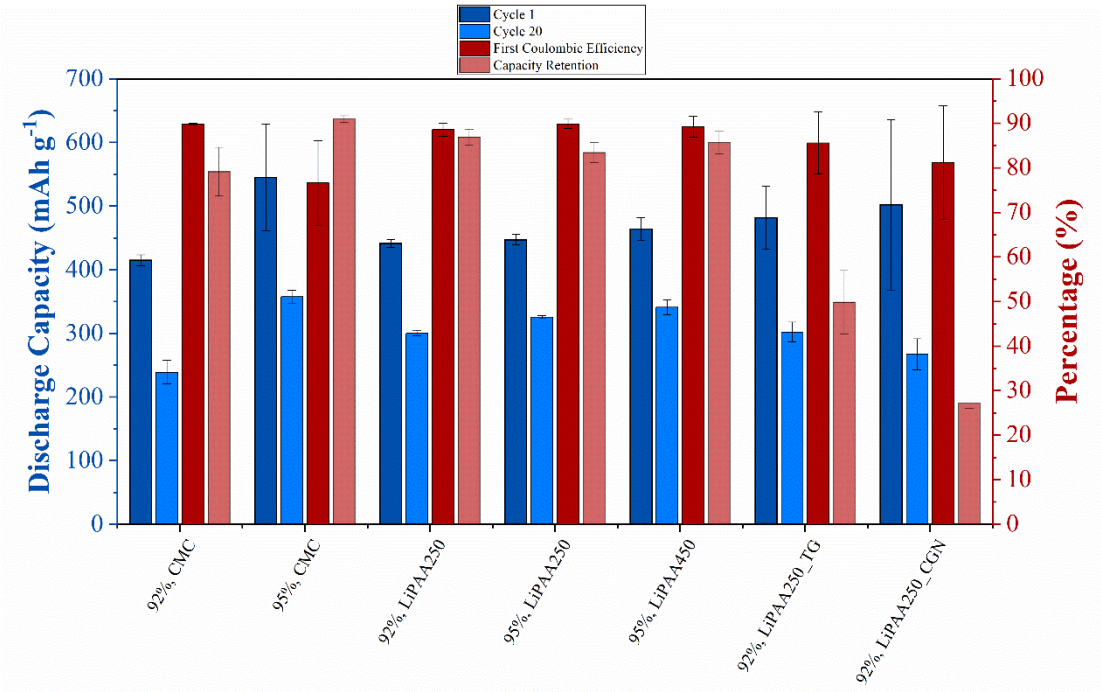

Figure 5.27 – Summary of the electrochemical behaviour of MTI SC electrodes prepared with different binders, including specific discharge capacity, coulombic efficiency of the first cycle and capacity retention during cycling.

Additional electrochemical investigations were performed by CV using a three-electrode configuration. In this case, both the working electrode and lithium metal were punched into 10 mm discs, and the electrolyte volume was reduced to 120 µL. Measurements were conducted for five cycles in the voltage window between 10 mV and 1.5 V at a scan rate of 0.1 mV s^{-1}.

5.2.1.2.1. Reference CMC-based binders

The first formulations employed CMC and SBR, consistent with graphite anodes. Although the combination of CMC and SBR is widely used in graphite production, researchers continue to debate the relative advantages and limitations of silicon-based electrodes. CMC-SBR systems can provide acceptable short-term performance, but studies have shown that conventional binders struggle to accommodate silicon's large volume expansion during prolonged cycling [150,407]. As a result, the stress generated during repeated volume changes is not effectively dissipated within the binder network, but instead accumulates locally, leading to polymer chain rearrangement and eventual electrode degradation [408]. Reviews of silicon anode binders highlight that linear polymer binders such as

CMC/SBR often fail to maintain electrode integrity over extended cycling, leading to rapid capacity decay [407]. Binders with a higher density of hydroxyl and carboxyl groups, such as PAA or Alg, generally ensure improved mechanical properties and long-term cycling stability [117,134].

Within this Ph.D. work, the CMC-SBR formulation provided the most satisfactory short-term electrochemical performance in line with the literature.

5.2.1.2.1.1. Laminate no. 1 (92%, CMC)

The first slurry was prepared by reducing the amount of AM compared to graphite to the value of 92 wt.%, in favor of a greater amount of binder, which improves electrode cohesion and adhesion [147,409]. The chosen composition of 92:2:2:4 (SC:C45:CMC:SBR) was in line with an already published patent [410]. SC was purchased from MTI Corp. [399], with a declared practical capacity between 420 and 470 mAh g^{-1} at 0.2C. Carbon black C45, CMC and SBR were the same materials used for the graphite anodes.

The production process was conducted at a very small scale, as for graphite, using a 5 mL beaker with a magnetic stirrer as the dispersing device. To choose the proper amount of material, the calculation was based on 0.7 g of solid material. Below the mixing process is described in detail:

5) The CMC was dissolved the day before and kept under stirring overnight as a 5 wt.% solution, to guarantee the proper dissolution of the polymer in the MilliQ water.
6) 0.280 g of the 5 wt.% CMC solution was further diluted in 0.2 mL of Milli-Q water and kept stirring at the highest speed (around 1.600 rpm) for 1 hour.
7) 0.014 g of C45 was added and the solution was kept stirring for 1 hour at the maximum speed.
8) 0.644 g of SC was finally slowly added; however, the viscosity was too high, blocking the movement of the magnetic stirrer and requiring the addition of 0.2 mL of water. Once all the powder was incorporated, the viscosity remained high, requiring the reduction of the mixing speed by half, while the solution was once again kept stirring for 1 hour.
9) The final step was the addition of 0.028 g of SBR, which was already suspended in solvent with a solid content of 18 wt.%, thus 0.17 g was added. In this case, the mixing speed was kept at around 800 rpm, while the mixing time was reduced to 30 minutes to avoid the degradation of the rubber.

Based on the amount of water added, the SF for this preparation was around 47 wt.%, and for further preparations this value was adjusted to 50 wt.%. In this way, the SF was increased by 10 wt.% compared to the graphite, supporting the

strategy of raising the solid content to reduce solvent demand during electrode fabrication and thereby favor industrial production and improve sustainability [411,412]. As done for graphite anodes, the SC slurry was coated onto 6 µm CC with the tape casting technique, using an Automatic Film Applicator (TQC SHEEN Standard AB4120). The doctor blade was set to a wet thickness of 100 µm and this value was kept constant for all subsequent electrode manufacturing with this material. The constant coating speed was set to 10 mm s^{-1}, and the laminate was dried in an oven at 50°C for 1 hour.

The laminate obtained with this production process is reported in ***Figure 5.28***. The slurry viscosity was not suitable for this type of deposition; in fact, at the edges of the laminate, the slurry receded. In addition, along the entire sheet, an unacceptable dispersion of the powders was observed, resulting in highly inhomogeneous electrodes. This behavior may be attributed to the two-step addition of water, which leads to insufficient mixing efficiency.

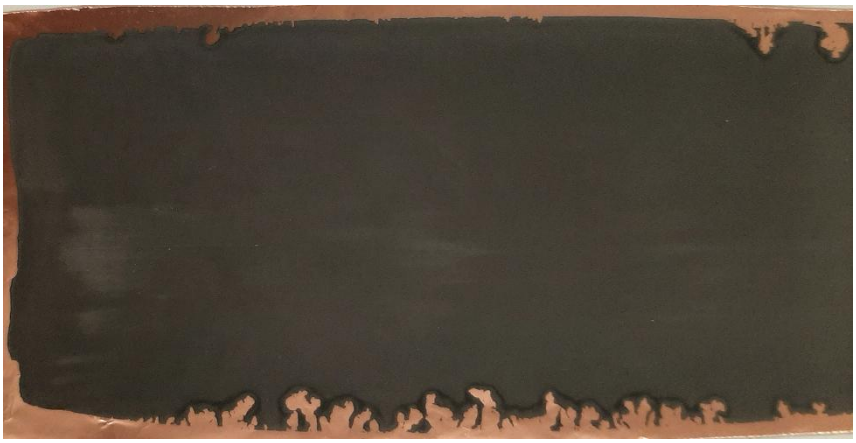

Figure 5.28 – First laminate produced with 92 wt.% of SC and CMC and SBR, the unoptimized viscosity is evident for the defects on the edges of the deposition and the bad dispersion in the middle

The electrodes were characterized by measuring their dry thickness at different locations across the surface to ensure a representative evaluation; the average value was calculated to be 46 ± 1 µm. This value was calculated excluding the thickness of the CC, indicating that the drying process reduced the coating layer thickness by approximately 50%. Although the surface was highly inhomogeneous, the dry thickness showed a small standard deviation.

As for the binder choice, the calendering step is also still under debate, with controversial results reported in the literature [266,268,413]. Compared to graphite, silicon-based electrodes need an even more strict calendering step control, as excessive pressure can hinder silicon volume variation during the lithiation and delithiation processes, thereby accelerating electrode degradation [268]. Hence, the calendering of silicon-based electrodes can effectively improve electrochemical performance only when the applied pressure is kept below a critical threshold, which strongly depends on electrode formulation, porosity, and binder system [267,268,414]. The high precision required for a proper calendering

step cannot currently be achieved with the facilities available at the Politecnico laboratories; therefore, it was decided to omit the calendering step.

The electrodes were punched into discs using a manual puncher, with a diameter of 15 mm. Based on the electrode weight, the ML was calculated to be 4.12 ± 0.08 mg cm^{-2}, and, based on the supplier-declared capacity, the areal capacity of the produced electrodes was calculated to be 1.85 ± 0.03 mAh cm^{-2}.

Even though the electrodes produced with this trial cannot be considered high-quality electrodes, electrochemical tests confirmed the low performance due to the poor manufacturing process (***Figure 5.29***): the capacity declared by the producer was not reached even at the lowest current density of 0.1C during the forming steps.

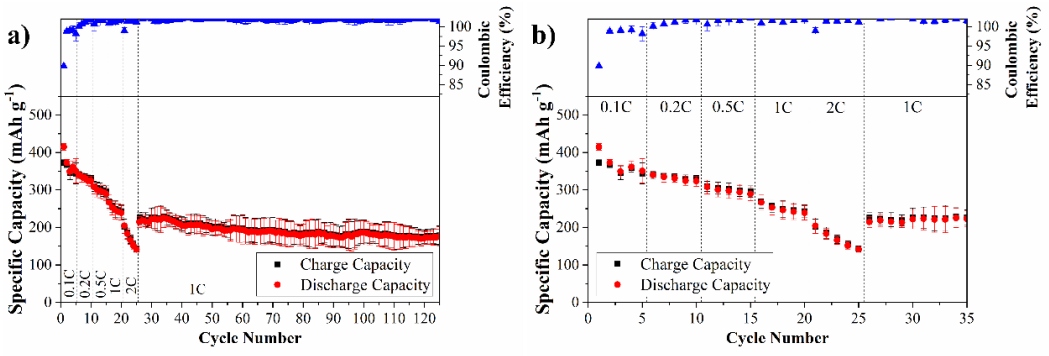

Figure 5.29 – Electrochemical characterization of the electrodes produced with 92 wt.% of SC and using CMC and SBR as binders: a) Entire test; b) Focus on the rate capability test

While the mean values of charge and discharge capacities were low and associated with poor performance, the reproducibility of the cells was quite good, with the dispersion of the values remaining within acceptable limits, especially during the first two cycles and at the highest current density (***Table 5.17***). During the first cycle, the discharge capacity, associated with the lithiation step, reached the highest mean value of 414.86 mAh g^{-1}, while the charge capacity (delithiation step) reached 379.59 mAh g^{-1}. The related average CE was 89.81%, corresponding to an average irreversible capacity loss in the first cycle of 10.19%, which is lower than the typical ~15% irreversible capacity loss reported for silicon-based electrodes [415,416]. This low value is undoubtedly a promising result; however, as the test progressed, further parasitic reactions occurred inside the cells that led to the poor electrochemical performance. With increasing current density, the electrochemical performance worsened, with the capacity decreasing continuously to values below 200 mAh g^{-1}. In addition, during long-term cycling beyond cycle 30, the three samples started to exhibit a higher capacity dispersion, related to intrinsic differences among electrodes produced with a not yet fully optimized production process. Apart from the formation steps, during both the rate capability test and long-term cycling, the CE exceeded 100%, which is not electrochemically acceptable. This behaviour can be attributed to the intrinsic

limitation of the half-cell configuration, where the excess lithium available at the counter electrode may compensate for lithium losses, leading to apparently overestimated values.

Table 5.17 – Values of charge and discharge capacities, normalized by the electrode weight, and relative values of coulombic efficiency for some representative cycles for the electrodes produced with 92 wt.% of SC and using CMC and SBR as binders

Cycle	***C-rate***	***Charge Capacity (mAh g^{-1})***	***Discharge Capacity (mAh g^{-1})***	***Coulombic Efficiency (%)***
1	*0.1C*	*372.59 ± 8.03*	*414.86 ± 8.73*	*89.81 ± 0.28*
2		*368.40 ± 9.13*	*372.71 ± 8.40*	*98.84 ± 0.30*
3		*345.69 ± 18.13*	*348.93 ± 16.24*	*99.054 ± 0.60*
10	*0.2C*	*329.46 ± 9.30*	*323.57 ± 13.49*	*101.86 ± 1.36*
15	*0.5C*	*295.49 ± 15.57*	*289.30 ± 17.40*	*102.17 ± 0.74*
20	*1C*	*242.96 ± 16.88*	*238.95 ± 18.88*	*101.73 ± 0.94*
25	*2C*	*142.93 ± 8.00*	*141.23 ± 7.81*	*101.20 ± 0.16*
30	*1C*	*226.35 ± 25.31*	*222.08 ± 25.74*	*101.95 ± 0.44*
50		*198.96 ± 19.29*	*195.14 ± 18.92*	*101.96 ± 0.01*
125		*178.38 ± 25.94*	*175.95 ± 26.26*	*101.42 ± 0.45*

Considering that the three samples presented comparable behavior, only one of the tested cells was chosen as an example to evaluate the charge and discharge curves (***Figure 5.30***). From the analysis of these charge/discharge profiles, as previously observed, the electrochemical performance is poor. Considering the discharge curve of the first cycle (dashed line, ***Figure 5.30a***) the rapid slope was attributed to the irreversible reaction that occurs between lithium and silicon. The discharge step was followed by the CVS, during which the plateau at 0.01 V was associated with two successive two-phase electrochemical reactions: the transformation of crystalline silicon nanoparticles into amorphous Li_xSi, followed by its conversion into the crystalline $Li_{15}Si_4$ phase [417,418]. For the second and third cycles, the discharge curves almost overlapped and the silicon contribution was evident in the broad shoulder that appeared below 0.2 V. Considering the charge curves, in this case, the curves almost overlapped from cycle 1 to cycle 3, meaning that the delithiation was highly reproducible during these cycles. Moving toward the rate capability test (***Figure 5.30b***) the shoulder associated with the silicon contribution was only partially visible in cycles 5 and 10. With increasing current density, the capacity contribution associated with silicon was progressively reduced, reflecting the kinetic limitations of silicon in composite electrodes [419]. In addition, an evident increment of the overvoltage between charge and discharge profiles is observed. At 2C, this behaviour was particularly severe, with the discharge capacity being almost entirely associated with the CVS contribution, while the charge curve started at potentials above 0.4 V. Considering the long-term cycling (***Figure 5.30c***) the overall capacity of the cell decreased

from cycle 30 to cycle 125 with the CVS becoming the dominant contributor to the discharge capacity.

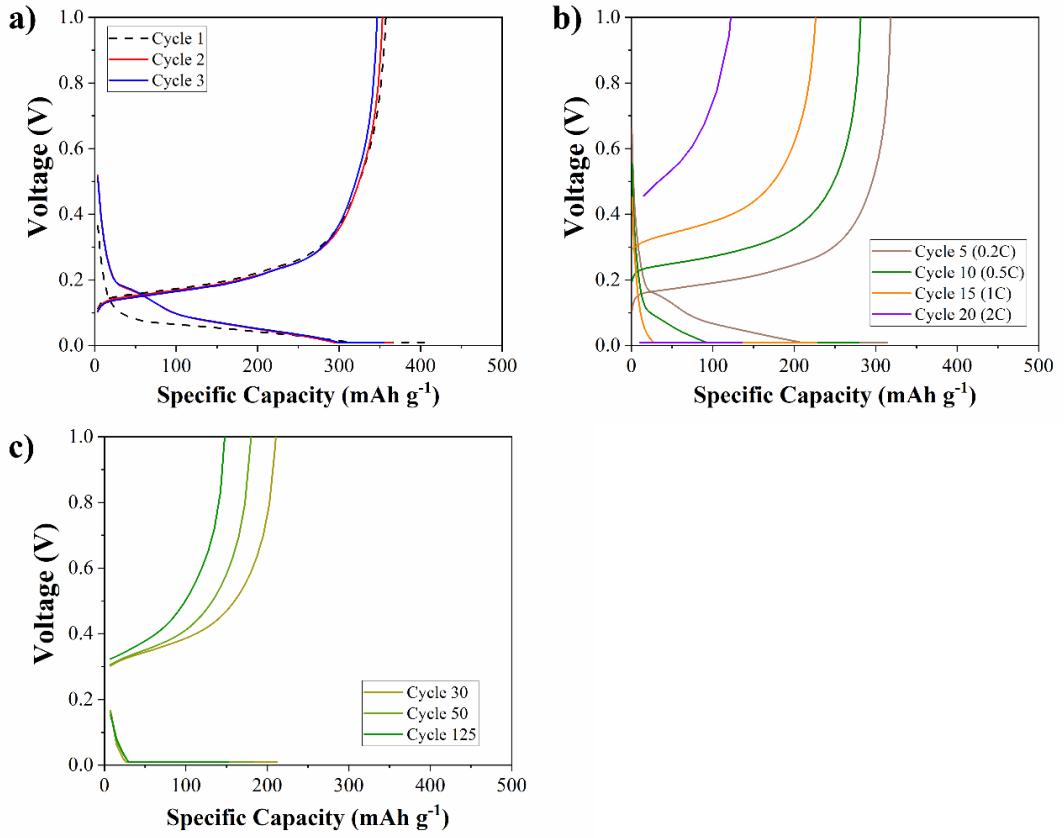

Figure 5.30 – Charge/discharge curves for some representative cycles of the electrodes produced with 92 wt.% of SC and using CMC and SBR as binders: a) Forming cycles; b) Rate capability test; c) Long cycling

A deeper investigation was performed by studying the CV profiles (***Figure 5.31***): the scan was performed over five cycles to observe the electrochemical reactions that occurred during the potential sweep. The curves were normalized by the weight of the AM. The CV measurements confirmed the silicon lithiation: the cathodic peak, present in each cycle, at voltage values lower than 0.2V was attributed to the formation of the metastable Li-Si phases [420–423]. At lower potentials, close to the cut-off, a second, slightly visible peak could be distinguished: in this case, this peak was associated with the transition from amorphous Li-Si phase to the crystalline structure [420]. During the anodic scan, two main oxidation peaks were detected at approximately 0.24 and 0.27 V. The first peak was associated with the delithiation of graphite and amorphous carbon, whereas the second peak corresponded to the dealloying of silicon [424,425]. In addition, a broader peak was partially observed at higher potentials, around 0.50 V, and was attributed to a further silicon dealloying process [426].

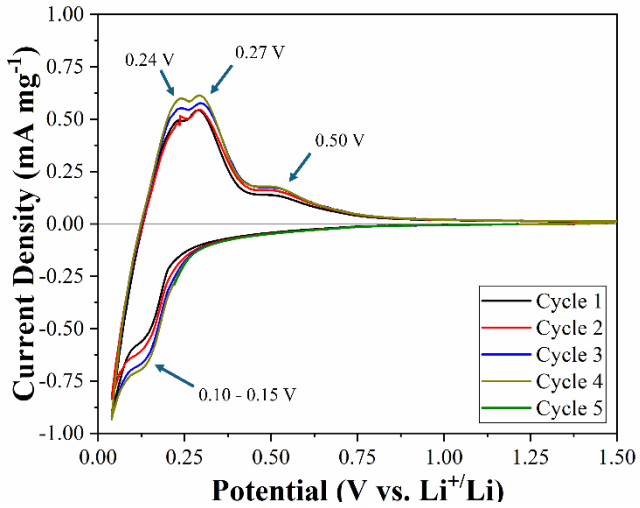

Figure 5.31 – CV test performed on 5 cycles for the electrodes produced with 92 wt.% of SC and using CMC and SBR as binders

5.2.1.2.1.2. Laminate no. 2 (92%, CMC_2)

The second trial aimed at improving the slurry processability observed in the previous laminate by increasing the SF to 50 wt.% and omitting the second water incorporation step during mixing. The slurry was prepared following the same general procedure adopted in the first trial and coated with a wet thickness of 100 µm. Despite the slight increase in SF, the resulting laminate still exhibited poor coating quality, with evident defects and pronounced inhomogeneities along the deposition direction (***Figure 5.32)***. The modification of the SF alone was therefore insufficient to achieve a stable slurry viscosity and homogeneous electrode structure. Due to the unsatisfactory laminate quality, no further physical or electrochemical characterization was performed on this sample.

Figure 5.32 – Second laminate produced with 92 wt.% of SC and CMC and SBR, the unoptimized viscosity is even more evident for the defects on the side of the deposition

5.2.1.2.1.3. Laminate no. 3 (95%, CMC)

For the third trial, a different approach was adopted, increasing the amount of AM content to reach the same amount as graphite anodes, and at the same time, trying to overcome the issue related to the unsuitable viscosity. Reducing the amount of binders also aimed to get closer to the industrial composition, while maintaining the binders functionality [150]. The resulting composition was 95:2:1:2 (SC:C45:CMC:SBR), while the slurry preparation followed the same optimized mixing route adopted in the previous trials, maintaining a SF of 50 wt.%. A new SBR batch was employed (always purchased from MTI), supplied with a higher solid content (50 wt.%) compared to the previously adopted material. After mixing, the slurry was coated with a wet thickness of 100 µm. Despite only minor modifications in the processing conditions, the laminate showed a noticeable improvement in surface homogeneity compared to the previous trials, although defects were still observed at the edges of the coating (***Figure 5.33***). These results indicated that increasing the AM fraction contributed to partially stabilizing the slurry behaviour, even if a fully uniform deposition was not yet achieved.

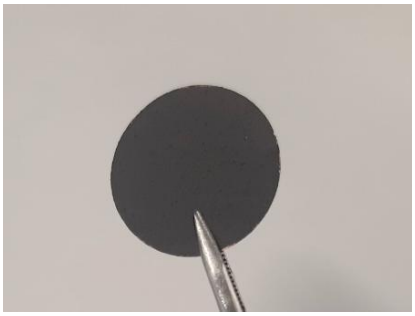

Figure 5.33 – Electrode with a diameter of 15 mm obtained at the third trial, with 95 wt.% of SC and using CMC and SBR as binders, with homogeneous and smooth surface

After punching the electrodes into 15 mm discs with a manual puncher, the samples exhibited a ML of 3.76 ± 0.20 mg cm^{-2}, corresponding to an areal capacity of 1.69 ± 0.09 mAh cm^{-2}. Despite the increase in SF and AM content, which should normally lead to higher ML, this trial showed a decrease in both electrode weight and ML values, compared to the first trial. This counterintuitive trend contrasts with the results of the first trial, where an opposite behavior was observed, and can be explained by inhomogeneities during the coating process and by slurry shrinkage effects at the electrode edges, leading to a greater accumulation of material in the central region.

This improvement was effectively observed throughout the forming, rate capability and long-term test (***Figure 5.34***). However, some issues were still observed, during the formation stage (***Figure 5.34b***). In particular, the discharge capacities recorded in the first three cycles (***Table 5.18***) were significantly higher than the practical capacity range declared by the supplier (420-470 mAh g^{-1}). The average discharge capacity reached 544.89 mAh g^{-1} in the first cycle, 473.32 mAh

g^{-1} in the second and 491.69 mAh g^{-1} the third cycles. Such anomalously high values indicate the occurrence of parasitic processes, mainly associated with the CVS, which led to an overestimation of the effective lithiation of the material. As confirmed by the analysis of the voltage profiles (***Figure 5.35***), the prolonged CVS contribution promoted excessive lithium consumption due to slow kinetic processes at low potentials, including lithium diffusion limitations, structural rearrangements, continuous SEI growth, lithium trapping and localized lithium plating [419,427]. This behaviour resulted in very low CE values during the formation cycles.

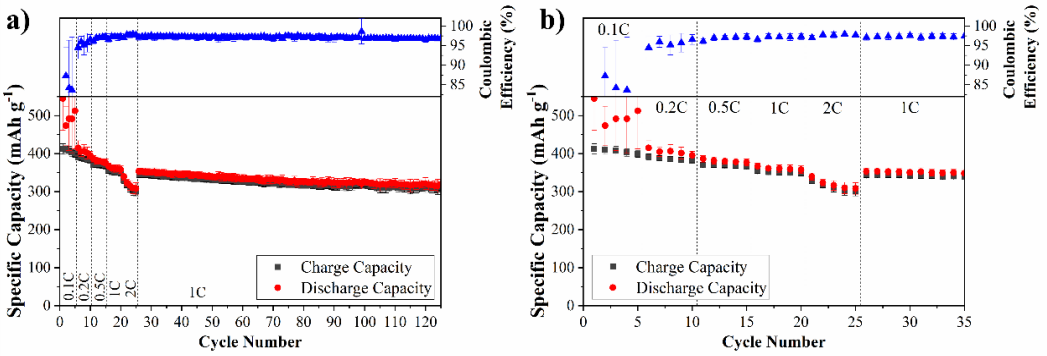

Figure 5.34 – Electrochemical characterization of the electrodes produced with 95 wt.% of SC and using CMC and SBR as binders: a) Entire test; b) Focus on the rate capability test

Table 5.18 – Values of charge and discharge capacities, normalized by the electrode weight, and relative values of coulombic efficiency for some representative cycles for the electrodes produced with 95 wt.% of SC and using CMC and SBR as binders

Cycle	***C-rate***	***Charge Capacity (mAh g^{-1})***	***Discharge Capacity (mAh g^{-1})***	***Coulombic Efficiency (%)***
1	*0.1C*	*412.40 ± 13.41*	*544.89 ± 83.82*	*76.66 ± 9.50*
2		*410.58 ± 12.07*	*473.32 ± 51.08*	*87.26 ± 7.23*
3		*407.43 ± 11.49*	*491.69 ± 83.39*	*84.23 ± 2.13*
10	*0.2C*	*381.73 ± 5.31*	*395.38 ± 10.54*	*96.57 ± 1.27*
15	*0.5C*	*366.37 ± 5.79*	*376.66 ± 8.89*	*97.28 ± 0.78*
20	*1C*	*348.08 ± 7.19*	*357.70 ± 10.07*	*97.33 ± 0.74*
25	*2C*	*301.55 ± 13.09*	*308.63 ± 15.34*	*97.73 ± 0.63*
30	*1C*	*342.04 ± 5.79*	*350.57 ± 7.54*	*97.57 ± 0.50*
50		*329.77 ± 7.60*	*339.29 ± 9.62*	*97.20 ± 0.57*
125		*309.16 ± 5.80*	*318.99 ± 7.02*	*96.87 ± 0.30*

During the rate capability test, the electrochemical behavior seemed improved, with capacity values in line with the expectations and no outliers were observed: with increasing current density, the discharge capacity decreased from 395.38 mAh g^{-1} at 0.2C to 308.63 mAh g^{-1} at 2C. However, the CE remained below 97% throughout the test, indicating that degradation processes had already occurred during the forming cycles, and highlighting once again the importance of

proper SEI formation [428]. A similar behavior was observed during long-term cycling, where the discharge capacity at 1C gradually decreased to an average value of 318.99 mAh g^{-1} and the CE dropped to values below 97%.

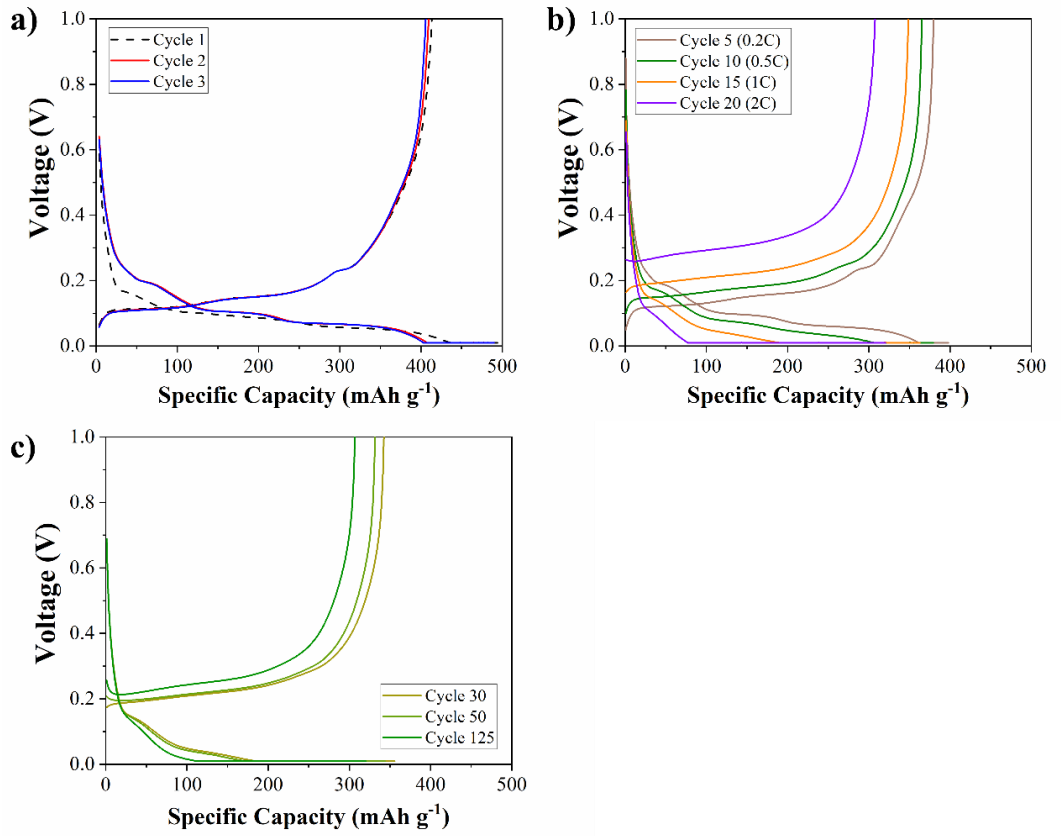

Figure 5.35 – Charge/discharge curves for some representative cycles of the electrodes produced with 95 wt.% of SC and using CMC and SBR as binders: a) Forming cycles; b) Rate capability test; c) Long cycling

Further insights were obtained from the analysis of the voltage profiles (***Figure 5.35***). Compared to Laminate no. 1, the discharge curves exhibited more clearly defined plateaus, reflecting a more effective contribution of the carbonaceous fraction to the overall capacity. The silicon-related shoulder below 0.2 V was still visible, although less pronounced. During the rate capability test, the silicon contribution remained detectable even at higher C-rates, while polarization effects increased at 2C, although less severely than in the previous trial.

CV measurements (***Figure 5.36***) confirmed the electrochemical behaviour already discussed for the previous laminate. The first cycle showed the expected differences due to irreversible processes associated with SEI formation [417], whereas subsequent cycles exhibited a more stable and reproducible response. The main cathodic feature related to silicon lithiation and the overlapping anodic contributions associated with both silicon dealloying and carbon de-intercalation were consistent with the trends previously described [424–426,429]. Only minor

polarization effects were observed with increasing cycle number, indicating a progressive stabilization of the electrode/electrolyte interface [429].

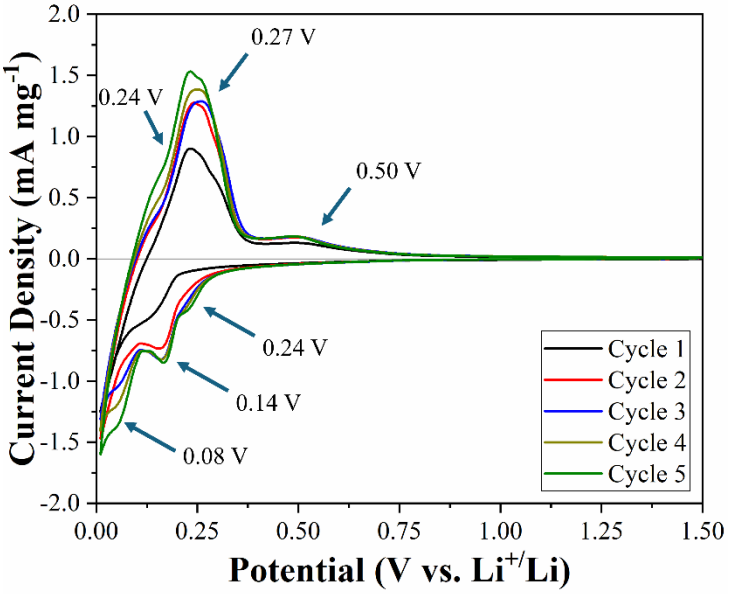

Figure 5.36 – CV test performed on 5 cycles for the electrodes produced with 95 wt.% of SC and using CMC and SBR as binders

Although this formulation does not enable optimal specific capacity values, it exhibits relatively high capacity retention, partially contrasting with literature reports that generally classify CMC–SBR binder systems as unsuitable for long-term cycling [401]. This discrepancy suggests that the detrimental effects of this formulation may become more pronounced over extended cycling beyond the duration explored in the present study, and therefore, additional long-term investigations would be required.

5.2.1.2.2. PAA as single binder

Given the poor results using the CMC-SBR binder composition, which confirmed the difficulties in the production of this type of anodes, the research focus shifted toward alternative binders, characterized by higher amounts of hydroxyl and carboxyl groups, able to create a stronger network around the silicon particles. In fact, for this study step, PAA was chosen thanks to its well-balanced characteristics between processability and electrochemical performance because its structural features allow it to accommodate the silicon expansion [145].

Different binders were evaluated: based on the literature research, PAA is one of the most widely used binders for Si-based electrodes [70,142,430]. PAA is a linear polymer available at various MWs; however, multiple studies report controversial results regarding which MW performs best for LIB applications [145–147,431]. In this work, two commonly adopted MWs were evaluated,

namely 250.000 and 450.000 g mol^{-1}, hereafter referred to as PAA250 and PAA450.

5.2.1.2.2.1. Laminate no. 4 (95%, PAA250)

The first formulation employed PAA250, purchased from Sigma-Aldrich as a 35 wt.% aqueous solution and used without further treatment. The electrode formulation was 95:2:3 (SC:C45:PAA), while the slurry was prepared as previously described (SF = 50 wt.%). One of the main advantages of using PAA instead of the combination of CMC and SBR is related to the use of a single binder, allowing for faster mixing. The slurry was coated using the same deposition parameters as previously adopted (wet thickness of 100 µm) and subsequently dried at 50 °C for 1 h. After drying, the laminate exhibited severe surface inhomogeneities across the entire coated area, characterized by a clear segregation of solid particles and solvent accumulation on opposite sides of the laminate (***Figure 5.37***). Due to the extremely poor coating quality, no further physical or electrochemical characterization was carried out on these samples.

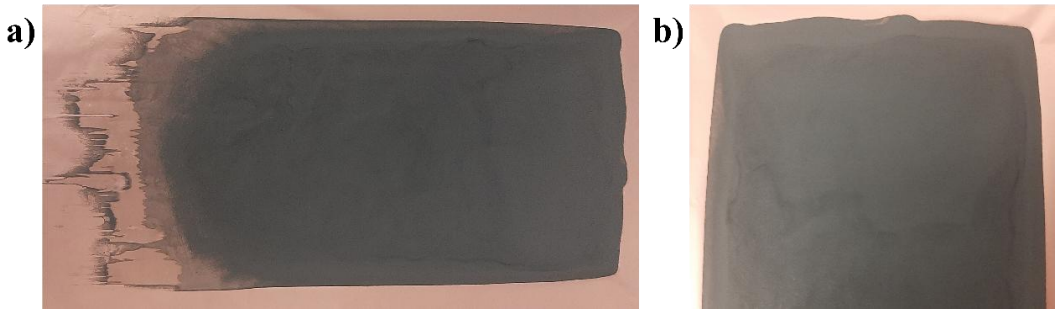

Figure 5.37 – Laminate produced with 95 wt.% of SC and using PAA250 as binder: a) Total laminate, the excess of solvent is evident on the left side; b) Focus on the deposition inhomogeneities

5.2.1.2.2.2. Laminate no. 5 (95%, PAA450)

Following the extremely poor coating behaviour observed with PAA250, a second trial was performed using PAA450, supplied in powder form and dissolved in water prior to slurry preparation. The electrode formulation was maintained at 95:2:3 (SC:C45:PAA), and the slurry was prepared following the same general mixing route adopted in the previous trial, keeping a SF of 50 wt.%. Despite the higher MW of the polymer, which was expected to increase slurry viscosity, the resulting coating still showed severe inhomogeneities, with pronounced accumulation of material on one side of the laminate (***Figure 5.38***). The viscosity increase was therefore insufficient to guarantee a stable slurry behaviour during deposition. Due to the unsatisfactory laminate quality, no further physical or electrochemical characterization was performed.

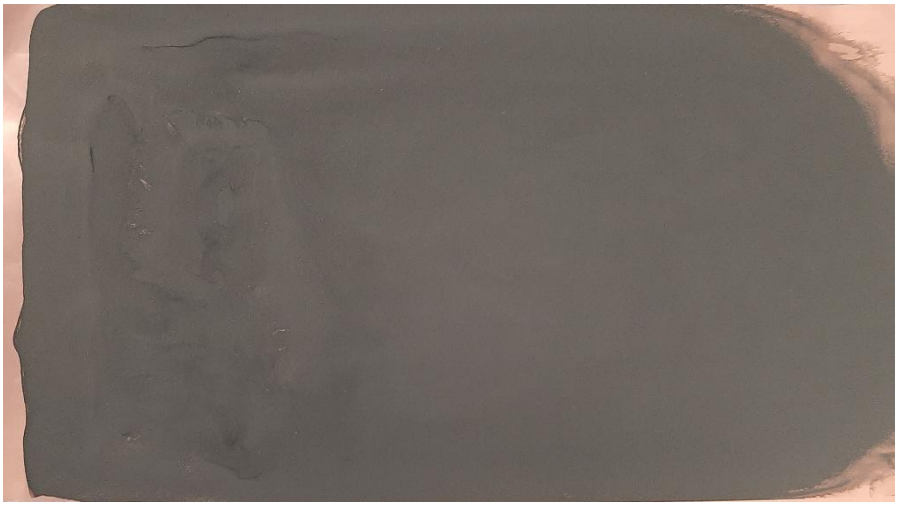

Figure 5.38 – Laminate produced with 95 wt.% of SC and using PAA450 as binder, on the left side is evident the inhomogeneities related to the accumulation of the slurry

The unsatisfactory behavior observed for both PAA-based slurries can be attributed to rheological limitations. Although PAA provides strong chemical interactions with silicon particles through hydrogen bonding and carboxyl groups, its linear polymer structure leads to predominantly Newtonian or weakly shear-thinning behavior in aqueous systems [432]. As demonstrated in silicon anode slurry studies employing different binders, including PAA and CMC/SBR, binder adsorption and polymer conformation play a critical role in determining slurry flowability and homogeneity during coating [432]. As a consequence, the slurry viscosity often remains insufficient to prevent particle migration during coating, especially at the laminate edges. Increasing the MW increases slurry viscosity; however, the formation of a sufficiently strong three-dimensional network able to stabilize the slurry during the coating process cannot be guaranteed [147]. In addition, the degree of neutralization and the conformation of PAA chains have been shown to strongly influence slurry processability, frequently failing to ensure homogeneous particle distribution during deposition [433].

Consequently, phase separation and material accumulation occur during solvent evaporation, leading to severe inhomogeneities in the dried electrodes [252]. Overall, these observations are consistent with broader analyses highlighting how binder-dependent rheological properties ultimately govern coating quality and slurry performance in LIB electrodes [434].

5.2.1.2.3. LiPAA as single binder: effect of pre-lithiation

The limitations observed for both PAA-based slurries indicate that strong chemical affinity between binder and silicon particles is not, by itself, sufficient to guarantee adequate slurry processability and coating quality. In particular, the linear structure of PAA limits its ability to form a stable three-dimensional network under shear, as polymer chains can only partially interact with each other

and with silicon particles to create a mechanically robust structure [157]. As a result, slurry homogeneity during coating remains inadequate, confirming the intrinsic limitations of using PAA alone for LIB applications.

To overcome these issues, the chemical structure of PAA must be modified to increase the number of effective interactions, particularly by enhancing the availability of carboxyl and hydroxyl groups capable of contributing to network formation. Several approaches have been reported in the literature, including the neutralization of PAA with LiOH or NaOH to form LiPAA or NaPAA [148,149,157], as well as cross-linking PAA with other polymers such as CMC and SBR [157,159,435]. Overall, appropriately neutralized PAA generally provides improved mechanical integrity and cycling stability compared to the acid form, due to the higher density of carboxylate groups that promote the formation of a stronger three-dimensional network [148,152,155,156,169,436].

In this study, LiPAA solutions with two MWs were prepared by titration [148,151] with solid LiOH, after a rough estimation of the residual -COOH groups. The LiOH powder was purchased from Sigma-Aldrich and used without further purification. The pH was monitored throughout the titration to confirm neutralization, and small final adjustments were made to achieve complete neutralization. Both solutions were prepared with a solid content of 10 wt.% and kept stirring overnight to guarantee optimal homogenization.

Based on these considerations, the subsequent investigation focused on alternative binder strategies aimed at modifying polymer conformation and interaction mechanisms, with the objective of improving slurry homogeneity during coating while preserving electrochemical performance.

5.2.1.2.3.1. Laminate no. 6 (92%, LiPAA250)

For the initial evaluation of Li-PAA, the first trial was based on a composition with a lower amount of AM (92 wt.%), favoring a higher amount of binder, which can help during the coating process [147,409]. The electrode formulation was prepared maintaining a SF of 50 wt.% and following the same general mixing route adopted in the previous trials. Compared to Laminate no. 3, produced with the CMC-SBR binder system at the same AM content, a clear improvement in slurry distribution on the CC surface was observed. Nevertheless, the coating still presented localized defects in the central region, indicating non-uniform deposition (***Figure 5.39a***). After drying, significant mechanical stresses were visible along the laminate edges (highlighted by red arrows in ***Figure 5.39b***), probably associated with the formation of a rigid network attributed to the lithiated PAA behaviour.

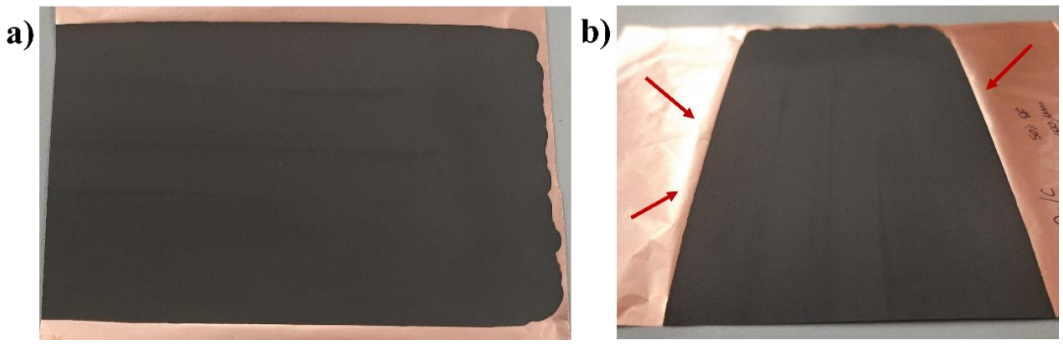

Figure 5.39 – Laminate produced with 92 wt.% of SC and LiPAA250 as binder, to be noted the tensions along the side highlighted with the red arrows

Even though the quality of the laminate was not as good as expected, the 15 mm electrodes were punched and characterized. The dry thickness was measured to be 53 ± 3 µm. The calculated ML was 4.26 ± 0.14 mg cm^{-2} and the areal capacity calculated from the theoretical capacity was 1.92 ± 0.06 mAh cm^{-2}.

Three replicate cells were tested, showing excellent reproducibility (***Figure 5.40***, ***Table 5.19***). Considering the formation cycles, the average first-cycle discharge capacity was 441.45 mAh g^{-1}, while the average first-cycle charge capacity was 391.00 mAh g^{-1}, resulting in a CE of 88.59%. This value is consistent with typical irreversible capacity losses reported for silicon-based electrodes [415,416]. During the rate capability test (***Figure 5.40b***), the discharge capacity gradually decreased with increasing current density, as expected from kinetic limitations, while CE remained consistently above 99%. These results demonstrate that LiPAA improves electrochemical reversibility compared to the CMC-SBR system.

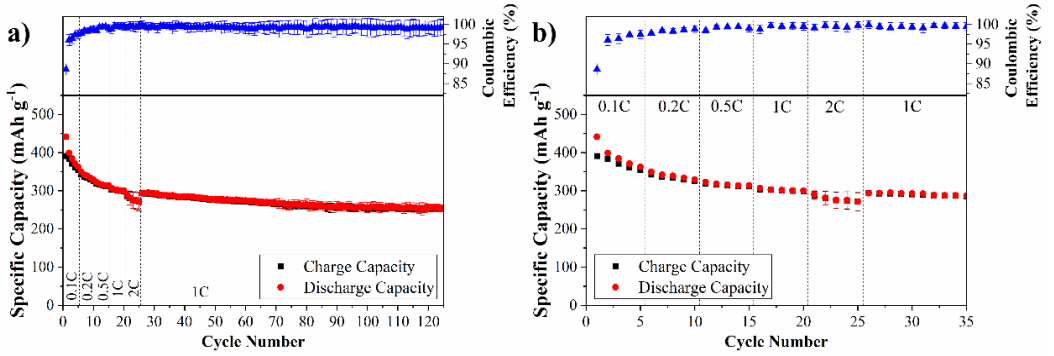

Figure 5.40 – Electrochemical characterization of the electrodes produced with 92 wt.% of SC and using LiPAA250 as binder: a) Entire test; b) Focus on the rate capability test

Table 5.19 – Values of charge and discharge capacities, normalized by the electrode weight, and relative values of coulombic efficiency for some representative cycles for the electrodes produced with 92 wt.% of SC and using LiPAA250 as binder

Cycle	***C-rate***	***Charge Capacity (mAh g^{-1})***	***Discharge Capacity (mAh g^{-1})***	***Coulombic Efficiency (%)***
1	*0.1C*	*391.00 ± 0.85*	*441.45 ± 6.30*	*88.59 ± 1.44*

2		*383.04 ± 1.85*	*398.82 ± 4.94*	*96.05 ± 1.38*
3		*370.87 ± 3.75*	*384.56 ± 2.60*	*96.44 ± 1.29*
10	*0.2C*	*325.43 ± 3.67*	*329.37 ± 2.27*	*98.80 ± 0.85*
15	*0.5C*	*311.18 ± 2.77*	*314.13 ± 0.44*	*99.06 ± 0.94*
20	*1C*	*298.69 ± 5.09*	*300.15 ± 3.93*	*99.51 ± 0.94*
25	*2C*	*270.83 ± 23.75*	*271.50 ± 24.60*	*99.77 ± 0.93*
30	*1C*	*290.86 ± 3.94*	*292.76 ± 3.29*	*99.35 ± 0.93*
50		*275.63 ± 5.83*	*277.31 ± 7.22*	*99.41 ± 1.22*
125		*252.34 ± 6.49*	*254.53 ± 8.32*	*99.17 ± 1.97*

Therefore, this binder positively affected the overall performance, partly due to the CVS contribution to the total discharge capacity during formation (***Figure 5.34a***). As for the previous case, the discharge curves were characterized by the three plateaus of the graphite intercalation mechanism coupled with the silicon contribution. During the rate capability test (***Figure 5.34b***), the charge/discharge profiles are consistent with the expectations: with the increase of the current density, the plateaus were gradually shortened while the polarization effects increased. The discharge curve at 2C (purple curve) presented a sharp profile because the sampling time was not properly tailored.

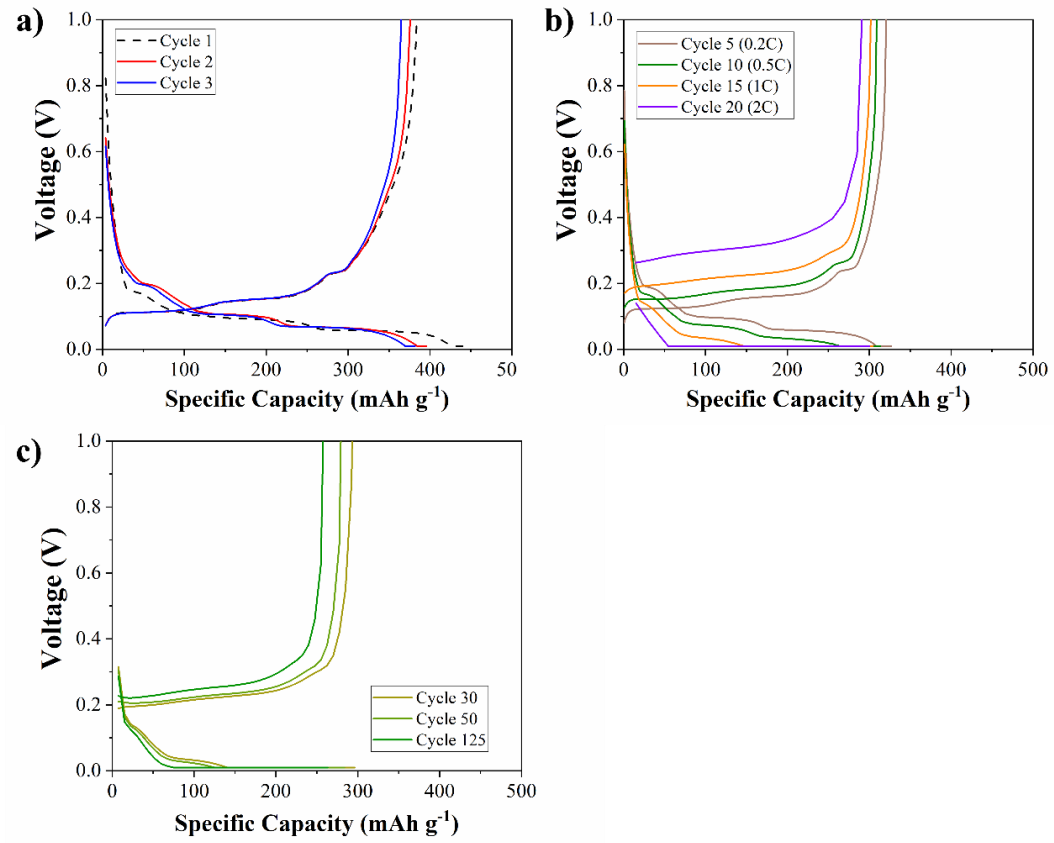

Figure 5.41 – Charge/discharge curves for some representative cycles of the electrodes produced with 92 wt.% of SC and using LiPAA250 as binder: a) Forming cycles; b) Rate capability test; c) Long cycling

5.2.1.2.3.2. Laminate no. 7 (95%, LiPAA250)

Following the encouraging results obtained in the previous trial, the AM content was increased to 95 wt.% while the binder fraction was reduced to 3 wt.% in order to approach a more industrially relevant electrode formulation. The slurry was prepared maintaining a SF of 50 wt.% and following the same general mixing procedure adopted in the previous LiPAA-based trials. Compared to the laminate produced with the same AM content using the CMC-SBR binder system (Laminate no. 3), a clear improvement in coating quality was observed, confirming the beneficial role of LiPAA in stabilizing slurry behaviour. The resulting laminate exhibited very good surface homogeneity with no evident defects across the coated area, although residual mechanical stresses were still visible along the deposition edges (***Figure 5.42***)

Figure 5.42 – Laminate produced with 95 wt.% of SC and LiPAA250 as binder, to be noted the tensions along the side highlighted with the red arrow

The electrodes were manually punched into discs with a diameter of 15 mm. The dry thickness of the electrodes was measured and the average value was 49 ± 2 µm. The ML was calculated to be 4.24 ± 0.18 mg cm^{-2}, and the areal capacity was 1.91 ± 0.08 mAh cm^{-2}.

The electrochemical performance (***Figure 5.43***, ***Table 5.20***) was consistent, with the values of charge and discharge capacities that were almost constant above 300 mAh g^{-1}, with the only exception of the highest C-rate of 2C. During the forming cycles, the average discharge capacity values of the first cycle reached 447.09 mAh g^{-1}, while the average charge capacity value was 401.66 mAh g^{-1}, which corresponded to an average CE of 89.85% and an average irreversible capacity of 10.15%, which is highly promising for SC electrodes [415,416].

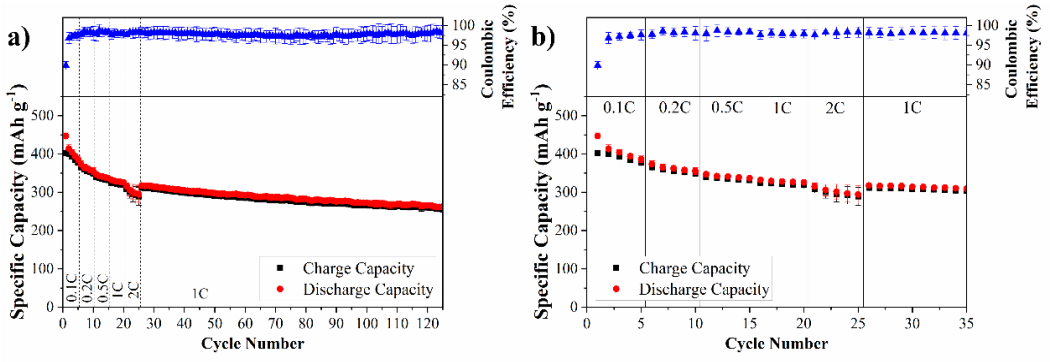

Figure 5.43 – Electrochemical characterization of the electrodes produced with 95 wt.% of SC and using LiPAA250 as binder: a) Entire test; b) Focus on the rate capability test

Table 5.20 – Values of charge and discharge capacities, normalized by the electrode weight, and relative values of coulombic efficiency for some representative cycles for the electrodes produced with 95 wt.% of SC and using LiPAA250 as binder

Cycle	***C-rate***	***Charge Capacity (mAh g^{-1})***	***Discharge Capacity (mAh g^{-1})***	***Coulombic Efficiency (%)***
1	*0.1C*	*401.66 ± 3.86*	*447.09 ± 8.35*	*89.85 ± 1.05*
2		*400.52 ± 4.33*	*413.75 ± 10.34*	*96.82 ± 1.40*
3		*392.89 ± 3.38*	*404.22 ± 7.06*	*97.21 ± 0.87*
10	*0.2C*	*348.40 ± 3.59*	*355.46 ± 8.98*	*98.04 ± 1.76*
15	*0.5C*	*331.58 ± 2.28*	*336.94 ± 1.78*	*98.41 ± 0.64*
20	*1C*	*318.78 ± 3.65*	*325.72 ± 2.41*	*97.87 ± 1.05*
25	*2C*	*289.21 ± 23.54*	*294.14 ± 22.90*	*98.31 ± 1.32*
30	*1C*	*308.77 ± 2.62*	*314.39 ± 2.58*	*98.22 ± 1.59*
50		*291.04 ± 2.18*	*297.62 ± 4.31*	*97.80 ± 1.78*
125		*257.54 ± 9.35*	*262.20 ± 6.93*	*98.21 ± 1.76*

During the rate capability test (***Figure 5.43b***), the electrodes confirmed good performance, with average capacity values above 300 mAh g^{-1} throughout the test, except at the highest current density of 2C, where, at cycle 25, the average discharge capacity dropped to 294.14 mAh g^{-1}, and the average charge capacity reached 289.21 mAh g^{-1}. Compared to the previous case, the CE never exceeded 99%. Voltage profile analysis (***Figure 5.44***) confirmed the coexistence of lithiation processes associated with both silicon and carbonaceous phases. These features remained clearly visible during formation and up to 1C, whereas at 2C the lithiation stages became less distinguishable and the contribution of the CVS increased. During long-term cycling, the progressive reduction in the visibility of these features was accompanied by a growing contribution of the CVS to the overall discharge capacity.

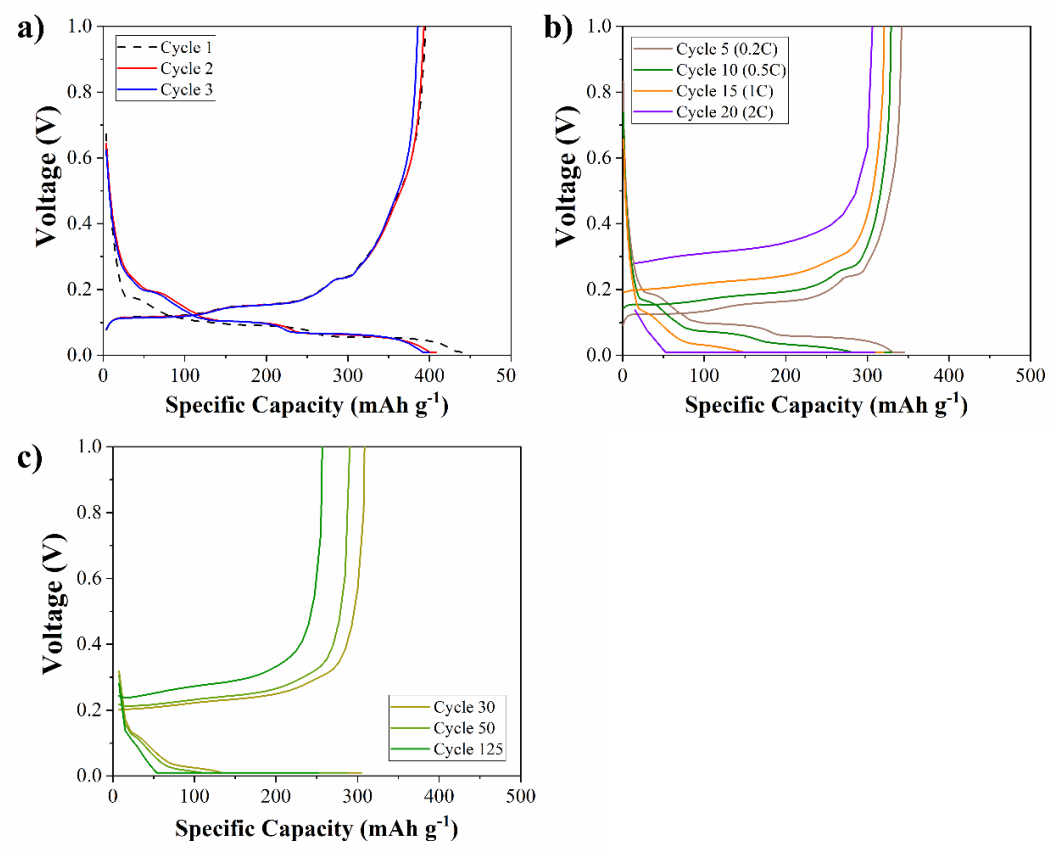

Figure 5.44 – Charge/discharge curves for some representative cycles of the electrodes produced with 95 wt.% of SC and using LiPAA250 as binder: a) Forming cycles; b) Rate capability test; c) Long cycling

CV analysis (***Figure 5.45***) further supported the trends observed in galvanostatic cycling. The cathodic peaks were consistent with those already discussed for laminate no. 6. During the anodic scan, two well-defined oxidation peaks were detected at approximately 0.24 and 0.27 V, associated respectively with the delithiation of carbonaceous phases and the dealloying of silicon [424,425]. Compared with previous samples, these peaks remained distinguishable with increasing cycle number, indicating relatively limited polarization effects.

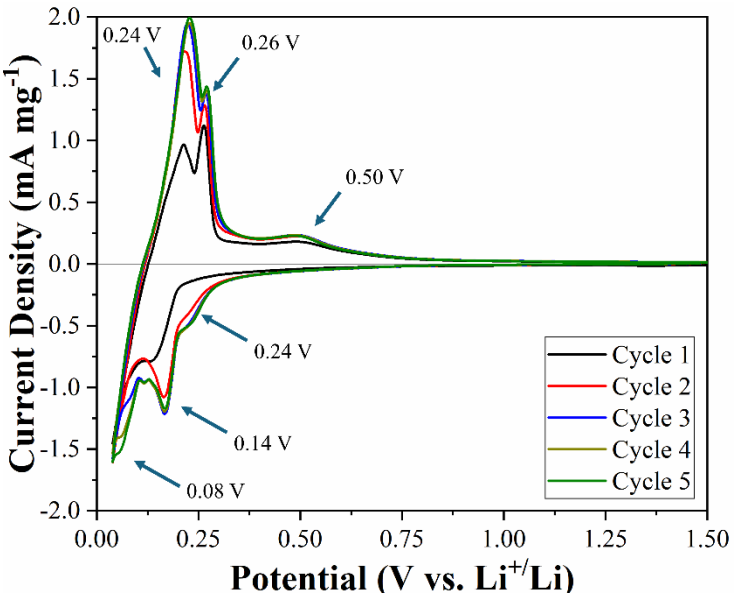

Figure 5.45 – CV test performed on 5 cycles for the electrodes produced with 95 wt.% of SC and using LiPAA250 as binder

5.2.1.2.3.3. Laminate no. 8 (95%, LiPAA450)

Following the positive results obtained with LiPAA250, a further trial was performed using LiPAA450 in order to investigate the influence of binder MW on slurry processability and coating quality. The electrode formulation was maintained at 95:2:3 (SC:C45:LiPAA), and the slurry was prepared according to the same general mixing procedure adopted in the previous LiPAA-based trials, keeping a SF of 50 wt.%. The resulting laminate showed a highly homogeneous surface, with no visible defects either in the central region or along the coating edges (***Figure 5.46***), indicating a further improvement in slurry stability compared to the lower MW binder.

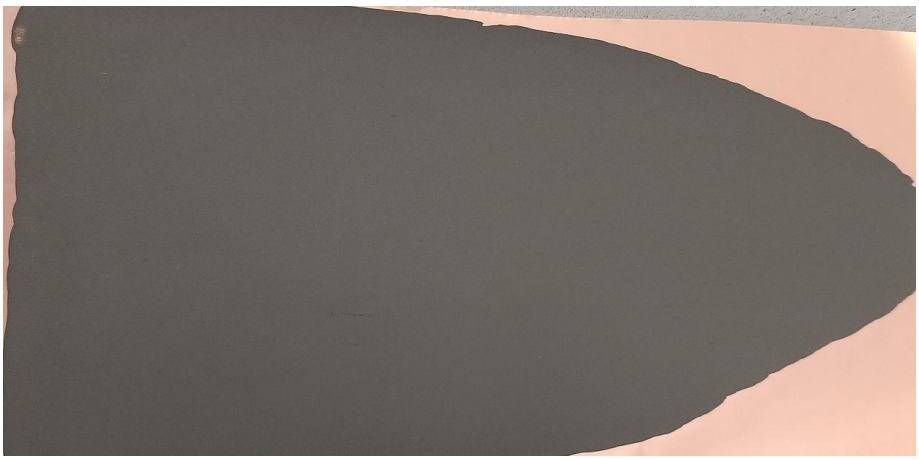

Figure 5.46 – Laminate produced with 95 wt.% of silicon and LiPAA450 as binder, with a smooth and homogeneous surface

The electrodes were manually punched into discs with a diameter of 15 mm. The average dry thickness was 57 ± 2 µm. The ML was calculated to be 4.41 ± 0.30 mg cm^{-2} and consequently, the areal capacity was 1.98 ± 0.13 mAh cm^{-2}.

This formulation resulted in very high electrochemical performance, although a larger dispersion of the results was observed, particularly during long-term cycling (***Figure 5.47***, ***Table 5.21***). During the formation cycles, the average first-cycle discharge capacity reached 464.21 mAh g^{-1}, while the corresponding charge capacity was 418.99 mAh g^{-1}. These values led to an average CE of 89.23%, which was comparable to that obtained with LiPAA250 and can be considered a promising result for silicon-based electrodes.

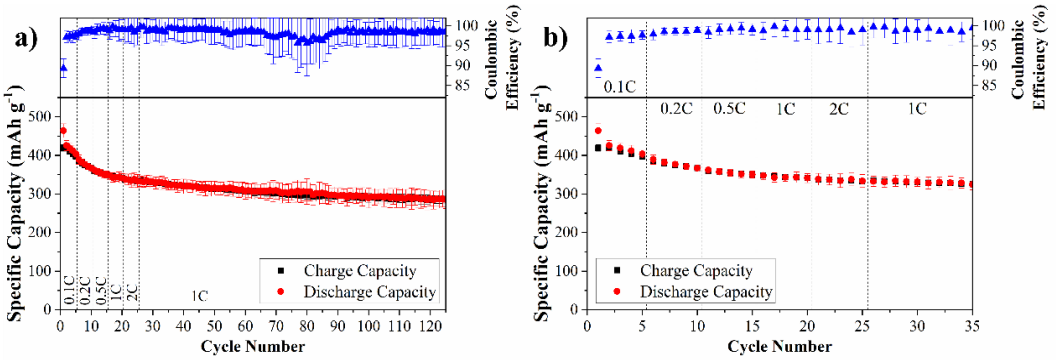

Figure 5.47 – Electrochemical characterization of the electrodes produced with 95 wt.% of SC and using LiPAA450 as binder: a) Entire test; b) Focus on the rate capability test

Table 5.21 – Values of charge and discharge capacities, normalized by the electrode weight, and relative values of coulombic efficiency for some representative cycles for the electrodes produced with 95 wt.% of SC and using LiPAA450 as binder

Cycle	***C-rate***	***Charge Capacity (mAh g^{-1})***	***Discharge Capacity (mAh g^{-1})***	***Coulombic Efficiency (%)***
1	*0.1C*	*418.99 ± 8.47*	*464.21 ± 17.72*	*89.23 ± 2.36*
2		*418.01 ± 9.01*	*425.53 ± 13.30*	*97.21 ± 1.49*
3		*412.51 ± 9.22*	*418.93 ± 12.03*	*97.40 ± 1.16*
10	*0.2C*	*366.98 ± 7.05*	*367.06 ± 5.61*	*98.92 ± 0.69*
15	*0.5C*	*350.96 ± 6.71*	*350.48 ± 9.03*	*99.15 ± 1.42*
20	*1C*	*341.03 ± 6.06*	*341.06 ± 11.99*	*99.09 ± 2.50*
25	*2C*	*332.91 ± 5.71*	*333.64 ± 16.85*	*99.02 ± 3.81*
30	*1C*	*330.41 ± 5.52*	*331.21 ± 12.02*	*98.92 ± 2.64*
50		*315.29 ± 6.63*	*316.05 ± 17.18*	*98.90 ± 3.56*
125		*285.49 ± 10.83*	*286.09 ± 23.88*	*98.62 ± 4.00*

The rate capability test (***Figure 5.47b***) was particularly promising for these samples. Even at 2C, the electrodes delivered an average discharge capacity of 333.64 mAh g^{-1} and the average charge capacity of 332.91 mAh g^{-1}, indicating improved kinetic behaviour compared with the other formulations. However, during the long-term cycling, the capacity decreased to 286.09 mAh g^{-1} for the

average discharge and 285.49 mAh g^{-1} for the charge, which corresponded to an average calculated capacity retention of 85.70%, significantly lower than in the case of 95%,CMC composition. Analysis of the voltage profiles (***Figure 5.48***) confirmed behaviour consistent with that previously discussed for LiPAA-based electrodes, with no additional features requiring specific discussion.

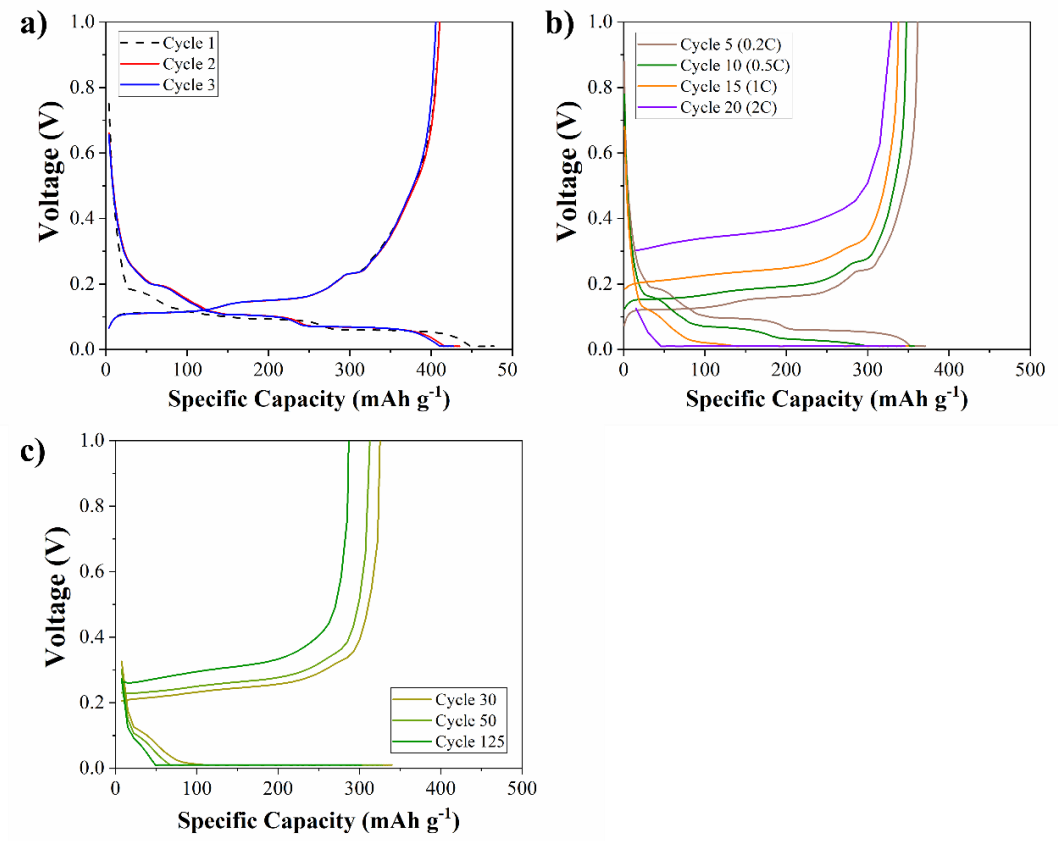

Figure 5.48 – Charge/discharge curves for some representative cycles of the electrodes produced with 95 wt.% of SC and using LiPAA450 as binder: a) Forming cycles; b) Rate capability test; c) Long cycling.

Overall, this composition provided the highest capacity values during the rate capability test. Nevertheless, the improved high-rate performance was not accompanied by a proportional enhancement in long-term stability, as the capacity retention remained comparable to that of the other investigated formulations.

5.2.1.2.4. LiPAA-based formulations with natural polysaccharide additives

After the confirmation of Li-PAA as a superior binder for silicon-based electrodes, in line with the literature [148,402,437], further investigations were performed on Li-PAA250 to improve its viscosity through the use of natural polysaccharides as additives. In particular, the introduction of natural polysaccharides, in combination with PAA, aimed to enhance electrode mechanical stability through their elastic behaviour and to explore potential synergistic effects between different binder networks, thereby reducing stress

concentration at the laminate edges. In addition, the choice of the polysaccharides was based primarily on the objective of improving the sustainability of the overall process by reducing the amount of PAA, due to its petroleum-based origin [438].

The natural polysaccharides chosen for this work were TG and CGN, whose chemical structures and further characteristics were discussed in detail in ***Chapter 2***. In the first case, TG was selected due to its large availability, and complex chemical structure, rich in carboxyl and hydroxyl groups, as described in ***Chapter 2***. In addition, its application in LIBs is still limited in the literature, although promising results have been reported for high-voltage cathodes [182] and anode materials such as graphite [172] and SC [439]. The other polysaccharide selected was CGN, which exists in three configurations (κ, ι, λ) depending on the number and position of the ester sulfate groups. Its application in LIB production has been widely investigated: in silicon-based systems, λ-CGN appears to be the most commonly employed form [174,440], while in graphite-based electrodes the specific form is often not specified [124]. Several examples of its application in high-voltage cathodes have also been reported [175,441–443]. In this work, the specific CGN composition used consisted predominantly of κ-CGN with a lower fraction of λ-CGN.

5.2.1.2.4.1. Laminate no. 9 (92%, LiPAA250_TG)

To further improve slurry stability, the natural polysaccharide TG was introduced into the LiPAA-based formulation. The AM content was set to 92 wt.%, while the binder fraction was partially replaced by TG, maintaining the conductive carbon content unchanged. Before slurry preparation, LiPAA and TG were premixed and stirred overnight to promote complete solubilization of the polysaccharide. The slurry was subsequently prepared following the same general mixing route adopted in the previous trials, maintaining a SF of 50 wt.%, and coated with a wet thickness of 100 µm. The resulting laminate exhibited a highly homogeneous surface, with no visible defects or tensile stresses along the coating edges (***Figure 5.49***), indicating a significant improvement in slurry processability.

Figure 5.49 – Laminate produced using 92 wt.% of SC and LiPAA250 as binder with the addition of 1 wt.% of tragacanth gum

After the drying process, the electrodes were manually punched into 15 mm discs, as previously done. The measured dry thickness was 42 ± 2 µm, while the average weight was 15.32 ± 0.54 mg. From this value, the calculated average ML was 3.24 ± 0.28 mg cm^{-2} and the average areal capacity was 1.46 ± 0.13 mAh cm^{-2}.

The introduction of TG as an additive resulted in a marked deterioration of the electrochemical performance (***Figure 5.50***, ***Table 5.22***). The tested cells showed poor reproducibility, with large standard deviations particularly evident during long-term cycling. This behaviour may be attributed to an incomplete dispersion of the binder system in the slurry, leading to local particle aggregation and non-uniform electrochemical activity. During the formation cycles, the electrodes delivered an average first-cycle discharge capacity of 481.58 mAh g^{-1} and a corresponding charge capacity of 410.05 mAh g^{-1}, which led to an average CE of 85.62%. This value was lower than that observed for the other LiPAA-based formulations, indicating less efficient stabilization of the electrode-electrolyte interface. The rate capability test further confirmed the limited performance of this composition (***Figure 5.50b***). At 1C, the average discharge capacity remained only slightly above 300 mAh g^{-1}, while at 2C it decreased to 255.80 mAh g^{-1} with an associated increase in data dispersion among replicate cells.

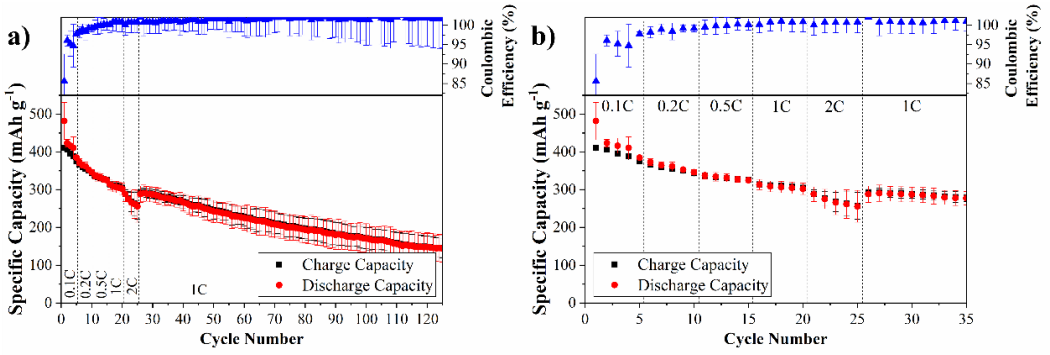

Figure 5.50 – Electrochemical characterization of the electrodes produced with 92 wt.% of SC and using LiPAA250 and TG as binders: a) Entire test; b) Focus on the rate capability test

Table 5.22 – Values of charge and discharge capacities, normalized by the electrode weight, and relative values of coulombic efficiency for some representative cycles for the electrodes produced with 92 wt.% of SC and using LiPAA250 and TG as binders

Cycle	***C-rate***	***Charge Capacity (mAh g^{-1})***	***Discharge Capacity (mAh g^{-1})***	***Coulombic Efficiency (%)***
1	*0.1C*	*410.05 ± 6.86*	*481.58 ± 49.55*	*85.62 ± 6.98*
2		*406.45 ± 4.24*	*423.08 ± 10.21*	*96.09 ± 1.41*
3		*395.95 ± 5.59*	*416.21 ± 20.07*	*95.23 ± 3.21*
10	*0.2C*	*343.20 ± 5.75*	*346.15 ± 6.87*	*99.16 ± 0.85*
15	*0.5C*	*325.48 ± 3.90*	*325.04 ± 8.58*	*100.16 ± 1.46*
20	*1C*	*304.61 ± 7.76*	*302.27 ± 15.39*	*100.86 ± 2.54*
25	*2C*	*257.19 ± 35.91*	*255.80 ± 42.14*	*100.83 ± 2.80*
30	*1C*	*289.17 ± 11.70*	*287.24 ± 19.39*	*100.80 ± 2.92*
50		*245.50 ± 23.96*	*242.00 ± 29.55*	*101.66 ± 2.80*
125		*145.49 ± 25.87*	*144.36 ± 35.87*	*101.96 ± 7.72*

Analysis of the voltage profiles (***Figure 5.51***) indicated lithiation and delithiation features consistent with the previously discussed SC behaviour. Nevertheless, the overall capacity remained lower, despite the contribution of the CVS than that of the other investigated formulations. These results suggest that even a small fraction of TG (1 wt.%) can significantly affect the electrochemical response of SC electrodes.

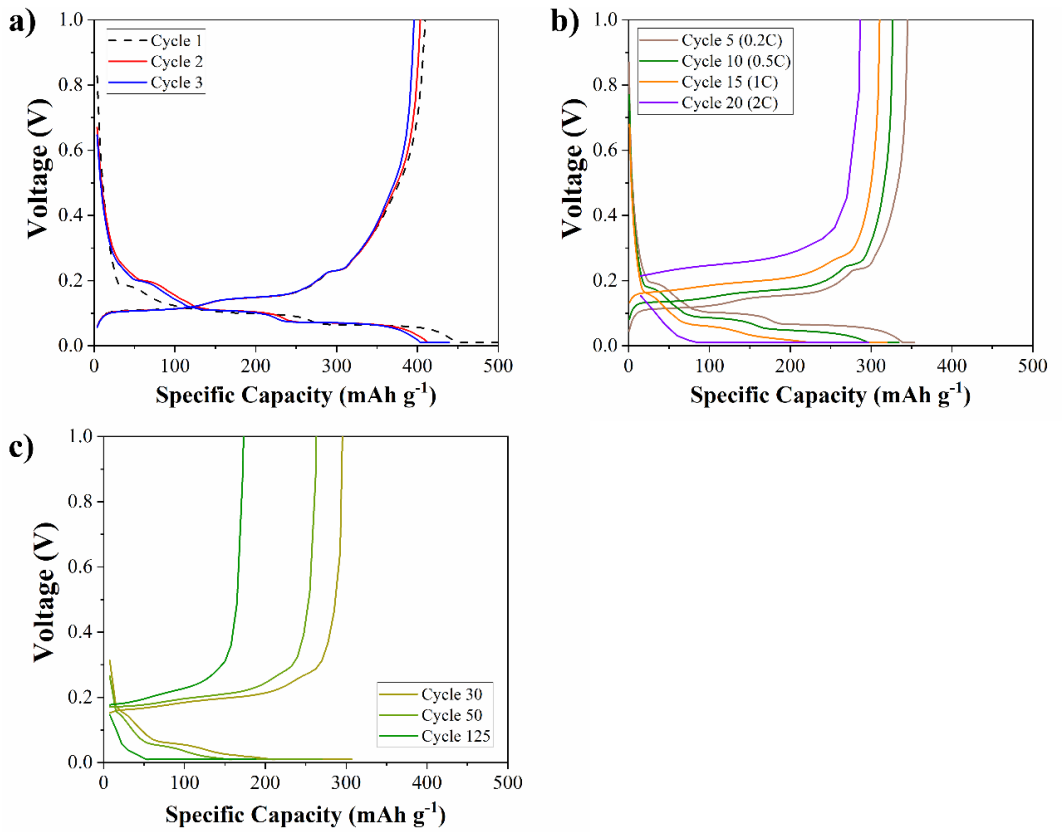

Figure 5.51 – Charge/discharge curves for some representative cycles of the electrodes produced with 92 wt.% of SC and using LiPAA250 and TG as binders: a) Forming cycles; b) Rate capability test; c) Long cycling

5.2.1.2.4.2. Laminate no. 10 (92 wt.%, LiPAA250_CGN)

Despite the improved coating quality obtained with TG, its poor electrochemical performance led to the investigation of CGN as an alternative natural polysaccharide additive in combination with LiPAA. The electrode formulation and production procedure were maintained unchanged, keeping a SF of 50 wt.%. The resulting laminate exhibited a highly homogeneous and smooth surface, with no visible coating defects (***Figure 5.52***), confirming the beneficial role of polysaccharide additives in improving slurry processability. After drying, fewer residual stresses were observed compared to the TG-based formulation. However, partial detachment of the electrode layer from the CC was noted during the manual punching of 15 mm discs, suggesting a reduction in adhesion strength that could negatively affect the electrochemical performance.

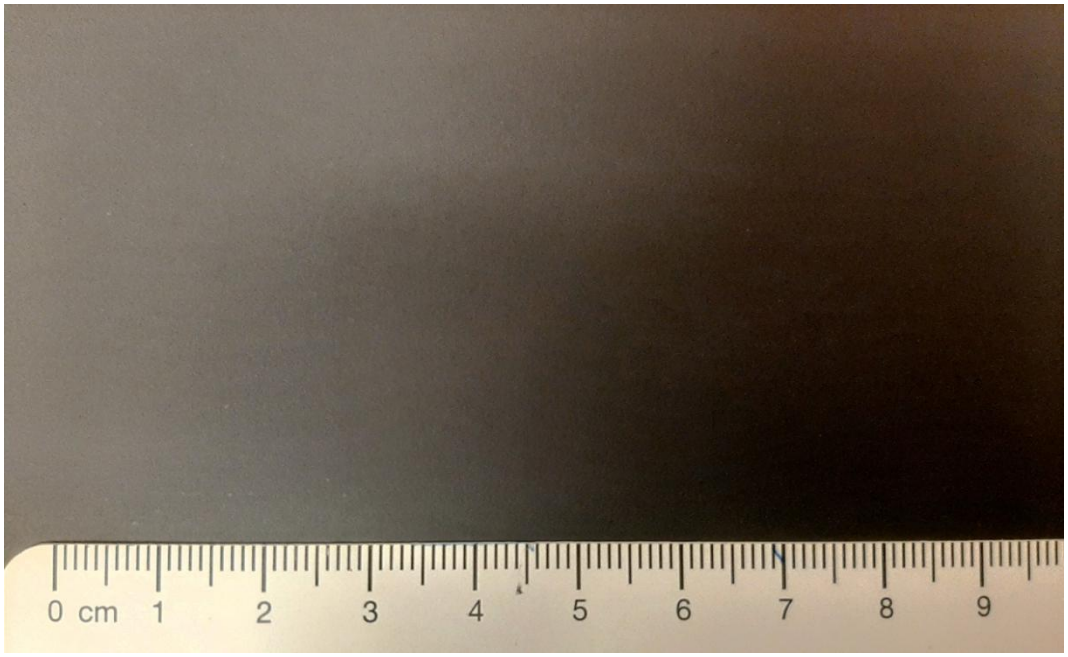

Figure 5.52 – Laminate produced with 92 wt.% of SC and using LiPAA250 as binder with the addition of 1 wt.% of Carrageenan

Despite this limitation, the electrode properties were measured. The dry thickness was 40 ± 1 µm, indicating very good dispersion and an exceptionally smooth surface compared with the other samples. The average ML value was 3.40 ± 0.18 mg cm^{-2} and a theoretical areal capacity of 1.53 ± 0.08 mAh cm^{-2}.

The addition of CGN affected the electrochemical performance even more severely than the addition of TG (***Figure 5.53***, ***Table 5.23***). The average charge and discharge capacities were the lowest among all the tested formulations, with values rapidly dropping below 300 mAh g^{-1}. During the forming step (***Figure 5.53b***), the discharge capacities showed extremely high variability, which resulted in equally high variability of the CE. Considering the long-term cycling test (***Figure 5.53a***), the capacity retention was 27.16%, the lowest value observed in this study, using SC as AM.

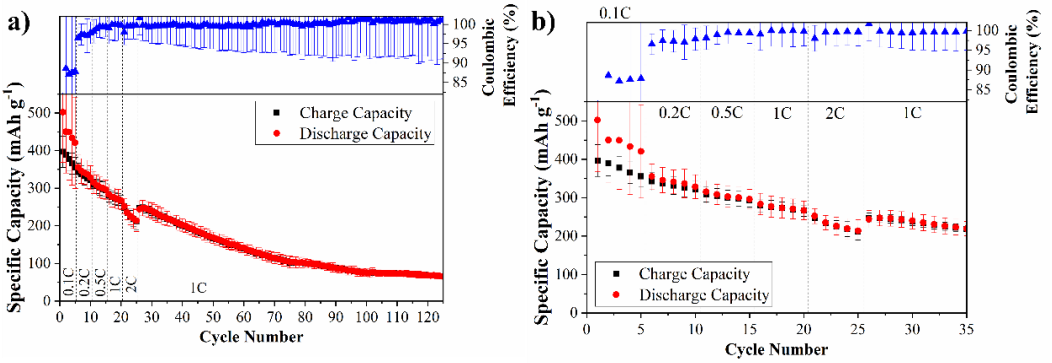

Figure 5.53 – Electrochemical characterization of the electrodes produced with 92 wt.% of SC and using LiPAA250 and CGN as binders: a) Entire test; b) Focus on the rate capability test

Table 5.23 – Values of charge and discharge capacities, normalized by the electrode weight, and relative values of coulombic efficiency for some representative cycles for the electrodes produced with 92 wt.% of SC and using LiPAA250 and CGN as binders

Cycle	***C-rate***	***Charge Capacity (mAh g^{-1})***	***Discharge Capacity (mAh g^{-1})***	***Coulombic Efficiency (%)***
1	*0.1C*	*396.83 ± 41.44*	*502.12 ± 133.75*	*81.24 ± 12.70*
2		*389.25 ± 32.53*	*450.28 ± 110.17*	*88.63 ± 13.62*
3		*377.77 ± 30.52*	*449.16 ± 127.40*	*87.20 ± 16.58*
10	*0.2C*	*321.05 ± 21.99*	*328.74 ± 30.93*	*97.82 ± 2.84*
15	*0.5C*	*293.98 ± 18.12*	*296.23 ± 25.59*	*99.39 ± 2.60*
20	*1C*	*266.00 ± 14.83*	*267.22 ± 24.31*	*99.76 ± 3.67*
25	*2C*	*212.50 ± 22.42*	*213.84 ± 29.20*	*99.67 ± 3.56*
30	*1C*	*238.12 ± 10.45*	*240.13 ± 21.01*	*99.42 ± 4.38*
50		*167.40 ± 4.83*	*168.69 ± 14.79*	*99.58 ± 5.87*
125		*65.75 ± 2.34*	*65.23 ± 5.92*	*101.37 ± 10.26*

The deeper investigation of the charge and discharge curves (***Figure 5.54***) allowed to observe how the lithiation and delithiation processes were performed correctly but, especially during the long-term cycling (***Figure 5.54c***) the lithiation plateaus were absent from cycle 30, and the CVS were not sufficient to contribute to the capacity to reach the same values as before. As for the TG, also in this case, the addition of CGN, even in so small quantities, badly affected the electrochemical results. The poor electrochemical results were mainly related to the detachments observed during the punching step; in fact, the losses in adhesion during the testing are one of the main common causes of poor performance.

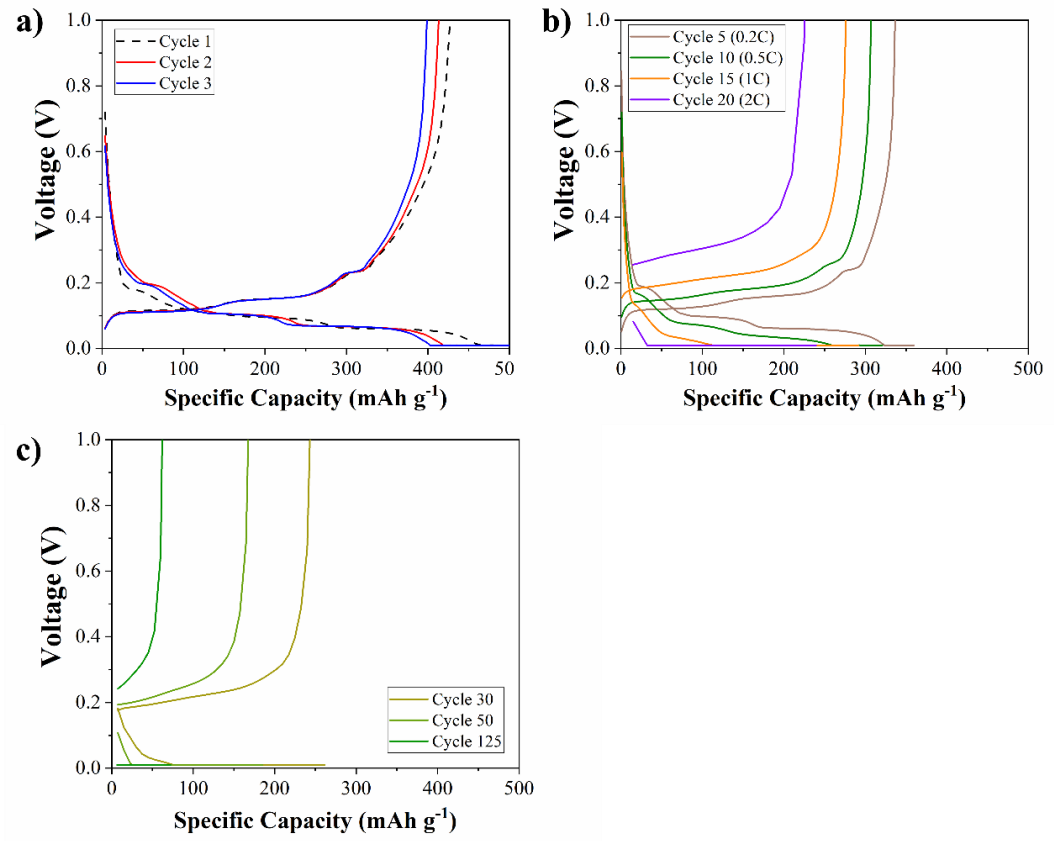

Figure 5.54 – Charge/discharge curves for some representative cycles of the electrodes produced with 92 wt.% of SC and using LiPAA250 and CGN as binders: a) Forming cycles; b) Rate capability test; c) Long cycling

5.2.1.3. Processing-performance correlation at laboratory scale

Table 5.15 collects and summarizes the characteristics of the laminates described in the previous paragraphs. Laminate no. 1 (92%,CMC) presented good homogeneity in terms of dry thickness, which was reflected in small deviations from the average value, also for the ML and all related characteristics. A greater difference was instead observed in the laminate no. 3 (95%, CMC, where the ML value showed an error more than double that of laminate no. 1 (92%, CMC). In addition, despite the increased SF for this preparation, the expected result was a higher ML; however, this expectation was not satisfied, indicating that, also in this case, the internal homogeneity of the slurry was quite poor.

As previously described, the use of PAA alone, independently from the MW, resulted in electrodes of such poor quality that no further characterizations were possible. When LiPAA (both MWs) was introduced as a binder, smaller differences were observed in the electrode characteristics. Interestingly, the increase of the AM between laminates no. 6 (92%, LiPAA250) and no. 7 (95%, LiPAA250) led to a decrease in both dry thickness and ML. This counterintuitive behavior could be due to a non-controlled variation of the doctor-blade gap, due to the manual setting of the deposition thickness. In fact, when LiPAA450 was used

as the binder in laminate no. 8, the measured dry thickness was slightly higher, as well as the ML. This behavior could be related to the higher MW of PAA, which in this case favored the formation of a thicker electrode. Consequently, both the ML and the areal capacity were higher due to the higher amount of AM in the electrode. In addition, the use of LiPAA resulted in a clear improvement in process reproducibility, as indicated by the reduced dispersion of dry thickness and ML values across different laminates, suggesting a more robust and controllable coating process.

Interestingly, the addition of both natural polysaccharides in laminate no. 9 (92%, LiPAA250_TG) and laminate no. 10 (92%, LiPAA250_CGN) led to a decrease in all the measured values compared to laminate no. 6, suggesting a reduction in slurry viscosity. The reduction in dry thickness and ML observed with the addition of natural polysaccharides suggested a predominant rheological effect, leading to improved coating uniformity while partially reducing the structural contribution of the binder network, with a consequent detrimental impact on the electrochemical performance (***Figure 5.55***).

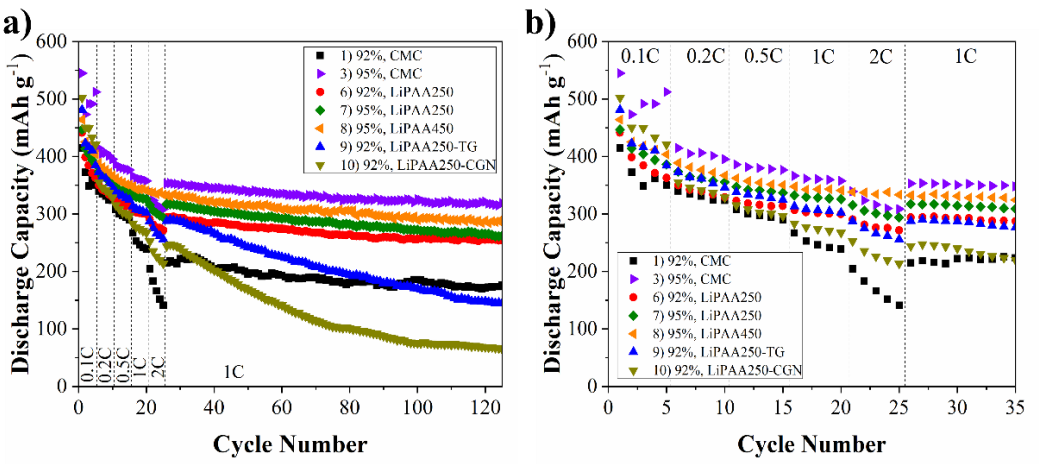

Figure 5.55 – Comparison of the average discharge capacities of the electrodes produced at laboratory level: a) Entire test; b) Focus on the rate capability test

In ***Figure 5.55*** a comprehensive comparison of the electrochemical results is reported, where the average discharge capacity values are collected in the same graph. For a cleaner data interpretation, the statistical error bars are not reported. Excluding the electrodes produced with the natural polysaccharides, CMC-based slurries presented both the best and the worst results. As described during the production process, the laminate no. 1 (92%, CMC) presented a poor quality surface that consequently led to the poor electrochemical results. The laminate no. 3 (95%, CMC) was still characterized by some defects at the edges, but the good homogeneity in the central region led to the best electrochemical results. All the laminates prepared with the LiPAA presented similar performance, with a slight increase in capacity when the AM was increased from laminate no. 6 (92%, LiPAA250) to laminate no. 7 (95%, LiPAA250). A comparable capacity increase

was observed when the MW of LiPAA was increased from 250.000 g mol^{-1} to 450.000 g mol^{-1} (laminate no. 8).

These results indicate that, for silicon-based anodes, binder chemistry plays a more dominant role than the SF in determining laminate quality, as variations in SF alone did not result in systematic improvements in ML or homogeneity.

5.2.2. Pilot-line manufacturing study

Similarly to graphite-based electrodes, the scale-up of silicon-based electrodes was carried out using the planetary mixer and the roll-to-roll coating machine with two representative slurries selected for this study. The first one was based on CMC and SBR (laminate no. 3), to have a proper comparison with the graphite anodes. The second slurry chosen was the one with the LiPAA450 (laminate no. 8), for its higher electrochemical performance within the LiPAA family (***Figure 5.55***). The slurry composition was maintained the same as at the laboratory level (95:2:1:2), while, thanks to the automatic slurry feeder of the roll-to-roll coating machine, a systematic thickness screening was possible. This part of the study aimed to evaluate a wider range of thicknesses and how they affected the electrode characteristics, such as ML.

However, as expected, the use of different facilities negatively affected electrode preparation, even though the laboratory-scale electrodes had shown good performance. Electrode production at pilot-line level was acceptable; however, further optimization is still required when production facilities change.

5.2.2.1. Electrode preparation and electrochemical validation at pilot scale of the reference CMC-based slurry

The first trial was based on the same composition as laminate no. 3, using the composition of 95 wt.% SC, 2 wt.% C45, 1 wt.% CMC and 2 wt.% SBR. As previously optimized at laboratory level, the SF was set to 50%, with an increase of 10% compared to the graphite-based formulation. As expected, the scale-up required an increase of the total amount of materials, reaching 50 g. The mixing step was based on the same protocol already optimized at laboratory level, with a multistep process based on the sequential addition of all the components:

1) First, 0.5 g of CMC was dissolved in 49 mL of MilliQ water and kept stirring at maximum speed of 600 rpm for 1 hour.
2) Second, 1 g of C45 was added and kept stirring for 1 hour at the same speed.
3) Third, the SC was slowly added by hand in a total amount of 47.5 g to facilitate dispersion; after preliminary manual mixing and once a homogeneous slurry was obtained, the planetary mixer was kept stirring at the maximum speed for 1 hour.

4) Finally, 2.0 g of SBR (solid content: 50%) was added. For this step, the speed was reduced to 100 rpm to avoid rubber degradation and mixing was maintained for 30 minutes.
5) For the final 5 minutes, the vacuum was turned on to favor slurry degassing.

For the coating step, the procedure of operating with the R2R was the same as that adopted for graphite anodes: different thickness (100 µm, 90 µm, 80 µm and 70 µm, ***Figure 5.56***) were imposed to evaluate the relation between the imposed wet thickness and the ML of the electrodes. The imposed coating speed was 300 mm min^{-1} and the in-line oven temperature was kept constant at 80°C.

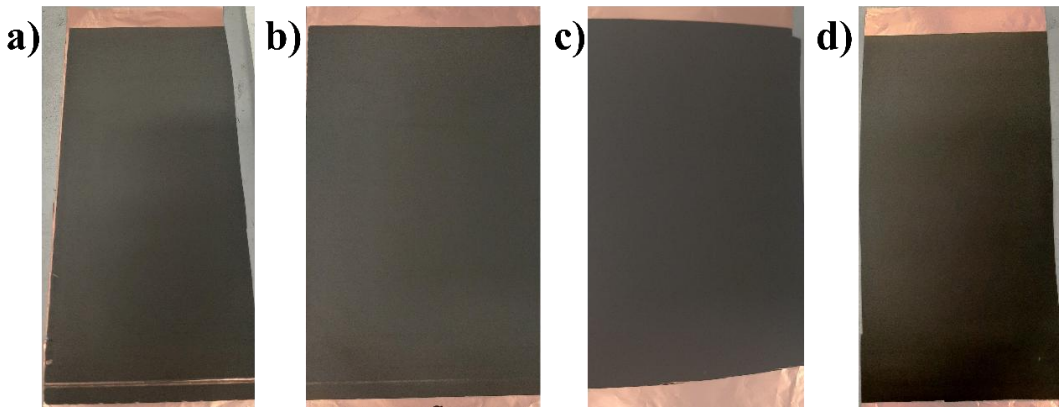

Figure 5.56 – Laminates produced at the pliot plant with the CMC-SBR composition at different thicknesses: a) 100 µm; b) 90 µm; c) 80 µm; d) 70 µm

Regardless of coating thickness, all the electrodes presented a highly homogenous surface without any evident defects. After the drying procedure, the electrodes were punched into discs with a diameter of 15 mm using a manual EL-Cell puncher. For better characterization, the electrodes were punched randomly along the entire electrode laminate to guarantee a proper analysis. The average ML values and the relative average areal capacities are reported in ***Table 5.24***. Regarding the thickness, all the electrodes presented quite homogeneous values, with statistical errors between 1 and 3 µm. On the other hand, the ML values were more widespread, with the wet thickness of 100 µm leading to a large variation of 0.59 mg cm^{-2}. Surprisingly, the wet thickness of 90 µm resulted in the narrowest range of variation of 0.09 mg cm^{-2}**.**

Table 5.24 – Summary of the electrode characteristics (dry thickness, ML, and areal capacity) as a function of the roll gap applied during the coating step for electrodes produced at pilot-line scale using CMC and SBR as binders.

Wet thickness Deposition (µm)	***Dry thickness (µm)***	***Mass Loading (mg cm^{-2})***	***Areal Capacity (mAh cm^{-2})***
100	*70 ± 1*	*6.26 ± 0.59*	*2.81 ± 0.26*
90	*60 ± 2*	*5.44 ± 0.09*	*2.45 ± 0.04*
80	*53 ± 1*	*4.57 ± 0.39*	*2.06 ± 0.17*
70	*48 ± 3*	*4.22 ± 0.46*	*1.90 ± 0.21*

Both the wet thicknesses of 80 µm and 70 µm presented higher variations than that of 90 µm. The motivation behind this behavior could be related to two aspects: firstly, every time that the thickness was changed, the variation was manually set, which can greatly affect the final result of the doctor-blade deposition, even if, in the case of the pilot line, the thickness should be more precise. Secondly, it is possible that the planetary mixer does not represent the best choice for this type of electrodes and that some agglomerations, not detectable, were still present. The inhomogeneous distribution of these agglomerates led to uneven coating on the CC.

The electrodes were assembled in CR2032 coin-cell configuration, following the same procedure used for laboratory-scale electrodes. All electrochemical tests were performed under identical conditions to enable a direct comparison with laboratory-scale results. An identical cycling protocol was employed, comprising five formation cycles, a rate capability test, and long-term cycling (***Table 5.16***). In addition, CV measurements were conducted to investigate the electrochemical reaction mechanisms.

For the electrochemical characterization of the electrodes produced at the pilot line using CMC and SBR binders, the electrodes with a wet thickness of 80 µm were selected for the electrochemical testing, because the areal capacity value of 2.06 mAh cm^{-2} represents a value in line with commercial values [397].

The electrochemical performance (***Figure 5.57***, ***Table 5.25***) was generally consistent with that observed at laboratory scale for the same formulation (laminate no. 3). However, a higher variability among replicate cells was evident, particularly during the formation cycles, leading to large fluctuations in CE. The first cycle showed an average discharge capacity of 511.16 mAh g^{-1} and a charge capacity of 415.74 mAh g^{-1}, corresponding to an average CE of 83.85% and an irreversible capacity loss exceeding 16%. During the rate capability test (***Figure 5.57b***), the dispersion among replicates decreased and the electrodes maintained acceptable performance even at high current density, reaching average discharge capacities close to 290.36 mAh g^{-1} at 2C. In contrast, during long-term cycling the variability progressively increased again, suggesting limited process robustness after scale-up. The calculated capacity retention was 86.11%.

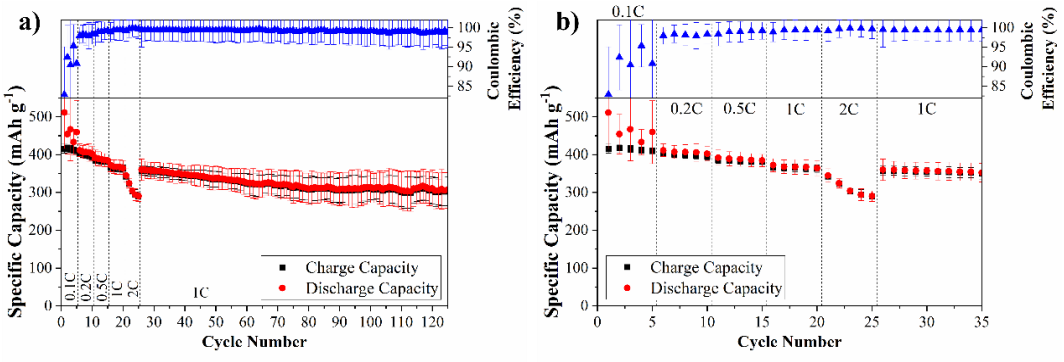

Figure 5.57 – Electrochemical characterization of the electrodes produced at the pilot line, with 95 wt.% of SC and using CMC and SBR as binders: a) Entire test; b) Focus on the rate capability test

Table 5.25 – Values of charge and discharge capacities, normalized by the electrode weight, and relative values of coulombic efficiency for some representative cycles for the electrodes produced at the pilot line, with 95 wt.% of SC and using CMC and SBR as binders

Cycle	***C-rate***	***Charge Capacity (mAh g^{-1})***	***Discharge Capacity (mAh g^{-1})***	***Coulombic Efficiency (%)***
1	*0.1C*	*415.74 ± 11.94*	*511.16 ± 95.37*	*83.85 ± 12.24*
2		*416.89 ± 9.95*	*454.41 ± 52.24*	*92.38 ± 8.36*
3		*415.17 ± 9.14*	*466.97 ± 83.00*	*90.47 ± 13.21*
10	*0.2C*	*395.23 ± 8.57*	*402.12 ± 19.07*	*98.37 ± 2.53*
15	*0.5C*	*381.46 ± 7.94*	*384.55 ± 16.31*	*99.26 ± 2.20*
20	*1C*	*362.24 ± 10.53*	*364.32 ± 19.94*	*99.52 ± 2.62*
25	*2C*	*289.29 ± 12.64*	*290.36 ± 13.82*	*99.67 ± 2.45*
30	*1C*	*354.87 ± 11.36*	*357.44 ± 21.21*	*99.39 ± 2.79*
50		*335.31 ± 20.82*	*338.17 ± 31.52*	*99.36 ± 3.24*
125		*302.95 ± 37.52*	*307.78 ± 49.92*	*98.87 ± 4.07*

Analysis of the voltage profiles (***Figure 5.58***) confirmed behaviour consistent with that previously discussed for laboratory-scale electrodes, with no additional features requiring detailed discussion. Similarly, CV measurements (***Figure 5.59***) showed trends comparable to those already described for laminate no. 3, confirming that the main electrochemical processes remained unchanged after scale-up.

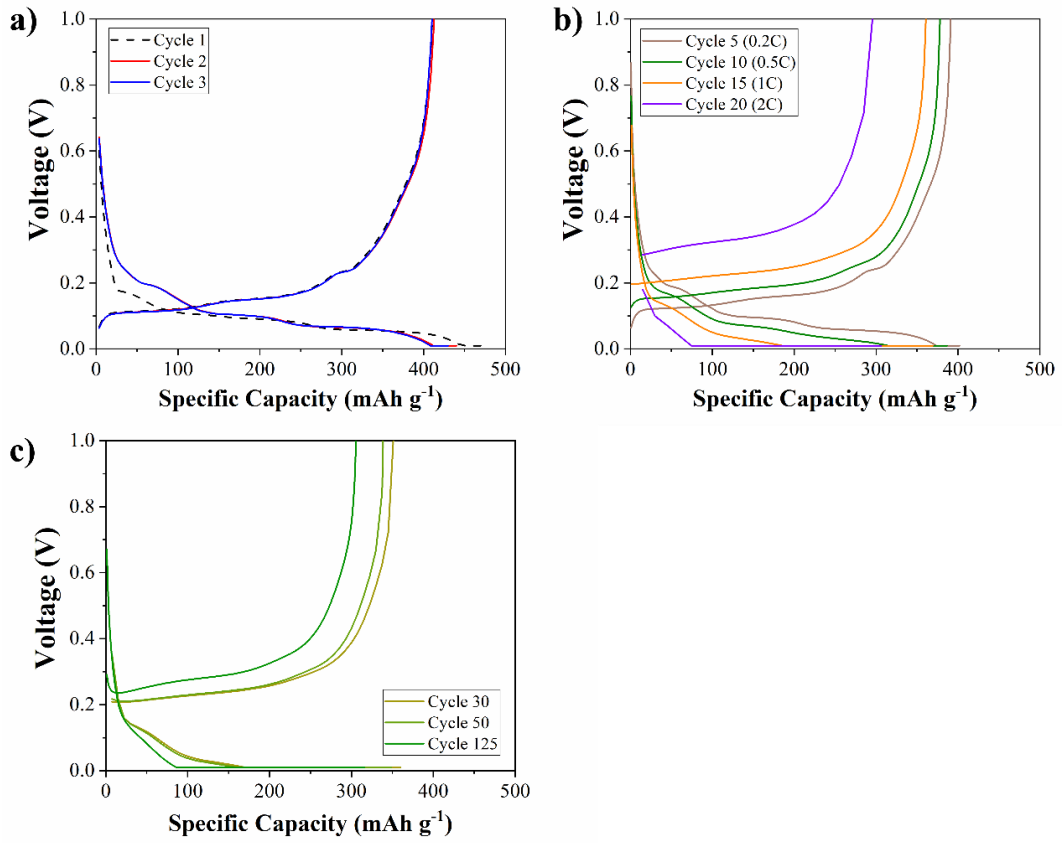

Figure 5.58 – Charge/discharge curves for some representative cycles of the electrodes produced at pilot line with 95 wt.% of SC and using CMC and SBR as binders: a) Forming cycles; b) Rate capability test; c) Long cycling

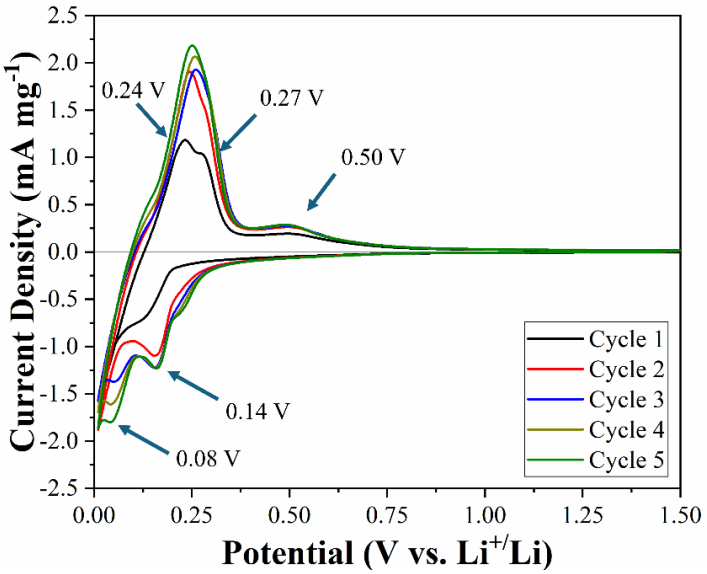

Figure 5.59 – CV test performed on 5 cycles for the electrodes produced at pilot line with 95 wt.% of SC and using CMC and SBR as binders

5.2.2.2. Li-PAA450-based slurry

The second formulation selected for the pilot line scale-up was the LiPAA450 based slurry, corresponding to laminate no. 8, composed of 95 wt.% SC, 2 wt.% carbon black C45 and 3 wt.% LiPAA450. Compared with the CMC–SBR system, slurry preparation was simplified due to the use of a single binder, which reduced the number of mixing steps. Because of the limited availability of AM, a smaller batch size was adopted, corresponding to a total solid content of 30 g while maintaining a SF of 50%. The mixing procedure followed the same sequential approach previously optimized, including binder dilution, conductive carbon dispersion, progressive addition of SC and final vacuum degassing.

Coating was performed under the same pilot line conditions used for the CMC–SBR formulation, with imposed wet thicknesses of 100, 90 and 80 µm, a coating speed of 300 mm min^{-1} and an in line drying temperature of 80 °C. The resulting laminates exhibited smooth and visually homogeneous surfaces (***Figure 5.60***).

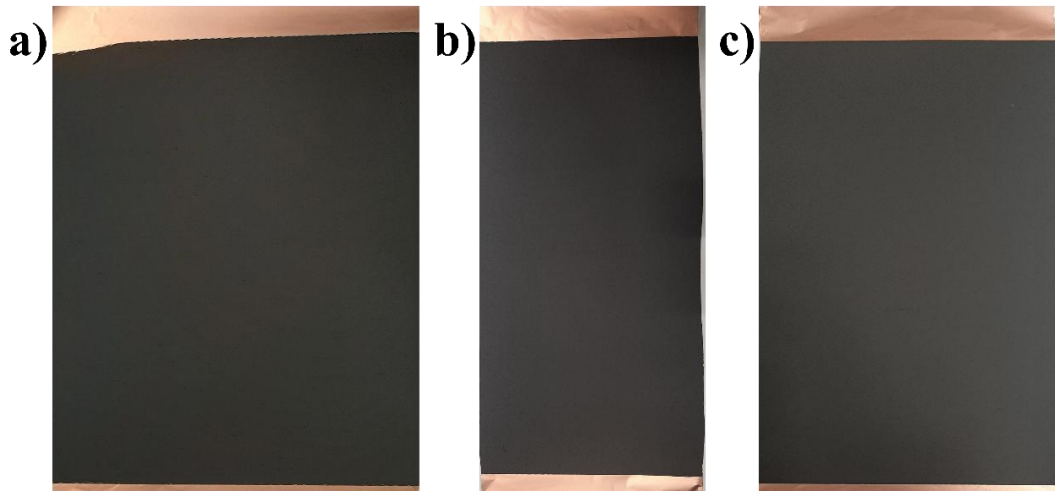

Figure 5.60 – Laminates produced at the pilot line with the LiPAA450 binder at different thicknesses: a) 100 µm; b) 90 µm; c) 80 µm

However, after drying, severe mechanical issues emerged during electrode punching. Significant delamination occurred along the entire electrode circumference (***Figure 5.61***), indicating insufficient adhesion and mechanical compliance of the coating. This behaviour can be partly attributed to the higher dry layer thickness compared with the CMC-SBR electrodes, which may promote cracking and interfacial failure. In addition, the intrinsic rigidity of PAA based binders, even after lithiation, can lead to reduced flexibility and poorer electrode integrity [444].

Figure 5.61 – Example of one 15 mm disc electrodes punched from the laminate produced with 80 µm wet slurry, the signs of the detachments are very evident along the borders.

The electrode characteristics are collected in ***Table 5.26***. Although the higher ML and areal capacity values were suitable for electrochemical testing, the extensive surface detachment prevented reliable cell assembly. Consequently, these electrodes were not further electrochemically investigated. Overall, this result highlights that formulations providing excellent laboratory-scale electrochemical performance may still present critical mechanical limitations during scale-up, emphasizing the importance of balancing electrochemical properties with processability and structural robustness.

Table 5.26 – Summary of the electrode characteristics (dry thickness, ML, and areal capacity) as a function of the roll gap applied during the coating step for electrodes produced at pilot-line scale using LiPAA450 as binders.

Wet thickness Deposition (µm)	***Dry thickness (µm)***	***Mass Loading (mg cm^{-2})***	***Areal Capacity (mAh cm^{-2})***
100	*75 ± 1*	*6.76 ± 0.21*	*3.04 ± 0.10*
90	*68 ± 1*	*6.20 ± 0.09*	*2.79 ± 0.04*
80	*65 ± 1*	*5.66 ± 0.11*	*2.55 ± 0.05*

5.2.3. Comparison of manufacturing behaviour at laboratory and pilot-line scale

The direct comparison between the production processes was possible thanks to a first comparison of the electrode characteristics (***Table 5.27***): as for the graphite anode, the different coating procedures (doctor blade at laboratory level vs reverse comma at pilot line) greatly affected the electrode characteristics, even when keeping the same wet thickness of 100 µm, resulting in significantly different electrode characteristics. Starting with the CMC-SBR system, with the doctor blade, the average ML was 3.76 mg cm^{-2}, but at the pilot-line, this value almost doubled, reaching 6.26 mg cm^{-2}. The same was observed for the LiPAA450 electrodes: in fact, at the laboratory level the average ML was 4.41 mg cm^{-2} but at the pilot line, it reached 6.76 mg cm^{-2}. Even by reducing the thicknesses by 40 µm, with the R2R process, a deposition thickness of 70 µm still resulted in values quite too high to reach comparable results.

Table 5.27 – Comparison of the electrode characteristics (dry thickness, ML and areal capacity) based on CMC and SBR composition, using different facilities

Laminate no.	***Wet thickness Deposition (µm)***	***Dry Thickness (µm)***	***Mass Loading (mg cm^{-2})***	***Areal Capacity (mAh cm^{-2})***
		Laboratory Level		
3 (CMC-SBR)	*100*	*--*	*3.76 ± 0.20*	*1.69 ± 0.09*
8 (LiPAA450)	*100*	*57 ± 2*	*4.41 ± 0.30*	*1.98 ± 0.13*
		Pilot line		
CMC-SBR	*100*	*70 ± 1*	*6.26 ± 0.59*	*2.81 ± 0.26*
	90	*60 ± 2*	*5.44 ± 0.09*	*2.45 ± 0.04*
	80	*53 ± 1*	*4.57 ± 0.39*	*2.06 ± 0.17*
	70	*48 ± 3*	*4.22 ± 0.46*	*1.90 ± 0.21*
LiPAA450	*100*	*75 ± 1*	*6.76 ± 0.21*	*3.04 ± 0.10*
	90	*68 ± 1*	*6.20 ± 0.09*	*2.79 ± 0.04*
	80	*65 ± 1*	*5.66 ± 0.11*	*2.55 ± 0.05*

The comparison between the electrochemical results is reported in ***Figure 5.62*** and ***Table 5.28***,where the discharge capacity of the electrodes produced with laminate no. 3, with 95% SC and CMC and SBR as binders, is compared with the same composition produced at the pilot line. The two production processes showed almost overlapping behavior, independently of the different ML of the electrodes assembled. The main differences were perceived during the formation cycles, where the two production processes led to high variability independently of the production process used for the electrode production. Considering that this effect was less marked for LiPAA binder, effectively the CMC-SBR composition may not represent the best solution for silicon-based electrodes.

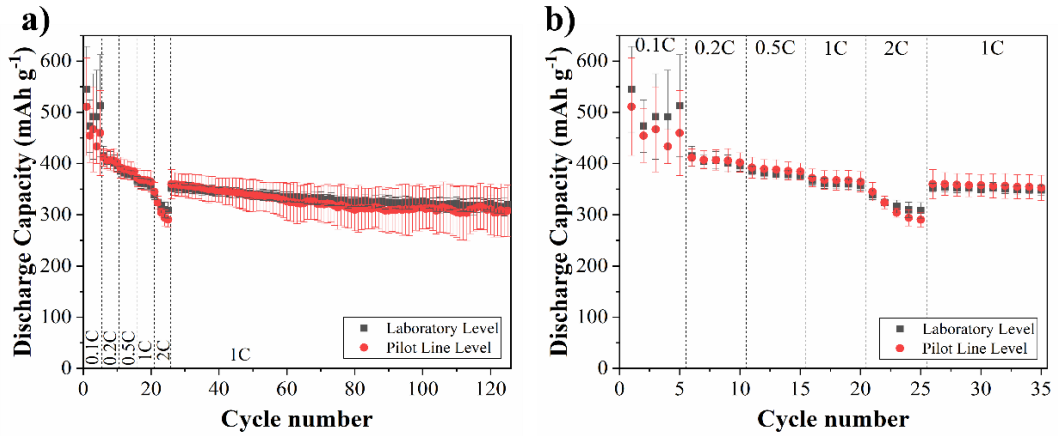

Figure 5.62 – Comparison of the discharge capacity of the CMC-SBR based electrodes depending on the two production processes

Table 5.28 – Comparison of the discharge capacity values of the CMC-SBR based electrodes depending on the two production processes

Cycle	***C-rate***	***Laboratory Level Discharge Capacity (mAh g^{-1})***	***Pilot line Level Discharge Capacity (mAh g^{-1})***
1		*544.89 ± 83.82*	*511.16 ± 95.37*
2	*0.1C*	*473.32 ± 51.08*	*454.41 ± 52.24*
3		*491.69 ± 83.39*	*466.97 ± 83.00*
10	*0.2C*	*395.38 ± 10.54*	*402.12 ± 19.07*
15	*0.5C*	*376.66 ± 8.89*	*384.55 ± 16.31*
20	*1C*	*357.70 ± 10.07*	*364.32 ± 19.94*
25	*2C*	*308.63 ± 15.34*	*290.36 ± 13.82*
30		*350.57 ± 7.54*	*357.44 ± 21.21*
50	*1C*	*339.29 ± 9.62*	*338.17 ± 31.52*
125		*318.99 ± 7.02*	*307.78 ± 49.92*

5.2.4. Key outcomes and implications for silicon-anode manufacturability

This work investigated the manufacturing and electrochemical behaviour of SC anodes containing approximately 10 wt.% silicon and processed using water-based binder systems, with particular attention to binder chemistry and scalability from laboratory to pilot-line production. At the laboratory scale, binder chemistry was identified as the dominant factor governing slurry homogeneity and coating quality, which directly reflects on electrochemical performance. The conventional CMC–SBR binder system, although suitable for graphite anodes, showed clear limitations for silicon-based electrodes, particularly during formation cycles, where parasitic reactions and high variability were observed. While acceptable capacity retention was achieved in some cases, the overall electrochemical results remained insufficient. PAA used as a single binder, regardless of MW, resulted in severe rheological issues, leading to phase separation during coating and highly inhomogeneous electrodes. These results confirmed that chemical affinity alone is not sufficient to ensure adequate slurry processability. In contrast, pre-lithiation of PAA to form LiPAA significantly improved slurry processability, electrode homogeneity, and consequently, electrochemical performance. Both LiPAA250 and LiPAA450 enabled stable cycling and initial CE around 89%, with the highest MW favoring improved high performance during the rate capability test at the expense of less reproducibility between different samples during long-term cycling. The addition of natural polysaccharides as binder additives did not lead to performance improvements. Despite enhanced coating uniformity, both TG and CGN negatively affected electrode adhesion and cycling stability, resulting in poor capacity retention and large variability between samples. These findings indicate that additional natural polysaccharides should be explored in combination with LiPAA to improve electrode performance.

Scale-up experiments highlighted the challenges associated with transferring laboratory-optimized formulations to pilot-line production. Differences in coating technology led to substantial variations in ML, even at comparable wet thicknesses, confirming the strong process sensitivity of the investigated systems. In this context, Li-PAA-based formulations showed markedly lower robustness to process variations compared to CMC-SBR systems, exhibiting a higher occurrence of mechanical defects on the electrode surface. These results indicate that, when processed under different manufacturing facilities and coating configurations, Li-PAA does not yet represent a sufficiently reliable binder choice for pilot-scale application. Further systematic investigations are therefore required to better understand its rheological behavior and adhesion mechanisms, under pilot-scale conditions, to improve its scalability and practical applicability.

Overall, the results demonstrate that, for silicon-based anodes, binder chemistry plays a critical role in determining electrode quality and electrochemical performance. LiPAA emerges as the most promising binder among those investigated, at least at laboratory level; however, further optimization at pilot-scale of processing conditions and long-term cycling stability are required for industrial applicability.

5.3. Development of silicon anodes within the GIGAGREEN project: electrode production optimization process and laser-treated current collectors

To further investigate the challenges associated with the manufacturing of silicon-based electrodes, a second SC material was considered within the framework of the GIGAGREEN European project (***Figure 5.63*** [352]). The objective was to compare its electrochemical performance with previously investigated systems and evaluate the transferability of the electrode production process under different material design conditions. SCs can exhibit markedly different rheological behaviour during slurry preparation and distinct electrochemical responses, making process optimization a critical aspect when targeting scalable manufacturing.

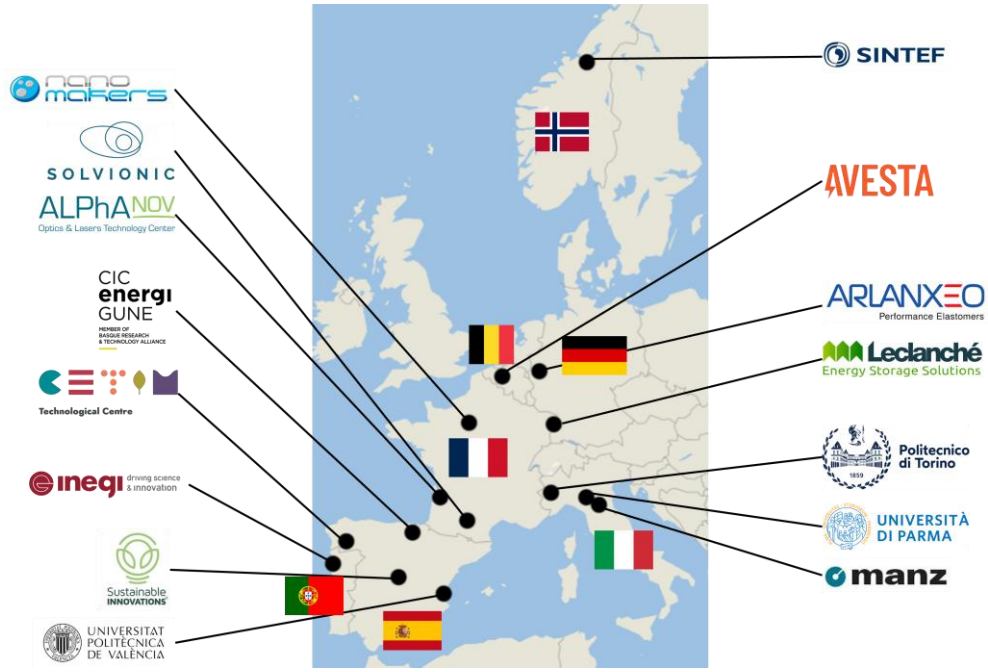

Figure 5.63 – Map of the European partners involved in the GIGAGREEN project [352].

Within the GIGAGREEN project, Politecnico di Torino was responsible for optimizing the laboratory-scale production of silicon-based anodes and for validating their electrochemical performance, to support the subsequent transfer of the developed processing conditions to larger-scale facilities operated by other partners. Particular attention was devoted to defining suitable slurry preparation protocols, coating conditions and interface engineering strategies compatible with industrial processing requirements.

The first phase of the work focused on the optimization of the electrode manufacturing procedure. Although an initial protocol was provided by the AM supplier Nanomakers [445], its direct implementation under the available laboratory conditions did not ensure adequate electrode quality. A systematic adjustment of slurry formulation and coating parameters was therefore required to achieve a stable and reproducible process. Electrochemical characterization was carried out through galvanostatic CC-CV cycling and CV, allowing the reproducibility of the optimized electrodes to be verified versus the reference results obtained at the supplier's facilities.

Once a reliable electrode formulation had been established, the investigation was extended to interface engineering strategies aimed at further improving electrode performance. In particular, the second phase addressed the use of laser-treated Cu CC, developed in collaboration with project partners. ALPhANOV [446] performed the laser surface treatments, while the Università di Parma [447] carried out the corresponding surface modelling and post-processing analyses. This stepwise approach enabled the specific contribution of each modification to be clearly identified. The main outcomes of this activity were subsequently reported in a dedicated research publication [206].

5.3.1. Process optimization at laboratory scale

The AM used in this study was supplied by Nanomakers. The material consists of a pitch-derived carbon-graphite Si/C/Gr composite with a silicon content of 12 wt.% [448]. Silicon nanoparticles and graphite particles are embedded in an amorphous carbon matrix formed by pitch pyrolysis, which becomes soft carbon, with crystalline silicon particles uniformly coated by an approximately 2 nm amorphous carbon layer [448].

The optimization was performed at laboratory scale, and only a limited number of trials were sufficient to reach the desired performance. The main challenge was associated with the dispersion of the SC material and the resulting slurry rheology, which strongly affected coating homogeneity and electrode integrity. The composition suggested by Nanomakers was 90:2:4:4 (wt.%):

- 90 wt.%: amount of AM, in this case the SC supplied by Nanomakers [448].
- 2 wt.%: amount of CA, in this case the carbon black C65 (Imerys Timcal). The use of C65, instead of C45, which is widely regarded as one of the most suitable conductive additives for water-based applications [355], was suggested by the supplier, who indicated a better compatibility with the AM.
- 4 wt.%: amount of CMC 2200 (Daicel Corporation).
- 4 wt.%: amount of SBR supplied by Arlanxeo [449], one of the project partners, containing 40 wt.% solid content; the detailed chemical composition is not disclosed.

The optimization strategy was based on the progressive modification of mixing conditions, SF and coating parameters, to identify the key factors governing electrode homogeneity and reproducibility. Compared to the initial procedure suggested by the partner, the optimization process required several adjustments, mainly consisting of an extension of the mixing time and an increase in the solid fraction from approximately 25 wt.% to 33 wt.%. This modification was followed by a corresponding reduction in the wet coating thickness in order to achieve the targeted electrode characteristics. Most of the experimental effort was therefore devoted to improving slurry dispersion and coating uniformity, also considering the different mixing facilities available. A qualitative overview of the optimization pathway, including the main processing changes adopted and the corresponding observations in terms of coating homogeneity and electrode manufacturability, is reported in ***Table 5.29***. As can be observed, the initial trials resulted in poor coating quality, highlighting the need for progressive adjustments to obtain reproducible and defect-free laminates.

Table 5.29 – Summary of the experimental trials carried out to optimize the slurry formulation and coating parameters of Gigagreen SC anodes at laboratory scale. The table highlights the evolution of binder composition, SF and processing conditions, together with the main qualitative outcomes observed in terms of coating homogeneity and electrode manufacturability.

Trial Number	***Solid Fraction***	***Wet thickness coating (µm)***	***Changes adopted***	***Main conclusions***
1	25%	220	Reference trial, performed with a magnetic stirrer.	Scarce homogeneity, with high amount of clumps and poor adhesion with the CC.
2	25%	220	Increase of the total amount of material to favor the use of disperser mixer.	Still scarce homogeneity, with high amount of clumps.
3	33%	100	Increase of the SF to improve the mixing step.	No evident improvement was observed.
4	33%	100	Increase of the total amount of material to favor the use of disperser mixer. Elongation of the mixing time after the addition of CMC, SC and SBR.	Still high inhomogeneities but smaller clumps on the surface.
5	33%	100	Further elongation of the mixing time after the addition of SBR.	Good homogeneous and smooth surface without visible clumps.
6	33%	120	Increase of wet thickness coating to reach the ML project target.	Good homogeneous and smooth surface without visible clumps. ML reached the targeted value.

For each laboratory trial, the produced electrodes were directly characterized in order to evaluate the effect of the selected processing conditions on their physical properties and estimated electrochemical performance, by the calculation of the areal capacity. A quantitative overview of these results is reported in ***Table 5.30*** and complements the qualitative description of the optimization pathway summarized in ***Table 5.29***. Further details on the individual trials are discussed in the following sections.

Table 5.30 – Summary of the laboratory-scale trials for Gigagreen SC anodes, reporting solid fraction, coating thickness and the resulting electrode properties. The areal capacity was calculated based on the material theoretical capacity.

Trial Number	***Solid Fraction (%)***	***Wet Thickness (µm)***	***Dry Thickness (µm)***	***Mass Loading (mg cm^{-2})***	***Areal Capacity (mAh cm^{-2})***
1	25%	220	*63 ± 4*	*3.43 ± 0.38*	*2.06 ± 0.23*
2	25%	220	--	--	--
3	33%	100	--	--	--
4	33%	100	*37 ± 4*	*2.29 ± 0.20*	*1.38 ± 0.12*
5	33%	100	*52 ± 2*	*3.04 ± 0.20*	*1.82 ± 0.12*
6	33%	120	*48 ± 1*	*3.33 ± 0.09*	*2.00 ± 0.06*

The declared theoretical capacity of this material was 700 mAh g^{-1} while the declared practical capacity was 600 mAh g^{-1}. These values, provided by Nanomakers, were based on theoretical calculations derived from the silicon content and preliminary electrochemical tests performed on the first synthesized material. Throughout the project, different synthesis batches were produced, with the aim of continuously improving the electrochemical performance. Given the long-term nature of the project and its focus on performance optimization, the AM producer progressively refined the synthesis process to improve the AM characteristics. Consequently, when higher capacities were observed, a deeper investigation of the electrodes was required to exclude parasitic reactions; in the absence of such effects, the capacity increase could be attributed to an effective improvement of the AM itself, as observed in this case.

5.3.1.1. Trial no. 1

The first trial was based on the production protocol suggested by Nanomakers, combined with the already optimized process developed in the laboratory. The mixing facility used was a magnetic stirrer, as previously done for graphite anodes, which allows the mixing of low amounts of water-based electrode slurries. The calculation for the components was based on 1 g of SC, with a composition of 90:2:4:4 (SC:C65:CMC:SBR) and a SF of around 25 wt.%.

1) 0.044 g of CMC were diluted in 3.22 mL of MilliQ water and kept under stirring at around 1000 rpm for 30 minutes.
2) 0.022 g of C65 were added and the solution was kept under stirring for 1 hour at the maximum speed (around 1600 rpm).
3) 1.00 g of SC was finally slowly added, and once all the powder was incorporated, the slurry was kept under stirring for 1 hour at maximum speed.
4) The final step was the addition of 0.044 g of SBR; however, in this case the material was already suspended in solvent with a solid content of 40 wt.%, thus 0.111 g were added instead. The mixing speed was reduced to 400 rpm for 20 minutes to guarantee the proper homogenization and avoid the degradation of the polymer.

The slurry was directly transferred to a doctor blade coating machine (TQC SHEEN Standard AB4120) immediately after mixing. The blade was set to deposit a 220 µm layer on a 17 µm thick copper foil. The blade speed was at 20 mm s^{-1}. The as-coated film was left to dry in air at room temperature (RT) for 2 h and then placed in an oven under air at 80 °C for 12 h. The resulting laminate (***Figure 5.64 a***) was characterized by a large number of clumps and inhomogeneities distributed over the entire surface, with significant dimensions (***Figure 5.64 b***). Afterwards, the electrodes were manually punched into 14 mm

diameter discs and individually pressed with a hydraulic press at 1 ton. The final electrodes (***Figure 5.64 c***) were characterized by clearly visible pressed clumps, confirming the presence of severe surface inhomogeneities.

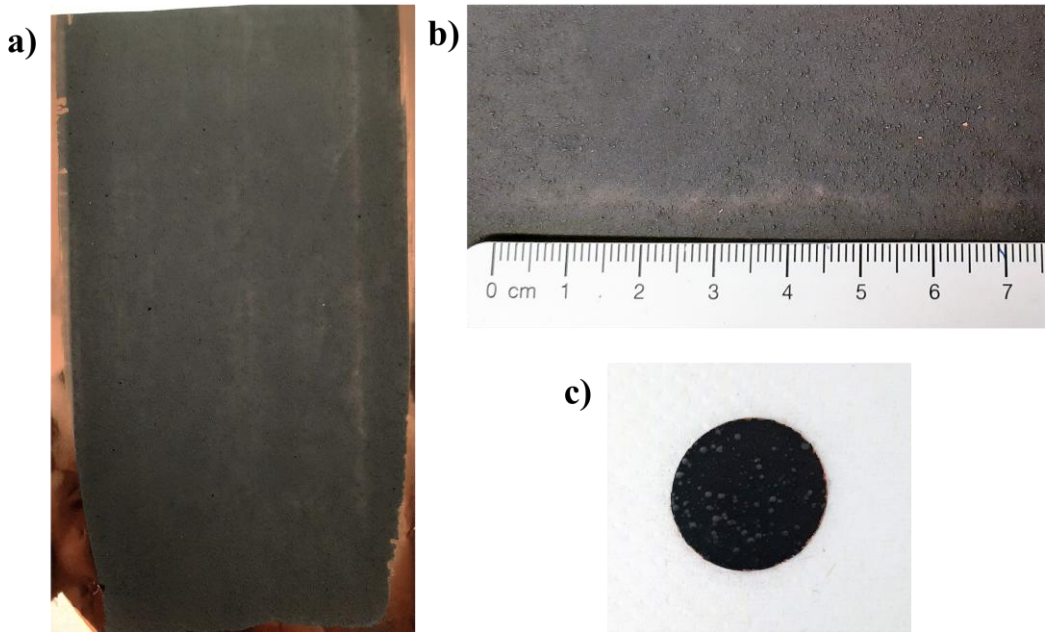

Figure 5.64 – Laminate produced at the first trial where the clumps and the inhomogeneities are very visible: a) Entire laminate; b) Focus on the clumps, macroscopically visible; c) Electrode with a diameter of 14 mm

The electrode surface was investigated through SEM analysis (***Figure 5.65***), highlighting the presence of agglomerates mainly associated with the binder phase, as suggested by the high oxygen content detected by EDX analysis. Considering that purely polymeric agglomerates are expected to collapse under the electron beam, these structures are more likely binder-rich regions in which the binder promotes the aggregation of AM particles. The origin of these inhomogeneities can be attributed to the type of mixer used, as the magnetic stirrer was not able to provide sufficient shear forces for the proper dispersion of highly viscous slurries. As a result, the formation of these agglomerates led to severe structural inhomogeneities, which negatively affected the electrochemical performance and hindered the achievement of the target performance, particularly during long-term cycling.

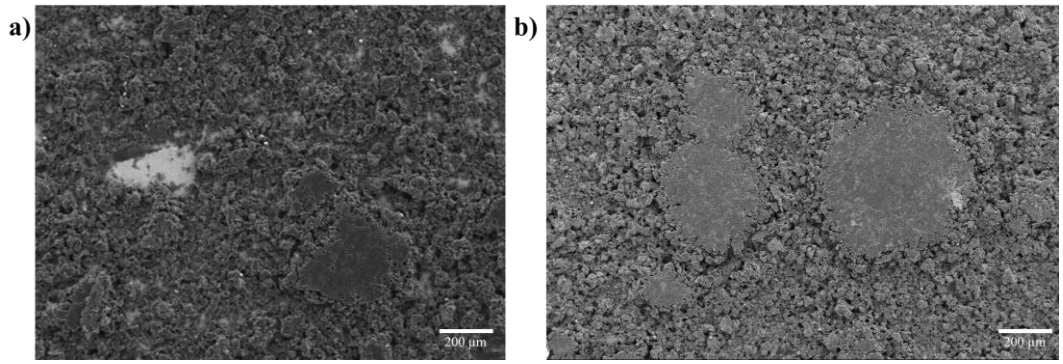

Figure 5.65 – SEM of the surface of two different regions with evident pressed clumps

Even though these electrodes could not be considered acceptable for LIB applications, they were weighed and their characteristics were measured, thus allowing the definition of a baseline. After the pressing step, the electrodes were characterized by a dry thickness, excluding the CC, of 63 ± 4 µm, and a ML of 3.43 ± 0.38 mg cm^{-2}. Based on the practical capacity of 600 mAh g^{-1} declared by the supplier, the AC was 2.06 ± 0.23 mAh cm^{-2}. These observations indicate that the magnetic stirrer was intrinsically unsuitable for the homogeneous dispersion of this silicon-based slurry, motivating the transition to higher-shear mixing strategies in the subsequent trial.

5.3.1.2. Trial no. 2

For the second trial, the amount of materials was tripled to reach a sufficient amount for a proper mixing with an homogenizer mixer (***Figure 3.4c***), which enables the mixing of higher viscosity slurries. The SF was maintained at around 25 wt.%, as in the previous case. The mixing procedure was largely maintained, and only minor optimizations of the rotational speed were required:

1) 0.133 g of CMC was diluted in 9.66 mL of MilliQ water and kept under stirring at around 1000 rpm for 30 minutes. The Dispermat device (20 mm disk) required a 25 mL beaker with an inner diameter of 25 mm, as the closer the diameter of the disk is to that of the beaker, the better the dispersion efficiency. The disk was positioned at approximately one-third of the solution height to ensure optimal dispersion.
2) 0.067 g of C65 was added, and the solution was kept under stirring for 30 minutes at the maximum speed of 2200 rpm.
3) 3.00 g of SC was finally slowly added, and once all the powder was incorporated, the solution was kept stirring for 30 minutes at maximum speed.
4) The final step was the addition of 0.133 g of SBR; however, in this case, the material was already suspended in solvent with a weight percentage of 40 wt.%, thus 0.333 g were added instead. The mixing speed was reduced to 400

rpm for 20 minutes to guarantee proper homogenization and avoid polymer degradation.

The coating was performed with a wet deposition thickness of 220 µm. As for the previous case, the amount of clumps and agglomeration remained very high, as observed in ***Figure 5.66***. Due to the poor quality of the resulting laminate, no further characterization of this sample was performed.

Figure 5.66 – Focus on the clumps presented on the dried laminate produced with the second trial

The results obtained from Trial no. 1 and no. 2 indicated that the main limitation was not only related to the mixing device itself, but also to the slurry formulation, which did not allow efficient dispersion under the tested conditions.

5.3.1.3. Trial no. 3

To achieve improved mixing, during the third trial, the SF was increased to 33 wt.%, while, at the same time, the wet coating thickness was reduced to 100 µm. The mixing procedure followed the same steps as previously described. Despite the increase in SF, similarly to the previous case, the laminates were characterized by a large number of clumps (***Figure 5.67***), and no further characterization of the electrodes was performed.

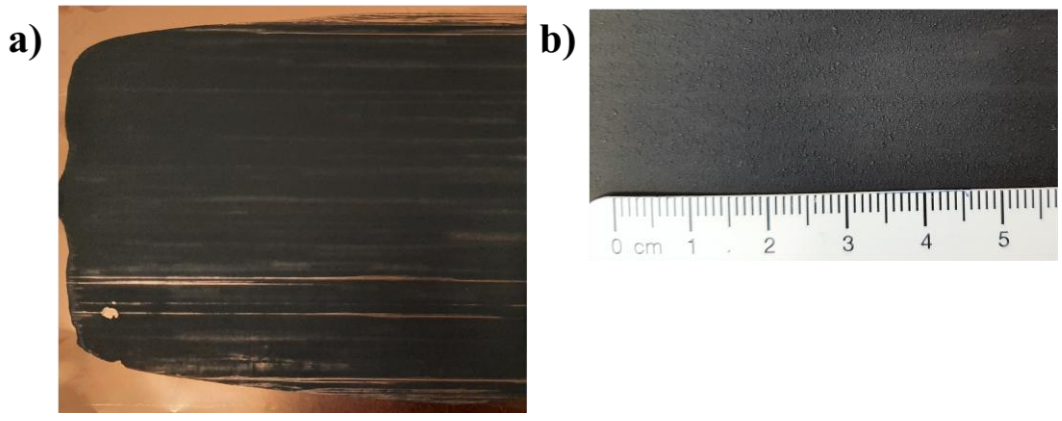

Figure 5.67 – Dry laminate produced with the third trial: a) Entire laminate; b) Focus on the clumps

5.3.1.4. Trial no. 4

During this trial, following the project partners' suggestions, multiple adjustments were performed to the production protocol, starting from an increased amount of mixed materials, while the SF was kept constant at 33 wt.%. In addition, some steps were extended with the aim of reducing clump formation. Finally, a specific procedure was introduced for the addition of the SBR: the mixer was kept at maximum speed for a few seconds, and only after that the mixing speed was reduced to 400 rpm. In this way, the SBR was completely dispersed in the slurry. The mixing procedure is described in detail below:

1) 0.197 g of CMC were added to 9.70 g of MilliQ water and the solution was stirred with the Dispermat device for 1 hour at 1000 rpm in a 25 mL beaker.
2) 0.099 g of C65 was dispersed in the CMC/water solution at 2200 RPM for 30 minutes.
3) 4.43 g of the composite SC was added to the solution and kept under stirring at 2200 RPM for 1 hour.
4) 0.493 g of SBR solution was finally added, reducing the mixing speed at 400 RPM for 30 minutes.

As in the previous trial, the slurry was coated on a 17 µm thick copper CC, imposing a wet thickness of 100 µm and a coating speed of 20 mm s^{-1}. The drying step was a multi step procedure, which started with the as-cast electrode sheets left to dry for about 2 hours under air at RT and then dried overnight in an oven at 80°C, still under air. Compared with the previous trials, the situation improved significantly, as shown in ***Figure 5.68***, where the clumps were smaller than in the previous case, but some surface inhomogeneities were still present. Finally, the electrodes were punched into discs with a diameter of 14 mm using a manual puncher.

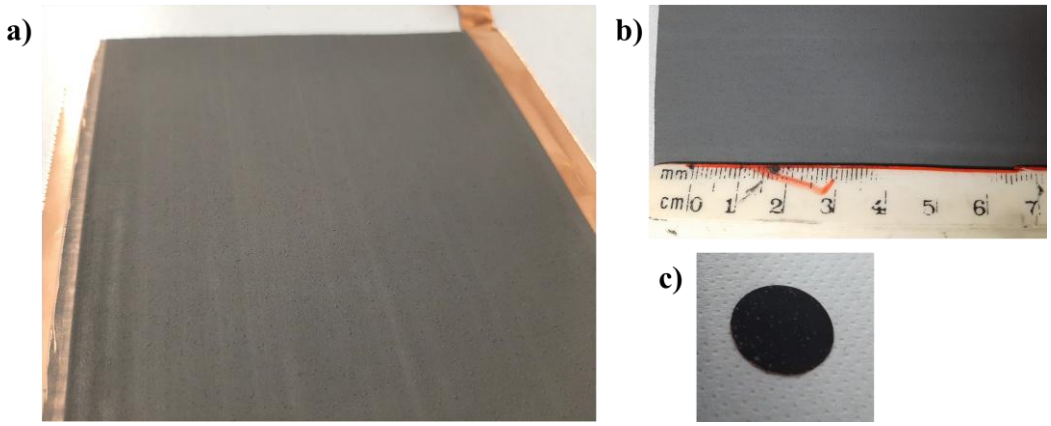

Figure 5.68 – Dry laminate produced with the fourth trial: a) Entire laminate; b) Focus on the clumps; c) Electrode with a diameter of 14 mm

The electrode characteristics were measured: the dry thickness was 37 ± 4 µm, the ML was 2.29 ± 0.20 mg cm^{-2}. Based on the practical capacity of 600 mAh g-1, the calculated AC was 1.38 ± 0.12 mAh cm^{-2}, which was lower than the project target of 2 mAh cm^{-2}. The increase in solid fraction improved the process stability but was not sufficient alone to eliminate binder agglomeration, highlighting the need for further optimization of mixing sequence and duration. However, the electrode characteristics showed a clear improvement compared to the previous trials, indicating that only a limited number of additional optimization steps were required to reach the desired target.

5.3.1.5. Trial no. 5

The fifth trial allowed the production of good-quality electrodes, in line with those produced by the other project partners. The main change in this trial was the extension of the final mixing step after the addition of SBR from 30 minutes to 1 hour. Multiple laminates were produced to verify that the production procedure was sufficiently robust to satisfy the amount of electrodes required within the project. The solid content in water was maintained at around 33 wt.%, as in the previous case. The mixing procedure was identical to that of the previous trial, apart from the elongation of the final step from 30 minutes to 1 h.

The laminates were produced with the same coating parameters described in the previous trial and the results are shown in ***Figure 5.69***. The laminate surface was smooth and homogeneous, without clump or other visible defects, as desired. In this case, the electrodes (***Figure 5.69 c***) were not pressed as electrochemical analysis confirmed that the expected performance of the material was already achieved in the unpressed state. Moreover, the calendering of silicon-based anodes remains a challenging step, as the large volume expansion of silicon during lithiation can induce mechanical stress, particle fracture, loss of electrical contact, and accelerated electrode degradation, which can lead to mechanical degradation and premature performance decay, even when higher electrode

density and reduced porosity are achieved [70,266,268,413,450]. A more detailed discussion of the advantages and limitations of the calendering process applied to silicon-based electrodes is supplied in ***Chapter 3***.

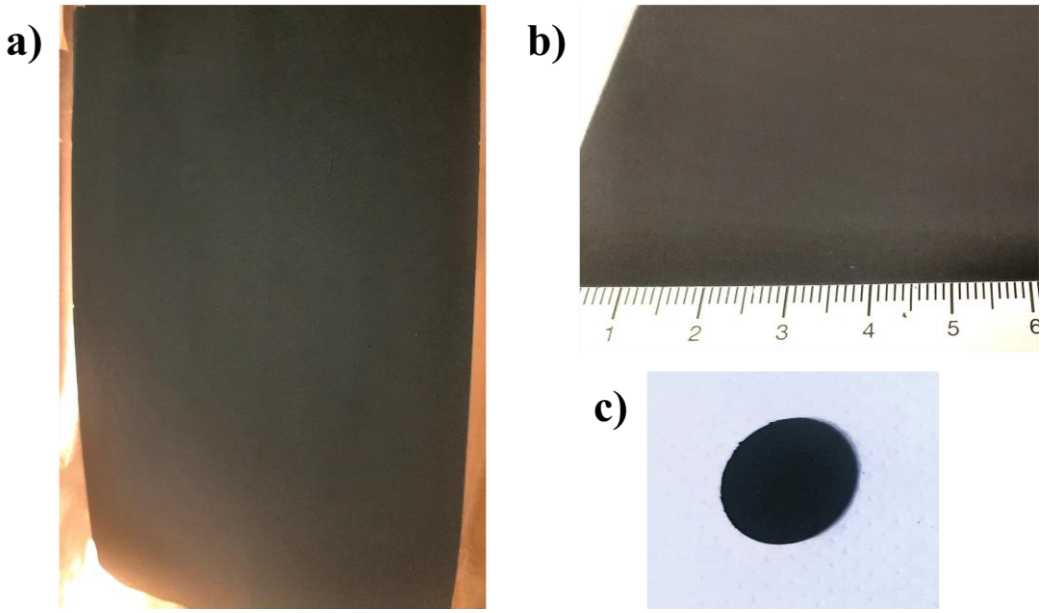

Figure 5.69 – Dry laminate produced with the fifth trial: a) Entire laminate; b) Focus on the clumps; c) Electrode with a diameter of 14 mm

The FESEM analysis (***Figure 5.70a***) performed on non-pressed electrodes confirmed a significant improved material dispersion compared to the first trial (***Figure 5.65***), with a highly homogeneous surface. The EDX analysis (***Figure 5.70b***) was used to map the elemental distribution, with a particular focus on silicon, carbon and oxygen. This analysis confirmed the improved dispersion of the binder, which contains oxygen, characterized by dark blue dots homogeneously distributed over the surface without visible agglomeration.

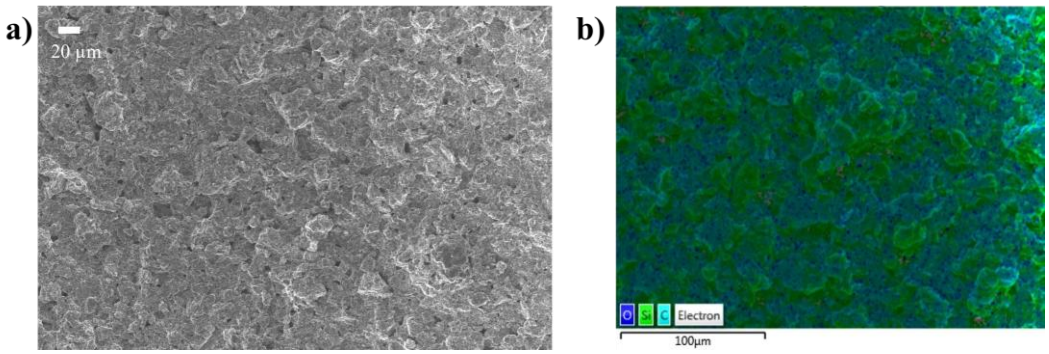

Figure 5.70 – a) SEM of the surface of electrode produced with the fifth trial, for this image the acquisition parameters were Magnification 500 X; WD 3,0 mm; EHT 5,00 kV; b) Map of the electrode surface

After the drying step, the dry layer thickness was measured and resulted approximately half of the imposed wet thickness with a value of 52 ± 2 µm. The

ML reached 3.04 ± 0.20 mg cm^{-2}, corresponding to an AC of 1.82 ± 0.12 mAh cm^{-2}. These electrodes were electrochemically tested as part of the activity focused on laser treatments of the copper CCs, the results of which are presented in the following section. The electrochemical performance was satisfactory, although further improvements were indicated as possible by the supplier; therefore, a different AM batch was used in the subsequent trial.

5.3.1.6. Trial no. 6

During this trial, a new batch of AM was employed: after the electrochemical tests, the synthesis had been optimized to improve the electrochemical performance. This trial was based on a small adjustment of the wet coating thickness to reach the project target values of ML and AC. The mixing step was kept identical to the optimized protocol used in the previous trial, which had already confirmed the high quality of the produced electrodes. During the coating step, the wet thickness was increased to 120 µm. In this way, the values of ML and AC of the electrodes were fully aligned with the project AC target of 2 mAh cm^{-2}. Thanks to the proper optimization of the mixing procedure, the homogeneity of the electrodes was further improved, resulting in a dry thickness of 48 ± 1 µm, without applying any calendering step. The calculated ML was 3.33 ± 0.09 mg cm^{-2}, characterized by a lower dispersion compared to the previous sample, corresponding to an AC of 2.00 ± 0.06 mAh cm^{-2}, matching the target value. Based on the average values of dry thickness and ML, the coating density was calculated to be 0.78 g cm^{-3}. Based on the equation reported in several studies [261,451,452], the calculated porosity was 63% before the pressing step. This value was calculated and is therefore associated with relatively high uncertainty. Nevertheless, this porosity value was consistent with those reported for other silicon-based electrodes in the literature [450,453]. To obtain a more accurate value, direct porosity measurements should be performed using dedicated techniques such as mercury intrusion porosimetry. Before performing the pressing step, the electrodes were electrochemically tested and the results are reported in the following section, to compare the electrochemical performance with that declared by the supplier and, if possible, avoid the calendering step. Indeed, the presence of silicon requires specific precautions during calendering, as already discussed in ***Chapter 3***. After the electrochemical results presented below in the chapter, it was decided to avoid the calendering step, thanks to the good electrode performance. The final protocol allowed the definition of a stable manufacturing procedure, ensuring homogeneous coating quality and target electrode properties.

5.3.2. Electrochemical validation of optimized electrodes

After the optimization of the electrode production process, the electrodes with a diameter of 14 mm were dried with an additional step under vacuum at 80°C for

24 hours. The electrodes were assembled in half-cell configuration using coin-cell 2032 geometry; the procedure was conducted inside a controlled-atmosphere glovebox filled with argon (O_2 < 1ppm, H_2O < 1ppm). The silicon composite electrodes were used as working electrodes, coupled with lithium metal chips from MTI Corp, with a diameter of 15.6 mm and a thickness of 0.56 mm, used as counter electrodes. A glass fiber separator GF/A (Whatman, 18 mm diameter, 0.65 mm thickness) was soaked with 150 µL of electrolyte (1M $LiPF_6$ in EC:DEC 1:1 + 10 wt.% FEC + 2 wt.% VC) supplied by Solvionic. The choice of this electrolyte was aimed at promoting the formation of a stable solid electrolyte interphase (SEI), which enhances the stability of silicon-based electrodes [403]. An excess amount of electrolyte was employed to prevent electrolyte limitation during electrochemical testing.

The electrodes produced with the optimized production process were electrochemically tested through a rate capability test followed by long term cycling, whose protocol is reported in ***Table 5.31***. This protocol was defined jointly by the project partners and kept constant throughout the project. The tests were conducted in a voltage window between 0.01 V and 1.5 V. The cycling protocol consisted of three initial formation cycles at a low current density of 0.1C, including a CVS after the lithiation step, in which the voltage was held at 0.01 V with a current cut-off of 0.01C. In silicon-based electrodes, the application of a CVS at 0.01 V, maintained until the current decays to a defined cut-off value (0.01C), is a commonly adopted procedure for half-cell electrochemical testing [405,406]. The duration of this step may vary across cycles and electrodes, as the current decay at low potentials is governed by time-dependent interfacial and transport processes; consequently, reaching a fixed current threshold does not necessarily occur within a constant time. This variability arises because multiple simultaneous processes (SEI formation, structural changes, interfacial reactions) evolve at different rates depending on material and cell design, making the kinetics of current decay inherently non-uniform [427]. After the formation step, a rate capability test was performed to evaluate the performance of the silicon composite at different current densities (0.2C, 0.5C, 1C, and 2C). In agreement with the project partners, the highest current-density step was performed using an asymmetric charge/discharge protocol: the lithiation step was maintained at 1C, while the delithiation step was increased to 2C, to apply a more severe electrochemical stress and simulate faster delithiation, as typically experienced during battery operation by the end user, whereas the charging step is generally more controlled by the manufacturer [454]. The final step consisted of long term cycling of 80 cycles to evaluate the preliminary capacity retention of these electrodes.

Throughout both the rate capability test and the long-term cycling, consistent with the procedure adopted for the previous materials, a CVS at 0.01 V was

applied after each lithiation step, using a current cut-off of 0.05C. The inclusion of a CVS after lithiation has been shown to support the stabilization of silicon-based anodes by promoting more uniform SEI formation and mitigating continuous electrolyte decomposition during cycling, which is essential for improved cycle stability in silicon-based half-cells [455].

Table 5.31 – Cycling protocol for the rate capability test coupled with the long term cycling, adopted for the electrochemical test throughout all the project, it was agreed between the partners

Cycle	***Mode***	***Discharge***	***Charge***
1-3	*Formation*	*CCS: 0.1C* *CVS: 0.01V / 0.01 C*	*CCS: 0.1C*
4-8	*Rate Capability*	*CCS: 0.2C* *CVS: 0.01V / 0.05 C*	*CCS: 0.2C*
9-13	*Rate Capability*	*CCS: 0.5C* *CVS: 0.01V / 0.05 C*	*CCS: 0.5C*
14-18	*Rate Capability*	*CCS: 1C* *CVS: 0.01V / 0.05 C*	*CCS: 1C*
19-23	*Rate Capability*	*CCS: 1C* *CVS: 0.01V / 0.05 C*	*CCS: 2C*
24-103	*Long Cycling*	*CCS: 1C* *CVS: 0.01V / 0.05 C*	*CCS: 1C*

Multiple samples have been electrochemically tested throughout the project; however, only those prepared using the final trial are presented here. The results reported below were not obtained using the first AM batch produced by Nanomakers, but rather a second batch, which exhibited improved performance compared to the initially declared values, although the extent of this improvement was not quantitatively specified.

The electrochemical tests were performed on three replicas to evaluate the reproducibility of the performance (***Figure 5.71***). Overall, the replicates showed good agreement, with low variability among them for both average charge and average discharge capacities (***Table 5.32***). The low variability among replicate cells confirmed the robustness of the optimized electrode processing protocol. Focusing on the first cycle, the average discharge capacity was 742.53 mAh g^{-1} while the average charge capacity was 619.06 mAh g^{-1}. This corresponded to an average coulombic efficiency of 83.43%, indicating a first irreversible capacity loss of 16.57% which is consistent with the ICE typically reported for silicon composite materials [415,416]. The rate capability test (***Figure 5.71b***) showed stable capacity values even at the highest current densities, with an average discharge capacity of 568.69 mAh g^{-1} and an average charge capacity of 563.25 mAh g^{-1}. By increasing the current density of the discharge step at 1C and of the charge step at 2C, the electrodes exhibited robust electrochemical performance: at cycle 23, the average discharge capacity was 568.69 mAh g^{-1} and the average charge capacity was 563.24 mAh g^{-1}. Considering the long term cycling (from

cycle 24 to cycle 103), the average capacity retention was calculated to be 91.21%, based on the ratio between the discharge capacity value of the cycles number 100 and 30.

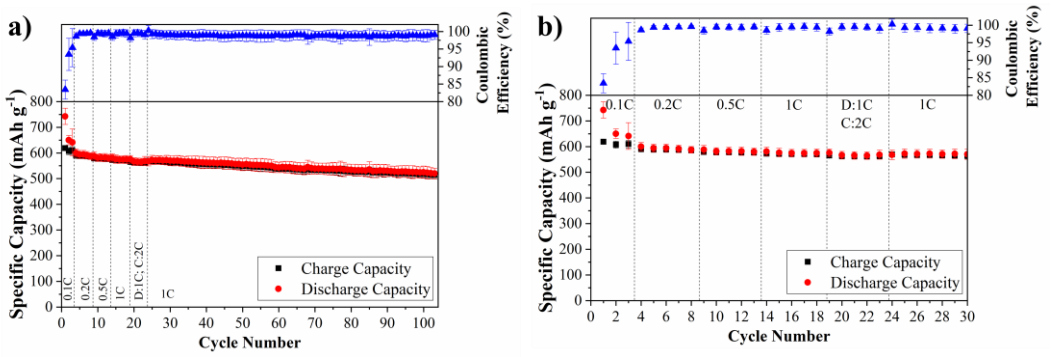

Figure 5.71 – Electrochemical characterization of the electrodes produced with the optimized procedure: a) Entire test; b) Focus on the rate capability test

Table 5.32 – Values of charge and discharge capacities, normalized by the electrode weight, and relative values of coulombic efficiency for the electrodes produced with the optimized production process

Cycle	***C-rate***	***Charge Capacity (mAh g^{-1})***	***Discharge Capacity (mAh g^{-1})***	***Coulombic Efficiency (%)***
1	*0.1C*	*619.06 ± 6.08*	*742.53 ± 31.56*	*83.43 ± 2.73*
2		*607.23 ± 13.66*	*650.15 ± 18.49*	*93.48 ± 4.58*
3		*609.69 ± 14.80*	*641.01 ± 52.15*	*95.41 ± 5.44*
8	*0.2C*	*585.30 ± 10.61*	*587.68 ± 12.86*	*99.60 ± 0.39*
13	*0.5C*	*577.24 ± 10.07*	*579.87 ± 14.42*	*99.56 ± 0.76*
18	*1C*	*571.24 ± 9.45*	*574.73 ± 15.47*	*99.41 ± 1.05*
23	*D:1C, C:2C*	*563.24 ± 10.85*	*568.69 ± 17.96*	*99.07 ± 1.27*
30	*1C*	*564.82 ± 12.65*	*570.08 ± 19.54*	*99.11 ± 1.22*
50		*548.40 ± 15.34*	*554.85 ± 23.48*	*98.88 ± 1.52*
103		*514.97 ± 14.01*	*519.99 ± 20.71*	*99.07 ± 1.27*

To gain a deeper understanding of the AM behavior during charge and discharge processes, the voltage profiles of selected representative cycles are reported in ***Figure 5.72***. The voltage profiles exhibited the characteristic features of the SC material, confirming the correct electrochemical activation of both phases: the shape of the first cycle (black curve, ***Figure 5.72a***) showed significant differences compared to the subsequent cycles, due to irreversible reactions occurring during SEI formation. The profile is characterized by a pronounced slope, followed by two small plateaus and a longer one. As already described, the AM is a composite of silicon, graphite, and soft carbon; therefore, during the profile analysis it is important to consider that multiple lithiation and delithiation processes can occur simultaneously. In general, the pronounced slope can be

attributed mainly to silicon, while the plateaus are more closely related to the graphitic component and the carbon matrix [456,457]. Following the discharge step, a CVS was applied, during which the plateau at 0.01 V was attributed to two consecutive two-phase electrochemical reactions: the amorphization of crystalline silicon nanoparticles into Li_xSi, followed by the formation of the crystalline $Li_{15}Si_4$ phase [417,418]. Focusing on the second and third cycles, the contributions of silicon and carbon lithiation processes become easier to distinguish. During the discharge process, the shoulder appearing at around 0.3 V is mainly associated with the lithiation of the soft carbon component within the composite [456,457]. However, in SC electrodes, the interpretation of this feature is intrinsically complex, as the broad nature of the shoulder suggests overlapping electrochemical contributions. In particular, part of this capacity may also originate from the lithiation of amorphous silicon, which typically occurs over a wide low-potential range around ~0.25 V [458]. Subsequently, the graphitic plateaus become clearly visible again, confirming the concurrent electrochemical contribution of both silicon and carbon phases within the electrode. During the formation cycles, the contribution of the CVS was marginal, indicating that the majority of the lithiation capacity was directly accommodated by the AM rather than being associated with kinetically limited processes. During the charge process, the delithiation mechanisms were more clearly distinguishable, proceeding from the delithiation of the soft carbon matrix at higher potentials to the complete delithiation of the silicon nanoparticles at lower potentials.

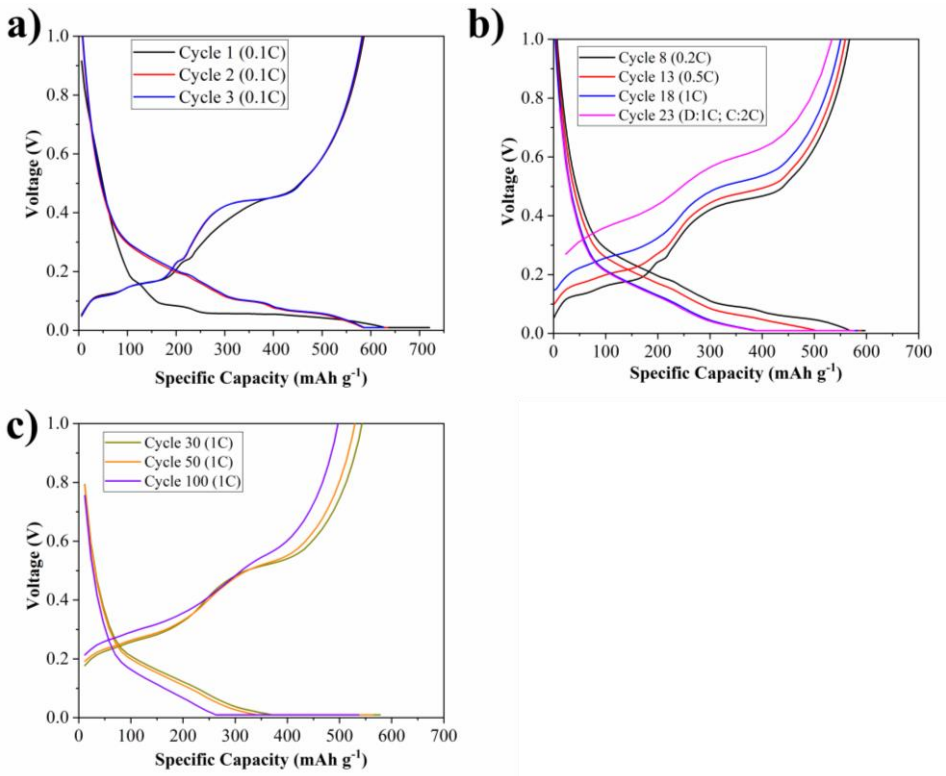

Figure 5.72 – Charge/discharge curves for some representative cycles of the electrodes produced with the optimized production process: a) Forming cycles; b) Rate capability test; c) Long cycling.

Considering the rate capability test (***Figure 5.72b***), even at the highest applied current density, the curves maintained a shape that allowed the distinction of both the silicon and soft carbon contributions. The contribution of the CVS became more pronounced, but remained lower than that observed for the previously discussed SC material (***Chapter 5.2***), indicating that the Nanomakers material, when coupled with a properly optimized electrode production process, enables improved electrochemical performance. It is important to note that during the charging step performed at 2C, the curves exhibited larger deviations, characterized by increased polarization; however, as already discussed, this behavior was consistent with the more severe delithiation conditions imposed during the asymmetric rate protocol. The good stability of the AM was also observed during the long-term cycling (***Figure 5.72c***). In fact, the curves at cycle 30 and cycle 50 were almost overlapping, while at cycle 100 a slight increase in overpotential became visible, although it remained within acceptable limits [459]. At the same time, the CVS contribution stabilized at approximately half of the measured discharge capacity.

Based on the electrochemical performance presented here, the synthesis of the AM and the electrode production process were considered successfully optimized at laboratory scale. All the data shared with the project partners were subsequently used to support the optimization at larger pilot scale, which was carried out by other partners.

5.3.3. Laser texturing of copper current collector

Once a stable and reproducible electrode manufacturing protocol had been established, the investigation was extended to interface engineering strategies aimed at further improving electrode performance. In particular, laser texturing of the CC was explored to enhance interfacial adhesion and electronic contact.

This activity was carried out within the GIGAGREEN project through the collaboration between Politecnico di Torino, responsible for electrode preparation and electrochemical testing, ALPhANOV, which performed the laser surface treatments, and the Università di Parma, which supported surface modelling and post-mortem analysis. The treatments were applied to CC with an average thickness of 17.5 µm, with the objective of improving the electrode-CC interface and, consequently, the electrochemical response.

The surface morphology of the laser-modified CCs is shown in ***Figure 5.73*** together with the corresponding SEM images, highlighting the structural changes induced by femtosecond laser processing. Further details on the laser treatments are reported in the dedicated publication [206]. The three samples were named according to the laser treatment used for their production:

1. Cu1L (***Figure 5.73a,d***): the first laser treatment produced submicrometric laser-induced periodic surface structures (LIPSS), leading to the formation of asymmetric wave-like patterns on the surface.
2. Cu2L (***Figure 5.73b,e***): the second laser treatment was based on the LIPSS combined with micro-grooves (μ-grooves).
3. Cu3L (***Figure 5.73c,f***): the third laser treatment was obtained using direct laser interference patterning (DLIP).

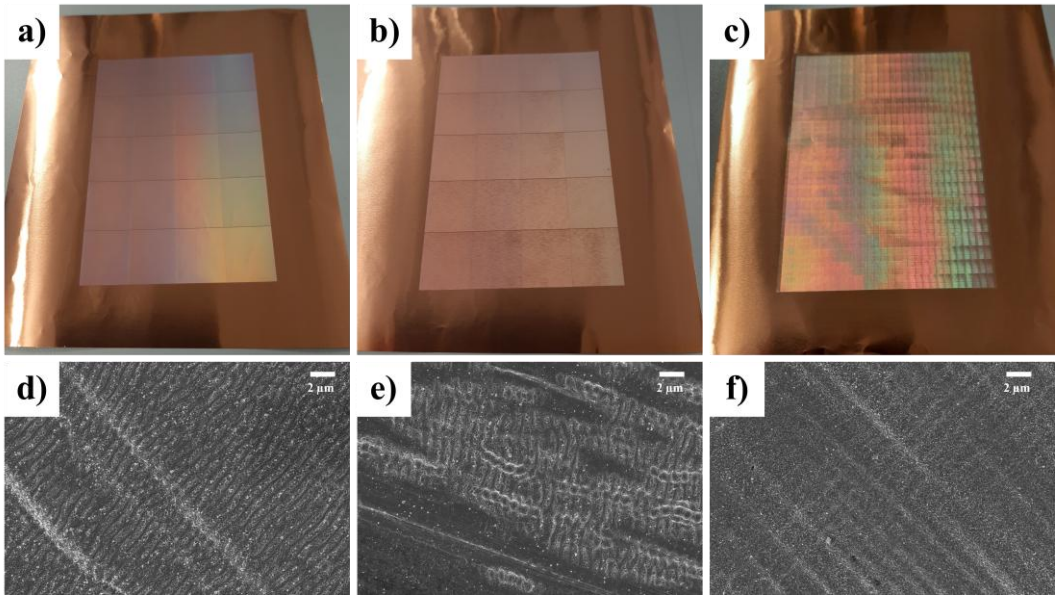

Figure 5.73 – Copper current collector modified with three treatments: a-d) Cu1L; b-e) Cu2L; c-f) Cu3L. The SEM images were captured using a magnification of 10KX

5.3.3.1. Impact of surface texturing on electrode fabrication and mass loading

The electrode production process was performed using the optimized procedure reported, based on Trial no. 5. The use of this procedure, rather than the final one, was solely due to the timing of this activity, as the final trial was optimized after this work had already been completed. As a result, the only significant difference among the samples was related to the use of different copper CCs. The electrode characteristics corresponding to the different CCs involved in the production process are reported below.

After the surface treatment of the CCs, their thickness was measured using a digital thickness gauge, and some differences were observed (***Table 5.33***). For all the laser-treated samples, an increase of at least 1 μm was measured, which was attributed to the edges formed around the surface modifications. The digital thickness gauge was not sufficiently sensitive to resolve thickness variations associated with the micrometric surface features. As a baseline, the electrodes produced using untreated CCs, named CuP, were characterized by the highest

value of dry thickness and ML, while all laser-treated samples exhibited different results. Despite the differences in CC thickness, the dry electrode layer thickness remained constant at 47 µm for all samples, with negligible statistical variations. In contrast, significant differences were observed in the ML, which depended on the laser treatment applied. For Cu1L, the average ML was 2.81 mg cm^{-2}, for Cu2L, 2.57 mg cm^{-2}, and for Cu3L, 2.36 mg cm^{-2}. The gradual reduction in ML was accompanied by a decrease in its statistical dispersion, from 0.33 mg cm^{-2} for Cu1L to 0.03 mg cm^{-2} for Cu3L. This trend may be attributed to the more regular surface pattern of the Cu3L CC, which favored a more homogeneous wet slurry distribution, resulting in highly reproducible electrodes in terms of ML. The average areal capacity calculated for Cu1L was 1.69 mAh cm^{-2}, for Cu2L was 1.54 mAh cm^{-2}, and for Cu3L was 1.42 mAh cm^{-2}.

Table 5.33 – Characteristics of the electrodes produced using the modified current collectors. The dry thickness was calculated excluding the current collectors

Sample	***CC Thickness (µm)***	***Dry Thickness (µm)***	***Mass Loading (mg cm^{-2})***	***Areal Capacity (mAh cm^{-2})***
CuP	*17.5*	*52 ± 2*	*3.04 ± 0.20*	*1.82 ± 0.12*
Cu1L	*18.5*	*47 ± 3*	*2.81 ± 0.33*	*1.69 ± 0.20*
Cu2L	*18*	*47 ± 2*	*2.57 ± 0.17*	*1.54 ± 0.10*
Cu3L	*19*	*47 ± 2*	*2.36 ± 0.03*	*1.42 ± 0.02*

5.3.3.2. Comparative electrochemical behaviour as a function of surface morphology

The cell assembly followed the same procedure previously described. The electrodes were tested according to the cycling protocol reported in ***Table 5.31***: the electrodes were assembled in 2032-type coin half-cells using lithium metal as the counter electrode and cycled under CC-CV mode during lithiation, and CC mode during delithiation.

The results presented in this analysis were based on the three assembled cells per each sample allowing a reproducibility comparison. To further investigate the electrochemical behavior of the AM, CV measurements were performed on all samples using a three-electrode cell configuration. In this setup, both the working electrode and the lithium counter electrode were punched into 10 mm diameter discs, and the electrolyte volume was reduced to 120 µL. As in the coin-cell tests, the electrolyte was supplied in excess to prevent it from acting as a limiting factor. CV measurements were carried out for three cycles within a voltage window of 10 mV to 1.5 V at a scan rate of 0.1 mV s^{-1}. To enable a direct comparison among samples, all CV curves were normalized to the corresponding AM mass.

Before discussing the electrochemical results, it is important to note that the average charge and discharge capacities presented in the following section are

higher than those previously reported. This difference is attributed to the use of different AM batches for the preparation of the corresponding electrodes. Although maximizing electrochemical performance was one of the project objectives, the highest capacity values were also associated with lower capacity retention during long-term cycling. This unfavorable behavior led the partner responsible for AM production to further optimize the synthesis process, prioritizing improved capacity retention. Within the scope of the project, whose final objective is the assembly of a full cell employing a water-based LNMO cathode, a slightly lower electrochemical performance of the silicon-based anode does not compromise the overall outcome. On the contrary, achieving long-term stability in a silicon composite anode represents a significant and highly relevant result.

5.3.3.2.1. Pristine current collector (CuP)

The electrochemical performance of electrodes produced on pristine copper CCs (***Figure 5.74***, ***Table 5.34***) was generally consistent with that previously observed for the optimized electrodes. During the first cycle, a relatively low coulombic efficiency of about 84% was measured, in line with the initial irreversible capacity typically associated with silicon-based materials. At higher C-rates, the electrodes maintained high charge and discharge capacities, reaching values close to 600 mAh g^{-1} at 2C. Despite this overall good rate capability, the capacity retention during long-term cycling remained limited, with an average value of about 86%, which was considered unsatisfactory by the AM supplier and motivated further optimization of the synthesis process. Indeed, improved electrochemical behaviour was later observed when using a second batch of AM, confirming the strong influence of material quality on the final electrode performance.

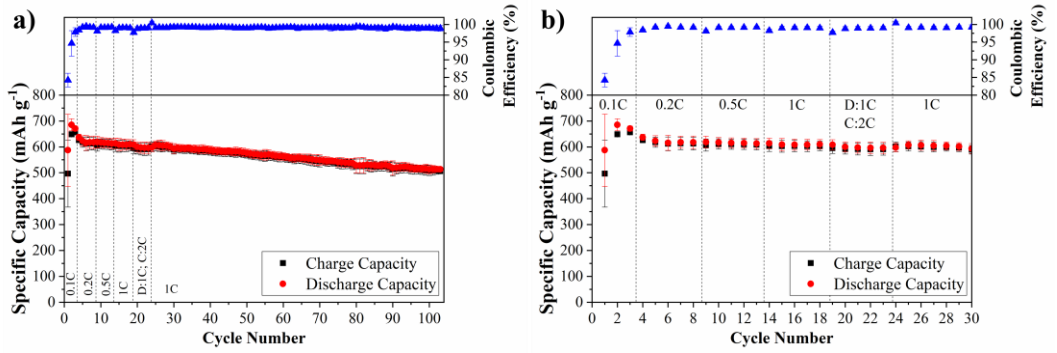

Figure 5.74 – Electrochemical characterization of the electrodes produced with the pristine CC: a) Entire test; b) Focus on the rate capability test

Table 5.34 – Values of charge and discharge capacities, normalized by the electrode weight, and relative values of coulombic efficiency for the electrodes produced with the pristine CC

Cycle	*C-rate*	*Charge Capacity (mAh g^{-1})*	*Discharge Capacity (mAh g^{-1})*	*Coulombic Efficiency (%)*
1		*496.46 ± 129.30*	*587.28 ± 139.30*	*84.25 ± 1.93*
2	*0.1C*	*648.35 ± 9.90*	*685.42 ± 23.32*	*94.67 ± 3.61*
3		*656.27 ± 8.53*	*670.60 ± 9.36*	*97.87 ± 1.22*
8	*0.2C*	*612.66 ± 24.43*	*617.88 ± 24.40*	*99.16 ± 0.29*
13	*0.5C*	*608.36 ± 19.90*	*612.98 ± 18.95*	*99.24 ± 0.33*
18	*1C*	*603.88 ± 18.48*	*610.04 ± 18.39*	*98.99 ± 0.56*
23	*2C*	*590.62 ± 2.28*	*596.29 ± 21.45*	*99.04 ± 0.43*
30		*589.03 ± 16.81*	*593.49 ± 19.05*	*99.26 ± 0.69*
50	*1C*	*571.13 ± 14.61*	*576.79 ± 14.59*	*99.02 ± 0.47*
103		*507.96 ± 12.23*	*513.60 ± 8.72*	*98.89 ± 0.81*

The voltage profiles (***Figure 5.75***) during formation and rate capability test showed the characteristic electrochemical features of SC electrodes, with differences among cycles mainly related to polarization and progressive capacity fading. Similarly, CV (***Figure 5.76***) confirmed the reproducibility of the main lithiation and delithiation processes, indicating that all expected electrochemical reactions occurred correctly throughout cycling.

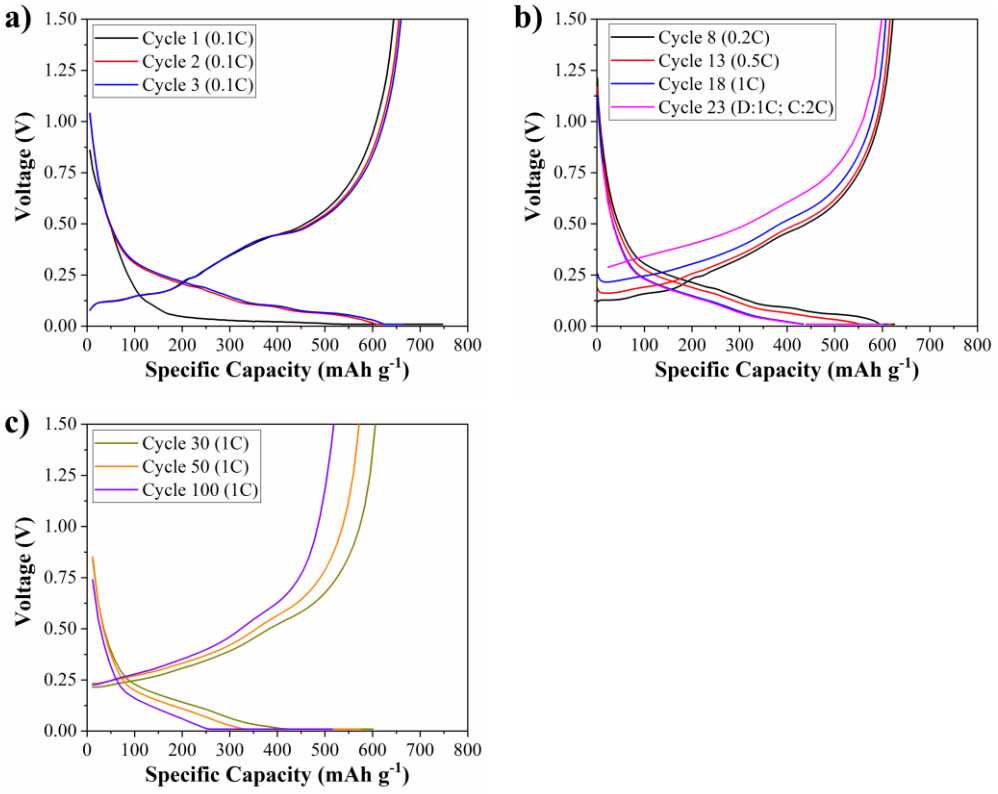

Figure 5.75 – Charge/discharge curves for some representative cycles of the electrodes produced with the pristine CC: a) Forming cycles; b) Rate capability test; c) Long cycling

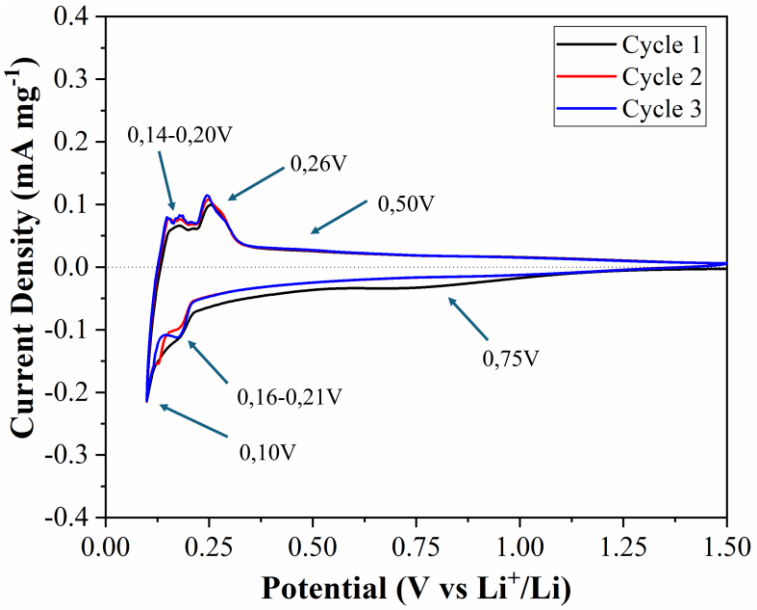

Figure 5.76 – Cyclic voltammetry performed on the CuP electrodes. The analysis was performed in the potential window between 0.1 V and 1.5 V with a scan rate of 0.1 mV s^{-1}.

5.3.3.2.2. LIPSS treatment (Cu1L)

The electrodes produced on LIPSS-textured CCs (Cu1L) showed generally high electrochemical performance (***Figure 5.77***, ***Table 5.35***) with first-cycle lithiation capacities approaching 860 mAh g^{-1}. However, the associated CE remained relatively low, mainly due to the extended CVS observed in some samples. This behaviour was reflected in a larger variability of the first-cycle capacities compared to pristine CC. During rate capability test (***Figure 5.77b***), the electrodes maintained high charge and discharge capacities, remaining close to 650 mAh g^{-1}, even at 2C. Nevertheless, long-term cycling revealed a progressive capacity decay, resulting in an average capacity retention of about 83%. In addition, the average CE did not systematically exceed 99% throughout the test, suggesting that interfacial stabilization was not fully achieved.

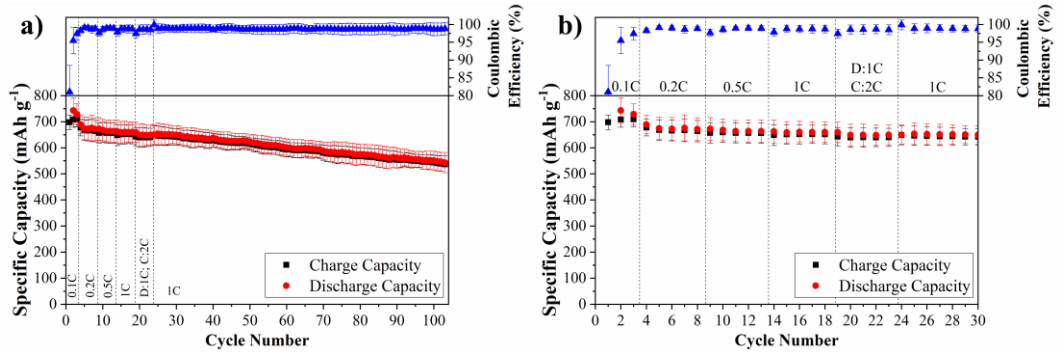

Figure 5.77 – Electrochemical characterization of the electrodes produced with the Cu1L: a) Entire test; b) Focus on the rate capability test

Table 5.35 – Values of charge and discharge capacities, normalized by the electrode weight, and relative values of coulombic efficiency for the electrodes produced with the Cu1L

Cycle	*C-rate*	*Charge Capacity (mAh g^{-1})*	*Discharge Capacity (mAh g^{-1})*	*Coulombic Efficiency (%)*
1		*697.70 ± 28.42*	*866.21 ± 92.16*	*81.05 ± 7.48*
2	*0.1C*	*708.84 ± 29.69*	*743.15 ± 49.20*	*95.51 ± 3.62*
3		*709.37 ± 28.71*	*728.51 ± 39.48*	*97.43 ± 1.85*
8	*0.2C*	*663.87 ± 40.86*	*671.48 ± 43.81*	*98.88 ± 0.65*
13	*0.5C*	*656.53 ± 39.47*	*663.59 ± 42.89*	*98.96 ± 0.72*
18	*1C*	*651.44 ± 36.05*	*659.96 ± 39.19*	*98.73 ± 1.08*
23	*2C*	*639.96 ± 34.80*	*649.65 ± 37.90*	*98.53 ± 1.38*
30		*641.75 ± 31.56*	*649.63 ± 34.67*	*98.81 ± 1.07*
50	*1C*	*614.40 ± 23.18*	*622.75 ± 26.65*	*98.68 ± 1.20*
103		*536.55 ± 32.17*	*543.34 ± 39.21*	*98.82 ± 1.69*

The voltage profiles (***Figure 5.78***) and CV curve (***Figure 5.79***) were consistent with those observed for electrodes produced on pristine CC, indicating that the main electrochemical processes remained unchanged. A reduced contribution of the CVS was observed, suggesting improved kinetic accessibility of the AM.

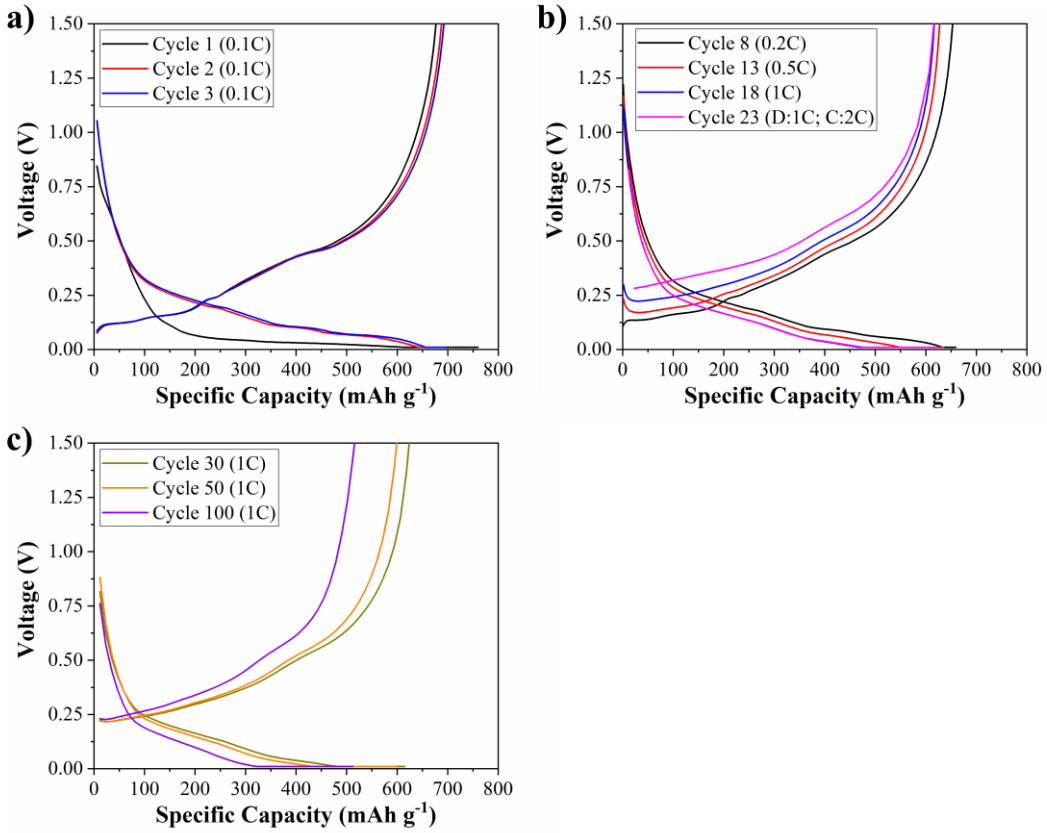

Figure 5.78 – Charge/discharge curves for some representative cycles of the electrodes produced with the Cu1L: a) Forming cycles; b) Rate capability test; c) Long cycling

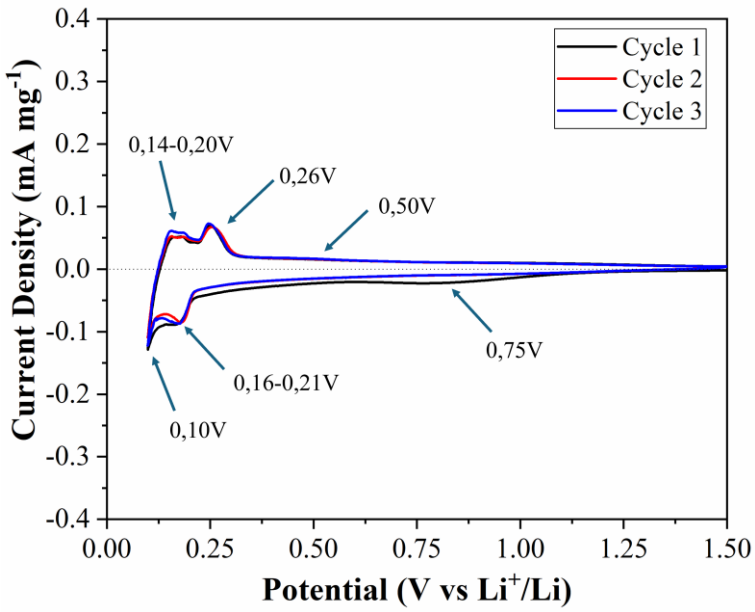

Figure 5.79 – Cyclic voltammetry performed on the Cu1L electrodes. The analysis was performed in the potential window between 0.1 V and 1.5 V with a scan rate of 0.1 mV s^{-1}.

5.3.3.2.3. LIPSS + micro-grooves treatment (Cu2L)

The electrodes produced on CCs treated with LIPSS combined with randomly distributed micro-grooves (Cu2L) showed improved electrochemical performance compared to pristine CC (***Figure 5.80***, ***Table 5.36***). In fact, during the rate capability test (***Figure 5.80b***), both the average charge and discharge capacities remained consistently above 615 mAh g^{-1}, however, the results were characterized by a relatively high variability among samples. This behaviour can be attributed to the irregular surface morphology, which may locally affect slurry spreading and electrode-CC contact. The variability progressively decreased during long-term cycling, resulting in an average capacity retention of about 86%. Although the overall performance was satisfactory, the electrochemical response remained less stable than expected, suggesting that the random distribution of surface features does not provide a fully controlled interface.

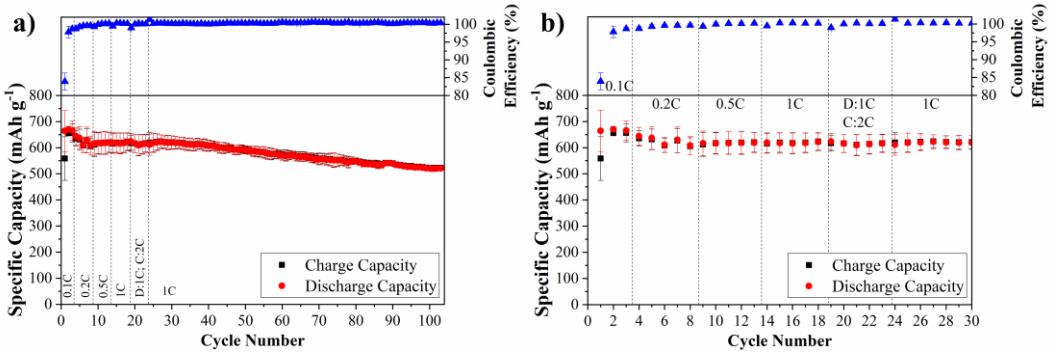

Figure 5.80 – Electrochemical characterization of the electrodes produced with the Cu2L: a) Entire test; b) Focus on the rate capability test

Table 5.36 – Values of charge and discharge capacities, normalized by the electrode weight, and relative values of coulombic efficiency for the electrodes produced with the Cu2L

Cycle	*C-rate*	*Charge Capacity (mAh g^{-1})*	*Discharge Capacity (mAh g^{-1})*	*Coulombic Efficiency (%)*
1		*558.62 ± 83.22*	*664.24 ± 78.85*	*83.91 ± 2.40*
2	*0.1C*	*655.66 ± 0.14*	*670.39 ± 10.78*	*97.82 ± 1.61*
3		*656.45 ± 33.94*	*665.32 ± 37.34*	*98.68 ± 0.45*
8	*0.2C*	*605.81 ± 32.07*	*608.15 ± 34.52*	*99.63 ± 0.40*
13	*0.5C*	*620.59 ± 37.78*	*619.16 ± 38.72*	*100.24 ± 0.17*
18	*1C*	*623.70 ± 33.43*	*622.32 ± 33.67*	*100.22 ± 0.05*
23	*2C*	*616.91 ± 32.94*	*616.11 ± 35.48*	*100.15 ± 0.44*
30		*620.94 ± 24.59*	*619.72 ± 25.86*	*100.20 ± 0.22*
50	*1C*	*592.83 ± 14.77*	*591.22 ± 15.31*	*100.27 ± 0.10*
103		*523.02 ± 5.75*	*520.86 ± 5.07*	*100.41 ± 0.13*

The voltage profiles (***Figure 5.81***) and CV curves (***Figure 5.82***) were consistent with those observed for the other CCs, confirming that the main lithiation and delithiation processes were unaffected by surface structuring. As previously observed for Cu1L, a reduced contribution of the CVS was detected, indicating improved kinetic accessibility of the AM. A detailed comparison among the different surface treatments is discussed in the following section.

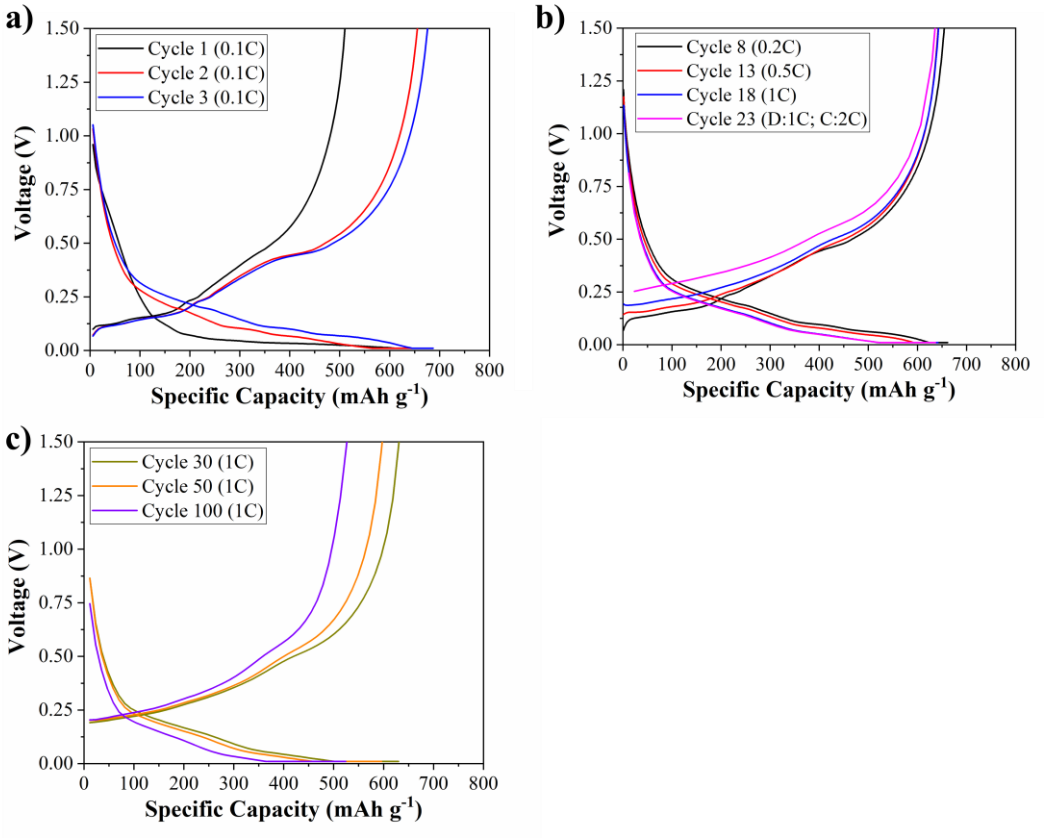

Figure 5.81 – Charge/discharge curves for some representative cycles of the electrodes produced with the Cu2L: a) Forming cycles; b) Rate capability test; c) Long cycling

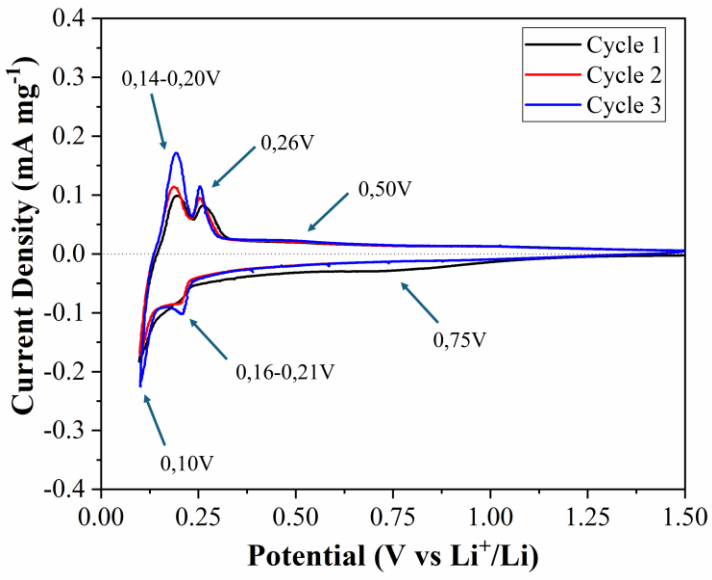

Figure 5.82 – Cyclic voltammetry performed on the Cu2L electrodes. The analysis was performed in the potential window between 0.1 V and 1.5 V with a scan rate of 0.1 mV s^{-1}.

5.3.3.2.4. DLIP treatment (Cu3L)

The electrodes produced on DLIP-structured CC (Cu3L), characterized by a regular 3D surface morphology, showed the best overall electrochemical performance among all the investigated samples (***Figure 5.83***, ***Table 5.37***). High first-cycle lithiation capacities close to 880 mAh g^{-1} were measured, together with good reproducibility and a rapid stabilization of coulombic efficiency above 99%. During rate capability testing, the electrodes maintained high charge and discharge capacities, remaining around 700 mAh g^{-1} even at high current densities. Long-term cycling revealed stable behaviour up to approximately 40 cycles, followed by a gradual capacity decay. Nevertheless, the average capacity retention reached about 88%, representing the highest value obtained in this study on the effect of CC surface modification.

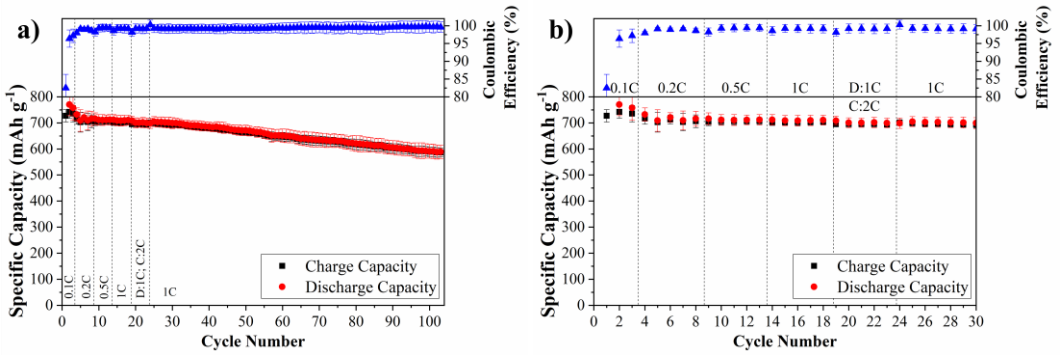

Figure 5.83 – Electrochemical characterization of the electrodes produced with the Cu3L: a) Entire test; b) Focus on the rate capability test

Table 5.37 – Values of charge and discharge capacities, normalized by the electrode weight, and relative values of coulombic efficiency for the electrodes produced with the Cu3L

Cycle	*C-rate*	*Charge Capacity (mAh g^{-1})*	*Discharge Capacity (mAh g^{-1})*	*Coulombic Efficiency (%)*
1		*727.22 ± 23.86*	*883.63 ± 68.17*	*82.49 ± 3.83*
2	*0.1C*	*741.87 ± 24.38*	*770.27 ± 42.57*	*96.39 ± 2.41*
3		*735.74 ± 31.52*	*757.63 ± 47.27*	*97.19 ± 1.90*
8	*0.2C*	*706.22 ± 24.53*	*715.89 ± 28.63*	*98.66 ± 0.68*
13	*0.5C*	*707.28 ± 12.90*	*711.79 ± 20.00*	*99.38 ± 1.00*
18	*1C*	*704.58 ± 10.87*	*710.72 ± 18.83*	*99.16 ± 1.16*
23	*2C*	*694.05 ± 9.72*	*699.71 ± 18.33*	*99.21 ± 1.28*
30		*692.93 ± 11.86*	*699.28 ± 20.73*	*99.12 ± 1.27*
50	*1C*	*665.63 ± 12.13*	*671.49 ± 19.86*	*99.15 ± 1.30*
103		*586.71 ± 17.18*	*589.16 ± 25.73*	*99.63 ± 1.48*

The improved electrochemical response can be attributed to the regular and controlled surface topology generated by DLIP processing, which promotes more homogeneous slurry spreading, enhanced electronic contact and a more effective

accommodation of silicon volume changes during cycling. Consistently with the other laser-treated CCs, a reduced contribution of the CVS was observed, indicating improved kinetic accessibility of the AM. The voltage profiles (***Figure 5.84***) and CV cycles (***Figure 5.82***) were comparable to those observed for the other samples, confirming that the main electrochemical mechanisms remained unchanged. The differences in performance can therefore be mainly associated with interfacial effects rather than intrinsic material behaviour.

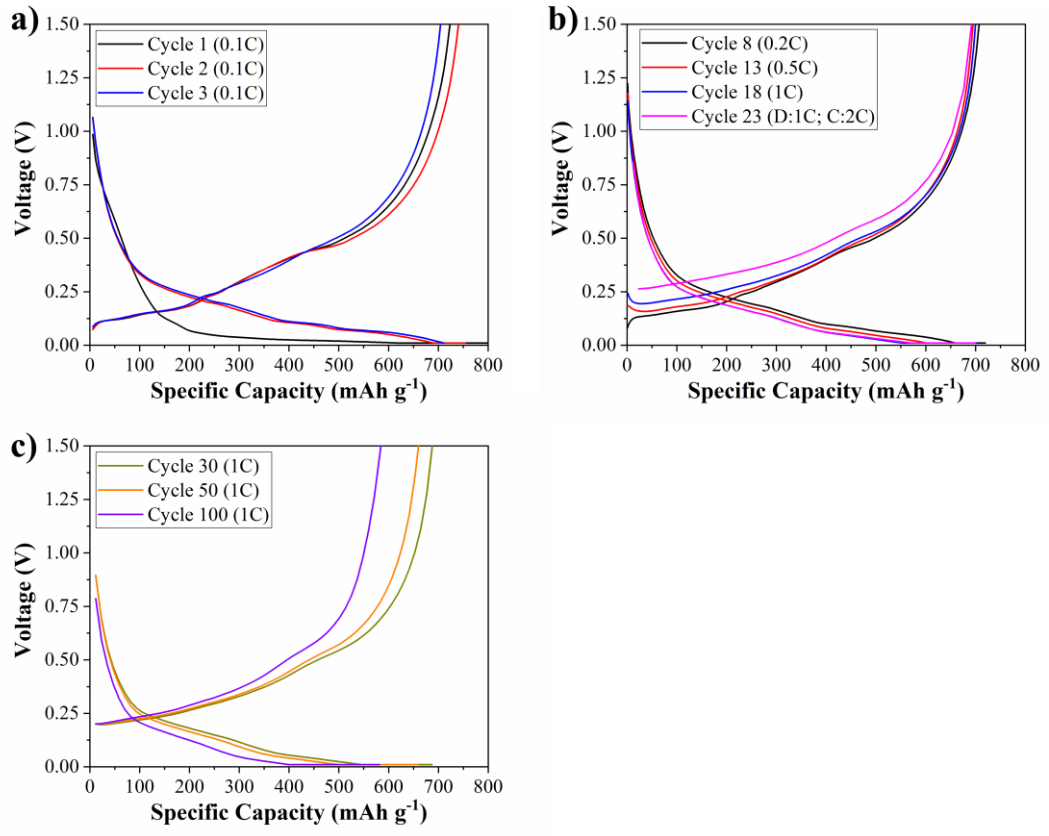

Figure 5.84 – Charge/discharge curves for some representative cycles of the electrodes produced with the Cu3L: a) Forming cycles; b) Rate capability test; c) Long cycling.

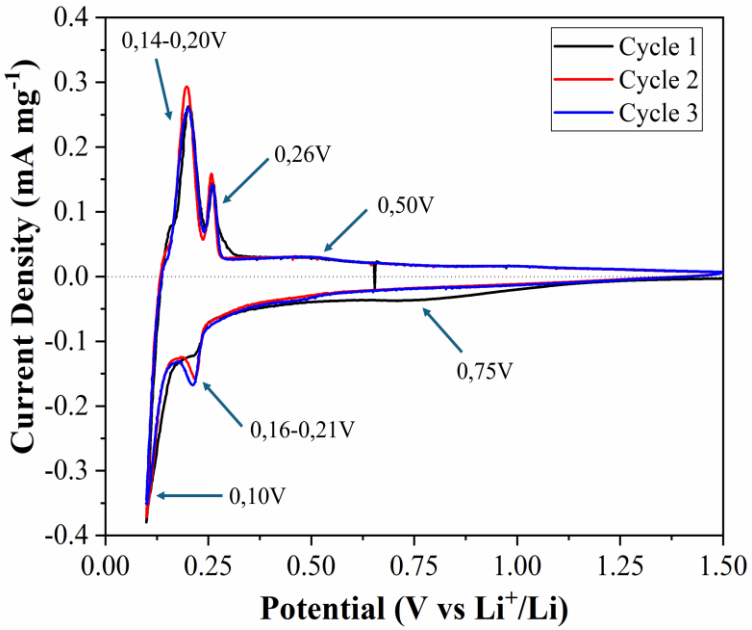

Figure 5.85 – Cyclic voltammetry performed on the Cu3L electrodes. The analysis was performed in the potential window between 0.1 V and 1.5 V with a scan rate of 0.1 mV s^{-1}.

5.3.3.3. Relationship between surface topology, interfacial resistance and electrochemical performance

The comparison of the electrochemical results, considering the discharge values and reported in ***Figure 5.86*** and ***Table 5.38***, showed that all laser treatments led to an overall improvement in electrochemical performance, except Cu2L, which exhibited results comparable to those of the CuP. The most pronounced improvement was observed for Cu3L, where the highly regular 3D structure generated by the DLIP treatment enabled enhanced capacities even at high C-rates (***Figure 5.86b***). In particular, at 2C, Cu3L exhibited an average discharge capacity approximately 100 mAh g^{-1} higher than that of CuP. However, when the capacity contribution associated with the CVS was excluded (***Figure 5.86c***), a markedly different trend emerges. In this case, CuP shows the lowest discharge capacity, followed sequentially by Cu1L, Cu2L, and Cu3L. Cu3L remained the laser treatment providing the greatest improvement in electrochemical performance; indeed, at 2C it delivered an average discharge capacity approximately 140 mAh g^{-1} higher than CuP.

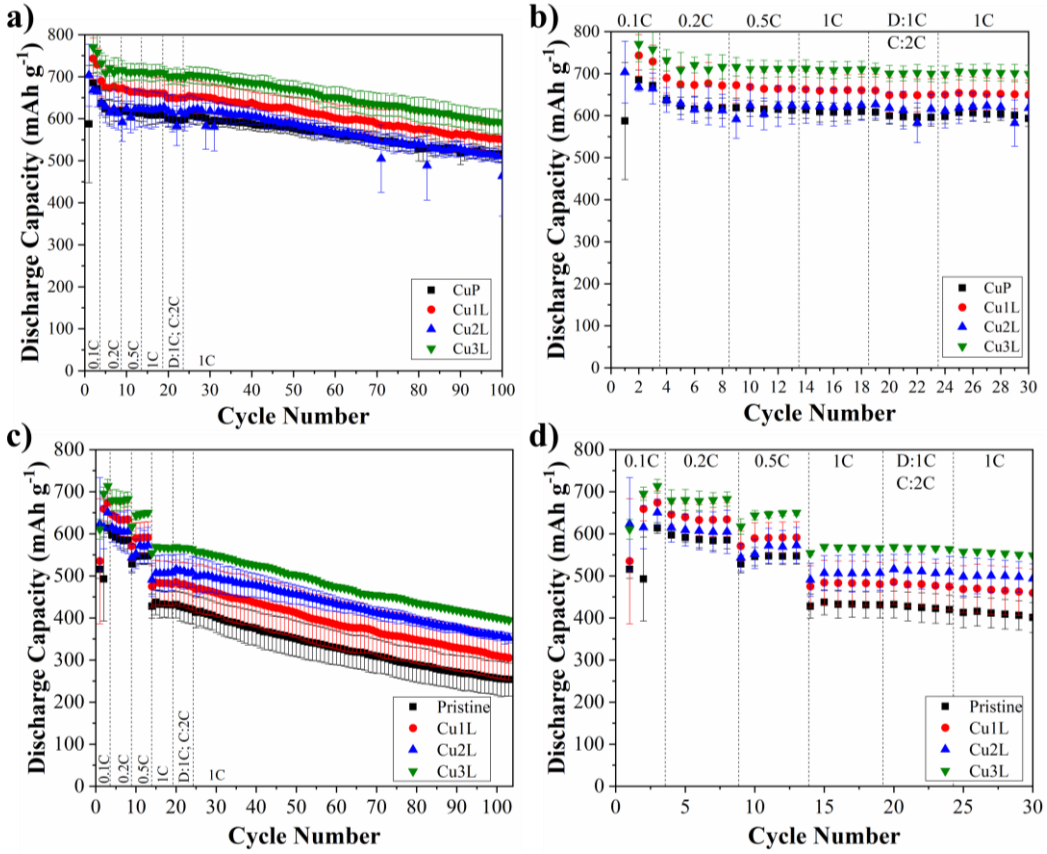

Figure 5.86 – Comparison of the discharge capacities of electrodes produced with laser-treated current collectors. Results are shown including the contribution of the CVS: a) the entire test; b) the rate capability test. Excluding the CVS:c) the entire test; d) the rate capability test.

Table 5.38 – Discharge capacity values, including and excluding the CVS and relative capacity retention (%) of silicon-based electrodes prepared on different CCs. Values are reported as average ± standard deviation calculated from replicate cells.

Cycle	***C-rate***	***Discharge Capacity (mAh g^{-1}) – Including CVS***			
		CuP	***Cu1L***	***Cu2L***	***Cu3L***
1		*587.28 ± 139.30*	*866.21 ± 92.16*	*664.24 ± 78.85*	*883.63 ± 68.17*
2	*0.1C*	*685.42 ± 23.32*	*743.15 ± 49.20*	*670.39 ± 10.78*	*770.27 ± 42.57*
3		*670.60 ± 9.36*	*728.51 ± 39.48*	*665.32 ± 37.34*	*757.63 ± 47.27*
8	*0.2C*	*617.88 ± 24.40*	*671.48 ± 43.81*	*608.15 ± 34.52*	*715.89 ± 28.63*
13	*0.5C*	*612.98 ± 18.95*	*663.59 ± 42.89*	*619.16 ± 38.72*	*711.79 ± 20.00*
18	*1C*	*610.04 ± 18.39*	*659.96 ± 39.19*	*622.32 ± 33.67*	*710.72 ± 18.83*
23	*2C*	*596.29 ± 21.45*	*649.65 ± 37.90*	*616.11 ± 35.48*	*699.71 ± 18.33*
30		*593.49 ± 19.05*	*649.63 ± 34.67*	*619.72 ± 25.86*	*699.28 ± 20.73*
50	*1C*	*576.79 ± 14.59*	*622.75 ± 26.65*	*591.22 ± 15.31*	*671.49 ± 19.86*
103		*513.60 ± 8.72*	*543.34 ± 39.21*	*520.86 ± 5.07*	*589.16 ± 25.73*
		Discharge Capacity (mAh g^{-1}) – Excluding CVS			
1		*515.87 ± 17.43*	*534.94 ± 121.41*	*623.60 ± 89.79*	*610.54 ± 19.28*
2	*0.1C*	*492.69 ± 81.61*	*658.94 ± 22.97*	*615.48 ± 41.55*	*695.44 ± 12.63*
3		*613.83 ± 10.72*	*673.83 ± 22.84*	*650.66 ± 25.62*	*713.59 ± 13.24*
8	*0.2C*	*585.39 ± 17.34*	*634.25 ± 33.24*	*604.78 ± 41.96*	*682.81 ± 13.77*

13	*0.5C*	*547.19 ± 15.74*	*591.13 ± 30.67*	*572.94 ± 34.87*	*649.93 ± 5.05*
18	*1C*	*431.24 ± 25.38*	*482.27 ± 42.42*	*506.63 ± 35.37*	*566.47 ± 2.95*
23	*2C*	*422.59 ± 28.87*	*476.61 ± 44.09*	*506.04 ± 27.69*	*565.56 ± 3.92*
30		*301.39 ± 152.32*	*459.34 ± 45.85*	*493.36 ± 28.92*	*548.90 ± 2.70*
50	*1C*	*350.53 ± 34.57*	*411.92 ± 47.46*	*455.47 ± 18.39*	*502.34 ± 4.62*
103		*253.69 ± 32.07*	*305.14 ± 42.48*	*352.49 ± 9.24*	*395.12 ± 4.36*
		Capacity Retention (%)			
		86.54	*83.50*	*85.81*	*87.70*

The significant increase in discharge capacity can be attributed to a reduction in the contribution of the CVS in favor of the CCS discharge capacity. A similar behavior has already been reported in previous studies related to the application of laser processing in LIBs; however, in those cases, a pulsed femtosecond laser was used to directly structure the electrode layer rather than the surface of the CC, as performed in the present work [406].

In general, for all laser-treated CCs, surface modification promoted a more homogeneous current distribution and improved electronic contact at the electrode-CC interface, thereby enhancing the overall electrochemical performance. This effect was more pronounced for Cu3L, whose surface exhibited a higher degree of regularity compared to the other treatments, leading to a stronger impact on electrode behavior.

To further investigate the electrodes, the electrode resistance and the interfacial resistance between the active layer and the CC were measured at room temperature using a 46-point probe system [460–462], and the results are reported in ***Table 5.39***. The internal resistance of an electrochemical cell is typically reflected in an IR drop during charge–discharge processes, which has a direct impact on both specific capacity and energy efficiency [463]. The results show that the composite volume resistivity remained essentially unchanged across all samples, as the electrode composition was identical. In contrast, the interface resistance clearly emerged as the most relevant differentiating parameter among the different CCs. In particular, the Cu3L, produced with the DLIP technology, exhibited the lowest interfacial resistance, which could be attributed to its more uniform surface morphology compared to Cu1L and Cu2L. This reduction in interface resistance promotes improved electronic transport at the electrode-CC interface, thereby contributing to the enhanced electrochemical performance observed for this configuration.

Table 5.39 – Resistivity of the composite dry layer and interface resistance of electrodes produced with different laser-treated current collector

	CuP	***Cu1L***	***Cu2L***	***Cu3L***
Composite Resistivity (Ω cm)	$1.89\ 10^{-1}$	$2.85\ 10^{-1}$	$2.45\ 10^{-1}$	$1.63\ 10^{-1}$
Interface Resistance (Ω cm^{-2})	$8.64\ 10^{-4}$	$4.16\ 10^{-3}$	$3.37\ 10^{-3}$	$5.30\ 10^{-4}$

Considering the comparison between the CV curves (***Figure 5.87***), the analysis of the first cycle (***Figure 5.87a***) confirmed the lithiation of silicon and the associated structural transition from crystalline silicon to amorphous Li_xSi phases [420–425,464]. Overall, all samples exhibited similar electrochemical features, although differences in peak intensity and position were observed depending on the CC treatment. During the cathodic scan, the broad peak at approximately 0.75 V related to SEI formation, was observed for all samples, indicating that laser texturing did not significantly affect this process. At lower potentials, a characteristic peak around 0.2 V associated with silicon lithiation was detected, with noticeable variations in definition and intensity. In particular, the Cu3L exhibited a sharper and more intense peak shifted toward higher potentials, indicating reduced polarization and more efficient utilization of the AM [465]. A second cathodic peak close to 0.1 V, attributed to the phase transition from amorphous to crystalline $Li_{15}Si_4$, was also more pronounced for Cu3L. During the anodic scan, two main oxidation peaks related to graphite delithiation and silicon dealloying were identified at around 0.14-0.26 V, along with a broader feature at higher potential (~0.50 V) attributed to further silicon dealloying. Laser-textured CCs, particularly Cu2L and Cu3L, showed better-defined anodic peaks, consistent with lower overpotential and improved electronic conductivity [465]. Comparison of the third cycle (***Figure 5.87b***) revealed similar peak positions to those of the first cycle, with increased current intensity due to electrode activation and stabilization of the SEI layer [466]. Overall, the enhanced performance observed for laser-textured CCs, especially CuL3, was attributed to improved interfacial contact and reduced charge-transfer resistance, resulting from a more homogeneous and controlled surface roughness. Further post-mortem analysis performed by another project partner showed that the 3D structure of the CC surface enabled a more effective accommodation of the AM expansion during cycling, resulting in reduced electrode deformation, particularly for Cu3L. Additional details and a comprehensive discussion of these findings are reported in the related publication [206].

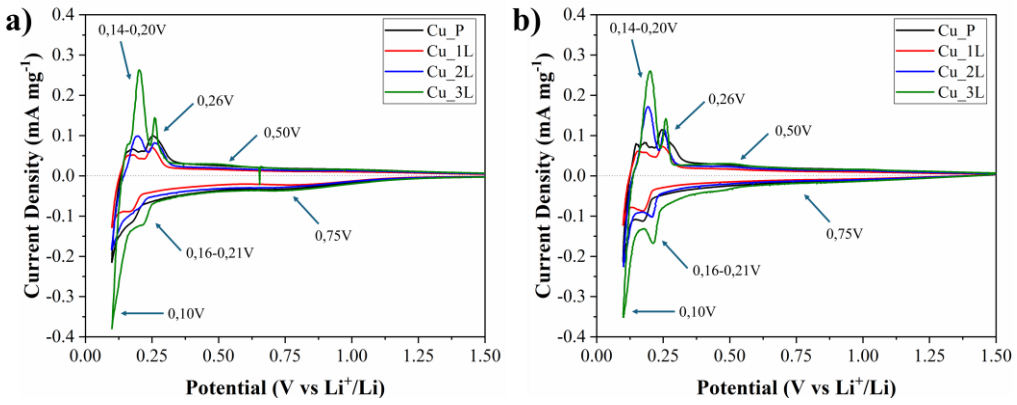

Figure 5.87 – Comparison between the cyclic voltammetry of the electrodes produced with the laser treated CCs: a) Cycle 1; b) Cycle 3.

5.3.4. Process implications and perspectives for scale-up

This work focused on the development of silicon-based anodes by addressing two critical aspects: the robustness of the electrode production process and the engineering of the electrode-CC interface. A stable and reproducible laboratory-scale process was established for the fabrication of water-based SC electrodes, enabling consistent ML and areal capacity while avoiding calendering, which remains challenging for silicon-based anodes.

Starting from the optimized baseline, laser texturing of copper CCs proved to be an effective approach to further enhance electrochemical performance without altering the AM composition. Among the investigated treatments, the DLIP-modified CC (Cu3L) supplied the most significant and reproducible benefits, including higher capacities at high C-rates, improved capacity retention, and a reduced contribution of the CVS in favor of capacity directly associated with the AM. Electrochemical characterization and resistance measurements indicated that these improvements are mainly related to reduced interfacial resistance and enhanced electronic contact between the active layer and the CC. Post-mortem analysis further suggested that the regular three-dimensional surface morphology of Cu3L enables a more controlled accommodation of AM expansion during cycling.

Overall, this work demonstrates that the performance of silicon-based anodes is governed not only by material design but by the coupled optimization of processing and interface engineering. From an industrial perspective, this integrated approach represents a necessary step toward the implementation of silicon anodes in scalable manufacturing processes.

5.4. Nanoporous Silicon for the production of Si-dominant anodes

The LIBs generation 3b aims at increasing the silicon content inside the anode to achieve higher volumetric energy in the final batteries. Generally, it is possible to define as “silicon-dominant” (SD) those electrodes in which the amount of silicon is more than 50%. Increasing the silicon content in silicon-based anodes can reduce the electrode thickness to about 19% of that of a graphite-dominant electrode at the same areal capacity, highlighting silicon’s contribution to improved volumetric energy density, in addition to its higher specific capacity [467]. In this study, the amount of silicon used for the anode production reached 80 wt.%. However, as already widely explained in ***Chapter 2***, this great advantage in terms of capacity and energy density is associated with the significant issue of expansion and contraction during the lithiation and de-lithiation process. To overcome this issue, multiple strategies have been investigated in the literature,

such as tailored synthesis approaches, the use of suitable binders, and capacity limitation.

To overcome the volume change issue, in this work, the three strategies were simultaneously applied to enhance the production of high-performing electrodes. The silicon produced by E-Magy [101,468], thanks to its nanoporous structure, (***Figure 5.88***) allows a near-zero volume expansion [469]. More in detail, in this particular material, the lithiation occurs along all the silicon particle surface, but the presence of the pores distributes the expansion toward the interior of the particle, so the external expansion is more limited. This material is characterized by an internal porosity of approximately 35%; therefore, the calendering process was not performed to avoid the collapse of the nanoporous structure [469]. Secondly, the binder chosen for the trials was PAA, which is already widely used for silicon-based electrodes [136,137,142,149]. However, its limited processability, as described in the previous chapter, led to the decision of adding some natural polysaccharides to improve the processability of the slurry even at higher TRL levels. The use of natural polysaccharides like TG, CGN, Na-Alg and Pec also aims to improve the sustainability of the production process by partially substituting PAA, which is a petroleum-based polymer [470].

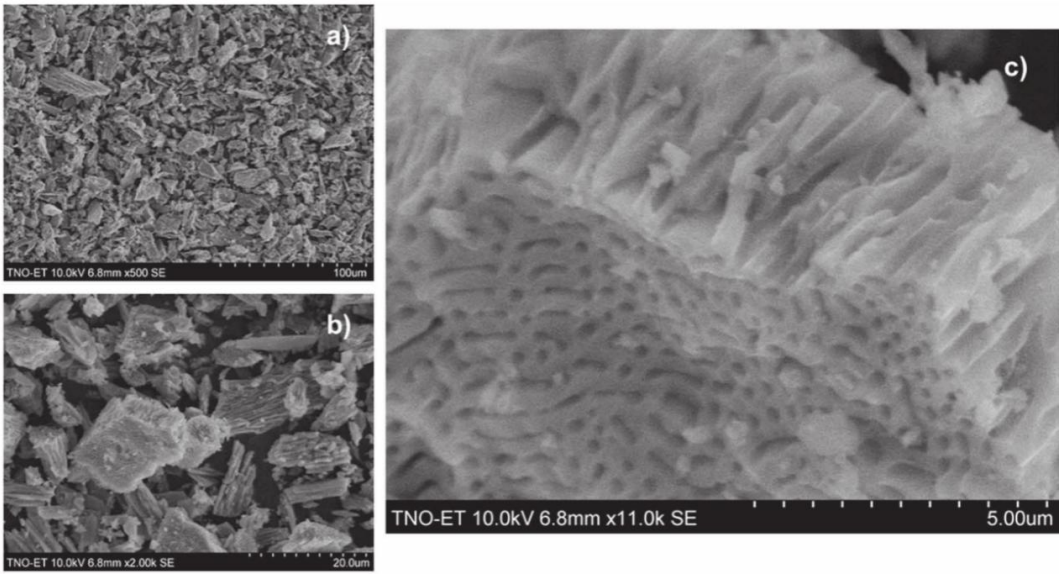

Figure 5.88 – SEM images of the silicon supplied by E-Magy at different magnifications: a) 500X; b) 2kX; c) 11kX. Reproduced from [469]

Finally, the silicon capacity was limited to 1000 mAh g^{-1}. In practical full-cell configurations, the anode capacity must be balanced with that of the cathode to ensure an appropriate N/P ratio; consequently, accessing the fully theoretical capacity of silicon is neither required nor desirable, as it would induce excessive volume changes and lithium consumption without providing additional usable energy at the cell level [471]. Capacity limitation is one of the most efficient ways to enhance the cycle life of the material, because less stress is applied during the

lithiation and de-lithiation processes, avoiding the pulverization of the material [106,469].

The first part of this work was performed in Politecnico di Torino, with the aim of optimizing the production process tailored to the facilities used and confirming the electrochemical performance declared by the supplier. The slurry optimization was based on a SF of 45 wt.%, in line with the previous materials, which was sufficient to obtain suitable deposition. In the case of these SD electrodes, however, the composition was quite different, with a reduction of the amount of active material from 95% to 80%, in favor of a higher binder content. The higher amount of binder was necessary to improve the mechanical integrity of the electrodes, in terms of cohesion and adhesion [409]. Within this work, the electrodes were produced both at laboratory level and at pilot-line level, to compare how the different facilities involved in the process affected the final results.

The second part of the work was performed during the period abroad at the laboratories of CIC energiGUNE (Vitoria-Gasteiz, Spain), where the already optimized slurries were further investigated through rheological measurements, leading to the necessity of increasing the SF to 60 wt.% for producing slurries with a viscosity in the range required for LIBs application. The mechanical characterization of the electrodes, coupled with their electrochemical characterization enabled a deeper understanding of the role of the binders in electrode performance.

5.4.1. Small scale production: Laboratory Level

This section focuses on the comprehensive description of the optimization procedure performed at laboratory level, along with the relative electrochemical performance. After the preliminary optimization of the slurry production process based on the precise supplier guidelines, the focus shifted to improving the sustainability of the process through the use of natural polysaccharides as binder additives. The electrodes were characterized using rapid measurements, such as dry-layer thickness and weight distribution to evaluate the homogeneity of the coating step and the reproducibility of this production process.

In the second section, the electrochemical results of the electrodes produced are presented, highlighting how the natural polysaccharides, even when added in a small amount of 1%, can influence electrochemical performance.

5.4.1.1. Electrode production

The electrode production procedure was based on the Argolab mixer (***Figure 3.5***), already adopted for the previous silicon composite material, which allowed efficient mixing of high-viscosity slurries and the preparation of larger slurry volumes compared to a simple magnetic stirrer. The composition of 80:5:5:10 and

the materials (Si, graphite, C45, binder) involved in the production of SD electrodes were based on the supplier suggestion, in line also with patents [410,472] and the literature [147,473]:

- 80 wt.% of Nanoporous Silicon supplied by E-Magy, whose additional characteristics and investigations are reported in [420]
- 5 wt.% of Graphite (Actilion GHDR 15-4, Imerys Timcal) as both conductive and structural additive: the addition of graphite to improve these characteristics was not necessary in previous silicon-based electrodes due to the lower silicon content involved [270,474]
- 5 wt.% of C45 (Imerys Timcal) as conductive additive
- 10 wt.% of PAA (Sigma Alrich) as polymeric binder, with a molecular weight of 450,000 g mol^{-1}

The choice of PAA instead of CMC/SBR binder system had already been introduced as one of the most promising binder for silicon-based anodes, thanks to its improved mechanical properties in the slurry, guaranteeing higher electrochemical performance and longer cycle life [141–143]. The electrode composition of 80:5:5:10 was maintained unaltered throughout the optimization process, apart from the substitution of 1% of PAA with natural polysaccharides. The introduction of a natural polysaccharide in this content is still scarcely reported in literature, particularly for electrochemical applications. An overall summary of the trials is reported in ***Table 5.40***, highlighting the changes adopted per each deposition trial and the subsequent conclusions.

Table 5.40 – Summary of the experimental trials carried out to optimize the slurry formulation and coating parameters of silicon-dominant anodes at laboratory scale. The table highlights the evolution of binder composition, SF and processing conditions, together with the main qualitative outcomes observed in terms of coating homogeneity and electrode manufacturability.

Trial Number	***Trial ID***	***Solid Fraction***	***Changes adopted***	***Main conclusions***
1	PAA_1	31.25%	First adaptation of supplier mixing procedure. Manual dry mixing of powders.	Slurry too liquid. Sedimentation effects. Very low ML and poor electrochemical performance.
2	PAA_2	45 wt.%	Increased SF. Same mixing conditions.	Reduced excess water but strong agglomeration and coating defects. Mixing shear too high.
3	PAA_3	45 wt.%	Reduced mixing speed and time. Improved dispersion protocol.	Homogeneous slurry and reproducible coatings. Selected as optimized baseline process.
4	PAA_SBR	45 wt.%	Replacement of 1 wt.% PAA with SBR additive.	Similar electrode morphology but worse electrochemical performance and poor reproducibility. Possible binder incompatibility.
5	PAA_Alg	45 wt.%	Addition of Alg as natural polysaccharide additive.	Improved ML and significantly enhanced long-term electrochemical stability.
6	PAA_TG	45 wt.%	Addition of TG additive.	Higher dry thickness at high wet deposition but lower electrochemical performance. Limited mechanical stability.

7	PAA_Pec	45 wt.%	Addition of Pec additive.	Very stable electrochemical behavior and high retained capacity. Promising sustainable binder system.

In addition to the binder change, a study on the impact of wet deposition thickness was conducted (***Table 5.41***); for each slurry preparation, multiple laminates were produced with different imposed wet thicknesses. The electrode characteristics were strictly dependent on the coating deposition parameters: the results show a generally consistent increase in ML with increasing wet thickness, indicating that the coating process was able to reasonably scale the deposited material across the investigated conditions.

Table 5.41 – Summary of the laboratory-scale trials for E-Magy SD anodes, reporting trial ID, coating thickness and the resulting electrode properties.

Trial ID	***Wet Thickness (µm)***	***Dry Thickness (µm)***	***Average Weight (mg)***	***Mass Loading (mg cm^{-2})***
PAA_1	*50*	*11*	*10.19 ± 0.10*	*0.45 ± 0.05*
	100	*41 ± 3*	*15.13 ± 1.66*	*2.69 ± 0.21*
PAA_2	*50*	*23 ± 7*	*12.46 ± 1.12*	*1.48 ± 0.51*
	100	*47 ± 6*	*15.54 ± 0.80*	*2.87 ± 0.39*
PAA_3	*50*	*22 ± 1*	*11.61 ± 0.43*	*1.09 ± 0.09*
	70	*31 ± 5*	*13.23 ± 0.60*	*1.82 ± 0.27*
	100	*41 ± 2*	*14.91 ± 0.38*	*2.59 ± 0.17*
PAA_SBR	*50*	*24 ± 1*	*11.78 ± 0.70*	*1.17 ± 0.12*
	70	*41 ± 4*	*13.78 ± 0.50*	*2.07 ± 0.22*
	100	*46 ± 2*	*14.78 ± 0.33*	*2.53 ± 0.15*
PAA_Alg	*50*	*26 ± 1*	*12.69 ± 0.17*	*1.58 ± 0.08*
	70	*33 ± 1*	*13.51 ± 0.10*	*1.95 ± 0.05*
	100	*46 ± 3*	*15.31 ± 0.22*	*2.77 ± 0.09*
PAA_TG	*50*	*27 ± 2*	*11.73 ± 0.14*	*1.15 ± 0.06*
	70	*43 ± 2*	*14.51 ± 0.17*	*2.41 ± 0.08*
	100	*54 ± 1*	*16.02 ± 0.26*	*3.09 ± 0.12*
PAA_Pec	*50*	*23 ± 1*	*11.85 ± 0.23*	*1.20 ± 0.10*
	70	*32 ± 1*	*13.64 ± 0.31*	*2.01 ± 0.14*
	100	*44 ± 1*	*14.78 ± 0.20*	*2.53 ± 0.09*

However, significant variability in dry thickness was observed for some formulations, particularly for PAA_1 and PAA_2, where large standard deviations and inconsistent values suggest limited process stability. This behavior can be attributed to differences in slurry dispersion, rheological properties, and coating

uniformity, highlighting that not all formulations ensured reproducible electrode fabrication and further optimizations were required. In contrast, systems containing additives exhibited more stable and consistent thickness values, together with higher ML at comparable wet thicknesses. This indicates an improved slurry processability and particle packing, likely associated with enhanced rheological control. Below, a comprehensive description of the electrode production processes and relative electrochemical performance is presented.

5.4.1.2. Electrochemical Characterization

After electrode production, the electrodes were vacuum dried for 4h at 120°C to ensure complete evaporation of residual water from electrode porosities. To guarantee a proper statistical evaluation of the electrochemical performance, three cells were assembled for each sample. The cells were electrochemically tested by galvanostatic charge-discharge analysis and CV.

Cell assembly was performed in the argon-filled glovebox, following the same procedure described for the SC anodes of the previous chapters. For the galvanostatic charge-discharge test, the SD electrodes were assembled in half-cell configurations, using metallic lithium as the counter electrode and G/F Whatman separator soaked with 150 µl of 1 M $LiPF_6$ dissolved in a solution of EC:DEC in ratio 1:1 with the addition of 10 wt.% of FEC and 2 wt.% of VC. The charge and discharge test was performed in the voltage range between 0.04 and 1.00 V. The cycling protocol for the first trial is reported in ***Table 5.42*** and consisted of two formation cycles, followed by a rate capability test and a long-term cycling at 1C. However, the electrochemical performances during long-term test were worse than expected, and after a discussion with the supplier, the cycling protocol was modified (***Table 5.43***) by adding a 2C step during the rate capability test and reducing the current density to 0.5C during long-term cycling. It is worth noting that, compared to the graphite- and SC anodes, in this case, CVS was not adopted during the test. The capacity retention was calculated as the ratio of the discharge capacity at cycle 120 to the discharge capacity at cycle 30.

Table 5.42 – Cycling protocol adopted for the first charge-discharge test for silicon-dominant anodes

Cycle	***Mode***	***Discharge***	***Charge***
1-2	*Formation*	*CCS: 0.1C*	*CCS: 0.1C*
3-7	*Rate Capability*	*CCS: 0.2C*	*CCS: 0.2C*
8-12	*Rate Capability*	*CCS: 0.5C*	*CCS: 0.5C*
13-17	*Rate Capability*	*CCS: 1C*	*CCS: 1C*
18-20	*Recovering*	*CCS: 0.1C*	*CCS: 0.1C*
21-120	*Long Cycling*	*CCS: 1C*	*CCS: 1C*

Table 5.43 – Cycling protocol adopted after the production optimization for the charge-discharge test for silicon-dominant anodes

Cycle	Mode	Discharge	Charge
1-2	Formation	CCS: 0.1C	CCS: 0.1C
3-7	Rate Capability	CCS: 0.2C	CCS: 0.2C
8-12	Rate Capability	CCS: 0.5C	CCS: 0.5C
13-17	Rate Capability	CCS: 1C	CCS: 1C
18-22	Rate Capability	CCS: 2C	CCS: 2C
23-27	Recovering	CCS: 0.1C	CCS: 0.1C
28-120	Long Cycling	CCS: 0.5C	CCS: 0.5C

For the CV test, the cells were assembled into three-electrodes configuration, both the working electrode and the lithium counter electrode were punched into 10 mm diameter discs, and the electrolyte volume was reduced to 120 µL. For both measurements, the electrolyte was in excess to prevent it from acting as a limiting factor. The CV test was performed in the voltage window between 0.04 and 1.50 V at a scan rate of 0.1 mV s^{-1}, performing five cycles for each sample. To enable direct comparison among samples, all CV curves were normalized to the corresponding AM mass.

As previously discussed, the use of a half-cell configuration with lithium as counter electrode represents a limitation for a rigorous evaluation of CE, since the virtually unlimited lithium reservoir hinders an accurate quantification. In addition, localized lithium plating phenomena can generate parasitic reactions that increase the value of CE. Nevertheless, the corresponding values are reported for completeness, and specific remarks are supplied when relevant to the overall discussion.

5.4.1.3. PAA-based

The optimization process started with the use of pure PAA, to adapt the optimized production process proposed by the supplier to the facilities available at PoliTo laboratories. The slurry optimization required a few trials to reach satisfactory electrode properties. The first trial was based on the process suggested by the silicon supplier, then both the time and the rotation speed of the mixers were adjusted based on PoliTo facilities to reach the optimal conditions while avoiding material degradation. The electrodes produced with the PAA as a single binder were electrochemically tested to confirm the optimization of the production process with the cycling protocol reported in ***Table 5.42***. The results of the first trial are presented below, as the preliminary outcomes did not meet the expected performance. These initial electrochemical data were not discarded; instead, they were critically analyzed to identify possible limitations related both to the production process and to the applied testing protocol. On this basis, adjustments were implemented in the slurry preparation and in the cycling conditions.

Subsequently, the electrochemical results obtained after these optimizations are reported, showing performance more consistent with the expected behavior of the material.

5.4.1.3.1. First trial: PAA_1

The first trial was prepared considering a total solid amount of 5 g, from which the amount of each component was calculated. Compared to the previous mixing procedures described for graphite and SC anodes, where each powder component was added one by one, in this case, silicon and graphite were first manually mixed and then added to the binder solution. This modification was introduced because the order of material addition can significantly affect slurry rheology and component dispersion, ultimately influencing the final electrode microstructure and electrochemical performance [360,361]. The detailed mixing process is reported below:

1. The first step consisted of the overnight dilution of PAA in MilliQ water to produce a 10 wt.% solution. This step was performed using a magnetic stirrer in a closed vessel, to avoid the evaporation of the solvent.
2. 5 g of diluted PAA were further diluted in 6.5 mL of MilliQ to reach the desired SF, and the mixture was stirred for 15 minutes at 1,000 rpm to ensure proper homogenization.
3. 0.25 g C45 was added to the PAA solution and, using the Argolab mixer, the mixture was stirred at 1,500 rpm for 15 minutes.
4. 4.0 g of silicon and 0.25 g of graphite were dry mixed and then manually added to the solution. Initially, the mixture appeared very dry and lacking water; however, after a few minutes of manual mixing, the slurry became more homogenous. Once adequate dispersion was achieved, the automatic mix was started at 2,000 rpm for 30 minutes.

The total mixing time, excluding PAA dissolution, was approximately 1 hour, including the manual mixing step. This corresponds to a reduction of around 70% in processing time compared to graphite and SC anode production. The slurry produced in this way was characterized by a SF of 31.25%, significantly lower than the 40% used for graphite and 50% for silicon composite. After mixing, the slurry exhibited an almost liquid-like behavior, which created some issues during the coating step; however, it appeared homogenous and free of visible clumps or aggregates.

The coating step was performed on the 6 µm-thick Cu CC using the automatic film applicator previously adopted. The manual doctor blade was set to two different wet thicknesses (50 and 100 µm) to evaluate the impact of this parameter on the final electrodes.

The laminates were dried at room temperature (RT) [469]: immediately after coating, the dry process started immediately and was completed in less than half an hour under ambient conditions. This approach, which avoids forced drying, is partially supported by the work of Real Hernandez et al. [475], who reported that storing silicon-based electrodes under high-humidity conditions promotes the transformation of certain covalent bonds between silicon and the binder into hydrogen bonds, resulting in a more balanced distribution between ester and hydrogen interactions. This rearrangement is suggested to enhance the mechanical integrity of the electrode film, thereby contributing to improved cycling stability.

The laminates produced at both wet thicknesses showed good homogeneity and uniform dispersion across the surface, without visible clumps and defects (***Figure 5.89***). In line with previous studies on this specific silicon material, the electrodes were not pressed or calendered [270,469]. However, the laminate produced with the lower wet thickness (***Figure 5.89a***) exhibited an excess of water on one side, likely due to the low SF used in this formulation.

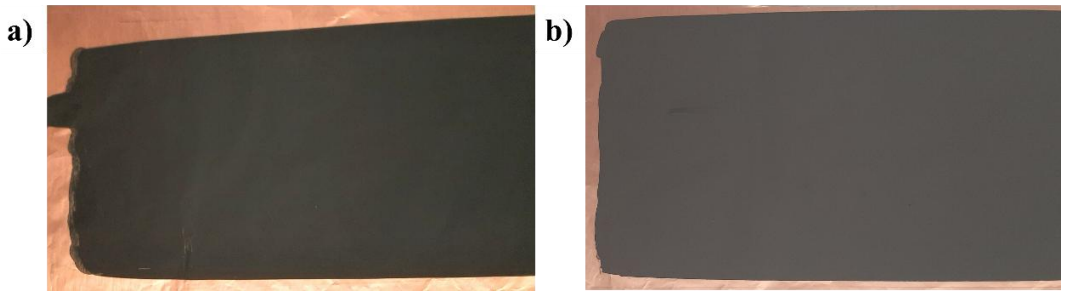

Figure 5.89 – Laminates produced during the first trial with a SF of 31% and a formulation containing 80 wt.% Si and 10 wt.% PAA, deposited at different wet thicknesses: a) 50 µm; b) 100 µm.

The electrodes were manually punched into 15 mm discs to be weighed and electrochemically tested. The dry thickness was calculated excluding the contribution of the CC. The 50 µm deposition thickness led to exceptionally low dry layer values (11 µm) and a ML of 0.45 ± 0.05 mg cm^{-2}, as collected in ***Table 5.41***. When the wet thickness was doubled (100 µm), the dry thickness reached 41 ± 3 µm and the ML increased to 2.69 ± 0.21 mg cm^{-2}. The explanation for these markedly different values is likely related to an accumulation of slurry at the bottom of the beaker, which was not clearly detected during coating. The low SF promoted a form of sedimentation: the first laminate was produced using the upper portion of the slurry, which was richer in solvent and poorer in solid particles, leading to the observed low dry thickness and ML values.

The electrochemical results of the electrodes, with an average ML of 2.83 mg cm^{-2} were far from expectations (***Figure 5.90***). Considering the long-term test up to 120 cycles (***Figure 5.90a***), the replicas were characterized by an overall capacity decay as soon as the current density was improved at 1C and a general low reproducibility between the samples, which led to the high statistical variation

observed in the graph. When considering only the rate capability test (***Figure 5.90b***), the variation between the samples was less evident, and the cells presented high reproducibility. However, after the two formation cycles at 0.1C, all the replicas were characterized by an important decay of the capacity already at 0.2C, which was far from the declared capacity of the material [469].

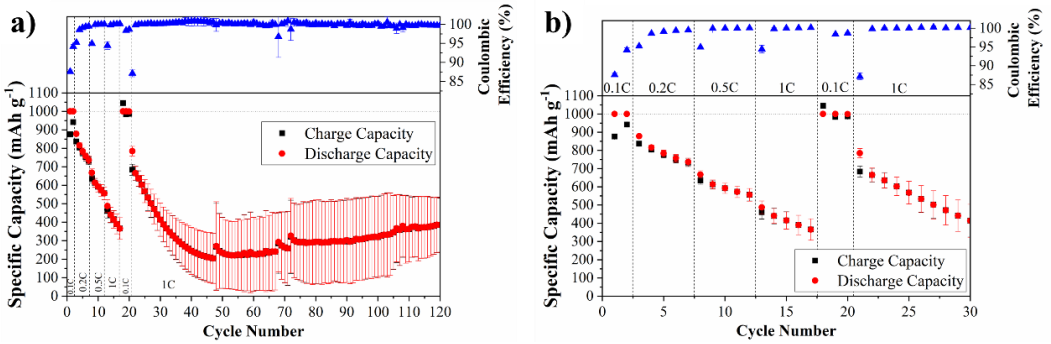

Figure 5.90 – Values of charge and discharge capacity and relative coulombic efficiency for the first production trial using 10 wt.% PAA as binder: a) Entire test, up to 120 cycles; b) Focus on the rate capability test.

Considering the forming cycles (***Table 5.44***), because of the limitation of the silicon capacity at 1000 mAh g^{-1}, this value was the one observed for the lithiation process of the material. In contrast, the charge capacity, which corresponds to the de-lithiation process from silicon, presented lower values: for cycle 1, the average value was around 875 mAh g^{-1}, which corresponded to an average initial CE of 87.60 wt.%. This value is in line with the average first cycle CE of SD materials [476,477] but far from the remarkable value of 92% reported by Maroni et al. [478]. When considering the rate capability test, the overall performance of the samples gradually decreased as the current density increased. At 1 C, the average discharge capacity was 365.72 mAh g^{-1} and the average charge capacity was 366.18 mAh g^{-1}, corresponding to an average CE above 100%. It is important to highlight that, when the current density was decreased to 0.1C for cycle 18, 19 and 20, the discharge capacity increased again at 1000 mAh g^{-1}, implying that the silicon material did not suffer from any degradation mechanism when the current density was increased but kinetic limitation factors limited the electrode performance [419].

Table 5.44 – Values of charge and discharge capacities, normalized by the electrode weight, and relative values of coulombic efficiency for some representative cycles for the electrodes produced with the first production trial using 10 wt.% PAA as binder.

Cycle	*C-rate*	*Charge Capacity (mAh g^{-1})*	*Discharge Capacity (mAh g^{-1})*	*Coulombic Efficiency (%)*
1	*0.1C*	*875.92 ± 4.20*	*999.95 ± 0.02*	*87.60 ± 0.42*
2		*941.88 ± 5.50*	*999.89 ± 0.02*	*94.20 ± 0.55*
7	*0.2C*	*732.62 ± 20.93*	*736.22 ± 20.85*	*99.51 ± 0.04*

12	*0.5C*	*556.62 ± 34.61*	*556.34 ± 34.76*	*100.05 ± 0.04*
17	*1C*	*366.18 ± 59.10*	*365.72 ± 59.12*	*100.13 ± 0.08*
20	*0.1C*	*986.49 ± 1.70*	*999.86 ± 0.05*	*98.66 ± 0.17*
30		*414.38 ± 90.08*	*413.83 ± 90.38*	*100.15 ± 0.12*
50	*1C*	*234.21 ± 192.00*	*233.67 ± 191.78*	*100.38 ± 0.30*
120		*384.10 ± 146.59*	*384.99 ± 147.18*	*99.78 ± 0.10*

During the long-term test at 1C, the average capacities significantly decay in the first 20 cycles: the average discharge capacity dropped from 413.83 mAh g^{-1} in cycle 30 to 233.67 mAh g^{-1} in cycle 50. After that, a gradual recovery was observed up to 384.99 mAh g^{-1} of cycle 120. This behavior was probably due to microcracking and intermittent loss of the electronic network, which increased the internal resistance of the electrodes [479,480]. As cycling proceeded, structural rearrangement and partial reconnection led to an apparent capacity recovery [481]. The average capacity retention was 93.03 %, thanks to the great recovery observed after cycle 50.

A deeper investigation of the lithiation and de-lithiation processes was possible thanks to the voltage profile analysis of one exemplary cell (***Figure 5.91***). Considering the forming cycles (***Figure 5.91a***), the lithiation process of the first cycle presented the typical shape of the important voltage drop and the subsequent voltage plateau, associated with SEI formation [91,482,483]. The de-lithiation profile, in line with expectations, highlighted the typical ICE observed during the first cycle. Considering the voltage profiles during the rate capability test (***Figure 5.91b***), the lithiation and de-lithiation processes maintained a consistent profile but exhibited shorter voltage plateaus, which ultimately led to increased polarization as the current density increased. Regarding the long-term test, the voltage profile of cycle 30 (***Figure 5.91c***, blue curves) was characterized by shapes consistent with the previous profiles but with an even shorter plateau. This effect was even more evident in cycle 50 (green curves), which showed the highest polarization among the observed curves. The increase in capacity was confirmed by the profile of cycle 120 (red curves), characterized by slightly longer plateaus than cycle 50 and lower polarization.

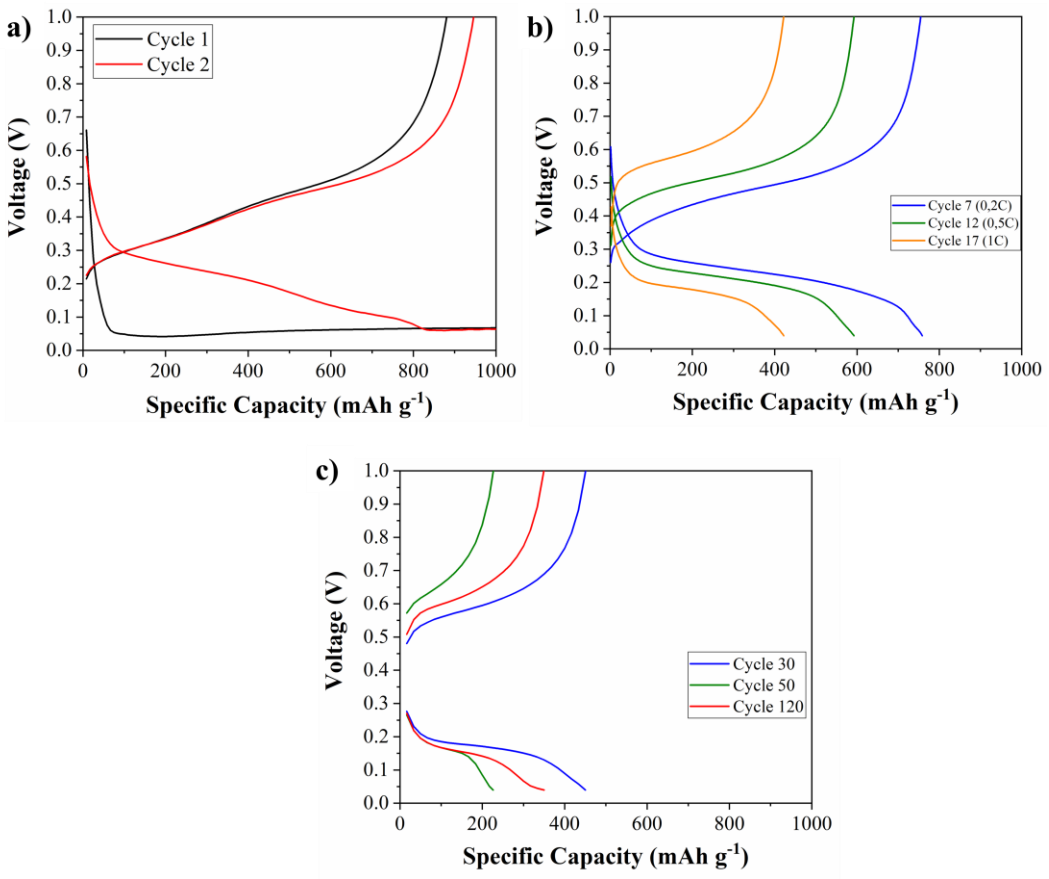

Figure 5.91 – Charge/discharge profiles for some representative cycles for the first production trial using 10 wt.% PAA as binder: a) Forming cycles; b) Rate capability test; b) Long-term test.

The CV profiles of the first three cycles (***Figure 5.92***) revealed the typical electrochemical behavior of silicon-based anodes. The cathodic scan of the first cycle (black curve) presented a different shape compared to the other cycles, with the typical behavior due to the SEI formation [417]. During the anodic scan, peaks centered at ~0.31 V and ~0.50 V are associated with the de-lithiation of Li_xSi phases, reflecting the characteristic multi-step dealloying process of silicon [484]. Although almost negligible, the peak at 0.24 V corresponded to one of the three de-lithiation peaks of the graphite, the peaks around 0.11 and 0.16 V were barely visible [484]. During the second and third scans, the cathodic broad peaks observed at approximately 0.23 and 0.27 V correspond to two silicon lithiation steps, from initial formation of alloy Li_xSi to deeper lithiation [485]. The gradual increase in intensity and the sharper definition of cathodic and anodic peaks can be associated with progressive electrode activation and an increase in the electrochemically accessible active area, as commonly observed in silicon-based anodes [429,486]. The absence of significant peak shifts or the emergence of additional side reactions suggests that, within the initial cycles, the system undergoes structural and interfacial stabilization rather than severe degradation. Overall, the observed evolution was consistent with the early-stage activation and

structural reorganization phenomena typically reported for silicon-based electrodes [484,487].

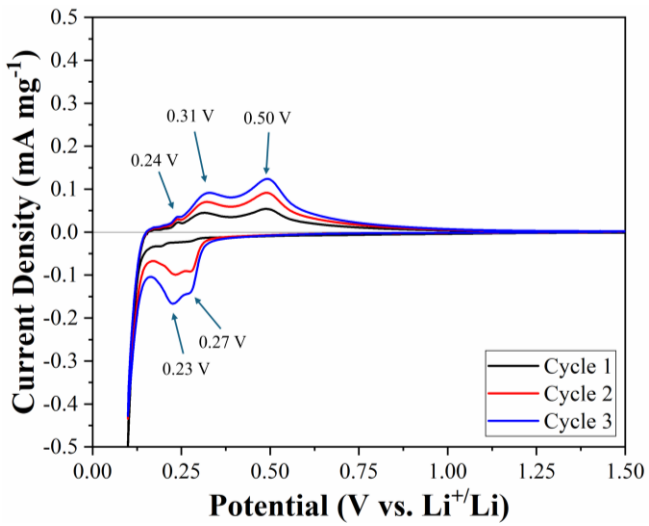

Figure 5.92 – Cycling voltammetry for the first production trial using 10 wt.% PAA as binder.

Although no unexpected redox peaks, or evident parasitic reactions were detected, the overall electrochemical performance remained significantly below the expected values for this SD system. The huge capacity decay at moderate current densities and the pronounced polarization observed during long-term cycling suggested that the limitations were predominantly related to electrode characteristics and processing parameters rather than intrinsic material instability. In particular, inhomogeneous particle distribution and local detachments may have contributed to the observed performance loss. These findings indicate that the electrochemical response was strongly process-dependent, highlighting the necessity of optimizing slurry preparation to fully exploit the potential of this nanoporous silicon material.

5.4.1.3.2. Second trial: PAA_2

The second trial aimed to increase the SF to 45 wt.% to produce slurries without the excess water, favoring a more uniform coating and at the same time, improve the electrochemical performance. The mixing procedure was kept the same as the previous trial, except a lower amount of water and the simplification of dry-mixing of the powders before their addition to the binder solution:

1. The first step of the process was the dilution overnight of PAA in MilliQ water to prepare a solution of 10 wt.%. This step was performed using a magnetic stirrer in a closed vessel, to avoid the evaporation of the solvent.

2. 5 g of diluted PAA were further diluted in 1.6 mL of MilliQ to reach the desired value of SF, and the mixture was kept stirred for 15 minutes at 1,000 rpm to ensure proper homogenization.
3. 4.0 g of silicon, 0.25 g of graphite and 0.25 g C45 were dry mixed and then manually added to the solution of PAA. At the beginning, the mixture resulted very dry and lacking water, even more than in the previous trial; however, after few minutes of manually mixing, the slurry started to be more homogeneous. Once good dispersion was achieved, the automatic mixing was started at 2,000 rpm for 30 minutes.

At the end of the mixing, inside the beaker, a deposit at the bottom of the beaker was observed, likely due to powder sedimentation, indicating that the applied shear conditions may not be optimal for this formulation. This behavior suggests that the high shear conditions may have affected the binder-induced particle network, promoting particle sedimentation. Despite this observation, the coating process was carried out, and the slurry was coated on the 6 µm Cu CC, using two imposed wet thicknesses (50 and 100 µm).

As observed in the previous trial, the laminates dried rapidly in air. However, in this case, visible surface defects were present on the electrode (***Figure 5.93***). For the laminate produced with a wet thickness of 50 µm (***Figure 5.93a***), several defects were observed, including inhomogeneities along the edges of the powder agglomerates, highlighted by the black markers on the left of the laminate. These features led to localized heterogeneities within the coating layer. Such defects were less evident in the laminate produced at 100 µm wet thickness (***Figure 5.93b***), likely because the agglomerates, being smaller than the deposition thickness, remained embedded within the wet layer. Nevertheless, the presence of these agglomerates must be considered a significant indicator of a not suitable mixing process.

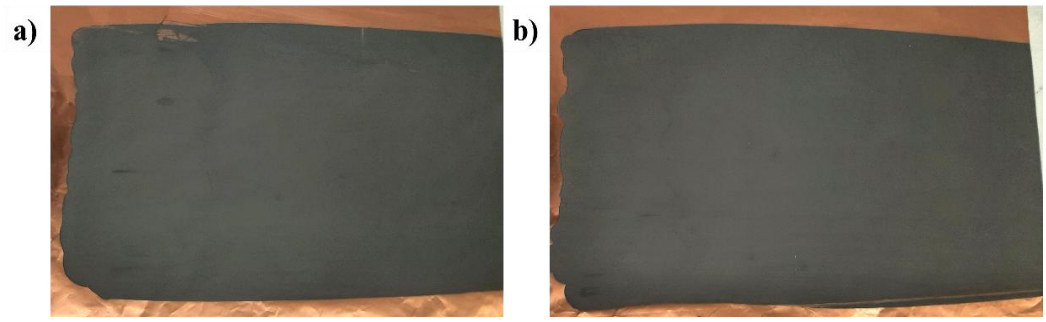

Figure 5.93 – Laminates produced during the second trial with a SF of 45 wt.% and a formulation containing 80 wt.% Si and 10 wt.% PAA, deposited at different wet thicknesses: a) 50 µm; b) 100 µm.

After drying, even though the poor aspect, the electrodes were manually punched into 15 mm diameter discs, and their characteristics are reported in ***Table 5.41***. Compared to the previous deposition, the laminate produced with a wet

thickness of 50 µm showed nearly double the dry thickness, reaching 23 ± 7 µm, and approximately triple the ML, with the value of 1.48 ± 0.51 mg cm^{-2}. For the 100 µm deposition, the differences compared to the previous slurry were smaller: the dry thickness reached 47 ± 6 µm, while the ML was 2.87 ± 0.39 mg cm^{-2}. The poor surface homogeneity makes further electrochemical characterization not relevant.

5.4.1.3.3. Third trial: PAA_3

During the third trial, the focus was on the optimization of the mixing process, specifically mixing speed and time, while all the components were maintained exactly the same. The only change was the reduction of the mixing speed from 2,000 rpm to 1,000 rpm and the time from 30 minutes to 20 minutes to avoid the powder deposition at the bottom of the beaker. After mixing, the slurry appeared more homogeneous and exhibited a more uniform viscosity. As previously performed, the slurry was coated onto the 6 µm Cu CC using an automatic film applicator, imposing wet thicknesses of 50, 70 and 100 µm. Although no pictures are available, the laminate surfaces appeared smooth and uniform, independently from the imposed wet deposition thickness.

After the drying step in air at RT, the electrodes were manually punched into 15 mm discs, and their characteristics are collected in ***Table 5.41.*** The dry thickness values measured for these electrodes were similar to those obtained in the previous trial but showed a significant improvement in coating uniformity, which can be attributed to the improved powder dispersion achieved through the optimized mixing procedure. The dry thickness and ML increased consistently with the imposed wet deposition thickness, indicating good process control and reproducibility of the coating step. The relatively low standard deviations further confirm the improved homogeneity of the laminates. This result suggests that slurry instability observed in the previous trial was primarily related to excessive shear conditions rather than to the SF itself.

This production process was considered as the optimized one. The reduction of the mixing step to 20 minutes represented a significant improvement, as even when including the initial manual mixing, the overall processing time was substantially lower than that required for graphite-based or SC-based electrodes.

The electrochemical results significantly improved compared to those obtained in the first trial, highlighting the importance of an optimized production process. The charge-discharge test was performed using the cycling protocol reported in ***Table 5.43***, characterized by the addition of the 2C step during the rate capability test and the reduction of the current density to 0.5C during the long-term cycling.

Electrodes with an average ML of 2.23 mg cm^{-2} were selected for the electrochemical characterization, whose results were reported in ***Figure 5.94***: as previously introduced, the results of the long-term test (***Figure 5.94a***) were

significantly improved due to the reduction of the current density. Moreover, thanks to the improved electrode characteristics, the rate capability performance was also notably enhanced (***Figure 5.94b***), with significantly higher capacities throughout the entire test. Although the average values were markedly improved, the variability among the samples remained relatively high, especially during long-term cycling. The sudden capacity decay and subsequent recovery observed during long-term cycling had already been reported by Karkar et al. [70] in comparable SD electrodes. Although the phenomenon was not investigated in detail by the authors, it is likely associated with localized interruptions in electronic conductivity induced by silicon volume changes, which, even if limited at the particle level, can significantly affect the overall electrochemical response.

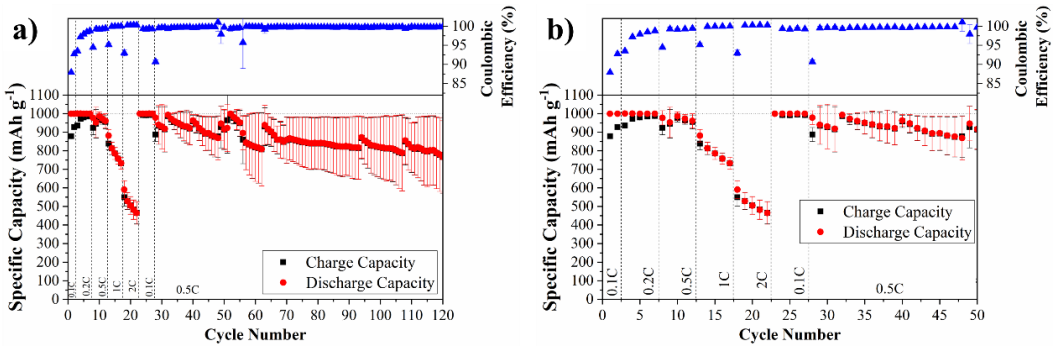

Figure 5.94 – Values of charge and discharge capacity and relative coulombic efficiency for the optimized process using 10 wt.% PAA as binder: a) Entire test, up to 120 cycles; b) Focus on the rate capability test.

The SEM analysis performed on the not-cycled electrode surface (***Figure 5.95***) confirmed the presence of significant cracks along the surface, which could be partially responsible for the electrochemical performance limitations.

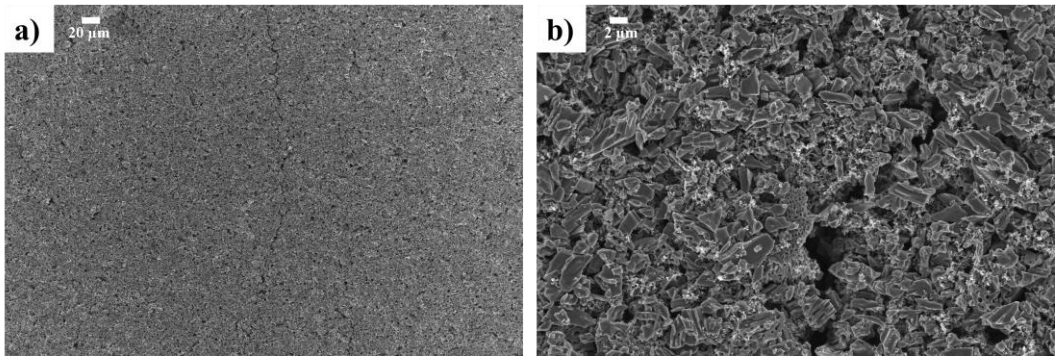

Figure 5.95 – SEM images produced with the optimized process using 10 wt.% PAA as binder at different magnification: a) 500X; b) 5kX.

Compared to the previously presented unoptimized electrodes, the modified production process led to noticeably higher average charge and discharge capacities, as well as improved average CE (***Table 5.45***). The forming cycles exhibited average values comparable to the previous samples. However,

significant improvements became evident when the current density was increased to 0.2C. Up to cycle 7, the lithiation capacity remained stable at approximately 1000 mAh g^{-1}, coupled with a gradual increase in the average de-lithiation capacity up to 987.52 mAh g^{-1}. When the current density was increased to 0.5C, a moderate capacity decay was observed, reaching the lowest point at 2C. Nevertheless, even at this stage, the average discharge capacity (464.98 mAh g^{-1}) and the average charge capacity (466.20 mAh g^{-1}) were significantly higher than those measured in the previous trial at lower current densities. These results confirmed the effectiveness of the production process optimization. During long-term cycling, the performance significant improved, with the capacity at cycles 120 being approximately double that of the previous sample. The average capacity retention calculated for these electrodes was 82.42%. Although this value is lower than that of the PAA_1 samples (93.03%), it is worth noting that the discharge capacity values in this case are significantly higher.

Table 5.45 – Values of charge and discharge capacities, normalized by the electrode weight, and relative values of coulombic efficiency for some representative cycles for the electrodes produced with the optimized production process using 10 wt.% PAA as binder.

Cycle	***C-rate***	***Charge Capacity (mAh g^{-1})***	***Discharge Capacity (mAh g^{-1})***	***Coulombic Efficiency (%)***
1	*0.1C*	*879.02 ± 2.45*	*999.73 ± 0.47*	*87.93 ± 0.28*
2		*927.42 ± 4.87*	*999.73 ± 0.47*	*92.77 ± 0.49*
7	*0.2C*	*987.52 ± 0.03*	*999.74 ± 0.27*	*98.78 ± 0.02*
12	*0.5C*	*955.25 ± 37.34*	*960.70 ± 38.28*	*99.43 ± 0.12*
17	*1C*	*732.84 ± 32.55*	*732.89 ± 32.43*	*99.99 ± 0.02*
22	*2C*	*466.20 ± 60.22*	*464.98 ± 60.57*	*100.27 ± 0.12*
27	*0.1C*	*992.46 ± 0.64*	*999.73 ± 0.47*	*99.27 ± 0.09*
30	*1C*	*926.93 ± 116.31*	*930.71 ± 119.77*	*99.62 ± 0.39*
50		*912.96 ± 106.49*	*915.80 ± 106.90*	*99.69 ± 0.06*
120		*766.52 ± 195.04*	*767.13 ± 194.67*	*99.91 ± 0.10*

The analysis of charge-discharge voltage profiles (***Figure 5.96***) further confirmed the improved behavior. The forming cycles presented the typical profile, with the first cycle characterized by an important slope and a long plateau associated with SEI formation, irreversible reactions and transition of crystalline Si into an amorphous Li_xSi phase, followed by its crystallization into $Li_{15}Si_4$ [417,418]. The profile obtained during the rate capability test (***Figure 5.96b***), showed longer voltage plateaus and reduced polarization compared to the previous trial. This improvement was also evident during long-term cycling (***Figure 5.96c***), where the polarization observed at cycle 120 (red curves) was substantially lower than in the previous trial.

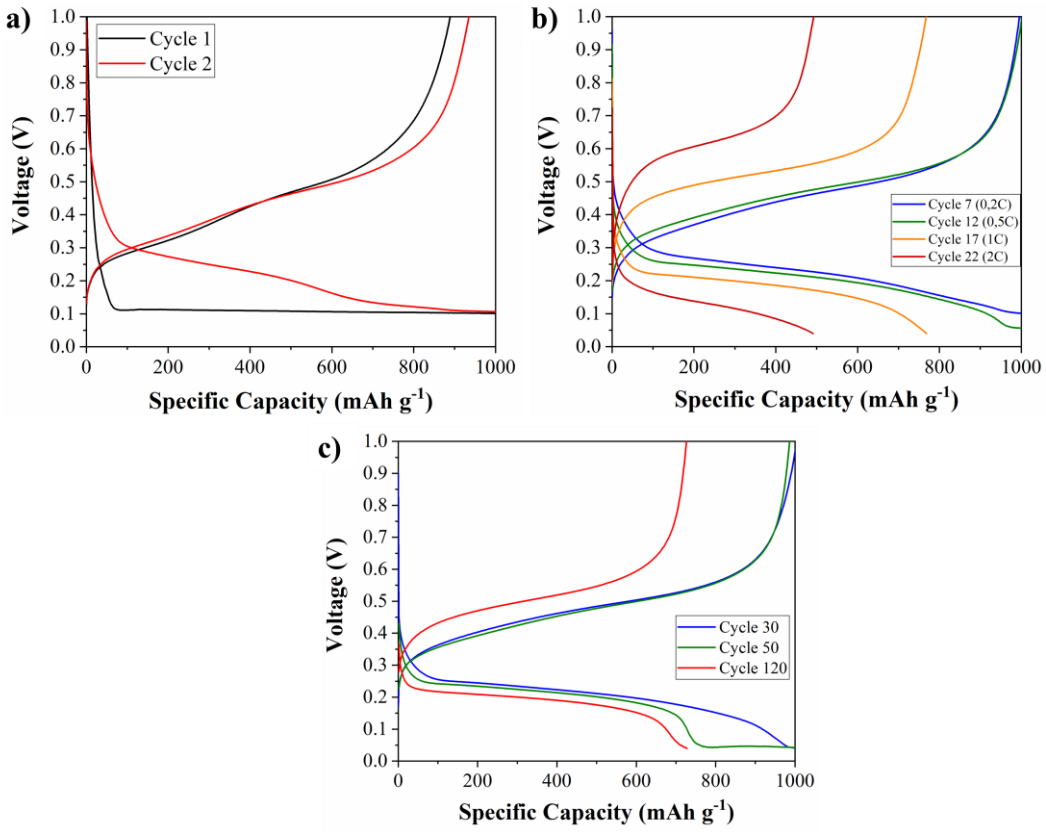

Figure 5.96 – Charge/discharge profiles for some representative cycles for the optimized production process using 10 wt.% PAA as binder: a) Forming cycles; b) Rate capability test; b) Long-term test.

Regarding the CV analysis (***Figure 5.97***), the peak positions were consistent with those observed for the previously prepared electrode, confirming the absence of parasitic reactions even after the optimized process. Overall, these SD electrodes presented acceptable electrochemical results during both rate capability and long-term cycling, and are therefore considered the baseline for comparison with the additive-based formulations.

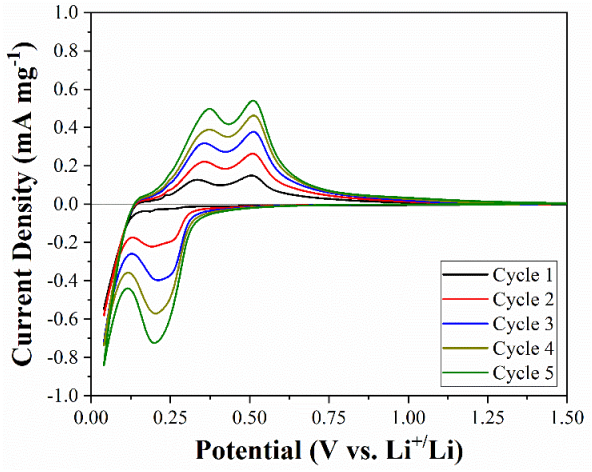

Figure 5.97 – Cycling voltammetry for the optimized production trial using 10 wt.% PAA as binder.

5.4.1.4. PAA and additives

After the optimization of the mixing procedure using PAA alone, the implementation of additional polymers in the system was considered as a suitable strategy to improve the mechanical properties of the slurry. The electrode composition was maintained unchanged, with the exception of reducing the PAA content to 9 wt.% in favor of the addition of a 1 wt.% polymeric additive. The first additive selected was SBR, which is already widely used in combination with CMC for graphite and SC-based anodes; however, only a limited number of studies have investigated the combination of SBR with PAA as a dual binder system [159,435].

Secondly, natural polysaccharides were selected to improve the sustainability of the overall process while simultaneously promoting the formation of robust polymeric networks within the slurry. The chosen polysaccharides were Na-Alg, Pec, and TG. The selection of these materials was based on their widespread use in the food industry as thickening agents, together with evidence from previous studies on Si-based anodes, as discussed in ***Chapter 2***.

The electrodes prepared with the use of additives to the PAA-binder were electrochemically tested by galvanostatic charge-discharge analysis using the same cycling protocol previously adopted (***Table 5.43***).

5.4.1.4.1. Addition of SBR: PAA_SBR

The first additive investigated was SBR, already extensively used in combination with CMC. The mixing procedure was maintained identical to the optimized PAA-based process, with the exception that SBR was added at the beginning together with the PAA solution, followed by the addition of the powder components. In contrast to graphite and SC anodes, where SBR is typically added at the end of the mixing process to prevent degradation, in this case, the reduced mixing speed and time allowed its incorporation at the beginning without detrimental effects. The detailed production procedure is reported below:

1. The first step consisted of the overnight dilution of PAA in MilliQ water to produce a 10 wt.% solution. This step was performed using a magnetic stirrer in a closed bottle to avoid solvent evaporation.
2. 4.5 g of diluted PAA were further diluted in 2.0 mL of MilliQ, and 0.1 g of SBR (previously diluted to 50 wt.%) was added to the solution. The mixture was stirred for 15 minutes at 1,000 rpm to ensure proper homogenization.
3. 4.0 g of silicon, 0.25 g of graphite and 0.25 g of C45 were dry mixed and then manually added to the PAA/SBR solution. Initially, the mixture appeared very dry and lacking water, even more than in the previous trial; however, after a few minutes of manual mixing, the slurry became more homogenous. Once

adequate dispersion was achieved, an automatic mix was performed at 1,000 rpm for 20 minutes.

After the mixing step, the slurry was coated onto the same 6 µm Cu CC with imposed wet thicknesses of 50, 70 and 100 µm, and left to dry in air at RT. The resulting laminates (***Figure 5.98***) exhibited smooth and homogeneous surfaces, independently of the wet deposition thickness.

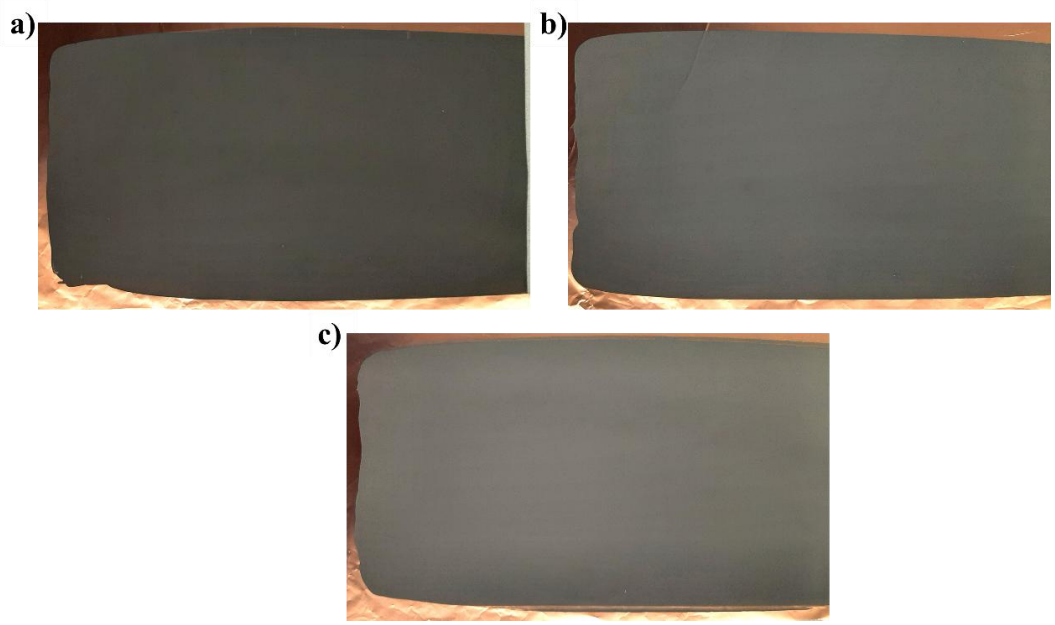

Figure 5.98 – Laminates produced with a SF of 45 wt.% and a formulation containing 9 wt.% PAA and 1 wt.% SBR, deposited at different wet thicknesses: a) 50 µm; b) 70 µm; c) 100 µm.

After the drying step, the dry thickness was randomly measured (***Table 5.41***), and after the manual punching into 15 mm discs, the electrodes were individually weighted. The laminate produced with a wet deposition thickness of 100 µm exhibited values extremely similar to those obtained for the 70 µm deposition. This similarity is probably related to the inherent variability associated with the manual adjustment of the doctor blade. In fact, the average weight of the 100 µm laminate showed a relatively large deviation compared to the other samples. The dry thickness values obtained for the 50 and 100 µm wet depositions were comparable to those of the optimized PAA-based electrodes prepared with the same wet thicknesses.

Overall, the results indicate that the addition of 1 wt.% SBR did not significantly alter the electrode thickness or ML compared to the optimized PAA formulation, suggesting that the processability and coating behavior remained stable under these conditions.

The electrochemical results of the electrodes prepared with SBR as an additive are reported in ***Figure 5.99*** and ***Table 5.46***. The average ML of the electrodes was

1.93 mg cm^{-2}. Compared to the sample containing just PAA, the addition of SBR led to lower electrochemical performance, especially during the rate capability test. At 2C, the average charge and discharge capacities were not able to reach even half of the values obtained for the PAA electrodes. It is worth noting that at cycle 120 the variability among samples exceeded 150 mAh g^{-1}, which significantly compromised reproducibility. The average capacity retention was calculated to be 89.16%

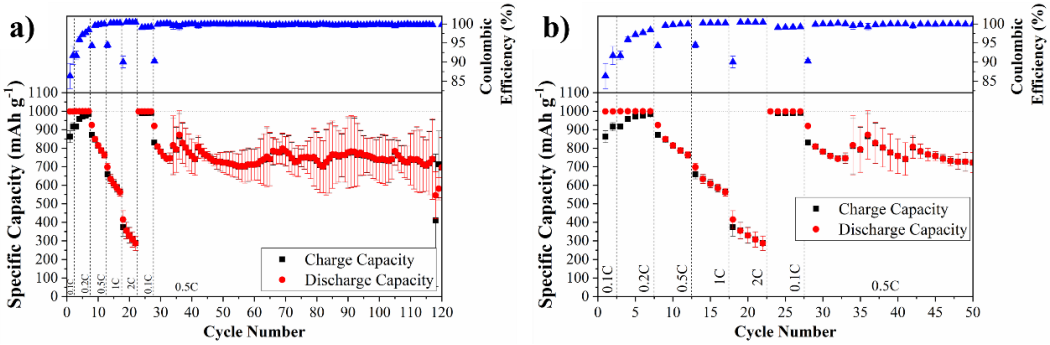

Figure 5.99 – Values of charge and discharge capacity and relative coulombic efficiency for the electrodes produced using 9 wt.% PAA and 1 wt.% SBR as binders: a) Entire test, up to 120 cycles; b) Focus on the rate capability test.

Table 5.46 – Values of charge and discharge capacities, normalized by the electrode weight, and relative values of coulombic efficiency for some representative cycles for the electrodes produced using 9 wt.% PAA and 1 wt.% SBR as binders.

Cycle	*C-rate*	*Charge Capacity (mAh g^{-1})*	*Discharge Capacity (mAh g^{-1})*	*Coulombic Efficiency (%)*
1	*0.1C*	*862.43 ± 31.93*	*998.56 ± 1.17*	*86.37 ± 3.30*
2		*916.15 ± 22.53*	*998.67 ± 1.00*	*91.74 ± 2.35*
7	*0.2C*	*983.15 ± 1.35*	*999.38 ± 0.83*	*98.38 ± 0.21*
12	*0.5C*	*763.57 ± 16.47*	*763.87 ± 16.96*	*99.96 ± 0.07*
17	*1C*	*564.15 ± 20.73*	*562.85 ± 21.15*	*100.23 ± 0.09*
22	*2C*	*287.98 ± 39.02*	*286.77 ± 38.97*	*100.42 ± 0.06*
27	*0.1C*	*990.90 ± 0.92*	*998.45 ± 0.95*	*99.24 ± 0.09*
30		*781.13 ± 2.50*	*781.23 ± 2.84*	*99.99 ± 0.04*
50	*1C*	*721.99 ± 53.84*	*722.63 ± 54.71*	*99.92 ± 0.11*
120		*695.17 ± 161.15*	*696.53 ± 162.55*	*99.83 ± 0.15*

The charge-discharge profiles (***Figure 5.100***) confirmed this behavior, showing a pronounced shortening of the plateaus and a marked increase in polarization during the rate capability test (***Figure 5.100b***). Due to the high variability among samples, ***Figure 5.100c*** reports the long-term cycling profile of the best-performing electrode, selected as the most representative of the achievable behavior. As a consequence, the capacity values visible in the plot for

the displayed cycles can approach 800 mAh g^{-1}, whereas the values listed in ***Table 5.46*** remain lower because they do not refer exclusively to that specific electrode. Although at cycle 120 the discharge capacity appeared higher than at cycles 30 and 50, the increased polarization and the different profile shape suggested the appearance of resistive phenomena rather than an effective improvement in electrochemical stability.

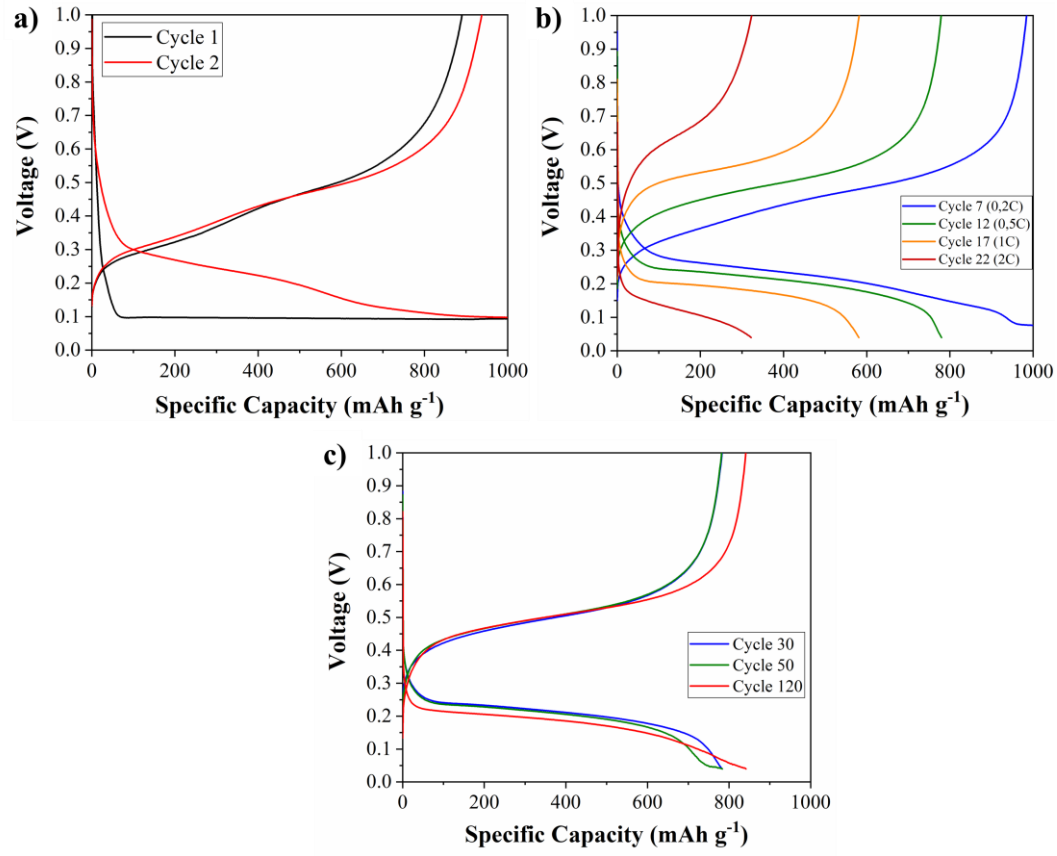

Figure 5.100 – Charge/discharge profiles for some representative cycles for the optimized production process using 9 wt.% PAA and 1 wt.% SBR as binders: a) Forming cycles; b) Rate capability test; b) Long-term test.

A similar behavior was observed also for the other replicas, indicating that the limitations associated with SBR addition may be related to a phase separation between the two binders, as deeper investigated below in the chapter. This phenomenon, occurring during slurry preparation or coating, may ultimately affect electrode homogeneity and electronic percolation, resulting in poor electrochemical performance.

5.4.1.4.2. Addition of Sodium Alginate: PAA_Alg

As previously done for the SC system, natural polysaccharides were selected as additives. The mixing procedure followed the same steps adopted for SBR,

with the only difference that Na-Alg was added in powder form and, to ensure proper dissolution, it was added the day before and kept under stirring overnight.

After the mixing process, the slurry was coated applying three wet deposition thicknesses (50, 70 and 100 µm), and the dried laminates are shown in ***Figure 5.101***. All three laminates exhibited smooth and homogeneous surfaces without visible clumps or agglomerates.

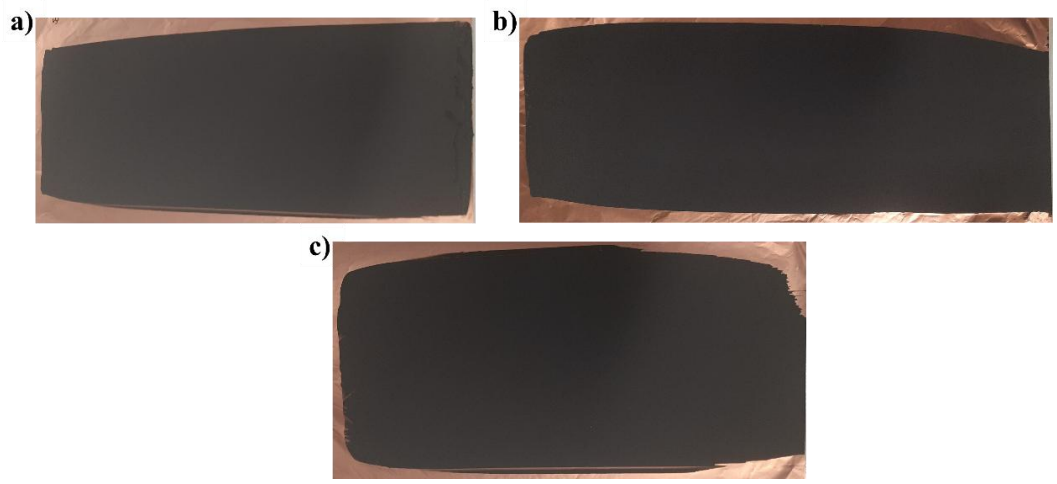

Figure 5.101 – Laminates produced with a SF of 45 wt.% and a formulation containing 9 wt.% PAA and 1 wt.% Alg, deposited at different wet thicknesses: a) 50 µm; b) 70 µm; c) 100 µm.

From these laminates, the 15 mm diameter electrodes were manually punched and characterized as previously described (***Table 5.41***). The dry thicknesses of the laminates produced with a gap of 50 and 100 µm were comparable to those produced with the SBR additive. However, for the same wet thicknesses, the electrode weight and corresponding ML were higher. This behavior may be attributed to the formation of a more structured polymeric network between PAA and Alg, which could enhance particle retention within the coating layer, enabling a higher effective solid deposition at comparable thickness. Such an effect represents a potentially advantageous feature for increasing the achievable areal capacity and, consequently, the energy density of the electrodes.

The electrodes with an average ML of 2.1 mg cm^{-2} were selected for the electrochemical characterization. The use of Alg as additive led to interesting electrochemical results with improved performance compared to the use of PAA alone formulation (***Figure 5.102***, ***Table 5.47***). The use of Alg is not new in the literature, and promising results for SD anodes have already been reported, both when used as a binder alone [137,488] and when combined with other natural polymers [165]. Overall, the rate capability test exhibited average values comparable to those of the PAA alone electrodes, with slightly higher variability at 0.5C but narrower dispersion at 2C. Remarkably, the most significant improvement was observed during the long-term test, where discharge capacities

above 900 mAh g^{-1} were maintained even at cycle 120. The capacity retention reached the exceptional value of 99.35%. In addition, the variability among samples was significantly reduced compared to the PAA baseline, with an almost complete elimination of the abrupt capacity decay previously observed.

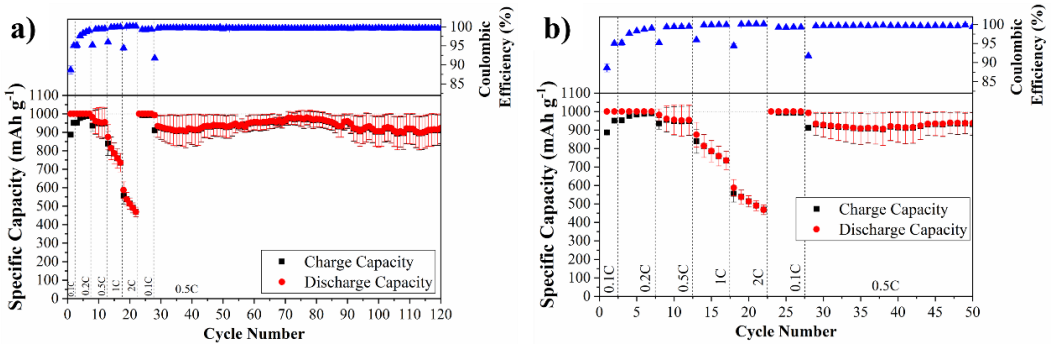

Figure 5.102 – Values of charge and discharge capacity and relative coulombic efficiency for the electrodes produced using 9 wt.% PAA and 1 wt.% Alg as binders: a) Entire test, up to 120 cycles; b) Focus on the rate capability test.

Table 5.47 – Values of charge and discharge capacities, normalized by the electrode weight, and relative values of coulombic efficiency for some representative cycles for the electrodes produced using 9 wt.% PAA and 1 wt.% Alg as binders.

Cycle	*C-rate*	*Charge Capacity (mAh g^{-1})*	*Discharge Capacity (mAh g^{-1})*	*Coulombic Efficiency (%)*
1	*0.1C*	*887.02 ± 10.04*	*1000.54 ± 0.94*	*88.65 ± 1.09*
2		*950.98 ± 1.90*	*1000.54 ± 0.94*	*95.05 ± 0.25*
7	*0.2C*	*990.63 ± 0.69*	*1000.36 ± 0.63*	*99.03 ± 0.13*
12	*0.5C*	*949.45 ± 78.80*	*954.19 ± 81.01*	*99.51 ± 0.20*
17	*1C*	*735.72 ± 49.73*	*736.06 ± 50.07*	*99.96 ± 0.05*
22	*2C*	*469.29 ± 26.11*	*468.68 ± 26.18*	*100.13 ± 0.02*
27	*0.1C*	*993.36 ± 0.85*	*1000.45 ± 0.79*	*99.29 ± 0.03*
30		*925.31 ± 63.79*	*928.16 ± 65.31*	*99.70 ± 0.14*
50	*1C*	*932.24 ± 60.79*	*937.20 ± 58.82*	*99.46 ± 0.34*
120		*918.39 ± 81.04*	*922.13 ± 81.92*	*99.60 ± 0.06*

The charge-discharge voltage profiles (***Figure 5.103***) were consistent with expectations, showing the typical increase in polarization during the rate capability test, which was largely recovered during long-term cycling. Notably, well-defined and extended voltage plateaus were still observed at cycle 120, confirming the improved electrochemical stability of the electrode. Similarly, CV analysis (***Figure 5.104***) exhibited the same characteristic peaks previously described in ***Figure 5.92***, without the appearance of unexpected peaks, or evidence of parasitic reactions. This behavior suggested that the PAA_Alg system supplied enhanced mechanical integrity during repeated silicon volume changes.

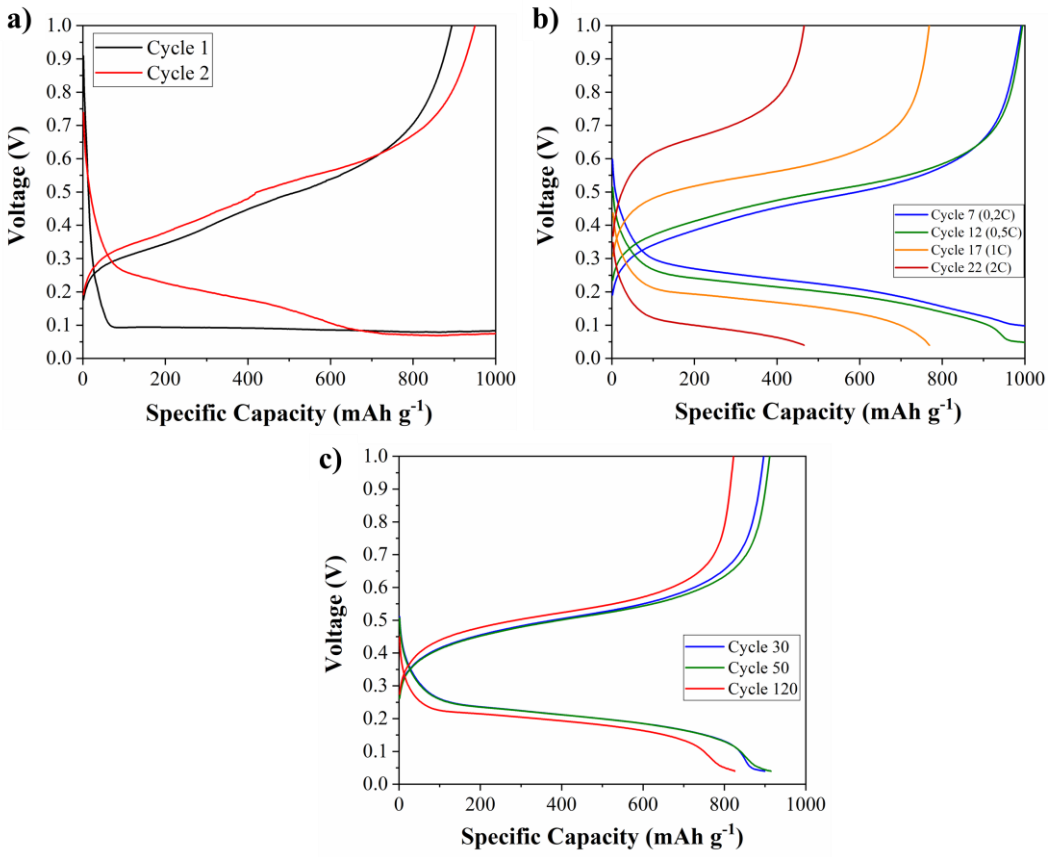

Figure 5.103 – Charge/discharge profiles for some representative cycles for the optimized production process using 9 wt.% PAA and 1 wt.% Alg as binders: a) Forming cycles; b) Rate capability test; b) Long-term test.

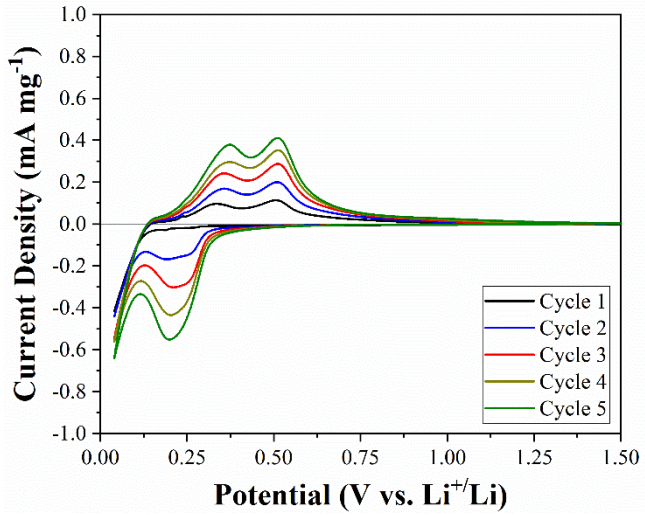

Figure 5.104 – Cycling voltammetry for the optimized production trial using 9 wt.% PAA and 1 wt.% Alg as binder.

5.4.1.4.3. Addition of Tragacanth Gum: PAA_TG

In addition to Na-Alg, another natural polysaccharide, TG, was investigated in this study. The mixing, coating and drying procedures were the same as those described for the previous trial. The laminates produced with the three imposed wet thicknesses are shown in ***Figure 5.105***. Overall, the surfaces appeared smooth and homogeneous, without visible defects.

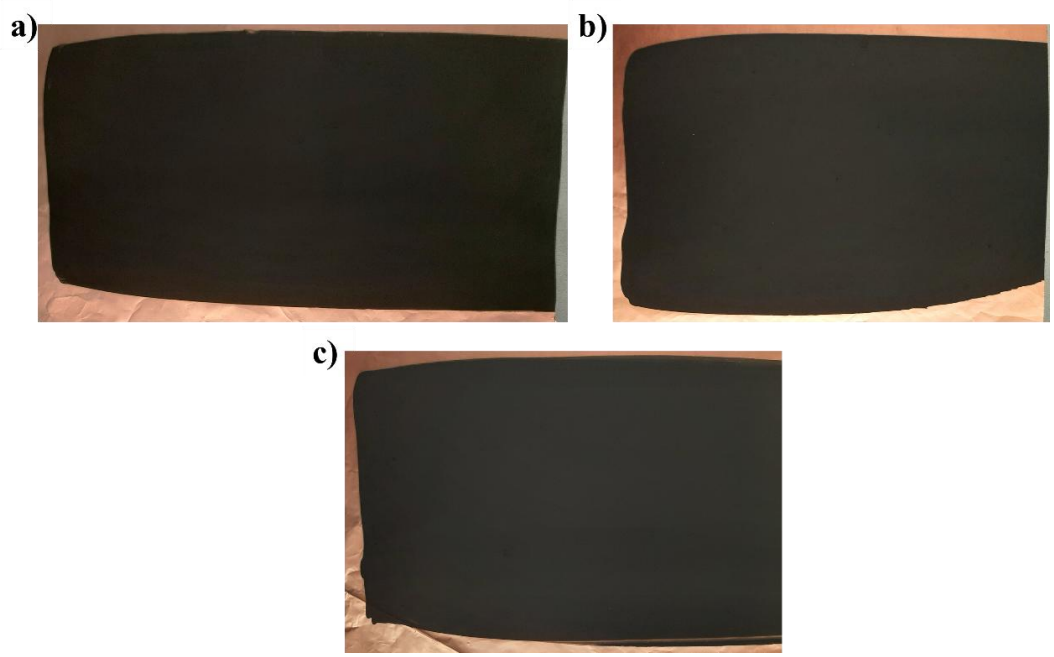

Figure 5.105 – Laminates produced with a SF of 45 wt.% and a formulation containing 9 wt.% PAA and 1 wt.% TG, deposited at different wet thicknesses: a) 50 µm; b) 70 µm; c) 100 µm.

The electrode characteristics (***Table 5.41***) were slightly different compared to the trial with Alg. For the wet thickness of 50 µm, the final dry thickness was comparable; however, increasing the blade gap resulted in a more pronounced increase in the dry layer thickness. A similar trend was observed for the average electrode weight and, consequently, for the ML. Although minor deviations may be related to the manual adjustment of the doctor blade, the more significant differences could be related to the polymeric network formed by the complex molecular structure of TG in combination with PAA. Overall, the addition of 1 wt.% TG led to a more pronounced increase in dry thickness and ML at higher blade gap, suggesting a stronger structuring effect of the PAA_TG network on slurry rheology and particle packing.

The electrodes with an average ML of 2.46 mg cm^{-2} were selected for electrochemical testing. The use of TG is less common in the literature compared to other binders, and the electrochemical performance observed in this work (***Figure 5.106***, ***Table 5.48***) likely reflects its limited adoption in battery applications. The rate capability test was characterized by lower performance than

the PAA alone formulation, and long-term cycling also exhibited reduced capacity values. In fact, the capacity retention was 75.42%, lower than the 82.42% calculated for the PAA_3 samples. However, the use of TG appeared to slightly improve the reproducibility among cells. Despite this, during long-term cycling the electrodes still showed abrupt capacity decay, similar to that observed for the PAA system. This behavior may be attributed to partial material detachment and localized interruption of the electronic conductive network, likely induced by repeated silicon volume changes, as reported by Karkar et al. [70].

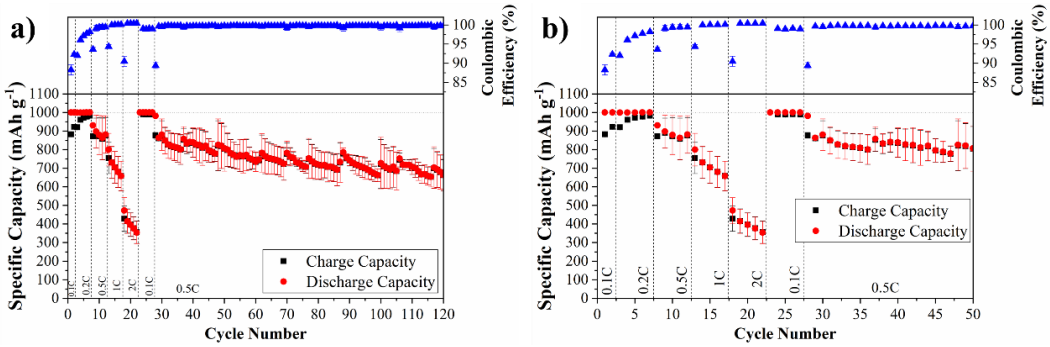

Figure 5.106 – Values of charge and discharge capacity and relative coulombic efficiency for the electrodes produced using 9 wt.% PAA and 1 wt.% TG as binders: a) Entire test, up to 120 cycles; b) Focus on the rate capability test.

Table 5.48 – Values of charge and discharge capacities, normalized by the electrode weight, and relative values of coulombic efficiency for some representative cycles for the electrodes produced using 9 wt.% PAA and 1 wt.% TG as binders.

Cycle	***C-rate***	***Charge Capacity (mAh g^{-1})***	***Discharge Capacity (mAh g^{-1})***	***Coulombic Efficiency (%)***
1	*0.1C*	*882.83 ± 13.33*	*1000*	*88.28 ± 1.33*
2		*923.15 ± 4.06*	*1000*	*92.32 ± 0.41*
7	*0.2C*	*982.26 ± 2.18*	*999.93 ± 0.13*	*98.23 ± 0.21*
12	*0.5C*	*876.57 ± 96.07*	*881.86 ± 100.40*	*99.43 ± 0.50*
17	*1C*	*658.52 ± 79.14*	*657.78 ± 79.76*	*100.12 ± 0.12*
22	*2C*	*355.74 ± 60.10*	*354.30 ± 60.01*	*100.41 ± 0.09*
27	*0.1C*	*989.33 ± 0.92*	*999.93 ± 0.13*	*98.94 ± 0.08*
30		*875.93 ± 79.72*	*880.37 ± 84.76*	*99.53 ± 0.50*
50	*1C*	*804.76 ± 119.95*	*806.69 ± 122.10*	*99.78 ± 0.23*
120		*662.42 ± 83.59*	*663.96 ± 84.66*	*99.78 ± 0.150*

The charge-discharge voltage profiles (***Figure 5.107***) were consistent with the previously discussed samples, with no additional points of interest requiring further discussion. Similarly, the CV analysis (***Figure 5.108***) did not reveal unexpected peaks or parasitic reactions compared to the previously discussed systems.

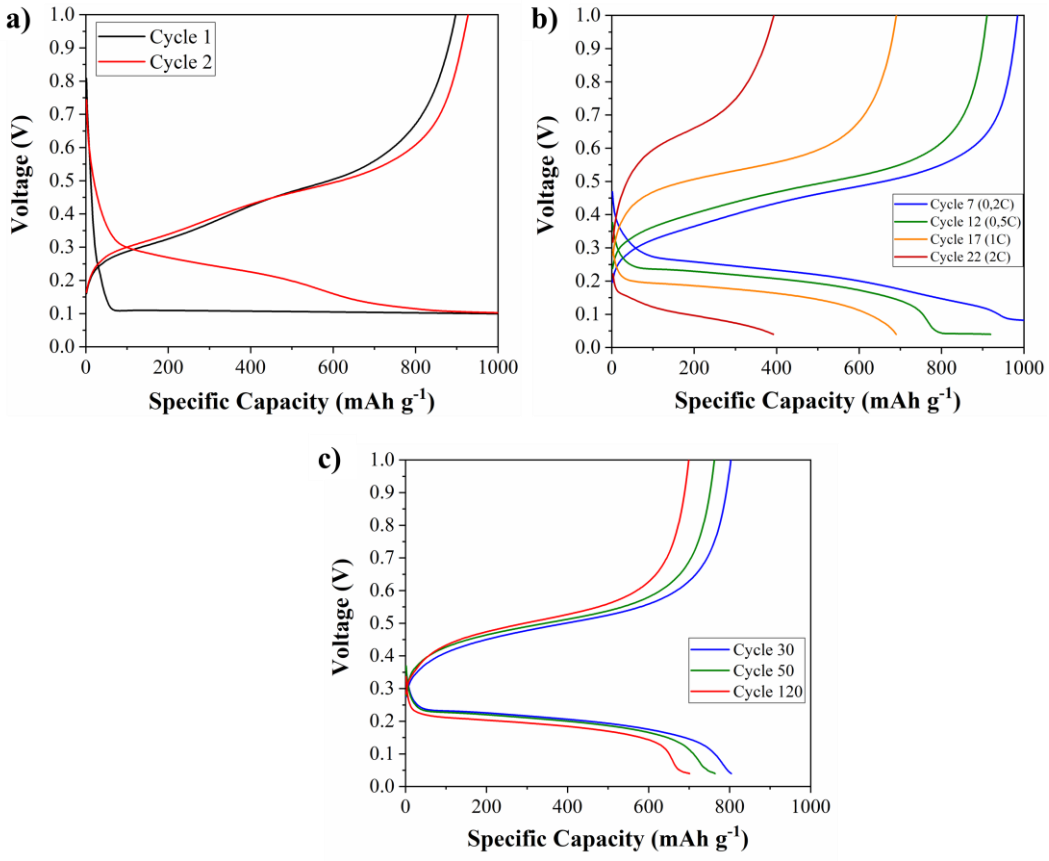

Figure 5.107 – Charge/discharge profiles for some representative cycles for the optimized production process using 9 wt.% PAA and 1 wt.% TG as binders: a) Forming cycles; b) Rate capability test; b) Long-term test.

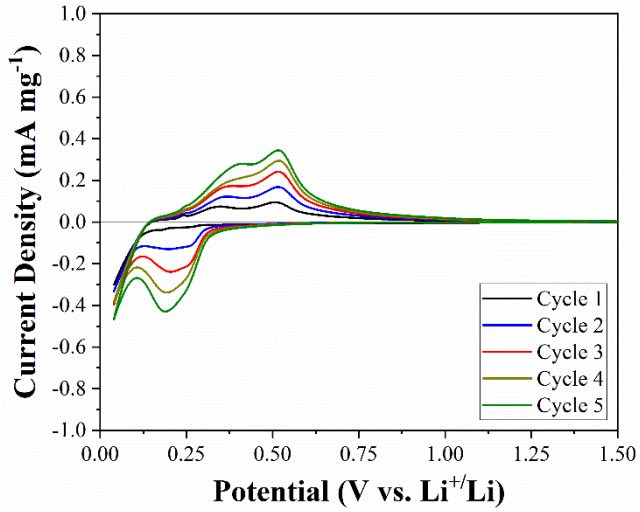

Figure 5.108 – Cycling voltammetry for the optimized production trial using 9 wt.% PAA and 1 wt.% TG as binder

The inferior electrochemical performance may be related to the complex and highly branched molecular structure of TG, which consists mainly of two

fractions, bassorin and tragacanthin, which can promote the formation of a heterogeneous polymer network within the slurry. Such a network may not efficiently accommodate the repeated silicon volume changes, leading to mechanical stress accumulation and progressive disruption of the electronic percolation pathways.

5.4.1.4.4. Addition of Pectin: PAA_Pec

The last natural polysaccharide investigated at this stage of the work was Pec. It is worth noting that the use of Pec as a binder is relatively limited in the literature, thereby limiting direct comparison with other studies. The mixing, coating, and drying procedures were identical to those described for the previous trials, with the only difference being the use of Pec instead of Alg or TG. The dried laminates obtained with different wet deposition thicknesses are shown in ***Figure 5.109***. All samples exhibited uniform coatings without visible defects.

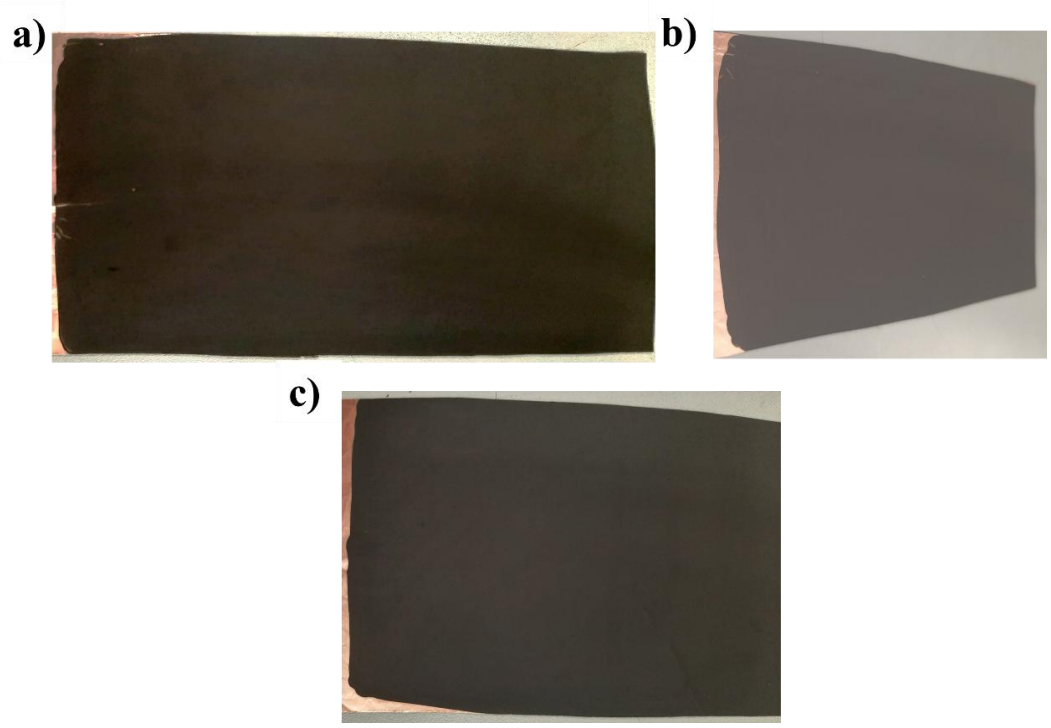

Figure 5.109 – Laminates produced with a SF of 45 wt.% and a formulation containing 9 wt.% PAA and 1 wt.% Pec, deposited at different wet thicknesses: a) 50 µm; b) 70 µm; c) 100 µm.

The electrodes characteristics (***Table 5.41***) were consistent with the previous trials, particularly with the formulation containing Alg. Overall, the incorporation of 1 wt.% pectin did not significantly modify the coating behavior or the resulting electrode thickness and ML, indicating that the PAA_Pec system maintains comparable processability and structural uniformity to the optimized PAA-based formulation.

The use of pectin as a binder resulted in remarkable electrochemical performance in this study (***Figure 5.110***, ***Table 5.49***). The electrodes selected for the electrochemical testing were characterized by an average ML of 2.07 mg cm^{-2}. Throughout the entire test, the electrodes exhibited higher capacities than those of the PAA alone formulation, with an average discharge capacity slightly above 550 mAh g^{-1} at 2C. During the long-term cycling, both charge and discharge capacities remained close to 1000 mAh g^{-1} for more than 50 cycles and at cycle 120, the average discharge capacity was still above 988 mAh g^{-1}, corresponding to a reduction of less than 12 mAh g^{-1}, and with a stunning capacity retention of 98.86%. Similarly to the Alg-based system, the capacities remained stable throughout the test without the abrupt capacity decay previously observed for the PAA alone electrodes.

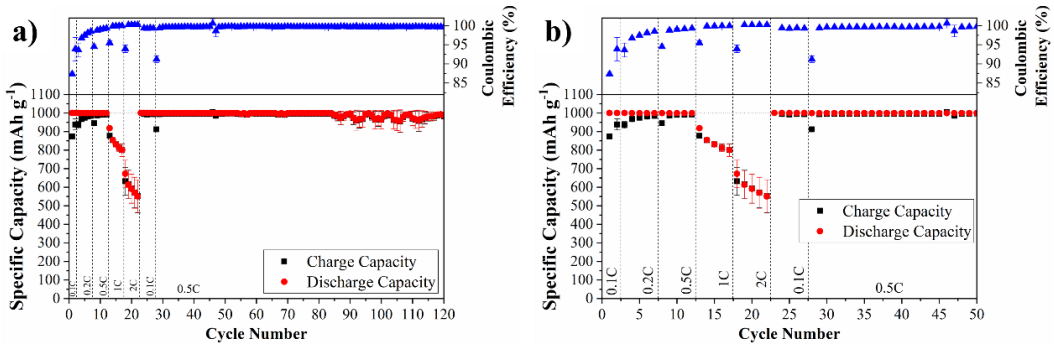

Figure 5.110 – Values of charge and discharge capacity and relative coulombic efficiency for the electrodes produced using 9 wt.% PAA and 1 wt.% Pec as binders: a) Entire test, up to 120 cycles; b) Focus on the rate capability test.

Table 5.49 – Values of charge and discharge capacities, normalized by the electrode weight, and relative values of coulombic efficiency for some representative cycles for the electrodes produced using 9 wt.% PAA and 1 wt.% Pec as binders.

Cycle	***C-rate***	***Charge Capacity (mAh g^{-1})***	***Discharge Capacity (mAh g^{-1})***	***Coulombic Efficiency (%)***
1	*0.1C*	*873.91 ± 4.72*	*1000.25 ± 0.35*	*87.37 ± 0.44*
2		*938.84 ± 30.18*	*1000.25 ± 0.35*	*93.86 ± 3.05*
7	*0.2C*	*984.62 ± 2.64*	*999.75 ± 0.35*	*98.49 ± 0.23*
12	*0.5C*	*992.55 ± 2.19*	*999.63 ± 0.53*	*99.29 ± 0.17*
17	*1C*	*799.98 ± 33.92*	*800.32 ± 34.39*	*99.96 ± 0.06*
22	*2C*	*551.75 ± 89.10*	*550.52 ± 89.83*	*100.24 ± 0.17*
27	*0.1C*	*993.50 ± 2.83*	*1000.25 ± 0.35*	*99.33 ± 0.32*
30		*995.30 ± 1.49*	*999.63 ± 0.53*	*99.57 ± 0.10*
50	*1C*	*997.02 ± 0.74*	*999.63 ± 0.53*	*99.74 ± 0.02*
120		*985.07 ± 16.37*	*988.25 ± 16.62*	*99.68 ± 0.02*

The electrode surface (***Figure 5.111***) exhibited improved homogeneity compared to the PAA alone samples, without visible cracks or significant surface defects.

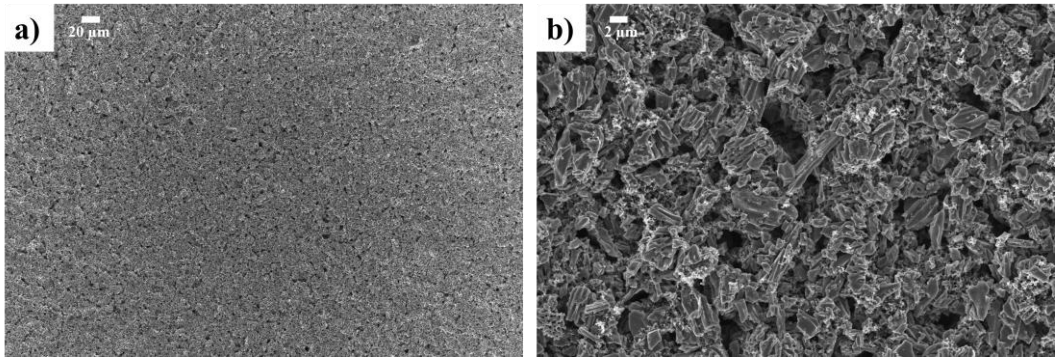

Figure 5.111 – SEM images of the electrodes produced using 9 wt.% PAA and 1 wt.% Pec as binders at different magnification: a) 500X; b) 5kX.

The charge-discharge voltage profiles (***Figure 5.112***), further confirmed the excellent stability during long-term cycling, as demonstrated by the nearly overlapping curves observed at cycles 30, 50, and 120 (***Figure 5.112c***). The CV analysis (***Figure 5.113***) showed slight differences compared to the previous systems. While cycle 1 was consistent with the expected behavior, cycles 2 and 3 exhibited lower peak intensities compared to the other formulations. However, cycles 4 and 5 showed a full recovery of peak intensity, resulting in profiles comparable to those observed for the Alg-based electrodes.

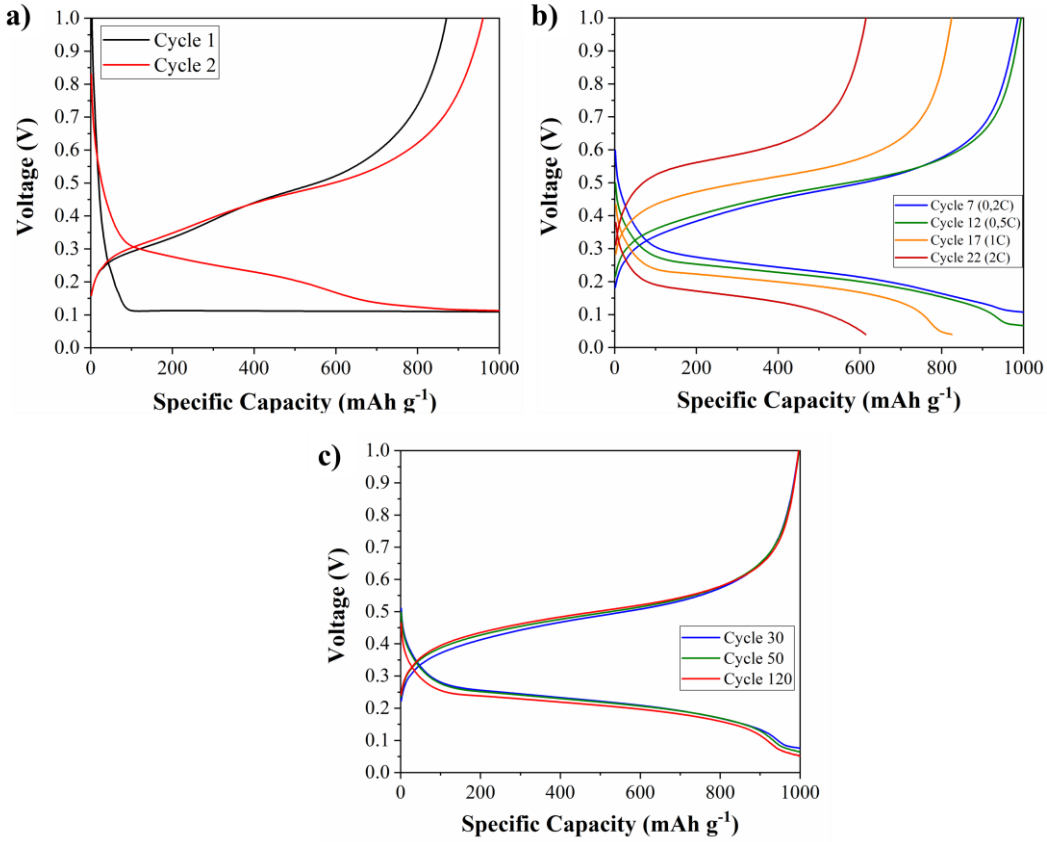

Figure 5.112 – Charge/discharge profiles for some representative cycles for the optimized production process using 9 wt.% PAA and 1 wt.% Pec as binders: a) Forming cycles; b) Rate capability test; b) Long-term test.

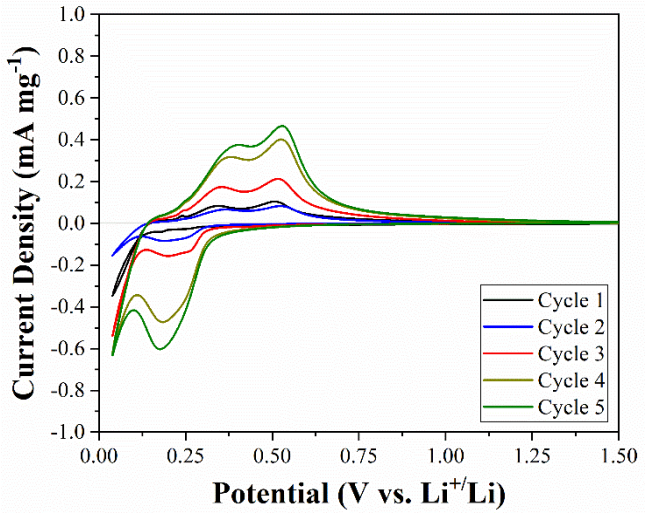

Figure 5.113 – Cycling voltammetry for the optimized production trial using 9 wt.% PAA and 1 wt.% Pec as binder

Overall, the exceptional electrochemical performance suggests that the PAA_Pec system may provide enhanced mechanical resilience during repeated

silicon volume changes. Nevertheless, the underlying stabilization mechanism remains not fully clarified, and further investigations are required.

5.4.1.5. Comparison between the additives

The comparative analysis of the laminates produced with different binders highlights the strong influence of binder chemistry on the final electrode properties, even under identical imposed coating thicknesses (***Table 5.50***, ***Figure 5.114***). Both dry thickness and ML increase with increasing wet coating thickness for all formulations, as expected. However, differences among binders are observed, with PAA_TG and PAA_Alg showing generally higher values, suggesting a greater ability to retain active material under comparable deposition conditions. It should also be noted that the manual setting of doctor blade may introduce additional variability, as small deviations in gap setting or operator handling can affect thickness uniformity and material deposition.

Table 5.50 – Comparison between the dry thicknesses and ML of the electrodes produced at laboratory level at Polito

Wet Thickness (µm)	***Parameter***	***PAA_3***	***PAA_SBR***	***PAA_Alg***	***PAA_TG***	***PAA_Pec***
50	*Dry Thickness (µm)*	22 ± 1	24 ± 1	26 ± 1	27 ± 2	23 ± 1
	Mass Loading (mg cm^{-2})	1.09 ± 0.09	1.17 ± 0.12	1.58 ± 0.08	1.15 ± 0.06	1.20 ± 0.10
70	*Dry Thickness (µm)*	31 ± 5	41 ± 4	33 ± 1	43 ± 2	32 ± 1
	Mass Loading (mg cm^{-2})	1.82 ± 0.27	2.07 ± 0.22	1.95 ± 0.05	2.41 ± 0.08	2.01 ± 0.14
100	*Dry Thickness (µm)*	41 ± 2	46 ± 2	46 ± 3	54 ± 1	44 ± 1
	Mass Loading (mg cm^{-2})	2.59 ± 0.17	2.53 ± 0.15	2.77 ± 0.09	3.09 ± 0.12	2.53 ± 0.09

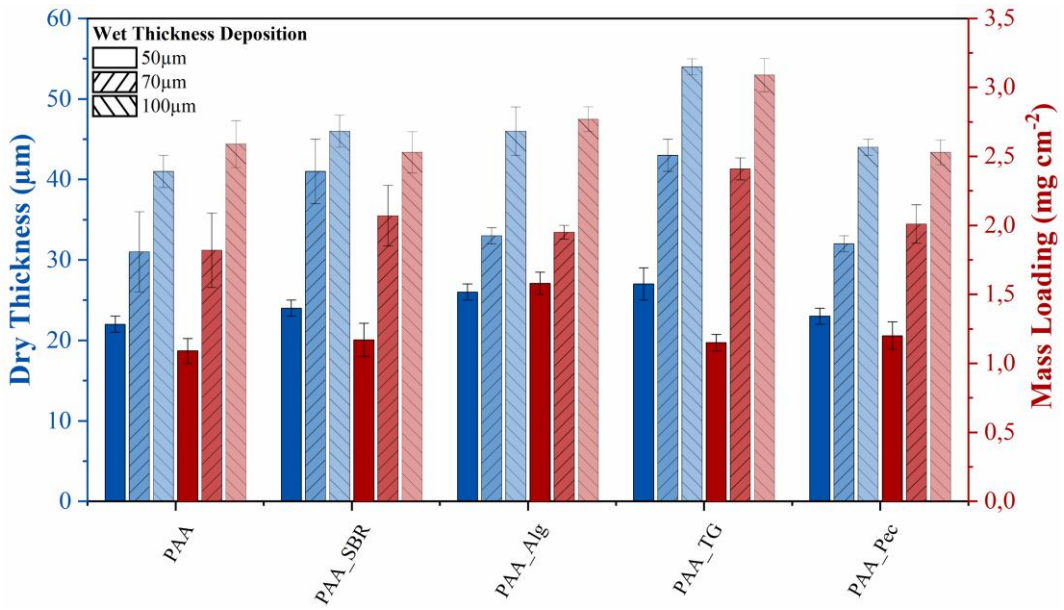

Figure 5.114 – Graphical comparison between the dry thicknesses and ML of the electrodes produced at laboratory level at Polito

At a wet thickness of 50 µm, differences in dry electrode thickness were already observed. TG and Alg exhibited slightly higher dry thickness values compared to SBR and Pec. Although the deviations appeared moderate at this thickness, suggesting that binder rheological properties and drying dynamics affected particle packing and shrinkage behavior. Slurry rheology and binder network formation are known to influence the structural evolution of the coating during solvent evaporation, ultimately determining the final electrode thickness [251,295]. In terms of ML, Alg showed the highest value, whereas SBR, TG, and Pec remained in a narrower range. This suggests that even at low coating thickness, the interactions between binder and powders and their dispersion stability could influence the effective amount of material retained after drying.

At 70 µm wet thickness, the differences in dry thickness became more pronounced. TG exhibited the highest value, closely followed by SBR, while Alg and Pec showed lower dry thicknesses. The larger standard deviation observed for SBR could reflect a higher sensitivity to processing conditions. Regarding ML, TG again showed the highest value, whereas Alg and Pec were slightly lower. These results indicated that, as the coating thickness increases, the influence of binder chemistry on shrinkage behavior and particle redistribution during drying became more pronounced.

At 100 µm wet thickness, the impact of binder selection became even more evident. TG-based electrodes displayed the highest dry thickness, while SBR and Alg showed similar intermediate values, and Pec resulted in the lowest thickness. At higher coating thicknesses, solvent evaporation gradients and capillary stresses were amplified, making binder-dependent shrinkage behavior more significant [489]. Polymeric binders capable of forming a structured internal network limited

particle rearrangement and mitigated thickness reduction during drying [490]. Consistently, TG also resulted in the highest ML, followed by Alg, whereas SBR and Pec showed comparable lower values.

Overall, the results confirmed that binder selection significantly affected both the final dry thickness and the ML of the electrodes. Even when the imposed wet thickness was kept constant, differences in binder chemistry led to systematic variations, highlighting the necessity of wider formulation investigations and process optimization.

For the electrochemical characterization, electrodes were selected with similar ML to ensure a proper comparison between the samples (***Table 5.51***). Starting from the PAA_3 sample onward, an ML value around 2 mg cm^{-2} was targeted, although this was not always achievable, as in the case of PAA_TG, which reached 2.46 mg cm^{-2}. However, the impact of different ML values does not appear to be significant. For instance, in the case of the PAA_SBR sample, characterized by a lower ML, the performance does not show a noticeable improvement.

Table 5.51 – Selected electrochemical performance results used for comparison among the investigated electrodes produced at Polito.

Sample ID	***Average Mass Loading (mg cm^{-2})***	***Discharge Capacity ($mAh\ g^{-1}$)***		***Initial Coulombic Efficiency (%)***	***Capacity retention (%)***
		Cycle 30	***Cycle 120***		
PAA 3	2.23	930.71	767.13	87.93	82.42
PAA SBR	1.93	781.23	696.53	86.37	89.16
PAA_Alg	2.10	928.16	922.13	88.65	99.35
PAA TG	2.46	880.37	663.96	88.28	75.42
PAA_Pec	2.07	999.63	988.25	87.37	98.86

The comparative electrochemical behavior of the different binder formulations is summarized in ***Figure 5.115***. Clear differences emerged both during the rate capability test and during long-term cycling, highlighting the strong impact of binder chemistry on electrode stability and performance. The first-cycle CE values are comparable across all samples (***Table 5.51***), ranging between 87% and 89%, which are still very good for silicon-based electrodes. During the rate capability test (***Figure 5.115a***), all samples exhibited the expected progressive decrease in discharge capacity with increasing current density; however, significant differences emerged among the formulations. The PAA_Pec system consistently delivered the highest capacities across all C-rates, while PAA_Alg showed slightly lower but still stable performance. The PAA baseline exhibited intermediate behavior, whereas PAA_TG and especially PAA_SBR displayed the lowest capacities and the most pronounced decay at high current densities. The capacity retention (***Table 5.51***) calculated between cycle 120 and cycle 30 is effectively improved for PAA_Alg and PAA_Pec, with values exceeding 98%.

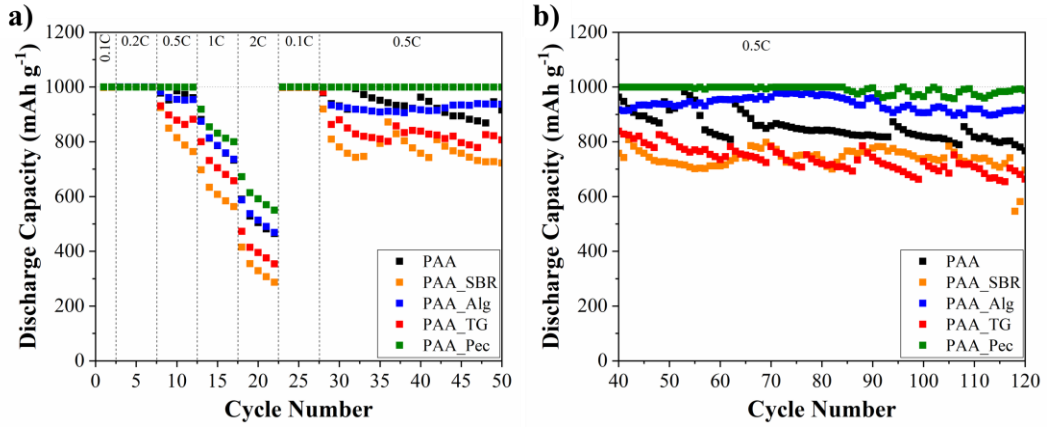

Figure 5.115 – Comparison of electrochemical performance of the electrodes produced at PoliTo based on the different binders combinations: a) Entire test, up to 120 cycles; b) Focus on the rate capability test.

These trends became even more evident during long-term cycling, where PAA_Pec exhibited the most stable behavior, maintaining discharge capacities close to 1000 mAh g^{-1} throughout the 120 cycles with minimal fading and low variability among replicas. PAA_Alg also showed remarkable stability, although with slightly lower average capacity compared to Pec, while the PAA baseline exhibited moderate decay and higher variability. Both TG and SBR systems were characterized by pronounced fluctuations and abrupt capacity drops, consistent with microstructural instability under repeated silicon volume variations. The absence of substantial decay phenomena in Pec and Alg-based systems suggested improved mechanical resilience, likely due to the formation of a more robust polymeric network. In particular, polysaccharides rich in carboxyl functional groups, such as Pec and Alg, may promote stronger hydrogen bonding and ionic interactions with both silicon and PAA, enhancing cohesion and accommodation of volume changes. Conversely, SBR, being less compatible with the aqueous PAA system, may induce microphase separation and weaker structural integrity, while the highly branched structure of TG may lead to heterogeneous network formation that does not efficiently sustain mechanical stress.

Overall, the combined analysis of rate capability and long-term cycling indicates a clear performance hierarchy among the investigated systems, with PAA_Pec and PAA_Alg with enhanced performance compared to the baseline PAA formulation, whereas PAA_TG and PAA_SBR exhibit inferior stability and reproducibility, demonstrating that binder selection is a critical parameter in governing the electrochemical response of SD electrodes.

5.4.2. Scale up process: Pilot-Line Scale

After the optimization of the production process at laboratory level, the formulation based on PAA alone was scaled up to the pilot-line level. The results

obtained during pilot-scale production are presented below, highlighting the main challenges encountered and the possible strategies to overcome them.

5.4.2.1. Electrode production

The slurry was prepared with the same composition (80:5:5:10) and SF (45 wt.%) used in the optimized laboratory-scale production process. The mixing procedure followed the same approach optimized with the Trial no.3 (PAA_3), with differences related to the increased batch size and the different equipment involved. At this stage, a planetary mixer (***Figure 3.4e***) was employed, requiring adjustments to the processing parameters:

1. 3.0 g of PAA (450,000 g mol^{-1}) was dissolved in 36.7 mL of MilliQ water for 30 minutes at 100 rpm. The low rotation speed was maintained to avoid splashing, although the system was closed. The planetary mixer enabled proper dissolution of the binder within this relatively short time.
2. 24.0 g of Si, 1.5 g of graphite and 1.5 g of C45 were manually pre-mixed and then added to the binder solution. After preliminary manual homogenization, the slurry was stirred at 100 rpm for 20 minutes.

Immediately after mixing, the slurry appeared highly homogeneous and free of visible clumps or aggregates. However, when transferred to the R2R coater, numerous agglomerates became visible on the slurry surface (***Figure 5.116***). In addition, the slurry exhibited excessively low viscosity, leading to uncontrolled spreading of the material along the rolls and over the CC (***Figure 5.116 b,c***).

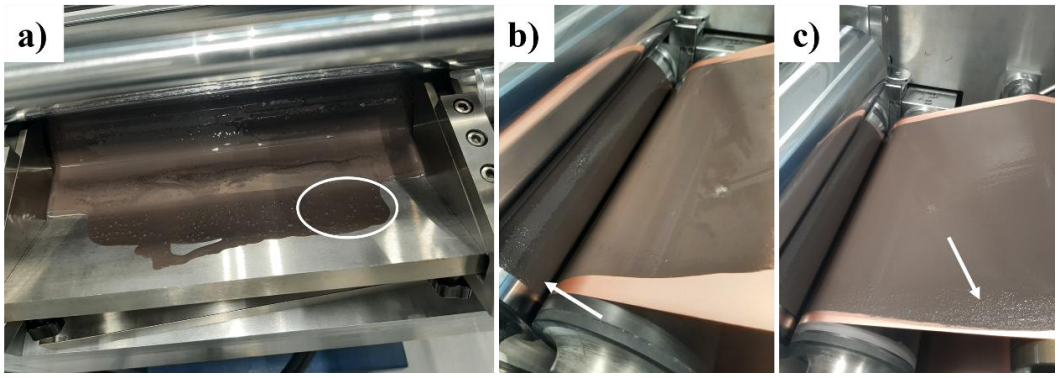

Figure 5.116 – Coating process at pilot line level, highlighting the defects encountered during the production process.

Despite these issues, electrodes were produced with different imposed wet thicknesses (20, 40 and 60 µm) to try to correlate wet deposition thickness with resulting dry thickness and ML. As reported in ***Table 5.52***, several discrepancies and inconsistencies were observed between the imposed wet thickness and the measured dry thickness values. This unexpected behavior was attributed to the

too-liquid slurry and the manual adjustment of the coating machine. Although the system provides greater precision compared to a laboratory doctor blade process, gap regulation was still performed manually, and at low thicknesses (20 or 40 µm), the deviation from the average values remains significant.

Table 5.52 – Characteristics of the electrodes produced at pilot line with a SF of 45 wt.% and a formulation containing 10 wt.% PAA.

Solid Fraction (%)	***Wet Thickness (µm)***	***Dry Thickness (µm)***	***Average Weight (mg)***	***Mass Loading (mg cm^{-2})***
45	*20*	*45 ± 6*	*12.58 ± 0.59*	*1.53 ± 0.27*
45	*40*	*49 ± 7*	*13.16 ± 0.31*	*1.79 ± 0.14*
45	*60*	*56 ± 1*	*14.61 ± 0.21*	*2.45 ± 0.09*

Due to the poor quality of the electrodes produced at pilot-line level, it was not possible to obtain samples suitable for reliable electrochemical testing. Consequently, no further electrochemical characterization was performed on these electrodes. These observations suggest that the slurry formulation optimized at laboratory scale was not directly transferable to pilot-scale processing, likely due to differences in mixing conditions.

5.4.3. Comparison between the production processes

When the two production processes (laboratory-scale and pilot-line scale) were compared, several relevant differences emerged (***Table 5.53***). The comparison between laboratory-scale and pilot-line production clearly highlighted the impact of process control on the final electrode properties. Despite maintaining the same SF (45 wt.%), the pilot-line electrode achieved a significantly higher dry thickness and ML at a lower imposed wet thickness, indicating a more efficient material deposition and reduced shrinkage during drying. In contrast, laboratory-scale coatings exhibited greater thickness variability and more pronounced contraction during solvent evaporation. Overall, these results confirmed that scaling up the coating process did not merely replicate laboratory conditions, but substantially increased the number of parameters that must be carefully controlled throughout the production process.

Table 5.53 – Comparison of the electrode's characteristics based on the different production processes.

Solid Fraction (%)	***Wet Thickness (µm)***	***Dry Thickness (µm)***	***Average Weight (mg)***	***Mass Loading (mg cm^{-2})***
		Laboratory Level		
45	*50*	*22 ± 1*	*11.61 ± 0.43*	*1.09 ± 0.09*
45	*70*	*31 ± 5*	*13.23 ± 0.60*	*1.82 ± 0.27*

45	*100*	*41 ± 2*	*14.91 ± 0.38*	*2.59 ± 0.17*
		Pilot line		
45	*20*	*45 ± 6*	*12.58 ± 0.59*	*1.53 ± 0.27*
45	*40*	*49 ± 7*	*13.16 ± 0.31*	*1.79 ± 0.14*
45	*60*	*56 ± 1*	*14.61 ± 0.21*	*2.45 ± 0.09*

5.4.4. Slurries optimization and further characterization at CIC energiGUNE Laboratories

During the research period at CIC energiGUNE laboratories, in Vitoria-Gasteiz, a deeper investigation on the rheological properties of the slurries was performed. The study started from the already optimized laboratory-scale production process developed at PoliTo, with a SF of 45 wt.%, and expanded the range of natural polysaccharides investigated, including CGN. However, rheological measurements confirmed the excessively low viscosity already observed during pilot-line production, and the SF was therefore increased to 60 wt.% for further analysis.

Compared to the mixer used at PoliTo, a larger Dispermat device was available at CIC energiGUNE for mixing water-based slurries. To accelerate the preparation process, the PAA solution was prepared the day before and kept under magnetic stirring overnight to ensure complete homogenization. The overall composition was maintained at 80:5:5:10 (E-Magy silicon, graphite, C45, and binder). When additives were introduced, the PAA content was reduced from 10 wt.% to 9 wt.%, replacing it with 1 wt.% of the selected additive.

Rheological measurements were carried out using a Thermo Scientific HAAKE RS1 rheometer, evaluating flow curves, thixotropic behavior, and creep recovery tests. Starting from the homogeneous PAA solution, each component (additive, C45, graphite and silicon) was sequentially incorporated while maintaining the same mass ratios, and for each slurry a rheological characterizations were performed. Flow curve and thixotropic behavior were measured with the test protocol reported in ***Table 5.54***. The test began with a rotational ramp in which the shear rate was increased from 0.1 to 1000 s^{-1} over 60 seconds to obtain the flow curve. The slurry was then maintained under steady shear conditions for 30 seconds, followed by a reverse ramp decreasing the shear rate from 1000 to 0.1 s^{-1} to evaluate thixotropic behavior. The importance of the evaluation of the thixotropic behavior relies in the degradation phenomena that the polymeric binders can encounter after shear application. The thixotropic test evaluates the time-dependent structural breakdown under shear and subsequent recovery when shear is reduced, providing insight into slurry stability and coating behavior after deposition.

Table 5.54 – Rheological testing protocol applied to the slurry to measure flow curve and thixotropic behavior

Parameter	Value	Measurement unit
1) Rot ramp – flow curve		
Shear rate ($\dot{\gamma}$)	0.1 → 1000	S^{-1}
Time	60	S
Temperature	23	°c
2) Rot time		
Shear rate ($\dot{\gamma}$)	1000	S^{-1}
Time	30	S
Temperature	23	°c
3) Rot ramp – thixotropic behavior		
Shear rate ($\dot{\gamma}$)	1000 → 0.1	S^{-1}
Time	60	S
Temperature	23	°c

An additional rheological characterization was performed using the creep recovery test, also referred to as 3-ITT, with the protocol reported in ***Table 5.55***. This test aimed to simulate slurry behavior during coating by applying a constant shear stress and monitoring the resulting deformation and its recovery after stress removal [147]. The creep recovery test allows differentiation between elastic and viscous contributions to the viscoelastic response of the slurry.

Table 5.55 – Rheological testing protocol applied to the slurry to measure creep recovery test

Parameter	Value	Measurement unit
1) Rot time		
Shear rate ($\dot{\gamma}$)	0.1	S^{-1}
Time	120	S
Temperature	23	°c
2) Rot time		
Shear rate ($\dot{\gamma}$)	10	S^{-1}
Time	10	S
Temperature	23	°c
3) Rot time		
Shear rate ($\dot{\gamma}$)	0.1	S^{-1}
Time	300	S
Temperature	23	°c

Rheological characterization represents a fundamental step in understanding slurry processability and its influence on final electrode properties. However,

when working with SD slurries, which exhibit faster drying behavior compared to other electrode formulations, extended rheological testing led to partial drying of the slurry during measurement (***Figure 5.117***). This phenomenon resulted in inconsistent and non-reproducible rheological data, as discussed in the following section.

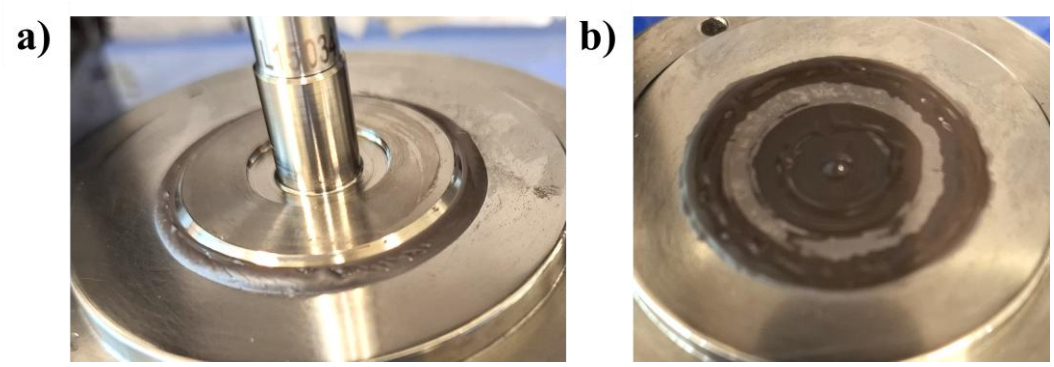

Figure 5.117 – Slurry drying process observed during rheological measurements.

5.4.4.1. Slurries optimization with a SF of 45 wt.%

The work performed at CIC energiGUNE started with the preparation of the slurries with a 45 wt.% SF. In this case, the PAA was dissolved in distilled water at 8.2 wt.% overnight, which corresponded to the dilution used for slurry preparation. The first step consisted of evaluating the mixture of PAA with selected additives; in particular, the first trials was performed using TG, Pec and SBR.

After proper mixing, all the slurries appeared transparent and homogeneous, except for the SBR-based slurry, which exhibited a milky appearance due to the characteristic whitish color of SBR. These slurries were first subjected to rheological testing, including flow curve and creep recovery measurements, as reported in ***Figure 5.118***. Both measurements were characterized by significant noise because the viscosity was too low to fall within the optimal detection window of the instrument.

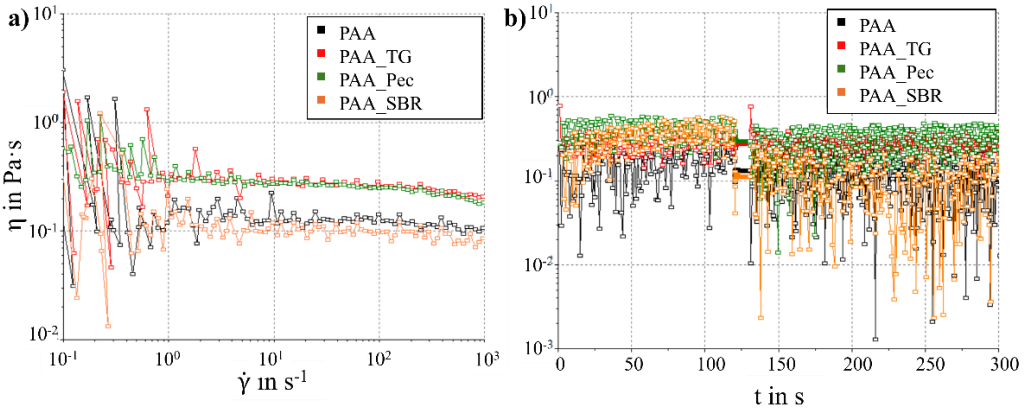

Figure 5.118 – Rheological characterization of the PAA and additive slurries: a) Flow curve and b) Creep recovery test.

Depending on the additive, some differences were observed. For the flow curves (***Figure 5.118a***), PAA alone (black curve) and PAA_SBR (orange curve) presented similar behavior, with PAA_SBR showing slightly lower viscosity than single PAA, likely due to phase heterogeneity within the system. In contrast, the addition of TG (red curve) and Pec (green curve) increased the viscosity of the slurry, with both systems showing overlapping trends. Overall, all binder systems exhibited the expected shear-thinning behavior, characterized by a reduction in viscosity at increasing shear rate. A similar trend was observed in the creep recovery test (***Figure 5.118b***). Although the high noise level hindered clear differentiation of the curves, PAA alone and PAA_SBR showed only a slight increase in viscosity at the beginning of the test, whereas TG and Pec presented higher initial viscosity values. These two systems (TG and Pec) also maintained higher viscosity during the second step of the test, when shear stress was consistently increased.

Even though the viscosity was far from the optimal range for LIBs application, the slurries were coated onto 6 µm Cu CC with an imposed wet thickness of 70 µm (***Figure 5.119***). After mixing, the PAA alone slurry appeared transparent and homogeneous, leading to smooth laminates (***Figure 5.119a***). A similar result was obtained for PAA_TG (***Figure 5.119b***) and PAA_Pec (***Figure 5.119c***). In contrast, the addition of SBR led to a different outcome (***Figure 5.119d***): the slurry appeared homogeneous during mixing, but after drying, the laminate surface exhibited blueish inhomogeneities, indicating a phase separation between PAA and SBR.

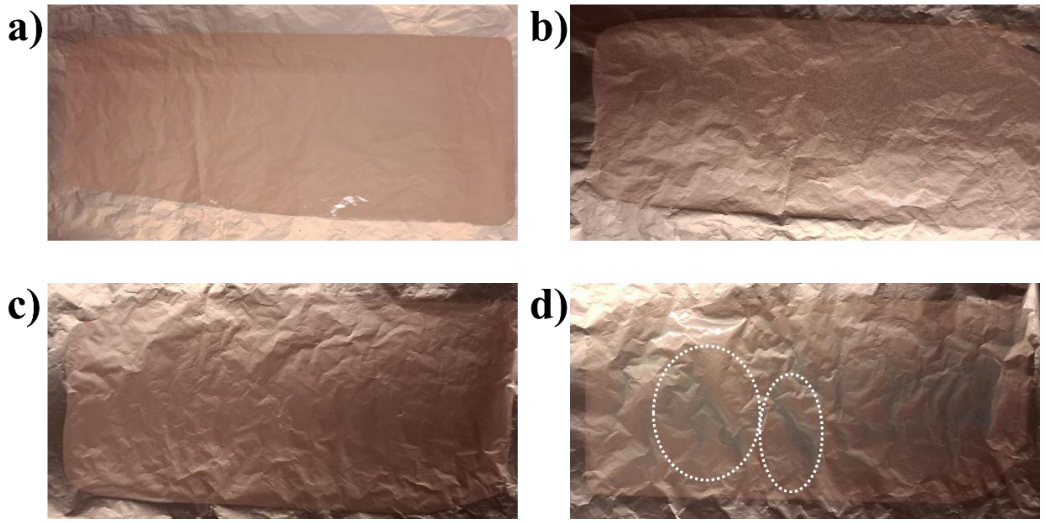

Figure 5.119 – Laminates with a thickness of 70 µm produced with the PAA and the additives: a) PAA alone; b) Tragacanth Gum; c) Pectin and d) SBR.

This phase separation can be explained by their chemical structures: PAA is highly polar due to its carboxylic functional groups (***Figure 5.120a***), whereas SBR contains apolar benzyl group (***Figure 5.120b***). Their combined use as binders for silicon electrodes generally requires chemical modification, as simple physical mixing is insufficient to ensure compatibility [159]. Based on these results, together with the poor electrochemical performance reported in ***Figure 5.100***, SBR was discarded for subsequent anodes preparation.

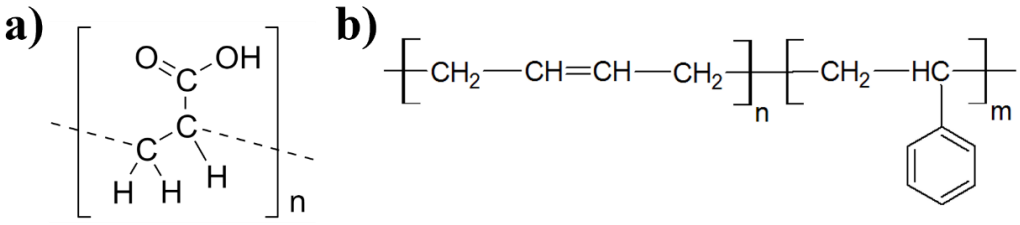

Figure 5.120 – Chemical structures of a) PAA and b) SBR.

To evaluate the impact of additional components in the anode formulation, PAA was mixed with 5 wt.% graphite and subjected to the same tests. ***Figure 5.121a*** shows the laminates produced with the PAA and graphite, which appeared very fluid, with graphite homogeneously dispersed across the surface. Accumulation of slurry was observed at the end of the coating path due to its low viscosity. The complete slurry containing graphite, carbon black, and silicon (***Figure 5.121b***) exhibited overall good homogeneity; however, defects observed on one side of the laminate were attributed to the insufficient viscosity of the slurry for stable deposition. The addition of graphite did not significantly affect the rheological behavior, as observed in both the flow curve and creep test

(***Figure 5.121c*** and ***Figure 5.121d***, respectively). In contrast, the complete slurry, obtained after the addition of graphite, C45, and silicon, exhibited an increase of approximately one order of magnitude, more similar to the desired viscosity.

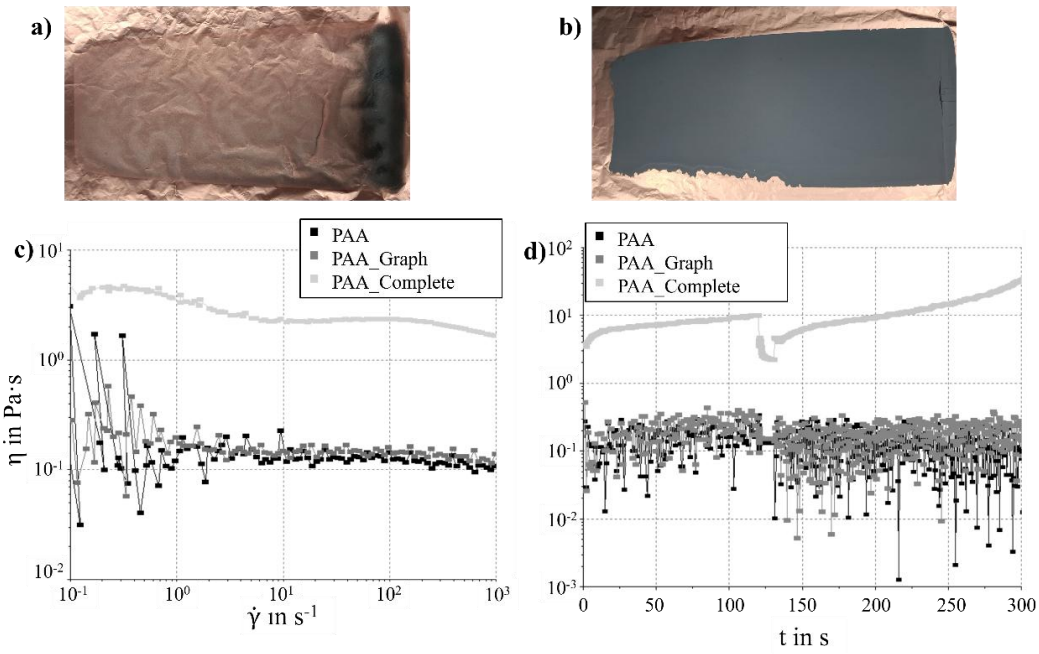

Figure 5.121 – a) Laminate produced with the PAA as binder and the graphite; b) Laminate complete with PAA graphite, carbon black and silicon; c) Flow curve with the comparison of the slurries produced with the different components; d) Creep recovery test with the comparison of the slurries produced with the different components.

A preliminary trial with TG was then conducted to assess the impact of the additive on slurry viscosity. ***Figure 5.122*** compares the rheological behavior of PAA alone (black curve) and PAA_TG (red curve). The addition of TG increased the viscosity while maintaining the desired shear-thinning behavior necessary for coating. Nevertheless, the absolute viscosity values remained outside the optimal range, which for silicon-based anodes has been reported to be in the range between 10^1-10^2 Pa·s [491]. For the flow curve (***Figure 5.122a***), TG increased viscosity across the entire shear rate range, although at high shear rates the viscosity of PAA_TG approached values similar to PAA alone. In the creep recovery test (***Figure 5.122b***), the initial viscosity values were consistent with those observed in the flow curve. After the huge increase in shear stress, pure PAA followed the expected trend, showing a significant reduction in viscosity, whereas PAA_TG maintained higher viscosity. After stress removal, PAA_TG exhibited a gradual viscosity recovery, while PAA alone showed a sharper recovery, likely associated with faster drying during the measurement.

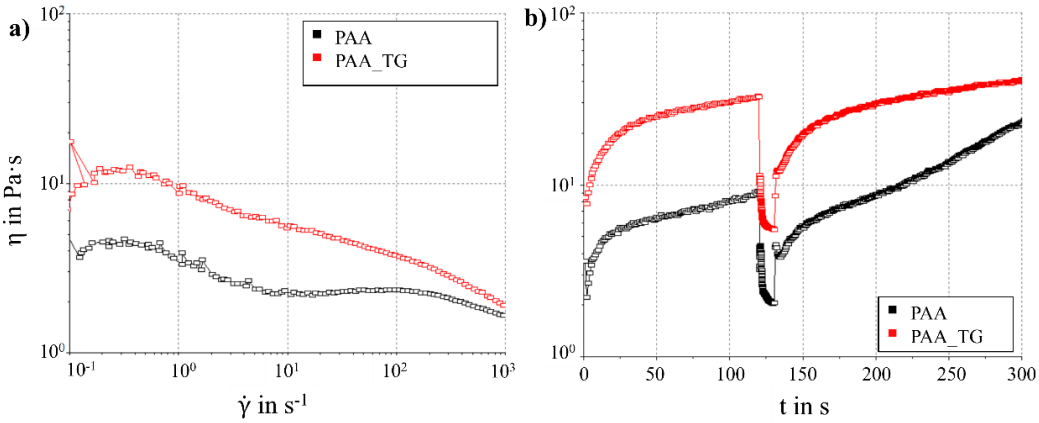

Figure 5.122 – Comparison of the rheological measurement for the slurries produced with the PAA alone (black curve) and the PAA with the TG (red curve): a) Flow curve; b) Creep recovery test.

The comparison of rheological results with existing literature results is difficult, due to the multiple parameters that can affect this parameter, starting from the specific silicon characteristics, binders and solvent involved in the production, the electrode composition and mixing procedure. Using a similar silicon grade, Karkar et al. [70] demonstrated that high-quality electrode films were obtained by tape casting with a SF between 24 and 28%, which provided an optimized rheological behavior. Although their composition also included PAA as binder, the silicon material differed, resulting in comparable viscosity at low shear rates but significantly different values at higher shear rates.

5.4.4.2. Increase of the SF up to 60 wt.%

After these evaluations, the SF was increased to 60 wt.%. In line with the observation reported by Kloker et al. [433], for SD anodes, a SF higher than 60 wt.%, compared to 50%, led to higher capacities for all C-rates with a stronger effect at higher C-rates and the capacity retention improved by almost 10 %.

The work started with the preparation of PAA alone, which was dissolved in water the day before at a concentration of 13.04 wt.%, and kept stirring overnight to guarantee proper homogenization. Starting from the PAA solution, the additives (natural polysaccharides) and the components were added one by one, and for each solution, pH and rheological measurement were performed. All the slurries presented similar pH values (***Table 5.56***), independently from the materials and the additives, with a range between 2 and 2.4.

Table 5.56 – pH values of all the solutions produced starting from the solution of PAA and with the natural polysaccharides added to the system.

Components	***pH***				
	PAA	**PAA_Alg**	**PAA_Pec**	**PAA_CGN**	**PAA_TG**
PAA	*2.07*	*2.83*	*2.22*	*2.22*	*2.35*
PAA_Graphite	*1.99*	--	--	--	--
PAA_C45	*2.02*	*2.90*	*2.23*	*2.25*	*2.37*
PAA_C45_Graphite	*2.02*	--	--	--	--
PAA_Complete	*2.05*	*2.87*	*2.21*	*2.21*	*2.32*

Successively, all the solutions were coated onto the 6 µm Cu CC, and the peel test was conducted on the resulting laminate. To guarantee proper comparison between laminates, a constant wet thickness deposition of 50 µm was maintained through the study. For each type of binder combination, 15 mm electrodes were manually punched and characterized by measuring the dry thickness, their average weight and the resulting ML (***Table 5.57***). The variations observed among the binder formulations can be attributed to changes in slurry rheology and polymer interactions, which ultimately influence drying behavior and electrode structure. It should be noted, however, that direct comparisons among exactly these binder systems under identical formulation and processing conditions are still lacking in literature. Therefore, some of the differences highlighted in this work may not clearly emerge when results from independent studies are compared, as variations in composition, SF, or coating parameters can mask binder-specific effects.

Table 5.57 – Characteristics of the electrodes produced at CIC energiGUNE with the different binder combinations

	Dry Thickness (µm)	*Average Weight (mg)*	*Average Mass Loading (mg cm^{-2})*
PAA	37 ± 5	14.83 ± 0.60	2.55 ± 0.27
PAA_Alg	38 ± 2	19.23 ± 0.46	4.54 ± 0.29
PAA_Pec	36 ± 2	14.72 ± 0.19	2.50 ± 0.09
PAA_CGN	53 ± 2	17.92 ± 0.43	3.95 ± 0.19
PAA_TG	39 ± 5	15.64 ± 0.29	2.92 ± 0.13

For each laminate produced, a sample of 30x60 mm was cut out to perform the 90° peel test and evaluate the adhesion strength between the coating layer and the CC [492]. The aim of this systematic characterization and investigation work was to better understand the role of each components regarding the mechanical behavior and how the different natural polysaccharides can affect the production process, even when added in a small amount of 1 wt.%.

The final electrochemical testing was performed at PoliTo. Following electrode fabrication, the electrodes were vacuum-dried at 120 °C for 4 hours to ensure complete removal of residual moisture. To guarantee statistical reliability

of the electrochemical results, three cells were assembled for each sample. Cell assembly was carried out inside an argon-filled glovebox, following the same procedure previously described for silicon-composite-based anodes. The SD electrodes were tested in half-cell configuration, using metallic lithium as the counter electrode and a G/F Whatman separator soaked with 150 µL of electrolyte consisting of 1 M $LiPF_6$ dissolved in EC:DEC (1:1 by volume), with the addition of 10 wt.% FEC and 2 wt.% VC. Electrochemical characterization was performed through galvanostatic charge-discharge measurements and CV. The galvanostatic tests were conducted within a voltage window of 0.04 - 1.00 V vs. Li^+/Li. The cycling protocol is reported in ***Table 5.58*** and included two formation cycles, followed by a rate capability test performed at 0.2C, 0.5C, 1C and 2C, and subsequent long-term cycling at 0.5C.

Table 5.58 – Cycling protocol adopted for electrochemical characterization of silicon-dominant electrodes produced at CIC energiGUNE

Cycle	***Mode***	***Discharge***	***Charge***
1-2	*Formation*	*CCS: 0.1C*	*CCS: 0.1C*
3-7	*Rate Capability*	*CCS: 0.2C*	*CCS: 0.2C*
8-12	*Rate Capability*	*CCS: 0.5C*	*CCS: 0.5C*
13-17	*Rate Capability*	*CCS: 1C*	*CCS: 1C*
18-22	*Rate Capability*	*CCS: 2C*	*CCS: 2C*
23-25	*Recovering*	*CCS: 0.1C*	*CCS: 0.1C*
26-120	*Long Cycling*	*CCS: 0.5C*	*CCS: 0.5C*

For CV measurements, the cells were assembled in a three-electrode configuration. Both the SD working electrode and the lithium counter and reference electrodes were punched into 10 mm diameter discs, and the electrolyte volume was reduced to 120 µL. The CV analysis was carried out within a voltage window of 0.04 - 1.0 V at a scan rate of 0.1 mV s^{-1}, performing five cycles for each sample. To ensure consistent comparison among the different formulations, all CV curves were normalized to the corresponding AM mass.

5.4.4.2.1. Single binder: PAA

Starting from pure PAA , the other components were added one by one to produce five different slurries, whose characteristics were independently measured. The pH values of the solutions prepared with the PAA alone are reported in ***Table 5.52***. The binder solution was characterized by the pH of 2.07, in line with the values reported in the literature [145]. The addition of slurry components did not lead to significant variations in pH.

The rheological measurement (***Figure 5.123***) presented interesting results. Regarding the flow curve (***Figure 5.123a***) the increase of SF effectively led to higher viscosity. PAA alone exhibited higher viscosity than the 45 wt.% SF formulation, reaching approximately 10^0 Pa·s at the lowest value of shear rate, remaining almost constant over a wide shear rate range, and decreasing at higher

shear rates, confirming shear-thinning behavior. The addition of graphite to the system led, as expected, to a significant increase in viscosity of approximately one order of magnitude while maintaining the same trend observed for PAA alone. The addition of C45 resulted in only a slight increase in viscosity, indicating that graphite acted as the main contributor to viscosity enhancement, as similarly observed by Reynolds et al. [299]. Interestingly, when graphite and C45 were simultaneously added, a slight decrease in viscosity was observed, which may be associated with changes in the carbonaceous particle network and interparticle interactions affecting slurry microstructure rather than a simple additive effect [493]. The preparation of the complete slurry containing all components led to the highest viscosity values, reaching levels consistent with those required for battery applications and maintaining the typical shear-thinning behavior necessary for proper coating procedures [299,491]. The addition of silicon led to a modification of the curve shape, with the appearance of a plateau of constant viscosity in the shear rate range between 10^1 and 10^2 s^{-1}. Interestingly, Zapata Dominguez at al, [494], reported a decrease in viscosity when the silicon content was increased from 8 to 15 wt.% in a graphite-silicon-blended anode. This effect can be used to explain the lower than expected viscosity increase observed here, despite the high silicon content (80 wt.%).

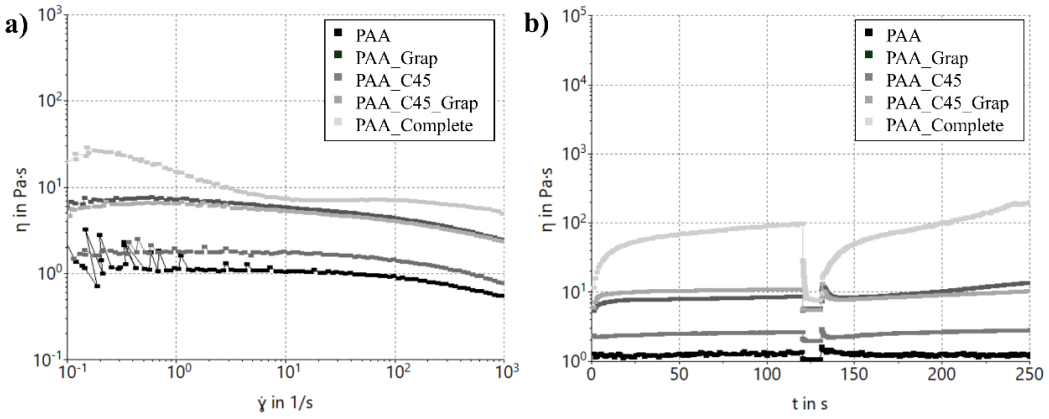

Figure 5.123 – Rheological characterization of the slurries produced with PAA alone: a) Flow curve; b) Creep recovery test.

When considering the creep recovery test (***Figure 5.123b***) increasing the SF to 60 wt.% led to a higher viscosity response. The viscosity of PAA_Complete was approximately one order of magnitude higher than that of the same slurry at an SF of 45 wt.%, although it remained close to the instrument detection limit. The separate addition of graphite and C45 both resulted in increased viscosity throughout the test. Interestingly, under steady-state conditions in this test, the viscosity of the slurry containing both C45 and graphite was higher than that of PAA_Graphite alone, in contrast to the trend observed in the flow curve. This behavior may be related to the lubricating properties of graphite, which under

shear can reduce resistance to flow and enhance polymer chain mobility. As expected, the complete slurry exhibited the highest viscosity values, which significantly decreased when higher shear stress was applied. Following stress removal, the slurry is expected to fully recover its original structure, which is typically confirmed when the viscosity returns to the plateau reached before stress application. However, in these samples, rapid solvent evaporation during the test leads to a continuous increase in viscosity, resulting in values that exceed the expected recovery plateau.

After rheological characterization, each solution was coated onto the CC with a constant wet thickness of 50 µm using a manual doctor blade as tape casting technique. The produced laminates are reported in ***Figure 5.124***: all were characterized by smooth and homogeneous surfaces, despite the different compositions.

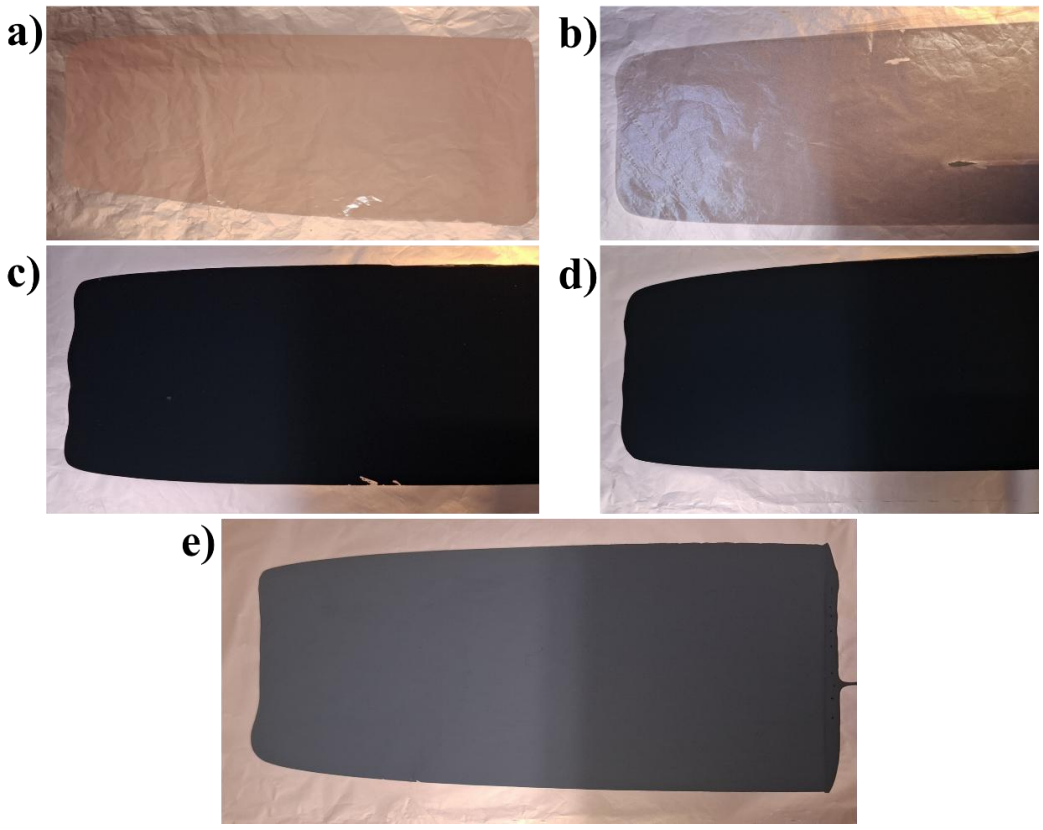

Figure 5.124 – Laminates produced with a constant wet thickness of 50 µm and starting from the solution of PAA alone: a) PAA alone; b)PAA_Graphite; c) PAA_C45; d) PAA_C45_Graphite; d) PAA_Complete.

Peel tests were also performed on these laminates (***Figure 5.125***). It is worth noting that the single PAA laminate exhibited complete adhesion to the CC, without visible removal or detachment. When graphite was added, only minor spots were detached. The addition of C45 alone significantly increased adhesion to the CC, even resulting in traces of adhesive remaining on the laminate surface.

A similar behavior was observed for the mixture of C45 and graphite. However, after the addition of the high silicon content, the adhesion behavior worsened significantly, with a considerable amount of material removed from the CC during the peel test.

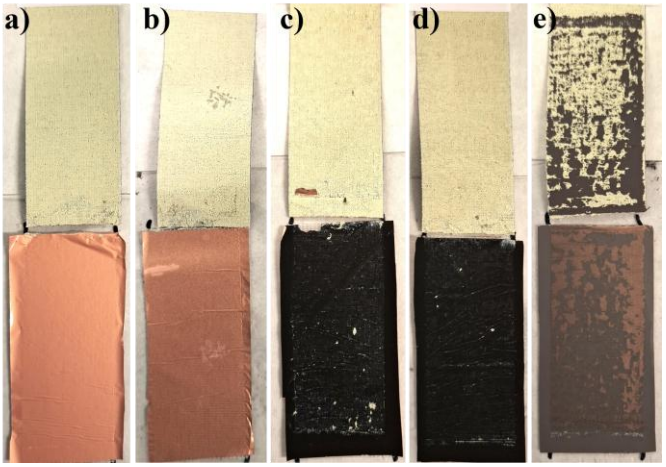

Figure 5.125 – Peel test performed o the laminates produced starting with the PAA alone solution: a) PAA alone; b)PAA_Graphite; c) PAA_C45; d) PAA_C45_Graphite; d) PAA_Complete.

The laminate produced with the complete slurry was further characterized by the measurement of dry thickness, average 15 mm diameter electrode weight and subsequent ML (***Table 5.57***). The laminate dry thickness was randomly measured along the electrode surface to ensure representative sampling and resulted in 37 ± 5 µm. The electrodes were characterized by an average weight of 14.83 ± 0.60 mg, corresponding to an average ML of 2.55 ± 0.27 mg cm^{-2}. This formulation was considered the reference for comparison.

Overall, the use of PAA as a standalone binder supplied consistent and reproducible rheological behavior. Due to the high similarity between some of the results, graphite appeared to have a limited additional impact on slurry rheology under these conditions. For this reason, in the subsequent investigation of natural polysaccharides, only C45 was retained as the single carbonaceous component for isolated evaluation.

The electrodes produced with the PAA alone as binder were considered as the baseline formulation and exhibited good electrochemical performance (***Figure 5.126***, ***Table 5.59***), with capacities remaining almost stable above 800 mAh g^{-1}, during most of the test. However, variability among the samples increased the statistical dispersion of the results throughout the cycling. Considering the rate capability test (***Figure 5.126b***), a significant capacity decay was observed at 2C, which can be attributed to kinetic limitations at high current density, as previously discussed. It is worth noting that the first cycle CE showed an average value of 88.92%, which is slightly higher than the typical values reported in the literature for silicon-based anodes [476,477].

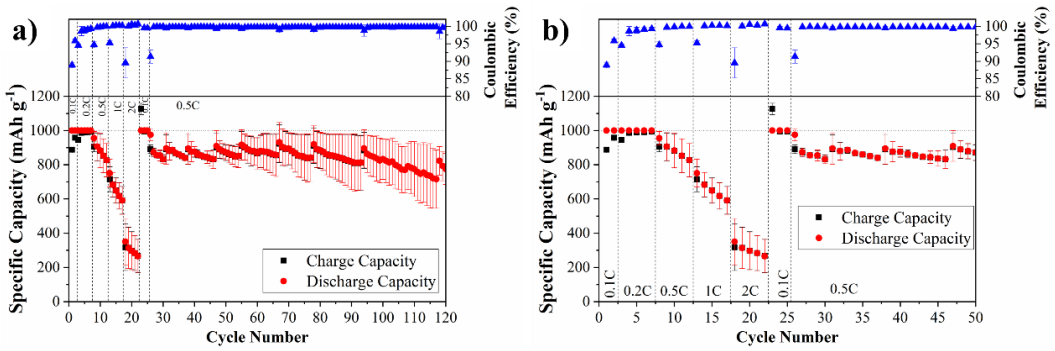

Figure 5.126 – Values of charge and discharge capacity and relative coulombic efficiency for PAA-based electrodes produced at CIC energiGUNE: a) Entire test, up to 120 cycles; b) Focus on the rate capability test.

Table 5.59 – Values of charge and discharge capacities, normalized by the electrode weight, and relative values of coulombic efficiency for some representative cycles for the PAA-based electrodes produced at CIC energiGUNE.

Cycle	*C-rate*	*Charge Capacity (mAh g^{-1})*	*Discharge Capacity (mAh g^{-1})*	*Coulombic Efficiency (%)*
1	*0.1C*	*887.84 ± 5.74*	*1000.00*	*88.92 ± 0.80*
2		*957.50 ± 3.19*	*1000.00*	*95.87 ± 0.52*
7	*0.2C*	*992.97 ± 4.42*	*1000.00*	*99.30 ± 0.44*
12	*0.5C*	*826.67 ± 97.56*	*826.95 ± 97.52*	*99.97 ± 0.06*
17	*1C*	*592.51 ± 81.09*	*591.37 ± 81.09*	*100.20 ± 0.12*
22	*2C*	*266.85 ± 97.28*	*265.36 ± 97.81*	*100.66 ± 0.38*
25	*0.1C*	*994.77 ± 2.43*	*1000.00*	*99.48 ± 0.24*
30		*831.60 ± 25.01*	*832.44 ± 26.00*	*99.90 ± 0.12*
50	*1C*	*870.51 ± 45.64*	*872.46 ± 45.99*	*99.78 ± 0.08*
120		*773.77 ± 89.70*	*776.09 ± 90.55*	*99.71 ± 0.07*

During the rate capability test, the discharge capacity decreased progressively with increasing C-rate, reaching 265.36 mAh g^{-1} at 2C. Upon returning to 0.1C (cycle 25), the discharge capacity recovered to approximately 1000 mAh g^{-1}, indicating that the capacity loss at high current density was predominantly due to kinetic limitations rather than irreversible degradation of the active material. During long-term cycling at 0.5C, the electrodes maintained relatively stable performance, with discharge capacities of 832.44 mAh g^{-1} at cycle 30, 872.46 mAh g^{-1} at cycle 50, and 776.09 mAh g^{-1} at cycle 120. Although some variability among samples persisted, the overall CE remained close to 100% throughout extended cycling, confirming stable electrochemical behavior after the formation stage. It is worth noting that, as previously discussed for graphite and SC-based, CE values slightly exceeding 100% at high C-rates can be attributed to the intrinsic limitations of the half-cell configuration with lithium metal counter electrode due to some localized lithium plating phenomenon.

The charge and discharge profiles (***Figure 5.127***) were consistent with those previously observed, showing the characteristic lithiation and de-lithiation plateaus and increased polarization at higher C-rates. Similarly, the CV curves (***Figure 5.128***) were consistent with the typical peaks already discussed.

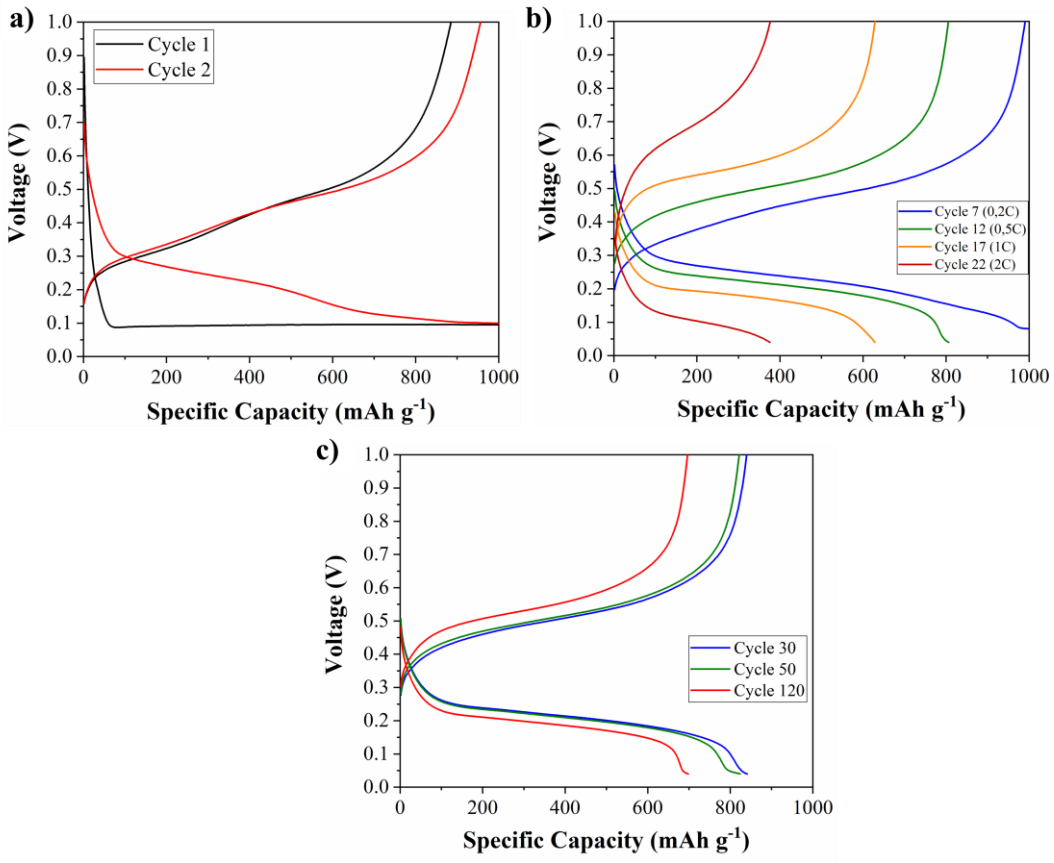

Figure 5.127 – Charge/discharge profiles for some representative cycles for PAA-based electrodes produced at CIC energiGUNE: a) Forming cycles; b) Rate capability test; b) Long-term test.

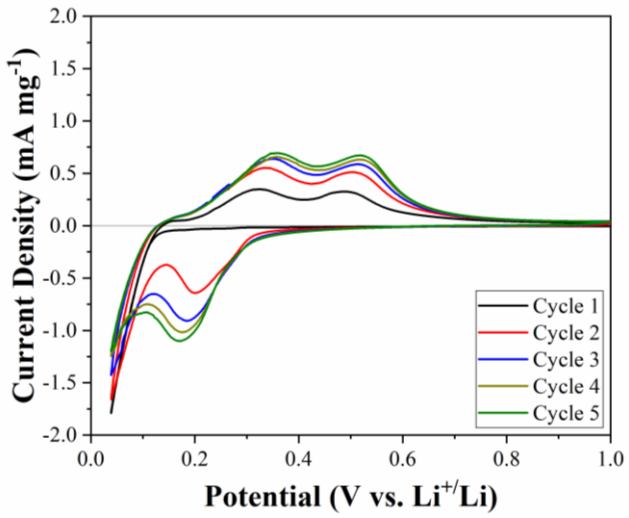

Figure 5.128 – Cycling voltammetry for the PAA-based electrodes produced at CIC energiGUNE.

5.4.4.2.2. PAA_Alg

The solutions prepared with Alg as additive exhibited slightly increased pH values (***Table 5.56***) for all three formulations. The increase in pH after the addition of Na-Alg to the value of 2.83 can be attributed to its sodium salt nature, which introduces Na^+ ions that partially neutralize the carboxylic acid groups of PAA, thereby reducing the concentration of free H^+ in solution. Apart from this effect, the addition of C45 or the other components did not significantly modify the pH of the solutions.

However, the incorporation of Na-Alg into the system substantially altered the slurry properties compared to PAA alone, leading to distinct rheological behavior (***Figure 5.129***). The main difference observed with the addition of 1 wt.% Alg was related to the viscosity observed for the binders-only solution, which exhibited higher viscosity at low shear rate and lower viscosity at high shear rate, resulting in a curve shape markedly different from that of PAA alone and from the other additives. When C45 and the other components were added, the flow curves regained a trend similar to that previously observed for PAA alone. The PAA_Alg_C45 formulation showed a slight increase in viscosity compared to PAA alone, as expected, while maintaining a similar curve shape. A comparable trend was observed for the complete slurry (PAA_Alg_Complete), although characterized by a more pronounced viscosity drop at higher shear rates. Despite these differences, all formulations maintained the desired shear-thinning behavior required for proper coating.

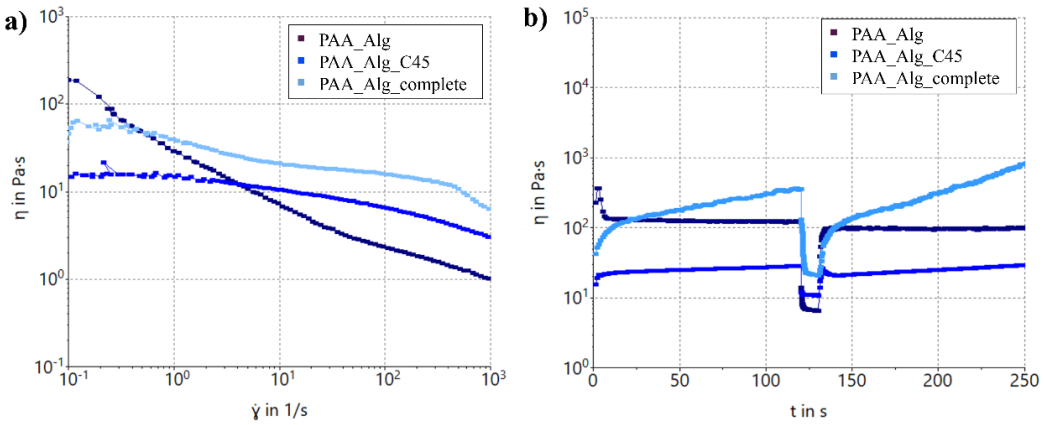

Figure 5.129 – Rheological characterization of the slurries produced with PAA_Alg: a) Flow curve and b) Creep recovery test.

Considering the creep recovery test, an analogous situation was observed: the PAA_Alg presented a viscous behavior completely different from the other slurries. This behavior may be related to the molecular structure of Alg, which is a block copolymer composed of mannuronic (M) and guluronic (G) units arranged in homopolymeric regions (***Figure 2.26***). The presence of these two blocks could

promote the formation of a more interconnected network with PAA through ionic interactions and hydrogen bonding, although this specific synergistic mechanism has not been extensively investigated in the literature.

The coating of the three laminates (***Figure 5.130***) resulted in smooth and homogeneous surfaces. The complete laminate (***Figure 5.130c***) presented some cracks due to an accidental drop of the sample; the very thin CC was not mechanically robust enough to prevent crack formation upon impact.

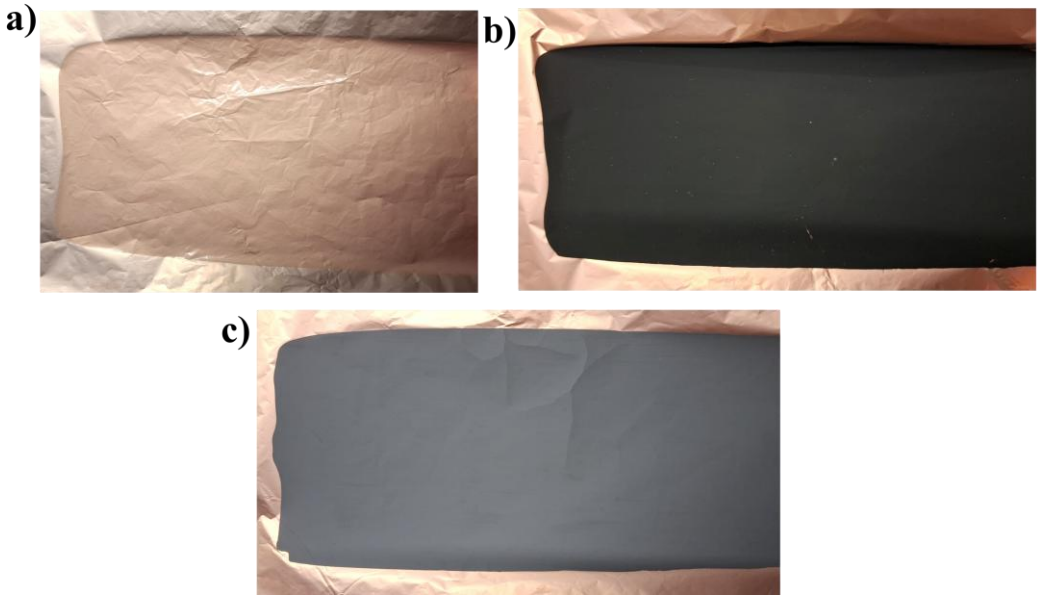

Figure 5.130 – Laminates produced with a constant wet thickness of 50 µm and starting from the solution of PAA_Alg: a) PAA_Alg; b)PAA_Alg_C45; c) PAA_Alg_Complete.

Samples for the peel test were directly cut from the laminates, and the results revealed notable differences (***Figure 5.131***). For the PAA_Alg formulation, the coating remained strongly attached to the CC, similarly to PAA alone. However, for the PAA_Alg_C45 formulation (***Figure 5.131b,c***), the adhesion between the coating and the CC was so strong that the peel test resulted in tearing of the thin Cu CC rather than delamination of the coating layer. The addition of silicon (***Figure 5.131d***) reduced the adhesion to the CC, as previously observed for PAA alone, favoring partial detachment of the coating layer.

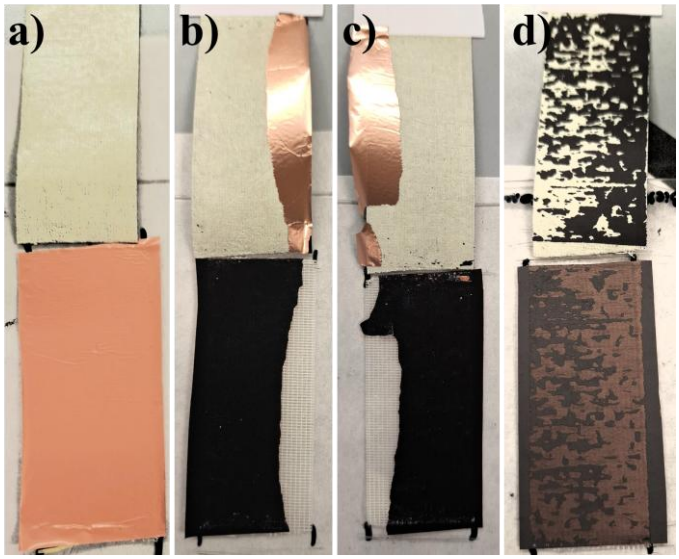

Figure 5.131 – Peel test performed o the laminates produced starting with the PAA_Alg solution: a) PAA_Alg; b)PAA_Alg_C45, first replica; c) PAA_Alg_C45, second replica; d) PAA_Alg_Complete.

For the PAA_Alg_Complete formulation, the dry thickness and ML were measured (***Table 5.57***), the laminate exhibited a dry thickness of 38 ± 2 µm. The punched 15 mm electrodes showed an average weight of 19.23 ± 0.46 mg, resulting in a significantly higher average ML of 4.54 ± 0.29 mg cm^{-2}. Compared to PAA alone, a similar dry thickness but a markedly higher ML was obtained.

Interestingly, the addition of Alg, even at a low amount of 1 wt.%, greatly impacts the properties of the slurries, influencing both rheological properties and adhesion performance compared to PAA alone. These results suggest that the introduction of alginate promotes the formation of a more interconnected polymeric network with PAA, which likely limits particle rearrangement during drying and enhances both packing density and interfacial adhesion. The combined rheological and mechanical evidence indicates that even a minor fraction of alginate can substantially modify the microstructural organization of the electrode.

In literature, the Na-Alg was already employed as binder for silicon-based electrodes, often leading to enhanced electrochemical performance [488,495]. However, the electrochemical performance obtained in this work (***Figure 5.132***, ***Table 5.60***) is significantly lower compared to PAA alone. This result is likely related to the electrode production parameters. Although the coating conditions were maintained constant, the PAA_Alg electrodes exhibited an average ML of 4.54 mg cm^{-2}, which is almost double the 2.55 mg cm^{-2} obtained for PAA alone. The higher ML, coupled with the increased electrode thickness, likely introduced transport limitations for both electron conduction and lithium-ion diffusion within the electrode, thereby reducing electrochemical performance [496].

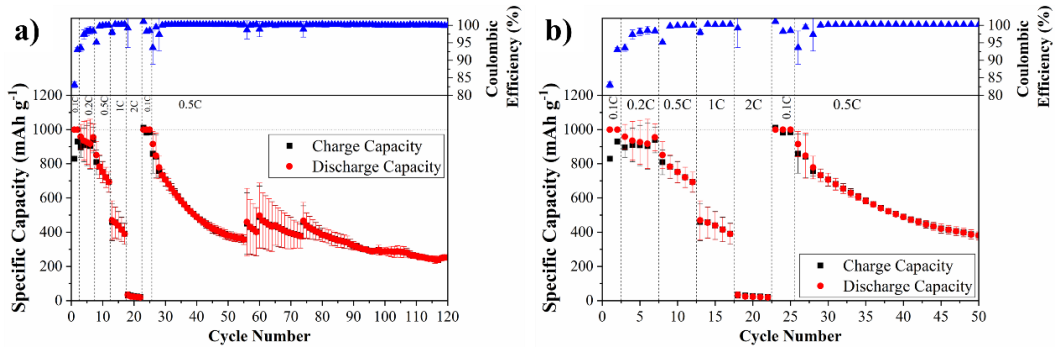

Figure 5.132 – Values of charge and discharge capacity and relative coulombic efficiency for PAA_Alg based electrodes produced at CIC energiGUNE: a) Entire test, up to 120 cycles; b) Focus on the rate capability test.

Table 5.60 – Values of charge and discharge capacities, normalized by the electrode weight, and relative values of coulombic efficiency for some representative cycles for the PAA_Alg based electrodes produced at CIC energiGUNE.

Cycle	*C-rate*	*Charge Capacity (mAh g^{-1})*	*Discharge Capacity (mAh g^{-1})*	*Coulombic Efficiency (%)*
1	*0.1C*	*829.27 ± 7.08*	*998.96 ± 1.80*	*83.01 ± 0.79*
2		*929.89 ± 4.53*	*999.21 ± 1.37*	*93.06 ± 0.57*
7	*0.2C*	*939.32 ± 75.52*	*954.79 ± 78.30*	*98.39 ± 0.17*
12	*0.5C*	*692.72 ± 58.24*	*692.32 ± 58.74*	*100.06 ± 0.09*
17	*1C*	*391.01 ± 61.74*	*389.76 ± 61.18*	*100.31 ± 0.14*
22	*2C*	*21.58 ± 11.67*	*18.97 ± 11.00*	*115.25 ± 4.49*
25	*0.1C*	*984.29 ± 2.24*	*999.46 ± 0.94*	*98.48 ± 0.32*
30		*707.75 ± 37.44*	*706.62 ± 38.14*	*100.16 ± 0.11*
50	*1C*	*381.41 ± 25.28*	*380.72 ± 25.28*	*100.18 ± 0.05*
120		*252.63 ± 16.34*	*252.61 ± 16.52*	*100.01 ± 0.10*

The increased ML strongly affected the rate capability test: at cycle 22 (2C), the average discharge capacity dropped to only 18.97 mAh g^{-1}. This dramatic reduction can be attributed to severe kinetic limitations rather than to intrinsic material degradation. Similarly, during long-term cycling, a rapid capacity decay was observed once the current density of 0.5C was applied. When the current density was reduced to 0.1C (cycle 25), the discharge capacity recovered to approximately 999.46 mAh g^{-1}, indicating that the AM itself did not undergo irreversible degradation and that the observed capacity loss at high current density was predominantly kinetic limitations. During long-term cycling at 0.5C, a progressive capacity decay was observed, with discharge capacities decreasing from 706.62 mAh g^{-1} at cycle 30 to 252.61 mAh g^{-1} at cycle 120. This behavior is consistent with the higher internal resistance and limited ion transport associated with thick, high ML electrodes.

The analysis of charge-discharge voltage profiles (***Figure 5.133***) did not reveal the presence of additional parasitic reactions. The polarization increase observed at higher C-rates further supports the hypothesis that the reduced electrochemical performance was primarily governed by transport limitations induced by the elevated ML rather than by chemical incompatibility of the binder system.

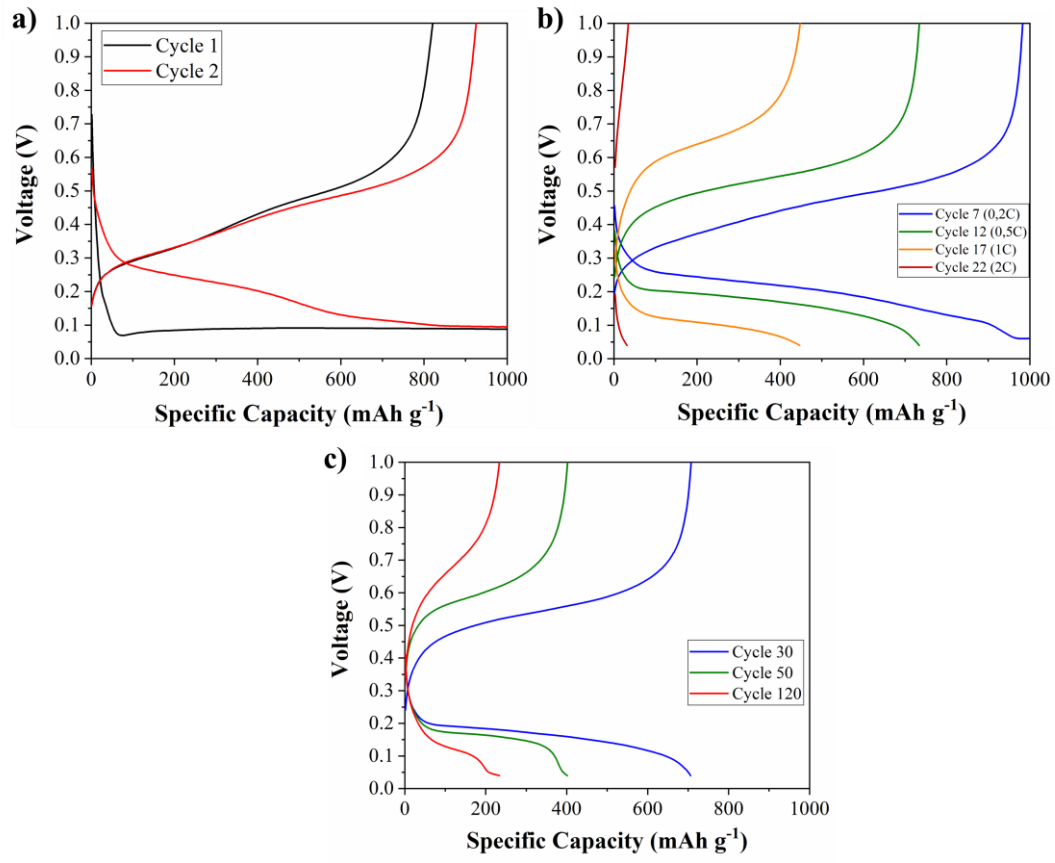

Figure 5.133 – Charge/discharge profiles for some representative cycles for PAA_Alg based electrodes produced at CIC energiGUNE: a) Forming cycles; b) Rate capability test; b) Long-term test.

5.4.4.2.3. PAA_Pec

The second additive involved in this study was Pec. The corresponding pH values are reported in ***Table 5.56*** and were only slightly affected by the addition of C45 and the other powder components. The increase of approximately 0.2 pH units compared to PAA alone can be attributed to the weakly acidic and partially esterified carboxylic groups of Pec, which reduce the effective concentration of free protons in the PAA solution through intermolecular interactions and partial acid-base compensation.

The rheological properties of the slurries produced with PAA_Pec (***Figure 5.134***) exhibited behavior comparable to PAA alone, with only a slight increase in viscosity due to the presence of the additive. Interestingly, in this case, the

difference in viscosity between PAA_Pec_C45 and PAA_Pec_Complete (***Figure 5.134a***) was minimal, with the distinction between the two formulations mainly reflected in the curve shape rather than in absolute viscosity values. Although only slightly appreciable, the complete slurry maintained the desired shear-thinning behavior. In contrast, the creep recovery test (***Figure 5.134b***) revealed more pronounced differences for PAA_Pec_Complete compared to the other slurries, highlighting how the two rheological tests probe different aspects of material behavior. The PAA_Pec_Complete formulation exhibited faster drying during the test, which resulted in a progressive increase in apparent viscosity under steady-state conditions, both before and after the increase in shear rate.

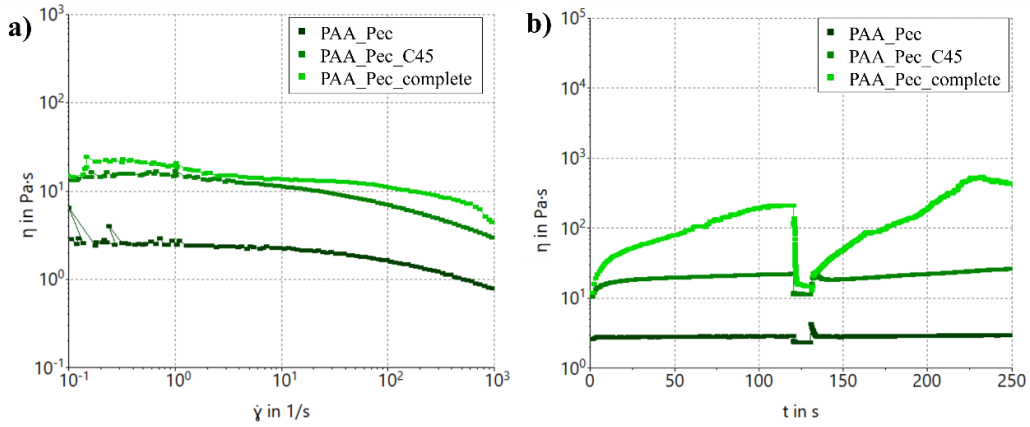

Figure 5.134 – Rheological characterization of the slurries produced with PAA_Pec: a) Flow curve and b) Creep recovery test.

The laminates produced (***Figure 5.135***) were characterized by a smooth and homogeneous surface, except PAA_Pec_C45 (***Figure 5.135b***), which showed the presence of a few bubbles after drying.

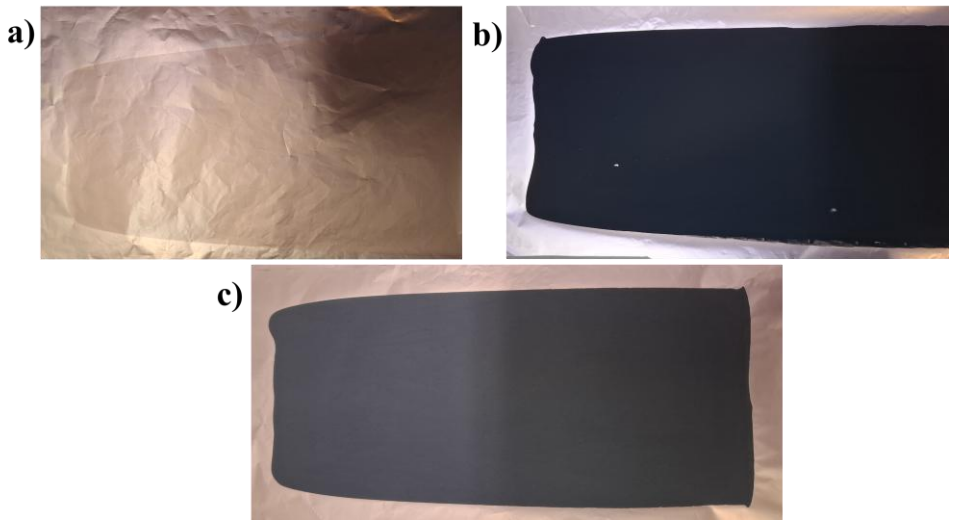

Figure 5.135 – Laminates produced with a constant wet thickness of 50 µm and starting from the solution of PAA_Pec: a) PAA_Pec; b)PAA_Pec_C45; c) PAA_Pec_Complete.

The peel test results (***Figure 5.136***) were comparable to those previously observed for PAA alone, indicating no significant improvement in adhesion performance.

Figure 5.136 – Peel test performed o the laminates produced starting with the PAA_Pec solution: a) PAA_Pec; b)PAA_Pec_C45; c) PAA_Pec_Complete.

The PAA_Pec electrode presented a dry thickness of 36 ± 2 µm. The 15 mm discs had an average weight of 14.72 ± 0.19 mg, corresponding to an average ML of 2.50 ± 0.09 mg cm^{-2}. Compared to the PAA reference, both dry thickness and ML remained essentially unchanged (***Table 5.57***).

Overall, the addition of Pec resulted in limited variations compared to PAA alone, suggesting that the introduction of Pec did not substantially modify the polymeric network within the slurry. This behavior may be related to the predominantly linear molecular structure of Pec, which could limit the formation of a strongly interconnected network with PAA and therefore reduce its impact on rheology and adhesion properties.

The use of Pec as a binder for LIBs is still limited in the literature; however, some innovative studies have started to investigate it as a promising component for cross-linked polymeric networks [176,177]. The electrochemical performance obtained in this work (***Figure 5.137***, ***Table 5.61***) confirmed its potential, with charge and discharge capacities comparable to those obtained with PAA alone.

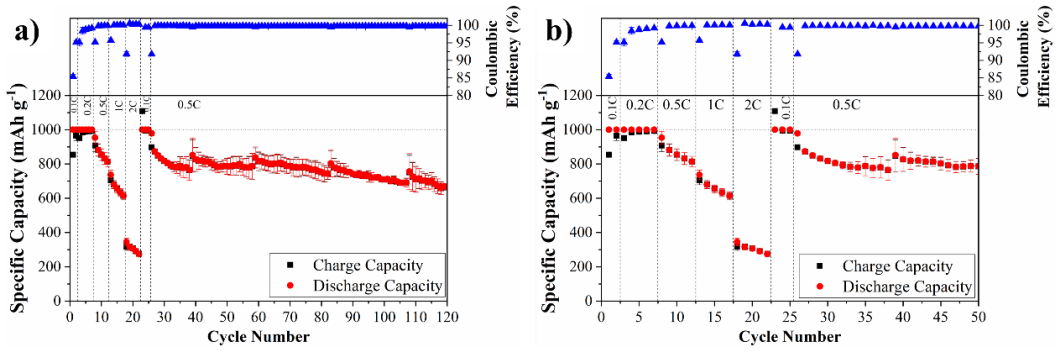

Figure 5.137 – Values of charge and discharge capacity and relative coulombic efficiency for PAA_Pec based electrodes produced at CIC energiGUNE: a) Entire test, up to 120 cycles; b) Focus on the rate capability test.

Table 5.61 – Values of charge and discharge capacities, normalized by the electrode weight, and relative values of coulombic efficiency for some representative cycles for the PAA_Pec based electrodes produced at CIC energiGUNE.

Cycle	***C-rate***	***Charge Capacity (mAh g^{-1})***	***Discharge Capacity (mAh g^{-1})***	***Coulombic Efficiency (%)***
1	*0.1C*	*854.17 ± 6.50*	*1000.00*	*85.42 ± 0.65*
2		*965.16 ± 28.06*	*1000.00*	*95.17 ± 0.49*
7	*0.2C*	*992.07 ± 3.47*	*1000.00*	*99.21 ± 0.35*
12	*0.5C*	*813.42 ± 31.19*	*814.04 ± 31.29*	*99.92 ± 0.01*
17	*1C*	*614.67 ± 23.63*	*614.06 ± 23.81*	*100.10 ± 0.04*
22	*2C*	*275.55 ± 7.07*	*274.72 ± 7.01*	*100.30 ± 0.04*
25	*0.1C*	*994.46 ± 1.38*	*1000.00*	*99.45 ± 0.14*
30		*816.60 ± 7.13*	*817.54 ± 7.40*	*99.88 ± 0.03*
50	*1C*	*785.66 ± 47.13*	*787.07 ± 47.70*	*99.82 ± 0.07*
120		*662.79 ± 11.70*	*664.09 ± 11.85*	*99.80 ± 0.05*

During the rate capability test, the discharge capacity decreased progressively with increasing C-rate, reaching 274.72 mAh g^{-1} at 2C. When returning to 0.1C (cycle 25), the discharge capacity recovered to approximately 1000 mAh g^{-1}, indicating that the capacity loss at high current density was mainly due to kinetic limitations rather than irreversible degradation. During long-term cycling at 0.5C, the electrodes maintained relatively stable performance, with discharge capacities of 817.54 mAh g^{-1} at cycle 30, 787.07 mAh g^{-1} at cycle 50, and 664.09 mAh g^{-1} at cycle 120. Compared to the outstanding performance previously observed (***Figure 5.110***), where the PAA_Pec composition exhibited a capacity retention above 98%. The higher SF adopted in this case, requiring lower coating thickness (50 µm), together with the use of a different mixer, may explain the poorer performance.

The charge-discharge curves (***Figure 5.138***) showed voltage profiles consistent with expectations for SD electrodes. Similarly, the CV analysis (***Figure***

5.139), did not reveal additional parasitic reactions; the redox peaks were slightly more intense than those observed for PAA alone, suggesting comparable or slightly enhanced electrochemical accessibility of the active material.

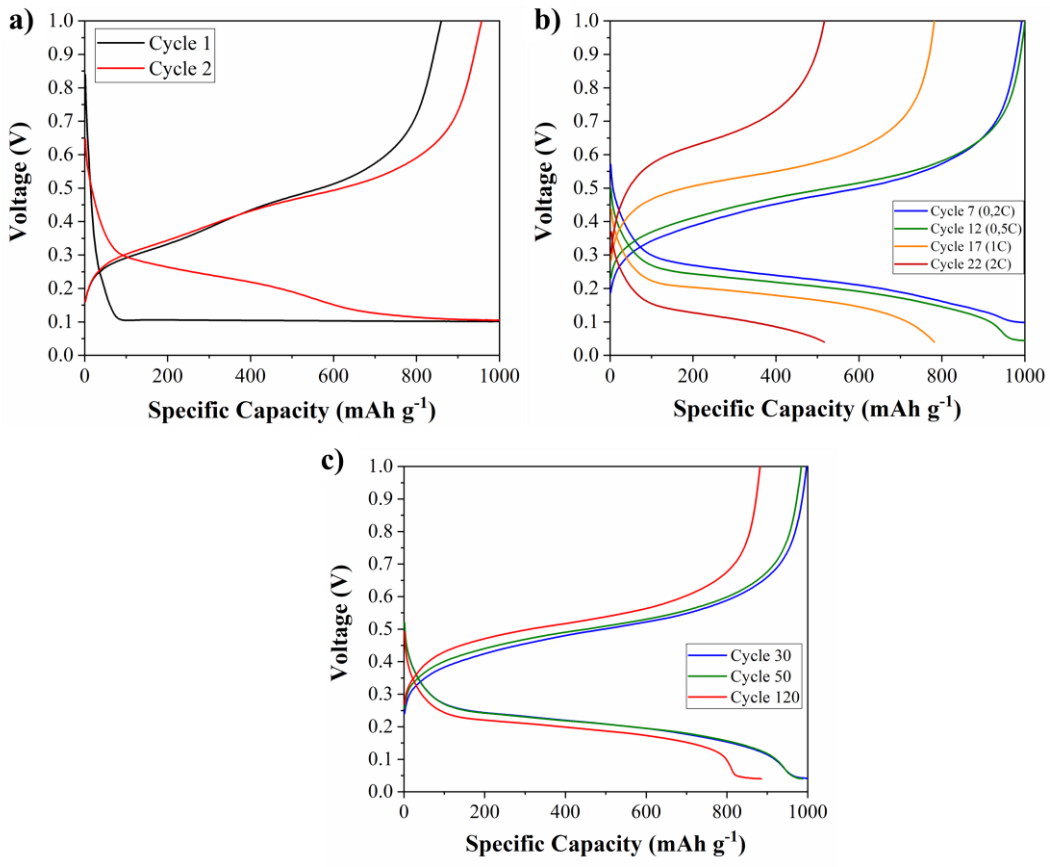

Figure 5.138 – Charge/discharge profiles for some representative cycles for PAA_Pec based electrodes produced at CIC energiGUNE: a) Forming cycles; b) Rate capability test; b) Long-term test.

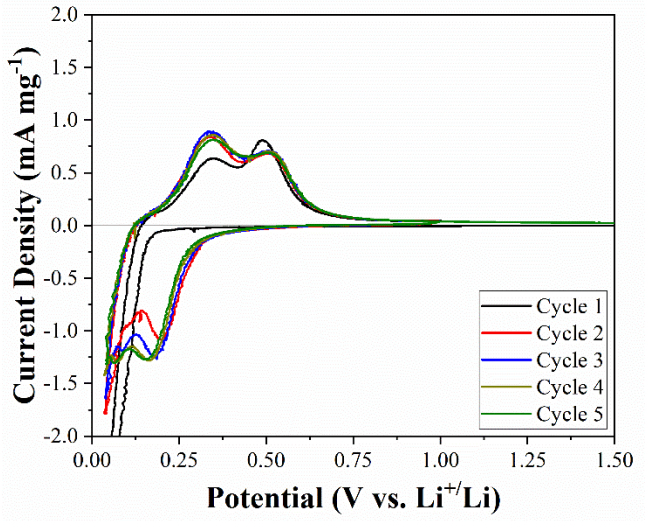

Figure 5.139 – Cycling voltammetry for the PAA_Pec based electrodes produced at CIC energiGUNE.

5.4.4.2.4. PAA_CGN

The third natural polysaccharide investigated in this study was CGN, whose chemical structure is reported in ***Figure 2.28***. This natural polysaccharide was already employed as an additive with the SC electrodes investigated in ***Chapter 5.2***, where it resulted in poor electrochemical performance. The wider investigation performed with these SD anodes allowed the poor electrochemical behavior to be correlated with the specific chemical structure of CGN. The impact of CGN on pH values (***Table 5.56***) was comparable to what was observed for Pec, with only a slight increase compared to PAA alone and almost negligible variations among the different compositions.

The rheological measurements (***Figure 5.140***), however, revealed viscosity behavior markedly different from that observed with the other additives explored in this work. The flow curves (***Figure 5.140a***) clearly showed shear-thinning behavior for all formulations, with viscosity progressively decreasing as shear rate increased. The slurry containing C45 exhibited the highest viscosity values across almost the entire shear rate range, whereas the PAA_CGN solution showed the lowest viscosity. The complete formulation (PAA_CGN_Complete) displayed intermediate values, suggesting a combined structural contribution of the different components to the overall rheological response.

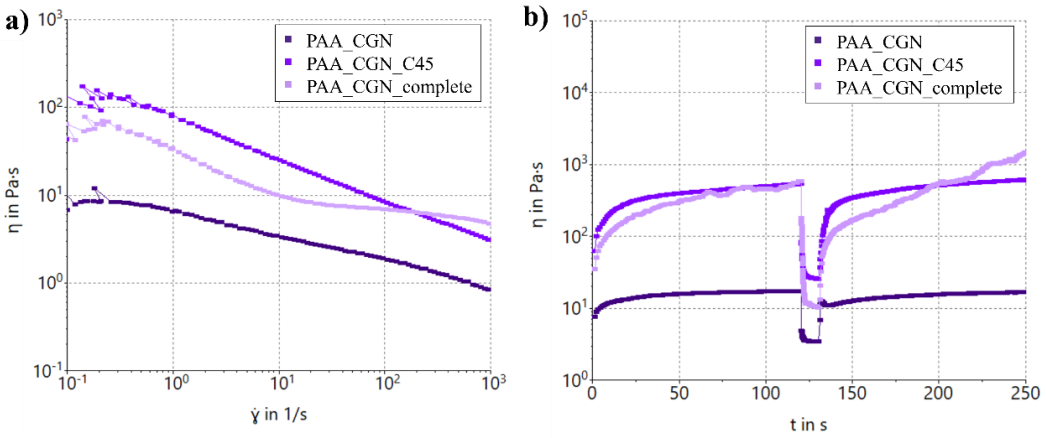

Figure 5.140 – Rheological characterization of the slurries produced with PAA_CGN: a) Flow curve and b) Creep recovery test.

The creep recovery test (***Figure 5.140b***) again presented distinctive results. The slurry containing C45 exhibited the highest initial viscosity, and this trend was maintained after the sudden increase in shear rate. In contrast, the complete slurry showed lower initial viscosity values, consistent with the flow curve results. However, its viscosity progressively increased during the steady-state phase, eventually approaching the values of PAA_CGN_C45 just before the shear rate increase. During the high-shear step, the complete slurry again exhibited

intermediate viscosity values, followed by a sharp increase after stress removal, likely due to progressive drying of the sample during measurement.

These interesting results can be partially explained by examining the laminate production process (***Figure 5.141***). The laminate produced with the binder composition PAA_CGN (***Figure 5.141a***) exhibited a bluish coloration, indicating evident phase separation between the two polymers, which significantly altered the properties of PAA. Although this phenomenon was clearly visible in the binder laminate, the laminates produced with C45 (***Figure 5.141b***) and with the complete formulation (***Figure 5.141c***), appeared macroscopically homogeneous and free of visible defects.

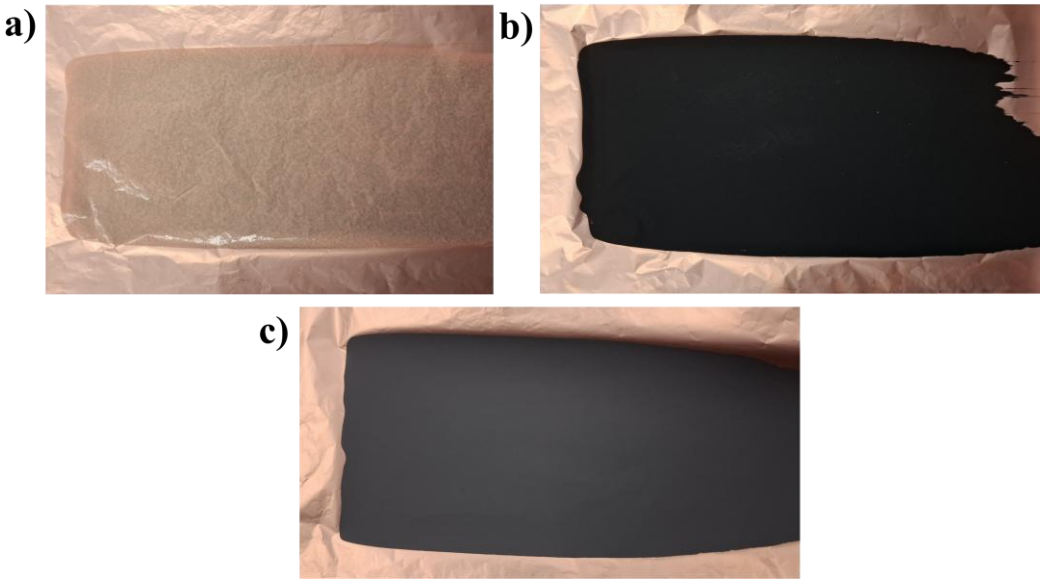

Figure 5.141 – Laminates produced with a constant wet thickness of 50 µm and starting from the solution of PAA_CGN: a) PAA_CGN; b)PAA_CGN_C45; c) PAA_CGN_Complete.

The impact of the phase separation on the adhesion properties became evident during the peel test (***Figure 5.142***). All formulations showed significant detachment from the CC, including the C45-containing laminate, which had exhibited strong adhesion behavior in previous samples with other additives.

Figure 5.142 – Peel test performed o the laminates produced starting with the PAA_CGN solution: a) PAA_CGN; b)PAA_CGN_C45; c) PAA_CGN_Complete.

For the PAA_CGN_Complete formulation, a higher dry thickness of 53 µm was measured. The average 15 mm electrode weight was 17.92 mg, corresponding to an average ML of 3.95 mg cm^{-2}. Compared to PAA alone, this formulation showed a substantial increase in both dry thickness and ML (***Table 5.57***).

These results clearly demonstrate how the structure of the polymeric network can strongly influence electrode properties. The phase separation observed between the two binders, although not macroscopically evident at the final electrode level, likely led to weaker interfacial cohesion and poor adhesion to the CC, ultimately contributing to inferior electrochemical performance due to easier detachment of the coating layer.

CGN, similarly to Pec, represents an emerging binder for LIB applications, although only a limited number of studies have focused on its use in anodes. In silicon-based systems, λ-CGN appears to be the most commonly employed form [174,440], with promising result. The poor electrochemical performance observed in this work (***Figure 5.143***, ***Table 5.62***) can be attributed to both the higher ML compared to PAA alone and the specific CGN composition used, which consisted predominantly of κ-CGN with a lower fraction of λ-CGN. These observation are consistent with those reported by Tamboia et al. [439], where the same CGN species was used as a binder for SiO_x/C electrodes.

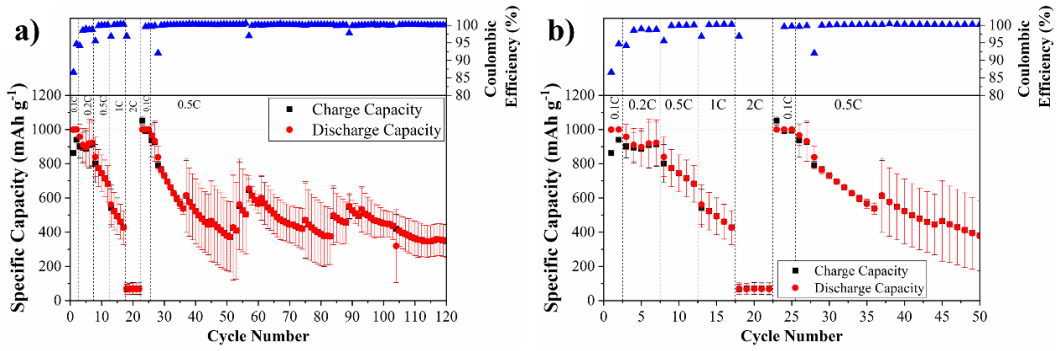

Figure 5.143 – Values of charge and discharge capacity and relative coulombic efficiency for PAA_CGN based electrodes produced at CIC energiGUNE: a) Entire test, up to 120 cycles; b) Focus on the rate capability test.

Table 5.62 – Values of charge and discharge capacities, normalized by the electrode weight, and relative values of coulombic efficiency for some representative cycles for the PAA_CGN based electrodes produced at CIC energiGUNE.

Cycle	***C-rate***	***Charge Capacity (mAh g^{-1})***	***Discharge Capacity (mAh g^{-1})***	***Coulombic Efficiency (%)***
1	*0.1C*	*861.80 ± 5.85*	*999.54 ± 1.2*	*86.22 ± 0.64*
2		*939.71 ± 5.35*	*999.77 ± 1.08*	*93.99 ± 0.64*
7	*0.2C*	*913.75 ± 129.86*	*922.29 ± 133.98*	*99.11 ± 0.36*
12	*0.5C*	*683.28 ± 107.53*	*682.89 ± 107.76*	*100.06 ± 0.07*
17	*1C*	*427.51 ± 98.84*	*426.33 ± 98.72*	*100.28 ± 0.04*
22	*2C*	*70.18 ± 34.02*	*68.26 ± 34.12*	*103.31 ± 1.50*
25	*0.1C*	*993.03 ± 3.47*	*999.77 ± 1.08*	*99.33 ± 0.45*
30		*730.66 ± 17.80*	*730.33 ± 17.73*	*100.04 ± 0.04*
50	*1C*	*379.64 ± 205.45*	*378.96 ± 206.04*	*100.27 ± 0.26*
120		*348.05 ± 94.97*	*348.11 ± 95.44*	*100.00 ± 0.13*

The charge-discharge profiles (***Figure 5.144***) confirmed the poor electrochemical behavior, particularly during the rate capability test, where a pronounced shortening of the silicon lithiation plateau and increased polarization were observed. The CV analysis of the first five cycles (***Figure 5.145***) confirmed the absence of parasitic reactions.

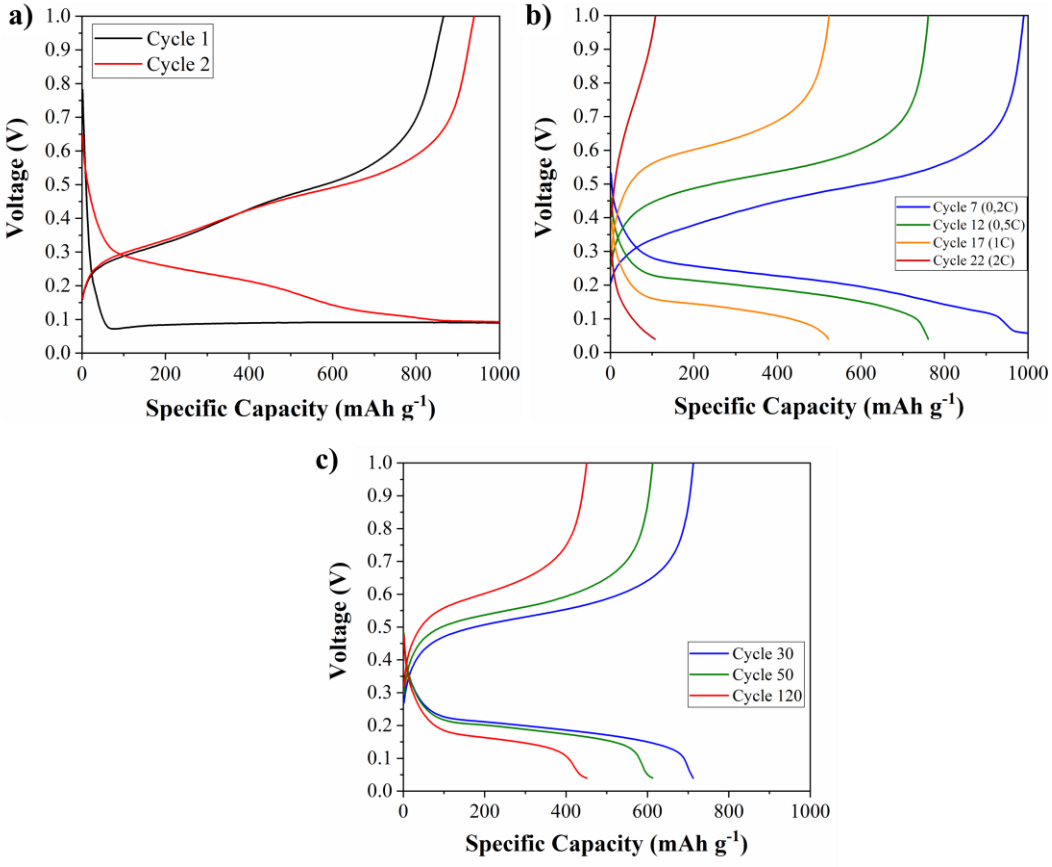

Figure 5.144 – Charge/discharge profiles for some representative cycles for PAA_CGN based electrodes produced at CIC energiGUNE: a) Forming cycles; b) Rate capability test; b) Long-term test.

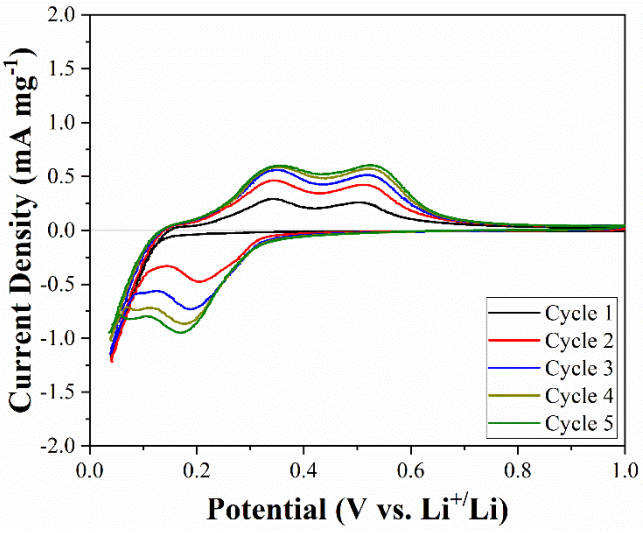

Figure 5.145 – Cycling voltammetry for the PAA_CGN based electrodes produced at CIC energiGUNE.

5.4.4.2.5. PAA_TG

The last polysaccharide investigated was TG, which, similarly to CGN, had already been employed in previous SC anodes. The chemical structure of TG (***Figure 2.27***) led to a slight change in pH compared to PAA alone (***Table 5.56***). However, as observed for the other additives, this variation cannot be considered as particularly significant.

The flow curve analysis (***Figure 5.146a***) presented similar behavior to PAA, especially when considering the PAA_TG solution. When the C45 was added to the system, the viscosity increased at low shear rates, while maintaining the characteristic shear-thinning behavior. At higher shear rates, viscosity values converged toward those expected for proper coating applications. When considering the complete slurry, slight differences in curve shape were observed: a more pronounced decrease in viscosity at low shear rates, followed by a longer plateau at intermediate shear rates and a final drop at higher shear rates. The creep recovery test (***Figure 5.146b***) revealed a more distinct behavior for the complete slurry compared to the other formulations. In particular, the complete slurry exhibited the most accelerated drying during the measurement, resulting in a rapid increase in apparent viscosity.

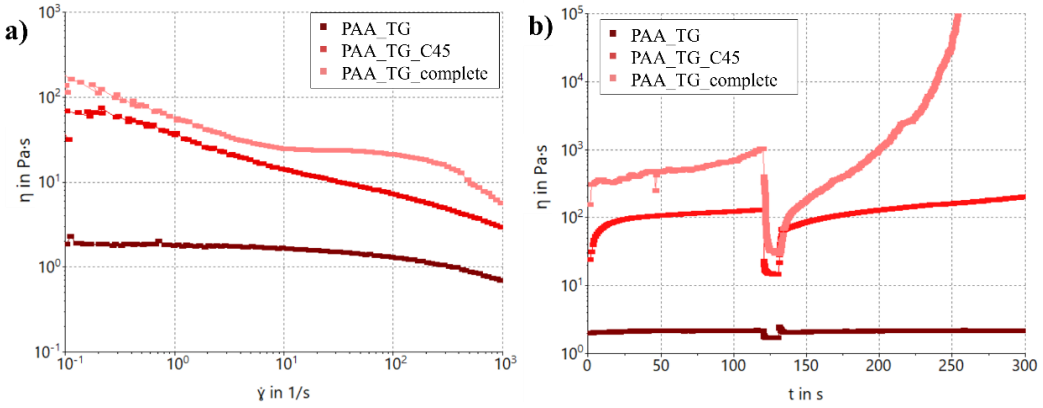

Figure 5.146 – Rheological characterization of the slurries produced with PAA_TG: a) Flow curve and b) Creep recovery test.

The laminates produced with TG were characterized by smooth and homogeneous surface (***Figure 5.147***). The samples subjected to peel-test analysis (***Figure 5.148***) showed adhesion behavior comparable to that observed for PAA alone.

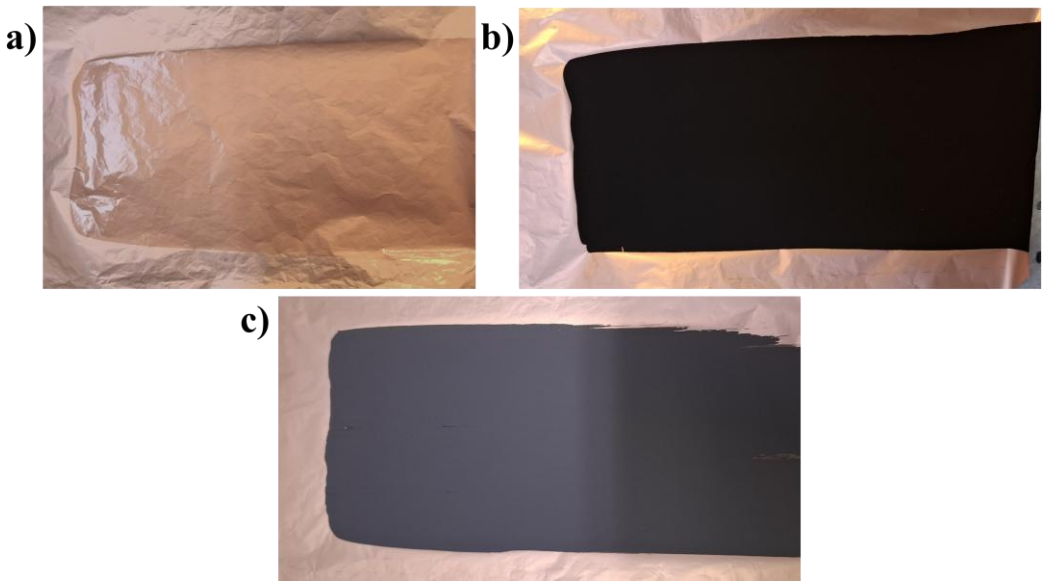

Figure 5.147 – Laminates produced with a constant wet thickness of 50 µm and starting from the solution of PAA_TG: a) PAA_TG; b)PAA_TG_C45; c) PAA_TG_Complete.

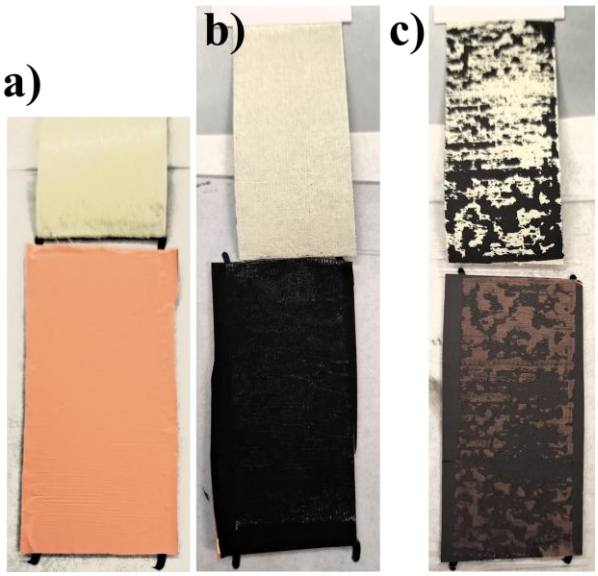

Figure 5.148 – Peel test performed o the laminates produced starting with the PAA_TG solution: a) PAA_TG; b)PAA_TG_C45; c) PAA_TG_Complete.

The PAA_TG_Complete laminate exhibited a dry thickness of 39 ± 5 µm. The manually punched discs showed an average weight of 15.64 ± 0.29 mg, corresponding to an average ML of 2.92 ± 0.13 mg cm^{-2}. Compared to the PAA electrode, a slight increase in ML was observed, while the thickness remained comparable (***Table 5.57***).

TG-based electrodes presented electrochemical performance (***Figure 5.149***, ***Table 5.63***) comparable to CGN, with the exception of reduced variability among samples during long-term cycling.

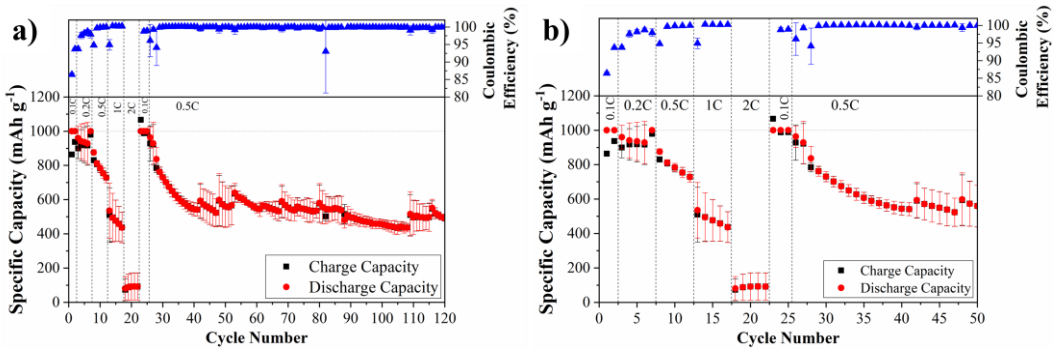

Figure 5.149 – Values of charge and discharge capacity and relative coulombic efficiency for PAA_TG based electrodes produced at CIC energiGUNE: a) Entire test, up to 120 cycles; b) Focus on the rate capability test.

Table 5.63 – Values of charge and discharge capacities, normalized by the electrode weight, and relative values of coulombic efficiency for some representative cycles for the PAA_TG based electrodes produced at CIC energiGUNE.

Cycle	***C-rate***	***Charge Capacity (mAh g^{-1})***	***Discharge Capacity (mAh g^{-1})***	***Coulombic Efficiency (%)***
1	*0.1C*	*983.98 ± 4.23*	*999.67 ± 1.09*	*86.43 ± 0.41*
2		*936.87 ± 2.11*	*999.86 ± 1.15*	*93.70 ± 0.29*
7	*0.2C*	*979.39 ± 10.20*	*999.87 ± 0.77*	*97.95 ± 1.07*
12	*0.5C*	*728.74 ± 29.89*	*728.80 ± 30.05*	*99.99 ± 0.04*
17	*1C*	*437.83 ± 89.38*	*436.66 ± 89.24*	*100.27 ± 0.03*
22	*2C*	*91.89 ± 79.63*	*91.35 ± 79.09*	*72.14 ± 49.33*
25	*0.1C*	*988.61 ± 2.87*	*999.67 ± 1.09*	*98.89 ± 0.34*
30		*730.56 ± 29.50*	*730.28 ± 29.76*	*100.04 ± 0.05*
50	*1C*	*559.89 ± 121.76*	*559.82 ± 122.15*	*100.02 ± 0.07*
120		*490.71 ± 10.69*	*490.90 ± 10.74*	*99.96 ± 0.04*

The analysis of charge-discharge profiles (***Figure 5.150***) confirmed the poor performance at 2C, characterized by a strongly shortened lithiation plateau and pronounced polarization. The CV analysis (***Figure 5.151***) did not show parasitic reactions during the first five cycles, and the observed peaks corresponded to the typical lithiation and de-lithiation processes previously described.

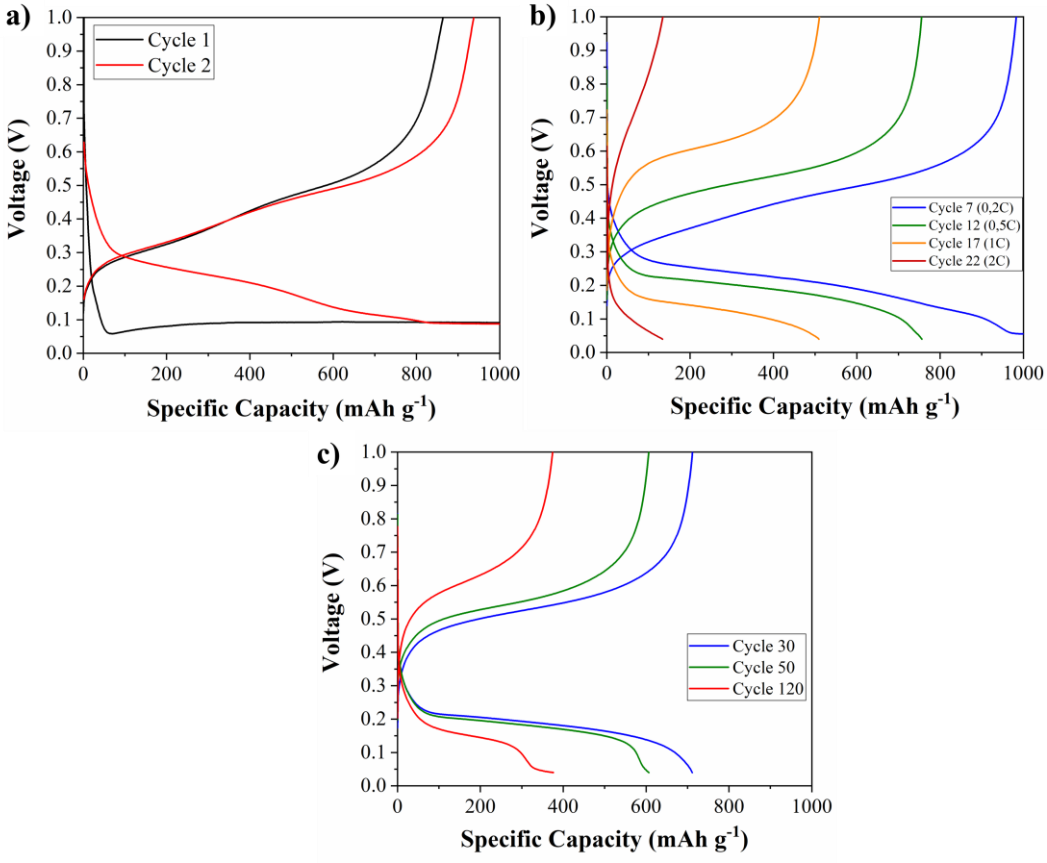

Figure 5.150 – Charge/discharge profiles for some representative cycles for PAA_TG based electrodes produced at CIC energiGUNE: a) Forming cycles; b) Rate capability test; b) Long-term test.

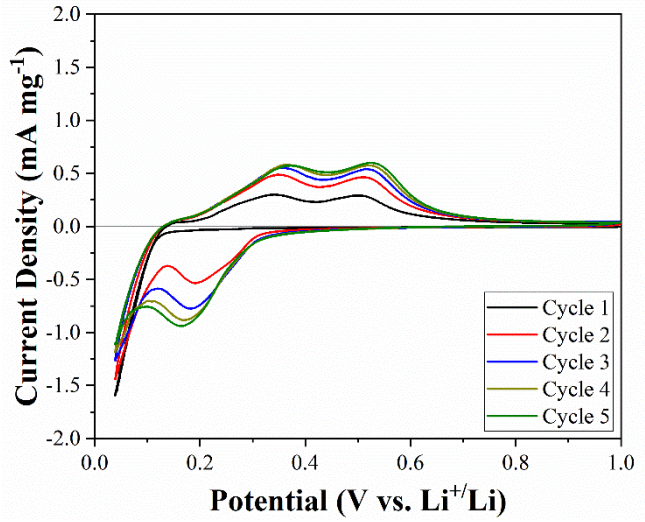

Figure 5.151 – Cycling voltammetry for the PAA_TG based electrodes produced at CIC energiGUNE.

5.4.4.3. Comparison between the additives

The comparative analysis of the natural polysaccharides added at 1 wt.% clearly demonstrates that even a minor modification in binder chemistry can significantly influence slurry behavior and, consequently, electrochemical performance.

All formulations exhibited acidic pH values below 3 (***Table 5.56***). This aspect is particularly relevant for silicon-based aqueous slurries, as alkaline conditions promote silicon hydrolysis ($Si + 2\ H_2O \rightarrow SiO_2 + H_2$), generating flammable hydrogen gas and compromising safety during large-scale fabrication. Maintaining an acidic environment, mitigates this dangerous reaction [497]. However, acidic conditions introduce the Cu CC corrosion, especially during the electrode drying step, which can require some hours. The rapid drying behavior of this material represents a critical factor that can significantly limit the extent of copper corrosion. In the study reported by Gil et al. [498], copper corrosion in PAA-based slurries was described as a time-dependent process occurring over several hours, mainly due to the presence of acidic PAA groups. The interaction between these acidic functionalities and the Cu CC promotes the formation of cuprous oxide, copper carboxylates, and other copper-derived compounds at the interface with the coated layer. While excessive corrosion is undesirable, controlled surface modification may generate beneficial effects. Hernandez et al. [499] proposed a maturation protocol aimed at improving the performance of silicon electrodes, consisting of storing the fabricated electrodes in a buffer solution at pH 3 under controlled humidity at 25 °C for several days. Their results suggested that atmospheric-induced corrosion of the Cu CC can release Cu^{2+} species, which are able to migrate into the humid electrode structure. These cations can physically cross-link binder chains, thereby modifying the mechanical resistance of the polymer network against silicon volume changes [500]. At the same time, the formation of copper carboxylate anchoring bonds at the interface between the coated layer and CC enhances adhesion strength [501]. A similar beneficial effect of multivalent cations has already been reported for Alg-based systems. The incorporation of Ca^{2+}, Ba^{2+}, Zn^{2+}, Mn^{2+}, or Al^{3+} into Na-Alg formulations leads to significant improvements in the cyclability of silicon anodes, as a result of coordination bonds that reinforce the polymeric network and enhance mechanical robustness compared to pure Na-Alg binders [500]. In the present work, the hypothesis is that the generation of Cu^{2+} species from mild corrosion likely acted as cross-linking agents within the binder network, substantially increasing the adhesion between the coating layer and the CC at the interface. Since Na-Alg is the only binder used in its salt form, it is likely the only one affected by this phenomenon. This effect was clearly evidenced during peel tests on Alg-based samples (***Figure 5.131***), where ripping of the copper foil occurred instead of coating delamination. Furthermore, Xiong et al. [497],

demonstrated that pH significantly influences both adhesion and cohesion strength, identifying an optimal region around pH 2.5, where the highest scratch resistance was obtained. The pH value of around 2.90 measured in this work for Alg-based systems effectively enhanced the adhesion with the CC. Thus, pH modulation represents a delicate balance between silicon stability and Cu integrity, and binder chemistry plays a decisive role in defining this equilibrium.

The rheological characterization revealed significant differences among the investigated slurries (***Figure 5.152***). The flow curves obtained for the PAA-based solutions containing the different natural polysaccharides (***Figure 5.152a***) all exhibited an overall shear-thinning behavior. The PAA-alone formulation showed the expected trend, and the addition of Pec and TG led to an increase in viscosity without substantially altering the overall curve profile. The incorporation of CGN induced a slight modification in the curve shape, whereas the most pronounced deviation was observed for Alg, whose flow curve differed markedly from the others. It is well established that the viscosity of alginate solutions depends strongly on molecular weight and pH. In particular, viscosity increases as pH decreases and typically reaches a maximum in the range of pH 3–3.5, where protonation of carboxyl groups enhances intermolecular hydrogen bonding [502]. The observed differences may also be associated with hysteresis phenomena (***Figure 5.152b***): after increasing the shear rate to determine the flow curve (represented by full squares), the stress was gradually reduced, and the recovery behavior (empty squares) was evaluated over the same shear-rate range. For PAA, Pec, and TG, the forward and backward curves nearly overlapped, indicating negligible hysteresis and suggesting that the systems exhibited elastic behavior with full recovery of the polymeric structure after shear removal [503]. CGN showed a slightly altered curve shape; however, at 10^{-1} s^{-1} returned to its initial value, indicating partial structural recovery. In contrast, Alg displayed a pronounced hysteresis behavior: the viscosity at 10^{-1} s^{-1} after shear was more than one order of magnitude different from the starting value. This behavior suggests partial degradation or restructuring of the polymer network under shear, with the area between the two curves representing the energy dissipated during the deformation-recovery cycle [504].

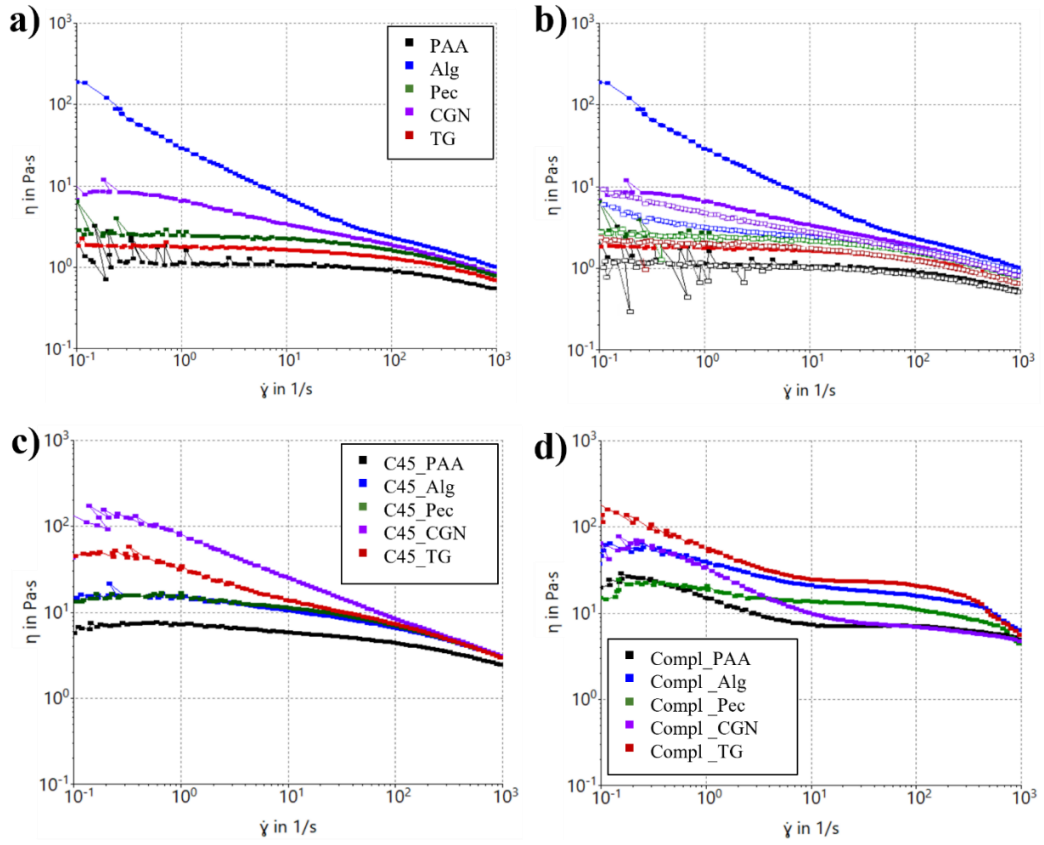

Figure 5.152 – Rheological characterization of the slurries with the different additives: a) Flow curves of the binders alone; b) Hysteresis effect observe for the binders alone; c) Flow curve of the binders added with the C45; d) Flow curves of the complete slurries containing all the components (binders, graphite, C45 and silicon)

Interestingly, the addition of C45 in the systems (***Figure 5.152c***) markedly altered the shape of the flow curves. In particular, the CGN-based formulation exhibited the highest viscosity at low shear rates. However, as the shear rate increased, the viscosities of all slurries progressively converged, becoming comparable at higher shear conditions. The influence of carbon black on binder suspensions has been systematically investigated by Ma et al. [505], who modeled its interaction with polymeric binders. Their study demonstrated that carbon black particles form an interconnected aggregate network that substantially contributes to the overall slurry viscosity. Both colloidal interparticle forces and hydrodynamic interactions were considered in their model to explain this behavior.

When the complete systems, composed of binders, C45, graphite and silicon were characterized (***Figure 5.152d***) the effect of the natural polysaccharides led to further modifications in the rheological response. All formulations exhibited the characteristic viscosity plateau commonly reported in the literature after the incorporation of solid particles into binder matrices (***Figure 5.153***, [506]). Among the formulations, the TG-based slurry showed the highest viscosity at low shear

rates, while CGN presented the most important slope as the shear rate increased. Nevertheless, all slurries maintained a clear shear-thinning behavior, and their viscosities became nearly overlapping at high shear rates.

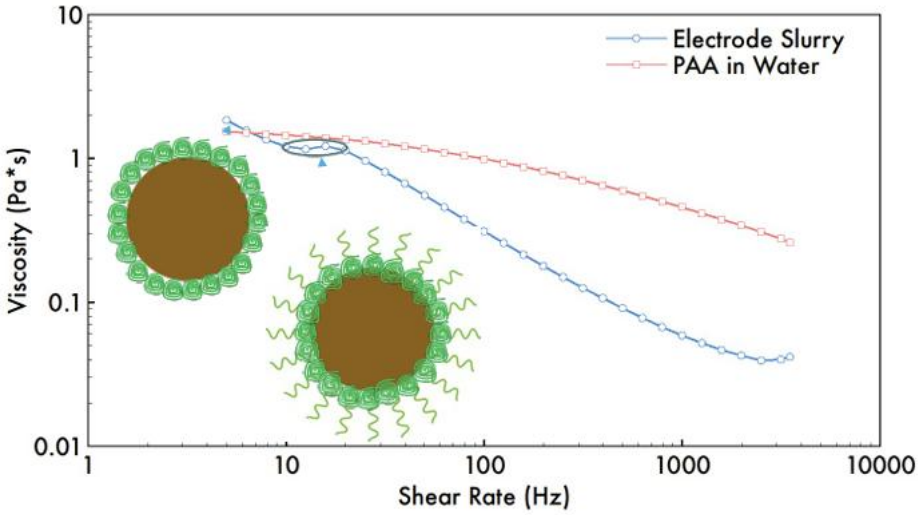

Figure 5.153 – Viscosity flow curve for silicon electrode slurry. Reproduced from [506]

The addition of silicon results in major changes in the solution polymer structure. In particular, the presence of silicon particles appears to reduce agglomeration and aggregation as the shear rate increases, a behavior that contrasts with what was observed for the PAA-alone system. This inversion in rheological response suggests that specific interactions occur between PAA chains and the silicon surface. One plausible explanation is that PAA chains strongly adsorb onto the silicon particles, and under shear they elongate and progressively disentangle, leading to a reduction in structural resistance. Alternatively, shear may promote partial desorption of PAA from the silicon surface, allowing the polymer chains to disentangle from one another and thereby lowering the overall viscosity. A further possibility is that excess PAA, which is not directly adsorbed onto silicon, forms lubrication layers within the slurry. These layers could reduce interactions between silicon particles coated with polymer chains, limiting the formation of a continuous interconnected network [506]. Interestingly, a comparable flow behavior has been reported for PAA-based systems at pH values close to 3, where a characteristic viscosity plateau is observed. At higher pH values, this plateau becomes less pronounced, indicating that the ionization state of PAA significantly influences interactions between polymer chains and silicon particles and, consequently, the macroscopic rheological response [432].

After the rheological characterization, the actual SF of the complete slurries was verified by the use of a moisture balance analysis (***Figure 5.154***). The measurements confirmed that solvent evaporation during mixing was negligible, as all formulations maintained a final solid fraction consistent with the theoretical

value of 60 wt.%. The gradual decrease in apparent solid fraction observed during the measurement reflects the controlled evaporation imposed by the instrument. The slightly faster apparent solvent evaporation observed for the CGN formulation may reflect differences in water binding capability associated with its polymeric network.

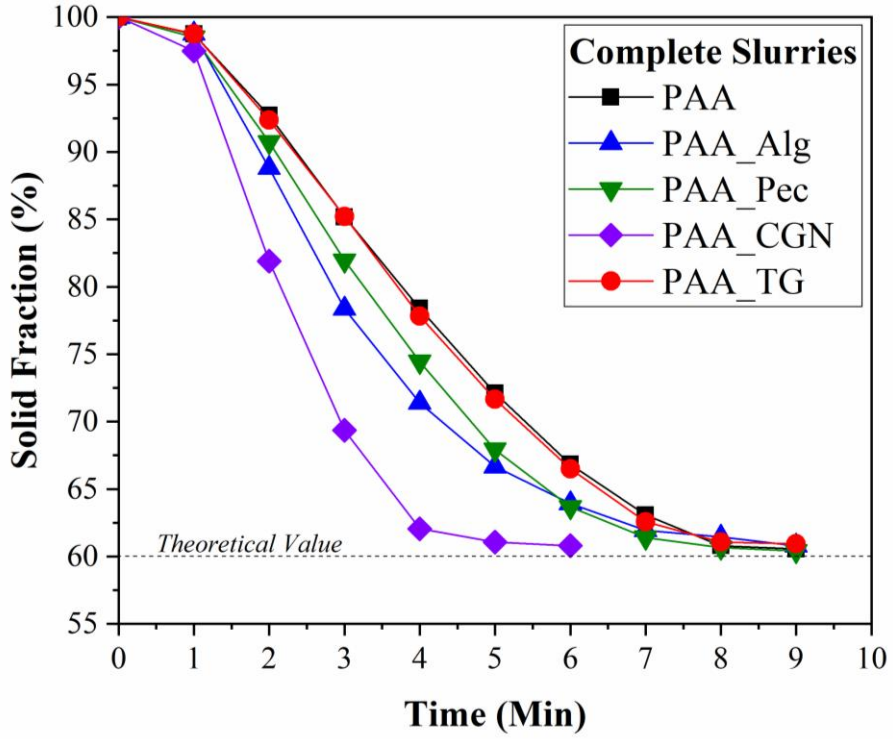

Figure 5.154 – Evolution of measured SF during moisture balance analysis for complete slurry formulations at 60 wt.% SF.

All laminates were prepared using a fixed wet thickness of 50 µm. From these coatings, 15 mm diameter electrodes were manually punched and subsequently characterized in terms of dry thickness, average weight, and resulting ML (***Table 5.53***). The addition of Alg to PAA resulted in a comparable dry thickness but a significantly higher ML, suggesting a modification of slurry organization and particle packing. Na-Alg, as a polysaccharide binder, is known to strongly affect the rheological behavior of aqueous electrode slurries through electrostatic interactions and hydrogen bonds formation [507]. Similarly, the ionization state of PAA has been shown to significantly influence slurry rheology and processing behavior, as the neutralization of carboxylic groups alters polymer particle interactions [152]. In contrast, the limited variation observed for the PAA_Pec formulation suggests a weaker structural contribution to slurry organization. The more pronounced increase in thickness and ML observed for PAA_CGN may be related to the strong polyelectrolyte nature of CGN, which can enhance interparticle interactions and viscosity, thereby affecting shrinkage during drying

[174]. Overall, these results confirm that binder chemistry plays a critical role not only in slurry flow behavior but also in determining the final electrode density and structural uniformity.

It worth noting that, based on the peel test results (***Figure 5.155***), it is difficult to clearly distinguish a real improvement associated with the addition of the additive. However, the adhesion between the coated layer and the current collector (CC) appears to be adequate, while the significant detachment is more likely related to poor cohesion among the active material particles.

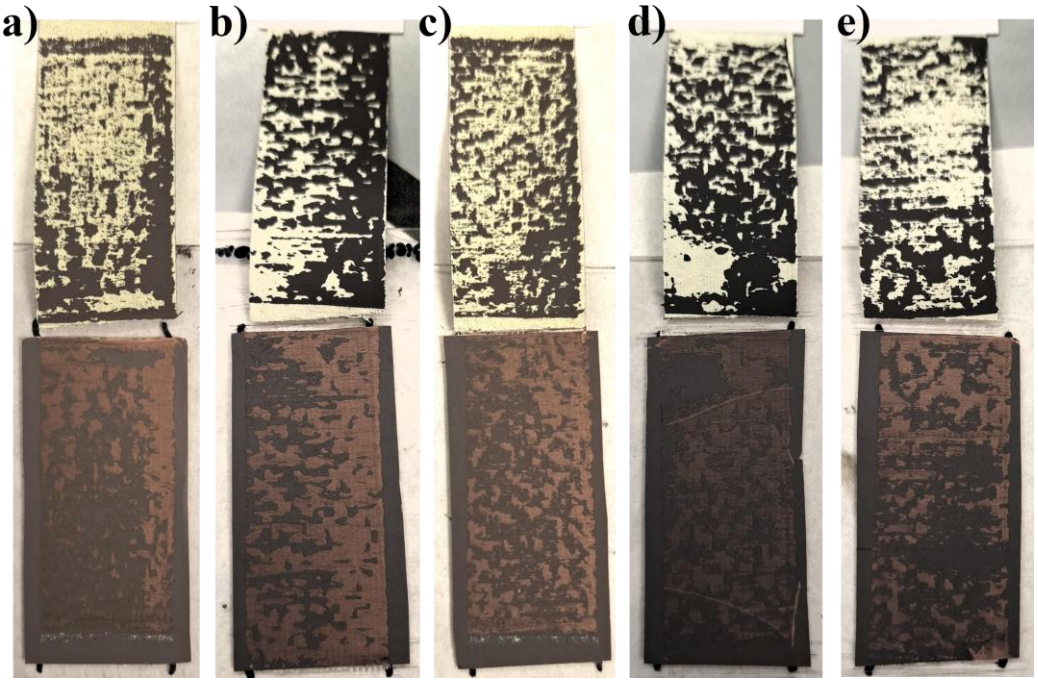

Figure 5.155 – Comparison of the peel-test results based on the different binder compositions: a) PAA; b) PAA_Alg; c) PAA_Pec; d) PAA_CGN; e) PAA_TG

The results reported in

Table 5.64 highlight that, in this stage of the work, the focus was placed on maintaining constant processing parameters, rather than achieving identical electrode properties. As a consequence, electrodes with significantly different ML were obtained, which must be considered when interpreting the electrochemical results. The influence of ML cannot be completely excluded, particularly in terms of capacity retention. This is especially evident for the PAA_Alg sample, which,

Sample ID	***Average Mass Loading (mg cm^{-2})***	***Discharge Capacity (mAh g^{-1})***		***Initial Coulombic Efficiency (%)***	***Capacity retention (%)***
		Cycle 30	***Cycle 120***		
PAA	2.48	834.44	776.09	88.92	93.23
PAA_Alg	4.39	706.62	252.61	83.01	35.75
PAA_Pec	2.55	817.54	664.09	85.42	81.23
PAA_CGN	3.90	730.33	348.11	86.22	47.66
PAA_TG	3.04	730.28	490.90	86.43	67.22

despite exhibiting the highest ML, shows the lowest capacity retention (35.75%). This suggests that the increased electrode thickness and ML may increase transport limitations and mechanical instability during cycling, ultimately accelerating performance degradation. In addition, when comparing these results with those obtained for the electrodes produced at PoliTo (***Table 5.51***), a general reduction in the initial CE is observed. This behavior may be associated with differences in electrode structure, slurry rheology, or processing conditions, further confirming the strong process-dependence of SD anodes.

Table 5.64 – Selected electrochemical performance results used for comparison among the investigated electrodes produced at CIC energiGUNE.

Sample ID	***Average Mass Loading (mg cm^{-2})***	***Discharge Capacity (mAh g^{-1})***		***Initial Coulombic Efficiency (%)***	***Capacity retention (%)***
		Cycle 30	***Cycle 120***		
PAA	2.48	834.44	776.09	88.92	93.23
PAA_Alg	4.39	706.62	252.61	83.01	35.75
PAA_Pec	2.55	817.54	664.09	85.42	81.23
PAA_CGN	3.90	730.33	348.11	86.22	47.66
PAA_TG	3.04	730.28	490.90	86.43	67.22

A more comprehensive comparison of the full electrochemical response (***Figure 5.156***) reveals that the addition of Pec does not significantly increase the achievable capacity compared to the PAA reference. Instead, its main effect is an improvement in cycling stability, as evidenced by the reduced occurrence of abrupt capacity decay events, which are clearly visible in the PAA sample. This behavior suggests that the use of natural additives such as Pec may enhance the mechanical resilience of the electrode, improving the ability of the binder network to accommodate silicon volume expansion during long-term cycling.

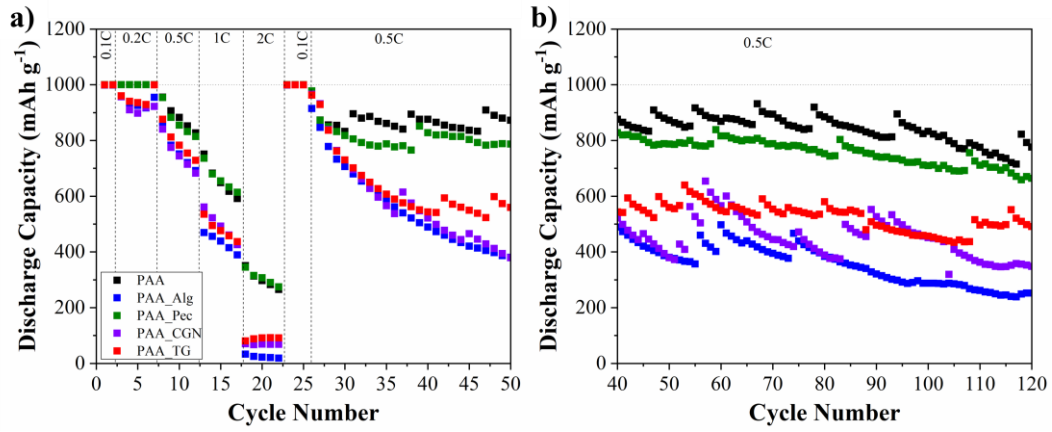

Figure 5.156 – Comparison of electrochemical performance of the electrodes produced at CIC energiGUNE based on the different binders combinations: a) Entire test, up to 120 cycles; b) Focus on the rate capability test.

After completing the electrochemical tests, the cells were disassembled in order to examine the possible occurrence of Cu CC corrosion. The electrodes were immersed in water and gently agitated; this simple procedure was sufficient to completely remove the active coating layer and expose the underlying CC. The pristine CC was characterized by a smooth surface with only regular marks associated with the rolling manufacturing process, at magnification of 500X (***Figure 5.157a***,***b***), these signs are just visible. In contrast, the CC recovered from cycled electrodes displayed heterogeneous surface conditions. In some areas (***Figure 5.157c***), localized pitting corrosion was clearly detected, whereas other regions remained unaffected (***Figure 5.157d***) retaining a surface morphology comparable to that of the pristine collector. Localized pitting corrosion has already been reported in previous studies [508,509]. Deguchi et al. [508] observed corrosion phenomena after subjecting electrodes to prolonged over-discharge conditions for two weeks, while Dai et al. [509] evaluated Cu degradation by immersing the CC directly in a conventional LIB electrolyte for 20 days. Both experimental conditions were considerably more aggressive than the standard galvanostatic cycling adopted in the present work. Accordingly, the corrosion observed here was less severe, suggesting that under the applied testing conditions the phenomenon remained moderate.

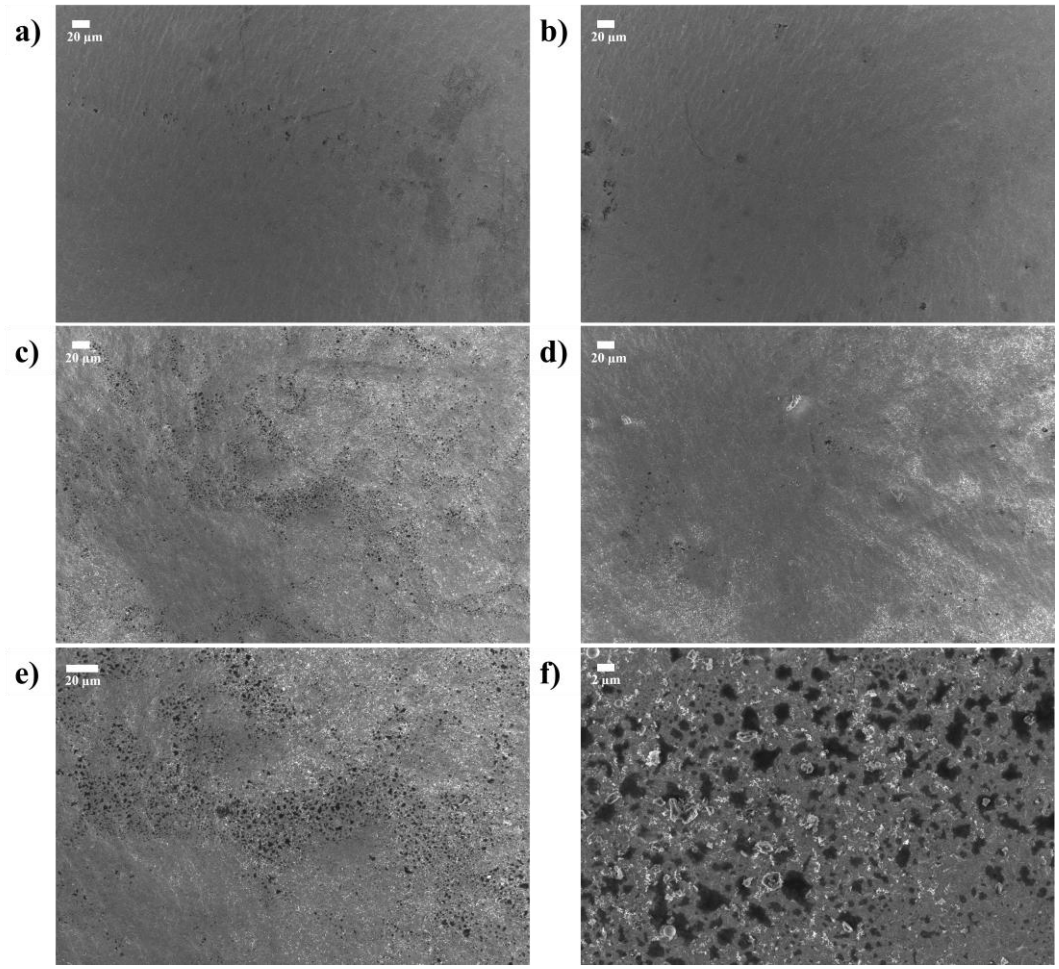

Figure 5.157 – SEM images of the C) surface at different magnifications. Before cycling (500X): a), b). After cycling of the PAA-based electrodes: c), d) at 500X, e) at 1kX, and f) at 5kX.

5.4.5. Main Outcomes and Implications

The results presented in this chapter clearly demonstrate that the electrochemical performance of SD anodes is strongly governed by the interplay between material design, slurry formulation, and processing parameters, rather than by the intrinsic properties of the AM alone. The use of nanoporous Si, combined with capacity limitation to 1000 mAh g^{-1} and the absence of calendering, proved effective in mitigating volume expansion while preserving high practical capacities.

The experimental work was structured in two consecutive stages, with the preliminary study carried out at PoliTo focusing on process optimization at laboratory level and providing the foundation for the subsequent investigations performed at CIC energiGUNE. In the first stage, the definition of a suitable mixing protocol and SF was essential to obtain homogeneous slurries and reproducible coatings. The transition from PAA_1 to PAA_3 clearly demonstrated that mixing conditions are a decisive parameter: reducing mixing speed and time

minimized particle sedimentation and improved slurry stability, directly translating into enhanced electrochemical performance. These results confirm that, for high-silicon systems, processing parameters are as critical as material composition.

The second stage, carried out at CIC energiGUNE, extended the analysis through rheological characterization, enabling a deeper understanding of slurry behavior and leading to the identification of higher SF values required to achieve viscosities compatible with industrial processing. This step allowed the correlation between slurry rheology, coating quality, and final electrode performance, bridging laboratory optimization with more application-relevant conditions.

Binder chemistry emerged as a key variable influencing both electrode structure and cycling stability. While PAA alone enabled acceptable performance after process optimization, the introduction of polymeric additives produced markedly different outcomes. The addition of SBR resulted in poorer electrochemical performance and reduced reproducibility, likely due to incompatibility between the two polymeric systems. Similarly, TG led to inferior performance, suggesting that its highly branched structure promotes a heterogeneous network that is not effective in maintaining electronic conductivity during cycling.

In contrast, natural polysaccharides such as Na-Alg and Pec significantly improved long-term stability and reduced variability among cells, effectively suppressing the abrupt capacity decay observed for PAA alone. Among all the investigated systems, the PAA_Pec formulation delivered the most stable electrochemical behavior, maintaining capacities close to the imposed limitation over extended cycling and exhibiting improved surface integrity without evident cracking. These results highlight that even minor modifications in binder composition, can substantially influence electrode properties and electrochemical durability. In addition, the use of Pec represents a promising strategy to enhance the sustainability of the process by partially replacing petroleum-based binders.

Overall, this study confirms that SD anodes can achieve stable and reproducible performance only when material design, binder interactions, and processing conditions are carefully balanced. The results provide practical guidelines for the formulation of SD electrodes and underline the necessity of coupling chemical design with process engineering to enable their scalable implementation.

5.5. Conclusion and final remarks

The experimental activities presented in this chapter demonstrate that the development of LIB anodes cannot be addressed solely from a material perspective, but requires a tightly integrated approach combining formulation, processing, and scale-up considerations.

Graphite-based anodes confirmed their role as a reliable benchmark, characterized by stable electrochemical performance and well-established manufacturability. However, the transition from laboratory-scale to pilot-line production highlighted the strong influence of processing conditions on electrode quality and reproducibility, underlining that even mature systems remain sensitive to manufacturing parameters.

The introduction of silicon in SC anodes (10 wt% Si) enabled a clear improvement in specific and areal capacity, but also revealed increasing challenges in terms of slurry stability, coating homogeneity, and electrode integrity. In this context, binder selection and formulation optimization emerged as critical factors, often having a greater impact on final performance than the active material itself. The comparison between laboratory and pilot-line production further emphasized the importance of adapting formulations to different processing environments, as direct scale-up without reformulation led to poor reproducibility and performance variability.

The activities carried out within the GIGAGREEN project confirmed that process optimization must be considered as an iterative and multi-variable problem, where material selection, electrode architecture, and manufacturing parameters are strongly interconnected. In particular, the implementation of laser-textured CCs demonstrated the potential to improve interfacial properties and electrochemical performance.

The transition toward SD anodes (80 wt% Si) represented the most challenging step. While a significant increase in capacity was achieved, this was accompanied by critical issues related to mechanical stability, electrode cohesion, and processability. The systematic investigation of aqueous binder systems and the incorporation of natural polysaccharides proved essential to partially mitigate these limitations, improving slurry rheology, coating quality, and cycling stability. Nevertheless, these systems remain highly sensitive to processing conditions, confirming that manufacturability remains a key bottleneck for high-silicon-content electrodes.

Overall, the results of this chapter clearly show that increasing silicon content leads to a progressive shift from a material-driven optimization to a process-driven one. While graphite systems showed stable and reproducible behaviour under the investigated conditions, silicon-based anodes require a much tighter control of slurry properties, coating conditions, and electrode architecture. From a broader perspective, this work highlights that the development of next-generation anodes must be approached as a multi-objective problem, where electrochemical performance, manufacturing scalability, and process robustness are equally critical. The insights gained in this chapter provide a fundamental basis for the subsequent LCA, where the interplay between performance improvements and process-related impacts is quantitatively evaluated.

Chapter 6

6. Life cycle assessment

Although research on LIBs remains extensive, this technology is approaching its theoretical performance limits [510]. As a result, further advances must not only target electrochemical performance but also address the environmental sustainability of battery production processes. In this context, LCA was adopted as a standardized methodology to quantify the environmental impacts associated with emissions and resource consumption in battery manufacturing.

The experimental activity presented in the previous chapter focused on the development and optimization of different types of anodes: graphite and silicon-based, distinguishing between SC and SD. Through this study, particular attention was placed on both electrochemical performance and processability of the wet slurry. As a logical extension of this optimization activity, a LCA was employed to quantify the environmental impacts associated with the production of anodes based on the AMs investigated throughout this work.

As already widely described in ***Chapter 4***, the LCA methodology was defined by detailing the main steps required to perform a complete assessment, together with its inherent limitations and sources of uncertainty. While experimental optimization enables performance-based comparisons, electrochemical improvements at the material or electrode level do not necessarily translate into environmental sustainability benefits, especially when energy consumption and process complexity are taken into account. For this reason, LCA was used to couple the experimental results with a environmental sustainability-oriented perspective, providing a broader environmental evaluation of the investigated active materials.

The LCA activity was structured into two main parts (***Figure 6.***). The first part focused on the production of anode electrodes, enabling a direct comparison among different active materials by jointly considering their environmental impacts and electrochemical performance. This analysis was based on experimental data generated in this work and complements the process

optimization discussed in the previous chapters from an environmental perspective. The LCA methodology and results presented in this section are based on a previous study by the author of this dissertation [511]. Here, the analysis was extended and structured to enable a coherent and systematic comparison among all the active materials investigated in this thesis. The second part of the chapter aimed to provide a more comprehensive perspective by extending the LCA to the production of full cells, assembled using LFP cathodes and the anodes previously introduced. This approach allowed the evaluation of how differences observed at the anode level propagate once additional components and manufacturing steps were included, thereby offering a more realistic assessment of battery production process.

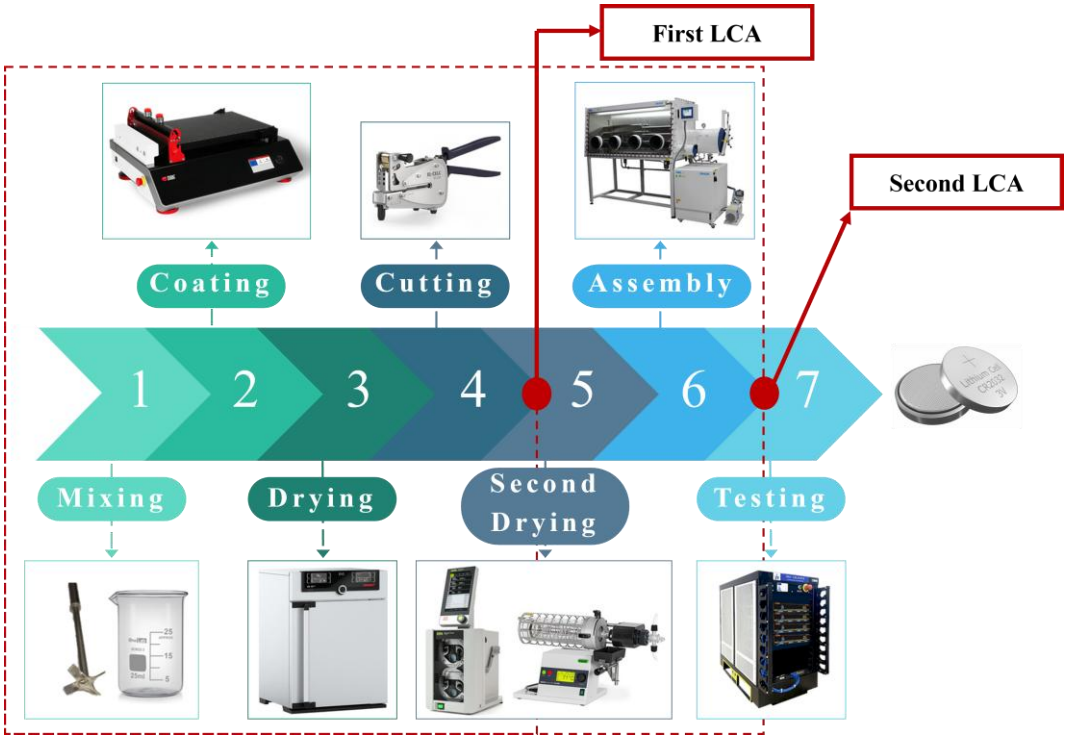

Figure 6.1 – Schematic overview of the production and assembly steps involved in coin-cell fabrication, from slurry preparation to electrochemical testing. The red markers indicate the system boundaries adopted for the two LCAs considered in this study.

It should be noted that LCA is inherently an iterative process. The analysis presented in this chapter represents the final and most complete assessment, consolidating all the information generated throughout the work. In practice, the LCA development involved multiple iterations, progressive refinements, and a gradual increase in system complexity.

6.1. Anode Production

The production of anode electrodes represented the point at which material choice and manufacturing processes concretely converge. In this work, the anode fabrication routes were not treated as abstract or idealized processes, but were derived from experimentally optimized procedures developed and discussed in the previous chapters. For this reason, the evaluation of the environmental impacts associated with anode production represented a necessary step to critically assess whether improvements achieved at the electrochemical level were effectively supported by the energy and material demands of the manufacturing process.

Several LCA studies have investigated the environmental impacts associated with LIBs, highlighting the relevance of both material selection and manufacturing processes [6,512]. Early works primarily focused on conventional full cells or entire battery packs, identifying energy consumption during electrode fabrication and the production of active materials as major contributors to global warming potential and cumulative energy demand [513–515]. More recent studies have extended the analysis to advanced anode materials, including silicon-based materials, often characterized by complex nanostructures and energy-intensive synthesis routes, [322,512,516–521]. Despite the growing number of LCAs addressing silicon-based anodes, a direct comparison among published results remains challenging, as these studies often adopt different, and in some cases insufficiently specified, system boundaries and FUs. To illustrate this variability, a selection of representative examples has been compiled in ***Table 6.1***, though this overview is not intended to be exhaustive of the entire body of literature. As highlighted by Erakca et al. [522], the omission or inconsistent definition of these parameters significantly limits the comparability of LCA outcomes across different electrode chemistries and cell configurations, particularly when attempting to relate environmental impacts to electrochemical performance. In addition, most existing LCA studies rely on generic datasets or literature-based assumptions for electrode manufacturing, often not related to experimentally validated processing conditions. As a consequence, the reported impacts may not fully reflect the limits arising from real electrode production processes, particularly when innovative active materials require modifications in slurry formulation, solid content, or drying conditions. Only a limited number of studies have attempted to integrate experimentally derived process data into LCA models for battery electrodes, despite the recognized importance of process parameters such as mixing energy, solvent content, and drying efficiency [522–524]. This limitation is particularly relevant for silicon-based anodes. In these systems, performance improvements are often accompanied by increased process complexity, making it difficult to assess whether electrochemical improvements are environmentally justified.

Table 6.1 – Summary of key methodological parameters (system boundaries, functional units, and LCIA methods) across a selection of published battery LCAs.

Chemistry	***System Boundaries***	***Functional Unit***	***LCIA Method***	***Reference***
Silicon/Li	Not Specified	1 kg of coated anode	CML	[512]
NCM622/Graphite	Cradle-to-gate	1 kWh 1 vehicle-kilometer	ReCiPe 2016 (H)	[322]
LCO/Graphite *LFP/Graphite*	Cradle-to-gate	1 kWh	Not Specified	[514]
NCM111/Graphite	Cradle-to-gate	1 battery pack kg kWh	ReCiPe V1.08	[515]
NMC111/Si Nanowires	Cradle-to-grave	1 km driven	Not Specified	[516]
NMC/Si Nanotubes	Cradle-to-gate	1 km driven	ReCiPe V1.08	[517]
NMC811/C-Si	Cradle-to-gate	1 kWh	ReCiPe 2016 (H)	[518]
Si Nanowire/Li	Cradle-to-grave	1 km driven	Not Specified	[520]
NCM111/Graphite *NCM111/Li* *NMC111/Si Nanowires*	Cradle-to-gate	1 kWh	ReCiPe 2016 (H)	[521]
NCM111/Graphite	Cradle-to-gate	1 kWh	ILCD 2011	[522]
NCM111/Graphite	Cradle-to-gate	1 kWh	Not Specified	[523]
NMC111/Graphite	Cradle-to-gate	1 kWh	EF V3.0	[524]
NMC/Graphite	Cradle-to-grave	1 km driven	Not Specified	[525]
NCA/C-Si	Cradle-to-gate	1 kWh	IPCC 2013 V1.03	[526]
NMC811/C-Si	Cradle-to-gate	1 battery pack	ReCiPe V1.08	[527]
NCM111/Graphite *NMC811/Graphite*	Cradle-to-gate	1 kg 1 kWh	ReCiPe 2016 (H)	[528]
LMO/Graphite *NCM111/Graphite*	Cradle-to-grave	1 battery pack	ReCiPe	[529]

In this work, all electrodes and cells were manufactured at laboratory scale, and the LCI was constructed entirely using primary data. Within this context, the present analysis aimed to bridge the identified gap by performing an LCA of anode production based on experimentally optimized electrode fabrication processes, ensuring consistency between materials, electrochemical performance, and production procedures discussed in the previous chapters.

The anodes investigated in this study represent different technological generations of European LIB development. The graphite-based anode (G-A) represented Generation 2 technology, introduced in commercial LIBs in 1991 and still dominating current industrial applications [12]. The silicon composite anode

(SC-A) corresponds to Generation 3a concepts, characterized by limited silicon contents (typically below 10 wt.%) introduced to enhance energy density and gradually adopted in commercial systems over the last decade [12]. Finally, the silicon-dominant anode (SD-A) represents Generation 3c concepts, in which silicon contents exceed 50 wt% and are expected to play a central role in future high-energy LIB technologies [13]. In this work, an SD-A with a silicon content of 80 wt% was selected based on the promising electrochemical performance reported in recent studies [13].

Given the complexity of LCA studies and the number of methodological choices involved, a synthetic overview of the methodological parameters adopted in this work is provided in ***Table 6.2***. This summary supports the interpretation of the results discussed in the following sections.

Table 6.2 – Summary of the methodological setup adopted for the LCA of anode production

Methodological parameters	***Adopted choice***
Functional Unit	*1 Ah of anode capacity* *1 kg of anode*
System boundaries	*Cradle-to-gate*
Software	*OpenLCA 2.4*
Database	*Ecoinvent 3.11*
LCIA calculation method	*Recipe 2016, Midpoint (H)* *Recipe 2016, Endpoint (H)*

6.1.1. Goal and scope definition

Following the methodological procedure and recommendations reported by Scrucca et al. [530], the goal of this study was to quantify the environmental impacts associated with the production processes of the three different types of anodes, with a specific focus on carbon footprint, which is described by the Climate Change (GW) category. The scope of the analysis was to assess, at the anode production level, whether improvements achieved at the electrochemical level were supported by the corresponding environmental impacts. Although similar approaches have already been proposed in the LCA literature, most existing studies do not rely on fully primary datasets for the construction of a complete LCI across all individual production steps [322,518]. In many cases, electrode manufacturing processes are reconstructed using generic datasets, literature assumptions, or simplified models, which limit the representativeness of the results when applied to real production conditions. In this context, the present study adopted a foreground system based on primary data, ensuring that all material flows, energy consumptions, and process parameters were derived from

experimentally optimized and validated electrode production procedures developed within this work.

6.1.2. Definition of the functional units

As already reported, several LCA studies on silicon-based anodes are available in the literature; however, direct comparison among published results is often difficult due to the adoption of different, and in some cases poorly specified, system boundaries and FUs. For this reason, the definition of the FU was addressed in accordance with ISO 14040 and ISO 14044 standards [309,310], and in line with previous LCA studies on battery systems [530]. In 2020, Tolomeo et al. [342] summarized the state of the art of the LCA applied to LIBs used in the automotive sector and clearly demonstrated the complexity underlying a proper comparison between different studies. The most commonly adopted FUs in LCA studies on LIBs depend on the system level under investigation, and multiple FUs can be used within the same study. In LCA studies focusing on electric vehicles, the most common FU is 1 vehicle-kilometer (vkm) [322,516,517,525]. At battery pack level, typical FUs include 1 kWh of storage capacity [322,518,521,526–528], 1 kg of battery mass [515] or 1 battery pack [529]. Similarly, mass-based FUs (1 kg) are frequently adopted for module, cell, and electrode-level assessments [512,515,521].

However, when the analysis is restricted to electrode production, the exclusive use of mass-based FUs limits the possibility of directly linking environmental impacts to electrochemical performance. For this reason, two FUs were defined in this study for the anode production phase. The first FU was 1 kg of anode produced, which allowed direct comparison with the existing literature. The second FU was a performance-based unit defined as 1 Ah of anode capacity, derived from experimentally measured electrochemical data. This second FU was particularly relevant when considering the integration of the anodes in full-cell configurations, where capacity rather than mass represents the functional output. Using both FUs provides a more comprehensive interpretation of the results, highlighting how FU selection influences the assessment of environmental impacts.

6.1.3. System boundaries

The system boundaries of the present LCA were defined in accordance with the goal of the study and the availability of primary experimental data. The analysis followed a cradle-to-gate approach, covering all processes from raw material supply to the production of finished anode electrodes at laboratory scale (***Figure 6.2***). The foreground system included the preparation of the electrode slurry, coating and drying of the electrodes, as experimentally performed within

this work. All electrodes and coin-cells were manufactured at laboratory level, and all material and energy flows were directly measured or calculated based on experimental data, enabling the construction of a LCI entirely based on primary data. Background processes, including electricity generation, transportation, and upstream material production, were modelled using secondary data obtained from the Ecoinvent 3.11 database.

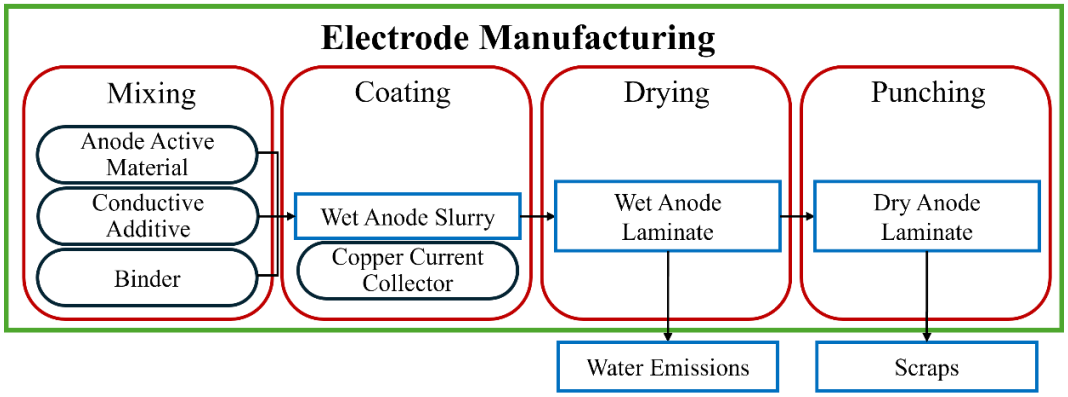

Figure 6.2 – The system boundary is indicated by the green rectangle, production steps are represented by red ovals, input materials and components by black ovals, and process outputs by blue squares.

Processes related to cell assembly, use phase, and EoL were excluded from this part of the analysis. A focus on cell assembly was addressed separately in the subsequent sections of this chapter, where the LCA on the full cell was investigated. This system boundary definition ensured internal consistency and allowed a focused comparison of the environmental impacts associated exclusively with the anode production process.

6.1.4. LCI for the anodes preparation

The LCI was constructed in accordance with the goal and scope previously defined, with a specific focus on the anode production process. The inventory was entirely based on primary experimental data for the foreground system, ensuring a high level of consistency between the laboratory-scale electrode production discussed in the previous chapters and the LCA perspective.

All material and energy flows were collected directly during experimental anode manufacturing activities carried out at laboratory scale. This approach allowed the LCI to reflect real processing conditions rather than idealized or literature-based assumptions, which is particularly relevant for emerging electrode chemistries, such as SD electrodes, and low-TRL manufacturing processes. Foreground data included material inputs, energy consumption, and process parameters associated with slurry preparation, coating, and drying steps. These data were obtained through direct measurements, calculated from experimental settings, or derived from equipment specifications provided by the manufacturers.

Background processes, including electricity generation, raw material production, and transportation, were modelled using secondary data from the Ecoinvent 3.11 database and implemented within the OpenLCA 2.4 software. This combination of primary data and standardized background datasets enabled a transparent and reproducible assessment while preserving comparability with existing LCA studies on LIB components.

6.1.4.1. Foreground system description

The foreground system included all processes directly related to the laboratory-scale production of anode electrodes, as experimentally performed and optimized in the previous chapters. In particular, the system included slurry preparation, electrode coating, and drying steps, which represented the core manufacturing phases of anode production and were strongly influenced by the choice of active material and formulation parameters. Slurry preparation involved the mixing of the active material, conductive additive, binder, and solvent, including the associated electricity consumption of the mixing equipment. The coating step included the deposition of the slurry onto the copper CC, while the drying stage accounted for solvent removal through thermal treatment under controlled conditions. No calendering step was included in the present inventory, in accordance with the experimental procedures adopted for the anodes considered in this study and to ensure consistency across the investigated chemistries. All these processes were modelled using primary data collected during experimental activities, ensuring that material compositions, solid content, process durations, and energy requirements accurately reflected the real manufacturing conditions. A set of key process parameters was identified and included in the LCI modelling to capture differences among anode chemistries. Only parameters directly affecting material and energy flows, such as wet deposition thickness and drying conditions, were considered, while purely operational settings were kept constant.

Processes related to upstream material extraction, synthesis of raw materials, and energy generation were excluded from the foreground system and were addressed within the background system. Similarly, downstream processes such as cell assembly, electrochemical testing, and EoL were excluded at this stage, as the present LCI focuses exclusively on the anode production phase. This choice allowed a clear isolation of the environmental contributions associated with electrode fabrication and enables a direct comparison among different anode chemistries under consistent processing assumptions.

6.1.4.2. Material and energy inventory

The material and energy inventory was constructed to accurately represent the foreground system associated with laboratory-scale anode production, in full consistency with the experimentally optimized procedures described in the

previous chapters. All inputs were quantified on the basis of direct measurements, mass balances, and equipment specifications, ensuring coherence between electrochemical experimentation and LCA modelling.

The material inventory included all components required for anode fabrication, such as active materials, binders, conductive additive, CC, and solvent. Three different active material formulations were investigated: G-A, SC-A and SD-A. The binder system consisted of CMC and SBR for G-A and SC-A, while PAA was employed for the SD-A formulation. Conductive carbon black was used as additive in all formulations, while copper foil was adopted as CC for all anode types. MilliQ water was used as solvent for slurry preparation. Upstream material production processes, including silicon production, were modelled in the background system using secondary data. Although silicon production is an established and industrially mature process, this primarily applies to conventional silicon materials. In contrast, the production of advanced silicon-based materials for battery anodes, such as silicon nanoparticles, nanoporous silicon, or SC structures, is still under active development. As a result, significant efforts are ongoing to improve the environmental sustainability of these materials through technological innovations [519,531], while corresponding LCI datasets are often limited or entirely unavailable.

All material inputs were quantified according to the slurry compositions, solid contents, and coating parameters experimentally optimized and reported in the previous chapters. A complete overview of the material and energy inputs for each unit process is reported in ***Table 6.3***, where differences among the three anode chemistries are explicitly highlighted.

Table 6.3 – Material inputs, process parameters, and energy consumption associated with the mixing, coating, and drying steps for the production of G-A, SC-A, and SD-A anodes at laboratory scale.

Process step	Parameter / input	Unit	G-A	SC-A	SD-A
Mixing	Time	Min	210	210	80
	Mixing speed	Rpm	2200	2200	1000
	Power	W	70	70	70
	Electricity	Wh	245	245	93.1
	Graphite	G	4.750	–	0.250
	Silicon carbide	G	–	4.750	–
	Nanoporous Silicon	G	–	–	4.000
	Carbon black	G	0.100	0.100	0.250
	CMC	G	0.050	0.050	–
	SBR	G	0.100	0.100	–

	PAA	G	–	–	0.500
	Water	G	7.500	5.000	3.333
	Solid Fraction	%	40	50	60
Coating	Time	Min	10	10	10
	Power	W	50	50	50
	Electricity	Wh	8.5	8.5	8.5
	Wet Slurry	G	1.693	1.366	1.129
	Copper foil	G	1.731	1.731	1.731
	Wet Deposition	µm	100	100	50
Drying	Time	Min	60	60	–
	Power	W	2000	2000	–
	Electricity	Wh	400	400	–

In addition to quantities, the geographical origin of raw materials was considered and documented in a dedicated table (***Table 6.4***), enabling subsequent assessment of transport-related impacts and the development of alternative European supply-chain scenario. However, due to the limited availability of detailed data, it was not possible to accurately identify the specific country of origin for all materials. Therefore, a generic non-European production was assumed, without further geographical specification.

Table 6.4 – Geographical origin of materials and energy inputs considered in the LCA of G-A, SC-A, and SD-A anodes, used for the assessment of transport-related impacts and supply-chain scenarios.

Material and Energy Inputs	*Supplier*	*Origin (Country)*
Graphite	Timcal	Outside Europe
Silicon Carbide	MTI Corp.	Outside Europe
Nanoporous Silicon	E-Magy	Netherlands
Carbon Black C45	Timcal	Outside Europe
Carboxy Methyl Cellulose	MTI Corp.	Outside Europe
Styrene Butadiene Rubber	MTI Corp.	Outside Europe
Polyacrylic Acid	Sigma Aldrich	Outside Europe
Water		Internal Production
Copper CC	MTI Corp.	Outside Europe
Electricity		Italian mix

Energy consumption was quantified for each unit process within the foreground system and included in the inventory as input. Slurry preparation energy was calculated based on the power of the mixing equipment and the

effective mixing time required for each formulation, reflecting the substantial differences between graphite and silicon-based slurries. For all formulations, slurry mixing was performed using the same laboratory mixer (Argolab Disperser, ***Figure 3.4***). Although this equipment had previously been employed only for the SD formulation (***Chapter 5.4***), it was adopted here for all anode types in order to ensure a consistent and comparable processing reference. Consequently, specific adjustments to the mixing protocols were required to achieve homogeneous slurries and acceptable coating quality across the different chemistries.

The coating process was identical for all slurry formulations in terms of processing time, electricity consumption, and CC mass. The only parameter varying among the anode types was the amount of wet slurry required to produce a single laminate, which decreased with increasing specific capacity. Drying emerged as the most energy-intensive step of anode production. Energy consumption was calculated using experimentally defined drying protocols, considering oven power, temperature, and time. Notably, differences in drying requirements among the three anode chemistries resulted in significantly different energy demands. Following the production procedures described in the previous chapter, G-A and SC-A required 1 hour of drying at 50°C, whereas the drying step for SD-A was performed in ambient air at room temperature.

During the design of the experimental work, a maximum theoretical yield per coating was assumed, corresponding to an ideal cutting of 15 mm diameter electrodes arranged in direct contact with each other. An illustrative layout of the coated area is shown in ***Figure 6.3***. In this configuration, a copper foil large enough to be processed with the doctor blade was considered, including a non-coated section required for mechanical anchoring during coating. Slurry deposition occurred over a maximum width of 10 cm (blade width), while the usable area was slightly reduced to exclude edge regions affected by thickness inhomogeneity. Based on the resulting usable area, a total of 75 electrodes could be obtained per coating, according to the scheme (***Figure 6.3***). Electrode punching was performed manually, and the associated material losses were quantified and included in the inventory as output of the system (***Table 6.5***). The punching process generated two types of waste: pure copper scraps, which can be directly recycled, and contaminated scraps, which require additional treatment before re-entering the recycling chain [532]. The relatively high scrap rate reflects the intrinsic inefficiency of manual punching, which contrasts with the higher material utilization typically achieved in industrial-scale electrode manufacturing [533].

Table 6.5 – Amount of scraps produced during the punching step of anode production, depending on the electrode chemistry

Punching	**Manual process**		**G-A**	**SC-A**	**SD-A**
	CC Scraps	g	0.546	0.546	0.546

	Electrode Scraps	g	0.789	0.888	0.789

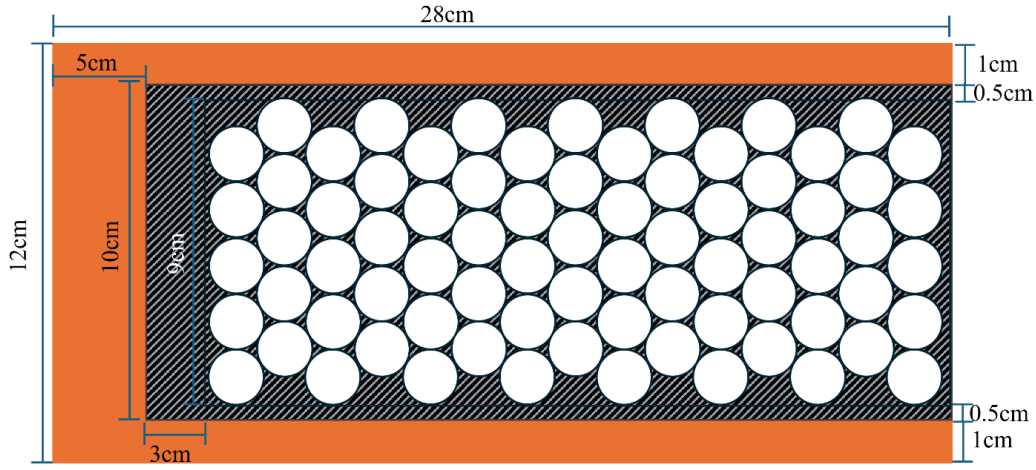

Figure 6.3 – Schematic representation of electrode laminates produced at laboratory scale, showing the waste generated by manual punching process.

Electricity consumption was modelled using the Italian electricity mix from the Ecoinvent 3.11 database (Cutoff Unit - Processes), in accordance with the geographical scope of the study and the location of the experimental activities. This approach ensured consistency between the foreground data and the background system.

To ensure full traceability and transparency of the LCI model, a comprehensive mapping of all system inputs is provided in ***Table 6.6***. This overview distinguishes between primary data gathered directly from laboratory activities and secondary data sourced from the Ecoinvent database, while explicitly highlighting where proxies were required due to dataset unavailability.

Table 6.6 – Correspondence between experimental inputs and Ecoinvent 3.11 background datasets, including data quality classification and proxy identification for the anode manufacturing processes.

Input	*Data Type*	*Proxy*	*Dataset*
Graphite	Primary	--	market for graphite | graphite | Cutoff, U - GLO
Silicon Composite	Primary	Silicon Carbide	market for silicon carbide | silicon carbide | Cutoff, U - GLO
Nanoporous Silicon	Primary	Silicon, Metallurgical Grade	silicon production, metallurgical grade | silicon, metallurgical grade | Cutoff, U - NO
Carbon Black	Primary	--	market for carbon black | carbon black | Cutoff, U - GLO
CMC	Primary	--	market for carboxymethyl cellulose, powder | carboxymethyl cellulose, powder | Cutoff, U - GLO
SBR	Primary	Latex	market for latex | latex | Cutoff, U - RoW
PAA	Primary	Acrylic Acid	market for acrylic acid | acrylic acid | Cutoff, U - RER
Ultrapure Water	Primary	--	water production, ultrapure | water,

			ultrapure | Cutoff, U - RER
Copper CC	Primary	--	market for sheet rolling, copper | sheet rolling, copper | Cutoff, U - GLO
Electricity, Medium Voltage	Secondary	--	market for electricity, medium voltage | electricity, medium voltage | Cutoff, U - IT

As extensively described in the previous chapters, the electrodes prepared in this work were individually weighed, and their thickness was measured to evaluate the coating uniformity achieved with the laboratory-scale coating process. The corresponding data, together with the average characteristics of the produced electrodes, are reported in ***Table 6.7***. Overall, a certain degree of variability was observed among the electrodes, which is also commonly reported at the industrial scale; however, in industrial settings, the coating quality can typically be monitored and controlled more effectively through dedicated inline inspection systems [281]. Among the reported parameters, volumetric capacity represents a key parameter and must be carefully considered, particularly when full cells are assembled. The higher energy density of the SD-A can enable a reduction in the environmental impact at cell level, primarily due to the lower amount of active material required to achieve the same electrochemical performance. When effectively translated into cell design, this reduction translates into lower material demand, reduced electrode volume, and consequently a lower amount of materials required for inactive cell components, such as casing and supporting elements [534]. Furthermore, the transition from conventional graphite anodes to silicon-based anodes may reduce the criticality associated with graphite, thereby lowering the overall demand for natural or synthetic graphite. This is particularly relevant in the context of current supply-chain issues [321,518], given the geographical concentration of graphite mining and processing and its classification as a critical raw material in several strategic assessments and policy documents [535]. As a consequence, the overall material demand at the LIB cell level may be reduced, provided that the volumetric and capacity advantages are effectively reflected in the cell design [521,536].

Table 6.7 – Overview of the main properties of the G-A, SC-A, and SD-A anodes produced at laboratory scale.

Chemistry	*Solid Fraction [%]*	*Dry Layer Thickness [µm]*	*Dry Layer Volume [cm^{-3}]*	*Weight [mg]*	*Practical Capacity [mAh]*	*Practical Capacity [mAh g^{-1}]*	*Volumetric Capacity [mAh cm^{-3}]*
G-A	40	46 ± 1	0.081	15.47	1.684	350	20.79
SC-A	50	50 ± 1	0.088	16.09	2.913	400	33.10
SD-A	60	37 ± 5	0.065	14.94	4.016	1000	61.78

As discussed previously, the electrodes were subsequently electrochemically tested to determine their practical capacity, following an approach comparable to

that reported by Philippot et al. [322]. The cells were assembled in a CR2032 coin-cell configuration inside an argon-filled glovebox with controlled atmosphere (O_2<0.5 ppm, H_2O <0.5 ppm). The prepared anode electrodes were used as working electrodes and paired with lithium metal foil as counter electrode. A GF/A Whatman separator was placed between the electrodes and soaked with 150 µL of electrolyte (1 M $LiPF_6$ in EC:DEC 1:1) to ensure consistent wetting conditions across all cells. All cells were assembled following the same procedure to ensure consistency among the different anode chemistries. The electrochemical characterization consisted of 10 consecutive charge–discharge cycles at a C-rate of 0.1C. For the G-A and SC-A electrodes, a CCCV protocol was adopted. During the CCS, the cells were cycled at 0.1C down to a cut-off voltage of 0.01 V vs. Li/Li^+, followed by a CVS at 0.01 V until the current cut-off of 0.01C. The electrochemical performance data obtained from these measurements are summarized in ***Figure 6.4***.

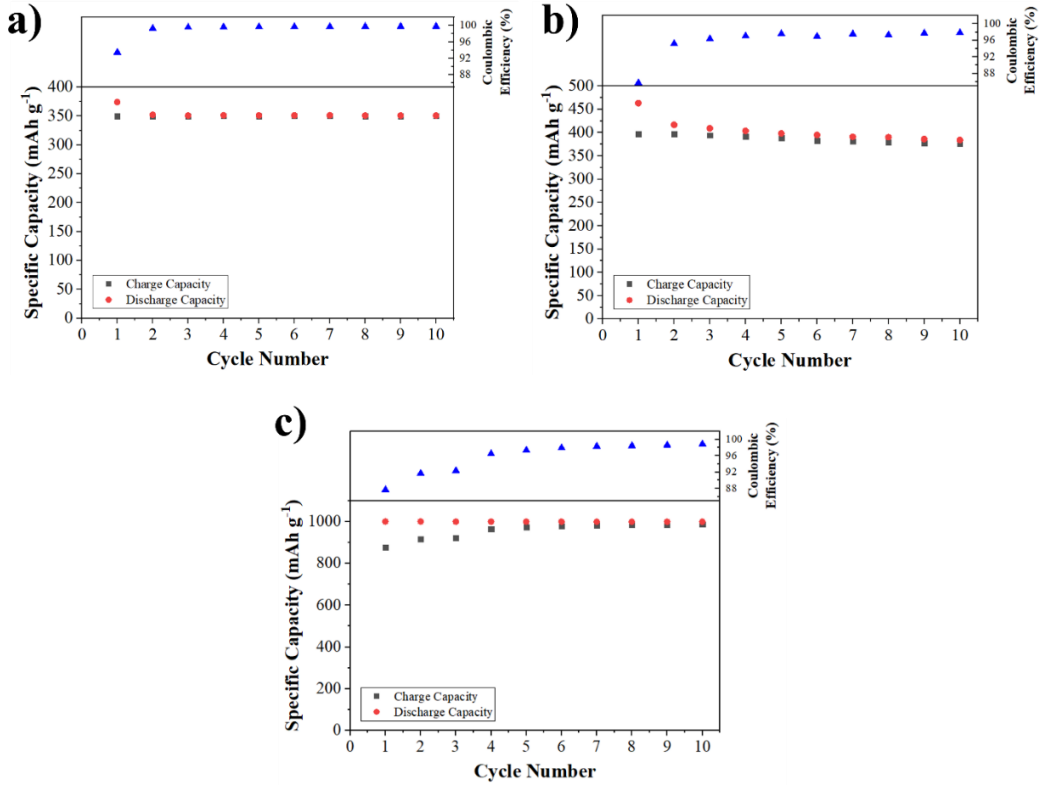

Figure 6.4 – Electrochemical results of the different anode materials tested in half-cell configuration using lithium metal as reference electrode: A) G-A; B) SC-A; C) SD-A.

6.1.5. Assumptions of the study

LCA inherently relies on a set of assumptions and modelling choices that can significantly influence the final results. This aspect becomes particularly relevant for emerging technologies and laboratory-scale processes, for which complete and

technology-specific datasets are often unavailable [317]. In this context, the present study can be classified as a Prospective Life Cycle Assessment (P-LCA), which aims to estimate the potential future environmental impacts of products and technologies that are still under development and not yet commercially available [537]. Such an approach typically relies on standard LCA databases and, where necessary, on assumptions regarding technological evolution or future process improvements [538]. As a consequence, transparency in the definition of assumptions becomes essential to ensure robustness, interpretability, and comparability of the results. While these assumptions introduce a degree of uncertainty, they also enable the consistent application of LCA to complex systems that would otherwise be impossible to assess quantitatively.

An original contribution of this work was related to the explicit quantification of production scrap rates. Due to the low TRL of the laboratory-scale manufacturing processes adopted, the scrap fraction was estimated to be slightly below 40%. In contrast, mature industrial processes typically report scrap rates close to 5% [533]. This discrepancy was non-negligible and must be carefully considered when interpreting the environmental results and evaluating the potential scalability of the investigated processes. Laboratory-scale production is intrinsically characterized by lower efficiency compared to optimized industrial manufacturing [522].

To complete the LCA, several modelling choices were required to address the limited availability of technology-specific datasets for emerging battery materials. In particular, when dedicated inventory data were not available in the Ecoinvent 3.11 database, representative proxies were selected following established practices in battery LCA studies. SBR was modelled using a generic latex dataset for the mixing step, while PAA was represented through an acrylic acid dataset, assuming the contribution of the polymerization process to be negligible, in line with the approach proposed by Nuss et al. [470]. Similarly, the SC investigated in this work, containing 10 wt.% silicon, was modelled using a silicon carbide dataset with a 50% silicon content, reflecting the lack of a more specific alternative. For SD-A, metallurgical-grade silicon was adopted as a representative proxy for the actual silicon material, consistently with previous LCA studies [322]. Finally, water used during slurry preparation was assumed to be completely removed during the drying step, in accordance with the experimentally defined processing conditions.

All energy-related calculations were based on the Italian electricity mix, reflecting the geographical location of the experimental activities carried out at the laboratories of Politecnico di Torino. Among the additional assumptions, no potential energy savings associated with reduced mixing intensity were considered. Although lower mixing speeds were adopted for the SD formulation compared to graphite-based slurries, the electricity consumption of the mixing

equipment was assumed to be identical for all formulations, since a reliable quantification of the resulting energy differences was not possible.

Regarding the geographical boundary selection for the baseline configuration, a crucial methodological assumption must be clarified. While a fully homogeneous extra European supply chain for all active materials could appear conceptually more uniform for a global scenario, the inclusion of European sourced silicon within the Global Actual Production case represents a deliberate and strategic modeling choice. This decision ensures absolute consistency throughout the dissertation, as the LCA is strictly based on the exact same active materials that were selected, characterized, and presented in the electrochemical section of this thesis. Furthermore, this configuration reflects real world supply chain shifts and emerging industrial realities. Advanced silicon solutions, such as those developed by specialized manufacturers like E-Magy, are explicitly declared as entirely sourced in Europe [539,540]. Incorporating this specific commercial reality into the model serves to highlight a concrete path toward strategic decoupling and independence from China for critical raw material procurement, showcasing how European supply chains can realistically mitigate geopolitical vulnerabilities. Therefore, while the baseline scenario features a hybrid geographic structure, this choice directly mirrors the actual experimental procurement of this doctoral work.

A key modelling assumption in this work concerns the use of water-based electrode fabrication processes, which allows electrode production to be carried out under ambient conditions without the need for strictly controlled dry-room environments. This assumption implies that, upon industrial scale-up, the environmental impacts associated with dry-room operation during electrode manufacturing could be reduced or partially avoided, leading to a further decrease in energy consumption and related emissions. In industrial battery manufacturing, dry-room facilities can account for approximately 29% of the total energy demand, as they are required to support moisture and temperature control during both electrode production and cell assembly [541]. Although dry-room conditions would still be necessary for specific cell-assembly steps, such as electrolyte filling and sealing, eliminating dry-room requirements during electrode manufacturing alone would already result in a substantial reduction in overall energy consumption [523,542]. In the present work, electrode fabrication was already carried out entirely in air, while coin-cell assembly was performed in an argon-filled glovebox; however, since cell assembly lies outside the defined system boundaries, this contribution was not included in the LCA. Nevertheless, the possibility of performing electrode manufacturing in air represents a relevant assumption in a prospective context, as it highlights an additional potential reduction of environmental impacts enabled by water-based electrode production processes [541].

6.1.6. Limitations and outlook

The use of primary foreground data ensures a high level of internal consistency between experimental results and environmental assessment. However, it should be noted that laboratory-scale production inherently tends to overestimate specific energy consumption compared to industrial-scale processes. For this reason, the LCI was intended to support comparative analysis between anode chemistries, rather than to provide absolute impact values representative of industrial manufacturing.

To ensure absolute methodological transparency and precisely address the boundaries of this evaluation, a clear distinction must be made between the empirical data of this work and the qualitative concepts derived from literature. This study does not develop a quantitative industrial scale or gigafactory scale modeling scenario, nor does it provide a numerical quantification of dry room energy savings. The LCA is strictly bounded to the laboratory scale scenario, constructed entirely from original primary data collected during the experimental campaigns. All inventory parameters, including specific slurry compositions, mixing parameters, and water based binder formulations, represent unique empirical findings generated within this research. Conversely, any reference to large scale prospective benefits is derived from existing scientific literature and intended solely as a qualitative outlook to contextualize the process. This includes the discussion regarding the potential to bypass dry room climate control systems during the electrode fabrication stage by shifting to water based processing, as well as general considerations on gigafactory efficiencies. These literature benchmarks serve exclusively to provide a qualitative understanding of future manufacturing trajectories. Consequently, all quantitative indicators and comparative profiles presented in this chapter constitute the original and independent empirical contribution of this thesis at the laboratory scale.

The main limitations of the present study were primarily related to the TRL of the investigated processes. All experimental activities were conducted at laboratory scale, and the resulting environmental impacts cannot be directly or linearly extrapolated to industrial production conditions. At larger scales, production processes are generally more efficient, characterized by reduced material losses, optimized energy use, and lower emissions per unit of output. Indeed, estimates for gigafactory-scale battery production consistently report significantly lower impacts compared to laboratory or pilot-scale lines [543]. Despite differences in absolute values, the relative trends observed among the investigated anode chemistries are expected to remain valid at larger scales, as they are driven by intrinsic differences in material composition and process requirements. In particular, the inherently higher specific capacity of SD anodes is expected to remain a key factor in reducing impacts when normalized to electrochemical performance. However, since scale-up involves non-linear

changes in both material and energy consumption, the results presented in this study should be interpreted with caution when considering industrial-scale scenarios.

The small quantities of materials involved in laboratory-scale production, often limited to a few grams or fractions of them, represent an additional limitation. This scale disparity complicated direct comparison with industrial LCA studies, where economies of scale significantly influence material efficiency and energy consumption. However, even at these reduced scales, the present results provided valuable insight into the relative environmental performance of alternative anode chemistries and constitute a meaningful starting point for future upscaling analyses. This aspect was particularly relevant in the prospective European supply chain scenario, where absolute variations in environmental impact were modest but still detectable, highlighting that supply-chain effects remained relevant even at small transport volumes.

An additional limitation concerns the definition of the system boundaries. The study was conducted following a cradle-to-gate LCA approach and therefore did not include the use phase and the EoL stage. As a consequence, while potential benefits related to the circular economy are qualitatively discussed within the text, they are not analytically quantified in the final footprint evaluation. This choice was motivated by the research-oriented nature of the investigated cells, which were fabricated exclusively for experimental purposes and not intended for commercial application. Coin cells were selected as the testing format due to their ease of assembly and the high level of control they allow over individual fabrication steps. Manual assembly also enables improved reproducibility at laboratory scale, although it remains partially influenced by operator-dependent variability. It should be noted that coin cells do not represent the dominant industrial formats, where cylindrical and prismatic cells are prevalent in the automotive sector and pouch cells are widely used in portable electronics. LCAs specifically focused on lithium-ion coin cells remain relatively scarce in the literature and are typically employed as benchmarking tools for emerging technologies, such as solid-state lithium batteries or sodium-ion batteries, rather than as direct representations of commercial products [544].

Finally, limitations also arise from the use of background databases. Although Ecoinvent 3.11 is one of the most comprehensive and widely adopted LCA databases, some datasets are still missing, while others remain partially outdated or based on older technological assumptions. One of the most significant gaps identified in this work concerns the lack of an adequate dataset for the production of SC materials. While proxy datasets based on technologically similar processes can be used to approximate such materials, as implemented in this study through the adoption of a silicon carbide proxy, these substitutions remain an approximation of the real production route. As a result, differences in synthesis pathways, energy intensity, and material efficiency cannot be fully captured, and

the lack of a dedicated and representative dataset for SC production constitutes one of the most relevant limitations of the background modelling.

In addition, several existing datasets rely on old, outdated datasets, reflecting assumptions that may no longer fully reflect current industrial practices. For example, datasets related to EURO6 lorry transportation still rely on values dating back to the 2013 update, while the dataset for European CMC production explicitly states that calculations are based on average technologies from the mid-1990s. These examples illustrate the inherent challenges in obtaining fully representative and up-to-date background data and underline how database limitations can influence the accuracy of LCA results, particularly when assessing emerging technologies and evolving supply chains. Similar issues have been highlighted by Surovtseva et al. [545], who showed that many LCIs for graphite production, which are widely used as reference in battery LCA studies, are based on incomplete and outdated data published between 2010 and 2015. The absence or simplification of key processes within these inventories can lead to a systematic underestimation of environmental impacts. Although graphite represents only one example among many, it clearly illustrates how performing a fully representative and up-to-date LCA remains a challenging task, particularly when assessing emerging technologies and rapidly evolving supply chains.

To complement these methodological limitations and align the environmental analysis with a broader environmental sustainability approach, a qualitative strategic and geopolitical perspective focused on raw material criticality must be considered. While the quantitative LCA highlights that the energy intensive synthesis of silicon can lead to higher upfront carbon footprints compared to graphite, this numerical penalty must be balanced against supply chain and macroeconomic risks. Graphite is currently classified as a Critical Raw Material (CRM) by the European Union due to its extreme geographical concentration and geopolitical vulnerability [546]. Conversely, silicon represents a globally abundant and strategically diversified resource [547]. Therefore, these qualitative strategic and supply chain factors, including regional technological independence and resource secureness, effectively complement the quantitative ecodesign indicators, justifying the choice of SD configurations within a comprehensive, long term environmental sustainability prospective.

6.1.7. LCIA methods

The LCIA was performed to translate the material and energy flows defined in LCI into potential environmental impacts. The ReCiPe 2016 methodology was selected as the LCIA elected methodology, considering both the Midpoint (H) and Endpoint (H) perspectives. The hierarchical cultural perspective (H) was adopted for both midpoint and endpoint calculations, as it represents a widely used compromise between short-term and long-term impact modelling and is widely

applied in battery LCA literature. This choice also facilitates comparison with previously published studies [322,515,518,521,548]. The 18 impact categories of the Midpoint method are reported in ***Table 6.8***, together with their abbreviations used during this work and the relative measurement unit.

Table 6.8 – List of the 18 impact categories evaluated with the ReCiPe (2016) Midpoint method, with their abbreviations and measurement unit.

Impact Category	***Abbreviation***	***Unit***
Acidification: terrestrial	TA	kg SO_2-Eq
Climate change	GW	kg CO_2-Eq
Ecotoxicity: freshwater	FE	kg 1,4-DCB-Eq
Ecotoxicity: marine	ME	kg 1,4-DCB-Eq
Ecotoxicity: terrestrial	TE	kg 1,4-DCB-Eq
Energy resources: non-renewable, fossil	FRS	kg oil-Eq
Eutrophication: freshwater	FET	kg P-Eq
Eutrophication: marine	MET	kg N-Eq
Human toxicity: carcinogenic	CHT	kg 1,4-DCB-Eq
Human toxicity: non-carcinogenic	NCHT	kg 1,4-DCB-Eq
Ionizing radiation	IR	kBq Co-60-Eq
Land use	LU	m^2*a crop-Eq
Material resources: metals/minerals	MRU	kg Cu-Eq
Stratospheric ozone depletion	SOD	kg CFC-11-Eq
Particulate matter formation	PMF	kg $PM_{2.5}$-Eq
Photochemical oxidant formation: human health	POFHH	kg NO_x-Eq
Photochemical oxidant formation: terrestrial ecosystems	POFTE	kg NO_x-Eq
Water use	WC	m^3

The midpoint approach was primarily used to analyze and compare the environmental impacts associated with anode production processes across the different active material configurations. Midpoint indicators allow a more direct interpretation of the contribution of individual processes and materials to specific impact categories, such as climate change, resource depletion, and human toxicity. The endpoint approach was employed as a complementary analysis to provide a more aggregated perspective on the overall environmental burden. By grouping midpoint impacts into damage categories related to human health, ecosystem quality, and resource availability, the endpoint results support a higher-level interpretation of the impacts associated with different anode chemistries [548]. While endpoint indicators inherently involve a higher degree of uncertainty compared to midpoint, they were included in this work to provide a broader environmental sustainability perspective and to support qualitative discussion of the results [343].

6.1.8. Sensitivity analysis

To further investigate the influence of material sourcing on environmental impacts, a sensitivity analysis was performed, partially inspired by the approach

proposed by Lavigne Philippot et al. [322]. The analysis focuses specifically on transportation routes and the electricity mix associated with raw material production, which are known to significantly affect the environmental footprint of LIBs. At present, a large fraction of the raw materials required for battery production originates from China and, more broadly, from Asian countries [549], resulting in long transportation distances and reliance on electricity mixes characterized by a high contribution from fossil-based energy sources.

In the context of the rapidly increasing demand for electric mobility, the European Union has introduced the European Critical Raw Materials Act, aiming to strengthen strategic autonomy by improving the resilience, environmental sustainability, and diversification of supply chains for critical raw materials [550]. Within this policy, evaluating the potential environmental benefits of localized supply chains becomes particularly relevant.

Several studies have already investigated supply-chain-related impacts of LIBs at different levels, either by focusing on the extraction and processing of specific materials such as graphite, cobalt, and manganese, or by analyzing the effect of manufacturing location on battery production impacts [526,536,551]. In particular, the work by Philippot et al. [526] demonstrated that the electricity mix, and therefore the country of production, can strongly influence the GW associated with battery manufacturing. However, a comprehensive evaluation of a fully European supply chain consistently applied across all materials remains limited in the literature.

In this study, a single sensitivity scenario was defined in which the entire supply chain was assumed to be located within Europe. The baseline scenario reflects the current situation, in which most materials required for anode production, including graphite, SC, carbon black, binders (CMC and SBR) and CC, are sourced from outside Europe. In the prospective scenario, the same materials were assumed to be supplied by European producers, while keeping all other parameters unchanged. Transportation processes were modelled using datasets from the Ecoinvent 3.11 database, based on data provided by Eurostat, the official statistical office of the European Union [552].

It should be noted that this sensitivity analysis accounts exclusively for changes in transportation routes and electricity mix associated with raw material production, while potential differences in production technologies and efficiencies were not considered. Despite this simplification, the results clearly indicated that strengthening the European supply chain could lead to a substantial reduction in the GW of battery production. This reduction was driven not only by shorter transport distances, but also by the higher share of renewable energy in the European electricity mix compared to countries such as China, in agreement with previous findings reported in the literature [526]. However, it should be noted that China is also significantly increasing its investment in renewable energy, with a growing contribution of renewable sources to its energy system, indicating

ongoing efforts toward decarbonization despite the continued use of fossil fuels [553].

6.1.9. Data quality assessment and uncertainty analysis based on the Pedigree approach

In line with the methodology proposed by Philippot et al. [322], uncertainty in this study was assessed using the Pedigree matrix approach, which allows a structured quantification of data uncertainties. This method distributes uncertainty across five independent qualitative indicators, each scored on a scale from 1 (lowest uncertainty) to 5 (highest uncertainty). Within the Ecoinvent Data Quality System, these indicators correspond to Reliability, Completeness, Temporal Correlation, Geographical Correlation, and Technological Correlation (***Figure 6.5***).

	1	2	3	4	5
Reliability	Verified data based on measurements	Verified data partly based on assumptions or non-verified data based on measurements	Non-verified data partly based on qualified estimates	Qualified estimate (e.g. by industrial expert)	Non-qualified estimates
Completeness	Representative data from all sites relevant for the market considered, over and adequate period to even out normal fluctuations	Representative data from > 50% of the sites relevant for the market considered, over an adequate period to even out normal fluctuations	Representative data from only some sites (<< 50%) relevant for the market considered or > 50% of sites but from shorter periods	Representative data from only one site relevant for the market considered or some sites but from shorter periods	Representativeness unknown or data from a small number of sites and from shorter periods
Temporal Correlation	Less than 3 years of difference to the time period of the data set	Less than 6 years of difference to the time period of the data set	Less than 10 years of difference to the time period of the data set	Less than 15 years of difference to the time period of the data set	Age of data unknown or more than 15 years of difference to the time period of the data set
Geographical Correlation	Data from area under study	Average data from larger area in which the area under study is included	Data from area with similar production conditions	Data from area with slightly similar production conditions	Data from unknown or distinctly different area (North America instead of Middle East, OECD-Europe instead of Russia)
Further Technological Correlation	Data from enterprises, processes and materials under study	Data from processes and materials under study (i.e. identical technology) but from different enterprises	Data from processes and materials under study but from different technology	Data on related processes or materials	Data on related processes on laboratory scale or from different technology

Figure 6.5 – Pedigree matrix developed by Ecoinvent

Despite its recognized importance, uncertainty analysis remains a relatively underdeveloped component of Life Cycle Assessment. Although more formalized working procedures have been proposed, such as the approach introduced by Igos et al. [554], a large fraction of LCA studies still do not explicitly address uncertainty. This limitation is particularly evident for emerging technologies and laboratory-scale systems, where data variability is often implicitly neglected, potentially compromising the robustness and interpretability of comparative assessments.

In the present work, primary foreground data were not explicitly associated with uncertainty distributions, as they were directly measured during electrode and cell preparation under controlled laboratory conditions. Material quantities, processing times, and equipment power ratings were experimentally determined, reducing uncertainty related to measurement accuracy. Nevertheless, it is acknowledged that laboratory-scale processes inherently exhibit some degree of variability; however, this variability was considered secondary compared to uncertainties associated with background data.

As a result, uncertainty analysis was mainly focused on background processes. For electricity generation and transportation processes, uncertainties were modelled using lognormal distributions, with squared geometric standard deviations derived from the corresponding uncertainty factors, consistently with common practice in LCA modelling [309,310,322]. The corresponding geometric standard deviations were calculated based on the Pedigree matrix scores. Uncertainty associated with electricity consumption was relatively limited, as energy use was calculated from known equipment power and operation times. However, residual uncertainty remains due to variability in the electricity supply and background dataset assumptions. In contrast, transportation processes were characterized by higher uncertainty, since detailed information on suppliers, routes, and logistics conditions were not fully available. In this case, uncertainty values provided by the Ecoinvent 3.11 database were adopted and considered representative. These uncertainties were particularly influential in the sensitivity analysis addressing the prospective European supply-chain scenario.

Uncertainty in the GW impact category was quantified through MCS, performed with 10,000 iterations. The number of iterations was selected following the approach adopted in comparable studies, as it represents an effective compromise between statistical robustness and computational efficiency [322,554]. The MCS enabled the evaluation of probability distributions for the impact results, allowing the identification of mean and median values. The deviation between these statistical indicators and the deterministic LCA results was used as a measure of the influence of uncertainty on the outcomes, with larger deviations indicating a stronger effect of uncertainty propagation through the model.

6.1.10. LCIA: linking electrochemical performance and environmental impacts

This section presents the results obtained from the LCA. It opens with an introductory overview describing the relative percentage contributions of the different electrode components to the overall impacts. The analysis was then structured into two separate subsections focusing on midpoint impact categories and comparing the FUs considered in this study. Subsequently, the results of the

sensitivity analysis assessing the influence of a fully European supply chain scenario are discussed, followed by a dedicated paragraph addressing the uncertainty analysis through MCS. Finally, the endpoint impact categories are presented and discussed.

Before discussing the individual impact categories in detail, it is important to highlight some general trends emerging from the results. In particular, the SD-A showed advantages not only in terms of higher specific capacity, but also in terms of material processability. Compared to the other formulations, SD-A enabled faster mixing and drying steps, reflecting more efficient slurry mixing and solvent removal, thanks to the drying process being conducted in ambient air at room temperature, which eliminated the need for an oven. The optimization of these manufacturing processes resulted in a significant reduction in electricity demand during electrode production, which contributed to an overall reduction of environmental impacts.

6.1.10.1. Environmental impacts assessment of 1 Ah anode production in a global supply chain

When the production of 1 Ah anodes was considered, the required number of electrodes emerged as a key parameter in interpreting the environmental results. Due to the differences in specific capacity, a substantially higher number of G-A electrodes was required to reach 1 Ah compared to silicon-based anodes: SC-A and especially SD-A achieved the same capacity with a considerably lower number of laminates. This reduction directly affected material consumption, processing time, and waste generation, providing a first indication of the potential advantages associated with silicon-rich anodes. All quantitative details regarding electrode numbers and laminates are reported in ***Table 6.9***.

Table 6.9 – Number of laminates and electrodes required to achieve the capacity of 1 Ah

Number of elements	***G-A***	***SC-A***	***SD-A***
Laminates	7.9	4.6	3.3
Electrodes	594	343	249

This effect was consistently reflected across the impact categories (***Figure 6.6***). Using G-A as the baseline reference, SC-A showed a moderate but systematic reduction of impacts, while SD-A exhibited a much stronger decrease in all categories. This reduction results from the combined effect of higher specific capacity, lower material demand per Ah, and process optimization. In particular, the simplified production route adopted for SD-A, which enabled faster mixing and eliminated the drying step, significantly lowered electricity consumption during electrode fabrication. In addition, the localized European production of SD-A further contributed to impact reduction. The higher share of renewable energy in the European electricity mix played a relevant role in

decreasing energy-related impacts, highlighting how material choice and supply chain assumptions jointly influence the overall environmental performance.

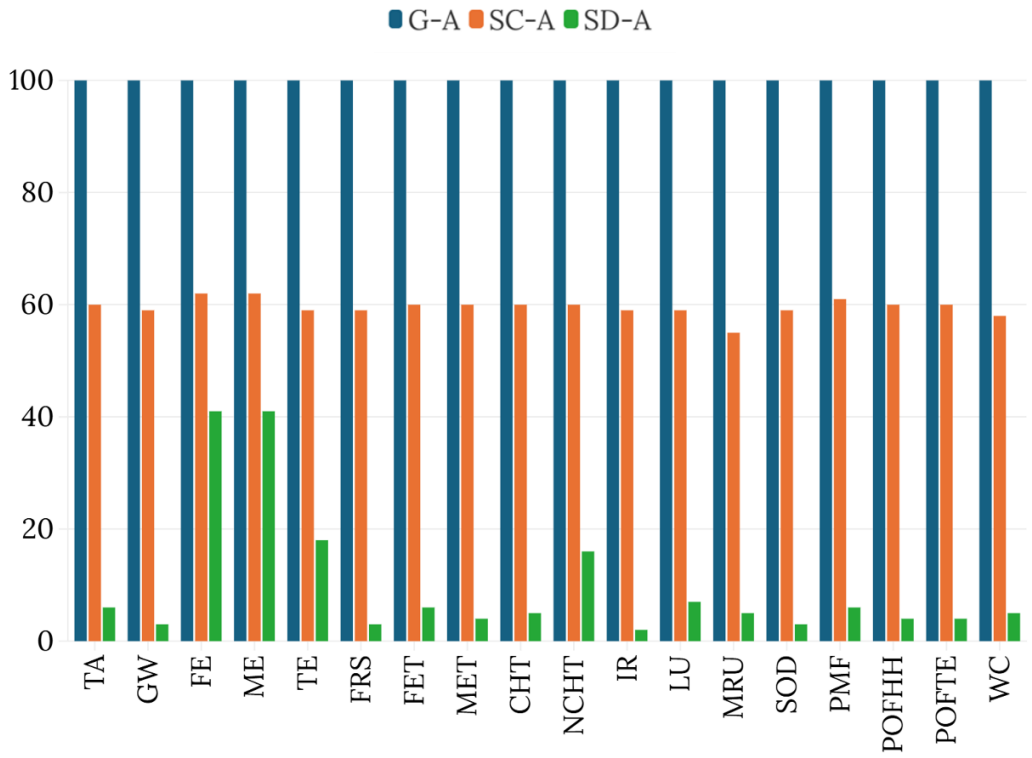

Figure 6.6 – Relative percentage reduction of environmental impacts for 1 Ah of anode production across the impact categories

Figure 6.7 presents a Sankey diagram illustrating the relative contribution of the different midpoint impact categories to the overall environmental performance of the three anode configurations. The width of each flow is proportional to its contribution, allowing the identification of the most influential impact categories for each system. In general, categories such as GW, freshwater ecotoxicity (FE), marine ecotoxicity (ME), terrestrial ecotoxicity (TE) and non-cancerogenic human toxicity (NCHT) represent the dominant contributions across all configurations, reflecting the energy-intensive nature of material production and electrode manufacturing. Differences among the three systems can be observed in the relative distribution of these contributions, highlighting how changes in material composition influence specific environmental impacts. This type of visualization allows an immediate understanding of impact distribution.

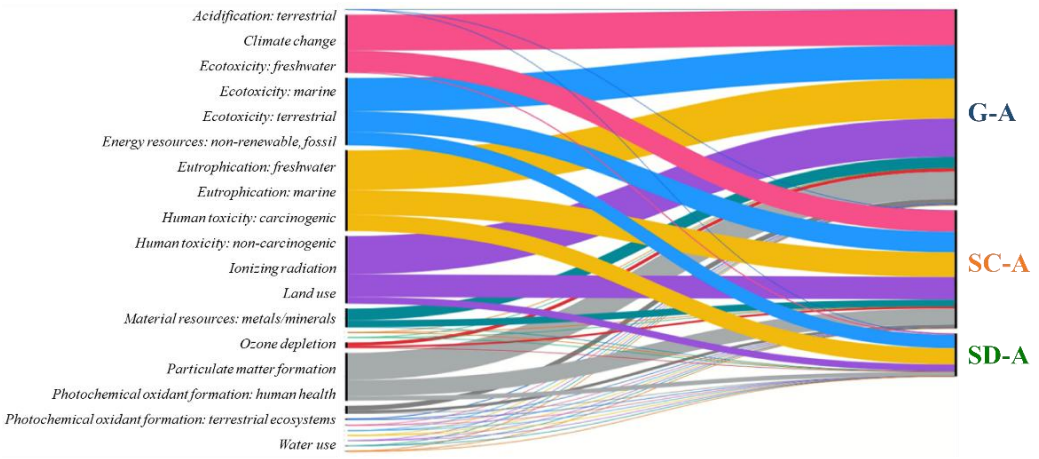

Figure 6.7 – Sankey diagram showing the contribution of different midpoint impact categories to the overall environmental impact of the three anode configurations (G-A, SC-A, SD-A). Each impact category is associated with a specific color, while the width of the flows represents their relative contribution. Due to scale differences, some contributions are not visually prominent, although all categories are reported for completeness.

An overview of the detailed impact values and the corresponding percentage reductions across the impact categories is reported in ***Table 6.10***, providing the basis for the discussion presented below. Starting from GW, which represents the most commonly used and discussed impact category, the results showed that GW was strongly dominated by energy consumption during electrode manufacturing. As a consequence, this category was particularly sensitive to variations in processing conditions and in the electricity mix. For GW, the G-A exhibited an impact of ~1.33 kg CO_2-eq per Ah, decreasing to ~0.79 kg CO_2-eq for SC-A and ~0.04 kg CO_2-eq for SD-A. The reduction observed for SC-A was primarily associated with the lower number of electrodes required to achieve the same capacity, whereas the pronounced decrease for SD-A was mainly due to the process optimizations coupled with the smaller number of electrodes. In particular, the simplified production route adopted for SD-A, enabling faster mixing and eliminating the drying step, substantially reduced electricity demand during electrode fabrication. Similar findings have been widely reported in the literature, where electricity consumption during electrode processing is identified as a dominant contributor to GW in LIB manufacturing, especially at laboratory and pilot scale [515,526]. This effect was further amplified by the use of the Italian electricity mix, characterized by a higher share of renewable energy sources, which has been shown to significantly lower GW compared to more fossil-based electricity mixes commonly associated with globalized supply chains [555].

Table 6.10 – Life cycle environmental impacts calculated for the actual production of 1Ah of different types of anodes and relative percentage reduction, considering the G-A as the baseline

Global Actual Production

Impact category	Results per 1 Ah of production			Percentage reduction (%)	
	G-A	SC-A	SD-A	SC-A	SD-A
TA	0.0031	0.0019	1.96E-04	40	94
GW	1.33	0.793	0.0409	41	97
FE	1.24	0.766	0.505	38	59
ME	1.48	0.916	0.602	38	59
TE	1.42	0.839	0.252	41	82
FRS	0.431	0.255	0.0120	41	97
FET	3.29E-04	1.98E-04	1.89E-05	40	94
MET	3.00E-05	1.80E-05	1.10E-06	40	96
CHT	0.123	0.0734	0.0056	40	95
NCHT	1.01	0.600	0.166	40	84
IR	0.178	0.105	0.00414	41	98
LU	0.0283	0.0167	0.00198	41	93
MRU	0.0163	0.00897	8.73E-04	45	95
SOD	6.01E-07	3.53E-07	1.83E-08	41	97
PMF	0.0012	7.28E-04	6.94E-05	39	94
POFHH	0.0021	0.0013	8.83E-05	40	96
POFTE	0.0022	0.0013	9.34E-05	40	96
WC	0.0181	0.0106	9.9E-04	42	95

Terrestrial acidification (TA) was mainly influenced by upstream mining and metallurgical processes [322], with G-A showing higher impacts due to the larger amount of materials required to reach the target capacity and the contribution of the copper CC. Ecotoxicity categories showed a different but still coherent behavior. While the reductions observed for FE and ME were less pronounced compared to energy-related categories, a clear improvement was still evident when moving from G-A to SC-A and further to SD-A. TE showed a stronger decrease, indicating a higher sensitivity to reductions in raw material extraction and upstream processing. These results highlighted the important role of mining-related processes in driving ecotoxicity impacts, in agreement with previous LCA studies on LIB materials [322], and suggested that additional improvements could be achieved by increasing the use of recycled materials, even though recycling was not explicitly considered within the system boundaries of this study. The energy resources category, including fossil and non-renewable resources (FRS), exhibited one of the most pronounced improvements with increasing silicon content. The higher impact associated with G-A reflected the contribution of petroleum-based materials, particularly SBR, whose influence progressively decreased for SC-A and became marginal for SD-A. This trend highlighted the relevance of binder selection and formulation strategies in reducing dependence

on fossil resources, an aspect that has been increasingly emphasized in recent studies on sustainable electrode design [556]. A similar behaviour was observed for eutrophication categories (FET and MET), where both SC-A and SD-A showed consistent improvements compared to G-A, with the most significant reductions associated with the SD formulation. Human toxicity categories (CHT and NCHT) followed comparable trends, with moderate improvements for SC-A and substantially lower impacts for SD-A. IR showed one of the strongest relative decreases among all categories, with a reduction of 98% from G-A to SD-A, reflecting the combined effect of reduced electricity demand and the characteristics of the electricity mix adopted. LU was mainly influenced by the contribution of biomass-based binders, particularly CMC, and showed a clear reduction with decreasing material demand per Ah. The impacts of material resources including metals and minerals (MRU) were predominantly due to the copper CC for all chemistries, while in G-A a substantial additional contribution originated from graphite production through the energy-intensive Acheson process. The remaining categories, including stratospheric ozone depletion (SOD), particulate matter formation (PMF), photochemical oxidant formation impacting human health (POFHH), or terrestrial ecosystems (POFTE), and water consumption (WC), followed trends consistent with those described above. In all cases, SC-A showed intermediate behaviour between G-A and SD-A, while SD-A consistently exhibited the lowest impacts.

Overall, the results demonstrated that increasing silicon content, when combined with optimized manufacturing processes and a localized supply chain, enabled a substantial reduction in the environmental impacts associated with the production of 1 Ah of anodes.

6.1.10.2. Environmental impacts assessment of 1 kg anode production in a global supply chain

In contrast to the 1 Ah FU, which emphasizes performance-based benefits, the 1 kg FU highlights the much larger material scale required for anode production. To produce 1 kg of anode material, tens of thousands of electrodes were required for all chemistries, with G-A and SD-A requiring a higher number of laminates than SC-A due to differences in electrode mass. These values, reported in detail in ***Table 6.11***, clearly show how the choice of FU strongly influences both the magnitude of the impacts and their interpretation, shifting the focus from electrochemical performance to a material-based perspective.

Table 6.11 – Number of laminates and electrodes required to achieve the capacity of 1 kg

Number of elements	***G-A***	***SC-A***	***SD-A***
Laminates	933	829	933
Electrodes	~70,000	~62,150	~70,000

Overall, the general trend observed for the performance-based FU was preserved (***Figure 6.8***): increasing the silicon content led to a reduction of the environmental impacts. However, the magnitude of these reductions was significantly smaller than in the 1 Ah case, highlighting the different perspective offered by a mass-based assessment.

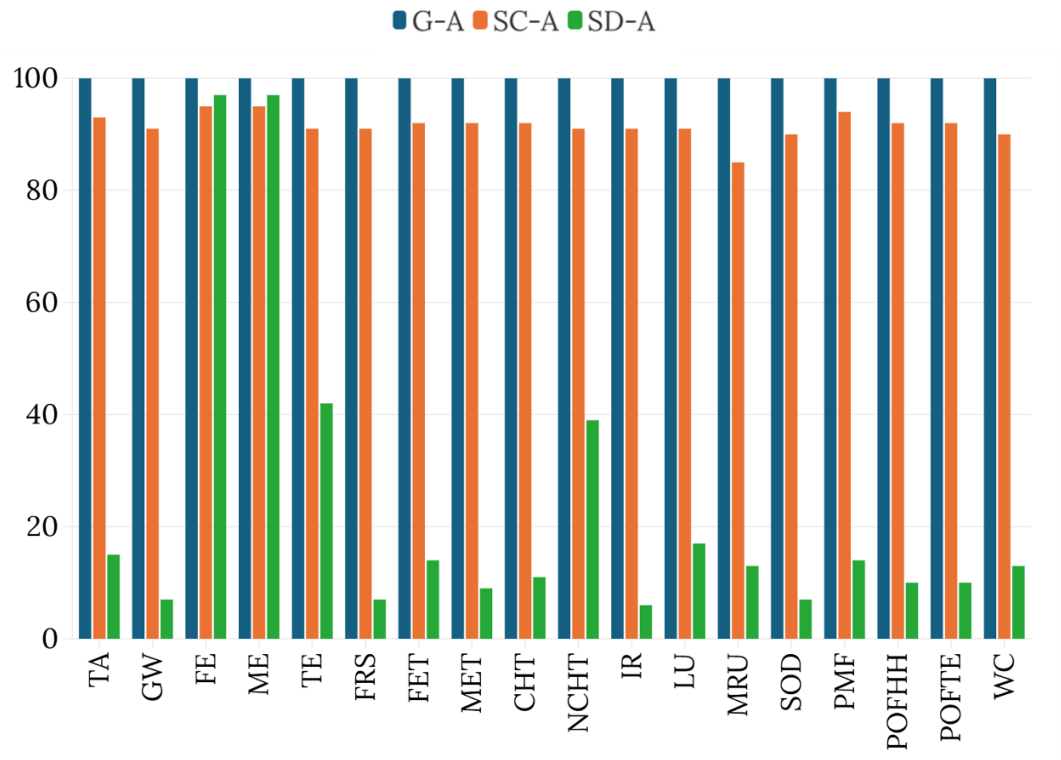

Figure 6.8 – Relative percentage reduction of environmental impacts for 1 kg of anode production across the impact categories

Consistently with previous findings reported in the literature [518], the addition of 10 wt% of silicon does not result in significant reductions in environmental impact. In the case of SC-A, which contains around 10 wt% of silicon, the reductions relative to G-A remained modest across most categories, typically below 10%, with MRU representing a notable exception, where a more visible decrease was observed. In contrast, SD-A, characterized by a silicon content of 80 wt%, exhibited pronounced reductions across the majority of the impact categories, generally ranging between about 60% and 90% (***Table 6.12***). Nevertheless, FE and ME showed more limited improvements, reflecting the high contribution of the silicon production process, which became more prominent when impacts were based on the electrode mass [521].

Table 6.12 – Life cycle environmental impacts calculated for the actual production of 1kg of different types of anodes and relative percentage reduction, considering the graphite anode as the baseline

	Global Actual Production				
Impact category	**Results per 1 kg of production**			**Percentage reduction (%)**	
	G-A	**SC-A**	**SD-A**	**SC-A**	**SD-A**
TA	0.364	0.337	0.0552	7	85
GW	157	144	11.5	9	93
FE	146	139	142	5	3
ME	174	166	169	5	3
TE	167	152	70.7	9	58
FRS	50.8	46.2	3.37	9	93
FET	0.0387	0.0358	0.0053	8	86
MET	0.0035	0.0033	0.0003	8	91
CHT	14.5	13.3	1.56	8	89
NCHT	119	109	46.5	9	61
IR	21.0	19.1	1.16	9	94
LU	3.33	3.02	0.556	9	83
MRU	1.92	1.62	0.245	15	87
SOD	7.08E-05	6.39E-05	5.14E-06	10	93
PMF	0.141	0.132	0.0195	6	86
POFHH	0.246	0.226	0.0248	8	90
POFTE	0.263	0.242	0.0262	8	90
WC	2.13	1.91	0.278	10	87

TA showed a clear decrease moving from G-A to SD-A, while SC-A exhibited only a minor reduction compared to G-A. A similar behaviour was observed for GW, where G-A presented the highest emissions, SC-A showed only a limited improvement, and SD-A exhibited a marked reduction. This confirmed that, even when adopting a mass-based FU, the SD chemistry benefited from process optimization and reduced energy demand during manufacturing, although the relative advantage was less pronounced than for the 1 Ah FU. A different trend emerged for ecotoxicity categories. For FE and ME, SC-A showed the expected decrease compared to G-A, consistently reflecting the lower material demand associated with the partial substitution of graphite. In contrast, although SD-A still exhibited a reduction relative to G-A, its impact values remained higher than those of SC-A. This indicates that the high silicon content, and in particular its energy-intensive production process, counterbalanced part of the benefits associated with reduced electrode quantity, resulting in intermediate performance between SC-A and G-A for these categories. FRS further highlighted the role of binder selection. While G-A and SC-A exhibited comparable values due to the contribution of petroleum-based SBR, SD-A showed a drastic reduction, reflecting the absence of SBR and the lower dependence on fossil-derived inputs. Similar considerations applied to eutrophication categories, where

SC-A showed limited improvements, while SD-A achieved substantial reductions. Human toxicity categories followed the same overall behavior. SC-A exhibited only minor improvements relative to G-A, while SD-A showed a strong decrease for both CHT and NCHT, confirming the dominant influence of material demand and production routes at this scale. IR also exhibited a pronounced reduction for SD-A, while the difference between G-A and SC-A remained limited. LU was mainly influenced by binder choice. The small difference between G-A and SC-A was associated with the use of CMC in both systems, whereas the adoption of PAA for SD-A resulted in a significantly lower impact. MRU similarly benefited from the SD formulation, although the contribution of the copper CC remained relevant across all chemistries. The remaining categories, including SOD, PMF, POFHH, POFTE, and WC, followed trends consistent with those described above, with SC-A showing limited reductions and SD-A consistently exhibiting the lowest impacts.

In summary, the comparison between the two FUs clearly showed that the environmental advantages of silicon-based anodes were more evident when evaluated using a performance-based FU, such as 1 Ah, rather than a mass-based metric like 1 kg. Nevertheless, even under the 1 kg FU, the SD anode demonstrated substantial reductions across most impact categories, confirming its potential to lower the environmental footprint of anode production when combined with optimized manufacturing processes and cleaner energy mixes.

6.1.10.3. Material composition and the relative contribution of anode components to environmental impacts

The contribution analysis of individual anode components considering the FU of 1 Ah, highlighted a strong dependence of environmental impacts on both material composition and anode chemistry. Overall, the impacts were distributed among AMs, CA, binders, and CC, with the relative importance of each component varying significantly depending on the anode formulation. In general, G-A electrodes were mainly influenced by the contribution of CC, while for silicon-based anodes the production of the active material itself contributed in a non-negligible amount. This change reflected the higher energy intensity and material demand associated with silicon-related processes compared to conventional graphite-based anodes.

For G-A, the copper CC represented the main contributor across most impact categories, often being responsible for the majority of the total impact (***Figure 6.9a***). This dominance was less evident in FRS, where the petroleum-based SBR binder played a role due to its fossil origin. In the case of MRU, both graphite and copper contributed significantly, as synthetic graphite in the Ecoinvent 3.11 database was modelled through the Acheson process, which relies on petroleum coke and energy-intensive processing. When the CC was excluded from the

analysis (***Figure 6.9b***), the relative contributions of the remaining components became more balanced, with graphite dominating MRU, conductive additives and SBR contributing to FRS, and CMC becoming relevant for LU due to its biomass-based production pathway.

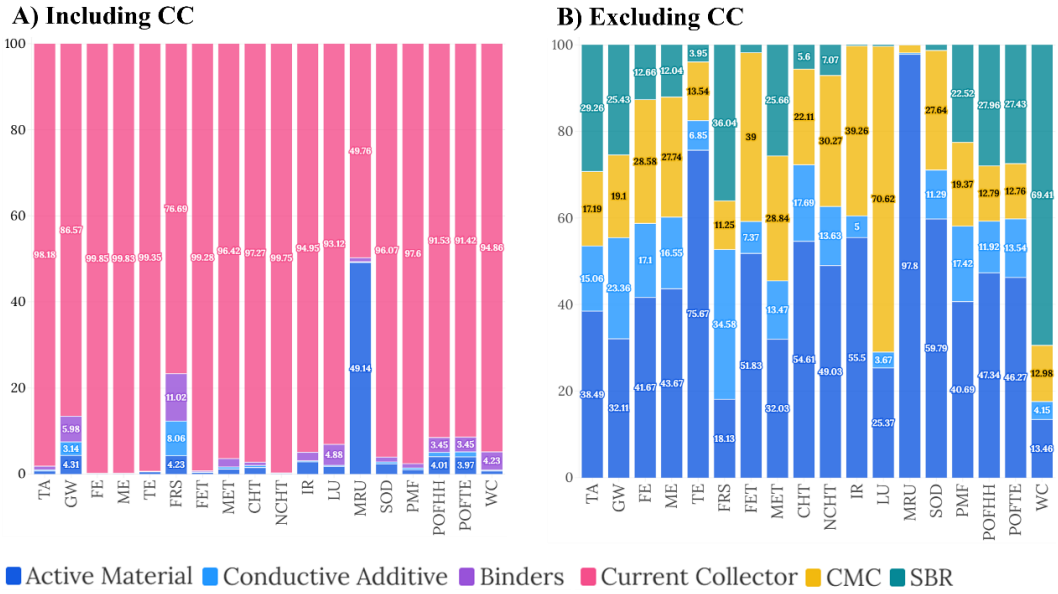

Figure 6.9 – Relative contribution of anode components for G-A: a) including active material, conductive additive, binders, and current collector; b) excluding the current collector.

In SC-A, the contribution percentages changed substantially (***Figure 6.10***). The precursors of silicon carbide emerged as the dominant contributor across most impact categories, largely outweighing the effects of binders, conductive additives, and CC (***Figure 6.10a***). This behaviour was primarily associated with the highly energy-intensive production process of silicon carbide, which resulted in higher impacts compared to graphite-based materials. When excluding the CC (***Figure 6.10b***), the predominance of the silicon carbide became even more pronounced, while the contributions of the other components remained marginal.

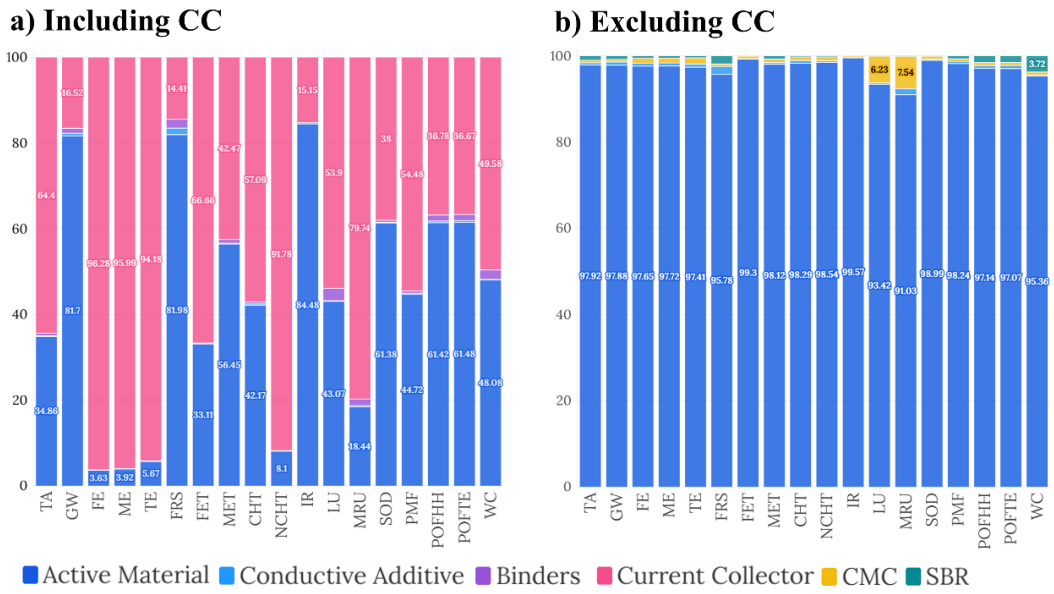

Figure 6.10 – Relative contribution of anode components for SC-A: a) including active material, conductive additive, binders, and current collector; b) excluding the current collector.

A similar trend was observed for SD-A (***Figure 6.11***). In this case, silicon production constituted the main driver of environmental impacts across nearly all categories, reflecting both its high mass fraction and the energy-intensive nature of its production process [521]. For this anode chemistry, when the CC is excluded (***Figure 6.11b***) the contribution of the binder becomes more noticeable than in the other anode formulations due to the higher binder content required for SD-A electrodes. In particular, the use of PAA, whose monomer originates from fossil resources, contributed to FRS and MRU [470].

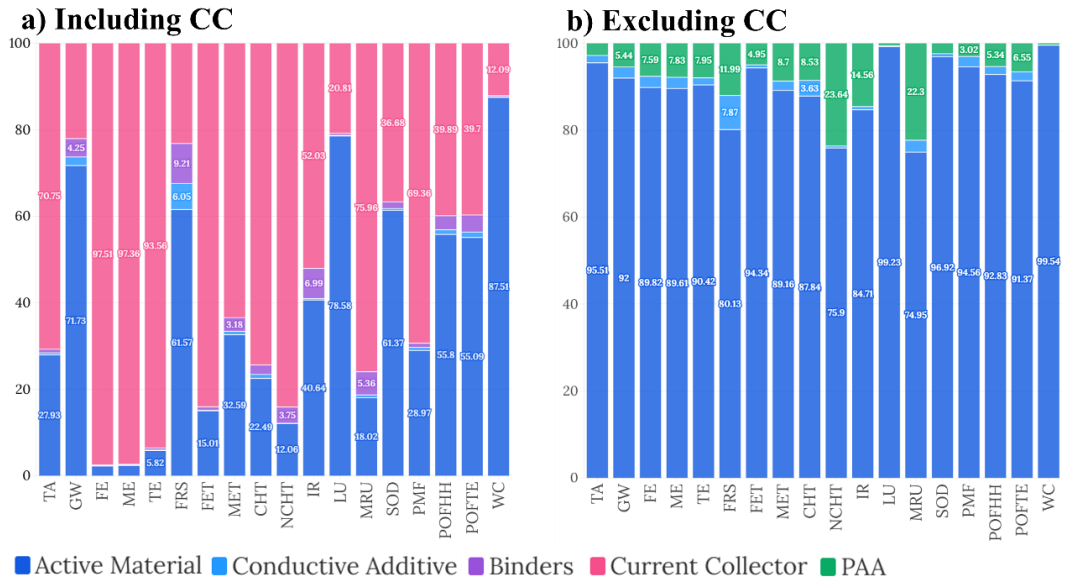

Figure 6.11 – Relative contribution of anode components for SD-A: a) including active material, conductive additive, binders, and current collector; b) excluding the current collector.

Based on these considerations, the following sections describe and discuss the calculated impacts in more detail, with a focus on the effects of anode chemistry, FU definition, supply chain assumptions, and uncertainty analysis.

6.1.10.4. Sensitivity analysis: how European supply chain impacts on the anodes production

To investigate the role of supply chain localization on the environmental performance of anode production, a sensitivity analysis was conducted by comparing the baseline global supply scenario with a hypothetical scenario in which all materials were sourced within Europe. This analysis was designed to support a broader discussion on the potential benefits of strengthening a European battery value chain, rather than to provide a detailed representation of alternative production technologies.

In the baseline scenario, most key inputs required for anode manufacturing, including active materials, conductive additive, binders, and CC, were supplied from outside Europe, reflecting current market conditions dominated by Asian producers. In the alternative scenario, the same materials were instead modelled as being supplied by European manufacturers, while maintaining identical material compositions and processing conditions. Transportation was modelled consistently with the methodology adopted in the previous chapters, using data from the Ecoinvent 3.11 database based on Eurostat statistics. Average transport distances were assigned according to material category, with chemicals modelled using the RER-08 classification and metallic components assigned to the RER-10 category. This ensured methodological coherence across the entire LCA framework.

It is important to emphasize that this sensitivity analysis focused exclusively on changes in transportation routes and the electricity mix associated with material supply. Production processes for raw materials were intentionally kept unchanged, even though European and non-European production routes may differ in terms of efficiency and technological maturity. This choice limits additional uncertainty and preserves the interpretability of the results. As a consequence, the analysis should be interpreted as a conservative estimate of the potential benefits associated with supply chain localization.

Figure 6.12 shows a chord diagram comparing the contribution of materials and processing steps to the overall environmental impact of G-A. This type of representation highlights the relative importance of raw materials (e.g., AM, CC, water) and manufacturing processes (e.g., mixing, coating, drying, transport, electricity), with the width of each segment proportional to its contribution. In both supply-chain scenarios, the dominant contributions are associated with the CC, water consumption, mixing and drying processes, confirming the relevance of both material inputs and energy-intensive manufacturing steps. However, a

noticeable difference between the two scenarios lies in the relative contribution of transport and electricity. In the global supply-chain scenario (***Figure 6.12a***), transport plays a more significant role due to longer distances and more complex logistics, whereas in the European scenario (***Figure 6.12b***) its contribution is reduced. Conversely, the impact associated with electricity remains relevant in both cases, reflecting the energy demand of the production process, although it may vary depending on the electricity mix. Overall, the comparison highlights how supply-chain localization can reduce transport-related impacts, while shifting the relative importance toward process-related contributions, emphasizing the need to optimize both material sourcing and manufacturing efficiency.

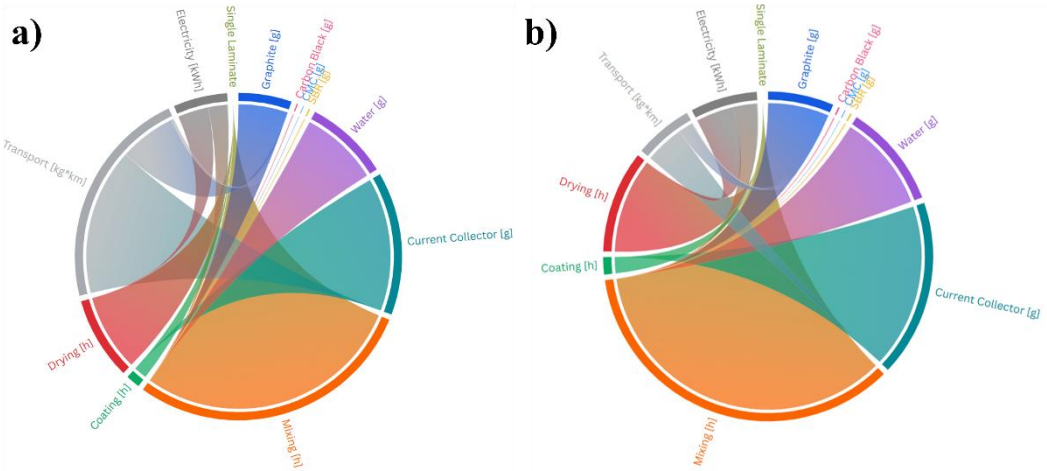

Figure 6.12 – Comparison of the contribution of materials and processing steps to the overall environmental impact of G-A under different supply-chain scenarios: a) global and b) European.

A similar distribution is observed for the SC-A configuration (***Figure 6.13***), with the main contributions still associated with the CC, water consumption, and energy-intensive processing steps such as mixing and drying. Compared to the G-A, the presence of the SC slightly shifts the relative contribution of material inputs, although process-related impacts remain dominant. As in the G-A case, supply-chain localization primarily affects transport-related contributions, which are reduced in the European scenario, while the role of electricity remains significant due to the energy demand of the manufacturing process.

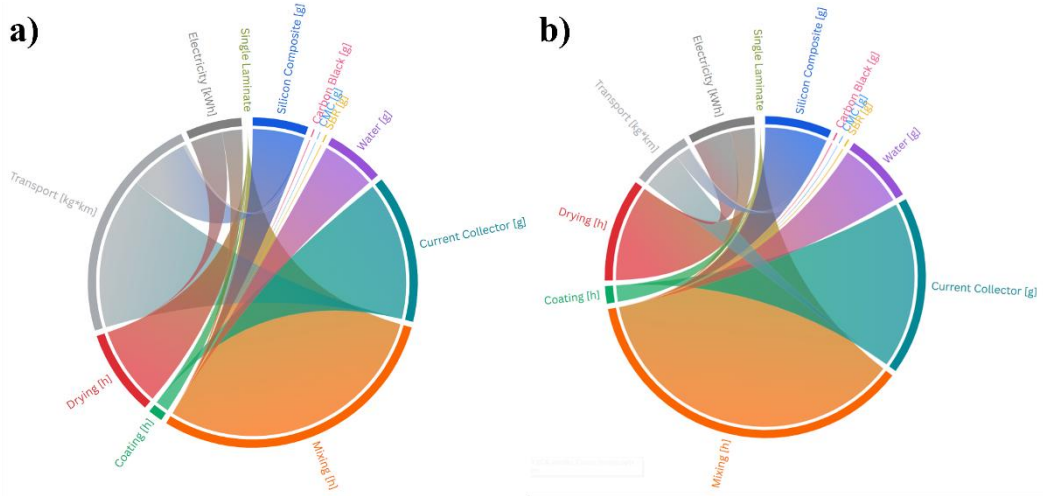

Figure 6.13 – Comparison of the contribution of materials and processing steps to the overall environmental impact of SC-A under different supply-chain scenarios: a) global and b) European.

For the SD-A configuration (***Figure 6.14***), the distribution of contributions shows a more pronounced shift toward material-related impacts, with silicon and the CC becoming the dominant contributors. Compared to both G-A and SC-A systems, the higher silicon content increases the relative importance of raw material production, while the contribution of processing steps such as mixing and coating becomes less relevant. As in the previous cases, supply-chain localization mainly reduces transport-related impacts, whereas the influence of electricity remains significant due to the energy requirements of the production process. This highlights how, for SD-A, material sourcing plays an even more critical role in determining the overall environmental performance.

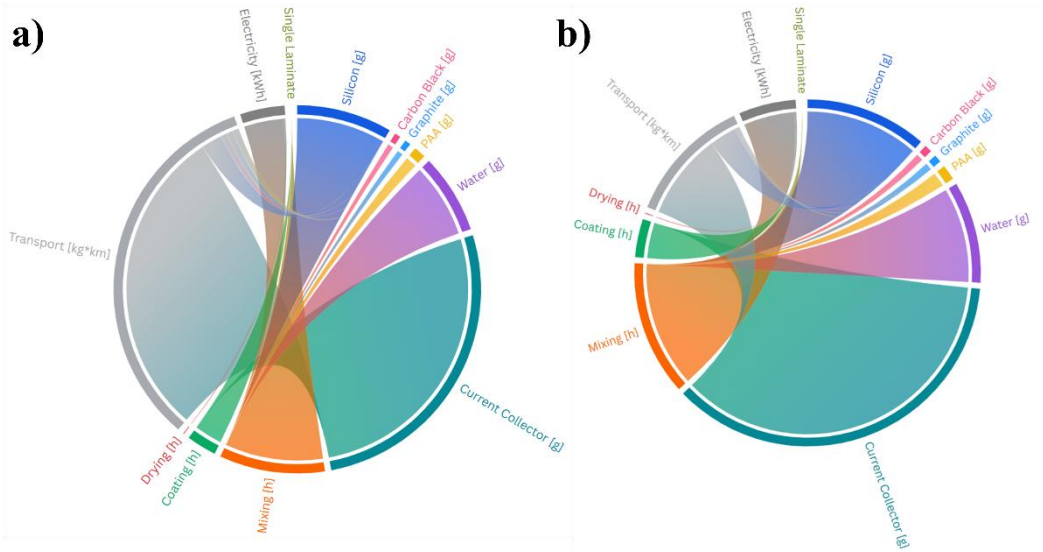

Figure 6.14 – Comparison of the contribution of materials and processing steps to the overall environmental impact of SD-A under different supply-chain scenarios: a) global and b) European.

Consistent trends are observed across all anode chemistries, as further quantified in ***Figure 6.15***. A fully European scenario consistently reduced GW

across all anode chemistries, mainly due to the higher share of renewable energy sources in the European electricity mix compared to the baseline scenario. These findings align with previous studies showing that the carbon footprint of battery materials is strongly influenced by the electricity mix, in particular, a higher share of electricity from renewable resources has been consistently associated with a significant reduction in cradle-to-gate emissions of battery production [557]. Beyond GW, improvements were also observed for FRS, reflecting a reduced dependence on fossil energy carriers when European electricity generation was assumed. These results are particularly relevant in the context of ongoing European strategies aimed at reducing reliance on imported fossil resources and critical raw materials, and at increasing regional self-sufficiency in battery manufacturing [550].

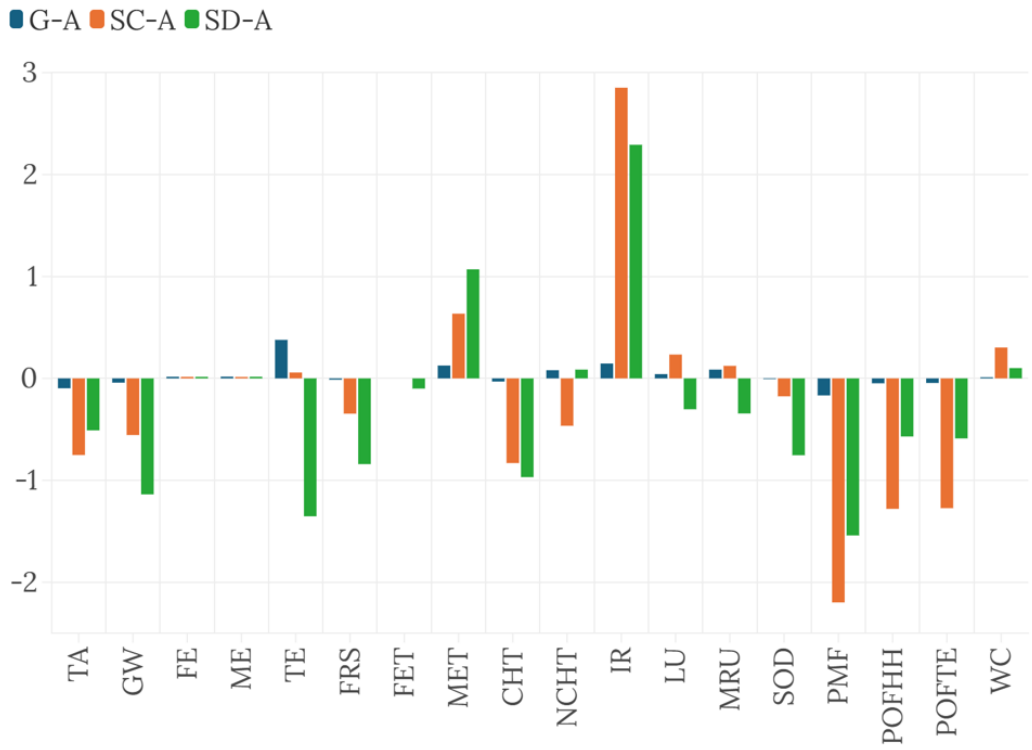

Figure 6.15 – Comparison between the current global supply chain and the hypothetical European supply chain scenario: the percentage variation is shown for each case: values below zero indicate a reduction in impacts, whereas values above zero indicate an increase in impacts.

Not all impact categories benefited equally from the European scenario. For FE and ME, impacts were slightly higher when materials were sourced within Europe. This trend can be attributed to differences in mining activities and upstream chemical processes. Primary extraction and metallurgical treatments are well-known drivers of ecotoxicity categories in battery LCAs, due to the release of heavy metals and the use of energy-intensive reagents during mineral processing [558]. Although transport distances are reduced in a European scenario, raw material extraction impacts remain dominant for these categories. A

similar consideration applies to MET, for which previous LCA studies have demonstrated that the use of recycled materials significantly reduces impacts associated with primary raw material extraction and processing [559]. This confirms that localization alone is insufficient to substantially lower ecotoxicity impacts without parallel improvements in circular economy flows. For IR, the European scenario showed higher impacts compared to the global baseline. This behavior is consistent with the higher share of nuclear energy in the European electricity mix, which is the main contributor to the IR category [515]. Therefore, while electricity decarbonization reduces GW, it may simultaneously increase IR depending on the specific composition of the energy mix.

Overall, these results indicate that strengthening a European supply chain can contribute to reducing the environmental impacts of anode production, particularly for GW and FRS. However, the benefits are not uniform across all impact categories: while climate-related and fossil resource indicators improve depending on localization, ecotoxicity and IR remain strongly influenced by the regional electricity mix. Although this sensitivity analysis does not account for potential differences in production technologies or efficiencies, it provides a robust indication of the direction and magnitude of the expected benefits, supporting the strategic relevance of supply chain localization for the environmental sustainability of future battery technologies.

6.1.10.5. Uncertainties evaluation through MCS

The uncertainty trends observed in this work are consistent with previous probabilistic LCAs on LIB systems, where Monte Carlo approaches are commonly used to propagate uncertainty from background datasets to impact results. For instance, Lavigne Philippot et al. [322] quantified uncertainty via Monte Carlo analysis in an LCA of a prototype LIB with a silicon-rich anode, showing that uncertainty propagation is particularly relevant when upstream processes are energy-intensive and strongly dependent on the electricity mix. Similarly, Cox et al. [560] highlighted that uncertainty in electricity-related parameters and upstream material datasets can substantially affect climate-related indicators, reinforcing the need to report uncertainty when comparing emerging battery technologies. In this context, the use of a Pedigree-matrix-based approach to derive uncertainty factors is aligned with the Ecoinvent 3.11 uncertainty methodology, whose pedigree factors and their empirical basis have been critically discussed and refined in the literature [561]. Finally, the relatively limited dispersion obtained here, and the consistently narrower distribution for SD-A, are coherent with the idea that tighter control of foreground processes and better-defined sourcing reduce uncertainty propagation; comparable conclusions have also been reported in battery-focused uncertainty studies adopting Monte Carlo and Bayesian Monte Carlo approaches [554].

To evaluate the robustness of the results and quantify the influence of input data variability, a MCS was conducted focusing on GW. This category was selected as the primary target of the uncertainty analysis because it represents the most relevant indicator in battery environmental sustainability assessment and is strongly influenced by energy-related background processes, which are typically among the main sources of uncertainty in LCA studies.

For each configuration, three independent simulation runs were performed with 10,000 iterations each. The number of iterations was selected to ensure statistical convergence of the distributions and stability of the mean and variance values, in line with common practice in probabilistic LCA studies. Only one representative run is presented here, as the three simulations showed negligible deviations, confirming reproducibility.

Uncertainty modelling was primarily concerned with background processes, since all foreground data were derived from direct laboratory measurements. Material quantities, process times, and equipment power ratings were experimentally recorded, which significantly reduced the variability associated with foreground data. However, background processes, such as electricity production, transport, and upstream material production, were characterized by inherent uncertainty due to their reliance on generic datasets. Electricity consumption was quantified with high precision in terms of kWh demand. Nevertheless, the exact electricity sourcing could not be specified beyond the regional mix, and therefore uncertainty was introduced through the Pedigree matrix. Low uncertainty scores were assigned for reliability and completeness, while moderate uncertainty was associated with geographical and technological representativeness. Transport modelling exhibited comparatively higher uncertainty. Distances and transport modes were derived from representative Ecoinvent 3.11 datasets rather than direct tracking. As a result, higher uncertainty factors were assigned to transport processes. This distinction between electricity and transport uncertainties reflects the different levels of controllability of these parameters within a laboratory-scale system.

The coefficient of variability for the FU of 1 Ah, reported in ***Table 6.13***, was calculated from the MCS results following the approach described by Gao et al. [554]. The values obtained were systematically lower than those reported in the cited study, indicating a limited dispersion of results. In particular, G-A and SC-A exhibited a coefficient of variability of approximately 2.4 %, while SD-A showed a slightly lower value of 2.0 %, consistently representing the lowest variability among the investigated chemistries. This behaviour can be attributed to several factors. First, the SD-A configuration was characterized by a more simplified and optimized production process. Second, the lower electricity demand per FU reduced the contribution of energy-related uncertainty. Finally, the more localized sourcing of silicon reduced the uncertainty associated with transport modelling, further contributing to the overall robustness of the results.

Table 6.13 – Monte Carlo simulation results for GW for the electrode production system per 1 Ah under both Global and European supply chain scenarios.

	Unit	Actual Global Production - 1Ah			European Supply Chain - 1Ah		
		G-A	SC-A	SD-A	G-A	SC-A	SD-A
Trials	-	10,000	10,000	10,000	10,000	10,000	10,000
Base Case	kg CO_2-Eq	1.3341	0.7928	0.0409	1.3335	0.7884	0.0404
Mean	kg CO_2-Eq	1.3338	0.7930	0.0409	1.3346	0.7883	0.0404
Median	kg CO_2-Eq	1.3306	0.7911	0.0408	1.3313	0.7863	0.0403
Standard Deviation	kg CO_2-Eq	0.0328	0.0196	0.0008	0.0334	0.0198	0.0008
5% percentile	kg CO_2-Eq	1.2856	0.7644	0.0396	1.2857	0.7596	0.0391
95% percentile	kg CO_2-Eq	1.3914	0.8279	0.0423	1.3941	0.8231	0.0419
Coefficient of variability	%	2.4621	2.4755	2.0407	2.5028	2.5149	2.0830
Minimum	kg CO_2-Eq	1.2422	0.7394	0.0382	1.2267	0.7306	0.0376
Maximum	kg CO_2-Eq	1.5116	0.9064	0.0472	1.4994	0.9015	0.0444

For the 1 Ah FU (***Figure 6.16***), mean and median values deviated only marginally from the deterministic base-case results, confirming that uncertainty propagation did not alter the comparative ranking of the anodes. The distributions were quasi-Gaussian for G-A and SC-A, whereas SD-A exhibited a narrower and slightly asymmetric profile, indicating lower sensitivity to background variability.

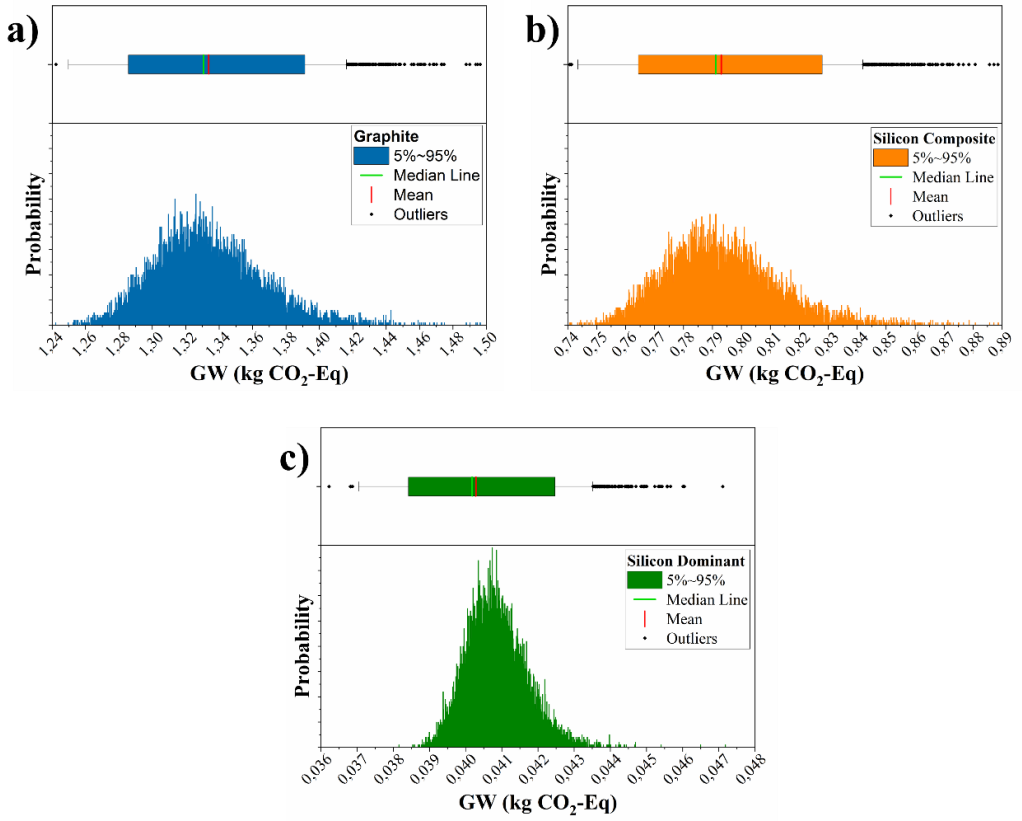

Figure 6.16 – Normal distributions obtained from 10,000 MCS for GW related to the actual production of 1 Ah. For each chemistry, the upper panel shows the box plot including mean, median, and outliers, while the lower panel presents the corresponding frequency histogram: a) G-A; b) SC-A; c) SD-A.

The coefficient of variability calculated for the FU of 1 kg (***Table 6.2***) was fully consistent with the values obtained for the FU of 1 Ah. For both G-A and SC-A, the coefficient of variability remained around 2.4 %, while for SD-A it remained stable at around 2.0 %. These results confirm that the level of uncertainty, described by the coefficient of variability, was comparable across the two FUs. These findings indicate that changing the FU from a performance-based to a mass-based perspective did not significantly affect the overall uncertainty variability of the system.

Table 6.14 – Monte Carlo simulation results for GW for the electrode production system per 1 kg under both Global and European supply chain scenarios.

	Unit	Actual Global Production - 1Ah			European Supply Chain - 1Ah		
		G-A	SC-A	SD-A	G-A	SC-A	SD-A
Trials	-	10,000	10,000	10,000	10,000	10,000	10,000
Base Case	kg CO_2-Eq	157.1142	143.5169	11.4718	157.0483	142.7188	11.3415
Mean	kg CO_2-Eq	157.0985	143.5425	11.4709	157.0415	142.7508	11.3463
Median	kg CO_2-Eq	156.7379	143.2377	11.4541	156.6737	142.3461	11.3295
Standard Deviation	kg CO_2-Eq	3.8911	3.5115	0.2303	3.9534	3.5295	0.2363
5% percentile	kg CO_2-Eq	151.4691	138.3827	11.1235	151.2893	137.6299	10.9925
95% percentile	kg CO_2-Eq	164.1089	149.786	11.8776	164.0672	149.0629	11.7608
Coefficient of variability	%	2.4769	2.4463	2.0073	2.5174	2.4725	2.0823
Minimum	kg CO_2-Eq	145.6578	133.9103	10.7473	144.804	133.1589	10.6145
Maximum	kg CO_2-Eq	179.3978	161.2133	12.6341	179.4976	165.1889	12.7485

The normal distributions presented a similar pattern also for the 1 kg FU (***Figure 6.17***). However, in this case, the distributions of G-A and SC-A were closer, reflecting the reduced performance advantage when impacts are normalized per unit mass rather than per delivered capacity.

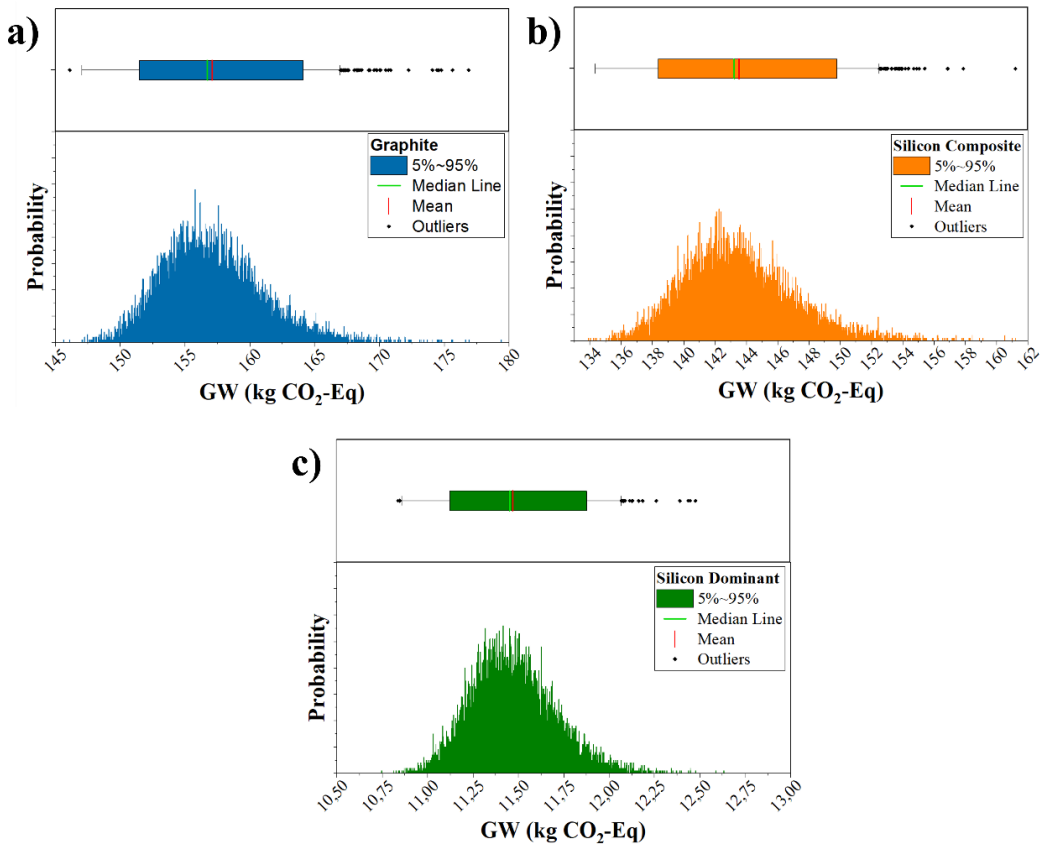

Figure 6.17 – Normal distributions obtained from 10,000 MCS for GW related to the actual production of 1 kg. For each chemistry, the upper panel shows the box plot including mean, median, and outliers, while the lower panel presents the corresponding frequency histogram: a) G-A; b) SC-A; c) SD-A.

When comparing the global and European supply chain scenarios both for 1 Ah (***Figure 6.18***) and 1 kg (***Figure 6.19***), the distribution shapes remained consistent, but SC-A and especially SD-A showed a visible shift of the GW distributions toward lower values under the European configuration. G-A, in contrast, exhibited only marginal variation. This suggests that localizing the supply chain contributes more effectively to reducing uncertainty when the system is strongly influenced by energy-intensive materials, such as silicon.

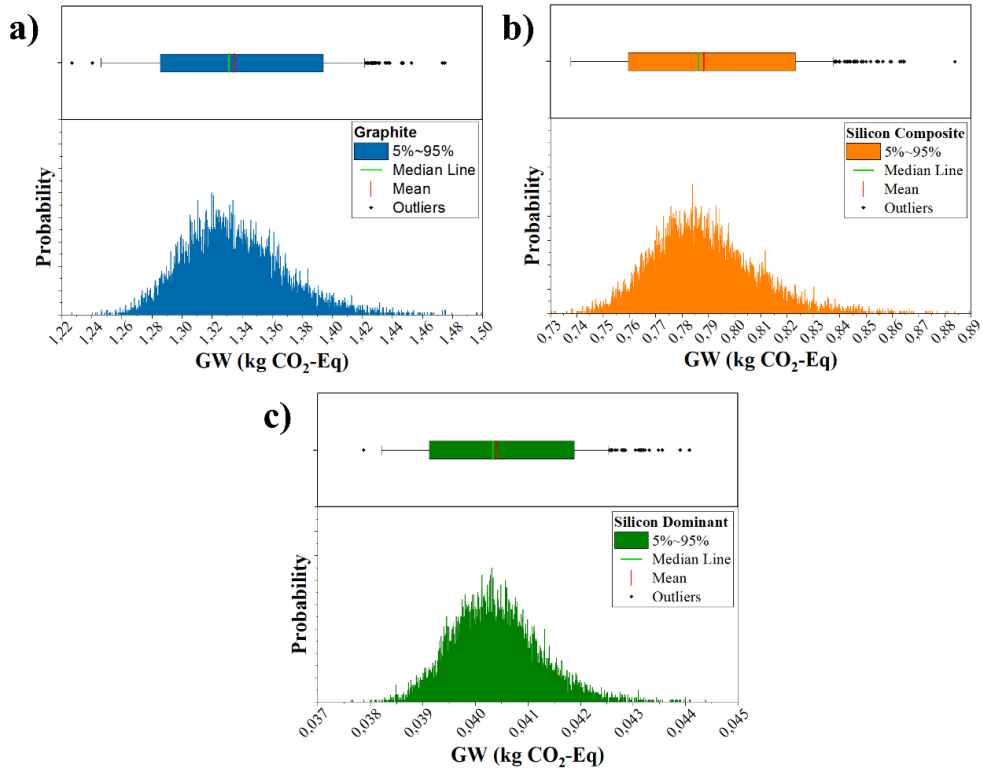

Figure 6.18 – Normal distributions obtained from 10,000 MCS for GW related to the theoretical European supply chain of 1 Ah. For each chemistry, the upper panel shows the box plot including mean, median, and outliers, while the lower panel presents the corresponding frequency histogram: a) G-A; b) SC-A; c) SD-A.

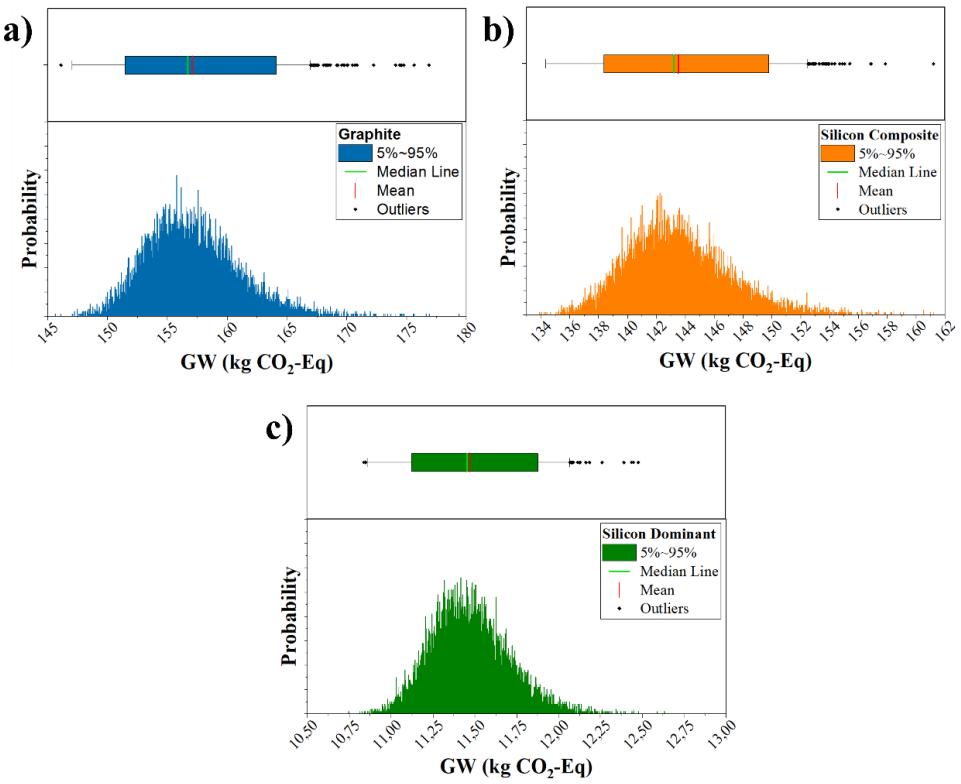

Figure 6.19 – Normal distributions obtained from 10,000 MCS for GW related to the theoretical European supply chain of 1 kg. For each chemistry, the upper panel shows the box plot including mean, median, and outliers, while the lower panel presents the corresponding frequency histogram: a) G-A; b) SC-A; c) SD-A.

A total comparison of the MCS is reported in ***Figure 6.20***. The figure clearly shows that the differences in GW among the three chemistries are clear and remain visible even when uncertainty is considered. The distributions have limited overlap, especially for the 1 Ah FU, where SD-A is consistently separated from G-A and SC-A within the 5–95% range (***Figure 6.21***). This confirms that the lower impact of SD-A is not only a deterministic result, but also remains valid under stochastic analysis. Moreover, the narrower distribution observed for SD-A reflects a lower sensitivity to uncertain inputs, particularly under the European supply chain scenario, confirming that process optimization and localized sourcing improve both environmental performance and result stability.

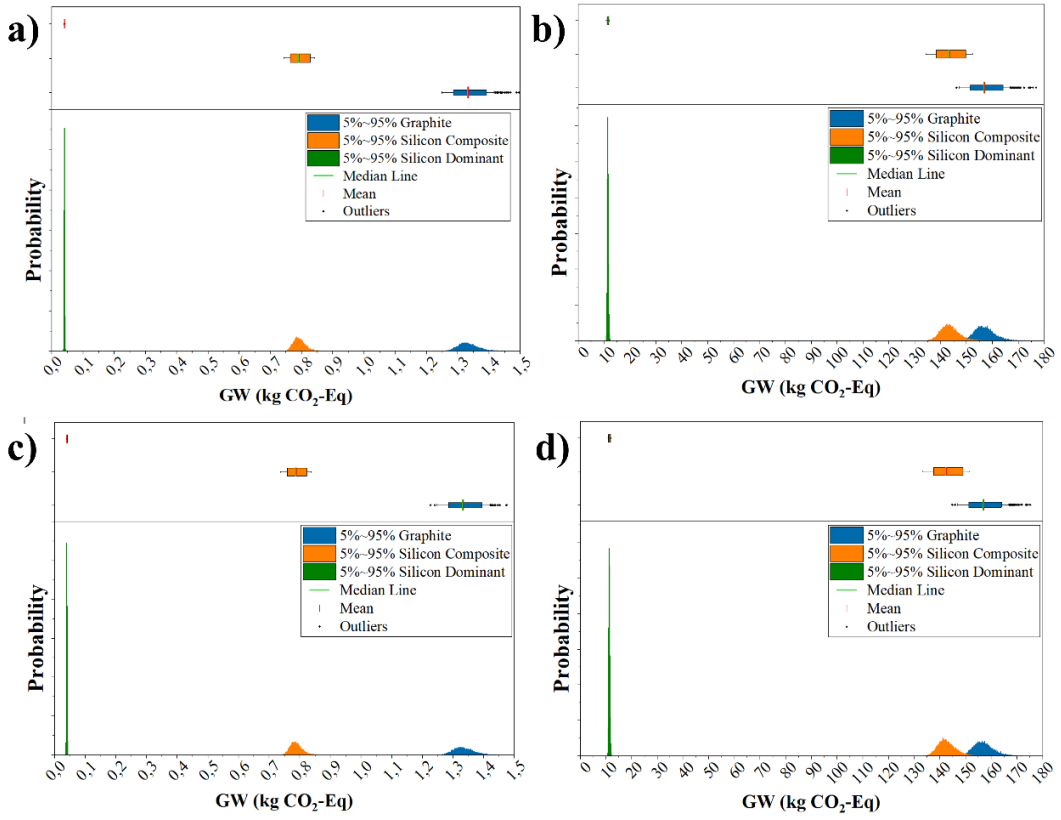

Figure 6.20 – Comparison of the normal distributions obtained from 10,000 MCS for GW across the three anode chemistries: (a) actual production of 1 Ah; (b) actual production of 1 kg; (c) European theoretical supply chain for 1 Ah; (d) European theoretical supply chain for 1 kg.

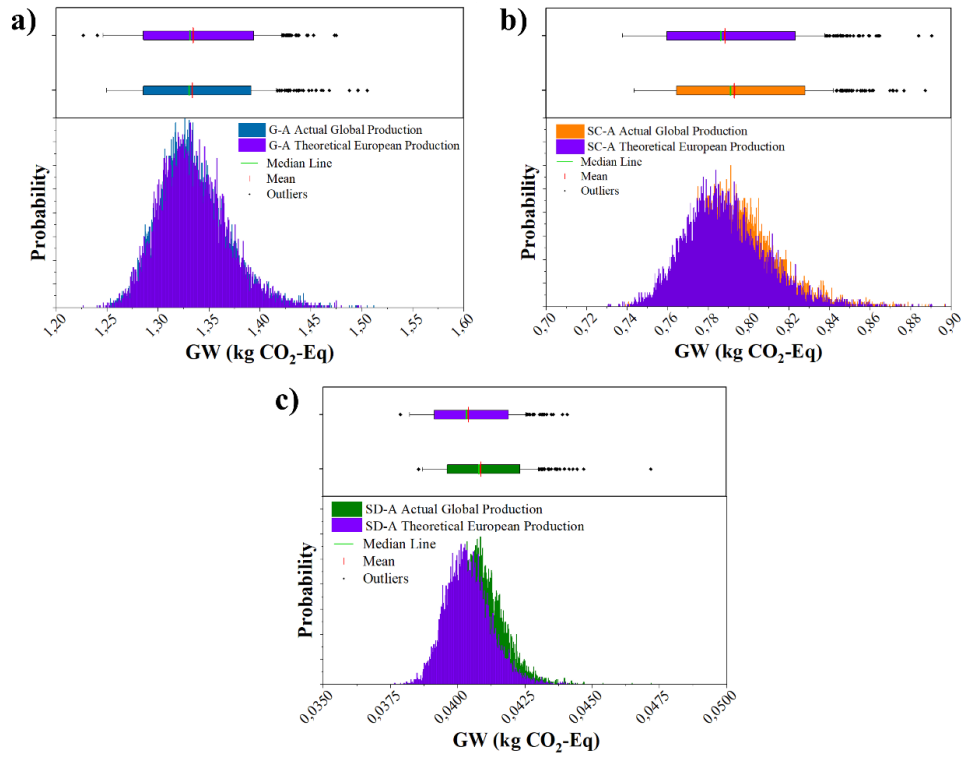

Figure 6.21 – Comparison of the MCS conducted for the actual global production and the theoretical European supply chain of 1 Ah: a) G-A; b) SC-A; c) SD-A.

It is important to underline that the Monte Carlo analysis captures uncertainty embedded in background datasets but does not account for structural uncertainty, such as alternative modelling assumptions, future technological changes, or potential improvements in industrial efficiency. In particular, the Pedigree matrix approach, while widely adopted, relies on qualitative judgement and cannot fully represent technological variability in emerging materials such as advanced silicon-based anodes. Moreover, the laboratory-scale nature of the system implies that some uncertainties, especially those related to scaling effects, are not captured in this probabilistic assessment. Industrial-scale production could introduce additional variability associated with continuous processes, quality control systems, and different supply-chain dynamics. Despite these limitations, the limited spread of the distributions, especially for SD-A, indicates that the observed reductions in GW are not artefacts of modelling variability but reflect structural differences in material intensity, process simplification, and supply-chain configuration. The lower dispersion associated with SD-A suggests that higher technological maturity and process control not only reduce environmental burdens but also decrease modelling uncertainty.

Overall, the uncertainty analysis strengthens the reliability of the comparative conclusions and supports the robustness of the identified environmental advantages of SD-A when combined with optimized manufacturing and localized sourcing strategies.

6.1.10.6. Evaluation of endpoint impact categories

To complement the midpoint discussion and provide a higher-level interpretation of the results, the inventory data were also evaluated using the ReCiPe 2016 Endpoint (H) method, which aggregates the 18 midpoint indicators into three damage categories: EQ, HH, and NR. This aggregation enables a systematic interpretation of potential long-term damage, linking material selection and manufacturing choices to overall environmental performance.

The endpoint results for the actual global production (***Table 6.15***) revealed a clear and consistent ranking among chemistries. Under the 1 Ah FU, a marked separation emerged across all three damage categories. EQ and HH progressively decreased from G-A to SC-A, while SD-A showed a reduction of approximately one order of magnitude. For NR, the reduction associated with SD-A reached nearly two orders of magnitude compared to G-A. This confirmed that higher electrochemical capacity, translated into lower material demand per unit of delivered energy, strongly affected endpoint resource depletion.

Table 6.15 – Endpoint impact results for the production of 1 Ah and 1 kg of anodes under the actual global supply chain scenario.

	Global Actual Production					
Endpoint Category	**Results per 1 Ah of production**			**Results per 1 kg of production**		
	G-A	**SC-A**	**SD-A**	**G-A**	**SC-A**	**SD-A**
Ecosystem quality [species.yr]	6.422E-09	3.846E-09	6.271E-10	7.563E-07	6.962E-07	1.761E-07
Human health [DALYs]	2.671E-06	1.599E-06	1.401E-07	3.146E-04	2.895E-04	3.933E-05
Natural resources [USD 2013]	0.141	0.083	0.004	16.628	15.090	1.100

When the analysis was conducted using the 1 kg FU, the same reduction order among chemistries was preserved, but the relative differences were less pronounced. Although SD-A still exhibited the lowest damage, the magnitude of the reduction was smaller than the 1 Ah FU. This confirmed that mass-based FU reduced the environmental advantage of SD-A by focusing on material production rather than electrochemical performance. In contrast, performance-based FU more effectively highlighted the environmental sustainability benefits of innovative anode chemistries. Across both FUs, NR consistently represented the dominant damage category. This behaviour indicated that resource extraction and primary material production remain the main responsible of environmental impacts in anode production.

When the theoretical European supply chain scenario was considered (***Table 6.16***), the variations relative to the global case were measurable but limited for both FUs. For the 1 Ah FU, EQ for G-A shifted only marginally from $6.422 \cdot 10^{-9}$

to $6.420 \cdot 10^{-9}$ species·yr, with similarly small reductions for SC-A and SD-A. HH decreased slightly for all chemistries, with SD-A moving from $1.40 \cdot 10^{-7}$ to $1.39 \cdot 10^{-7}$ DALYs. NR remained essentially unchanged for G-A and SC-A and showed only a minor decrease for SD-A.

Table 6.16 – Endpoint impact results for the production of 1 Ah and 1 kg of anodes under the actual global supply chain scenario.

	Theoretical European Supply Chain					
Endpoint Category	**Results per 1 Ah of production**			**Results per 1 kg of production**		
	G-A	**SC-A**	**SD-A**	**G-A**	**SC-A**	**SD-A**
Ecosystem quality [species.yr]	6.420E-09	3.830E-09	6.254E-10	7.561E-07	6.933E-07	1.756E-07
Human health [DALYs]	2.669E-06	1.582E-06	1.388E-07	3.143E-04	2.865E-04	3.898E-05
Natural resources [USD 2013]	0.141	0.083	0.004	16.632	15.092	1.094

These results indicated that geographic relocation alone did not fundamentally reduce aggregated damage. While shorter transport distances and a cleaner electricity mix slightly benefited EQ and HH, the NR category remained primarily governed by upstream extraction processes, which were not structurally modified by localization alone. As illustrated in ***Figure 6.22***, percentage reductions are evident for the EQ and HH, while for the NR showed marginal changes and even slight increased for G-A and SC-A, reflecting the limited availability of certain raw materials within Europe and the associated mining dynamics.

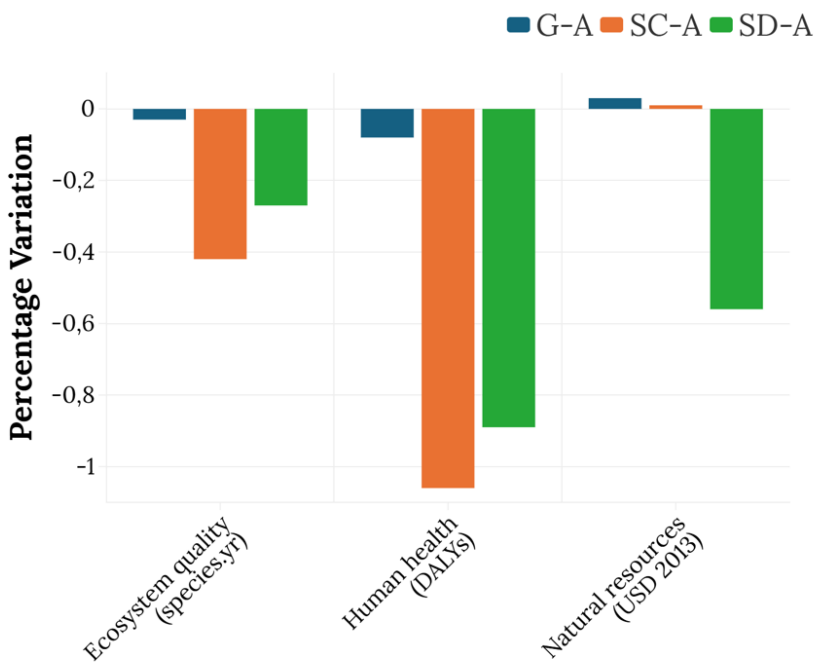

Figure 6.22 – Percentage change in endpoint results under the European supply chain scenario relative to the actual global production [511].

The endpoint analysis confirmed the trends identified at the midpoint level, but also highlighted important methodological aspects. At midpoint level, differences among chemistries were clearly visible across categories such as GW, FRS and MRU, where SD-A exhibited substantial reductions for the 1 Ah FU. These improvements were directly linked to lower electricity demand and reduced material consumption. At endpoint level, however, the aggregation of multiple impact pathways into three damage categories smoothed these reductions. In this study, midpoint results were more informative for identifying the specific process responsible, while endpoint indicators provided a synthetic validation of the overall environmental sustainability effect. Both approaches consistently identified SD-A as the most favorable chemistry when assessed on a performance basis.

Overall, the endpoint results reinforced the central conclusion of this work: material efficiency, when translated into electrochemical performance, had a stronger influence on long-term environmental damage than supply chain localization alone. However, coupling high-capacity chemistries with regionalized and circular supply strategies would likely generate synergistic improvements, enabling a more comprehensive transition toward sustainable battery technologies.

6.2. Full cell production

In the previous chapter, the environmental assessment was focused on the production of anode electrodes, with the aim of quantifying the impacts associated with different AMs and their experimentally optimized manufacturing conditions. While that material-level analysis provided valuable results in terms of environmental sustainability, considering both electrochemical performance and production-related environmental impacts, it did not fully capture the implications arising from the integration of these electrodes into a complete battery system. In practice, electrode materials are not used alone, but are assembled into cells through a sequence of additional processing steps that introduce further material and energy requirements. When assembling coin cells at the laboratory scale, key steps such as adding the electrolyte, stacking the electrodes and separator, and sealing the cell are performed. These procedures are often simplified or even omitted in material-focused LCAs, especially one that covers the full cell, even at laboratory scale, all assembly processes should be included.

For this reason, the present chapter shifts the analytical focus from electrode production alone to the assembly of the complete coin cell. The material inventory was completely redefined starting from the electrode level because some further optimizations were required. In fact, a different methodological approach was adopted compared to the previous study: all the electrodes were prepared again, in order to ensure a realistic balancing between anode and cathode under laboratory-scale conditions. The target areal capacity of the cathode was first defined at the cell level at around 2.5 mAh cm^{-2}, based on the practical capacity of 150 mAh g^{-1} of the LFP electrodes prepared at laboratory level. The balancing between anode and cathode capacities was defined based on the negative-to-positive capacity ratio (N/P), which was maintained within the range 1.05–1.15 [472]. This criterion reflects commonly adopted cell design practices and ensures realistic capacity matching without excessive material overbalancing. Cathodes were therefore produced by targeting the maximum areal capacity achievable at laboratory scale, and the anode fabrication processes were subsequently adapted to meet the resulting capacity requirements. This approach, which more closely reflects industrial cell design strategies, introduced additional challenges at the electrode manufacturing level. In particular, multiple electrode laminates with different wet thicknesses were produced and optimized in order to reach the desired areal capacity. As a consequence, further adjustments to the anode production processes were required. For instance, in the case of G-A, the solid fraction was increased up to 50 wt.%, resulting in manufacturing conditions that became more comparable to those adopted for SC-A. For SD-A, the requirement of achieving an areal capacity balanced with the LFP cathode was based on a conservative reference specific capacity of 3800 mAh g^{-1} for silicon, and led to substantial manufacturing restrictions. This value was intentionally selected

instead of the theoretical maximum (4200 mAh g^{-1}) to account for incomplete silicon lithiation under practical conditions. As a result, the production of SD-A was characterized by extremely low mass loadings, highlighting the significant practical challenges associated with the fabrication of high-silicon-content anodes at laboratory scale.

Within this work, all coin cells were assembled at laboratory scale, and the LCI was constructed entirely using primary data. By extending the system boundaries from electrode production to full coin-cell assembly, this chapter provides a more comprehensive assessment of how material choices and manufacturing procedures influence the environmental performance of emerging LIB technologies. Considering the inherent complexity of LCAs and the variety of methodological decisions required, a concise overview of the key assumptions and modelling parameters adopted in this study is presented in ***Table 6.18***. This overview is intended to facilitate the interpretation of the results discussed in the subsequent sections.

Table 6.17 – Summary of the methodological setup adopted for the LCA of full cells

Methodological aspect	***Adopted choice***
Functional unit	*1 coin cell* *1 kWh of energy stored by coin cells*
System boundaries	*Cradle-to-gate*
Software	*OpenLCA 2.4*
Database	*Ecoinvent 3.11*
LCIA calculation method	*Recipe 2016, Midpoint (H)* *Recipe 2016, Endpoint (H)*

6.2.1. Goal and scope definition

The goal and scope definition of this study was consistent with the approach previously applied to the life cycle assessment of anode production, ensuring methodological continuity. Nevertheless, the scope of the analysis was expanded to the full coin cell, with the system boundaries which also included the assembly process. As a result, the assessment addressed the environmental impacts associated with the complete coin-cell manufacturing chain, rather than focusing exclusively on anode fabrication.

6.2.2. Definition of the functional units

By changing the product level of the analysis, the FUs were necessarily adapted. In this study, the primary FU was defined as a single coin cell. Although this choice is relatively uncommon in battery LCAs, it is consistent with the

experimental focus of this work, where coin cells represent the fundamental configuration used to investigate and compare emerging technologies. Indeed, coin-cell-based FU is typically adopted only in specific contexts, such as the early-stage assessment of innovative systems including solid-state batteries or lithium–sulfur batteries, where cell-level comparisons are required [544,562,563].

For comparison with the broader LCA literature on LIBs, a secondary FU of 1 kWh of stored energy was chosen, which represents the most widely adopted reference in battery LCA studies [322,518,521,526–528]. Nevertheless, even in this case, direct comparability remained limited, as the technological characteristics and assembly processes of coin cells differ significantly from those of commercial cells. As a consequence, the use of both FUs allowed the results to be interpreted within their appropriate technological context, while highlighting the limitations associated with scaling laboratory-scale coin-cell data to industrial-level impacts.

6.2.3. System boundaries

At this stage, the system boundaries were expanded to include additional processes required at the coin-cell level. In particular, the analysis was extended to account for the secondary drying step, which was necessary before transferring the electrodes into the glovebox, as well as the coin-cell assembly process itself (***Figure 6.23***). The assessment followed a cradle-to-gate approach, covering all processes from raw material supply to the production of finished coin cells at laboratory scale. Accordingly, all internal components of the coin cell were included in the system boundaries, including the electrolyte, the separator, the spring and stainless-steel spacers used to maintain internal pressure, as well as the external coin-cell casing. In addition, the electricity consumption associated with glovebox operation was considered, together with the argon required to maintain the inert atmosphere during cell assembly.

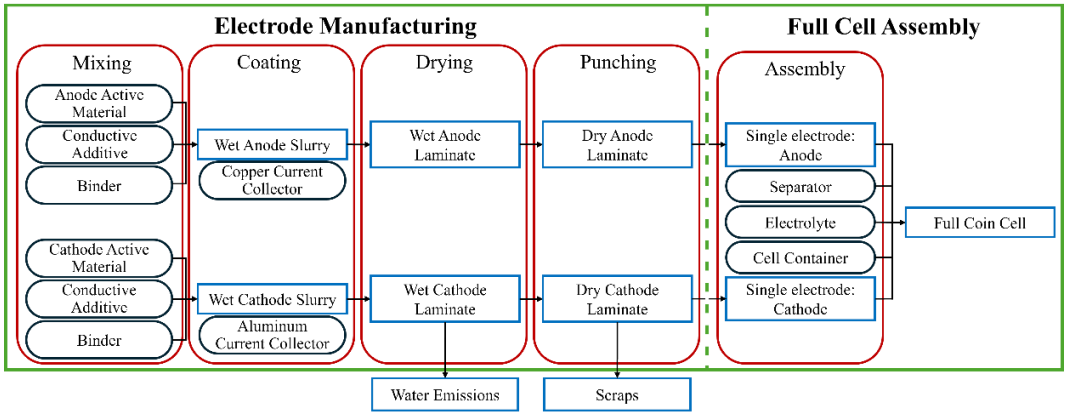

Figure 6.23 – The limit of the system boundaries is highlighted by the green rectangle, which include both the electrode manufacturing and full cell assembly processes, while production steps, input materials and components, and process outputs are represented by red ovals, black ovals, and blue squares, respectively.

As already sone for the anode-related study presented in ***Chapter 6.1***, all material and energy flows within the defined system boundaries were directly measured or calculated based on experimental data, enabling the construction of a LCI entirely based on primary data for the foreground system. Background processes, including electricity generation, transportation, and upstream material production, were modelled using secondary datasets obtained from the Ecoinvent 3.11 database.

6.2.4. LCI of the full cell assembly

LCI was constructed in accordance with the goal and scope definition introduced above. While the overall inventory structure remained consistent with the earlier analysis, it was extended to include additional downstream steps that had been excluded previously, in order to account for the complete coin-cell production process.

Material consumption and electricity demand were carefully measured and calculated throughout the entire production process. All foreground data originated from directly measured experimental values, whereas background processes such as electricity supply, raw material production, and transportation were represented using secondary datasets from the Ecoinvent 3.11 database and modelled within the OpenLCA 2.4 software environment.

6.2.4.1. Foreground system description

Foreground data were collected directly during the laboratory-scale production and assembly of the coin cells considered in this study. All material inputs and energy consumptions associated with electrode fabrication, secondary drying, glovebox operation, and coin-cell assembly were measured or calculated based on experimental activities specifically performed for this work. Particular attention was devoted to the accurate quantification of material masses, electricity demand, and processing times, in order to ensure internal consistency with the defined system boundaries and FUs. The use of primary foreground data allows the environmental assessment to reflect realistic manufacturing conditions and supports a reliable comparison among the different anode configurations integrated at the cell level.

6.2.4.2. Material and energy inventory

The material and energy inventory was compiled to quantitatively describe all relevant input and output flows associated with the laboratory-scale production and assembly of the coin cells considered in this study. The LCI included the consumption of materials for electrode fabrication, as done in the previous work, cell components (electrolyte, separator, spacers, spring, and casing), as well as the

energy requirements associated with mixing, coating, drying, secondary drying and glovebox operation.

Material flows were quantified based on measured masses and experimentally defined formulations, while energy demands were calculated from equipment power ratings and operating times recorded during the production and assembly processes. The inventory was developed in accordance with the defined FUs and system boundaries, ensuring consistency across all modelling stages. This detailed material and energy inventory constituted the basis for the subsequent LCIA and enabled a transparent evaluation of the contributions of individual processes and components to the overall environmental profile of the coin cells. The anodes were produced with the same procedure described for the previous study, with the only exception of the G-A, whose SF was increased to 50%. The LFP cathodes were produced with a similar procedure of G-A and SC-A, involving the Argolab mixer and the CMC-SBR water-based binder composition. Obviously, the LFP cathode was coated on the aluminum CC. A complete overview of the material and energy inputs for each unit process is reported in ***Table 6.18***, where differences among the electrodes are explicitly highlighted.

Table 6.18 – Material inputs, operating conditions, and energy requirements related to the mixing, coating, and drying stages of the production processes of G-A, SC-A, SD-A, and LFP electrodes at laboratory scale.

Process step	Parameter / input	Unit	G-A	SC-A	SD-A	LFP
Mixing	Time	min	210	210	80	210
	Mixing speed	rpm	2200	2200	1000	2200
	Power	W	70	70	70	70
	Electricity	Wh	245	245	93.1	245
	Graphite	g	4.750	–	0.250	–
	Silicon carbide	g	–	4.750	–	–
	Nanoporous Silicon	g	–	–	4.000	–
	LFP	g	–	–	–	9.500
	Carbon black	g	0.100	0.100	0.250	0.200
	CMC	g	0.050	0.050	–	0.100
	SBR	g	0.100	0.100	–	0.200
	PAA	g	–	–	0.500	–
	Water	g	5.000	5.000	3.333	10.000
	Solid Fraction	%	50	50	60	50
Coating	Time	min	10	10	10	10
	Power	W	50	50	50	50

	Electricity	Wh	8.5	8.5	8.5	8.5
	Wet Slurry	g	4.037	3.125	0.425	8.099
	CC	g	1.807	1.807	1.807	1.834
	Wet Deposition	µm	110	100	20	350
Drying	Time	min	60	60	–	60
	Power	W	2000	2000	–	2000
	Electricity	Wh	400	400	–	400

The scraps produced after the punching step were included in the LCI as waste flows (***Table 6.19***). As in the previous case, an optimized cutting configuration was assumed in order to minimize material losses (***Figure 6.3***). This approach was applied to both copper and aluminum CCs. The resulting scraps were distinguished between pure CC residues and coated electrode scraps. Although these waste streams were quantitatively assessed, within the LCI they were conservatively modelled as generic waste. From a circular economy perspective, however, a distinction is necessary: clean CC scraps could be directly recycled and reintroduced into the production cycle with limited additional treatment, whereas coated electrode scraps would require more complex separation and recovery processes. As already discussed, the relative quantities of scrap at laboratory scale are considerably higher than in industrial production environments [533]. Nevertheless, their inclusion in the inventory remains essential, since even a 1% reduction in scrap rate can become highly significant at a larger scale, both economically and environmentally, due to the magnitude of materials involved.

Table 6.19 – Amount of scraps produced during the punching step of electrode production, depending on the electrode chemistry

	Manual process				
Punching	CC Scraps	g	0.570	0.570	0.570
	Electrode Scraps	g	1.381	1.188	0.615

After the production of both anodic and cathodic electrodes, the system boundaries were extended to include the assembly phase of the coin cell (***Table 6.20***). Since assembly was performed in an argon-filled glovebox with a strict humidity-controlled atmosphere, a secondary vacuum-drying step was required before transferring the electrodes into the glovebox. An average assembly time of approximately 15 minutes per cell was considered, including the associated electricity consumption and argon use necessary to maintain the inert atmosphere. All components required for coin-cell assembly were included in the inventory.

Each component was individually weighed, although variability among different production batches must be acknowledged. The structural components of the coin cell were predominantly made of stainless steel, with except the polymeric O-ring, which functions as an electrical insulator to prevent short-circuiting between the electrodes.

Table 6.20 – Material inputs, operating conditions, and energy requirements related to the second drying and cell assembly for the production of full cells

Process step	Parameter / input	Unit	Single coin cell
Second drying	Time	min	240
	Power	W	630
	Electricity	Wh	2520
Assembly	Time	min	10
	Power	W	2300
	Electricity	Wh	383.33
	Argon	g	12.5
	Electrolyte	µL	150
	Separator	g	0.032
	Top	g	0.872
	Bottom	g	0.838
	Plastic O-ring	g	0.003
	Spring	g	0.181
	Spacers	g	3.454

For the full-cell assembly stage, a detailed categorization of all system inputs is provided in ***Table 6.21***. This table identifies the origin of each inventory flow, clearly separating direct laboratory measurements from secondary background data, and lists the specific proxies implemented when dedicated datasets were not accessible.

Table 6.21 – Correspondence between experimental inputs and Ecoinvent 3.11 background datasets, including data quality classification and proxy identification for the full cell manufacturing processes.

Input	***Data Type***	***Proxy***	***Dataset***
Graphite	Primary	--	market for graphite | graphite | Cutoff, U - GLO
Silicon Composite	Primary	Silicon Carbide	market for silicon carbide | silicon carbide | Cutoff, U - GLO
Nanoporous Silicon	Primary	Silicon, Metallurgical Grade	silicon production, metallurgical grade | silicon, metallurgical grade | Cutoff, U - NO
LFP	Primary	--	market for lithium iron phosphate | lithium iron

			phosphate | Cutoff, U - RoW
Carbon Black	Primary	--	market for carbon black | carbon black | Cutoff, U - GLO
CMC	Primary	--	market for carboxymethyl cellulose, powder | carboxymethyl cellulose, powder | Cutoff, U - GLO
SBR	Primary	Latex	market for latex | latex | Cutoff, U - RoW
PAA	Primary	Acrylic Acid	market for acrylic acid | acrylic acid | Cutoff, U - RER
Ultrapure Water	Primary	--	water production, ultrapure | water, ultrapure | Cutoff, U - RER
Copper CC	Primary	--	market for sheet rolling, copper | sheet rolling, copper | Cutoff, U - GLO
Aluminum CC	Primary	--	market for sheet rolling, aluminium | sheet rolling, aluminium | Cutoff, U - GLO
Electricity, Medium Voltage	Secondary	--	market for electricity, medium voltage | electricity, medium voltage | Cutoff, U - IT
Stainless Steel Components	Secondary	--	market for metal working, average for chromium steel product manufacturing | metal working, average for chromium steel product manufacturing | Cutoff, U - GLO
Plastic O-ring	Secondary	--	market for extrusion of plastic sheets and thermoforming, inline | extrusion of plastic sheets and thermoforming, inline | Cutoff, U - GLO
Separator	Secondary	--	market for glass fibre | glass fibre | Cutoff, U - GLO
Argon	Secondary	--	market for argon, liquid | argon, liquid | Cutoff, U - RER
DEC	Primary	--	market for diethyl carbonate | diethyl carbonate | Cutoff, U - RER
EC	Primary	--	market for ethylene carbonate | ethylene carbonate | Cutoff, U - GLO
$LiPF_6$	Primary	--	market for lithium hexafluorophosphate | lithium hexafluorophosphate | Cutoff, U - RoW

As described in previous chapters, each electrode was individually weighed and its thickness measured to evaluate coating uniformity under laboratory-scale conditions. The corresponding data are reported in ***Table 6.22***. A certain variability among electrodes was observed, which is also reported at industrial scale; however, industrial production benefits from dedicated inline inspection systems that enable tighter process control and improved coating homogeneity [281]. Among the measured parameters, volumetric capacity represents a critical design variable, particularly when transitioning from half-cell testing to full-cell assembly. The higher specific and volumetric capacities associated with SD-A enable higher cell-level energy density. When effectively translated into cell design, this advantage reduces the amount of active material required to achieve a given electrochemical performance. As a consequence, electrode volume can be

reduced, leading to a lower demand for inactive materials such as casing and supporting components [534]. Moreover, the shift from conventional graphite-based systems to silicon-rich chemistries may decrease dependence on natural and synthetic graphite, potentially mitigating raw-material criticality concerns. More broadly, higher electrochemical performance per unit mass enables a reduction in total material demand per unit of stored energy [521,536]. Under such conditions, improvements achieved at the material level can propagate to the full-cell level, influencing both environmental impacts and long-term resource efficiency.

Table 6.22 – Overview of the main properties of the G-A, SC-A, SD-A anodes, and LFP cathode produced at laboratory scale.

Chemistry	***Solid Fraction [%]***	***Electrode Area [cm^2]***	***Dry Layer Thickness [µm]***	***Dry Layer Volume [cm^{-3}]***	***Weight [mg]***
G-A	*50*	*1.766*	*80 ± 5*	*0.0141*	*25.00 ± 0.16*
SC-A	*50*	*1.766*	*66 ± 5*	*0.0117*	*21.50 ± 0.22*
SD-A	*60*	*1.766*	*16 ± 5*	*0.0028*	*11.13 ± 0.05*
LFP	*50*	*1.538*	*180*	*0.0277*	*35.49 ± 1.35*

The electrochemical cells were assembled in a CR2032 coin-cell configuration inside an argon-filled glovebox under strict controlled atmosphere (O_2<0.5 ppm, H_2O <0.5 ppm). A GF/A Whatman separator was placed between the electrodes and soaked with 150 mL of electrolyte to guarantee uniform and reproducible wetting conditions. For G-A, a baseline electrolyte composed of 1M $LiPF_6$ in EC:DEC (1:1 v/v) was chosen. In contrast, for SC-A and SD-A, the electrolyte formulation was modified by adding 10% of FEC and 2% of VC to improve interfacial stability on the silicon surface [403]. All cells were assembled following the same procedure to ensure consistency among the different anode chemistries. Electrochemical characterization consisted of 10 consecutive charge–discharge cycles at a C-rate of 0.1C, followed by 5 cycles at 0.2C, in the potential range between 2.5 V and 3.65 V. For the G-A and SC-A electrodes, a CCCV protocol was adopted, as done in previous chapters. The resulting electrochemical performance data are summarized in ***Figure 6.24***.

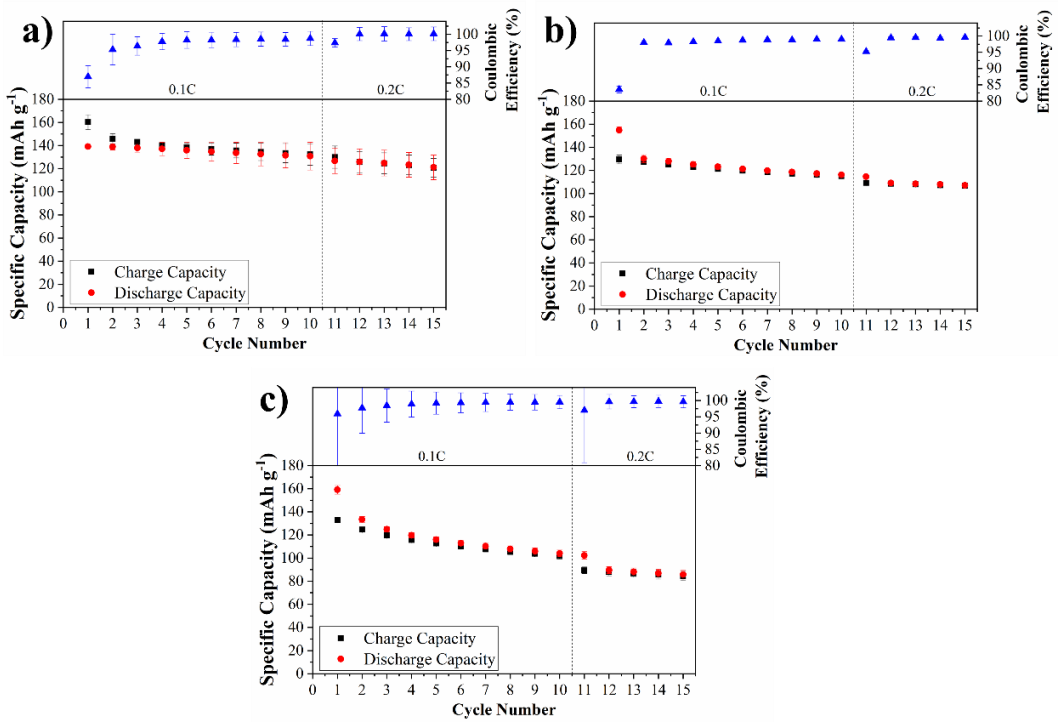

Figure 6.24 – Average electrochemical results of the different full cells assembled with the different anode chemistries: A) G-A; B) SC-A; C) SD-A.

The average discharge values are reported in ***Table 6.23*** and are consistent with the expected electrochemical behaviour of the investigated chemistries. G-A exhibited the highest discharge capacity, followed by a progressive decrease with increasing silicon content. However, G-A also showed a higher variability among replicates, whereas the cells assembled with silicon-based anodes displayed a more stable and reproducible response.

Table 6.23 – Average discharge capacity for the full cells assembled with the different anode chemistries

Cycle	C-rate	Discharge Capacity (mAh g^{-1})		
		G-A	SC-A	SD-A
1	0.1	139.13 ± 0.58	129.44 ± 3.70	132.80 ± 2.13
2		138.92 ± 2.67	127.58 ± 2.59	124.61 ± 2.03
3		137.98 ± 3.77	125.16 ± 2.41	119.49 ± 1.99
10		130.83 ± 11.97	115.13 ± 1.85	102.24 ± 2.95
15	0.2	121.14 ± 10.56	106.71 ± 0.72	84.50 ± 4.00

6.2.5. Assumptions of the study

The assumptions adopted in this study were largely aligned with those defined in the previous analysis on anode production, ensuring methodological continuity

within this work. However, additional assumptions were introduced to account for the extension of the system boundaries to the coin-cell assembly stage.

Regarding electrode drying, an optimized use of the oven was assumed by considering the simultaneous drying of four electrode sheets during the primary drying step. After coating, the electrodes were manually cut according to the defined cutting layout (***Figure 6.3***) and subsequently subjected to a secondary vacuum-drying. The electricity consumption associated with this step was allocated over the 100 electrodes assumed to be processed in parallel.

During coin-cell assembly, all operations were performed inside a glovebox. The corresponding electricity consumption and argon demand were estimated assuming an average assembly time of approximately 15 minutes per coin cell, corresponding to the duration required for the complete assembly procedure. The electrolyte was intentionally added in excess to prevent electrochemical limitations related to insufficient wetting. The selected amount corresponded to approximately twice the quantity typically required when scaled according to cell capacity under industrial conditions [564]. This conservative approach ensured consistent and reproducible electrochemical performance across all tested chemistries.

Finally, since FEC was not available as an independent process in the database, its contribution was approximated by associating it with the production process of EC, assuming comparable upstream production pathways.

6.2.6. Limitations and outlook

The limitations of this study are largely consistent with those previously discussed, with the primary constraint related to the TRL of the investigated processes. The manufacturing steps were carried out at laboratory scale and, therefore, cannot fully represent industrial production conditions in terms of process efficiency, material utilization, and operational optimization [522].

The system boundaries followed a cradle-to-gate approach, extending beyond the previous analysis by including not only electrode fabrication but also the coin-cell assembly stage. However, the use phase and EoL management were not considered within the scope of this study. Consequently, the results reflect the environmental impacts associated with material production and cell assembly only, without accounting for potential impacts or benefits related to battery operation, lifetime, or recycling pathways. For this reason, circular economy considerations are treated strictly qualitatively throughout the text and are excluded from the quantitative impact analysis.

In this context, the normalization of the experimental full cell data to a functional unit of 1 kWh must be interpreted strictly as an illustrative and theoretical exercise rather than a predictive industrial estimation. Scaling up inventory data from laboratory scale coin cells to a macro scale energy unit

involves a massive geometric and volumetric disparity. In a real coin cell, the inactive components, particularly the heavy stainless steel casing, represent a disproportionately high mass fraction relative to the active materials, which inherently distorts the absolute environmental footprint. Therefore, the 1 kWh environmental metrics presented in this section do not reflect the physical reality of a commercial battery pack or an industrial cell format. Instead, this mathematical extrapolation serves exclusively as a uniform comparative baseline to evaluate the inherent environmental footprint of different material formulations under equivalent functional parameters. Any absolute numbers reported under this FU must be viewed with caution and treated as indicative values meant to guide early stage ecodesign choices rather than absolute lifecycle indicators.

An additional limitation concerns the optimization level of the SD-A cell configuration, which cannot be considered fully achieved. Starting from the N/P ratio, several studies [565,566] suggest that the value typically adopted for graphite and low-silicon systems, around 1.1, may not be optimal for high-content silicon anodes. Moreover, the significant reduction in anode thickness would require further investigation of parameters such as the number of spacers to reach the optimal internal cell pressure. These aspects could influence electrochemical performance and long-term stability. However, such optimization studies are time-consuming and require extensive experimental validation, and therefore fall outside the scope of the present work.

6.2.7. LCIA methods

In line with the approach adopted for the anode study described in ***Chapter 6.1***, the ReCiPe 2016 methodology was applied using both the Midpoint (H) and Endpoint (H) perspectives.

6.2.8. Data quality assessment and uncertainty analysis based on the Pedigree approach

Uncertainty was evaluated following the same approach adopted in the previous study, based on the Pedigree matrix presented in ***Figure 6.5***. In the present work, to improve the robustness of the uncertainty assessment, foreground processes based on primary data were also assigned minimum variability factors. Although these data were experimentally measured and directly controlled, it was considered that upstream production and transportation stages associated with these materials are still subject to fluctuations. Therefore, even primary data were not treated as uncertainty-free, but characterized using the lowest variability scores within the Pedigree matrix. It is acknowledged that laboratory-scale processes inherently exhibit a certain degree of variability. However, this variability was considered secondary compared to the uncertainty associated with

background datasets. As in the previous analysis, the largest contribution to overall uncertainty remained linked to background processes, particularly electricity generation, raw material extraction, and transportation modelling.

By explicitly characterizing both foreground and background uncertainty, this LCA avoided overconfidence in experimentally measured data and provided a more realistic representation of the variability related to the innovative technology.

6.2.9. LCIA: linking electrochemical performance and environmental impacts

The results obtained from the LCA performed using the two previously introduced FUs are presented below. Considering the complexity of the system and the number of materials involved, a sensitivity analysis on a fully European supply chain was not conducted due to the lack of consistent primary data, which would have required the introduction of an even larger number of speculative assumptions compared to those already introduced in the previous case. However, the uncertainty analysis through MCS iterations on the Midpoint categories is presented for both FUs, together with the evaluation of the Endpoint categories.

As previously discussed in the paragraph addressing the limitations of this LCA approach, the different anodes represented a very small fraction of the overall system (***Table 6.24***), particularly considering the adopted coin cell geometry. The casing and spacers accounted for approximately 95 wt% of the total system mass for all three chemistries. Consequently, the contribution of the anodes at the cell level remained limited due to their mass fraction below 0.5%, although their specific impact intensity per unit mass was not negligible. The dominance of the casing mass limited the variability of material-specific differences among the anode chemistries within this laboratory-scale configuration.

Table 6.24 – Mass distribution of cell components for the three anode chemistries considering the complete coin cell configuration, including casing and spacers. Values are reported in grams and as weight percentage relative to the total cell mass.

Cell Components	***G-A***		***SC-A***		***SD-A***	
	g	**%**	**g**	**%**	**g**	**%**
Anode	0.025	0.44	0.022	0.39	0.011	0.20
Cathode	0.036	0.64	0.036	0.64	0.036	0.64
Separator	0.030	0.53	0.032	0.57	0.032	0.57
Electrolyte	0.195	3.46	0.189	3.36	0.189	3.37
Casing and Spacers	5.348	94.92	5.348	95.04	5.348	95.23
Total	5.634		5.627		5.616	

The contribution associated with the excess electrolyte becomes particularly evident when the casing was excluded from the overall calculation (***Table 6.25***). The exclusion of the casing from the calculation highlighted the structural imbalance of the laboratory-scale configuration: the electrolyte added in large amount accounted for approximately 68-71 wt% of the remaining system, becoming the dominant mass contributor across all chemistries. As expected, the cathode contributed largely to the system, in line with other studies [567], even though, in this case, its contribution was almost equivalent to that of the separator. This was due to the G/F Whatman separator, which is quite thick and was adopted to guarantee a uniform distribution of the electrolyte inside the cell. At the industrial level, PP or PE separators are chosen due to their reduced thickness which leads to almost negligible contribution to overall emissions [567]. Despite the significant reduction in anode mass from G-A (5.39 wt%) to SD-A (0.60 wt%), the overall mass distribution of the system remains essentially unchanged. This indicates that, in the present configuration, changes in anode chemistry have a limited influence on the overall impact distribution. The reduction of nearly one magnitude order in anode mass from G-A to SD-A does not translate into a proportional shift in system mass distribution, due to the structural dominance of the electrolyte and separator in the casing-free configuration.

Table 6.25 – Mass distribution of cell components for the three anode chemistries excluding case and spacers. Values are reported in grams and weight percentage relative to the system.

Cell Components	***G-A***		***SC-A***		***SD-A***	
	g	**%**	**g**	**%**	**g**	**%**
Anode AM	0.0155	5.39	0.012	4.32	0.0016	0.60
Cu foil	0.0095	3.31	0.0095	3.42	0.0095	3.55
Cathode AM	0.0271	9.43	0.0271	9.75	0.0271	10.13
Al foil	0.0084	2.92	0.0084	3.02	0.0084	3.14
Separator	0.0320	11.13	0.0320	11.51	0.0320	11.96
Electrolyte	0.1949	67.81	0.1890	67.99	0.1890	70.63
Total	0.2874		0.2780		0.2676	

Overall, the findings indicated that, within a laboratory-scale coin cell configuration, variations in anode chemistry alone are not sufficient to substantially modify the environmental impacts at the cell level, as the system remains structurally dominated by other components rather than by active materials.

6.2.9.1. Environmental impact assessment of 1 coin cell

As expected, the use of a coin-cell-based FU led to results that were only weakly comparable with most LCA studies available in the literature, which typically adopt FUs such as 1 kWh [322,518,521,526–528] or 1 battery pack [529]. In this second phase of the work, the analysis was extended to the entire

cell system, which is a more complex system than the production of individual electrodes. Hence, the present analysis was based on a laboratory-scale coin cell configuration, where other components. such as the stainless steel case and spacers dominate the total mass and influence the overall impact distribution. Since the anode contributes less than 0.5 wt% to the total cell mass, while the casing accounts for approximately 95 wt%, the influence of anode chemistry on the overall impact profile was inherently limited at this scale. As a consequence, the relative contribution of active materials could not be directly compared with studies conducted at the industrial cell scale.

The variability associated with changes in anode formulation became less evident within the full cell configuration. Unlike the electrode-level analysis, where impacts could be more directly attributed to material composition and processing steps, the increased system complexity made it considerably more difficult to associate variations in specific impact categories with individual components. The midpoint results calculated for the FU of 1 coin cell (***Figure 6.25***, ***Table 6.26***) confirmed this trend. Across all categories, the differences among G-A, SC-A and SD-A remained below approximately 1%, indicating that the environmental signal associated with anode chemistry was largely masked at the cell level.

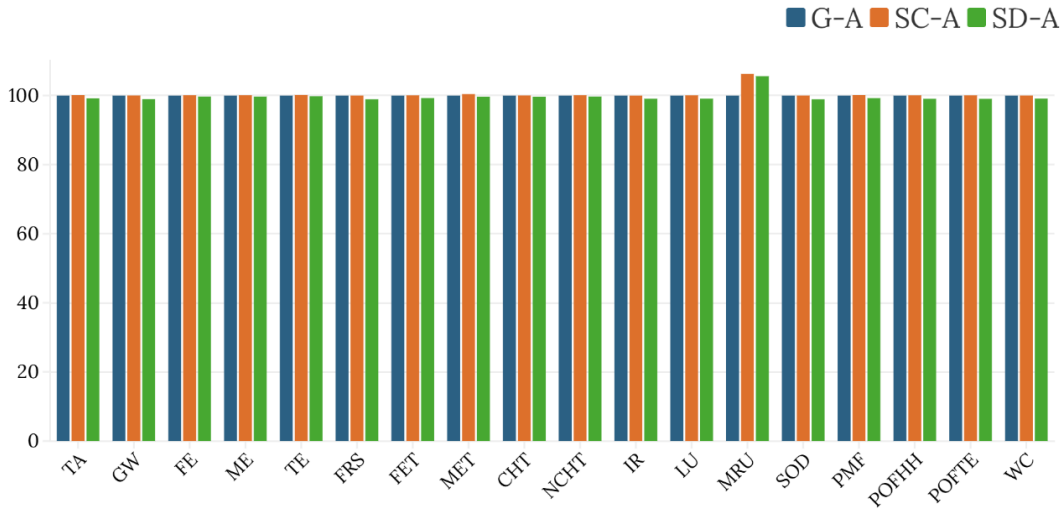

Figure 6.25 – Graphical representation of midpoint impact category results for the three anode chemistries calculated using the FU of 1 coin cell.

Table 6.26 – Midpoint impact category results for the three anode chemistries calculated using the FU of 1 coin cell.

Impact category	**Results per 1 coin cell**		
	G-A	**SC-A**	**SD-A**
TA	6.301E-04	6.309E-04	6.249E-04
GW	0.2717	0.2717	0.2689
FE	0.0122	0.0122	0.0121
ME	0.0158	0.0158	0.0158

TE	0.4154	0.4161	0.4145
FRS	0.0863	0.0864	0.0854
FET	7.852E-05	7.858E-05	7.794E-05
MET	8.140E-06	8.175E-06	8.112E-06
CHT	0.0632	0.0633	0.0630
NCHT	0.2994	0.2997	0.2985
IR	0.0422	0.0422	0.0418
LU	0.0059	0.0059	0.0058
MRU	0.0047	0.0050	0.0049
SOD	1.183E-07	1.183E-07	1.170E-07
PMF	2.613E-04	2.617E-04	2.593E-04
POFHH	4.325E-04	4.328E-04	4.284E-04
POFTE	4.612E-04	4.615E-04	4.569E-04
WC	4.206E-03	4.207E-03	4.169E-03

Among all impact categories, MRU showed the most pronounced variation, with slightly higher values for silicon-based anodes, both SC-A and SD-A. This trend could be attributed to the silicon production process itself, as already discussed in the previous chapter and to the higher complexity of the electrolyte formulation, due to the presence of additives [322,568,569]. In contrast, for GW, which represents the most commonly discussed category, the SD-A configuration led to a reduction of approximately 0.0028 kg CO_2-Eq compared to G-A. Although measurable, this reduction corresponded to roughly 1% of the total GW impact per coin cell, confirming that, within the adopted laboratory-scale configuration, the effect of anode chemistry remained marginal relative to the overall system structure.

6.2.9.2. Environmental impacts assessment of 1 kWh production in a global supply chain

When adopting the FU based on the production of 1 kWh, the geometry and performance of the produced cells became a determining factor once again, limiting the comparability of the results with the existing literature. For example, studies such as Ellingsen et al. [515] evaluated a full-battery pack with an energy capacity of approximately 26.6 kWh**,** using industrial-scale cells with optimized energy density and design that differ significantly from laboratory-scale coin cells. In the present work, achieving an energy output of 1 kWh using laboratory-scale coin cells requires the manufacturing of several hundred thousand units (***Table 6.27***). The number of cells was estimated based on the ratio between the target energy and the energy delivered per cell for each anode configuration. Considering what was previously observed for the FU of 1 coin cell, where the casing represented the dominant mass fraction of the system, the direct comparison with industrial-scale cell configurations became structurally

inappropriate. The imbalance between casing and other materials in coin cells led to a disproportionate increase in environmental impacts when scaled to a 1 kWh FU.

Table 6.27 – Number of coin cells required to reach the production of 1 kWh for the three anode chemistries, based on the experimentally measured cell capacities.

Parameters	***Units***	***G-A***	***SC-A***	***SD-A***
Practical capacity	*mAh*	3.28	2.58	2.22
Voltage window	*V*	1.15	1.15	1.15
Energy	*mWh*	3.77	2.97	2.55
Number of cells	*item*	265,252	336,700	392,157

To fully understand the shift in environmental trends when moving from the electrode level to the full-cell level, it is essential to analyze the relationship between single-cell energy and the scaling factor for the 1 kWh FU. This comparison reveals a crucial message of this work: material-level innovations are strictly bound by cell design efficiency. At the electrode level, the SD-A exhibits the lowest environmental impacts because its high specific capacity drastically reduces the mass of active material required per Ah. However, at the coin cell level, the unoptimized cell configuration, coupled with the fixed capacity of the cathode and the lower ICE typical of silicon-based anodes, results in a lower practical energy output per individual cell compared to the graphite baseline.

As reported in ***Figure 6.26*** and ***Table 6.28***, when using the FU of 1 kWh, silicon-based anodes led to an increase in emissions across all impact categories compared to the graphite-based configuration. This result contrasted with the electrode-level assessment and was primarily driven by the significantly higher number of cells required to achieve 1 kWh. In particular, the lower electrochemical performance observed for the SD-A configuration resulted in the need for a substantially larger number of cells, which directly increased the cumulative environmental impacts. Therefore, in this configuration, cell performance became the main driver of the overall impact rather than the intrinsic contribution of the active material itself.

The production of cells with improved energy density and optimized structural design would likely lead to a reduction in the resulting environmental impacts, as fewer individual units would be required to deliver the same output. In a performance-based LCA, such as 1 kWh used in this work, the number of cells needed became a critical driver of cumulative impacts. Consequently, improvements in energy density and ratio between active and inactive materials directly translate into a reduced number of cells required to deliver the same amount of energy. This directly decreases the need for components such as casing, spacers, CCs and other structural elements, which do not directly contribute to electrochemical performance but significantly affect the overall environmental

burden. This implies that design efficiency and electrochemical performance are not only technical optimization parameters but also key environmental drivers when the FU is energy-based. Therefore, the environmental profile of a battery system cannot be interpreted independently of its architectural efficiency, as design-related limits may amplify or mitigate the impacts associated with material choices.

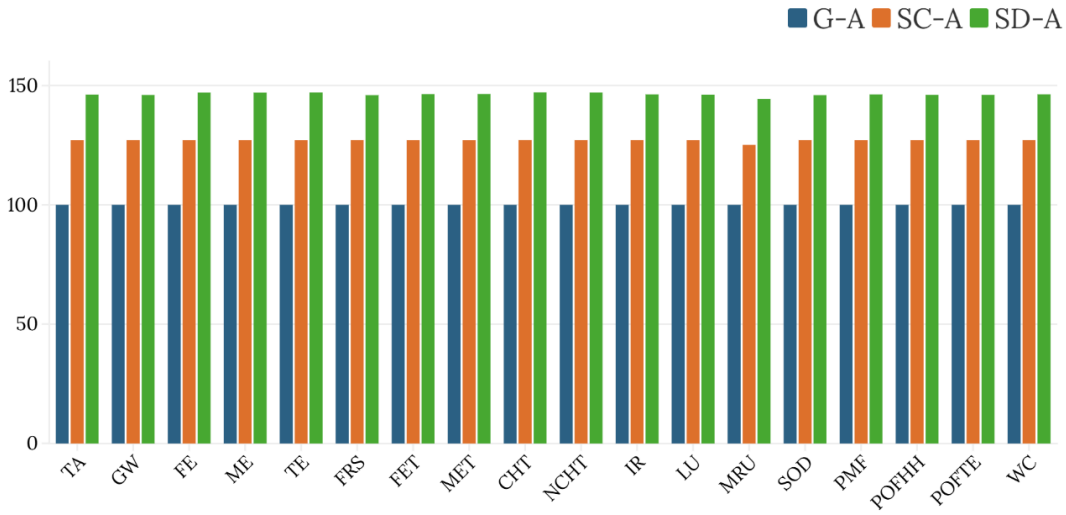

Figure 6.26 – Graphical representation of midpoint impact category results for the three anode chemistries calculated using the FU of 1 kWh.

Table 6.28 – Midpoint impact category results for the three anode chemistries calculated using the FU of 1kWh.

Impact category	**Results per 1 kWh of production**		
	Graphite	**Silicon Composite**	**Silicon Dominant**
TA	157.44	200.04	230.13
GW	6.77E+04	8.60E+04	9.88E+04
FE	3069.88	3900.87	4514.07
ME	3990.99	5071.33	5867.99
TE	1.05E+05	1.33E+05	1.54E+05
FRS	2.14E+04	2.72E+04	3.12E+04
FET	19.64	24.96	28.75
MET	2.04	2.59	2.98
CHT	1.62E+04	2.06E+04	2.39E+04
NCHT	7.61E+04	9.67E+04	1.12E+05
IR	1.07E+04	1.35E+04	1.56E+04
LU	1472.55	1871.09	2151.98933933
MRU	1134.21	1419.57	1638.09
SOD	0.0297	0.0377	0.0433
PMF	65.34	83.02	95.56
POFHH	107.39	136.46	156.88
POFTE	114.35	145.31	167.04
WC	1063.09	1351.10	1555.27

These findings underline that, when the FU was defined in terms of delivered energy, electrochemical performance became a dominant parameter in determining the overall environmental profile. In this context, differences in active material composition could be partially or entirely masked by the amount of case and spacers components. As a consequence, the environmental sustainability advantages observed at the electrode level did not necessarily translate into improved results at the cell level when the assessment was scaled to a performance-based FU.

This highlighted the critical importance of FU selection and system boundary definition in LCA studies of emerging technologies. Depending on whether the analysis is conducted at material, electrode, cell, or entire battery pack level, the relative contribution of material innovation can shift significantly, leading to different environmental sustainability interpretations.

6.2.9.3. Material composition and the relative contribution to environmental impacts

The relative contribution analysis of the full cell components, considering the FU of 1 kWh, highlights a strong dependence of the environmental impacts on the selected anode chemistry. The comparison between G-A, SC-A, and SD-A full cells allows the identification of the main impact drivers and how the progressive increase in silicon content affects the overall environmental profile.

When the full assembly process using G-A as anode is considered (***Figure 6.27a***), electricity emerges as the dominant contributor across several impact categories for all chemistries, in some cases exceeding 80%, highlighting the strong influence of laboratory-scale production. In contrast, argon, casing, and other components contribute to a much smaller extent. In particular, the casing and stainless steel components show a highly variable contribution: despite accounting for approximately 95% of the total cell mass (***Table 6.24***), their impact is significant only in specific categories, such as toxicity-related indicators (e.g., TE, MET, CHT, NCHT), where contributions can exceed 50–60%. This behaviour is mainly associated with the presence of alloying elements such as nickel and chromium, whose extraction and refining processes are known to be particularly relevant for human toxicity, ecotoxicity, and resource depletion categories [570,571]. In contrast, categories related to energy use and emissions, such as GW and TA, are predominantly driven by electricity consumption, which emerges as the main contributor when the full assembly process is included. This result is consistent with previous studies on LIBs, which highlight the strong influence of energy demand, especially under laboratory-scale or non-optimized production conditions [555,572]. The contribution of argon, although secondary, is not negligible in some categories, due to the energy-intensive nature of industrial gas production, typically based on cryogenic air separation

processes[573]. When excluding the assembly process (***Figure 6.27b***), the contribution shifts almost entirely to the active materials, with the cathode representing the main hotspot, followed by the anode and the electrolyte, in agreement with previous LCA studies [515]. A distinct behaviour is observed for the MRU category, where the electrolyte shows a relatively higher contribution compared to other impact categories. This can be attributed to the characteristics of the electrolyte salt, typically lithium hexafluorophosphate ($LiPF_6$), whose production involves multi-step synthesis routes based on fluorinated precursors and non-renewable raw materials [574]. As a result, despite its low mass fraction, the electrolyte contributes significantly to resource depletion due to the complexity of its production process and the use of critical elements.

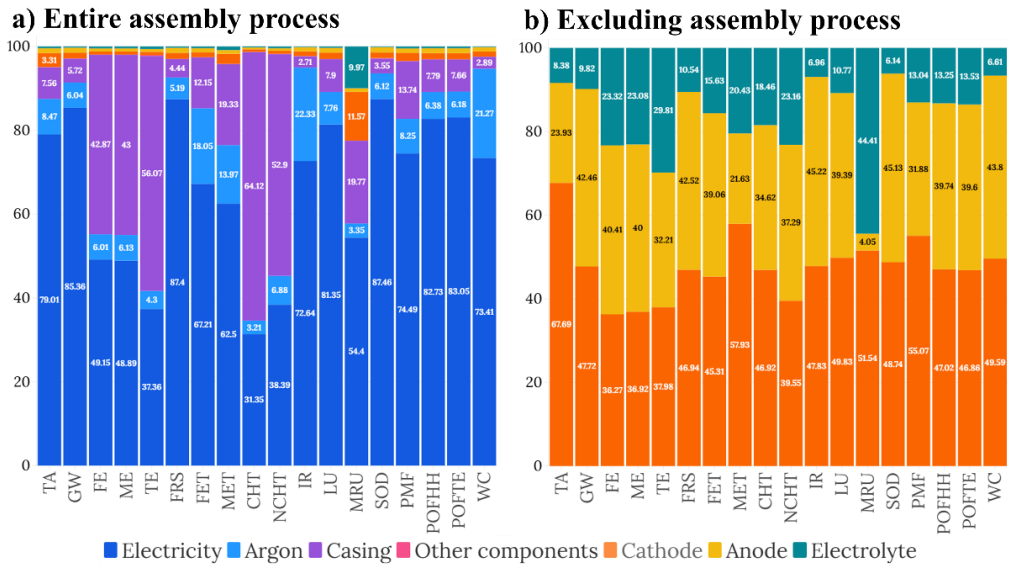

Figure 6.27 – Relative contribution of full cell components produced using G-A as anode: a) including the entire assembly process, accounting for electricity, argon consumption in the glovebox, and all other components; b) excluding the assembly process, focusing only on anode, cathode, and electrolyte.

The relative contribution analysis for SC-A (***Figure 6.28***), does not show substantial differences compared to the graphite-based system. When the full assembly process is considered, electricity remains the dominant contributor across most impact categories, while argon, casing, and other auxiliary components play a minor role. When excluding the assembly process, the impact is mainly governed by the active materials, with the cathode representing the primary hotspot, followed by the anode and the electrolyte.

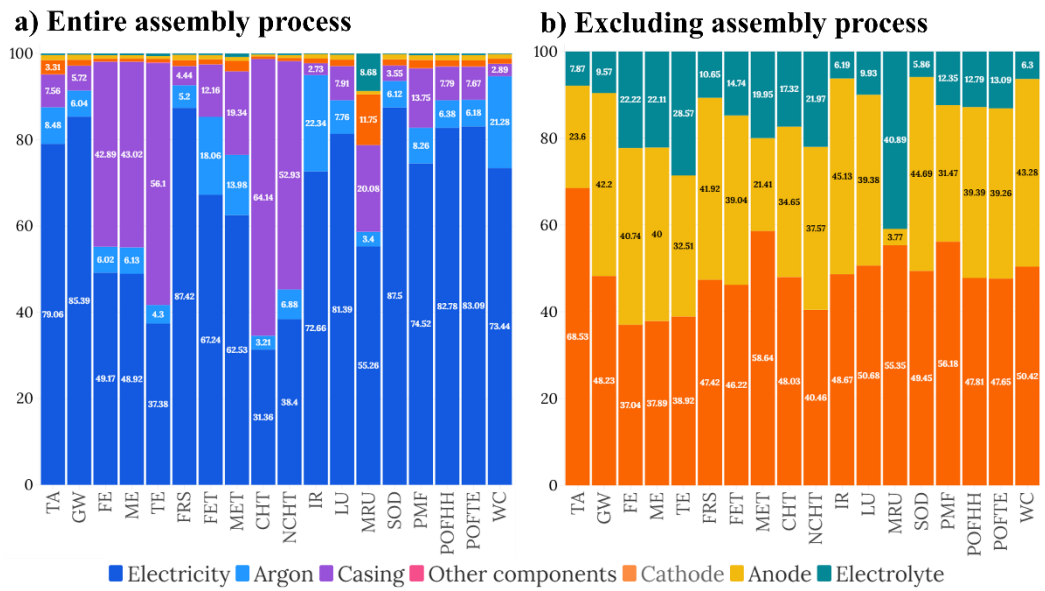

Figure 6.28 – Relative contribution of full cell components produced using SC-A as anode: a) including the entire assembly process, accounting for electricity, argon consumption in the glovebox, and all other components; b) excluding the assembly process, focusing only on anode, cathode, and electrolyte.

The relative contribution analysis for SD-A (***Figure 6.29***) highlights a clear difference between the results obtained including and excluding the assembly process. When the full assembly process is considered (***Figure 6.29a***), electricity dominates the environmental impact across all categories, typically accounting for 70–85% of the total impact. In this scenario, the contribution of the anode becomes almost negligible, dropping below 1% in several categories, such as GW, MET, and POFHH, indicating that the impact of AMs is largely masked by process-related energy consumption. When excluding the assembly process (***Figure 6.29b***), the contribution shifts entirely to the AMs, revealing a markedly different distribution. The cathode remains the dominant contributor across most categories, reaching values above 80% in several cases, while the anode contribution is significantly reduced compared to both G-A and SC-A systems, remaining below 10% in most categories and dropping to values close to zero in MRU. At the same time, the electrolyte shows a relevant contribution in specific categories, particularly in MRU, highlighting its importance in resource-related impacts [574].

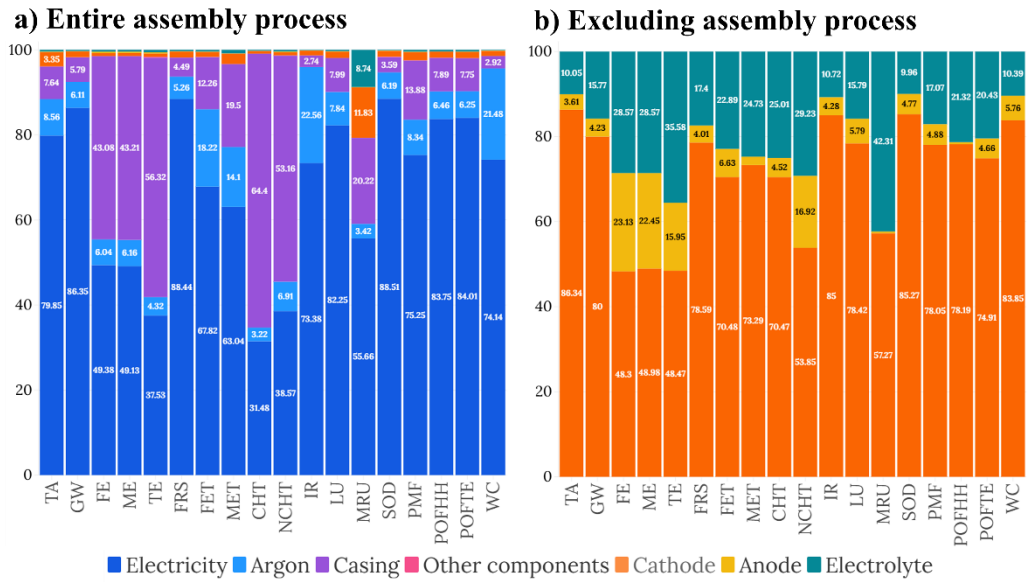

Figure 6.29 – Relative contribution of full cell components produced using SD-A as anode: a) including the entire assembly process, accounting for electricity, argon consumption in the glovebox, and all other components; b) excluding the assembly process, focusing only on anode, cathode, and electrolyte.

Overall, the results demonstrate that the environmental impact is governed by a strong interplay between process conditions and material composition, with their relative importance depending on the system boundary. When the full assembly process is included, electricity consumption dominates the impact across all anode chemistries, masking the contribution of individual components and highlighting the limitations of laboratory-scale production. In contrast, excluding the assembly process reveals the intrinsic impact distribution of the cell, where the cathode consistently represents the main contributing component. The transition from G-A to SC-A does not significantly alter this behaviour, while the adoption of SD-A leads to a more unbalanced system, characterized by a further concentration of impacts on the cathode and a marked reduction in the relative contribution of the anode. At the same time, electrolyte emerges as relevant contributors in selected categories, particularly in resource-related impacts. These findings confirm that, although anode chemistry influences the distribution of impacts, the overall environmental profile remains largely governed by cathode materials and process-related energy demand, emphasizing the need for combined strategies targeting both material design and process optimization to achieve a meaningful reduction in the environmental footprint.

6.2.9.4. Uncertainties evaluation through MCS

The uncertainty analysis was performed on the GW category to assess how the greater structural and compositional complexity of the full cell system is reflected in the propagation of uncertainty within the impact results. Consistently with the previous case, 10,000 MCS iterations were carried out to evaluate the

robustness of the outcomes. The coefficient of variability (***Table 6.29***) obtained for the full cell configuration remains remarkably consistent with the values previously observed for the electrode production study. For the FU of 1 coin cell, the coefficient of variability values were 2.44%, 2.40% and 2.41% for G-A, SC-A and SD-A, respectively. A similar trend was observed for the FU of 1 kWh, where the coefficient of variability ranges between 2.38% and 2.44%.

Table 6.29 – Monte Carlo simulation results for GW for the full cell system, considering both the FUs.

	Unit	FU: 1 coin cell			FU: 1 kWh		
		G-A	SC-A	SD-A	G-A	SC-A	SD-A
Trials	-	10,000	10,000	10,000	10,000	10,000	10,000
Base Case	kg CO_2-Eq	0.2717	0.2717	0.2689	67677	86007	98839
Mean	kg CO_2-Eq	0.2564	0.2561	0.2558	63445	80746	93678
Median	kg CO_2-Eq	0.2558	0.2556	0.2552	63311	80583	93481
Standard Deviation	kg CO_2-Eq	0.0062	0.0061	0.0062	1546	1957	2235
5% percentile	kg CO_2-Eq	0.2473	0.2471	0.2468	61183	77852	90328
95% percentile	kg CO_2-Eq	0.2676	0.2671	0.2669	66177	84271	97675
Coefficient of variability	%	2.4351	2.4007	2.4134	2.4367	2.4244	2.3865
Minimum	kg CO_2-Eq	0.2388	0.2371	0.2368	59160	74920	87576
Maximum	kg CO_2-Eq	0.2915	0.2854	0.2857	73940	89983	104835

Despite the increased structural and compositional complexity associated with the full cell configuration, the overall level of uncertainty did not increase significantly. This indicated that the additional system components, including casing, separator and electrolyte, introduced variability that remained proportionally consistent with the dispersion already observed at electrode level. A notable difference emerged when comparing these results with those obtained for the electrode production LCA. In the previous case, SD-A exhibited a lower coefficient of variability compared to G-A and SC-A, likely due to the simplified and geographically defined silicon supply chain. In the full cell configuration, however, this advantage disappeared, and SD-A aligned with the variability of the other chemistries. This suggested that, once the entire cell system was considered, the uncertainty contributions associated with additional materials and processes outweigh the reduced supply chain variability previously observed for silicon. In other words, the greater structural complexity of the full cell reduced the relative benefit derived from the more controlled silicon sourcing.

Figure 6.30 shows the Gaussian-shaped probability distributions associated with the FU of 1 coin cell for the three anode chemistries. The curves displayed a very similar Gaussian-shaped profile, with comparable spread and symmetry around their central values. The distributions largely overlapped along the entire range of impact values, indicating that the variability patterns were nearly identical across configurations. The tails of the distributions extended to similar

minimum and maximum values, and no chemistry exhibited a markedly broader or more asymmetric profile. Overall, in the comparison between the chemistries (***Figure 6.30d***), the strong overlap and the analogous shape of the curves suggested that the propagation of uncertainty remains consistent regardless of the anode composition at cell level.

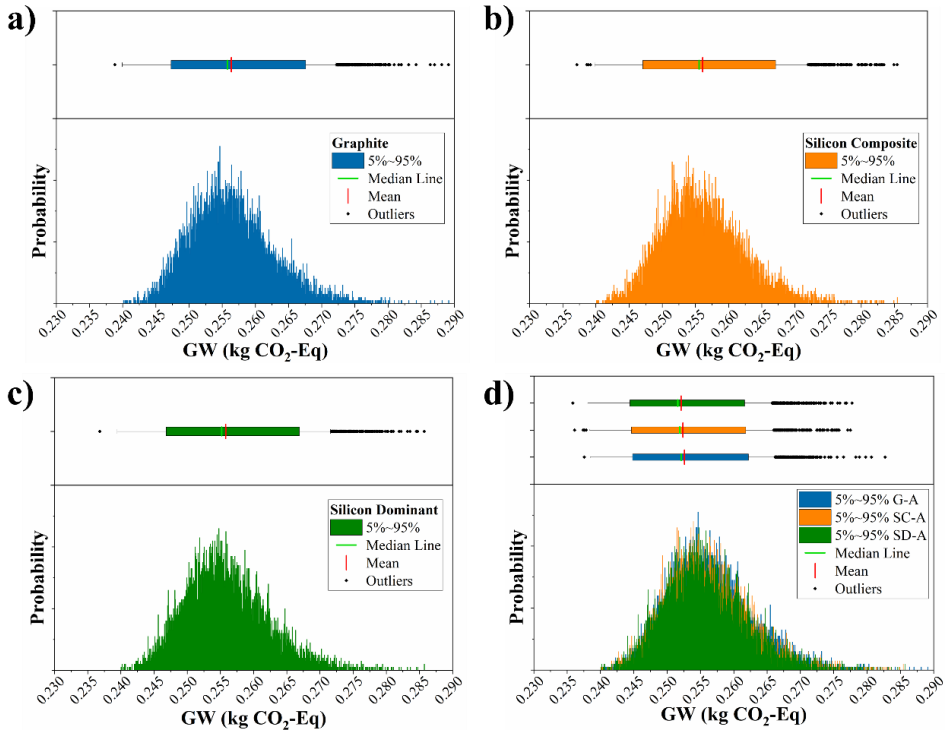

Figure 6.30 – Normal distributions obtained from 10,000 MCS for GW related to the full cell production using the FU of 1 coin cell. For each chemistry, the upper panel shows the box plot including mean, median, and outliers, while the lower panel presents the corresponding frequency histogram: a) G-A; b) SC-A; c) SD-A; d) Comparison between the three chemistries.

In contrast, for the FU of 1 kWh (***Figure 6.31***), the probability distributions were clearly separated in terms of absolute impact values, reflecting the different number of cells required to achieve the FU. Nevertheless, the relative spread of each distribution remained comparable, as confirmed by the similar coefficient of variability values. Although the standard deviation increases in absolute terms due to the scaling effect, the proportional variability remains stable across chemistries.

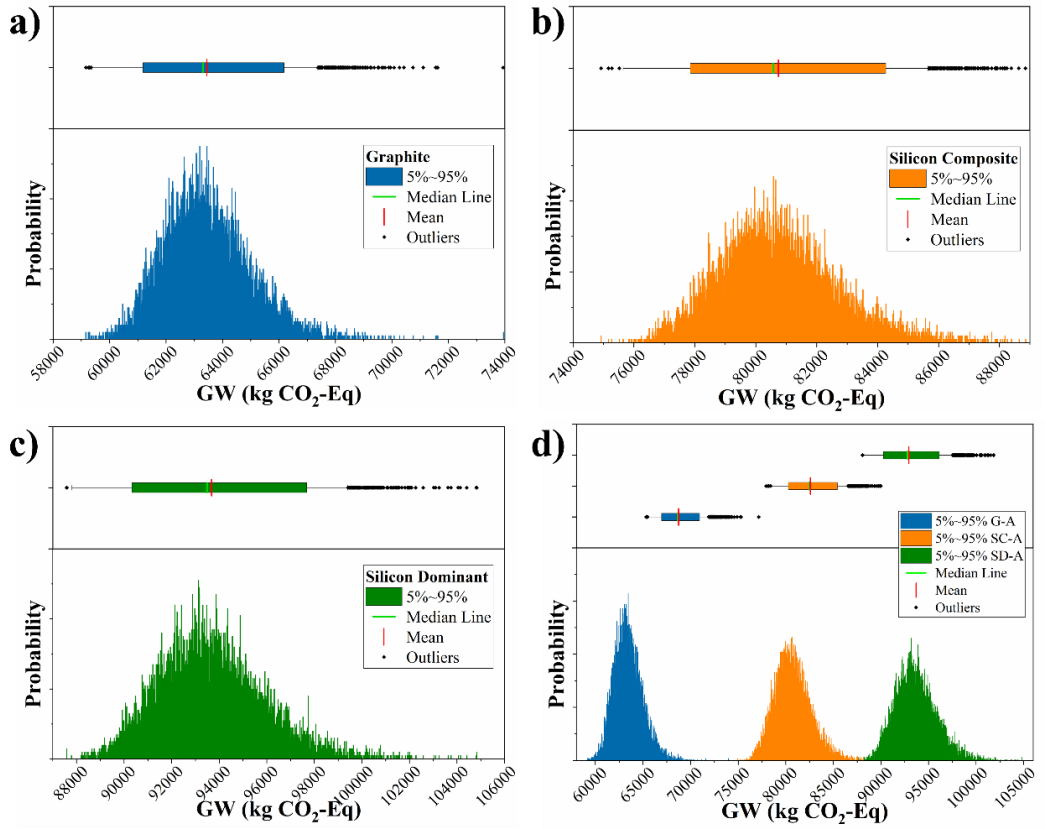

Figure 6.31 – Normal distributions obtained from 10,000 MCS for GW related to the full cell production using the FU of 1 kWh. For each chemistry, the upper panel shows the box plot including mean, median, and outliers, while the lower panel presents the corresponding frequency histogram: a) G-A; b) SC-A; c) SD-A; d) Comparison between the three chemistries.

6.2.9.5. Evaluation of endpoint impact categories

For completeness, the endpoint impact categories were also calculated in this study. As expected, and consistently with the previous case, the endpoint results closely reflected the trends observed for the midpoint categories. This coherence is consistent with the structure of the ReCiPe 2016 method, in which endpoint indicators are derived through the aggregation and damage modeling of midpoint categories.

In particular, the endpoint results for both FUs (***Figure 6.32***, ***Table 6.30***) followed a pattern similar to that observed at midpoint level. When considering the production of 1 coin cell, the variations in environmental impacts among the three anode chemistries remained almost negligible. In contrast, when adopting the FU of 1 kWh, the differences became more pronounced. In this case, the SC-A configuration showed an increase in endpoint impacts of approximately 25% compared to G-A, while SD-A exhibited an increase of around 50%. This amplification was consistent with the higher number of cells required to achieve the same energy output and confirmed that, under an energy-based FU,

electrochemical performance became the dominant driver of the overall environmental profile.

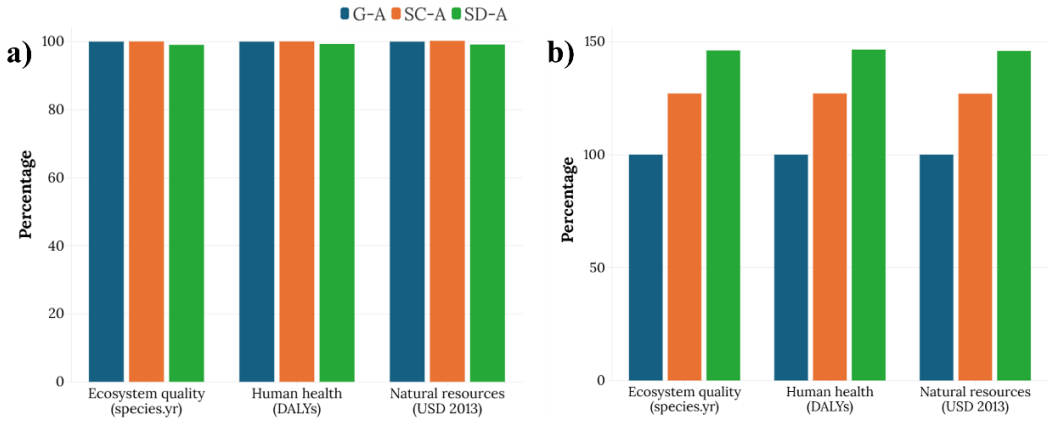

Figure 6.32 – Percentage change in endpoint results depending on the anode chemistries and FUs: a) 1 coin cell; b) 1 kWh

Table 6.30 – Endpoint impact category results for the three anode chemistries calculated using both the FUs.

Endpoint Category	Results per 1 coin cell			Results per 1 kWh of production		
	G-A	SC-A	SD-A	G-A	SC-A	SD-A
Ecosystem quality [species.yr]	1,130E-09	1,131E-09	1,119E-09	2,820E-04	3,583E-04	4,120E-04
Human health [DALYs]	7,046E-07	7,051E-07	6,997E-07	0,1777	0,2258	0,2604
Natural resources [USD 2013]	0,0280	0,0281	0,0278	6904,41	8769,55	10072,55

As observed in the previous case focused on the electrode production, the NR damage category remains the dominant contributor to total impacts also for the full cell configuration. This result is primarily attributable to the material intensity of the system, including both the raw materials required for electrode production and the contribution of stainless-steel components used in the casing. In detailed LCAs of LIBs, the steel housing has been shown to contribute significantly to abiotic resource depletion due to the presence of alloying metals such as chromium and nickel in the steel structure [575]. Moreover, dedicated studies on battery casing demonstrate that replacing steel with lighter materials reduces several impact categories, with steel exhibiting the highest impacts, including those related to resource use [575].

Overall, the LCA on endpoint categories reinforced the interpretation derived from the midpoint analysis and confirmed that cell geometry and electrochemical performance dominated the environmental profile of the coin cell configuration. The prevalence of the NR damage category further highlighted the high material demand of the system, where structural components and stainless steel elements

outweigh the contribution of active materials. These findings demonstrated that, within laboratory-scale architectures, environmental impacts were strongly governed by design efficiency and material choices rather than by variations in anode chemistry alone. Consequently, environmental sustainability improvements associated with material innovation must be evaluated in combination with geometry optimization and performance improvements to ensure meaningful environmental benefits.

6.3. Methodological sensitivity: comparison between ReCiPe and EF Methods

While the MCS performed in the previous sections allows for the quantification of parameter uncertainty derived from the variability of background inventory data, it does not safeguard the study against the structural (or model) uncertainty inherent to LCIA methodologies. Indeed, different characterization approach employ distinct modeling approaches, environmental mechanisms, and spatial-temporal assumptions to translate emission and resource flows into potential environmental impacts. As extensively highlighted in the battery literature review (***Table 6.1***), a uniform consensus on the preferred LCIA method has not yet been established. Sector-specific studies, as reported by Tolomeo et al. [342], frequently alternate between the ReCiPe approach and other methods, which often complicates cross-study comparisons. In addition, this comparison is highly important because the EF method is steadily becoming the mandatory standard in modern regulations, meaning that future battery environmental sustainability assessments will likely be required to use it by law. Therefore, introducing this methodological sensitivity analysis addresses the necessity of validating the robustness of the conclusions drawn so far. By recalculating the entire inventory at both the anode production level and the full-cell level using the EF 3.1 method, this section aims to verify whether the environmental hierarchy and the benefits associated with the different FUs and chemistries investigated remain almost invariant, regardless of the mathematical characterization model adopted.

6.3.1. Methodological Framework of EF vs ReCiPe

To properly interpret the outcomes of this cross-methodological sensitivity analysis, it is essential to first establish the foundational differences governing the two selected LCIA approaches. o ensure a rigorous comparison, it is important to emphasize that all system boundaries, data cutoff criteria, allocation rules, and technological assumptions previously established for the baseline model remain strictly unchanged throughout this analysis. By keeping the underlying LCI completely identical, this approach isolates the structural uncertainty of the

characterization models. Consequently, any observed variations or stabilities in the environmental profiles can be confidently attributed to the mathematical and conceptual differences between the ReCiPe 2016 [343] and EF 3.1 [345] approaches, rather than to alterations in data quality, proxy choices, or technical scope.

From a structural point of view, these two methods represent distinct modeling approaches. ReCiPe 2016 provides a harmonized midpoint-to-endpoint approach; its Hierarchist perspective is selected here as the baseline, representing the standard scientific consensus over a 100-year time frame. Conversely, the EF 3.1 approach, initiated by the JRC to support the PEF initiative, focuses strictly on a standardized set of midpoint categories paired with mandatory normalization and weighting factors. Crucially, EF 3.1 has been designated as the mandatory methodology under the European Battery Regulation [576] for computing the carbon footprint and environmental profiles of traction and industrial batteries, making its structural comparison against academic baselines highly relevant.

These conceptual distinctions yield prominent modeling discrepancies within the specific impact categories that drive battery value chains. For climate impacts, both frameworks utilize IPCC 100-year models, but while ReCiPe aggregates greenhouse effects into a single Global Warming metric, within EF 3.1, climate change is disaggregated into fossil, biogenic, and land use/land use change contributions, each with its own reporting structure, which improves transparency for products containing both fossil-based and biogenic carbon flows. Resource depletion modeling presents an even deeper divide: ReCiPe adopts a surplus energy cost approach, measuring resource scarcity in MJ based on the extra energy future generations must expend as ore grades deplete. In contrast, EF 3.1 utilizes the Abiotic Depletion Potential (ADP) model for non-fossil resources, measuring scarcity in kg Sb eq relative to ultimate crustal reserves. Consequently, EF 3.1 penalizes the consumption of geologically scarce elements far more severely than ReCiPe, which focuses instead on long-term extraction energy penalties.

Toxicological assessment also feature high structural uncertainty due to the complexity of modeling environmental transport, fate, and exposure pathways. ReCiPe 2016 relies on the EUSES model, expressing human and ecotoxicological impacts in kg 1,4-DCB eq, whereas EF 3.1 uniformly adopts the consensus-based USEtox 2.0 approach, utilizing CTUh and CTUe metrics. The USEtox model incorporates more stringent fate and exposure modeling for heavy metals, which heavily penalizes upstream metallurgical mining and CC manufacturing involving copper and aluminum foils. Furthermore, WC metrics diverge from simple volumetric accounting to stress-weighted modeling. While ReCiPe tracks unregionalized net consumption in m^3, EF 3.1 implements the regionalized AWARE model, weighting water volume by the local user-to-availability ratio to assess deprivation risks in water-stressed manufacturing regions. Ultimately,

mapping out these methodological boundaries allows the subsequent analysis to verify whether these distinct mathematical formulations alter the relative environmental competitiveness and engineering viability of the developed SD-A chemistry against the state-of-the-art commercial benchmarks.

6.3.2. Comparison at anode production level

The cross-methodological comparison for the performance-based capacity baseline of 1 Ah reveals a uniform and substantial environmental advantage for the SD-A chemistry across nearly all impact categories. As compiled in ***Table 6.31***, the total GW impact with the EF 3.1 approach drops drastically from 6.0026 kg CO_2 eq for the baseline G-A and 3.4917 kg CO_2 eq for the SC-A, down to a mere 0.0397 kg CO_2 eq for the SD-A. A highly consistent parallel is observed within the ReCiPe 2016 approach, which captures the same pronounced decrease.

Table 6.31 – Comparative results for 1 Ah of anode capacity across G-A, SC-A, and SD-A chemistries using EF 3.1 and ReCiPe 2016 approaches.

Results for 1 Ah of production						
Impact category	**EF 3.1**			**ReCiPe 2016**		
	G-A	**SC-A**	**SD-A**	**G-A**	**SC-A**	**SD-A**
TA	0.0199	0.0116	2.8E-04	0.0031	0.0019	1.96E-04
GW	6.0026	3.4917	0.0397	1.33	0.793	0.0409
GW-bio	0.0155	0.0090	4.77E-04			
GW-fos	5.9863	3.4821	0.0392			
GW-lu	8.35E-04	5.13E-04	1.26E-05			
FE	7.6728	4.4719	0.2067	1.24	0.766	0.505
FE-inorg	7.3370	4.2767	0.2037			
FE-org	0.3358	0.1952	0.0030			
FRS	100.64	58.5012	0.5902	0.431	0.255	0.0120
FET	0.0014	8.32E-04	1.89E-05	3.29E-04	1.98E-04	1.89E-05
MET	0.0037	0.0021	3.41E-05	3.00E-05	1.80E-05	1.10E-06
TET	0.0382	0.0223	0.0004			
CHT	7.97E-10	4.63E-10	2.64E-11	0.123	0.0734	0.0056
CHT-inorg	3.35E-10	1.95E-10	1.46E-11			
CHT-org	4.62E-10	2.68E-10	1.18E-11			
NCHT	2.77E-08	1.61E-08	1.9E-09	1.01	0.600	0.166
NCHT-inorg	2.59E-08	1.5E-08	1.39E-09			
NCHT-org	1.81E-09	1.05E-09	5.18E-10			
IR	0.8573	0.4983	0.0044	0.178	0.105	0.00414
LU	14.8899	8.6587	0.2407	0.0283	0.0167	0.00198
MRU	1.62E-05	9.39E-06	1.71E-06	0.0163	0.00897	8.73E-04
SOD	1.50E-07	8.68E-08	7.88E-10	6.01E-07	3.53E-07	1.83E-08
PMF	7.67E-08	4.53E-08	1.14E-09	0.0012	7.28E-04	6.94E-05
POFHH	0.0157	0.0091	1.41E-04	0.0021	0.0013	8.83E-05
WC	3.5629	2.0646	0.0425	0.0181	0.0106	9.9E-04

The sub-division provided by EF 3.1 demonstrates that the climate footprint is overwhelmingly dominated by the fossil component (GW-fos), which accounts for over 98% of the total GHG emissions across all three formulations, tracking the high energy demands of raw material processing. Resource-related metrics such as FRS and WC display a highly consistent decline when transitioning from graphite to SD configurations, regardless of the distinct characterization models, such as the regionalized AWARE water stress mechanism in EF 3.1 versus the unregionalized volumetric approach in ReCiPe, used by the two software frameworks.

When evaluating the environmental profiles of 1 kg of manufactured anode, the absolute indicator values scale up across all configurations, nonetheless, the performance hierarchy among the configurations remains unaltered for the main indicators, as shown in ***Table 6.32***. The GWP reaches 7.07E+05 kg CO_2 eq (EF 3.1) and 157 kg CO_2 eq (ReCiPe) for the G-A, dropping down to 1.11E+04 kg CO_2 eq (EF 3.1) and 11.5 kg CO_2 eq (ReCiPe) for the SD-A. Evaluating the data per kg is useful because it separates the environmental impact of the materials from their electrical performance. This allows for a direct weight comparison, making it easier to see specific differences between the two methods that the high capacity of the silicon anode might otherwise hide.

Table 6.32 – Comparative results for 1 kg of anode capacity across G-A, SC-A, and SD-A chemistries using EF 3.1 and ReCiPe 2016 approaches.

Results for 1 kg of production

Impact category	EF 3.1			ReCiPe 2016		
	G-A	SC-A	SD-A	G-A	SC-A	SD-A
TA	2347	2105	78	0.364	0.337	0.0552
GW	7.07E+05	6.32E+05	1.11E+04	157	144	11.5
GW-bio	1820	1622	134			
GW-fos	7.05E+05	6.30E+05	1.10E+04			
GW-lu	98	93	3.55			
FE	9.04E+05	8.09E+05	5.80E+04	146	139	142
FE-inorg	8.64E+05	7.74E+05	5.72E+04			
FE-org	3.95E+04	3.53E+04	840			
FRS	1.18E+07	1.06E+07	1.66E+05	50.8	46.2	3.37
FET	167	150	5.31	0.0387	0.0358	0.0053
MET	430	386	9.59	0.0035	0.0033	0.0003
TET	4499	4032	106			
CHT	9.39E-05	8.38E-05	7.43E-06	14.5	13.3	1.56
CHT-inorg	3.95E-05	3.53E-05	4.11E-06			
CHT-org	5.44E-05	4.85E-05	3.32E-06			
NCHT	0.0033	0.0029	5.35E-04	119	109	46.5
NCHT-inorg	0.0030	0.0027	3.89E-04			
NCHT-org	2.13E-04	1.9E-04	1.46E-04			
IR	1.01E+05	9.02E+04	1240	21.0	19.1	1.16

LU	1.75E+06	1.57E+06	6.76E+04	3.33	3.02	0.556
MRU	1.91	1.70	0.48	1.92	1.62	0.245
SOD	0.0176	0.0157	2.21E-04	7.08E-05	6.39E-05	5.14E-06
PMF	0.0090	0.0082	3.2E-04	0.141	0.132	0.0195
POFHH	1849	1655	40	0.246	0.226	0.0248
WC	4.20E+05	3.74E+05	1.19E+04	2.13	1.91	0.278

Despite this general structural alignment, a critical methodological divergence emerges when analyzing FE with the mass FU. While the EF 3.1 approach tracks a perfectly linear reduction in FE from G-A (9.04E+05) through SC-A (8.09E+05) down to SD-A (5.80E+04), the ReCiPe 2016 method undergoes a distinct structural rank inversion: the SC-A exhibits the lowest overall emissions at 139 kg P eq, whereas the SD-A formulation rises to 142 kg P eq. This difference happens because the two methodologies use completely different models to evaluate ecotoxicity. EF 3.1 relies on the USEtox model (measuring in CTUe), while ReCiPe 2016 applies the USES-LCA model (measuring in kg 1,4-DCB eq). However, this difference disappears when looking at the 1 Ah capacity FU, where the better performance of the SD-A reduces the total material weight needed, compressing its FE impact (0.2067 CTUe for EF 3.1 and 0.505 kg 1,4-DCB eq for ReCiPe).

To visually synthesize these GHG dynamics, ***Figure 6.33*** provides a comprehensive cross methodological comparison of the total GW impacts. ***Figure 6.33a*** illustrates the carbon footprint normalized per unit of electrochemical capacity, where the exceptional specific capacity of the SD-A collapses the environmental impact to a tiny fraction of the G-A. This profound visual decrease is replicated with high consistent parallel within the ReCiPe 2016 framework, confirming that the developed SD-A configuration delivers a substantial and robust mitigation of carbon emissions per unit of useful service. Conversely, ***Figure 6.33b*** isolates the intrinsic climate burden per 1 kg of manufactured anode, separating the environmental impact of the materials and processing from their electrochemical performance. While the overall hierarchy G-A > SC-A > SD-A is maintained, this dimension exposes a critical methodological divergence between EF 3.1 and ReCiPe 2016. In the EF 3.1 method, the absolute numbers are astronomically high and the visual comparison with the ReCiPe 2016 approach is almost impossible. The included dotted zoom box within the ReCiPe graph demonstrates a clear visual and numerical distinction for the three formulations. This graph visually clarifies that while SC-A does offer a slight performance benefit, it does not achieve a decisive environmental win over G-A from a purely material perspective, demonstrating only a minimal decrease in CO_2 emissions when performance is excluded. Only the developed SD-A delivers an environmental win across both performance and mass dimensions, a core validation which this image concisely and powerfully confirms.

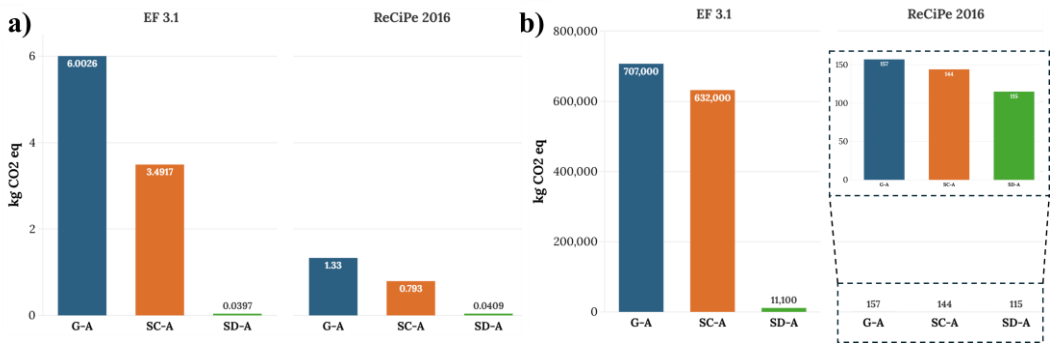

Figure 6.33 – Comparative evaluation of GW impacts, contrasting the EF 3.1 and ReCiPe 2016 characterization models: a) 1 Ah of electrochemical capacity; b) 1 kg of manufactured anode.

Ultimately, these findings show that the choice between EF 3.1 and ReCiPe 2016 does not alter the main conclusions of the study. Even with minor method-specific differences, both approaches clearly confirm that the developed SD-A is the most environmentally sustainable option when actual anode performance is taken into account.

6.3.3. Comparison at full cell level

Moving the analysis to the full-cell level allows for an evaluation of the material configurations within a complete battery system. When looking at the production of a single coin cell (***Table 6.33***), the environmental impacts of the three chemistries are remarkably similar. For example, under the EF 3.1 framework, the GW impact is 0.2658 kg CO_2 eq for G-A, 0.2659 kg CO_2 eq for SC-A, and 0.2631 kg CO_2 eq for SD-A. The ReCiPe 2016 method reflects this exact same trend, with GW values set at 0.2717 kg CO_2 eq for both G-A and SC-A, and dropping slightly to 0.2689 kg CO_2 eq for SD-A. At this level, the GW is heavily dominated by common cell components like the casing, separator, electrolyte, and manufacturing processes, rather than the active mass of the anode. Both characterization methods are in perfect agreement regarding this behavior.

Table 6.33 – Comparative results for 1 coin cell production across G-A, SC-A, and SD-A chemistries using EF 3.1 and ReCiPe 2016 approaches.

Results for 1 coin cell

Impact category	EF 3.1			ReCiPe 2016		
	G-A	SC-A	SD-A	G-A	SC-A	SD-A
TA	9.35E-04	9.36E-04	9.27E-04	0.6301	0.6309	0.6249
GW	0.2658	0.2659	0.2631	0.2717	0.2717	0.2689
GW-bio	1.078E-04	1.079E-03	1.072E-03			
GW-fos	0.26467	0.26476	0.26198			
GW-lu	9.76E-05	9.82E-05	9.78E-05			
FE	0.6536	0.6773	0.6741	0.0122	0.0122	0.0121
FE-inorg	0.6385	0.6622	0.6592			
FE-org	0.015073	0.01509	0.01493			

FRS	4.5030	4.5033	4.4561	0.0863	0.0864	0.0854
FET	7.85E-05	7.85E-05	7.79E-05	7.85E-02	7.86E-02	7.79E-02
MET	1.73E-04	1.73E-04	01.71E-04	8.14E-03	8.18E-03	8.11E-03
TET	1.831E-03	1.833E-03	1.815E-03			
CHT	5.24E-11	5.24E-11	5.21E-11	0.0632	0.0633	0.0630
CHT-inorg	2.16E-11	2.17E-11	2.15E-11			
CHT-org	3.08E-11	3.08E-11	3.06E-11			
NCHT	1.33E-09	1.33E-09	1.32E-09	0.2994	0.2997	0.2985
NCHT-inorg	1.24E-09	1.24E-09	1.23E-09			
NCHT-org	8.89E-11	8.9E-11	8.91E-11			
IR	0.044412	0.044414	0.044011	0.0422	0.0422	0.0418
LU	0.7149	0.7156	0.7090	0.0059	0.0059	0.0058
MRU	8.06E-07	8.09E-07	8.06E-07	0.0047	0.0050	0.0049
SOD	6.35E-09	6.35E-09	6.28E-09	1.18E-04	1.18E-04	1.17E-04
PMF	4.5E-09	4.51E-09	4.48E-09	0.2613	0.2617	0.2593
POFHH	7.05E-04	7.06E-04	6.99E-04	0.4325	0.4328	0.4284
WC	0.18065	0.18069	0.17905	4.206	4.207	4.169

However, a dramatic shift occurs when the results are scaled up to 1 kWh of full-cell capacity (***Table 6.34***). At this performance baseline, a clear environmental hierarchy emerges where the G-A shows the lowest impact and the SD-A shows the highest, for both the calculation methods (EF 3.1 and ReCiPe 2016). This same ranking is consistently maintained across all other impact categories in both methods. This overall trend happens because in this specific coin cell configuration, the lower electrochemical performance of SD-A compared to G-A, requires a significantly higher number of physical cells to reach a total capacity of 1 kWh.

Table 6.34 – Comparative results for 1 kWh of full cell capacity across G-A, SC-A, and SD-A chemistries using EF 3.1 and ReCiPe 2016 approaches.

Results for 1 kWh of production						
Impact category	**EF 3.1**			**ReCiPe 2016**		
	G-A	**SC-A**	**SD-A**	**G-A**	**SC-A**	**SD-A**
TA	234	297	341	157.44	200.04	230.13
GW	6.62E+04	8.42E+04	9.67E+04	6.77E+04	8.60E+04	9.88E+04
GW-bio	277	352	406			
GW-fos	6.59E+04	8.38E+04	9.63E+04			
GW-lu	24	31	36			
FE	1.27E+05	1.59E+05	1.84E+05	3069.88	3900.87	4514.07
FE-inorg	1.23E+05	1.55E+05	1.78E+05			
FE-org	3647	4636	5327			
FRS	1.12E+06	1.42E+06	1.63E+06	2.14E+04	2.72E+04	3.12E+04
FET	20	25	29	19.64	24.96	28.75
MET	43	55	63	2.04	2.59	2.98
TET	457	581	668			

CHT	1.16E-05	1.47E-05	1.7E-05	1.62E+04	2.06E+04	2.39E+04
CHT-inorg	5.44E-06	6.91E-06	7.98E-06			
CHT-org	6.18E-06	7.82E-06	9.01E-06			
NCHT	3.25E-04	4.13E-04	4.76E-04	7.61E+04	9.67E+04	1.12E+05
NCHT-inorg	3.06E-04	3.89E-04	4.49E-04			
NCHT-org	1.88E-05	2.39E-05	2.79E-05			
IR	1.12E+04	1.42E+04	1.64E+04	1.07E+04	1.35E+04	1.56E+04
LU	1.78E+05	2.27E+05	2.61E+05	1472	1871	2152
MRU	0.1910	0.2424	0.2805	1134	1420	1638
SOD	0.0016	0.0020	0.0023	0.0297	0.0377	0.0433
PMF	0.0011	0.0014	0.0016	65	83	95
POFHH	174	221	254	107	136	157
WC	4.57E+04	5.80E+04	6.68E+04	1063	135	1555

To provide complete methodological transparency regarding the full cell configurations, ***Figure 6.34*** illustrates the GW profiles across both FUs. ***Figure 6.34a*** highlights the impact at a single cell level, where the GHG contributions of G-A, SC-A, and SD-A are nearly indistinguishable, hovering around 0.26 kg CO_2 eq. This uniformity occurs because the heavy stainless steel coin cell housing completely overwhelms the inventory, masking the underlying variations in anode chemistry. Conversely, ***Figure 6.34b*** visually captures the massive numerical inflation that takes place when these laboratory metrics are mathematically scaled up to a macro scale functional unit of 1 kWh. Because a coin cell possesses an extremely unfavorable ratio of inactive structural mass to active material energy capacity, a literal linear multiplication to reach 1 kWh forces the model to replicate thousands of heavy inactive components. This structural overhead drives the values to extraordinary levels, where the SD-A configuration exhibits the highest footprint due to the worst cell capacity. Far from representing a prospective commercial battery pack, this visual divergence serves as a powerful validation of the extreme caution required when interpreting raw laboratory upscaling data, reinforcing that these macro scale values function strictly as theoretical indicators rather than industrial projections.

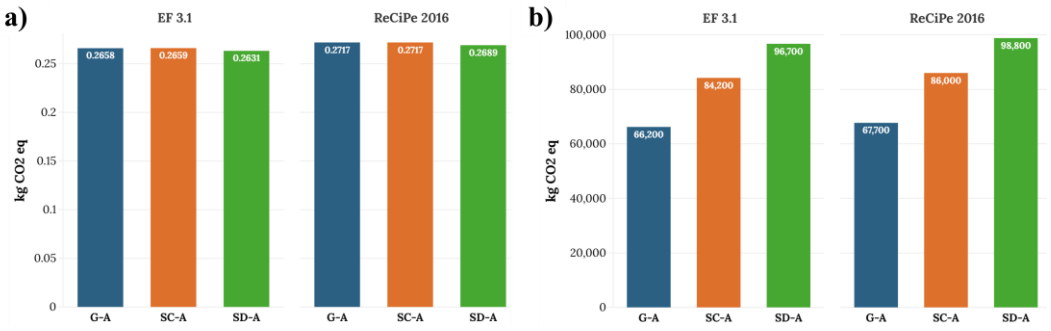

Figure 6.34 – Comparative evaluation of GW impacts, contrasting the EF 3.1 and ReCiPe 2016 characterization models: a) 1 coin cell; b) 1 kWh.

From a methodological point-of-view, the most important finding here is the total consistency between the two calculation frameworks. Even though EF 3.1 and ReCiPe 2016 use completely different mathematical models and units for categories like toxicity and acidification, they lead to identical rankings and proportional changes across the chemistries. This absolute alignment proves that model uncertainty does not affect the full-cell conclusions, providing a highly robustness for the study.

6.4. Main findings and implications

The LCA conducted in this chapter provided a comprehensive environmental evaluation of the anode chemistries developed and experimentally optimized throughout this work. By combining primary foreground data with background datasets, the analysis ensured methodological consistency between laboratory-scale processing conditions and environmental impacts.

The results demonstrated that the environmental impacts of silicon-based anodes strongly depend on the selected FU and system boundary. When assessed through a performance-based FU (1 Ah), the SD-A exhibited important reductions across most midpoint categories, primarily driven by its higher specific capacity and the associated decrease in material demand per unit of delivered capacity. In contrast, when adopting a mass-based FU (1 kg), the magnitude of these improvements was reduced, highlighting how the interpretation of environmental impacts shifted according to the different FU adopted.

The extension of the system boundaries to the full-cell configuration further emphasized the critical role of system architecture and energy density. At cell level, considering the FU of 1 coin cell, the dominance of structural components and casing mass partially masked the intrinsic differences between anode chemistries. When the FU was defined as delivered energy (1 kWh), electrochemical performance and design efficiency emerged as primary factors of the environmental impacts.

These findings underline that material innovation alone is not sufficient to guarantee environmental improvement. Instead, environmental sustainability benefits can only be fully realized when enhanced material properties are effectively translated into optimized cell design and manufacturing efficiency. Beyond the specific results obtained for the investigated anode chemistries, this work highlights the critical role of methodological choices in the LCA of emerging battery technologies. In particular, the combined use of mass-based and performance-based FUs, together with the progressive expansion of system boundaries from electrode to full cell level, proved essential to correctly interpret the environmental implications of material innovation. These aspects confirm that LCA outcomes for batteries cannot be meaningfully discussed without explicit reference to the FU and the technological scale considered.

Finally, the cross-methodological sensitivity analysis comparing EF 3.1 and ReCiPe 2016 verified that the study's findings are robust against model uncertainty. Although the two frameworks rely on different underlying characterization models, which led to important variations, both methods ultimately yielded the same environmental rankings and trends, proving that the choice of calculation framework does not alter the core conclusions of this work. Furthermore, aligning the analysis with the EF framework provides valuable future-proofing for the study, as this methodology is rapidly becoming the mandatory standard in modern battery regulations.

Overall, this chapter confirmed the necessity of integrating electrochemical development with environmental assessment from the early stages of technology design. The combination of experimental and LCA approach adopted in this work provided a robust framework for evaluating next-generation battery materials within a environmental sustainability perspective, while acknowledging the limitations inherent to laboratory-scale modelling and prospective assumptions.

Future research should focus on translating high-capacity anode materials into cell architectures that effectively exploit their potential, reducing the relative contribution of inactive components. In parallel, the integration of recycling scenarios and industrial-scale manufacturing data will be essential to fully assess the environmental sustainability potential of SD-A within realistic battery systems.

Chapter 7

7. Conclusion and perspectives

This Ph.D. work demonstrates that the development of LIB anodes cannot be effectively addressed through a sequential approach, where electrochemical performance, manufacturing, and environmental sustainability are considered independently. Instead, these aspects must be treated as strongly interconnected variables within a unified design framework.

From a materials perspective, the progressive transition from graphite to silicon-based anodes confirmed the potential of silicon to significantly enhance specific and areal capacity. However, this improvement is intrinsically associated with increased complexity in electrode design, processing, and stability. In particular, high-silicon-content systems highlighted critical challenges related to mechanical integrity and processability, which cannot be overcome by material selection alone.

The experimental results clearly show that electrode formulation, and especially binder chemistry, plays a central role in controlling both electrochemical performance and manufacturability. The development of aqueous binder systems, including the use of natural polysaccharides, proved to be an effective strategy to improve slurry stability, coating quality, and cycling behaviour, particularly for SD electrodes. At the same time, the rheological properties of the slurry emerged as a key parameter, especially when transitioning from laboratory-scale to pilot-line production.

From a manufacturing perspective, this work demonstrates that scale-up requires the adaptation of both formulations and process parameters to different facilities, as the direct application of laboratory conditions leads to variability and performance loss. The comparison between laboratory and pilot-line production demonstrated that electrode quality, reproducibility, and performance are strongly influenced by processing conditions, confirming that manufacturability must be considered from the early stages of material development.

The LCA results further reinforced this perspective, showing that environmental impact is not only due to material composition, but also to process-related factors such as energy consumption, drying conditions, and production scale. The integration of primary experimental data into the LCA framework enabled a more realistic evaluation of the environmental implications of different material and process configurations.

An important perspective emerging from this work is the possibility of integrating electrochemical performance and environmental assessment at the early stages of battery design. The combined use of primary experimental data and LCA models provides the basis for the development of a dynamic evaluation framework, in which material selection, electrode formulation, and process parameters can be directly linked to both performance indicators and environmental impacts. In this context, the LCA model developed in this work could be extended toward a more application-oriented tool, capable of interfacing with simplified design tools to simulate different cell configurations. Such an approach would enable the real-time evaluation of alternative design choices, allowing the identification of optimal combinations of energy density, manufacturability, and environmental impact. Although not fully implemented within this study, this perspective highlights the potential of transitioning from a static LCA analysis to a dynamic, design-support methodology, where environmental sustainability considerations are embedded directly within the battery development process rather than assessed a posteriori.

Overall, the results indicate that increasing energy density through the introduction of silicon-based anodes requires a redefinition of battery development strategies. Rather than focusing solely on material optimization, an integrated approach in which electrode formulation, processing conditions, and manufacturing aspects are considered from the early stages of design. In this context, silicon-based electrodes emphasize the strong interdependence between material properties and process parameters, showing that achieving high performance and reproducibility depends on the ability to control the entire manufacturing chain, from slurry formulation to electrode fabrication.

The main contribution of this dissertation lies in the demonstration that high-performance battery materials and sustainable manufacturing strategies are not mutually exclusive, but must be co-designed. The proposed integrated approach provides a framework for the development of next-generation LIBs in which performance, scalability, and environmental impact are simultaneously optimized. Future research should focus on further improving the stability of high-silicon-content electrodes, refining aqueous processing strategies, and extending the integrated methodology to full-cell systems and industrial-scale production. Particular attention should be devoted to the coupling between advanced materials and low-impact manufacturing technologies, to accelerate the transition toward more sustainable energy storage systems.

References

[1] The European Green Deal - European Commission. https://commission.europa.eu/strategy-and-policy/priorities-2019-2024/european-green-deal_en (accessed March 15, 2026).

[2] European Climate Law | EUR-Lex. https://eur-lex.europa.eu/EN/legal-content/summary/european-climate-law (accessed March 15, 2026).

[3] J. Amici, P. Asinari, E. Ayerbe, P. Barboux, P. Bayle-Guillemaud, R.J. Behm, M. Berecibar, E. Berg, A. Bhowmik, S. Bodoardo, I.E. Castelli, I. Cekic-Laskovic, R. Christensen, S. Clark, R. Diehm, R. Dominko, M. Fichtner, A.A. Franco, A. Grimaud, N. Guillet, M. Hahlin, S. Hartmann, V. Heiries, K. Hermansson, A. Heuer, S. Jana, L. Jabbour, J. Kallo, A. Latz, H. Lorrmann, O.M. Løvvik, S. Lyonnard, M. Meeus, E. Paillard, S. Perraud, T. Placke, C. Punckt, O. Raccurt, J. Ruhland, E. Sheridan, H. Stein, J.M. Tarascon, V. Trapp, T. Vegge, M. Weil, W. Wenzel, M. Winter, A. Wolf, K. Edström, A Roadmap for Transforming Research to Invent the Batteries of the Future Designed within the European Large Scale Research Initiative BATTERY 2030+, Adv. Energy Mater. 12 (2022). https://doi.org/10.1002/aenm.202102785.

[4] Can Europe go electric and remain sovereign? | T&E. https://www.transportenvironment.org/articles/can-europe-go-electric-and-remain-sovereign (accessed March 16, 2026).

[5] A. Racu, J. Poliscanova, An industrial blueprint for batteries in Europe How Europe can successfully build a sustainable battery value chain Transport & Environment Further information, (2024). www.transportenvironment.org (accessed June 30, 2025).

[6] J.C. Barbosa, R.S. Pinto, J.P. Serra, R. Gonçalves, E. Lizundia, C.M. Costa, S. Lanceros-Mendez, Batteries and sustainability: the relevance of life cycle assessment, Sustainable Energy Technologies and Assessments 82 (2025) 104488. https://doi.org/10.1016/j.seta.2025.104488.

[7] Impact and Challenges - Battery 2030+. https://battery2030.eu/battery2030/about-us/impact-and-challenges/ (accessed March 16, 2026).

[8] R. Korthauer, Lithium-ion batteries: Basics and applications, Springer Berlin Heidelberg, 2018. https://doi.org/10.1007/978-3-662-53071-9.

[9] The Nobel Prize in Chemistry 2019 - NobelPrize.org. https://www.nobelprize.org/prizes/chemistry/2019/summary/ (accessed October 20, 2025).

[10] M. Armand, P. Axmann, D. Bresser, M. Copley, K. Edström, C. Ekberg, D. Guyomard, B. Lestriez, P. Novák, M. Petranikova, W. Porcher, S. Trabesinger, M. Wohlfahrt-Mehrens, H. Zhang, Lithium-ion batteries – Current state of the art and anticipated developments, J. Power Sources 479 (2020). https://doi.org/10.1016/j.jpowsour.2020.228708.

[11] M. Krichen, Y. Basheer, S.M. Qaisar, A. Waqar, A Survey on Energy Storage: Techniques and Challenges, Energies (Basel). 16 (2023). https://doi.org/10.3390/en16052271.

[12] Armand M., Tarascon J. M., Building better batteries, Nature 2008 451:7179 451 (2008) 652–657. https://doi.org/10.1038/451652a.

[13] J.T. Frith, M.J. Lacey, U. Ulissi, A non-academic perspective on the future of lithium-based batteries, Nat. Commun. 14 (2023) 420. https://doi.org/10.1038/s41467-023-35933-2.

[14] S. Yan, C.-H. Yim, V. Pankov, M. Bauer, E. Baranova, A. Weck, A. Merati, Y. Abu-Lebdeh, C. Gerbaldi, Perovskite Solid-State Electrolytes for Lithium Metal Batteries, (2021). https://doi.org/10.3390/batteries7040075.

[15] D.E. Demirocak, S.S. Srinivasan, E.K. Stefanakos, A review on nanocomposite materials for rechargeable Li-ion batteries, Applied Sciences (Switzerland) 7 (2017). https://doi.org/10.3390/app7070731.
[16] X. Li, X. Sun, X. Hu, F. Fan, S. Cai, C. Zheng, G.D. Stucky, Review on comprehending and enhancing the initial Coulombic efficiency of anode materials in lithium-ion/sodium-ion batteries, Nano Energy 77 (2020) 105143. https://doi.org/10.1016/J.NANOEN.2020.105143.
[17] What are SOC and SOH of a battery, how to measure them?. https://www.biologic.net/topics/battery-states-state-of-charge-soc-state-of-health-soh/ (accessed November 28, 2025).
[18] J.T. Warner, The Handbook of Lithium-Ion Battery Pack Design: Chemistry, Components, Types, and Terminology, 2nd Edition, Elsevier Science, 2024.
[19] Y. Xing, E.W.M. Ma, K.L. Tsui, M. Pecht, Battery Management Systems in Electric and Hybrid Vehicles, Energies 2011, Vol. 4, Pages 1840-1857 4 (2011) 1840–1857. https://doi.org/10.3390/EN4111840.
[20] P.-A. Le, A general introduction to lithium-ion batteries: From the first concept to the top six commercials and beyond, Journal of Electrochemical Science and Engineering (2023). https://doi.org/10.5599/jese.1544.
[21] K. Xu, Nonaqueous Liquid Electrolytes for Lithium-Based Rechargeable Batteries, ChemInform 35 (2004). https://doi.org/10.1002/chin.200450271.
[22] R. Joy, N.T.M. Balakrishnan, A. Das, S. Shafeek, V.K. Thakur, K. Zaghib, J.F.M. Jaffarali, M.V.V. Reddy, P. Raghavan, Graphene: Chemistry and Applications for Lithium-Ion Batteries, Electrochem 3 (2022) 143–183. https://doi.org/10.3390/electrochem3010010.
[23] M. Winter, R.J. Brodd, What are batteries, fuel cells, and supercapacitors?, Chem. Rev. 104 (2004) 4245–4269. https://doi.org/10.1021/cr020730k.
[24] C. Liu, Z.G. Neale, G. Cao, Understanding electrochemical potentials of cathode materials in rechargeable batteries, Materials Today 19 (2016) 109–123. https://doi.org/10.1016/j.mattod.2015.10.009.
[25] J. Xiang, Y. Wei, Y. Zhong, Y. Yang, H. Cheng, L. Yuan, H. Xu, Y. Huang, Building Practical High-Voltage Cathode Materials for Lithium-Ion Batteries, Advanced Materials 34 (2022). https://doi.org/10.1002/adma.202200912.
[26] A. Kraytsberg, Y. Ein-Eli, A. Kraytsberg, Y. Ein-Eli, Higher, stronger, better ... A review of 5 volt cathode materials for advanced lithium-ion batteries, Adv. Energy Mater. 2 (2012) 922–939. https://doi.org/10.1002/aenm.201200068.
[27] D. Zhao, W. Chen, Analysis of polarization and thermal characteristics in lithium-ion battery with various electrode thicknesses, J. Energy Storage 71 (2023). https://doi.org/10.1016/j.est.2023.108159.
[28] W. Xie, P. Guo, X. Gao, Elucidating the rate limitation of lithium-ion batteries under different charging conditions through polarization analysis, J. Energy Storage 82 (2024). https://doi.org/10.1016/j.est.2024.110554.
[29] J. Diekmann, C. Hanisch, L. Froböse, G. Schälicke, T. Loellhoeffel, A.-S. Fölster, A. Kwade, Ecological Recycling of Lithium-Ion Batteries from Electric Vehicles with Focus on Mechanical Processes, J. Electrochem. Soc. 164 (2016) A6184. https://doi.org/10.1149/2.0271701JES.
[30] D. Romero Guillén, J. Guimarães Sanches, A. Barbosa Botelho Junior, L.A. Gobo, M. Guimarães Bergerman, D.C. Romano Espinosa, J.A.S. Tenório, Physical Process for Li-Ion Battery Recycling from Electric Vehicles, Ind. Eng. Chem. Res. 63 (2024) 19788–19803. https://doi.org/10.1021/ACS.IECR.4C03271.
[31] A.W. Golubkov, D. Fuchs, J. Wagner, H. Wiltsche, C. Stangl, G. Fauler, G. Voitic, A. Thaler, V. Hacker, Thermal-runaway experiments on consumer Li-ion batteries with

metal-oxide and olivin-type cathodes, RSC Adv. 4 (2013) 3633–3642. https://doi.org/10.1039/C3RA45748F.

[32] L.P. He, S.Y. Sun, X.F. Song, J.G. Yu, Recovery of cathode materials and Al from spent lithium-ion batteries by ultrasonic cleaning, Waste Management 46 (2015) 523–528. https://doi.org/10.1016/J.WASMAN.2015.08.035.

[33] C. Yuan, Y. Deng, T. Li, F. Yang, Manufacturing energy analysis of lithium ion battery pack for electric vehicles, CIRP Annals 66 (2017) 53–56. https://doi.org/10.1016/J.CIRP.2017.04.109.

[34] G. Berckmans, M. Messagie, J. Smekens, N. Omar, L. Vanhaverbeke, J. Van Mierlo, Cost projection of state of the art lithium-ion batteries for electric vehicles up to 2030, Energies (Basel). 10 (2017). https://doi.org/10.3390/en10091314.

[35] P.S. Grant, D. Greenwood, K. Pardikar, R. Smith, T. Entwistle, L.A. Middlemiss, G. Murray, S.A. Cussen, M.J. Lain, M.J. Capener, M. Copley, C.D. Reynolds, S.D. Hare, M.J.H. Simmons, E. Kendrick, S.P. Zankowski, S. Wheeler, P. Zhu, P.R. Slater, Y.S. Zhang, A.R.T. Morrison, W. Dawson, J. Li, P.R. Shearing, D.J.L. Brett, G. Matthews, R. Ge, R. Drummond, E.C. Tredenick, C. Cheng, S.R. Duncan, A.M. Boyce, M. Faraji-Niri, J. Marco, L.A. Roman-Ramirez, C. Harper, P. Blackmore, T. Shelley, A. Mohsseni, D.J. Cumming, Roadmap on Li-ion battery manufacturing research, JPhys Energy 4 (2022). https://doi.org/10.1088/2515-7655/ac8e30.

[36] Y.-L. Ding, Cathode for Thin-Film Lithium-Ion Batteries, in: Lithium-Ion Batteries - Thin Film for Energy Materials and Devices, IntechOpen, 2020. https://doi.org/10.5772/intechopen.84534.

[37] C. Julien, A. Mauger, K. Zaghib, H. Groult, Comparative Issues of Cathode Materials for Li-Ion Batteries, Inorganics (Basel). 2 (2014) 132–154. https://doi.org/10.3390/inorganics2010132.

[38] B. N, D. H, Review on Synthesis, Characterizations, and Electrochemical Properties of Cathode Materials for Lithium Ion Batteries, Journal of Material Science & Engineering 5 (2016). https://doi.org/10.4172/2169-0022.1000258.

[39] M. Akhilash, P.S. Salini, B. John, T.D. Mercy, A journey through layered cathode materials for lithium ion cells – From lithium cobalt oxide to lithium-rich transition metal oxides, J. Alloys Compd. 869 (2021). https://doi.org/10.1016/j.jallcom.2021.159239.

[40] N. Nitta, F. Wu, J.T. Lee, G. Yushin, Li-ion battery materials: Present and future, Materials Today 18 (2015) 252–264. https://doi.org/10.1016/j.mattod.2014.10.040.

[41] S. Kim, V.I. Hegde, Z. Yao, Z. Lu, M. Amsler, J. He, S. Hao, J.R. Croy, E. Lee, M.M. Thackeray, C. Wolverton, First-Principles Study of Lithium Cobalt Spinel Oxides: Correlating Structure and Electrochemistry, ACS Appl. Mater. Interfaces 10 (2018) 13479–13490. https://doi.org/10.1021/acsami.8b00394.

[42] I. Buchmann, Batteries in a portable world : a handbook on rechargeable batteries for non-engineers, Cadex Electronics Inc, 2011.

[43] G. Crabtree, E. Kócs, L. Trahey, The energy-storage frontier: Lithium-ion batteries and beyond, MRS Bull. 40 (2015) 1067–1076. https://doi.org/10.1557/mrs.2015.259.

[44] L. Song, Y. Zheng, Z. Xiao, C. Wang, T. Long, Review on Thermal Runaway of Lithium-Ion Batteries for Electric Vehicles, J. Electron. Mater. 51 (2022) 30–46. https://doi.org/10.1007/s11664-021-09281-0.

[45] Access to Cobalt in the EU – an Overview of Raw Materials Initiatives - Cobalt Institute. https://www.cobaltinstitute.org/news/access-to-cobalt-in-the-eu-an-overview-of-raw-materials-initiatives/ (accessed November 4, 2025).

[46] T. Li, X.Z. Yuan, L. Zhang, D. Song, K. Shi, C. Bock, Degradation Mechanisms and Mitigation Strategies of Nickel-Rich NMC-Based Lithium-Ion Batteries, Electrochemical Energy Reviews 3 (2020) 43–80. https://doi.org/10.1007/s41918-019-00053-3.

[47] Y. Lv, S. Huang, Y. Zhao, S. Roy, X. Lu, Y. Hou, J. Zhang, A review of nickel-rich layered oxide cathodes: synthetic strategies, structural characteristics, failure mechanism, improvement approaches and prospects, Appl. Energy 305 (2022). https://doi.org/10.1016/j.apenergy.2021.117849.

[48] S. Aryal, J.L. Durham, A.L. Lipson, K.Z. Pupek, O. Kahvecioglu, Roles of Mn and Co in Ni-rich layered oxide cathodes synthesized utilizing a Taylor Vortex Reactor, Electrochim. Acta 391 (2021). https://doi.org/10.1016/j.electacta.2021.138929.

[49] H. Zhao, W.Y.A. Lam, L. Sheng, L. Wang, P. Bai, Y. Yang, D. Ren, H. Xu, X. He, Cobalt-Free Cathode Materials: Families and their Prospects, Adv. Energy Mater. 12 (2022). https://doi.org/10.1002/aenm.202103894.

[50] X.-G. Sun, C.J. Jafta, S. Tan, A. Borisevich, R.B. Gupta, M.P. Paranthaman, Facile Surface Coatings for Performance Improvement of NMC811 Battery Cathode Material, J. Electrochem. Soc. 169 (2022) 020565. https://doi.org/10.1149/1945-7111/ac5302.

[51] J.M. Lim, T. Hwang, D. Kim, M.S. Park, K. Cho, M. Cho, Intrinsic Origins of Crack Generation in Ni-rich LiNi0.8Co0.1Mn0.1O2 Layered Oxide Cathode Material, Sci. Rep. 7 (2017). https://doi.org/10.1038/srep39669.

[52] S.M. Bak, E. Hu, Y. Zhou, X. Yu, S.D. Senanayake, S.J. Cho, K.B. Kim, K.Y. Chung, X.Q. Yang, K.W. Nam, Structural changes and thermal stability of charged LiNixMnyCozO2 cathode materials studied by combined in situ time-resolved XRD and mass spectroscopy, ACS Appl. Mater. Interfaces 6 (2014) 22594–22601. https://doi.org/10.1021/am506712c.

[53] S.-B. Son, D. Robertson, Y. Tsai, S. Trask, A. Dunlop, I. Bloom, Systematic Study of the Cathode Compositional Dependency of Cross-Talk Behavior in Li-Ion Battery, J. Electrochem. Soc. 167 (2020) 160508. https://doi.org/10.1149/1945-7111/abcb40.

[54] G. Liang, V.K. Peterson, K.W. See, Z. Guo, W.K. Pang, Developing high-voltage spinel LiNi0.5Mn1.5O4cathodes for high-energy-density lithium-ion batteries: Current achievements and future prospects, J. Mater. Chem. A Mater. 8 (2020) 15373–15398. https://doi.org/10.1039/d0ta02812f.

[55] I. Dienwiebel, M. Diehl, B. Heidrich, X. Yang, M. Winter, M. Börner, Enabling Aqueous Processing for LiNi 0.5 Mn 1.5 O 4 -Based Positive Electrodes in Lithium-Ion Batteries by Applying Lithium-Based Processing Additives , Advanced Energy and Sustainability Research 2 (2021) 2100075. https://doi.org/10.1002/aesr.202100075.

[56] G.Q. Liu, L. Wen, Y.M. Liu, Spinel LiNi 0.5Mn 1.5O 4 and its derivatives as cathodes for high-voltage Li-ion batteries, Journal of Solid State Electrochemistry 14 (2010) 2191–2202. https://doi.org/10.1007/s10008-010-1061-5.

[57] M. Fehse, N. Etxebarria, L. Otaegui, M. Cabello, S. Martín-Fuentes, M.A. Cabañero, I. Monterrubio, C.F. Elkjær, O. Fabelo, N.A. Enkubari, J.M. López Del Amo, M. Casas-Cabanas, M. Reynaud, Influence of Transition-Metal Order on the Reaction Mechanism of LNMO Cathode Spinel: An Operando X-ray Absorption Spectroscopy Study, Chemistry of Materials 34 (2022) 6529–6540. https://doi.org/10.1021/acs.chemmater.2c01360.

[58] H. Li, L. Wang, Y. Song, Y. Wu, H. Zhang, A. Du, X. He, Understanding the Insight Mechanism of Chemical-Mechanical Degradation of Layered Co-Free Ni-Rich Cathode Materials: A Review, Small (2023). https://doi.org/10.1002/smll.202302208.

[59] A. Mathew, M.J. Lacey, D. Brandell, Investigating oxidative stability of lithium-ion battery electrolytes using synthetic charge-discharge profile voltammetry, Journal of Power Sources Advances 11 (2021). https://doi.org/10.1016/j.powera.2021.100071.

[60] D. Versaci, R. Colombo, G. Montinaro, M. Buga, N. Cortes Felix, G. Evans, F. Bella, J. Amici, C. Francia, S. Bodoardo, Tailoring cathode materials: A comprehensive study on LNMO/LFP blending for next generation lithium-ion batteries, J. Power Sources 613 (2024). https://doi.org/10.1016/j.jpowsour.2024.234955.

[61] M. Armand, P. Axmann, D. Bresser, M. Copley, K. Edström, C. Ekberg, D. Guyomard, B. Lestriez, P. Novák, M. Petranikova, W. Porcher, S. Trabesinger, M. Wohlfahrt-Mehrens, H. Zhang, Lithium-ion batteries – Current state of the art and anticipated developments, J. Power Sources 479 (2020). https://doi.org/10.1016/j.jpowsour.2020.228708.

[62] A. Gören, C.M. Costa, M.M. Silva, S. Lanceros-Méndez, State of the art and open questions on cathode preparation based on carbon coated lithium iron phosphate, Compos. B Eng. 83 (2015) 333–345. https://doi.org/10.1016/j.compositesb.2015.08.064.

[63] J. Li, Z.-F. Ma, Past and Present of LiFePO4: From Fundamental Research to Industrial Applications, Chem 5 (2019) 3–6. https://doi.org/10.1016/j.chempr.2018.12.012.

[64] J.-M. Tarascon, M. Armand, Issues and challenges facing rechargeable lithium batteries, Nature (2001). https://doi.org/https://doi.org/10.1038/35104644.

[65] C. Julien, A. Mauger, A. Vijh, K. Zaghib, Lithium Batteries Science and Technology, Springer, 2016. https://doi.org/10.1007/978-3-319-19108-9.

[66] J. Lu, Z. Chen, F. Pan, Y. Cui, K. Amine, High-Performance Anode Materials for Rechargeable Lithium-Ion Batteries, Electrochemical Energy Reviews 1 (2018) 35–53. https://doi.org/10.1007/s41918-018-0001-4.

[67] S. Goriparti, E. Miele, F. De Angelis, E. Di Fabrizio, R. Proietti Zaccaria, C. Capiglia, Review on recent progress of nanostructured anode materials for Li-ion batteries, J. Power Sources 257 (2014) 421–443. https://doi.org/10.1016/j.jpowsour.2013.11.103.

[68] K. Guo, R. Kumar, X. Xiao, B.W. Sheldon, H. Gao, Failure progression in the solid electrolyte interphase (SEI) on silicon electrodes, Nano Energy 68 (2020). https://doi.org/10.1016/j.nanoen.2019.104257.

[69] H. Adenusi, G.A. Chass, S. Passerini, K. V. Tian, G. Chen, Lithium Batteries and the Solid Electrolyte Interphase (SEI)—Progress and Outlook, Adv. Energy Mater. 13 (2023). https://doi.org/10.1002/aenm.202203307.

[70] Z. Karkar, D. Guyomard, L. Roué, B. Lestriez, A comparative study of polyacrylic acid (PAA) and carboxymethyl cellulose (CMC) binders for Si-based electrodes, Electrochim. Acta 258 (2017) 453–466. https://doi.org/10.1016/j.electacta.2017.11.082.

[71] G.G. Eshetu, E. Figgemeier, Confronting the Challenges of Next-Generation Silicon Anode-Based Lithium-Ion Batteries: Role of Designer Electrolyte Additives and Polymeric Binders, ChemSusChem 12 (2019) 2515–2539. https://doi.org/10.1002/cssc.201900209.

[72] J. Shin, T.H. Kim, Y. Lee, E.A. Cho, Key functional groups defining the formation of Si anode solid-electrolyte interphase towards high energy density Li-ion batteries, Energy Storage Mater. 25 (2020) 764–781. https://doi.org/10.1016/j.ensm.2019.09.009.

[73] M. Srivastava, A.K. Anil, K. Zaghib, Binders for Li-Ion Battery Technologies and Beyond: A Comprehensive Review, Batteries 2024, Vol. 10, Page 268 10 (2024) 268. https://doi.org/10.3390/BATTERIES10080268.

[74] B.T. Young, C.C. Nguyen, A. Lobach, D.R. Heskett, J.C. Woicik, B.L. Lucht, Role of binders in solid electrolyte interphase formation in lithium ion batteries studied with hard X-ray photoelectron spectroscopy, Journal of Materials Research 2018 34:1 34 (2019) 97–106. https://doi.org/10.1557/JMR.2018.363.

[75] C. Xu, F. Lindgren, B. Philippe, M. Gorgoi, F. Björefors, K. Edström, T. Gustafsson, Improved performance of the silicon anode for li-ion batteries: Understanding the surface modification mechanism of fluoroethylene carbonate as an effective electrolyte additive, Chemistry of Materials 27 (2015) 2591–2599. https://doi.org/10.1021/acs.chemmater.5b00339.

[76] J. Collins, G. Gourdin, M. Foster, D. Qu, Carbon surface functionalities and SEI formation during Li intercalation, Carbon N. Y. 92 (2015) 193–244. https://doi.org/10.1016/j.carbon.2015.04.007.

[77] W. Xu, J. Wang, F. Ding, X. Chen, E. Nasybulin, Y. Zhang, J.G. Zhang, Lithium metal anodes for rechargeable batteries, Energy Environ. Sci. 7 (2014) 513–537. https://doi.org/10.1039/C3EE40795K.

[78] Y. Zhong, Y. Chen, Y. Cheng, Q. Fan, H. Zhao, H. Shao, Y. Lai, Z. Shi, X. Ke, Z. Guo, Li Alginate-Based Artificial SEI Layer for Stable Lithium Metal Anodes, ACS Appl. Mater. Interfaces 11 (2019) 37726–37731. https://doi.org/10.1021/acsami.9b12634.

[79] Y. Qiao, H. Zhao, Y. Shen, L. Li, Z. Rao, G. Shao, Y. Lei, Recycling of graphite anode from spent lithium-ion batteries: Advances and perspectives, EcoMat 5 (2023). https://doi.org/10.1002/eom2.12321.

[80] K.H. Chen, K.N. Wood, E. Kazyak, W.S. Lepage, A.L. Davis, A.J. Sanchez, N.P. Dasgupta, Dead lithium: Mass transport effects on voltage, capacity, and failure of lithium metal anodes, J. Mater. Chem. A Mater. 5 (2017) 11671–11681. https://doi.org/10.1039/c7ta00371d.

[81] A. Mauger, C.M. Julien, J.B. Goodenough, K. Zaghib, Tribute to Michel Armand: from Rocking Chair – Li-ion to Solid-State Lithium Batteries, J. Electrochem. Soc. 167 (2020) 070507. https://doi.org/10.1149/2.0072007jes.

[82] L. Zhao, B. Ding, X.Y. Qin, Z. Wang, W. Lv, Y.B. He, Q.H. Yang, F. Kang, Revisiting the Roles of Natural Graphite in Ongoing Lithium-Ion Batteries, Advanced Materials 34 (2022). https://doi.org/10.1002/adma.202106704.

[83] J. Asenbauer, T. Eisenmann, M. Kuenzel, A. Kazzazi, Z. Chen, D. Bresser, The success story of graphite as a lithium-ion anode material-fundamentals, remaining challenges, and recent developments including silicon (oxide) composites, Sustain. Energy Fuels 4 (2020) 5387–5416. https://doi.org/10.1039/d0se00175a.

[84] S.Y. Sun, N. Yao, C. Bin Jin, J. Xie, X.Y. Li, M.Y. Zhou, X. Chen, B.Q. Li, X.Q. Zhang, Q. Zhang, The Crucial Role of Electrode Potential of a Working Anode in Dictating the Structural Evolution of Solid Electrolyte Interphase, Angew. Chem. Int. Ed. 61 (2022). https://doi.org/10.1002/anie.202208743.

[85] A. Mauger, H. Xie, C.M. Julien, Composite anodes for lithium-ion batteries: Status and trends, AIMS Mater. Sci. 3 (2016) 1054–1106. https://doi.org/10.3934/matersci.2016.3.1054.

[86] B. Liu, X. Wang, H. Chen, Z. Wang, D. Chen, Y.B. Cheng, C. Zhou, G. Shen, Hierarchical silicon nanowires-carbon textiles matrix as a binder-free anode for high-performance advanced lithium-ion batteries, Sci. Rep. 3 (2013). https://doi.org/10.1038/srep01622.

[87] H. Zhang, Y. Yang, D. Ren, L. Wang, X. He, Graphite as anode materials: Fundamental mechanism, recent progress and advances, Energy Storage Mater. 36 (2021) 147–170. https://doi.org/10.1016/j.ensm.2020.12.027.

[88] E. Lewicka, K. Guzik, K. Galos, On the possibilities of critical raw materials production from the eu's primary sources, Resources 10 (2021). https://doi.org/10.3390/RESOURCES10050050.

[89] Y. Chen, X. Li, L. Zhou, Y.W. Mai, H. Huang, High-performance electrospun nanostructured composite fiber anodes for lithium-ion batteries, in: Multifunctionality of Polymer Composites: Challenges and New Solutions, Elsevier Inc., 2015: pp. 662–689. https://doi.org/10.1016/B978-0-323-26434-1.00021-0.

[90] Z. yuan Feng, W. jie Peng, Z. xing Wang, H. jun Guo, X. hai Li, G. chun Yan, J. xi Wang, Review of silicon-based alloys for lithium-ion battery anodes, International Journal of Minerals, Metallurgy and Materials 28 (2021) 1549–1564. https://doi.org/10.1007/s12613-021-2335-x.

[91] Z. Xiao, C. Wang, L. Song, Y. Zheng, T. Long, Research progress of nano-silicon-based materials and silicon-carbon composite anode materials for lithium-ion batteries, Journal

of Solid State Electrochemistry 26 (2022) 1125–1136. https://doi.org/10.1007/s10008-022-05141-x.

[92] Y. Mei, Y. He, H. Zhu, Z. Ma, Y. Pu, Z. Chen, P. Li, L. He, W. Wang, H. Tang, Recent Advances in the Structural Design of Silicon/Carbon Anodes for Lithium Ion Batteries: A Review, Coatings 13 (2023). https://doi.org/10.3390/coatings13020436.

[93] L. Sun, Y. Liu, R. Shao, J. Wu, R. Jiang, Z. Jin, Recent progress and future perspective on practical silicon anode-based lithium ion batteries, Energy Storage Mater. 46 (2022) 482–502. https://doi.org/10.1016/j.ensm.2022.01.042.

[94] C. Berg, R. Morasch, M. Graf, H.A. Gasteiger, Comparison of Silicon and Graphite Anodes: Temperature-Dependence of Impedance Characteristics and Rate Performance, J. Electrochem. Soc. 170 (2023) 030534. https://doi.org/10.1149/1945-7111/acc09d.

[95] Y. Zhang, B. Wu, G. Mu, C. Ma, D. Mu, F. Wu, Recent progress and perspectives on silicon anode: Synthesis and prelithiation for LIBs energy storage, Journal of Energy Chemistry 64 (2022) 615–650. https://doi.org/10.1016/j.jechem.2021.04.013.

[96] N. Sick, O. Krätzig, G.G. Eshetu, E. Figgemeier, A review of the publication and patent landscape of anode materials for lithium ion batteries, J. Energy Storage 43 (2021). https://doi.org/10.1016/j.est.2021.103231.

[97] B. Jin, L. Liao, X. Shen, Z. Mei, Q. Du, L. Liang, B. Lei, J. Du, Advancement in Research on Silicon/Carbon Composite Anode Materials for Lithium-Ion Batteries, Metals 2025, Vol. 15, Page 386 15 (2025) 386. https://doi.org/10.3390/MET15040386.

[98] T. Lee, M.J. Seong, H.C. Ahn, M. Baek, K. Park, J. Oh, T. Choi, J.W. Choi, Fast-chargeable lithium-ion batteries by μ-Si anode-tailored full-cell design, Proceedings of the National Academy of Sciences 122 (2024) e2417053121. https://doi.org/10.1073/PNAS.2417053121.

[99] X.H. Liu, L. Zhong, S. Huang, S.X. Mao, T. Zhu, J.Y. Huang, Size-dependent fracture of silicon nanoparticles during lithiation, ACS Nano 6 (2012) 1522–1531. https://doi.org/10.1021/NN204476H.

[100] C. Yang, K.S.R. Chandran, A critical review of silicon nanowire electrodes and their energy storage capacities in Li-ion cells, RSC Adv. 13 (2023) 3947. https://doi.org/10.1039/D2RA07326A.

[101] E-magy - The Battery Industry Is On With Silicon. https://e-magy.com/ (accessed September 6, 2025).

[102] B. Rage, D. Delbegue, N. Louvain, P.E. Lippens, Engineering of Silicon Core-Shell Structures for Li-ion Anodes, Chemistry – A European Journal 27 (2021) 16275–16290. https://doi.org/10.1002/CHEM.202102470.

[103] Y. Kim, M. Kim, N. Kim, H. Cha, S. Kim, J. Sung, J. Cho, Unraveling the impact of CNT on electrode expansion in silicon-based lithium-ion batteries, Energy Storage Mater. 74 (2025) 103983. https://doi.org/10.1016/J.ENSM.2024.103983.

[104] E. Feyzi, A.K. M R, X. Li, S. Deng, J. Nanda, K. Zaghib, A comprehensive review of silicon anodes for high-energy lithium-ion batteries: Challenges, latest developments, and perspectives, Next Energy 5 (2024) 100176. https://doi.org/10.1016/J.NXENER.2024.100176.

[105] J. Diao, D. Wang, X. Wang, Y. Liu, D. Li, L. Liu, L. Xiong, Research progress on binders for silicon-based anodes, J. Power Sources 625 (2025) 235665. https://doi.org/10.1016/J.JPOWSOUR.2024.235665.

[106] H.F. Andersen, C.E.L. Foss, J. Voje, R. Tronstad, T. Mokkelbost, P.E. Vullum, A. Ulvestad, M. Kirkengen, J.P. Mæhlen, Silicon-Carbon composite anodes from industrial battery grade silicon, Sci. Rep. 9 (2019). https://doi.org/10.1038/s41598-019-51324-4.

[107] J. Liu, M. Yue, S. Wang, Y. Zhao, J. Zhang, A Review of Performance Attenuation and Mitigation Strategies of Lithium-Ion Batteries, Adv. Funct. Mater. 32 (2022). https://doi.org/10.1002/adfm.202107769.

[108] X. Su, Q. Wu, J. Li, X. Xiao, A. Lott, W. Lu, B.W. Sheldon, J. Wu, Silicon-Based nanomaterials for lithium-ion batteries: A review, Adv. Energy Mater. 4 (2014). https://doi.org/10.1002/aenm.201300882.
[109] C. Zhang, F. Wang, J. Han, S. Bai, J. Tan, J. Liu, F. Li, Challenges and Recent Progress on Silicon-Based Anode Materials for Next-Generation Lithium-Ion Batteries, Small Struct. 2 (2021). https://doi.org/10.1002/sstr.202100009.
[110] J. Van Mierlo, M. Berecibar, M. El Baghdadi, C. De Cauwer, M. Messagie, T. Coosemans, V.A. Jacobs, O. Hegazy, Beyond the State of the Art of Electric Vehicles: A Fact-Based Paper of the Current and Prospective Electric Vehicle Technologies, World Electric Vehicle Journal 2021, Vol. 12, Page 20 12 (2021) 20. https://doi.org/10.3390/WEVJ12010020.
[111] J. Xiao, F. Shi, T. Glossmann, C. Burnett, Z. Liu, From laboratory innovations to materials manufacturing for lithium-based batteries, Nat. Energy (2023). https://doi.org/10.1038/s41560-023-01221-y.
[112] W.J. Zhang, A review of the electrochemical performance of alloy anodes for lithium-ion batteries, J. Power Sources 196 (2011) 13–24. https://doi.org/10.1016/j.jpowsour.2010.07.020.
[113] D. Bresser, S. Passerini, B. Scrosati, Leveraging valuable synergies by combining alloying and conversion for lithium-ion anodes, Energy Environ. Sci. 9 (2016) 3348–3367. https://doi.org/10.1039/c6ee02346k.
[114] S. Li, K. Wang, G. Zhang, S. Li, Y. Xu, X. Zhang, X. Zhang, S. Zheng, X. Sun, Y. Ma, Fast Charging Anode Materials for Lithium-Ion Batteries: Current Status and Perspectives, Adv. Funct. Mater. 32 (2022). https://doi.org/10.1002/adfm.202200796.
[115] S. Sudhakaran, T.K. Bijoy, A Comprehensive Review of Current and Emerging Binder Technologies for Energy Storage Applications, ACS Appl. Energy Mater. 6 (2023) 11773–11794. https://doi.org/10.1021/acsaem.3c02218.
[116] Y. Yang, S. Wu, Y. Zhang, C. Liu, X. Wei, D. Luo, Z. Lin, Towards efficient binders for silicon based lithium-ion battery anodes, Chemical Engineering Journal 406 (2021). https://doi.org/10.1016/j.cej.2020.126807.
[117] M. Srivastava, A.K. Anil, K. Zaghib, Binders for Li-Ion Battery Technologies and Beyond: A Comprehensive Review, Batteries 10 (2024). https://doi.org/10.3390/batteries10080268.
[118] T.-W. Kwon, J.W. Choi, A. Coskun, The emerging era of supramolecular polymeric binders in silicon anodes, 2014. http://doc.rero.ch.
[119] S. Ahmed, P.A. Nelson, K.G. Gallagher, D.W. Dees, Energy impact of cathode drying and solvent recovery during lithium-ion battery manufacturing, J. Power Sources 322 (2016) 169–178. https://doi.org/10.1016/j.jpowsour.2016.04.102.
[120] D. Bresser, D. Buchholz, A. Moretti, A. Varzi, S. Passerini, Alternative binders for sustainable electrochemical energy storage-the transition to aqueous electrode processing and bio-derived polymers, Energy Environ. Sci. 11 (2018) 3096–3127. https://doi.org/10.1039/c8ee00640g.
[121] L. Qiu, Z. Shao, D. Wang, W. Wang, F. Wang, J. Wang, Enhanced electrochemical properties of LiFePO4 (LFP) cathode using the carboxymethyl cellulose lithium (CMC-Li) as novel binder in lithium-ion battery, Carbohydr. Polym. 111 (2014) 588–591. https://doi.org/10.1016/j.carbpol.2014.05.027.
[122] N. Loeffler, T. Kopel, G.-T. Kim, S. Passerini, Polyurethane Binder for Aqueous Processing of Li-Ion Battery Electrodes, J. Electrochem. Soc. 162 (2015) A2692–A2698. https://doi.org/10.1149/2.0641514jes.
[123] R. Dallaev, T. Pisarenko, D. Sobola, F. Orudzhev, S. Ramazanov, T. Trčka, Brief Review of PVDF Properties and Applications Potential, Polymers (Basel). 14 (2022). https://doi.org/10.3390/polym14224793.

[124] N. Cuesta, A. Ramos, I. Cameán, C. Antuña, A.B. García, Hydrocolloids as binders for graphite anodes of lithium-ion batteries, Electrochim. Acta 155 (2015) 140–147. https://doi.org/10.1016/j.electacta.2014.12.122.
[125] REACH Regulation - Environment - European Commission. https://environment.ec.europa.eu/topics/chemicals/reach-regulation_en#protecting-consumers (accessed October 20, 2025).
[126] S. Ahmed, P.A. Nelson, K.G. Gallagher, D.W. Dees, Energy impact of cathode drying and solvent recovery during lithium-ion battery manufacturing, J. Power Sources 322 (2016) 169–178. https://doi.org/10.1016/J.JPOWSOUR.2016.04.102.
[127] A.M. Pillai, P.S. Salini, B. John, M.T. Devassy, Aqueous Binders for Cathodes: A Lodestar for Greener Lithium Ion Cells, Energy and Fuels (2022). https://doi.org/10.1021/acs.energyfuels.2c00346.
[128] D.L. Wood, J. Li, C. Daniel, Prospects for reducing the processing cost of lithium ion batteries, J. Power Sources 275 (2015) 234–242. https://doi.org/10.1016/j.jpowsour.2014.11.019.
[129] N. Lingappan, L. Kong, M. Pecht, The significance of aqueous binders in lithium-ion batteries, Renewable and Sustainable Energy Reviews 147 (2021). https://doi.org/10.1016/j.rser.2021.111227.
[130] M. Wolter, D. Leiva, M. Fritsch, S. Börner, Process development and optimization for Li-ion battery production, in: EVS27 International Battery, Hybrid and Fuel Cell Electric Vehicle Symposium, Barcelona, 2013.
[131] N. Loeffler, J. Von Zamory, N. Laszczynski, I. Doberdo, G.T. Kim, S. Passerini, Performance of LiNi1/3Mn1/3Co1/3O 2/graphite batteries based on aqueous binder, J. Power Sources 248 (2014) 915–922. https://doi.org/10.1016/j.jpowsour.2013.10.018.
[132] S.N. Bryntesen, I. Tolstorebrov, A.M. Svensson, P. Shearing, J.J. Lamb, O.S. Burheim, Introducing lignin as a binder material for the aqueous production of NMC111 cathodes for Li-ion batteries, Mater. Adv. (2022). https://doi.org/10.1039/d2ma00850e.
[133] H. Chen, M. Ling, L. Hencz, H.Y. Ling, G. Li, Z. Lin, G. Liu, S. Zhang, Exploring Chemical, Mechanical, and Electrical Functionalities of Binders for Advanced Energy-Storage Devices, Chem. Rev. 118 (2018) 8936–8982. https://doi.org/10.1021/acs.chemrev.8b00241.
[134] Y.M. Zhao, F.S. Yue, S.C. Li, Y. Zhang, Z.R. Tian, Q. Xu, S. Xin, Y.G. Guo, Advances of polymer binders for silicon-based anodes in high energy density lithium-ion batteries, InfoMat 3 (2021) 460–501. https://doi.org/10.1002/INF2.12185.
[135] T. Dong, P. Mu, S. Zhang, H. Zhang, W. Liu, G. Cui, How Do Polymer Binders Assist Transition Metal Oxide Cathodes to Address the Challenge of High-Voltage Lithium Battery Applications?, Electrochemical Energy Reviews 4 (2021) 545–565. https://doi.org/10.1007/s41918-021-00102-w.
[136] J.T. Li, Z.Y. Wu, Y.Q. Lu, Y. Zhou, Q. Sen Huang, L. Huang, S.G. Sun, Water Soluble Binder, an Electrochemical Performance Booster for Electrode Materials with High Energy Density, Adv. Energy Mater. 7 (2017). https://doi.org/10.1002/aenm.201701185.
[137] E.N. Primo, F. Eroles, M. del C. Rojas, F. Cometto, E. Leiva, D.E. Barraco, G.L. Luque, Mechanical properties vs. interaction strength: Comprehensive understanding of aqueous binders' formulation on Si-based anodes for lithium-ion batteries, J. Power Sources 563 (2023). https://doi.org/10.1016/j.jpowsour.2023.232800.
[138] W. Schlemmer, J. Selinger, M.A. Hobisch, S. Spirk, Polysaccharides for sustainable energy storage – A review, Carbohydr. Polym. 265 (2021). https://doi.org/10.1016/j.carbpol.2021.118063.
[139] P.S. Salini, S. V. Gopinadh, A. Kalpakasseri, B. John, M. Thelakkattu Devassy, Toward Greener and Sustainable Li-Ion Cells: An Overview of Aqueous-Based Binder Systems,

ACS Sustain. Chem. Eng. 8 (2020) 4003–4025. https://doi.org/10.1021/acssuschemeng.9b07478.

[140] A. Cholewinski, P. Si, M. Uceda, M. Pope, B. Zhao, Polymer binders: Characterization and development toward aqueous electrode fabrication for sustainability, Polymers (Basel). 13 (2021) 1–20. https://doi.org/10.3390/polym13040631.

[141] S. Komaba, K. Shimomura, N. Yabuuchi, T. Ozeki, H. Yui, K. Konno, Study on polymer binders for high-capacity SiO negative electrode of Li-Ion batteries, Journal of Physical Chemistry C 115 (2011) 13487–13495. https://doi.org/10.1021/jp201691g.

[142] A. Magasinski, B. Zdyrko, I. Kovalenko, B. Hertzberg, R. Burtovyy, C.F. Huebner, T.F. Fuller, I. Luzinov, G. Yushin, Toward efficient binders for Li-ion battery Si-based anodes: Polyacrylic acid, ACS Appl. Mater. Interfaces 2 (2010) 3004–3010. https://doi.org/10.1021/am100871y.

[143] T.R. Martin, R.T. Pekarek, J.E. Coyle, M.C. Schulze, N.R. Neale, Understanding why poly(acrylic acid) works: decarbonylation and cross-linking provide an ionically conductive passivation layer in silicon anodes, J. Mater. Chem. A Mater. 9 (2021) 21929–21938. https://doi.org/10.1039/d1ta04319f.

[144] V. Silano, J.M. Barat Baviera, C. Bolognesi, B.J. Brüschweiler, A. Chesson, P.S. Cocconcelli, R. Crebelli, D.M. Gott, K. Grob, E. Lampi, A. Mortensen, G. Riviere, I.L. Steffensen, C. Tlustos, H. Van Loveren, L. Vernis, H. Zorn, M. Kolf-Clauw, J.P. Cravedi, R. Franz, M.R. Milana, K. Pfaff, M. de F. Tavares Poças, K. Svensson, D. Wölfle, A. Lioupis, L. Castle, Safety assessment of the active substance polyacrylic acid, sodium salt, cross-linked, for use in active food contact materials, EFSA Journal 16 (2018). https://doi.org/10.2903/j.efsa.2018.5448.

[145] M.J. Jolley, T.S. Pathan, C. Jenkins, M.J. Loveridge, Exploration of High and Low Molecular Weight Polyacrylic Acids and Sodium Polyacrylates as Potential Binder System for Use in Silicon Graphite Anodes, ACS Appl. Energy Mater. 8 (2025) 1647–1660. https://doi.org/10.1021/ACSAEM.4C02672.

[146] Z. Wan, S. Li, W. Tang, C. Dai, J. Yang, Z. Lin, J. Qiu, M. Ling, Z. Lin, Z. Li, Exploring the optimal molecular weight of polyacrylic acid binder for silicon nanoparticle anodes in lithium-ion batteries, Journal of Energy Chemistry 105 (2025) 76–86. https://doi.org/10.1016/J.JECHEM.2025.01.040.

[147] R. Kasinathan, M. Marinaro, P. Axmann, M. Wohlfahrt–Mehrens, Influence of the Molecular Weight of Poly-Acrylic Acid Binder on Performance of Si-Alloy/Graphite Composite Anodes for Lithium-Ion Batteries, Energy Technology 6 (2018) 2256–2263. https://doi.org/10.1002/ente.201800302.

[148] K.A. Hays, R.E. Ruther, A.J. Kukay, P. Cao, T. Saito, D.L. Wood, J. Li, What makes lithium substituted polyacrylic acid a better binder than polyacrylic acid for silicon-graphite composite anodes?, J. Power Sources 384 (2018) 136–144. https://doi.org/10.1016/j.jpowsour.2018.02.085.

[149] B. Boz, K. Fröhlich, L. Neidhart, P. Molaiyan, G. Bertoni, M. Ricci, F. De Boni, M. Vuksanovic, M. Romio, K. Whitmore, M. Jahn, Evaluating Polyacrylic Acid as a Universal Aqueous Binder for Ni-Rich Cathodes NMC811 and Si Anodes in Full Cell Lithium-ion Batteries, Chempluschem 89 (2024). https://doi.org/10.1002/cplu.202400195.

[150] W. Zhu, J. Zhou, S. Xiang, X. Bian, J. Yin, J. Jiang, L. Yang, Progress of Binder Structures in Silicon-Based Anodes for Advanced Lithium-Ion Batteries: A Mini Review, Front. Chem. 9 (2021). https://doi.org/10.3389/fchem.2021.712225.

[151] J. Xiong, N. Dupré, D. Mazouzi, D. Guyomard, L. Roué, B. Lestriez, Influence of the Polyacrylic Acid Binder Neutralization Degree on the Initial Electrochemical Behavior of a Silicon/Graphite Electrode, ACS Appl. Mater. Interfaces 13 (2021) 28304–28323. https://doi.org/10.1021/acsami.1c06683.

[152] Z. Shi, S. Jiang, L.A. Robertson, Y. Zhao, E. Sarnello, T. Li, W. Chen, Z. Zhang, L. Zhang, Restorable Neutralization of Poly(acrylic acid) Binders toward Balanced Processing Properties and Cycling Performance for Silicon Anodes in Lithium-Ion Batteries, ACS Appl. Mater. Interfaces 12 (2020) 57932–57940. https://doi.org/10.1021/ACSAMI.0C18559.

[153] L. Anah, N. Astrini, A. Haryono, The Effect of Temperature on the Grafting of Acrylic Acid onto Carboxymethyl Cellulose, in: Macromol. Symp., Wiley-VCH Verlag, 2015: pp. 178–184. https://doi.org/10.1002/masy.201550324.

[154] A. Salama, N. Shukry, I.M. El-Sherbiny, A. Sarhan, A Carboxymethyl Cellulose-Graft-Polyacrylic Acid Hydrogel: A Cost Effective and Reusable Adsorbent for Cu 2+, 2015.

[155] S. Mishra, G. Usha Rani, G. Sen, Microwave initiated synthesis and application of polyacrylic acid grafted carboxymethyl cellulose, Carbohydr. Polym. 87 (2012) 2255–2262. https://doi.org/10.1016/j.carbpol.2011.10.057.

[156] P. Klinpituksa, P. Kosaiyakanon, Superabsorbent Polymer Based on Sodium Carboxymethyl Cellulose Grafted Polyacrylic Acid by Inverse Suspension Polymerization, Int. J. Polym. Sci. 2017 (2017). https://doi.org/10.1155/2017/3476921.

[157] L. Wei, C. Chen, Z. Hou, H. Wei, Poly (acrylic acid sodium) grafted carboxymethyl cellulose as a high performance polymer binder for silicon anode in lithium ion batteries, Sci. Rep. 6 (2016). https://doi.org/10.1038/srep19583.

[158] H. Cho, K. Kim, C.M. Park, G. Jeong, Partially carbonized poly (Acrylic acid) grafted to carboxymethyl cellulose as an advanced binder for si anode in li-ion batteries, Journal of Electrochemical Science and Technology 10 (2019) 131–138. https://doi.org/10.5229/JECST.2019.10.2.131.

[159] M.J. Jolley, T.S. Pathan, A.M. Wemyss, I. Prokes, S. Moharana, C. Wan, M.J. Loveridge, Development and Application of a Poly(acrylic acid)-Grafted Styrene-Butadiene Rubber as a Binder System for Silicon-Graphite Anodes in Li-Ion Batteries, ACS Appl. Energy Mater. 6 (2023) 496–507. https://doi.org/10.1021/acsaem.2c03489.

[160] L. Yue, L. Zhang, H. Zhong, Carboxymethyl chitosan: A new water soluble binder for Si anode of Li-ion batteries, J. Power Sources 247 (2014) 327–331. https://doi.org/10.1016/j.jpowsour.2013.08.073.

[161] Y. Gao, X. Qiu, X. Wang, A. Gu, L. Zhang, X. Chen, J. Li, Z. Yu, Chitosan-g-Poly(acrylic acid) Copolymer and Its Sodium Salt as Stabilized Aqueous Binders for Silicon Anodes in Lithium-Ion Batteries, ACS Sustain. Chem. Eng. 7 (2019) 16274–16283. https://doi.org/10.1021/acssuschemeng.9b03307.

[162] J. Qi, X. Yu, B. Chen, H. Zhuo, S. Chen, Enhanced cycling stability and rate capability of silicon/graphite anodes by chitosan-based aqueous binder, Ionics (Kiel). 29 (2023) 951–961. https://doi.org/10.1007/s11581-022-04877-w.

[163] X. Zhao, C.-H. Yim, N. Du, Y. Abu-Lebdeh, Crosslinked Chitosan Networks as Binders for Silicon/Graphite Composite Electrodes in Li-Ion Batteries, J. Electrochem. Soc. 165 (2018) A1110–A1121. https://doi.org/10.1149/2.114805jes.

[164] C. Chen, S.H. Lee, M. Cho, J. Kim, Y. Lee, Cross-Linked Chitosan as an Efficient Binder for Si Anode of Li-ion Batteries, ACS Appl. Mater. Interfaces 8 (2016) 2658–2665. https://doi.org/10.1021/acsami.5b10673.

[165] Z.H. Wu, J.Y. Yang, B. Yu, B.M. Shi, C.R. Zhao, Z.L. Yu, Self-healing alginate–carboxymethyl chitosan porous scaffold as an effective binder for silicon anodes in lithium-ion batteries, Rare Metals 38 (2019) 832–839. https://doi.org/10.1007/s12598-016-0753-0.

[166] J. He, H. Zhong, J. Wang, L. Zhang, Investigation on xanthan gum as novel water soluble binder for LiFePO4 cathode in lithium-ion batteries, J. Alloys Compd. 714 (2017) 409–418. https://doi.org/10.1016/j.jallcom.2017.04.238.

[167] Y. Zhang, X. Jin, R. Ji, S. Xie, X. Huang, Y. Zheng, L. Chang, T. Zhao, Xanthan gum with double-helix structure as a novel aqueous binder to stabilize lithium-rich cathode, Chem. Phys. Lett. 801 (2022). https://doi.org/10.1016/j.cplett.2022.139700.
[168] S. Kaur, S. Santra, Application of Guar Gum and its Derivatives as Green Binder/Separator for Advanced Lithium-Ion Batteries, ChemistryOpen 11 (2022). https://doi.org/10.1002/open.202100209.
[169] Z.J. Han, K. Yamagiwa, N. Yabuuchi, J.Y. Son, Y.T. Cui, H. Oji, A. Kogure, T. Harada, S. Ishikawa, Y. Aoki, S. Komaba, Electrochemical lithiation performance and characterization of silicon-graphite composites with lithium, sodium, potassium, and ammonium polyacrylate binders, Physical Chemistry Chemical Physics 17 (2015) 3783–3795. https://doi.org/10.1039/c4cp04939j.
[170] Z.Y. Wu, L. Deng, J.T. Li, Q. Sen Huang, Y.Q. Lu, J. Liu, T. Zhang, L. Huang, S.G. Sun, Multiple hydrogel alginate binders for Si anodes of lithium-ion battery, Electrochim. Acta 245 (2017) 371–378. https://doi.org/10.1016/j.electacta.2017.05.094.
[171] X. Feng, J. Yang, X. Yu, J. Wang, Y. Nuli, Low-cost SiO-based anode using green binders for lithium ion batteries, Journal of Solid State Electrochemistry 17 (2013) 2461–2469. https://doi.org/10.1007/s10008-013-2128-x.
[172] D. Versaci, R. Nasi, U. Zubair, J. Amici, M. Sgroi, M.A. Dumitrescu, C. Francia, S. Bodoardo, N. Penazzi, New eco-friendly low-cost binders for Li-ion anodes, Journal of Solid State Electrochemistry 21 (2017) 3429–3435. https://doi.org/10.1007/s10008-017-3665-5.
[173] M. Nejatian, S. Abbasi, F. Azarikia, Gum Tragacanth: Structure, characteristics and applications in foods, Int. J. Biol. Macromol. 160 (2020) 846–860. https://doi.org/10.1016/j.ijbiomac.2020.05.214.
[174] W. Jang, K.K. Rajeev, G.M. Thorat, S. Kim, Y. Kang, T.H. Kim, Lambda Carrageenan as a Water-Soluble Binder for Silicon Anodes in Lithium-Ion Batteries, ACS Sustain. Chem. Eng. 10 (2022) 12620–12629. https://doi.org/10.1021/acssuschemeng.2c03313.
[175] B. Chang, D.H. Yun, I. Hwang, J.K. Seo, J. Kang, G. Noh, S. Choi, J.W. Choi, Carrageenan as A Sacrificial Binder for 5 V LiNi 0.5 Mn 1.5 O 4 Cathodes in Lithium-Ion Batteries , Advanced Materials (2023). https://doi.org/10.1002/adma.202303787.
[176] B. Gendensuren, C. He, E.S. Oh, Preparation of pectin-based dual-crosslinked network as a binder for high performance Si/C anode for LIBs, Korean Journal of Chemical Engineering 37 (2020) 366–373. https://doi.org/10.1007/s11814-019-0438-0.
[177] J.T. Wang, C.C. Wan, J.L. Hong, Polymer Blends of Pectin/Poly(acrylic acid) as Efficient Binders for Silicon Anodes in Lithium-Ion Batteries, ChemElectroChem 7 (2020) 3106–3115. https://doi.org/10.1002/celc.202000666.
[178] C.Y. Chung, W.M. Chen, Y.R. Chen, L.Y. Chen, Y.H. Su, P.W. Chi, P.M. Wu, K.S. Chang-Liao, H.Y. Tang, M.K. Wu, Enhanced fast charging capabilities in natural graphite/iron cross-linked pectin electrodes for lithium-ion batteries, Mater. Adv. (2024). https://doi.org/10.1039/d4ma00584h.
[179] Y.R. Chen, L.Y. Chen, C.Y. Chung, Y.H. Su, F.Y. Wu, T.M. Hsu, P.W. Chi, P.M. Wu, K.S. Chang-Liao, H.Y. Tang, M.K. Wu, Enhanced electrochemical performance of a LiFePO4 cathode with an environmentally friendly pectin/polyethylene glycol binder, J. Power Sources 613 (2024). https://doi.org/10.1016/j.jpowsour.2024.234861.
[180] O.S. Taskin, D. Hubble, T. Zhu, G. Liu, Biomass-derived polymeric binders in silicon anodes for battery energy storage applications, Green Chemistry 23 (2021) 7890–7901. https://doi.org/10.1039/d1gc01814k.
[181] A. Dodero, S. Vicini, M. Alloisio, M. Castellano, Rheological properties of sodium alginate solutions in the presence of added salt: an application of Kulicke equation, Rheol. Acta 59 (2020) 365–374. https://doi.org/10.1007/s00397-020-01206-8.

[182] D. Versaci, O.D. Apostu, D. Dessantis, J. Amici, C. Francia, M. Minella, S. Bodoardo, Tragacanth, an Exudate Gum as Suitable Aqueous Binder for High Voltage Cathode Material, Batteries 9 (2023) 199. https://doi.org/10.3390/BATTERIES9040199/S1.
[183] M. Brestaz, W. Porcher, S. Jouanneau, Bio-Polymers As Binders For Nano-Silicon Negative Electrodes Of Lithium-Ion Batteries, 2012.
[184] D.E. Yoon, C. Hwang, N.R. Kang, U. Lee, D. Ahn, J.Y. Kim, H.K. Song, Dependency of Electrochemical Performances of Silicon Lithium-Ion Batteries on Glycosidic Linkages of Polysaccharide Binders, ACS Appl. Mater. Interfaces 8 (2016) 4042–4047. https://doi.org/10.1021/acsami.5b11408.
[185] P. Zhu, D. Gastol, J. Marshall, R. Sommerville, V. Goodship, E. Kendrick, A review of current collectors for lithium-ion batteries, J. Power Sources 485 (2021). https://doi.org/10.1016/j.jpowsour.2020.229321.
[186] M. Yamada, T. Watanabe, T. Gunji, J. Wu, F. Matsumoto, Review of the Design of Current Collectors for Improving the Battery Performance in Lithium-Ion and Post-Lithium-Ion Batteries, Electrochem 1 (2020) 124–159. https://doi.org/10.3390/electrochem1020011.
[187] H. Jeong, J. Jang, C. Jo, A review on current collector coating methods for next-generation batteries, Chemical Engineering Journal 446 (2022). https://doi.org/10.1016/j.cej.2022.136860.
[188] Y. Yang, W. Yuan, X. Zhang, Y. Ke, Z. Qiu, J. Luo, Y. Tang, C. Wang, Y. Yuan, Y. Huang, A review on structuralized current collectors for high-performance lithium-ion battery anodes, Appl. Energy 276 (2020). https://doi.org/10.1016/j.apenergy.2020.115464.
[189] H. Jeong, J. Jang, C. Jo, A review on current collector coating methods for next-generation batteries, Chemical Engineering Journal 446 (2022) 136860. https://doi.org/10.1016/J.CEJ.2022.136860.
[190] L. Guo, D.B. Thornton, M.A. Koronfel, I.E.L. Stephens, M.P. Ryan, Degradation in lithium ion battery current collectors, JPhys Energy 3 (2021). https://doi.org/10.1088/2515-7655/ac0c04.
[191] L. Guo, D.B. Thornton, M.A. Koronfel, I.E.L. Stephens, M.P. Ryan, Degradation in lithium ion battery current collectors, JPhys Energy 3 (2021). https://doi.org/10.1088/2515-7655/ac0c04.
[192] S. Jin, Y. Jiang, H. Ji, Y. Yu, Advanced 3D Current Collectors for Lithium-Based Batteries, Advanced Materials 30 (2018). https://doi.org/10.1002/adma.201802014.
[193] P. Zhu, D. Gastol, J. Marshall, R. Sommerville, V. Goodship, E. Kendrick, A review of current collectors for lithium-ion batteries, J. Power Sources 485 (2021). https://doi.org/10.1016/j.jpowsour.2020.229321.
[194] H. Jeong, J. Jang, C. Jo, A review on current collector coating methods for next-generation batteries, Chemical Engineering Journal 446 (2022). https://doi.org/10.1016/j.cej.2022.136860.
[195] M. Onsrud, A.O. Tezel, S. Fotedar, A.M. Svensson, Novel carbon coating on aluminum current collectors for lithium-ion batteries, SN Appl. Sci. 4 (2022). https://doi.org/10.1007/s42452-022-05103-y.
[196] R. Wang, W. Li, L. Liu, Y. Qian, F. Liu, M. Chen, Y. Guo, L. Liu, Carbon black/graphene-modified aluminum foil cathode current collectors for lithium ion batteries with enhanced electrochemical performances, Journal of Electroanalytical Chemistry 833 (2019) 63–69. https://doi.org/10.1016/j.jelechem.2018.11.007.
[197] I. Doberdò, N. Löffler, N. Laszczynski, D. Cericola, N. Penazzi, S. Bodoardo, G.T. Kim, S. Passerini, Enabling aqueous binders for lithium battery cathodes – Carbon coating of aluminum current collector, J. Power Sources 248 (2014) 1000–1006. https://doi.org/10.1016/J.JPOWSOUR.2013.10.039.

[198] S. Yoon, H.S. Jang, S. Kim, J. Kim, K.Y. Cho, Crater-like architectural aluminum current collectors with superior electrochemical performance for Li-ion batteries, Journal of Electroanalytical Chemistry 797 (2017) 37–41. https://doi.org/10.1016/J.JELECHEM.2017.05.017.
[199] S. Pedaballi, C.C. Li, Effects of surface modification and organic binder type on cell performance of water-processed Ni-rich Li(Ni0.8Co0.1Mn0.1)O2 cathodes, J. Power Sources 472 (2020). https://doi.org/10.1016/j.jpowsour.2020.228552.
[200] L. Romoli, A.H.A. Lutey, G. Lazzini, Laser texturing of Li-ion battery electrode current collectors for improved active layer interface adhesion, CIRP Annals (2022). https://doi.org/10.1016/j.cirp.2022.04.034.
[201] Y. Wang, Z. Zhao, J. Zhong, T. Wang, L. Wang, H. Xu, J. Cao, J. Li, G. Zhang, H. Fei, J. Zhu, Hierarchically Micro/Nanostructured Current Collectors Induced by Ultrafast Femtosecond Laser Strategy for High-Performance Lithium-ion Batteries, Energy and Environmental Materials (2021). https://doi.org/10.1002/eem2.12223.
[202] X. Fei, Z. Dong, B. Gong, X. Zhao, Lightweight Through-Hole Copper Foil as a Current Collector for Lithium-Ion Batteries, ACS Appl. Mater. Interfaces 13 (2021) 42266–42275. https://doi.org/10.1021/acsami.1c13233.
[203] X.X. Tang, W. Liu, B.Y. Ye, Y. Tang, Preparation of current collector with blind holes and enhanced cycle performance of silicon-based anode, Transactions of Nonferrous Metals Society of China (English Edition) 23 (2013) 1723–1727. https://doi.org/10.1016/S1003-6326(13)62654-0.
[204] Y. Zheng, Z. An, P. Smyrek, H.J. Seifert, T. Kunze, V. Lang, A.-F. Lasagni, W. Pfleging, Direct laser interference patterning and ultrafast laser-induced micro/nano structuring of current collectors for lithium-ion batteries, in: Laser-Based Micro- and Nanoprocessing X, SPIE, 2016: p. 97361B. https://doi.org/10.1117/12.2220111.
[205] E. Ravesio, A.H.A. Lutey, D. Versaci, L. Romoli, S. Bodoardo, Nanosecond pulsed laser texturing of Li-ion battery electrode current collectors: Electrochemical characterisation of cathode half-cells, Sustainable Materials and Technologies 38 (2023) e00751. https://doi.org/10.1016/J.SUSMAT.2023.E00751.
[206] E. Ravesio, G. Montinaro, G. Mincuzzi, M. Negozio, D. Versaci, V. Gartiser, A.H.A. Lutey, F. Bella, S. Bodoardo, Ultrashort pulsed laser texturing of current collector for Si/C Li-ion anodes: Characterization of electrochemical performance and evolution of interface morphology, J. Energy Storage 109 (2025) 115226. https://doi.org/10.1016/J.EST.2024.115226.
[207] K. Xu, Nonaqueous liquid electrolytes for lithium-based rechargeable batteries, Chem. Rev. 104 (2004) 4303–4417. https://doi.org/10.1021/cr030203g.
[208] C.F.J. Francis, I.L. Kyratzis, A.S. Best, Lithium-Ion Battery Separators for Ionic-Liquid Electrolytes: A Review, Advanced Materials 32 (2020) 1904205. https://doi.org/10.1002/ADMA.201904205.
[209] M. Ue, Y. Sasaki, Y. Tanaka, M. Morita, Nonaqueous Electrolytes with Advances in Solvents, in: Electrolytes for Lithium and Lithium-Ion Batteries, Modern Aspects of Electrochemistry, 2014: pp. 93–165. https://doi.org/10.1007/978-1-4939-0302-3_2.
[210] W.A. Henderson, Nonaqueous Electrolytes: Advances in Lithium Salts, in: Electrolytes for Lithium and Lithium-Ion Batteries, Modern Aspects of Electrochemistry, 2014: pp. 1–92. https://doi.org/10.1007/978-1-4939-0302-3_1.
[211] S.S. Zhang, A review on electrolyte additives for lithium-ion batteries, J. Power Sources 162 (2006) 1379–1394. https://doi.org/10.1016/j.jpowsour.2006.07.074.
[212] G. Yang, Y. Li, S. Liu, S. Zhang, Z. Wang, L. Chen, LiFSI to improve lithium deposition in carbonate electrolyte, Energy Storage Mater. 23 (2019) 350–357. https://doi.org/10.1016/j.ensm.2019.04.041.

[213] K. Abe, Nonaqueous Electrolytes and Advances in Additives, in: Electrolytes for Lithium and Lithium-Ion Batteries, Modern Aspects of Electrochemistry, 2014: pp. 167–207. https://doi.org/10.1007/978-1-4939-0302-3_3.
[214] S. Zhang, M. He, C.C. Su, Z. Zhang, Advanced electrolyte/additive for lithium-ion batteries with silicon anode, Curr. Opin. Chem. Eng. 13 (2016) 24–35. https://doi.org/10.1016/j.coche.2016.08.003.
[215] D. Aurbach, K. Gamolsky, B. Markovsky, Y. Gofer, M. Schmidt, U. Heider, On the use of vinylene carbonate (VC) as an additive to electrolyte solutions for Li-ion batteries, Electrochim. Acta 47 (2002) 1423–1439. https://doi.org/10.1016/S0013-4686(01)00858-1.
[216] W. Chae, B. Kim, W.S. Ryoo, T. Earmme, A Brief Review of Gel Polymer Electrolytes Using In Situ Polymerization for Lithium-ion Polymer Batteries, Polymers 2023, Vol. 15, Page 803 15 (2023) 803. https://doi.org/10.3390/POLYM15040803.
[217] M. Bai, X. Tang, M. Zhang, H. Wang, Z. Wang, A. Shao, Y. Ma, An in-situ polymerization strategy for gel polymer electrolyte Si||Ni-rich lithium-ion batteries, Nature Communications 2024 15:1 15 (2024) 1–13. https://doi.org/10.1038/s41467-024-49713-z.
[218] J. Mu, S. Liao, L. Shi, B. Su, F. Xu, Z. Guo, H. Li, F. Wei, Solid-state polymer electrolytes in lithium batteries: latest progress and perspective, Polym. Chem. 15 (2024) 473–499. https://doi.org/10.1039/D3PY01311A.
[219] X. Zhou, Y. Zhou, L. Yu, L. Qi, K.S. Oh, P. Hu, S.Y. Lee, C. Chen, Gel polymer electrolytes for rechargeable batteries toward wide-temperature applications, Chem. Soc. Rev. 53 (2024) 5291–5337. https://doi.org/10.1039/D3CS00551H.
[220] X. Lu, Y. Wang, X. Xu, B. Yan, T. Wu, L. Lu, X. Lu, X. Xu, L. Lu, Y. Wang, B. Yan, T. Wu, Polymer-Based Solid-State Electrolytes for High-Energy-Density Lithium-Ion Batteries – Review, Adv. Energy Mater. 13 (2023) 2301746. https://doi.org/10.1002/AENM.202301746.
[221] A. Balducci, Ionic Liquids in Lithium-Ion Batteries, Topics in Current Chemistry 2017 375:2 375 (2017) 20-. https://doi.org/10.1007/S41061-017-0109-8.
[222] K. Karuppasamy, J. Theerthagiri, D. Vikraman, C.J. Yim, S. Hussain, R. Sharma, T. Maiyalagan, J. Qin, H.S. Kim, Ionic Liquid-Based Electrolytes for Energy Storage Devices: A Brief Review on Their Limits and Applications, Polymers (Basel). 12 (2020) 918. https://doi.org/10.3390/POLYM12040918.
[223] M. Haarmann, W. Haselrieder, A. Kwade, Extrusion-Based Processing of Cathodes: Influence of Solid Content on Suspension and Electrode Properties, Energy Technology 8 (2020). https://doi.org/10.1002/ente.201801169.
[224] J.-H. Schunemann, H. Dreger, H. Bockholt, A. Kwade, Smart Electrode Processing for Battery Cost Reduction, ECS Trans. 73 (2016) 153–159. https://doi.org/10.1149/07301.0153ecst.
[225] W.B. Hawley, J. Li, Electrode manufacturing for lithium-ion batteries—Analysis of current and next generation processing, J. Energy Storage 25 (2019). https://doi.org/10.1016/j.est.2019.100862.
[226] R. Gonçalves, S. Lanceros-Méndez, C.M. Costa, Electrode fabrication process and its influence in lithium-ion battery performance: State of the art and future trends, Electrochem. Commun. 135 (2022). https://doi.org/10.1016/j.elecom.2022.107210.
[227] M. Keppeler, H.Y. Tran, W. Braunwarth, The Role of Pilot Lines in Bridging the Gap Between Fundamental Research and Industrial Production for Lithium-Ion Battery Cells Relevant to Sustainable Electromobility: A Review, Energy Technology 9 (2021). https://doi.org/10.1002/ente.202100132.
[228] O. Krätzig, F. Degen, A comprehensive review and analysis of technology performance characteristics of lithium-ion battery cell manufacturing: Introducing a Call-for-Innovation-Heatmap, Journal of Power Sources Advances 33 (2025) 100174. https://doi.org/10.1016/J.POWERA.2025.100174.

[229] C. Mao, S.J. An, H.M. Meyer, J. Li, M. Wood, R.E. Ruther, D.L. Wood, Balancing formation time and electrochemical performance of high energy lithium-ion batteries, J. Power Sources 402 (2018) 107–115. https://doi.org/10.1016/j.jpowsour.2018.09.019.
[230] M. Fichtner, K. Edström, E. Ayerbe, M. Berecibar, A. Bhowmik, I.E. Castelli, S. Clark, R. Dominko, M. Erakca, A.A. Franco, A. Grimaud, B. Horstmann, A. Latz, H. Lorrmann, M. Meeus, R. Narayan, F. Pammer, J. Ruhland, H. Stein, T. Vegge, M. Weil, Rechargeable Batteries of the Future—The State of the Art from a BATTERY 2030+ Perspective, Adv. Energy Mater. 12 (2022). https://doi.org/10.1002/aenm.202102904.
[231] S. Michaelis, E. Rahimzei, B. LabFactory Braunschweig, T. Braunschweig Achim Kampker, H. Heimes, C. Lienemann, C. Offermanns, M. Kehrer Axel Thielmann, T. Hettesheimer, C. Neef Arno Kwade, W. Haselrieder, S. Rahlfs, R. Uerlich, N. Bognar Editors Sarah Michaelis, L. Abraham, J. Zienow Professional support Thorge Thönnessen, M. Kirchhoff, P. Schulz, V. Seefeldt, Imprint Publisher VDMA Battery Production Lyoner Str. 18 60528 Frankfurt am Main, 2018. http://battprod.vdma.org.
[232] P.A. Le, A general introduction to lithium-ion batteries: From the first concept to the top six commercials and beyond, Journal of Electrochemical Science and Engineering 13 (2023) 591–604. https://doi.org/10.5599/jese.1544.
[233] S.N. Bryntesen, A.H. Strømman, I. Tolstorebrov, P.R. Shearing, J.J. Lamb, O. Stokke Burheim, Opportunities for the state-of-the-art production of lib electrodes—a review, Energies (Basel). 14 (2021). https://doi.org/10.3390/en14051406.
[234] M.D. Bouguern, A.K. Madikere Raghunatha Reddy, X. Li, S. Deng, H. Laryea, K. Zaghib, Engineering Dry Electrode Manufacturing for Sustainable Lithium-Ion Batteries, Batteries 10 (2024). https://doi.org/10.3390/batteries10010039.
[235] S. Haghi, M. Leeb, A. Molzberger, R. Daub, Measuring Instruments for Characterization of Intermediate Products in Electrode Manufacturing of Lithium-Ion Batteries, Energy Technology (2023). https://doi.org/10.1002/ente.202300364.
[236] Y. Liu, R. Zhang, J. Wang, Y. Wang, Current and future lithium-ion battery manufacturing, IScience 24 (2021) 102332. https://doi.org/10.1016/j.isci.
[237] P.S. Grant, D. Greenwood, K. Pardikar, R. Smith, T. Entwistle, L.A. Middlemiss, G. Murray, S.A. Cussen, M.J. Lain, M.J. Capener, M. Copley, C.D. Reynolds, S.D. Hare, M.J.H. Simmons, E. Kendrick, S.P. Zankowski, S. Wheeler, P. Zhu, P.R. Slater, Y.S. Zhang, A.R.T. Morrison, W. Dawson, J. Li, P.R. Shearing, D.J.L. Brett, G. Matthews, R. Ge, R. Drummond, E.C. Tredenick, C. Cheng, S.R. Duncan, A.M. Boyce, M. Faraji-Niri, J. Marco, L.A. Roman-Ramirez, C. Harper, P. Blackmore, T. Shelley, A. Mohsseni, D.J. Cumming, Roadmap on Li-ion battery manufacturing research, JPhys Energy 4 (2022). https://doi.org/10.1088/2515-7655/ac8e30.
[238] K.M. Kim, W.S. Jeon, I.J. Chung, S.H. Chang, Effect of mixing sequences on the electrode characteristics of lithium-ion rechargeable batteries, J. Power Sources 83 (1999) 108–113. https://doi.org/10.1016/S0378-7753(99)00281-5.
[239] G.W. Lee, J.H. Ryu, W. Han, K.H. Ahn, S.M. Oh, Effect of slurry preparation process on electrochemical performances of LiCoO2 composite electrode, J. Power Sources 195 (2010) 6049–6054. https://doi.org/10.1016/J.JPOWSOUR.2009.12.101.
[240] Y. He, L. Jing, Y. Ji, Z. Zhu, L. Feng, X. Fu, Y. Wang, Revisiting the electrode manufacturing: A look into electrode rheology and active material microenvironment, Journal of Energy Chemistry 72 (2022) 41–55. https://doi.org/10.1016/j.jechem.2022.04.038.
[241] T. Evans, D.M. Piper, Large-format battery anodes comprising silicon particles, 2021.
[242] J.P. Sullivan, A. Bose, On the connection between slurry rheology and electrochemical performance of graphite anodes in Lithium-ion batteries, Electrochem. Commun. 141 (2022). https://doi.org/10.1016/j.elecom.2022.107353.

[243] M. Kuenzel, D. Bresser, T. Diemant, D.V. Carvalho, G.T. Kim, R.J. Behm, S. Passerini, Complementary Strategies Toward the Aqueous Processing of High-Voltage LiNi0.5Mn1.5O4 Lithium-Ion Cathodes, ChemSusChem 11 (2018) 562–573. https://doi.org/10.1002/cssc.201702021.

[244] R. Tao, Y. Gu, Z. Du, X. Lyu, J. Li, Advanced electrode processing for lithium-ion battery manufacturing, Nature Reviews Clean Technology 2025 1:2 1 (2025) 116–131. https://doi.org/10.1038/s44359-024-00018-w.

[245] M.W. von Horstig, A. Schoo, T. Loellhoeffel, J.K. Mayer, A. Kwade, A Perspective on Innovative Drying Methods for Energy-Efficient Solvent-Based Production of Lithium-Ion Battery Electrodes, Energy Technology 10 (2022). https://doi.org/10.1002/ente.202200689.

[246] F. Font, B. Protas, G. Richardson, J.M. Foster, Binder migration during drying of lithium-ion battery electrodes: modelling and comparison to experiment, J. Power Sources 393 (2018) 177–185. https://doi.org/10.1016/j.jpowsour.2018.04.097.

[247] J. Li, J. Fleetwood, W.B. Hawley, W. Kays, From Materials to Cell: State-of-the-Art and Prospective Technologies for Lithium-Ion Battery Electrode Processing, Chem. Rev. 122 (2022) 903–956. https://doi.org/10.1021/acs.chemrev.1c00565.

[248] D.L. Wood, J.D. Quass, J. Li, S. Ahmed, D. Ventola, C. Daniel, Technical and economic analysis of solvent-based lithium-ion electrode drying with water and NMP, Drying Technology 36 (2018) 234–244. https://doi.org/10.1080/07373937.2017.1319855.

[249] J. Kumberg, M. Müller, R. Diehm, S. Spiegel, C. Wachsmann, W. Bauer, P. Scharfer, W. Schabel, Drying of Lithium-Ion Battery Anodes for Use in High-Energy Cells: Influence of Electrode Thickness on Drying Time, Adhesion, and Crack Formation, Energy Technology 7 (2019). https://doi.org/10.1002/ente.201900722.

[250] Y. Chen, H. Tao, B. Li, B. Li, C. Lian, H. Liu, Modeling and Optimizing the Drying Process of Electrode Manufacturing for Lithium-Ion Batteries, Energy Technology (2024). https://doi.org/10.1002/ente.202401146.

[251] Y.S. Zhang, N.E. Courtier, Z. Zhang, K. Liu, J.J. Bailey, A.M. Boyce, G. Richardson, P.R. Shearing, E. Kendrick, D.J.L. Brett, A Review of Lithium-Ion Battery Electrode Drying: Mechanisms and Metrology, Adv. Energy Mater. 12 (2022). https://doi.org/10.1002/aenm.202102233.

[252] M. Nikpour, B. Liu, P. Minson, Z. Hillman, B.A. Mazzeo, D.R. Wheeler, Li-ion Electrode Microstructure Evolution during Drying and Calendering, Batteries 8 (2022). https://doi.org/10.3390/batteries8090107.

[253] B.P.N. Nguyen, N. Mariage, R. Fredon, E.M. Kelder, B. Lestriez, Manufacturing of LiNi 0.5 Mn 1.5 O 4 Positive Composite Electrodes with Industry-Relevant Surface Capacities for Lithium Ion-Cells , J. Electrochem. Soc. 162 (2015) A1451–A1459. https://doi.org/10.1149/2.0261508jes.

[254] M.W. von Horstig, A. Schoo, T. Loellhoeffel, J.K. Mayer, A. Kwade, A Perspective on Innovative Drying Methods for Energy-Efficient Solvent-Based Production of Lithium-Ion Battery Electrodes, Energy Technology 10 (2022) 2200689. https://doi.org/10.1002/ENTE.202200689.

[255] J. Zhang, J. Sun, H. Huang, C. Ji, M. Yan, Z. Yuan, Deformation and fracture mechanisms in the calendering process of lithium-ion battery electrodes, Appl. Energy 373 (2024). https://doi.org/10.1016/j.apenergy.2024.123900.

[256] D. Schreiner, M. Oguntke, T. Günther, G. Reinhart, Modelling of the Calendering Process of NMC-622 Cathodes in Battery Production Analyzing Machine/Material–Process–Structure Correlations, Energy Technology 7 (2019). https://doi.org/10.1002/ente.201900840.

[257] F.A. Soto, J.M. Martinez de la Hoz, J.M. Seminario, P.B. Balbuena, Modeling solid-electrolyte interfacial phenomena in silicon anodes, Curr. Opin. Chem. Eng. 13 (2016) 179–185. https://doi.org/10.1016/j.coche.2016.08.017.
[258] C. Meyer, M. Kosfeld, W. Haselrieder, A. Kwade, Process modeling of the electrode calendering of lithium-ion batteries regarding variation of cathode active materials and mass loadings, J. Energy Storage 18 (2018) 371–379. https://doi.org/10.1016/j.est.2018.05.018.
[259] A.C. Ngandjong, T. Lombardo, E.N. Primo, M. Chouchane, A. Shodiev, O. Arcelus, A.A. Franco, Investigating electrode calendering and its impact on electrochemical performance by means of a new discrete element method model: Towards a digital twin of Li-Ion battery manufacturing, J. Power Sources 485 (2021). https://doi.org/10.1016/j.jpowsour.2020.229320.
[260] D. Mayer, A.K. Wurba, B. Bold, J. Bernecker, A. Smith, J. Fleischer, Investigation of the mechanical behavior of electrodes after calendering and its influence on singulation and cell performance, Processes 9 (2021). https://doi.org/10.3390/pr9112009.
[261] H. Zheng, L. Tan, G. Liu, X. Song, V.S. Battaglia, Calendering effects on the physical and electrochemical properties of Li[Ni 1/3Mn 1/3Co 1/3]O 2 cathode, J. Power Sources 208 (2012) 52–57. https://doi.org/10.1016/j.jpowsour.2012.02.001.
[262] C. Fongy, A.-C. Gaillot, S. Jouanneau, D. Guyomard, B. Lestriez, Ionic vs Electronic Power Limitations and Analysis of the Fraction of Wired Grains in LiFePO[sub 4] Composite Electrodes, J. Electrochem. Soc. 157 (2010) A885. https://doi.org/10.1149/1.3432559/XML.
[263] D. Antartis, S. Dillon, I. Chasiotis, Effect of porosity on electrochemical and mechanical properties of composite Li-ion anodes, in: J. Compos. Mater., SAGE Publications Ltd, 2015: pp. 1849–1862. https://doi.org/10.1177/0021998314568653.
[264] M. Abdollahifar, H. Cavers, S. Scheffler, A. Diener, M. Lippke, A. Kwade, Insights into Influencing Electrode Calendering on the Battery Performance, Adv. Energy Mater. (2023). https://doi.org/10.1002/aenm.202300973.
[265] W. Haselrieder, S. Ivanov, D.K. Christen, H. Bockholt, A. Kwade, Impact of the Calendering Process on the Interfacial Structure and the Related Electrochemical Performance of Secondary Lithium-Ion Batteries, ECS Trans. 50 (2013) 59–70. https://doi.org/10.1149/05026.0059ecst.
[266] Z. Karkar, T. Jaouhari, A. Tranchot, D. Mazouzi, D. Guyomard, B. Lestriez, L. Roué, How silicon electrodes can be calendered without altering their mechanical strength and cycle life, J. Power Sources 371 (2017) 136–147. https://doi.org/10.1016/j.jpowsour.2017.10.042.
[267] S. Scheffler, R. Jagau, N. Müller, A. Diener, A. Kwade, Calendering of Silicon-Containing Electrodes and Their Influence on the Mechanical and Electrochemical Properties, Batteries 8 (2022). https://doi.org/10.3390/batteries8050046.
[268] D. Li, H. Wan, J. Liu, H. Jiang, Y. Wang, J. Zhang, Y. Zheng, Effects of calendering state on coupled electrochemical-mechanical performance of silicon based composite electrodes, Green Energy and Intelligent Transportation 3 (2024). https://doi.org/10.1016/j.geits.2024.100154.
[269] J. Müller, M. Abdollahifar, S. Doose, P. Michalowski, N.L. Wu, A. Kwade, Effects of carbon coating on calendered nano-silicon graphite composite anodes of LiB, J. Power Sources 548 (2022) 232000. https://doi.org/10.1016/J.JPOWSOUR.2022.232000.
[270] Z. Du, R.A. Dunlap, M.N. Obrovac, High Energy Density Calendered Si Alloy/Graphite Anodes, J. Electrochem. Soc. 161 (2014) A1698–A1705. https://doi.org/10.1149/2.0941410jes.

[271] R. Schröder, M. Aydemir, G. Seliger, Comparatively Assessing different Shapes of Lithium-ion Battery Cells, in: Procedia Manuf., Elsevier B.V., 2017: pp. 104–111. https://doi.org/10.1016/j.promfg.2017.02.013.
[272] M.R. Kronthaler, F. Schloegl, J. Kurfer, R. Wiedenmann, M.F. Zaeh, G. Reinhart, Laser Cutting in the Production of Lithium Ion Cells, in: Phys. Procedia, Elsevier B.V., 2012: pp. 213–224. https://doi.org/10.1016/j.phpro.2012.10.032.
[273] W. Pfleging, A review of laser electrode processing for development and manufacturing of lithium-ion batteries, Nanophotonics 7 (2017) 549–573. https://doi.org/10.1515/nanoph-2017-0044.
[274] M.P. Lautenschlaeger, B. Prifling, B. Kellers, J. Weinmiller, T. Danner, V. Schmidt, A. Latz, Understanding Electrolyte Filling of Lithium-Ion Battery Electrodes on the Pore Scale Using the Lattice Boltzmann Method, Batter. Supercaps 5 (2022) e202200090. https://doi.org/10.1002/BATT.202200090.
[275] M. Hinkers, K. Borzutzki, O. Krätzig, F. Degen, Comprehensive Assessment of Novel Technologies for Electrolyte Filling in Lithium-Ion Battery Production, Batteries 2025, Vol. 11, Page 41 11 (2025) 41. https://doi.org/10.3390/BATTERIES11020041.
[276] A. Kampker, H. Heimes, C. Offermanns, S. Wennemar, T. Robben, N. Lackner, Optimizing the Cell Finishing Process: An Overview of Steps, Technologies, and Trends, World Electric Vehicle Journal 2023, Vol. 14, Page 96 14 (2023) 96. https://doi.org/10.3390/WEVJ14040096.
[277] F. Schomburg, B. Heidrich, S. Wennemar, R. Drees, T. Roth, M. Kurrat, H. Heimes, A. Jossen, M. Winter, J.Y. Cheong, F. Röder, Lithium-ion battery cell formation: status and future directions towards a knowledge-based process design, Energy Environ. Sci. 17 (2024) 2686–2733. https://doi.org/10.1039/D3EE03559J.
[278] F. Schomburg, B. Heidrich, S. Wennemar, R. Drees, T. Roth, M. Kurrat, H. Heimes, A. Jossen, M. Winter, J.Y. Cheong, F. Röder, Lithium-ion battery cell formation: status and future directions towards a knowledge-based process design, Energy Environ. Sci. 17 (2024) 2686–2733. https://doi.org/10.1039/D3EE03559J.
[279] C.D. Reynolds, P.R. Slater, S.D. Hare, M.J.H. Simmons, E. Kendrick, A review of metrology in lithium-ion electrode coating processes, Mater. Des. 209 (2021). https://doi.org/10.1016/j.matdes.2021.109971.
[280] A. Schoo, R. Moschner, J. Hülsmann, A. Kwade, Coating Defects of Lithium-Ion Battery Electrodes and Their Inline Detection and Tracking, Batteries 9 (2023). https://doi.org/10.3390/BATTERIES9020111.
[281] W. Li, A. Yanyachi, T. Sun, D. Wu, M.N. Banis, Z. Liu, J. Zhou, S. Kuppan, O. Ezekoye, Y. Liu, Multimodal Characterization of Coating Defects in Graphite Electrodes for Lithium-Ion Batteries, J. Electrochem. Soc. 172 (2025) 080523. https://doi.org/10.1149/1945-7111/ADF9CF.
[282] J. Kurfer, M. Westermeier, C. Tammer, G. Reinhart, Production of large-area lithium-ion cells – Preconditioning, cell stacking and quality assurance, CIRP Annals 61 (2012) 1–4. https://doi.org/10.1016/J.CIRP.2012.03.101.
[283] A. Amin, P.V. Geiping, A.S. Odungat, F. Özcan, D. Segets, Thermal Imaging for Quality Control in Thin Silicon-Based Coatings for Lithium-Ion Batteries: Defect Detection, Drying Dynamics, and Machine Learning-Based Mass Loading Estimation, Small Methods 9 (2025) 2402079. https://doi.org/10.1002/SMTD.202402079.
[284] P. Just, L. Ebert, T. Echelmeyer, M.A. Roscher, Infrared particle detection for battery electrode foils, Infrared Phys. Technol. 61 (2013) 254–258. https://doi.org/10.1016/j.infrared.2013.08.017.
[285] D. Mohanty, J. Li, R. Born, L.C. Maxey, R.B. Dinwiddie, C. Daniel, D.L. Wood, Non-destructive evaluation of slot-die-coated lithium secondary battery electrodes by in-line

laser caliper and IR thermography methods, Analytical Methods 6 (2014) 674–683. https://doi.org/10.1039/C3AY41140K.

[286] X. Lu, A. Bertei, D.P. Finegan, C. Tan, S.R. Daemi, J.S. Weaving, K.B. O'Regan, T.M.M. Heenan, G. Hinds, E. Kendrick, D.J.L. Brett, P.R. Shearing, 3D microstructure design of lithium-ion battery electrodes assisted by X-ray nano-computed tomography and modelling, Nature Communications 2020 11:1 11 (2020) 2079-. https://doi.org/10.1038/s41467-020-15811-x.

[287] A. Liu, W. Yao, S. Yang, D. Gonsoulin, A. Larson, A. Condon, P.M. Attia, Y. Shirley-Meng, Design and Performance of the BYD LFP/Graphite 4680 Cylindrical Cell, J. Electrochem. Soc. 172 (2025) 110536. https://doi.org/10.1149/1945-7111/AE1E33.

[288] Y. Jiang, A. Tian, L. Yan, X. Du, L. Yang, L. Li, J. Zhou, Q. Wang, S. Ruan, X. He, Y. Zhang, X. Yu, Y. Jiang, F. Tu, J. Xiang, W. Wan, C. Wang, Y. Xia, X. Xia, W. Zhang, X-Ray Computed Tomography (CT) Technology for Detecting Battery Defects and Revealing Failure Mechanisms, Journal of Electronic Materials 2024 53:10 53 (2024) 5776–5787. https://doi.org/10.1007/S11664-024-11300-9.

[289] D. Tang, C. Xu, G. Xu, S. Cui, S. Zhang, Non-Contact Laser Ultrasound Detection of Internal Gas Defects in Lithium-Ion Batteries, Sensors 2025, Vol. 25, Page 2033 25 (2025) 2033. https://doi.org/10.3390/S25072033.

[290] Interlude: Rheology Becomes an Independent Science: Societies, Congresses and Journals, Rheology Series 7 (1998) 43–71. https://doi.org/10.1016/S0169-3107(98)80004-X.

[291] D.I. Wilson, What is rheology?, Eye 2018 32:2 32 (2017) 179–183. https://doi.org/10.1038/eye.2017.267.

[292] T.G. Mezger, The Rheology Handbook For users of rotational and oscillatory rheometers, 5 th Revised Edition, Vincentz Network GmbH & Co. KG, Hanover, 2020.

[293] Pitch Drop experiment - School of Mathematics and Physics - University of Queensland. https://smp.uq.edu.au/pitch-drop-experiment (accessed September 8, 2025).

[294] H.A. Barnes, Chapter 18 The rheology of emulsions, in: Interface Science and Technology, Elsevier, 2004: pp. 721–759. https://doi.org/10.1016/S1573-4285(04)80020-6.

[295] C.D. Reynolds, H. Walker, A. Mahgoub, E. Adebayo, E. Kendrick, Battery electrode slurry rheology and its impact on manufacturing, Energy Advances 4 (2025) 84–93. https://doi.org/10.1039/D4YA00380B.

[296] Rheological measurements | Anton Paar Wiki. https://wiki.anton-paar.com/fi-en/basics-of-rheology/rheological-measurements/ (accessed November 17, 2025).

[297] Liu Ta-Jo, Tiu Carlos, Chen Li-Chun, Liu Darjen, The Influence of Slurry Rheology on Lithium-ion Electrode Processing, in: Printed Batteries: Materials, Technology and Applications, First Edition, John Wiley & Sons Ltd., 2018.

[298] N. Park, M. Lee, H. Jung, J. Nam, Complex rheological response of Li-ion battery anode slurries, J. Power Sources 608 (2024). https://doi.org/10.1016/j.jpowsour.2024.234607.

[299] C.D. Reynolds, S.D. Hare, P.R. Slater, M.J.H. Simmons, E. Kendrick, Rheology and Structure of Lithium-Ion Battery Electrode Slurries, Energy Technology 10 (2022). https://doi.org/10.1002/ente.202200545.

[300] P. Galek, J. Różański, K. Fic, Toward better porous carbon-based electrodes by investigation of the viscoelastic properties of carbon suspension, Chemical Engineering Journal 463 (2023). https://doi.org/10.1016/J.CEJ.2023.142476.

[301] H. Herrada-Manchón, M.A. Fernández, E. Aguilar, Essential Guide to Hydrogel Rheology in Extrusion 3D Printing: How to Measure It and Why It Matters?, Gels 2023, Vol. 9, Page 517 9 (2023) 517. https://doi.org/10.3390/GELS9070517.

[302] J. Alemán, A. V. Chadwick, J. He, M. Hess, K. Horie, R.G. Jones, P. Kratochvíl, I. Meisel, I. Mita, G. Moad, S. Penczek, R.F.T. Stepto, Definitions of terms relating to the structure and processing of sols, gels, networks, and inorganic-organic hybrid materials (IUPAC

recommendations 2007), Pure and Applied Chemistry 79 (2007) 1801–1829. https://doi.org/10.1351/PAC200779101801.
[303] Rheological Evaluation of Battery Slurries with Different Graphite Particle Size and Shape - TA Instruments. https://www.tainstruments.com/applications-notes/rheological-evaluation-of-battery-slurries-with-different-graphite-particle-size-and-shape/ (accessed September 8, 2025).
[304] A. Amin, M. Loewenich, L. Grebener, M. Hammad, S. Heckenbach, M.-A. Kräenbring, S. Odungat, A. Harshawardhan Ladole, T.B. Nguyen, D. Schwabenland, H.K. Salim, H. Wiggers, D. Segets, F. Özcan, Impact of Supraparticle Sizes and Morphology on Interparticle Spacing, Slurry Rheology, Coating Density, and Electrochemical Performance in Si/C Anodes for Li-Ion Batteries, ACS Appl. Energy Mater. (2025). https://doi.org/10.1021/acsaem.4c02578.
[305] L. Ouyang, Z. Wu, J. Wang, X. Qi, Q. Li, J. Wang, S. Lu, The effect of solid content on the rheological properties and microstructures of a Li-ion battery cathode slurry, RSC Adv. 10 (2020) 19360–19370. https://doi.org/10.1039/D0RA02651D.
[306] B. Zhao, D. Yin, Y. Gao, J. Ren, Concentration dependence of yield stress, thixotropy, and viscoelasticity rheological behavior of lithium-ion battery slurry, Ceram. Int. 48 (2022) 19073–19080. https://doi.org/10.1016/j.ceramint.2022.03.197.
[307] Rheological Evaluation of Battery Slurries with Different Graphite Particle Size and Shape - TA Instruments. https://www.tainstruments.com/applications-notes/rheological-evaluation-of-battery-slurries-with-different-graphite-particle-size-and-shape/ (accessed September 6, 2025).
[308] L. Ouyang, Z. Wu, J. Wang, X. Qi, Q. Li, J. Wang, S. Lu, The effect of solid content on the rheological properties and microstructures of a Li-ion battery cathode slurry, RSC Adv. 10 (2020) 19360–19370. https://doi.org/10.1039/d0ra02651d.
[309] BS EN ISO 14040: 2006 -- Environmental management -- Life cycle assessment -- Principles and framework, BSI Standards Limited, 2020.
[310] BS EN ISO 14044: 2006 -- Environmental management -- Life cycle assessment -- Requirements and guidelines, British Standards Institution, 2021.
[311] Communication from the Commission to the Council and the European Parliament: Integrated Product Policy Building on Environmental Life-Cycle Thinking, Brussels, 2003. http://europa.eu.int/comm/environment/ipp/ippsum.pdf.
[312] European Platform on LCA | EPLCA. https://eplca.jrc.ec.europa.eu/ (accessed September 6, 2025).
[313] European Platform on LCA | EPLCA. https://eplca.jrc.ec.europa.eu/projects.html (accessed September 6, 2025).
[314] European Platform on LCA | EPLCA. https://eplca.jrc.ec.europa.eu/EU_BatteryRegulation_Art7.html (accessed September 6, 2025).
[315] Under development - Batteries and parts thereof (c-PCR under PCR 2024:06) | EPD International. https://www.environdec.com/pcr-library/pcr_9b0f5b33-3add-4449-cbb1-08dba21ab132 (accessed November 28, 2025).
[316] Under development - Batteries and parts thereof (c-PCR under PCR 2024:06) | EPD International. https://www.environdec.com/pcr-library/pcr_9b0f5b33-3add-4449-cbb1-08dba21ab132 (accessed April 3, 2026).
[317] A. Accardo, A. Garofalo, G. Dotelli, E. Spessa, Prospective LCA of Next-Generation Cells for Electric Vehicle Applications, IEEE Access 12 (2024) 19584–19597. https://doi.org/10.1109/ACCESS.2024.3361312.
[318] S. Sala, F. Reale, G.J. Cristobal, L. Marelli, R. Pant, Life cycle assessment for the impact assessment of policies - Life thinking and assessment in the European policies and for

evaluating policy options, Joint Research Centre 28380 (2016) 53. https://doi.org/10.2788/318544.
[319] Understanding LCA – measuring environmental impact in design – Hera. https://hera.org.nz/lca-explained/ (accessed September 6, 2025).
[320] Life Cycle Assessment Stages: Explained. https://www.tunley-environmental.com/en/insights/life-cycle-assessment-stages (accessed September 6, 2025).
[321] E.A. Olivetti, G. Ceder, G.G. Gaustad, X. Fu, Lithium-Ion Battery Supply Chain Considerations: Analysis of Potential Bottlenecks in Critical Metals, Joule 1 (2017) 229–243. https://doi.org/10.1016/j.joule.2017.08.019.
[322] M. Lavigne Philippot, D. Costa, G. Cardellini, L. De Sutter, J. Smekens, J. Van Mierlo, M. Messagie, Life cycle assessment of a lithium-ion battery with a silicon anode for electric vehicles, J. Energy Storage 60 (2023) 106635. https://doi.org/10.1016/j.est.2023.106635.
[323] M. Etxandi-Santolaya, L. Canals Casals, C. Corchero, Extending the electric vehicle battery first life: Performance beyond the current end of life threshold, Heliyon 10 (2024) e26066. https://doi.org/10.1016/J.HELIYON.2024.E26066.
[324] L. Colarullo, J. Thakur, Second-life EV batteries for stationary storage applications in Local Energy Communities, Renewable and Sustainable Energy Reviews 169 (2022) 112913. https://doi.org/10.1016/J.RSER.2022.112913.
[325] M.Z. Hauschild, R.K. Rosenbaum, S.I. Olsen, Life Cycle Assessment, Theory and Practice, Springer Nature, 2018. https://doi.org/10.1007/978-3-319-56475-3.
[326] openLCA.org | openLCA is a free, professional Life Cycle Assessment (LCA) and footprint software with a broad range of features and many available databases, created by GreenDelta since 2006. https://www.openlca.org/ (accessed November 30, 2025).
[327] SimaPro - Sustainability insights for informed changemakers. https://simapro.com/ (accessed November 30, 2025).
[328] Life Cycle Assessment Software and Data | Sphera (GaBi). https://sphera.com/solutions/product-stewardship/life-cycle-assessment-software-and-data/ (accessed November 30, 2025).
[329] Ecoinvent v3.11 - ecoinvent. https://ecoinvent.org/ecoinvent-v3-11/ (accessed September 6, 2025).
[330] S. Sala, F. Reale, Cristobal-Garcia J, Life cycle assessment for the impact assessment of policies Life thinking and assessment in the European policies and for evaluating policy options, (2016). https://doi.org/10.2788/318544.
[331] Life Cycle Assessment & the EF methods - Green Forum. https://green-forum.ec.europa.eu/green-business/environmental-footprint-methods/life-cycle-assessment-ef-methods_en (accessed April 3, 2026).
[332] European Platform on LCA | EPLCA. https://eplca.jrc.ec.europa.eu/lifecycleassessment.html (accessed April 3, 2026).
[333] European Platform on LCA | EPLCA. https://eplca.jrc.ec.europa.eu/EnvironmentalFootprint.html (accessed April 3, 2026).
[334] Intergovernmental Panel on Climate Change - DCCEEW. https://www.dcceew.gov.au/climate-change/international-climate-action/intergovernmental-panel (accessed September 6, 2025).
[335] LCIA: the ReCiPe model | RIVM. https://www.rivm.nl/en/life-cycle-assessment-lca/recipe (accessed September 6, 2025).
[336] Tool for Reduction and Assessment of Chemicals and Other Environmental Impacts (TRACI) | US EPA. https://www.epa.gov/chemical-research/tool-reduction-and-assessment-chemicals-and-other-environmental-impacts-traci (accessed September 6, 2025).
[337] GREET | Department of Energy. https://www.energy.gov/eere/greet (accessed December 1, 2025).

[338] S. Toniolo, A. Mazzi, C. Pieretto, A. Scipioni, Allocation strategies in comparative life cycle assessment for recycling: Considerations from case studies, Resour. Conserv. Recycl. 117 (2017) 249–261. https://doi.org/10.1016/j.resconrec.2016.10.011.
[339] Life Cycle Assessment & the EF methods - European Commission. https://green-forum.ec.europa.eu/green-business/environmental-footprint-methods/life-cycle-assessment-ef-methods_en (accessed September 6, 2025).
[340] D. Paul, V. Pechancová, N. Saha, D. Pavelková, N. Saha, M. Motiei, T. Jamatia, M. Chaudhuri, A. Ivanichenko, M. Venher, L. Hrbáčková, P. Sáha, Life cycle assessment of lithium-based batteries: Review of sustainability dimensions, Renewable and Sustainable Energy Reviews 206 (2024) 114860. https://doi.org/10.1016/J.RSER.2024.114860.
[341] Huijbregts; M.A.J., Steinmann; Z.J.N., Elshout; P.M.F., Stam; G., Verones; F., Vieira; M.D.M., Hollander; A., Zijp; M., van Zelm; R., ReCiPe 2016 - A harmonized life cycle impact assessment method at midpoint and endpoint level - Report I: Characterization, 2017. https://doi.org/10.1007/S11367-016-1246-Y/TABLES/2.
[342] R. Tolomeo, G. De Feo, R. Adami, L.S. Osséo, Application of life cycle assessment to lithium ion batteries in the automotive sector, Sustainability (Switzerland) 12 (2020). https://doi.org/10.3390/su12114628.
[343] M.A.J. Huijbregts, Z.J.N. Steinmann, P.M.F. Elshout, G. Stam, F. Verones, M. Vieira, M. Zijp, A. Hollander, R. van Zelm, ReCiPe2016: a harmonised life cycle impact assessment method at midpoint and endpoint level, International Journal of Life Cycle Assessment 22 (2017) 138–147. https://doi.org/10.1007/s11367-016-1246-y.
[344] Global Guidance Principles for Life Cycle Assessment Databases, 2011. https://www.lifecycleinitiative.org/library/global-guidance-principles-for-lca-databases-a-basis-for-greener-processes-and-products/ (accessed May 17, 2025).
[345] S. Andreasi Bassi, F. Biganzoli, N. Ferrara, A. Amadei, A. Valente, S. Sala, F. Ardente, Updated characterisation and normalisation factors for the environmental footprint 3.1 method, 2023.
[346] E. Igos, E. Benetto, R. Meyer, P. Baustert, B. Othoniel, How to treat uncertainties in life cycle assessment studies?, International Journal of Life Cycle Assessment 24 (2019) 794–807. https://doi.org/10.1007/s11367-018-1477-1.
[347] S. Gavankar, S. Anderson, A.A. Keller, Critical Components of Uncertainty Communication in Life Cycle Assessments of Emerging Technologies: Nanotechnology as a Case Study, J. Ind. Ecol. 19 (2015) 468–479. https://doi.org/10.1111/JIEC.12183.
[348] F. Pomponi, Z. Barahmand, M.S. Eikeland, Life Cycle Assessment under Uncertainty: A Scoping Review, World 2022, Vol. 3, Pages 692-717 3 (2022) 692–717. https://doi.org/10.3390/WORLD3030039.
[349] F. Michiels, A. Geeraerd, How to decide and visualize whether uncertainty or variability is dominating in life cycle assessment results: A systematic review, Environmental Modelling and Software 133 (2020). https://doi.org/10.1016/j.envsoft.2020.104841.
[350] S. Freidberg, From behind the curtain: talking about values in LCA, International Journal of Life Cycle Assessment 23 (2018) 1410–1414. https://doi.org/10.1007/s11367-015-0879-6.
[351] B. Moutik, J. Summerscales, J. Graham-Jones, R. Pemberton, Life Cycle Assessment Research Trends and Implications: A Bibliometric Analysis, Sustainability 2023, Vol. 15, Page 13408 15 (2023) 13408. https://doi.org/10.3390/SU151813408.
[352] GIGAGREEN: Towards the sustainable giga-factory. https://gigagreenproject.eu/ (accessed September 10, 2025).
[353] R. Jacob Robin, Viability and Eco-Consequences of Synthetic and Natural Graphite for Lithium-Ion Battery Anodes in the USA, IEEE Engineering Management Review 52 (2024) 131–147. https://doi.org/10.1109/EMR.2024.3372697.

[354] Copper Foil with Various Width and Thickness as Battery Current Collec – MTI Online Store. https://mtixtl.com/en-euea/products/copper-foil-with-various-width-and-thickness-as-battery-current-collector-from-4-5%CE%BCm-to-25%CE%BCm?variant=44673887994104 (accessed September 5, 2025).
[355] M.E. Spahr, D. Goers, A. Leone, S. Stallone, E. Grivei, Development of carbon conductive additives for advanced lithium ion batteries, J. Power Sources 196 (2011) 3404–3413. https://doi.org/10.1016/j.jpowsour.2010.07.002.
[356] Anode active material, and lithium secondary battery comprising same, 2014. https://patents.google.com/patent/CN105659417A/en (accessed February 19, 2025).
[357] H. Buqa, M. Holzapfel, F. Krumeich, C. Veit, P. Novák, Study of styrene butadiene rubber and sodium methyl cellulose as binder for negative electrodes in lithium-ion batteries, J. Power Sources 161 (2006) 617–622. https://doi.org/10.1016/J.JPOWSOUR.2006.03.073.
[358] H. Chen, M. Ling, L. Hencz, H.Y. Ling, G. Li, Z. Lin, G. Liu, S. Zhang, Exploring Chemical, Mechanical, and Electrical Functionalities of Binders for Advanced Energy-Storage Devices, Chem. Rev. 118 (2018) 8936–8982. https://doi.org/10.1021/ACS.CHEMREV.8B00241
[359] K. Hofmann, A.D. Hegde, X. Liu-Theato, R. Gordon, A. Smith, N. Willenbacher, Effect of mechanical properties on processing behavior and electrochemical performance of aqueous processed graphite anodes for lithium-ion batteries, J. Power Sources 593 (2024) 233996. https://doi.org/10.1016/J.JPOWSOUR.2023.233996.
[360] M. Wang, D. Dang, A. Meyer, R. Arsenault, Y.-T. Cheng, Effects of the Mixing Sequence on Making Lithium Ion Battery Electrodes, J. Electrochem. Soc. 167 (2020) 100518. https://doi.org/10.1149/1945-7111/ab95c6.
[361] K. Kitamura, M. Tanaka, T. Mori, Effects of the mixing sequence on the graphite dispersion and resistance of lithium-ion battery anodes, J. Colloid Interface Sci. 625 (2022) 136–144. https://doi.org/10.1016/j.jcis.2022.06.006.
[362] W. Yourey, Theoretical Impact of Manufacturing Tolerance on Lithium-Ion Electrode and Cell Physical Properties, Batteries 2020, Vol. 6, Page 23 6 (2020) 23. https://doi.org/10.3390/BATTERIES6020023.
[363] B. Rowden, N. Garcia-Araez, Estimating lithium-ion battery behavior from half-cell data, Energy Reports 7 (2021) 97–103. https://doi.org/10.1016/j.egyr.2021.02.048.
[364] N. Meddings, M. Heinrich, F. Overney, J.S. Lee, V. Ruiz, E. Napolitano, S. Seitz, G. Hinds, R. Raccichini, M. Gaberšček, J. Park, Application of electrochemical impedance spectroscopy to commercial Li-ion cells: A review, J. Power Sources 480 (2020) 228742. https://doi.org/10.1016/J.JPOWSOUR.2020.228742.
[365] Z. Feng, X. Qiu, X. Chen, H. Wang, X. Guo, Interfacial Dynamics Study of NCM523-Based Semi-Solid-State Lithium-Ion Batteries by Electrochemical Impedance Spectroscopy, ACS Appl. Mater. Interfaces 16 (2024) 42995–43005. https://doi.org/10.1021/ACSAMI.4C09122.
[366] U. Westerhoff, K. Kurbach, F. Lienesch, M. Kurrat, Analysis of Lithium-Ion Battery Models Based on Electrochemical Impedance Spectroscopy, Energy Technology 4 (2016) 1620–1630. https://doi.org/10.1002/ENTE.201600154.
[367] F. Santoni, A. De Angelis, A. Moschitta, P. Carbone, M. Galeotti, L. Cinà, C. Giammanco, A. Di Carlo, A guide to equivalent circuit fitting for impedance analysis and battery state estimation, J. Energy Storage 82 (2024) 110389. https://doi.org/10.1016/J.EST.2023.110389.
[368] A.C. Lazanas, M.I. Prodromidis, Electrochemical Impedance Spectroscopy─A Tutorial, ACS Measurement Science Au 3 (2023) 162–193. https://doi.org/10.1021/ACSMEASURESCIAU.2C00070.

[369] A.C. Lazanas, M.I. Prodromidis, Electrochemical Impedance Spectroscopy─A Tutorial, ACS Measurement Science Au 3 (2023) 162–193. https://doi.org/10.1021/ACSMEASURESCIAU.2C00070.
[370] Y. Li, L. Jiang, N. Zhang, Z. Wei, W. Mei, Q. Duan, J. Sun, Q. Wang, Early warning method for thermal runaway of lithium-ion batteries under thermal abuse condition based on online electrochemical impedance monitoring, Journal of Energy Chemistry 92 (2024) 74–86. https://doi.org/10.1016/J.JECHEM.2023.12.049.
[371] Q. Zhang, W. Cai, Y.X. Yao, G.L. Zhu, C. Yan, L.L. Jiang, C. He, J.Q. Huang, A review on energy chemistry of fast-charging anodes, Chem. Soc. Rev. 49 (2020) 3806–3833. https://doi.org/10.1039/c9cs00728h.
[372] D. Rehnlund, Z. Wang, L. Nyholm, D. Rehnlund, L. Nyholm, Z. Wang, Lithium-Diffusion Induced Capacity Losses in Lithium-Based Batteries, Advanced Materials 34 (2022) 2108827. https://doi.org/10.1002/ADMA.202108827.
[373] W. Zhao, C. Zhao, H. Wu, L. Li, C. Zhang, Progress, challenge and perspective of graphite-based anode materials for lithium batteries: A review, J. Energy Storage 81 (2024) 110409. https://doi.org/10.1016/J.EST.2023.110409.
[374] S. Weng, G. Yang, S. Zhang, X. Liu, X. Zhang, Z. Liu, M. Cao, M.N. Ateş, Y. Li, L. Chen, Z. Wang, X. Wang, Kinetic Limits of Graphite Anode for Fast-Charging Lithium-Ion Batteries, Nanomicro Lett. 15 (2023) 215. https://doi.org/10.1007/S40820-023-01183-6.
[375] J. Li, L. Wang, J. Xu, Investigation of the lithium plating triggering criterion in graphite electrodes, J. Mater. Chem. A Mater. 12 (2024) 12581–12591. https://doi.org/10.1039/D4TA00244J.
[376] X. Lu, M. Lagnoni, A. Bertei, S. Das, R.E. Owen, Q. Li, K. O'Regan, A. Wade, D.P. Finegan, E. Kendrick, M.Z. Bazant, D.J.L. Brett, P.R. Shearing, Multiscale dynamics of charging and plating in graphite electrodes coupling operando microscopy and phase-field modelling, Nat. Commun. 14 (2023) 5127. https://doi.org/10.1038/S41467-023-40574-6.
[377] S. Sun, T. Guan, X. Cheng, P. Zuo, Y. Gao, C. Du, G. Yin, Accelerated aging and degradation mechanism of LiFePO 4 /graphite batteries cycled at high discharge rates, RSC Adv. 8 (2018) 25695–25703. https://doi.org/10.1039/C8RA04074E.
[378] J. Guo, Y. Li, J. Meng, K. Pedersen, L. Gurevich, D.I. Stroe, Understanding the mechanism of capacity increase during early cycling of commercial NMC/graphite lithium-ion batteries, Journal of Energy Chemistry 74 (2022) 34–44. https://doi.org/10.1016/J.JECHEM.2022.07.005.
[379] Z. Wang, R. Deng, Y. Wang, F. Pan, Comparison of Construction Strategies of Solid Electrolyte Interface (SEI) in Li Battery and Mg Battery—A Review, Molecules 29 (2024) 4761. https://doi.org/10.3390/MOLECULES29194761.
[380] T. Insinna, E.N. Bassey, K. Märker, A. Collauto, A.L. Barra, C.P. Grey, Graphite Anodes for Li-Ion Batteries: An Electron Paramagnetic Resonance Investigation, Chemistry of Materials 35 (2023) 5497–5511. https://doi.org/10.1021/acs.chemmater.3c00860.
[381] R.S. Kadam, K.P. Gadkaree, Thermodynamics of Lithium Intercalation in Randomly Oriented High Graphene Carbon, International Journal of Electrochemistry 2017 (2017) 5391794. https://doi.org/10.1155/2017/5391794.
[382] S. Jovanovic, P. Jakes, S. Merz, R.A. Eichel, J. Granwehr, Lithium intercalation into graphite: In operando analysis of Raman signal widths, Electrochemical Science Advances 2 (2022) e2100068. https://doi.org/10.1002/ELSA.202100068.
[383] T. Ohzuku, Y. Iwakoshi, K. Sawai, Formation of Lithium-Graphite Intercalation Compounds in Nonaqueous Electrolytes and Their Application as a Negative Electrode for a Lithium Ion (Shuttlecock) Cell, Journal of Electrochemistry Society 140 (1993). https://doi.org/10.1149/1.2220849.

[384] Y. Guo, R.B. Smith, Z. Yu, D.K. Efetov, J. Wang, P. Kim, M.Z. Bazant, L.E. Brus, Li Intercalation into Graphite: Direct Optical Imaging and Cahn-Hilliard Reaction Dynamics, Journal of Physical Chemistry Letters 7 (2016) 2151–2156. https://doi.org/10.1021/ACS.JPCLETT.6B00625.

[385] W. Zhou, P.H.L. Sit, First-Principles Understanding of the Staging Properties of the Graphite Intercalation Compounds towards Dual-Ion Battery Applications, ACS Omega 5 (2020) 18289–18300. https://doi.org/10.1021/ACSOMEGA.0C01950.

[386] M.D. Levi, C. Wang, J.S. Gnanaraj, D. Aurbach, Electrochemical behavior of graphite anode at elevated temperatures in organic carbonate solutions, in: J. Power Sources, 2003: pp. 538–542. https://doi.org/10.1016/S0378-7753(03)00279-9.

[387] J.R. Dahn Moli, R.F. Moli, M.J. Spoon, Suppression of staging in lithium-intercalated carbon by disorder in the host, Phys. Rev. B 42 (1990). https://doi.org/10.1103/PhysRevB.42.6424.

[388] J.R. Dahn, Phase diagram of Li"C6, 1991.

[389] Z. Zhang, K. Smith, R. Jervis, P.R. Shearing, T.S. Miller, D.J.L. Brett, Operando Electrochemical Atomic Force Microscopy of Solid-Electrolyte Interphase Formation on Graphite Anodes: The Evolution of SEI Morphology and Mechanical Properties, ACS Appl. Mater. Interfaces 12 (2020) 35132–35141. https://doi.org/10.1021/ACSAMI.0C11190.

[390] S.S. Zhang, Is Li/Graphite Half-Cell Suitable for Evaluating Lithiation Rate Capability of Graphite Electrode?, J. Electrochem. Soc. 167 (2020) 100510. https://doi.org/10.1149/1945-7111/ab945e.

[391] J. Xiao, Q. Li, Y. Bi, M. Cai, B. Dunn, T. Glossmann, J. Liu, T. Osaka, R. Sugiura, B. Wu, J. Yang, J.G. Zhang, M.S. Whittingham, Understanding and applying coulombic efficiency in lithium metal batteries, Nature Energy 2020 5:8 5 (2020) 561–568. https://doi.org/10.1038/s41560-020-0648-z.

[392] Application Note: Graphite against Lithium – A poor Battery | EL-CELL. https://www.el-cell.com/app-note_a-poor-battery/ (accessed September 5, 2025).

[393] C-NERGY™ | Imerys. https://www.imerys.com/product-ranges/c-nergy (accessed September 5, 2025).

[394] Y.K. Huang, J. Pettersson, L. Nyholm, Diffusion-Controlled Lithium Trapping in Graphite Composite Electrodes for Lithium-Ion Batteries, Advanced Energy and Sustainability Research 3 (2022). https://doi.org/10.1002/AESR.202200042.

[395] S.S. Zhang, Is Li/Graphite Half-Cell Suitable for Evaluating Lithiation Rate Capability of Graphite Electrode?, J. Electrochem. Soc. 167 (2020) 100510. https://doi.org/10.1149/1945-7111/AB945E.

[396] T. Kornas, D. Wittmann, R. Daub, O. Meyer, C. Weihs, S. Thiede, C. Herrmann, Multi-Criteria Optimization in the Production of Lithium-Ion Batteries, Procedia Manuf. 43 (2020) 720–727. https://doi.org/10.1016/j.promfg.2020.02.113.

[397] Li-Ion Battery Anode - Single Layer CMS Graphite Coated on Cu Foil (24 – MTI Online Store. https://mtixtl.com/en-euea/products/li-ion-battery-anode-single-layer-cms-graphite-coated-on-cu-foil-241-l-x-200-w-x-0-05thickness-mm-5-sheets-bag-bc-cf-241-ss-005?_pos=20&_fid=27ded501e&_ss=c (accessed September 8, 2025).

[398] F. Dai, M. Cai, Best practices in lithium battery cell preparation and evaluation, Commun. Mater. 3 (2022). https://doi.org/10.1038/s43246-022-00286-8.

[399] Silicon/Carbon (Si/C) Composite Powder as Lithium Ion Battery Anode, 2 – MTI Online Store. https://mtixtl.com/products/lib-sc450b?_pos=8&_fid=735f12be2&_ss=c (accessed September 6, 2025).

[400] M.N. Obrovac, V.L. Chevrier, Alloy negative electrodes for Li-ion batteries, Chem. Rev. 114 (2014) 11444–11502. https://doi.org/10.1021/cr500207g.

[401] D. Mazouzi, Z. Karkar, C. Reale Hernandez, P. Jimenez Manero, D. Guyomard, L. Roué, B. Lestriez, Critical roles of binders and formulation at multiscales of silicon-based composite electrodes, J. Power Sources 280 (2015) 533–549. https://doi.org/10.1016/j.jpowsour.2015.01.140.

[402] W. Porcher, S. Chazelle, A. Boulineau, N. Mariage, J.P. Alper, T. Van Rompaey, J.-S. Bridel, C. Haon, Understanding Polyacrylic Acid and Lithium Polyacrylate Binder Behavior in Silicon Based Electrodes for Li-Ion Batteries, J. Electrochem. Soc. 164 (2017) A3633–A3640. https://doi.org/10.1149/2.0821714jes.

[403] J. Nam, H. Lee, O. Chae, Overcoming Challenges in Silicon Anodes: The Role of Electrolyte Additives and Solid-State Electrolytes, Micromachines (Basel). 16 (2025) 800. https://doi.org/10.3390/mi16070800.

[404] K. Ogata, S. Jeon, D.-S. Ko, I.S. Jung, J.H. Kim, K. Ito, Y. Kubo, K. Takei, S. Saito, Y.-H. Cho, H. Park, J. Jang, H.-G. Kim, J.-H. Kim, Y.S. Kim, W. Choi, M. Koh, K. Uosaki, S.G. Doo, Y. Hwang, S. Han, Evolving affinity between Coulombic reversibility and hysteretic phase transformations in nano-structured silicon-based lithium-ion batteries, Nat. Commun. 9 (2018) 479. https://doi.org/10.1038/s41467-018-02824-w.

[405] T.K. Pham, G.A. Snook, D. Glass, A. V. Ellis, Lithium-ion diffusion behaviour in silicon nanoparticle/graphite blended anodes, J. Power Sources 638 (2025). https://doi.org/10.1016/j.jpowsour.2025.236623.

[406] Y. Zheng, D. Yin, H.J. Seifert, W. Pfleging, Investigation of fast-charging and degradation processes in 3d silicon–graphite anodes, Nanomaterials 12 (2022). https://doi.org/10.3390/nano12010140.

[407] Z. Hu, R. Zhao, J. Yang, C. Wu, Y. Bai, Binders for Si based electrodes: Current status, modification strategies and perspective, Energy Storage Mater. 59 (2023). https://doi.org/10.1016/j.ensm.2023.102776.

[408] S. Woo, M. Song, H. Park, W.-J. Song, Designing a Dual-Functional Binder for High-Energy-Density Silicon Anodes in Lithium-Ion Batteries, ACS Appl. Mater. Interfaces 17 (2025) 54786–54798. https://doi.org/10.1021/acsami.5c12431.

[409] A. Li, J.L. Hempel, M.P. Balogh, Y.-T. Cheng, A.I. Taub, Effect of Binder Content on Silicon Microparticle Anodes for Lithium-Ion Batteries, J. Electrochem. Soc. 170 (2023) 010533. https://doi.org/10.1149/1945-7111/acb388.

[410] R.C. Ionescu, C. Liu, Silicon material and method of manufacture, EP4347540A1, 2024. https://patents.google.com/patent/EP4347540A1/en?q=(silicon+composite+anode+composition+for+secondary+battery+cell)&oq=silicon+composite+anode+composition+for+secondary+battery+cell (accessed May 22, 2025).

[411] C. Reynolds, M. Faraji Niri, M.F. Hidalgo, R. Heymer, L. Román, G. Alsofi, H. Khanom, B. Pye, J. Marco, E. Kendrick, Impact of Formulation and Slurry Properties on Lithium-ion Electrode Manufacturing, Batter. Supercaps 7 (2024). https://doi.org/10.1002/batt.202300396.

[412] C.D. Reynolds, S.D. Hare, P.R. Slater, M.J.H. Simmons, E. Kendrick, Rheology and Structure of Lithium-Ion Battery Electrode Slurries, Energy Technology 10 (2022). https://doi.org/10.1002/ente.202200545.

[413] N. Dimov, H. Noguchi, M. Yoshio, A chemometric investigation of the effect of the process parameters on the performance of mixed Si/C electrodes, J. Power Sources 156 (2006) 567–573. https://doi.org/10.1016/j.jpowsour.2005.06.006.

[414] Z. Karkar, T. Jaouhari, A. Tranchot, D. Mazouzi, D. Guyomard, B. Lestriez, L. Roué, How silicon electrodes can be calendered without altering their mechanical strength and cycle life, J. Power Sources 371 (2017) 136–147. https://doi.org/10.1016/j.jpowsour.2017.10.042.

[415] F. Zhang, J. Yang, Boosting initial coulombic efficiency of Si-based anodes: a review, (2010). https://doi.org/10.1007/s42247-020-00080-7/Published.

[416] Q. Xu, J. Li, Y. Yin, Y. Kong, Y. Guo, L. Wan, Nano/Micro-Structured Si/C Anodes with High Initial Coulombic Efficiency in Li-Ion Batteries, Chem. Asian J. 11 (2016) 1205–1209. https://doi.org/10.1002/asia.201600067.
[417] M.N. Obrovac, L. Christensen, Structural changes in silicon anodes during lithium insertion/extraction, Electrochemical and Solid-State Letters 7 (2004). https://doi.org/10.1149/1.1652421.
[418] M.N. Obrovac, L.J. Krause, Reversible Cycling of Crystalline Silicon Powder, J. Electrochem. Soc. 154 (2007) A103. https://doi.org/10.1149/1.2402112.
[419] C. Chen, R. Agrawal, C. Wang, High Performance Li4Ti5O12/Si Composite Anodes for Li-Ion Batteries, Nanomaterials 5 (2015) 1469–1480. https://doi.org/10.3390/nano5031469.
[420] W.J. Legerstee, T. Noort, T.K. van Vliet, H. Schut, E.M. Kelder, Characterisation of defects in porous silicon as an anode material using positron annihilation Doppler Broadening Spectroscopy, Applied Nanoscience (Switzerland) 12 (2022) 3399–3408. https://doi.org/10.1007/s13204-022-02550-2.
[421] A. Mukanova, A. Nurpeissova, S. Kim, M. Myronov, Z. Bakenov, N-Type Doped Silicon Thin Film on a Porous Cu Current Collector as the Negative Electrode for Li-Ion Batteries, ChemistryOpen 7 (2018) 92–96. https://doi.org/10.1002/open.201700162.
[422] S. Yin, Q. Ji, X. Zuo, S. Xie, K. Fang, Y. Xia, J. Li, B. Qiu, M. Wang, J. Ban, X. Wang, Y. Zhang, Y. Xiao, L. Zheng, S. Liang, Z. Liu, C. Wang, Y.-J. Cheng, Silicon lithium-ion battery anode with enhanced performance: Multiple effects of silver nanoparticles, J. Mater. Sci. Technol. 34 (2018) 1902–1911. https://doi.org/10.1016/j.jmst.2018.02.004.
[423] Y. Liu, X. Liu, Y. Zhu, J. Wang, W. Ji, X. Liu, Scalable Synthesis of Pitch-Coated Nanoporous Si/Graphite Composite Anodes for Lithium-Ion Batteries, Energy & Fuels 37 (2023) 4624–4631. https://doi.org/10.1021/acs.energyfuels.2c03702.
[424] Z. Yan, S. Yi, X. Li, J. Jiang, D. Yang, N. Du, A scalable silicon/graphite anode with high silicon content for high-energy lithium-ion batteries, Mater. Today Energy 31 (2023) 101225. https://doi.org/10.1016/J.MTENER.2022.101225.
[425] Q. Xu, Q. Wang, D. Chen, Y. Zhong, Z. Wu, Y. Song, G. Wang, Y. Liu, B. Zhong, X. Guo, Silicon/graphite composite anode with constrained swelling and a stable solid electrolyte interphase enabled by spent graphite, Green Chemistry 23 (2021) 4531–4539. https://doi.org/10.1039/d1gc00630d.
[426] Y. Xu, G. Yin, Y. Ma, P. Zuo, X. Cheng, Nanosized core/shell silicon@carbon anode material for lithium ion batteries with polyvinylidene fluoride as carbon source, J. Mater. Chem. 20 (2010) 3216–3220. https://doi.org/10.1039/b921979j.
[427] F. Schomburg, B. Heidrich, S. Wennemar, R. Drees, T. Roth, M. Kurrat, H. Heimes, A. Jossen, M. Winter, J.Y. Cheong, F. Röder, Lithium-ion battery cell formation: status and future directions towards a knowledge-based process design, Energy Environ. Sci. 17 (2024) 2686–2733. https://doi.org/10.1039/d3ee03559j.
[428] H. Seo, D. Kim, S. Park, E. Seo, P. Kim, J. Choi, J. Yoo, A comprehensive review of liquid electrolytes for silicon anodes in lithium-ion batteries, Advances in Industrial and Engineering Chemistry 1 (2025) 3. https://doi.org/10.1007/s44405-025-00004-1.
[429] H. Bashirpour-bonab, Investigation and electrochemical analysis of SEI layer formation in natural graphite anode formation process in lithium-ion battery, E-Prime - Advances in Electrical Engineering, Electronics and Energy 5 (2023) 100261. https://doi.org/10.1016/j.prime.2023.100261.
[430] P. Parikh, M. Sina, A. Banerjee, X. Wang, M.S. D'Souza, J.M. Doux, E.A. Wu, O.Y. Trieu, Y. Gong, Q. Zhou, K. Snyder, Y.S. Meng, Role of Polyacrylic Acid (PAA) Binder on the Solid Electrolyte Interphase in Silicon Anodes, Chemistry of Materials 31 (2019) 2535–2544. https://doi.org/10.1021/acs.chemmater.8b05020.

[431] B. Hu, I.A. Shkrob, S. Zhang, L. Zhang, J. Zhang, Y. Li, C. Liao, Z. Zhang, W. Lu, L. Zhang, The existence of optimal molecular weight for poly(acrylic acid) binders in silicon/graphite composite anode for lithium-ion batteries, J. Power Sources 378 (2018) 671–676. https://doi.org/10.1016/j.jpowsour.2017.12.068.

[432] B. Kim, Y. Song, B. Youn, D. Lee, Dispersion Homogeneity of Silicon Anode Slurries with Various Binders for Li-Ion Battery Anode Coating, Polymers (Basel). 15 (2023). https://doi.org/10.3390/polym15051152.

[433] G. Kloker, D. Vrankovic, N. Arya, T. Diemant, M. Anjass, Enabling Si-Dominant Anodes: Influence of Neutralization Degree of Polyacrylic Acid on Low-Cost Micron-Sized Silicon Anode in High-Energy Li-Ion Full Cell, Batter. Supercaps 7 (2024). https://doi.org/10.1002/batt.202400330.

[434] L. Zhang, X. Wu, W. Qian, K. Pan, X. Zhang, L. Li, M. Jia, S. Zhang, Exploring More Functions in Binders for Lithium Batteries, Electrochemical Energy Reviews 6 (2023). https://doi.org/10.1007/s41918-023-00198-2.

[435] D. Shin, H. Park, U. Paik, Cross-linked poly(acrylic acid)-carboxymethyl cellulose and styrene-butadiene rubber as an efficient binder system and its physicochemical effects on a high energy density graphite anode for Li-ion batteries, Electrochem. Commun. 77 (2017) 103–106. https://doi.org/10.1016/j.elecom.2017.02.018.

[436] T.B.T. Truong, Y.R. Chen, G.Y. Lin, H.T. Lin, Y.S. Wu, C.C. Yang, Lithium polyacrylate polymer coating enhances the performance of graphite/silicon/carbon composite anodes, Electrochim. Acta 365 (2021). https://doi.org/10.1016/j.electacta.2020.137387.

[437] R. Zhu, S. Liu, T. Li, D. Yang, Precisely Prelithiated Polyacrylic Acid Binder Improving Electrochemical Performance of Micron-Sized Silicon Anodes for Lithium-Ion Batteries, ChemElectroChem (2024). https://doi.org/10.1002/celc.202400326.

[438] A.C. Dimian, C.S. Bildea, Sustainable process design for manufacturing acrylic acid from glycerol, Chemical Engineering Research and Design 166 (2021) 121–134. https://doi.org/10.1016/j.cherd.2020.12.002.

[439] L. Tamboia, G. Montinaro, E. Ravesio, J. Amici, C. Francia, S. Bodoardo, F. Bella, D. Versaci, Optimization of binary binder blends for aqueous-based slurries of SiOx/C for next-generation lithium-ion batteries, J. Clean. Prod. 554 (2026) 148153. https://doi.org/10.1016/j.jclepro.2026.148153.

[440] S.W. Kim, R. K.K, Y. Kang, J.H. Han, S.J. Yeon, S. Kannan, T.-H. Kim, Oxidized λ-Carrageenan as an Aqueous Silicon-Anode Polymer Binder with Reduced Viscosity for Lithium-Ion Batteries, ACS Sustain. Chem. Eng. 12 (2024) 16041–16051. https://doi.org/10.1021/acssuschemeng.4c05808.

[441] A.C. Rolandi, C. Pozo-Gonzalo, I. de Meatza, N. Casado, M. Forsyth, D. Mecerreyes, Carrageenans as Sustainable Water-Processable Binders for High-Voltage NMC811 Cathodes, ACS Appl. Energy Mater. 6 (2023) 8616–8625. https://doi.org/10.1021/acsaem.3c01662.

[442] M. Binder, E. Keller, D. Bresser, Carrageenan as Water-Soluble Binder for High Mass Loading $LiNi_{0.5}Mn_{1.5}O_4$ Cathodes, ECS Meeting Abstracts MA2025-02 (2025) 543–543. https://doi.org/10.1149/MA2025-023543mtgabs.

[443] M. Binder, E. Keller, D. Bresser, Realization of high mass loading LiNi0.5Mn1.5O4 Li-ion cathodes using water-soluble carrageenan as binder, J. Power Sources 603 (2024) 234487. https://doi.org/10.1016/j.jpowsour.2024.234487.

[444] J. He, C. Das, F. Yang, J. Maibach, Crosslinked poly(acrylic acid) enhances adhesion and electrochemical performance of Si anodes in Li-ion batteries, Electrochim. Acta 411 (2022) 140038. https://doi.org/10.1016/j.electacta.2022.140038.

[445] Nanomakers - when small makes a difference. https://nanomakers.fr/en/ (accessed September 10, 2025).

[446] ALPhANOV | Centre technologique Optique & Lasers. https://www.alphanov.com/en (accessed September 10, 2025).
[447] Università degli studi di Parma. https://www.unipr.it/ (accessed December 23, 2025).
[448] M. Gutierrez, M. Morcrette, L. Monconduit, Y. Oudart, P. Lemaire, C. Davoisne, N. Louvain, R. Janot, Towards a better understanding of the degradation mechanisms of Li-ion full cells using Si/C composites as anode, J. Power Sources 533 (2022) 231408. https://doi.org/10.1016/J.JPOWSOUR.2022.231408.
[449] Company | ARLANXEO Website / Customer Portal. https://www.arlanxeo.com/company (accessed December 23, 2025).
[450] S. Scheffler, R. Jagau, N. Müller, A. Diener, A. Kwade, Calendering of Silicon-Containing Electrodes and Their Influence on the Mechanical and Electrochemical Properties, Batteries 8 (2022) 46. https://doi.org/10.3390/BATTERIES8050046/S1.
[451] K. Eun Kyung, S. Sun Young, K. Je Young, W. Sang Wook, Methods of measuring electrode density and electrode porosity, US9719905B2, 2014. https://patents.google.com/patent/US9719905B2/en (accessed September 10, 2025).
[452] D. Zapata Dominguez, B. Mondal, M. Gaberscek, M. Morcrette, A.A. Franco, Impact of the manufacturing process on graphite blend electrodes with silicon nanoparticles for lithium-ion batteries, J. Power Sources 580 (2023) 233367. https://doi.org/10.1016/J.JPOWSOUR.2023.233367.
[453] D. Li, H. Wan, J. Liu, H. Jiang, Y. Wang, J. Zhang, Y. Zheng, Effects of calendering state on coupled electrochemical-mechanical performance of silicon based composite electrodes, Green Energy and Intelligent Transportation 3 (2024) 100154. https://doi.org/10.1016/J.GEITS.2024.100154.
[454] J. Li, N.J. Dudney, X. Xiao, Y. Cheng, C. Liang, M.W. Verbrugge, Asymmetric Rate Behavior of Si Anodes for Lithium-Ion Batteries: Ultrafast De-Lithiation versus Sluggish Lithiation at High Current Densities, Adv. Energy Mater. 5 (2015). https://doi.org/10.1002/aenm.201401627.
[455] B. Liu, M. Luo, Z. Wang, C. Passolano, L. Shaw, On the Specific Capacity and Cycle Stability of Si@void@C Anodes: Effects of Particle Size and Charge/Discharge Protocol, Batteries 8 (2022). https://doi.org/10.3390/batteries8100154.
[456] Y. Abe, I. Saito, M. Tomioka, M. Kabir, S. Kumagai, Effects of Excessive Prelithiation on Full-Cell Performance of Li-Ion Batteries with a Hard-Carbon/Nanosized-Si Composite Anode, Batteries 8 (2022) 210. https://doi.org/10.3390/batteries8110210.
[457] G.M. Overhoff, R. Nölle, V. Siozios, M. Winter, T. Placke, A Thorough Analysis of Two Different Pre-Lithiation Techniques for Silicon/Carbon Negative Electrodes in Lithium Ion Batteries, Batter. Supercaps 4 (2021) 1163–1174. https://doi.org/10.1002/batt.202100024.
[458] H.-W. Jung, G.-E. Lee, H.-C. Shin, In Situ Electrochemical Detection of Silicon Anode Crystallization for Full-Cell Health Management, Energies (Basel). 19 (2026) 279. https://doi.org/10.3390/en19010279.
[459] T.K. Pham, G.A. Snook, D. Glass, A. V. Ellis, Lithium-ion diffusion behaviour in silicon nanoparticle/graphite blended anodes, J. Power Sources 638 (2025) 236623. https://doi.org/10.1016/j.jpowsour.2025.236623.
[460] D. Lepage, L. Savignac, M. Saulnier, S. Gervais, S.B. Schougaard, Modification of aluminum current collectors with a conductive polymer for application in lithium batteries, Electrochem. Commun. 102 (2019) 1–4. https://doi.org/10.1016/j.elecom.2019.03.009.
[461] M.J. Lain, G. Apachitei, D.-E. Dogaru, W.D. Widanage, J. Marco, M. Copley, Measurement of anisotropic volumetric resistivity in lithium ion electrodes, RSC Adv. 13 (2023) 33437–33445. https://doi.org/10.1039/D3RA06412C.

[462] N. Kumano, Y. Yamaguchi, Y. Akimoto, A. Ohshima, H. Nakamura, M. Yamamura, Migration of binder and conductive agent during drying process of Li-ion battery cathodes, J. Power Sources 591 (2024) 233883. https://doi.org/10.1016/j.jpowsour.2023.233883.
[463] H. Oh, G.-S. Kim, B.U. Hwang, J. Bang, J. Kim, K.-M. Jeong, Development of a feasible and scalable manufacturing method for PTFE-based solvent-free lithium-ion battery electrodes, Chemical Engineering Journal 491 (2024) 151957. https://doi.org/10.1016/j.cej.2024.151957.
[464] A.L. Michan, M. Leskes, C.P. Grey, Voltage Dependent Solid Electrolyte Interphase Formation in Silicon Electrodes: Monitoring the Formation of Organic Decomposition Products, Chemistry of Materials 28 (2016) 385–398. https://doi.org/10.1021/acs.chemmater.5b04408.
[465] J. Gu, A.J. Lovett, M. Füredi, T. Dore, S. Guldin, T.S. Miller, Tracking Lithium Intercalation in Battery Electrodes via Their Electrochromic Properties Using *Operando* Ellipsometry, J. Am. Chem. Soc. 147 (2025) 40967–40980. https://doi.org/10.1021/jacs.5c14539.
[466] E. Barcaro, V. Marangon, M. Mutarelli, J. Hassoun, A lithium-ion battery with cycling stability promoted by the progressive activation of a silicon oxide anode in graphene-amorphous carbon matrix, J. Power Sources 595 (2024) 234059. https://doi.org/10.1016/j.jpowsour.2024.234059.
[467] W. Yourey, Silicon Negative Electrodes—What Can Be Achieved for Commercial Cell Energy Densities, Batteries 9 (2023) 576. https://doi.org/10.3390/BATTERIES9120576/S1.
[468] A. Osmanpour, J. Poen, V. Ruiz, K. Tariq, W.P. Kalisvaart, Stable, Scalable Micron-Sized Porous Silicon for High Energy Density Li-Ion Batteries, Batter. Supercaps (2025). https://doi.org/10.1002/batt.202500500.
[469] F. Maroni, M. Spreafico, A. Schönecker, M. Wohlfahrt-Mehrens, M. Marinaro, Near-Zero Volume Expansion Nanoporous Silicon as Anode for Li-ion Batteries, J. Electrochem. Soc. 169 (2022) 080506. https://doi.org/10.1149/1945-7111/ac8628.
[470] P. Nuss, K.H. Gardner, Attributional life cycle assessment (ALCA) of polyitaconic acid production from northeast US softwood biomass, International Journal of Life Cycle Assessment 18 (2013) 603–612. https://doi.org/10.1007/s11367-012-0511-y.
[471] H.F. Andersen, C.E.L. Foss, J. Voje, R. Tronstad, T. Mokkelbost, P.E. Vullum, A. Ulvestad, M. Kirkengen, J.P. Mæhlen, Silicon-Carbon composite anodes from industrial battery grade silicon, Sci. Rep. 9 (2019) 1–9. https://doi.org/10.1038/S41598-019-51324-4.
[472] R.C. Ionescu, C. Liu, Silicon anode battery, WO2022177914A1, 2022. https://patents.google.com/patent/WO2022177914A1/en?q=(silicon+composite+anode+composition+for+secondary+battery+cell)&oq=silicon+composite+anode+composition+for+secondary+battery+cell (accessed May 22, 2025).
[473] T. Chartrel, M. Ndour, V. Bonnet, S. Cavalaglio, L. Aymard, F. Dolhem, L. Monconduit, J.P. Bonnet, Revisiting and improving the preparation of silicon-based electrodes for lithium-ion batteries: ball milling impact on poly(acrylic acid) polymer binders, Mater. Chem. Front. 3 (2019) 881–891. https://doi.org/10.1039/c8qm00660a.
[474] Y. Son, N. Kim, T. Lee, Y. Lee, J. Ma, S. Chae, J. Sung, H. Cha, Y. Yoo, J. Cho, Calendering-Compatible Macroporous Architecture for Silicon–Graphite Composite toward High-Energy Lithium-Ion Batteries, Advanced Materials 32 (2020) 2003286. https://doi.org/10.1002/ADMA.202003286.
[475] C. Real Hernandez, Z. Karkar, D. Guyomard, B. Lestriez, L. Roué, A film maturation process for improving the cycle life of Si-based anodes for Li-ion batteries, Electrochem. Commun. 61 (2015) 102–105. https://doi.org/10.1016/j.elecom.2015.10.014.

[476] I.-H. Lee, Y. Jin, H.-S. Jang, D. Whang, Enhancing the Stability and Initial Coulombic Efficiency of Silicon Anodes through Coating with Glassy ZIF-4, Nanomaterials 14 (2023) 18. https://doi.org/10.3390/nano14010018.
[477] B. Peng, W. Bao, K. Sun, J. Xiao, Enhancing Silicon Anode Performance in Lithium-Ion Batteries Through Hybrid Artificial SEI Layer and Prelithiation, Nanomaterials 15 (2025) 690. https://doi.org/10.3390/nano15090690.
[478] F. Maroni, A. Kryeziu, J. Chen, M. Marinaro, Between Pilot-Production and Lab-Scale: How to Approach Silicon-Dominant Li-Ion Battery Anodes Performance Consistency, Adv. Mater. Technol. (2026). https://doi.org/10.1002/admt.202502167.
[479] S. Chae, M. Ko, K. Kim, K. Ahn, J. Cho, Confronting Issues of the Practical Implementation of Si Anode in High-Energy Lithium-Ion Batteries, Joule 1 (2017) 47–60. https://doi.org/10.1016/j.joule.2017.07.006.
[480] T. Li, J. Yang, S. Lu, H. Wang, H. Ding, Failure mechanism of bulk silicon anode electrodes for lithium-ion batteries, Rare Metals 32 (2013) 299–304. https://doi.org/10.1007/s12598-013-0045-x.
[481] N. Yuca, I. Kalafat, E. Guney, B. Cetin, O.S. Taskin, Self-Healing Systems in Silicon Anodes for Li-Ion Batteries, Materials 15 (2022) 2392. https://doi.org/10.3390/ma15072392.
[482] D. Ma, Z. Cao, A. Hu, Si-Based Anode Materials for Li-Ion Batteries: A Mini Review, Nanomicro Lett. 6 (2014) 347–358. https://doi.org/10.1007/s40820-014-0008-2.
[483] G. Zhu, S. Yang, Y. Wang, Q. Qu, H. Zheng, Dimethylacrylamide, a novel electrolyte additive, can improve the electrochemical performances of silicon anodes in lithium-ion batteries, RSC Adv. 9 (2019) 435–443. https://doi.org/10.1039/C8RA07988A.
[484] M. Wetjen, D. Pritzl, R. Jung, S. Solchenbach, R. Ghadimi, H.A. Gasteiger, Differentiating the Degradation Phenomena in Silicon-Graphite Electrodes for Lithium-Ion Batteries, J. Electrochem. Soc. 164 (2017) A2840–A2852. https://doi.org/10.1149/2.1921712jes.
[485] B. Jerliu, E. Hüger, L. Dörrer, B.K. Seidlhofer, R. Steitz, M. Horisberger, H. Schmidt, Lithium insertion into silicon electrodes studied by cyclic voltammetry and *operando* neutron reflectometry, Physical Chemistry Chemical Physics 20 (2018) 23480–23491. https://doi.org/10.1039/C8CP03540G.
[486] E. Barcaro, V. Marangon, M. Mutarelli, J. Hassoun, A lithium-ion battery with cycling stability promoted by the progressive activation of a silicon oxide anode in graphene-amorphous carbon matrix, J. Power Sources 595 (2024) 234059. https://doi.org/10.1016/j.jpowsour.2024.234059.
[487] S. Hansen, E. Quiroga-González, J. Carstensen, H. Föll, Size-dependent cyclic voltammetry study of silicon microwire anodes for lithium ion batteries, Electrochim. Acta 217 (2016) 283–291. https://doi.org/10.1016/j.electacta.2016.09.088.
[488] F. Zou, A. Manthiram, F. Zou, A. Manthiram, A Review of the Design of Advanced Binders for High-Performance Batteries, Adv. Energy Mater. 10 (2020) 2002508. https://doi.org/10.1002/AENM.202002508.
[489] S. Jaiser, M. Müller, M. Baunach, W. Bauer, P. Scharfer, W. Schabel, Investigation of film solidification and binder migration during drying of Li-Ion battery anodes, J. Power Sources 318 (2016) 210–219. https://doi.org/10.1016/j.jpowsour.2016.04.018.
[490] C.D. Reynolds, J. Lam, L. Yang, E. Kendrick, Extensional rheology of battery electrode slurries with water-based binders, Mater. Des. 222 (2022). https://doi.org/10.1016/j.matdes.2022.111104.
[491] Y. Song, B.-Y. Song, B. Kim, Y. Ju, I.-S. Jang, J. Chun, D. Lee, Designing highly packed silicon anode slurries for high capacity and prolonged lifespan of lithium-ion batteries, Chemical Engineering Journal 474 (2023) 145606. https://doi.org/10.1016/j.cej.2023.145606.

[492] M. Zarei-Jelyani, S. Baktashian, M. Babaiee, R. Eqra, Improved Mechanical and Electrochemical Properties of Artificial Graphite Anode Using Water-Based Binders in Lithium-Ion Batteries, 2018.
[493] T. Larsen, J.R. Royer, F.H.J. Laidlaw, W.C.K. Poon, T. Larsen, S.J. Andreasen, J. de C. Christiansen, Controlling the rheo-electric properties of graphite/carbon black suspensions by 'flow switching,' Rheol. Acta 63 (2024) 283–289. https://doi.org/10.1007/s00397-024-01439-x.
[494] D.Z. Dominguez, B. Mondal, A.A. Franco, Understanding the Processability of Graphite Blend Electrodes with Silicon Nanoparticles, ECS Meeting Abstracts MA2023-01 (2023) 711. https://doi.org/10.26434/chemrxiv-2022-p891w.
[495] I. Kovalenko, B. Zdyrko, A. Magasinski, B. Hertzberg, Z. Milicev, R. Burtovyy, I. Luzinov, G. Yushin, A Major Constituent of Brown Algae for Use in High-Capacity Li-Ion Batteries, Science (1979). 334 (2011) 75–79. https://doi.org/10.1126/science.1209150.
[496] D. Sarker, R.K. Bordia, U.D. Schiller, Numerical modeling of electrochemical transport and discharge mechanisms in hierarchically porous lithium-ion electrodes, Mater. Adv. 7 (2026) 2362–2378. https://doi.org/10.1039/D5MA00902B.
[497] J. Xiong, N. Dupré, D. Mazouzi, D. Guyomard, L. Roué, B. Lestriez, Influence of the Polyacrylic Acid Binder Neutralization Degree on the Initial Electrochemical Behavior of a Silicon/Graphite Electrode, ACS Appl. Mater. Interfaces 13 (2021) 28304–28323. https://doi.org/10.1021/ACSAMI.1C06683.
[498] H. Gil, C. Leygraf, Initial Atmospheric Corrosion of Copper Induced by Carboxylic Acids, J. Electrochem. Soc. 154 (2007) C611. https://doi.org/10.1149/1.2773627.
[499] C.R. Hernandez, A. Etiemble, T. Douillard, D. Mazouzi, Z. Karkar, E. Maire, D. Guyomard, B. Lestriez, L. Roué, A Facile and Very Effective Method to Enhance the Mechanical Strength and the Cyclability of Si-Based Electrodes for Li-Ion Batteries, Adv. Energy Mater. 8 (2018) 1701787. https://doi.org/10.1002/AENM.201701787.
[500] D. Mazouzi, R. Grissa, M. Paris, Z. Karkar, L. Huet, D. Guyomard, L. Roué, T. Devic, B. Lestriez, CMC-citric acid Cu(II) cross-linked binder approach to improve the electrochemical performance of Si-based electrodes, Electrochim. Acta 304 (2019) 495–504. https://doi.org/10.1016/j.electacta.2019.03.026.
[501] V. Vanpeene, J. Villanova, A. King, B. Lestriez, E. Maire, L. Roué, Dynamics of the Morphological Degradation of Si-Based Anodes for Li-Ion Batteries Characterized by In Situ Synchrotron X-Ray Tomography, Adv. Energy Mater. 9 (2019). https://doi.org/10.1002/aenm.201803947.
[502] O.D. Frent, L.G. Vicas, N. Duteanu, C.M. Morgovan, T. Jurca, A. Pallag, M.E. Muresan, S.M. Filip, R.L. Lucaciu, E. Marian, Sodium Alginate—Natural Microencapsulation Material of Polymeric Microparticles, International Journal of Molecular Sciences 2022, Vol. 23, Page 12108 23 (2022) 12108. https://doi.org/10.3390/IJMS232012108.
[503] C.M. Yakacki, R. Shandas, C. Lanning, B. Rech, A. Eckstein, K. Gall, Unconstrained Recovery Characterization of Shape-Memory Polymer Networks for Cardiovascular Applications, Biomaterials 28 (2007) 2255. https://doi.org/10.1016/J.BIOMATERIALS.2007.01.030.
[504] S. Wang, Y. Shi, Y. Li, H. Lin, K. Fan, X. Teng, Solid-state refrigeration of shape memory alloy-based elastocaloric materials: A review focusing on preparation methods, properties and development, Renewable and Sustainable Energy Reviews 187 (2023) 113762. https://doi.org/10.1016/J.RSER.2023.113762.
[505] F. Ma, Y. Fu, V. Battaglia, R. Prasher, Microrheological modeling of lithium ion battery anode slurry, J. Power Sources 438 (2019) 226994. https://doi.org/10.1016/J.JPOWSOUR.2019.226994.
[506] J. Vaughey, B. Cunningham, Next Generation Lithium-Ion Batteries: Advanced Anodes R&D, 2019.

[507] C. Toigo, M. Kracalik, E. Bradt, K.H. Pettinger, C. Arbizzani, Rheological properties of aqueous sodium alginate slurries for lto battery electrodes, Polymers (Basel). 13 (2021). https://doi.org/10.3390/polym13203582.
[508] M. Deguchi, Y.M. Todorov, K. Abe, Functional electrolyte: Design of corrosion inhibition additives to protect Cu current collectors in over-discharged state, J. Power Sources 625 (2025). https://doi.org/10.1016/j.jpowsour.2024.235613.
[509] S. Dai, J. Chen, Y. Ren, Z. Liu, J. Chen, C. Li, X. Zhang, X. Zhang, T. Zeng, Electrochemical corrosion behavior of the copper current collector in the electrolyte of lithium-ion batteries, Int. J. Electrochem. Sci. 12 (2017) 10589–10598. https://doi.org/10.20964/2017.11.28.
[510] Y. Gao, Z. Pan, J. Sun, Z. Liu, J. Wang, High-Energy Batteries: Beyond Lithium-Ion and Their Long Road to Commercialisation, Nanomicro Lett. 14 (2022). https://doi.org/10.1007/s40820-022-00844-2.
[511] E. Ravesio, V. Sumini, L. Genovese, D. Versaci, S. Bodoardo, Life Cycle Assessment of Graphite, Silicon Composite, and Silicon-Dominant Anodes for Lithium-Ion Batteries: Environmental Impacts, Uncertainties, and Supply Chain Considerations, Adv. Sustain. Syst. 10 (2026). https://doi.org/10.1002/adsu.202501576.
[512] M.J. Lain, Y. Wu, A. Smith, S. Bolloju, S.R. Coles, L.F.J. Piper, A comparative life cycle assessment of different lithium ion anode manufacturing routes based on graphite and/or silicon, Sustainable Materials and Technologies 45 (2025) e01609. https://doi.org/10.1016/j.susmat.2025.e01609.
[513] L. Gaines, J.L. Sullivan, A. Burnham, Life-Cycle Analysis for Lithium-Ion Battery Production and Recycling, (2011). https://www.researchgate.net/publication/265158823.
[514] D. Kushnir, B.A. Sandén, Multi-level energy analysis of emerging technologies: A case study in new materials for lithium ion batteries, J. Clean. Prod. 19 (2011) 1405–1416. https://doi.org/10.1016/j.jclepro.2011.05.006.
[515] L.A.W. Ellingsen, G. Majeau-Bettez, B. Singh, A.K. Srivastava, L.O. Valøen, A.H. Strømman, Life Cycle Assessment of a Lithium-Ion Battery Vehicle Pack, J. Ind. Ecol. 18 (2014) 113–124. https://doi.org/10.1111/jiec.12072.
[516] B. Li, X. Gao, J. Li, C. Yuan, Life cycle environmental impact of high-capacity lithium ion battery with silicon nanowires anode for electric vehicles, Environ. Sci. Technol. 48 (2014) 3047–3055. https://doi.org/10.1021/es4037786.
[517] Y. Deng, L. Ma, T. Li, J. Li, C. Yuan, Life Cycle Assessment of Silicon-Nanotube-Based Lithium Ion Battery for Electric Vehicles, ACS Sustain. Chem. Eng. 7 (2019) 599–610. https://doi.org/10.1021/acssuschemeng.8b04136.
[518] Vijaya, P.K. Nema, P. Kalita, R. Thangavel, Life cycle assessment of lithium-ion batteries with carbon-coated silicon-graphite composite anodes: impact of silicon content on cradle-to-gate environmental footprint, Environmental Science and Pollution Research (2025) 1–15. https://doi.org/10.1007/s11356-025-36270-1.
[519] C. Nøstvold, E. Pastor-Vallés, V. Andersen, G. Tranell, J.B. Pettersen, Life Cycle Assessment of Metallurgical Grade Silicon Comparing Charge Mixtures and Yields, Journal of Sustainable Metallurgy 11 (2025) 436–455. https://doi.org/10.1007/S40831-024-00941-Z/TABLES/14.
[520] B. Li, J. Li, C. Yuan, Life Cycle Assessment of Lithium Ion Batteries with Silicon Nanowire Anode for Electric Vehicles, Proceedings of the International Symposium on Sustainable Systems and Technologies (2013). https://doi.org/10.6084/m9.figshare.805147.
[521] Z. Wu, D. Kong, Comparative life cycle assessment of lithium-ion batteries with lithium metal, silicon nanowire, and graphite anodes, Clean Technol. Environ. Policy 20 (2018) 1233–1244. https://doi.org/10.1007/s10098-018-1548-9.

[522] M. Erakca, S. Pinto Bautista, S. Moghaddas, M. Baumann, W. Bauer, L. Leuthner, M. Weil, Closing gaps in LCA of lithium-ion batteries: LCA of lab-scale cell production with new primary data, J. Clean. Prod. 384 (2023) 135510. https://doi.org/10.1016/j.jclepro.2022.135510.
[523] M. Erakca, M. Baumann, W. Bauer, L. de Biasi, J. Hofmann, B. Bold, M. Weil, Energy flow analysis of laboratory scale lithium-ion battery cell production, IScience 24 (2021) 102437. https://doi.org/10.1016/j.isci.2021.102437.
[524] M.L. Carvalho, A. Temporelli, E. Brivio, P.C. Brambilla, G. Mela, P. Girardi, Batteries in motion: A life cycle assessment and critical resource use analysis of micromobility vehicles with primary Li-ion battery data, J. Energy Storage 125 (2025) 116965. https://doi.org/10.1016/j.est.2025.116965.
[525] D. Khanna, E. Gemechu, N. Mahbub, J. Joy, A. Kumar, Assessment of life cycle environmental impacts of materials, driving pattern, and climatic conditions on battery electric and hydrogen fuel cell vehicles in a cold region, Environ. Impact Assess. Rev. 110 (2025) 107680. https://doi.org/10.1016/j.eiar.2024.107680.
[526] M. Philippot, G. Alvarez, E. Ayerbe, J. Van Mierlo, M. Messagie, Eco-Efficiency of a Lithium-Ion Battery for Electric Vehicles: Influence of Manufacturing Country and Commodity Prices on GHG Emissions and Costs, Batteries 2019, Vol. 5, Page 23 5 (2019) 23. https://doi.org/10.3390/batteries5010023.
[527] E. Kallitsis, A. Korre, G. Kelsall, M. Kupfersberger, Z. Nie, Environmental life cycle assessment of the production in China of lithium-ion batteries with nickel-cobalt-manganese cathodes utilising novel electrode chemistries, J. Clean. Prod. 254 (2020). https://doi.org/10.1016/j.jclepro.2020.120067.
[528] M. Chordia, A. Nordelöf, L.A.W. Ellingsen, Environmental life cycle implications of upscaling lithium-ion battery production, International Journal of Life Cycle Assessment 26 (2021) 2024–2039. https://doi.org/10.1007/S11367-021-01976-0/FIGURES/6.
[529] S. Zhao, F. You, Comparative Life-Cycle Assessment of Li-Ion Batteries through Process-Based and Integrated Hybrid Approaches, ACS Sustain. Chem. Eng. 7 (2019) 5082–5094. https://doi.org/10.1021/acssuschemeng.8b05902.
[530] F. Scrucca, A. Presciutti, G. Baldinelli, G. Barberio, L. Postrioti, C. Karaca, Life cycle assessment of Li-ion batteries for electric vehicles: A review focused on the production phase impact, J. Power Sources 639 (2025) 236703. https://doi.org/10.1016/j.jpowsour.2025.236703.
[531] H. Hoover, R. Bell, K. Rippy, Emerging Technologies for Decarbonizing Silicon Production, Journal of Sustainable Metallurgy 10 (2024) 1921–1932. https://doi.org/10.1007/S40831-024-00913-3/FIGURES/8.
[532] P. Wiechers, A. Hermann, S. Koob, F. Glaum, M. Gleiß, Development of a Process for Direct Recycling of Negative Electrode Scrap from Lithium-Ion Battery Production on a Technical Scale and Its Influence on the Material Quality, Batteries 10 (2024) 218. https://doi.org/10.3390/batteries10070218.
[533] N. Hayagan, C. Aymonier, L. Croguennec, C. Faure, J.-B. Ledeuil, M. Morcrette, R. Dedryvère, J. Olchowka, G. Philippot, Direct Recycling Process Using Pressurized CO2 for Li-Ion Battery Positive Electrode Production Scraps, ACS Sustain. Chem. Eng. 13 (2024) 105–118. https://doi.org/10.1021/acssuschemeng.4C05591.
[534] F. Arshad, J. Lin, N. Manurkar, E. Fan, A. Ahmad, M. un N. Tariq, F. Wu, R. Chen, L. Li, Life Cycle Assessment of Lithium-ion Batteries: A Critical Review, Resour. Conserv. Recycl. 180 (2022). https://doi.org/10.1016/j.resconrec.2022.106164.
[535] Critical Raw Materials Resilience: Charting a Path towards greater Security and Sustainability, Brussels, 2020. http://info.worldbank.org/governance/wgi/.
[536] N.B. Manjong, V. Bach, L. Usai, S. Marinova, O. Stokke Burheim, M. Finkbeiner, A.H. Strømman, A comparative assessment of value chain criticality of lithium-ion battery cells,

Sustainable Materials and Technologies 36 (2023). https://doi.org/10.1016/j.susmat.2023.e00614.
[537] R. Arvidsson, A.M. Tillman, B.A. Sandén, M. Janssen, A. Nordelöf, D. Kushnir, S. Molander, Environmental Assessment of Emerging Technologies: Recommendations for Prospective LCA, J. Ind. Ecol. 22 (2018) 1286–1294. https://doi.org/10.1111/jiec.12690.
[538] J.B. Guinée, S. Cucurachi, P.J.G. Henriksson, R. Heijungs, Digesting the alphabet soup of LCA, International Journal of Life Cycle Assessment 23 (2018) 1507–1511. https://doi.org/10.1007/s11367-018-1478-0.
[539] High-Energy Density Lithium Ion Batteries for Unmanned Systems. https://www.unmannedsystemstechnology.com/company/e-magy/ (accessed July 7, 2026).
[540] The silicon solution: how E-magy is building Europe's battery independence | EIT. https://www.eit.europa.eu/news-events/success-stories/silicon-solution-how-e-magy-building-europes-battery-independence (accessed July 7, 2026).
[541] C. Yuan, Y. Deng, T. Li, F. Yang, Manufacturing energy analysis of lithium ion battery pack for electric vehicles, CIRP Ann. Manuf. Technol. 66 (2017) 53–56. https://doi.org/10.1016/j.cirp.2017.04.109.
[542] A. Jinasena, O.S. Burheim, A.H. Strømman, A Flexible Model for Benchmarking the Energy Usage of Automotive Lithium-Ion Battery Cell Manufacturing, Batteries 2021, Vol. 7, Page 14 7 (2021) 14. https://doi.org/10.3390/batteries7010014.
[543] S. Davidsson Kurland, Energy use for GWh-scale lithium-ion battery production, Environ. Res. Commun 2 (2020) 12001. https://doi.org/10.1088/2515-7620/ab5e1e.
[544] J. Zhang, X. Ke, Y. Gu, F. Wang, D. Zheng, K. Shen, C. Yuan, Cradle-to-gate life cycle assessment of all-solid-state lithium-ion batteries for sustainable design and manufacturing, International Journal of Life Cycle Assessment 27 (2022) 227–237. https://doi.org/10.1007/s11367-022-02023-2.
[545] D. Surovtseva, E. Crossin, R. Pell, L. Stamford, Toward a life cycle inventory for graphite production, J. Ind. Ecol. 26 (2022) 964–979. https://doi.org/10.1111/JIEC.13234.
[546] M. Grohol, C. Veeh, Study on the Critical Raw Materials for the EU 2023 - Final Report, 2023.
[547] S. Bobba, S. Carrara, J. Huisman, F. Mathieux, C. Pavel, Critical raw materials for strategic technologies and sectors in the EU: A foresight study, 2020.
[548] D. Paul, V. Pechancová, N. Saha, D. Pavelková, N. Saha, M. Motiei, T. Jamatia, M. Chaudhuri, A. Ivanichenko, M. Venher, L. Hrbáčková, P. Sáha, Life cycle assessment of lithium-based batteries: Review of sustainability dimensions, Renewable and Sustainable Energy Reviews 206 (2024) 114860. https://doi.org/10.1016/j.rser.2024.114860.
[549] Global battery supply chain: Hidden regional trends | McKinsey. https://www.mckinsey.com/features/mckinsey-center-for-future-mobility/our-insights/the-hidden-trends-in-battery-supply-and-demand-a-regional-analysis (accessed September 5, 2025).
[550] Critical Raw Materials Act - European Commission. https://single-market-economy.ec.europa.eu/sectors/raw-materials/areas-specific-interest/critical-raw-materials/critical-raw-materials-act_en#actions-under-the-critical-raw-materials-act (accessed September 2, 2025).
[551] J.L. Popien, J. Husmann, A. Barke, C. Thies, F. Cerdas, C. Herrmann, T.S. Spengler, Comparison of lithium-ion battery supply chains – a life cycle sustainability assessment, Procedia CIRP 116 (2023) 131–136. https://doi.org/10.1016/J.PROCIR.2023.02.023.
[552] Database - Transport - Eurostat. https://ec.europa.eu/eurostat/web/transport/database (accessed September 2, 2025).
[553] Green energy sector drove more than 90% of China's investment growth last year, analysis finds | China | The Guardian. https://www.theguardian.com/world/2026/feb/05/china-green-energy-sector-investment-growth (accessed February 5, 2026).

[554] B. Gao, S. Yang, S. Peng, Bayesian Monte Carlo-assisted life cycle assessment of lithium iron phosphate batteries production for electric vehicles under uncertainty, Green Manufacturing Open 2024 2 (2024) 18. https://doi.org/10.20517/gmo.2024.092201.
[555] Q. Dai, J.C. Kelly, L. Gaines, M. Wang, Life cycle analysis of lithium-ion batteries for automotive applications, Batteries 5 (2019). https://doi.org/10.3390/batteries5020048.
[556] I. Dobryden, C. Montanari, D. Bhattacharjya, J. Aydin, A. Ahniyaz, Bio-Based Binder Development for Lithium-Ion Batteries, Materials 16 (2023) 5553. https://doi.org/10.3390/ma16165553.
[557] M. Clemente, P. Maharjan, M. Salazar, T. Hofman, Meta-analysis of life cycle assessments for Li-ion batteries production emissions, Int. J. Life Cycle Assess. 30 (2025) 2625–2641. https://doi.org/10.1007/s11367-025-02541-9.
[558] J.F. Peters, M. Weil, Providing a common base for life cycle assessments of Li-Ion batteries, J. Clean. Prod. 171 (2018) 704–713. https://doi.org/10.1016/j.jclepro.2017.10.016.
[559] J.B. Dunn, C. James, L. Gaines, K. Gallagher, Q. Dai, J.C. Kelly, Material and Energy Flows in the Production of Cathode and Anode Materials for Lithium Ion Batteries, 2015. https://greet.anl.gov/ (accessed February 13, 2025).
[560] B. Cox, C.L. Mutel, C. Bauer, A. Mendoza Beltran, D.P. Van Vuuren, Uncertain Environmental Footprint of Current and Future Battery Electric Vehicles, Environ. Sci. Technol. 52 (2018) 4989–4995. https://doi.org/10.1021/acs.est.8b00261.
[561] A. Ciroth, S. Muller, B. Weidema, P. Lesage, Empirically based uncertainty factors for the pedigree matrix in ecoinvent, International Journal of Life Cycle Assessment 21 (2016) 1338–1348. https://doi.org/10.1007/s11367-013-0670-5.
[562] F. Degen, M. Mitterfellner, A. Kampker, Comparative life cycle assessment of lithium-ion, sodium-ion, and solid-state battery cells for electric vehicles, J. Ind. Ecol. (2024). https://doi.org/10.1111/JIEC.13594.
[563] E. Batuecas, C.S. Martínez-Cisneros, D. Serrano, A. Várez, Life cycle assessment of lab-scale solid sodium-ion batteries: A sustainable alternative to liquid lithium-ion batteries, J. Energy Storage 80 (2024) 110355. https://doi.org/10.1016/J.EST.2023.110355.
[564] M.S. Ziegler, J. Song, J.E. Trancik, Determinants of lithium-ion battery technology cost decline, Energy Environ. Sci. 14 (2021) 6074–6098. https://doi.org/10.1039/D1EE01313K.
[565] M.-T.F. Rodrigues, A.Y.R. Prado, S.E. Trask, S. Ahmed, A.N. Jansen, D.P. Abraham, Modulating electrode utilization in lithium-ion cells with silicon-bearing anodes, J. Power Sources 477 (2020) 229029. https://doi.org/10.1016/j.jpowsour.2020.229029.
[566] G. Mu, S. Agrawal, P. Sittisomwong, P. Bai, Impacts of negative to positive capacities ratios on the performance of next-generation lithium-ion batteries, Electrochim. Acta 406 (2022) 139878. https://doi.org/10.1016/j.electacta.2022.139878.
[567] C. Xu, B. Steubing, M. Hu, C. Harpprecht, M. van der Meide, A. Tukker, Future greenhouse gas emissions of automotive lithium-ion battery cell production, Resour. Conserv. Recycl. 187 (2022). https://doi.org/10.1016/j.resconrec.2022.106606.
[568] R. Zhang, Y. Wu, G. Ge, J. Liu, J. Wang, S. Wang, Z. He, Electrolyte additives in Li-ion batteries: from mechanisms to application, Sustain. Energy Fuels 10 (2026) 150–190. https://doi.org/10.1039/D5SE01310K.
[569] S. Wickerts, R. Arvidsson, A. Nordelöf, M. Svanström, P. Johansson, Prospective Life Cycle Assessment of Lithium-Sulfur Batteries for Stationary Energy Storage, ACS Sustain. Chem. Eng. 11 (2023) 9553–9563. https://doi.org/10.1021/acssuschemeng.3c00141.
[570] C. Harpprecht, B. Miranda Xicotencatl, S. van Nielen, M. van der Meide, C. Li, Z. Li, A. Tukker, B. Steubing, Future environmental impacts of metals: A systematic review of

impact trends, modelling approaches, and challenges, Resour. Conserv. Recycl. 205 (2024) 107572. https://doi.org/10.1016/j.resconrec.2024.107572.
[571] G. Omar Barrionuevo, J. Andrade-Garz, L. Llatance-Guevara, F. E. Alarc, Life Cycle Assessment of Tensile Specimens of Stainless Steel Obtained by Additive Manufacturing versus Conventional Manufacturing, Advanced Materials & Sustainable Manufacturing 2 (2025) 10004–10004. https://doi.org/10.70322/amsm.2025.10004.
[572] M. Clemente, P. Maharjan, M. Salazar, T. Hofman, Meta-analysis of life cycle assessments for Li-ion batteries production emissions, Int. J. Life Cycle Assess. 30 (2025) 2625–2641. https://doi.org/10.1007/s11367-025-02541-9.
[573] M. Zhang, C. Cheng, Y. Zhao, B. Wang, Life Cycle Assessment for Industrial Gas Production in China, (2024). https://doi.org/10.21203/rs.3.rs-4335748/v1.
[574] T.F. Burton, J.L. Gómez Urbano, Y. Zhu, A. Balducci, O. Fontaine, The urgent electrolyte sustainability challenges for electric vehicle batteries, Nat. Commun. 16 (2025) 5957. https://doi.org/10.1038/s41467-025-60711-7.
[575] X. Li, Y. Zhang, Y. Liao, G. Yu, Environmental impact assessment of battery boxes based on lightweight material substitution, Sci. Rep. 14 (2024) 2594. https://doi.org/10.1038/s41598-024-53238-2.
[576] European Battery Regulation. https://environment.ec.europa.eu/topics/waste-and-recycling/batteries_en (accessed July 8, 2026).

Appendix A – List of Abbreviation

3 ITT – 3 Interval Thixotropic Test
AC – Areal Capacity
ADP – Abiotic Depletion Potential
ALG – Sodium Alginate
AM – Active Material
AoP – Areas of Protection
AW – Average Weight
AWARE – Available Water Remaining
CA – Conductive Additive
CC – Current Collector
CC-CV - Constant Current – Constant Voltage
CCS – Constant Current Step
CE – Coulombic Efficiency
CEI – Cathode Electrolyte Interphase
CFB – Carbon Footprint of Batteries
CGN – Carrageenan
CHT – Human toxicity: carcinogenic
CMC – Carboxy Methyl Cellulose
CPG – Cone-Plate Geometry
CRM – Critical Raw Material
CT – Computed Tomograpy
CTUh – Comparative Toxic Unit for Human
CTUe – Comparative Toxic Unit for Ecosystem
CV – Cyclic Voltammetry
CVS – Constant Voltage Step
DALY – Disability-Adjusted Life Years
DEC – Diethylene Carbonate
DLIP – Direct Laser Interference Patterning
DMC – Dimethyl Carbonate
DT – Dry Thickness
EC – Ethylene Carbonate
EDS – Energy Dispersive Spectrometer
EDX – Energy Dispersive X-ray Analysis
EHT – Electron High Tension
EIS – Electrochemical Impedance Spectroscopy
EMC – Ethyl Methyl Carbonate
EOFP – Photochemical Oxidant Formation Potential: Ecosystems
EoL – End of Life
EPD – Environmental Product Declaration
EPLCA – European Platform on Life Cycle Assessment
EV – Electric Vehicle
FE – Ecotoxicity Freshwater
FEC – Fluoroethylene Carbonate
FEP – Freshwater Eutrophication Potential
FESEM – Field Emission Scanning Electron Microscopy
FET – Eutrophication: freshwater
FETP – Freshwater Ecotoxicity Potential
FFP – Fossil Fuel Potential
FRS – Energy resources: non-renewable, fossil
FU – Functional Unit
G-A – Graphite Anodes
GHG – Greenhouse gases

GIC – Graphite Intercalation Compound
GLO – Global
GPE – Gel Polymer Electrolyte
GW – Climate Change
GWP – Global Warming Potential
HH – Human Health
HOFP – Photochemical Oxidant Formation Potential: Humans
HTPc – Human Toxicity Potential: carcinogenic
HTPnc – Human Toxicity Potential: non-carcinogenic
ICE – Initial Coulombic Efficiency
ICL – Irreversible Capacity Loss
iFFT – Inverse Fast Fourier Transform
IL – Ionic Liquid
IPCC – Intergovernmental Panel on Climate Change
IR – Ionizing radiation
IRP – Ionising Radiation Potential
JRC – Joint Research Centre
LCA – Life Cycle Assessment
LCC – Life Cycle Costing
LCI – Life Cycle Inventory
LCO – Lithium Cobalt Oxide
LCSA - Life Cycle Sustainability Assessment
LCT – Life Cycle Thinking
LE – Liquid Electrolyte
LFP – Lithium Iron Phosphate
LIB – Lithium Ion Battery
LiPAA – Lithiated Polyacrylic Acid
$LiPF_6$ – Lithium Hexafluorophosphate
LIPSS – Laser-Induced Periodic Surface Structures
LMB – Lithium Metal Battery
LNMO – Lithium Nickel Manganese Oxide
LOP – Agricultural Land Occupation
LU – Land Use
LVR – Linear Viscoelasticity Region
MCS – Monte Carlo Simulation
ME – Ecotoxicity Marine
MEP – Marine Eutrophication Potential
MET – Eutrophication: marine
METP – Marine Ecotoxicity Potential
MJ – Mega Joule
ML – Mass Loading
MRU – Material resources: metals/minerals
MW – Molecular Weight
NCHT – Human toxicity: non-carcinogenic
NE – Natural Environment
NMC – Lithium Nickel Manganese Cobalt Oxide
NMP – N-Methyl Pyrrolidone
NOx – Nitrogen Oxides
NR – Natural Resources
OCV – Open-Circuit Voltage
ODP – Ozone Depletion Potential
PAA – Polyacrylic Acid
PC – Propylene Carbonate
PCR – Product Category Rules
PE – Polyethylene
PEC – Pectin
PEF – Product Environmental Footprint
P-LCA – Prospective Life Cycle Assessment

PM – Particulate Matter
PMF – Particulate Matter Formation
PMFP – Particulate Matter Formation Potential
POFHH – Photochemical oxidant formation: human health
POFTE – Photochemical oxidant formation: terrestrial ecosystems
PP – Polypropylene
PPG – Plate-Plate Geometry
PVDF – Polyvinylidene Fluoride
R2R – Roll-to-Roll
RER – Europe
RoW – Rest of the World
RPM – Rotation per minute
RT – Room Temperature
SBR – Styrene Butadiene Rubber
SC – Silicon Composite
SC-A – Silicon Composite Anodes
SD – Silicon Dominant
SD-A - Silicon Dominant Anodes
SEI – Solid Electrolyte Interphase
SEM – Scanning Electron Microscopy
SF – Solid Fraction
sLCA – Social Life Cycle Assessment
SoC – State of Charge
SOD – Stratospheric Ozone Depletion
SoH – State of Health
SOP – Surplus Ore Potential
SPE – Solid Polymer Electrolyte
TA – Terrestrial Acidification
TAP – Terrestrial Acidification Potential
TE – Ecotoxicity terrestrial
TEP – Terrestrial Eutrophication Potential
TET – Terrestrial Eutrophication
TETP – Terrestrial Ecotoxicity Potential
TG – Tragacanth Gum
TRACI – Tool for Reduction and Assessment of Chemicals and Other Environmental Impacts
VC – Vinyl Carbonate
Vkm – Vehicle kilometer
VOC – Volatile Organic Compounds
WC – Water Use
WCP – Water Consumption Potential
WD – Working Distance
XRD – X-Ray Diffraction

Appendix B – List of Publications

"*Nanosecond pulsed laser texturing of Li-ion battery electrode current collectors: process optimisation and electrochemical characterisation of cathode half-cells"*
E. Ravesio, A.H.A. Lutey, D. Versaci, L.Romoli, S. Bodoardo
Sustainable Materials and Technologies (**2023**), 38, e00751
(https://doi.org/10.1016/j.susmat.2023.e00751)

"*Ultrashort pulsed laser texturing of current collector for Si/C Li-ion anodes: Characterization of electrochemical performance and evolution of interface morphology*"
E. Ravesio, G. Montinaro, G. Mincuzzi, M. Negozio, D. Versaci, V. Gartiser, A.H.A. Lutey, F. Bella, S. Bodoardo
Journal of Energy Storage (**2025**), 109, 115226
(https://doi.org/10.1016/j.est.2024.115226)

"Characterization of adhesion in lithium-ion battery electrodes with laser-textured current collectors"
A.H.A. Lutey, M. Negozio, E. Ravesio, D. Versaci
Journal of Manufacturing Science and Engineering (**2025**), 147 (7), 071006
(https://doi.org/10.1115/1.4068239)

"High throughput femtosecond laser processing for new generation battery"
G. Mincuzzi, Q. Mocaer, V. Rouffiange, P. Tallone, E. Ravesio, V. Gartiser, M. Negozio, A.H.A. Lutey
Proceedings Volume 13351, Laser-based Micro and Nanoprocessing XIX (**2025**)
(https://doi.org/10.1117/12.3041941)

"Life Cycle Assessment of Graphite, Silicon Composite, and Silicon-Dominant Anodes for Lithium-Ion Batteries: Environmental Impacts, Uncertainties, and Supply Chain Considerations"
E. Ravesio, V. Sumini, L. Genovese, D. Versaci, S. Bodoardo
Advanced Sustainable Systems (**2026**), 10:e01576
(https://doi.org/10.1002/adsu.202501576)

"Optimization of binary binder blends for aqueous-based slurries of SiOx/C for next-generation lithium-ion batteries"

L. Tamboia, G. Montinaro, E. Ravesio, J. Amici, C. Francia, S. Bodoardo, F. Bella, D. Versaci
Journal of Cleaner Production (**2026**), 148153
(https://doi.org/10.1016/j.jclepro.2026.148153)

Appendix C – List of Oral/Poster Publications

Poster: "*The GigaGreen Project. Towards the sustainable giga-factory: developing green cell manufacturing processes*"
E. Ravesio, G. Montinaro, D. Versaci, F. Bella, S. Bodoardo
Battery 2030+ Annual Conference; 9-10 May 2023; Uppsala (Sweden)

Oral Presentation: "*Towards scale-up in sustainable electrode production with a small pilot line*"
E. Ravesio, V. Sumini, G. Montinaro, D. Versaci, F. Bella, S. Bodoardo
Giornate dell'Elettrochimica Italiana (GEI) 2023; 17-21 September 2023; Cefalù (Italy)

Oral Presentation: "*Towards scale-up in sustainable electrode production with a small pilot line*"
E. Ravesio, V. Sumini, G. Montinaro, D. Versaci, F. Bella, S. Bodoardo
24th International Conference "New Cryogenic and Isotope Technologies for Energy and Environment"; 18-20 October 2023; Govora Bay (Romania)

Oral Presentation: "*Towards scale-up in sustainable electrode production with a small pilot line*"
E. Ravesio, V. Sumini, G. Montinaro, D. Versaci, F. Bella, S. Bodoardo
Merck Young Chemists' Symposium (MYCS) 2023; 13-15 November 2023, Rimini (Italy)

Poster: "*Towards scaling up in the production of Silicon-rich anodes with water-based binders*"
E. Ravesio, V. Sumini, G. Montinaro, D. Versaci, S. Bodoardo
37th Topical Meeting of the International Society of Electrochemistry; 9-12 June 2024; Stresa (Italy)

Oral Presentation: "*Silicon-dominant anodes: how the TRL level can influence the production process*"
E. Ravesio, V. Sumini, G. Montinaro, D. Versaci, F. Bella, S. Bodoardo
The 2024 Fall Meeting of the European Materials Research Society (E-MRS); 16-20 September 2024; Warsaw (Poland)

Oral Presentation: "*Evaluating the impact of natural polysaccharides on the production process of silicon-dominant anodes*"

E. Ravesio, V. Sumini, L. Genovese, L. Otaegui, D. Giraldo, D. Versaci, S. Bodoardo
Giornate dell'Elettrochimica Italiana (GEI) 2025; 15-19 September 2025; San Benedetto del Tronto (Italy)